UNIVERSITY OF SOUTHAMPTON

FACULTY OF NATURAL AND ENVIRONMENTAL SCIENCES

Chemistry

Volume 1 of 1

Novel Multi-Component Systems of Propyphenazone and Lonidamine: Characterisation, Physicochemical Properties and Quantum Crystallography Studies

by

Lucy Kristina Mapp

Thesis for the degree of Doctor of Philosophy

September 2017

UNIVERSITY OF SOUTHAMPTON

ABSTRACT

FACULTY OF NATURAL AND ENVIRONMENTAL SCIENCES

Chemistry

Thesis for the degree of Doctor of Philosophy

NOVEL MULTI-COMPONENT SYSTEMS OF PROPYPHENAZONE AND LONIDAMINE: CHARACTERISATION, PHYSICOCHEMICAL PROPERTIES AND QUANTUM CRYSTALLOGRAPHY STUDIES

Lucy Kristina Mapp

This thesis reports novel multi-component systems of two APIs, PROPY and LON. Design and prediction strategies, tailored for each API, have been used to select appropriate co-former molecules used for subsequent screening and synthesis. Comprehensive characterisation of the products was followed by single crystal X-ray diffraction structural analysis and physicochemical property measurements. These include thermal properties, stability, dissolution and solubility which were characterised by DSC, TGA, PXRD and HPLC.

A subset of PROPY systems were selected to probe the nature of the API···co-former interactions. The experimental electron density distribution, based on very high resolution single crystal diffraction, was modelled and a topological analysis undertaken using Bader's Atoms in Molecules (AIM) approach. Atomic charges, intermolecular interactions and their energies have been subsequently derived and compared between systems. Complementary theoretical calculations using the PIXEL and Crystal Explorer interaction energy approaches were undertaken and used to investigate the intermolecular interactions beyond atom···atom contacts. These permitted the decomposition of the intermolecular interactions into their constituent energy components for a comprehensive analysis. This novel approach provided new insight into the driving forces behind the formation of the solid state. Furthermore, this quantum crystallography approach enabled an analysis of the effect of the co-former on structure and the range of influencing factors that determine the physicochemical properties of these multi-component systems.

Table of Contents

Table of Contents ..... **i**

List of Figures ..... **xii**

List of Accompanying Materials ..... **xix**

DECLARATION OF AUTHORSHIP ..... **xxi**

Acknowledgements ..... **xxiii**

Definitions and Abbreviations ..... **xxv**

Chapter 1: Crystal Engineering, Co-Crystals and Multi-component Systems **1**

1.1 Engineering the Solid State 1

1.1.1 Non-Covalent Interactions 2

1.2 Hydrogen Bonding 3

1.2.1 The Importance of Hydrogen Bonding 4

1.2.2 Hydrogen Bonding Interaction Preferences 4

1.2.3 Proton Transfer in Hydrogen Bonds 5

1.3 Multi-Component Materials: Co-Crystals and Salts 5

1.3.1 Salt or Co-Crystal? 6

1.3.2 Advantages of Co-Crystals and Salts 7

1.3.3 Pharmaceutical Applications of Co-Crystals and Salts 8

1.3.4 Design and Prediction Approaches for Co-Crystals and Salts 9

1.3.5 Synthetic Approaches for Co-Crystals and Salts 12

1.4 Conclusions 13

Chapter 2: Analytical Methods **15**

2.1 Crystallography 15

2.1.1 Background Theory 16

2.1.2 Solving the X-ray Crystal Structure 17

2.1.3 Standard Resolution Structure Analysis 18

2.1.4 Beyond Standard Resolution 18

2.2 Theoretical Approaches to Structural Analysis 22

2.2.1 PIXEL 23
2.2.2 Crystal Explorer 25
2.2.3 Hirshfeld Surface Analysis 26
2.3 Analysis of Intermolecular Interactions in Crystal Structures 26
2.3.1 Interaction Information Obtained from Experimental Studies 26
2.3.2 Theoretical Approaches to Interaction Analysis 27
2.4 Physicochemical Properties 28
2.4.1 Thermal Properties Characterisation 28
2.4.2 Solution Properties 30
2.4.3 Stability 33
2.4.4 pK_a 34
2.5 Conclusions 34
Chapter 3: Aims 37
Chapter 4: Novel Co-Crystals of Propyphenazone 41
4.1 Propyphenazone 41
4.1.1 Polymorphs of PROPY 41
4.1.2 PROPY Co-Crystal and Studies on Structurally Similar APIs 42
4.2 Design of Co-Crystals 43
4.2.1 Interaction Searching for Preferences of the Carbonyl Group 43
4.2.2 Analysis of Structurally Related Molecules and Their Co-Crystals 49
4.2.3 Co-Former Selection and Screening Approach 51
4.2.4 Application of the Molecular Complementarity (QSAR) Prediction Method 53
4.3 Structural Analysis of the Novel Co-crystals 54
4.3.1 Analysis of Co-Crystals Containing a Hydroxyl Functional Group 55
4.3.2 Analysis of Co-Crystals Containing a Carboxylic Acid Functional Group 57
4.3.3 Analysis of Co-Crystals Containing both Carboxylic Acid and Hydroxyl Functional Groups 59
4.3.4 Hirshfeld Surface Analysis 63
4.3.5 Structural Similarities and Trends in Interactions 67

4.4 Thermal Analysis 68
4.5 Stability of Co-Crystals 70
4.5.1 Slurry Tests 70
4.5.2 Accelerated Storage 71
4.5.3 Dynamic Vapour Sorption 71
4.6 Analysis of the Solution Properties 72
4.6.1 Dissolution Rate 72
4.6.2 Solubility 73
4.7 Conclusions 75
Chapter 5: Quantum Crystallography Studies of PROPY Co-Crystals 79
5.1 Reasoning Behind Quantum Crystallography and Charge Density Studies 79
5.2 Selection of Co-Crystal Family 80
5.3 Methodology 82
5.3.1 Molecular Pair Interaction Energies 82
5.3.2 Detailed Molecular Pair Interaction Energies 83
5.3.3 Experimental Charge Density 84
5.3.4 Summary 85
5.4 Overview of Co-Crystal Interactions 85
5.4.1 PROPY-MPAR 85
5.4.2 PROPY-4HBA 90
5.4.3 PROPY-HQ 94
5.4.4 PROPY-FA 98
5.5 Deconvolution of Interaction Energies 103
5.5.1 Interaction Strengths 103
5.5.2 Contributions of the Coulombic and Dispersion Energy Components 106
5.5.3 Types and Contributions of the Molecular Pairs 108
5.6 Experimental Charge Analysis 110
5.6.1 Analysis of the Ring Critical Points 111
5.6.2 PROPY···Co-Former Interactions and Assemblies 112
5.6.3 Experimental Hydrogen Bond Energies 114

5.7 Evaluation and Rationale of Physicochemical Properties 114
5.7.1 Melting Point 115
5.7.2 Stability 117
5.7.3 Dissolution 117
5.7.4 Solubility 119
5.8 Evaluation of Additional Co-Crystal Systems 120
5.8.1 PROPY-PGL·0.5ACN 121
5.8.2 PROPY-25DHBA 123
5.8.3 PROPY-45DClPA 125
5.8.4 PROPY 126
5.9 Physicochemical Properties Analysis of All Systems 128
5.9.1 Melting Point 128
5.9.2 Stability 130
5.10 Conclusions 131
5.10.1 Aim 1: Structural Similarities 131
5.10.2 Aim 2: Stoichiometry 132
5.10.3 Aim 3: The Primary Hydrogen Bond 133
5.10.4 Aim 4: Structural Diversity 134
5.10.5 Physicochemical Properties 134
5.10.6 Additional Findings 135
Chapter 6: Novel Salts and Co-Crystals of Lonidamine 137
6.1 Lonidamine 137
6.1.1 Polymorphs of LON 137
6.2 Design of Co-Crystals 139
6.2.1 Interaction Analysis to Identify the Preferred Co-Former Functional Groups 139
6.2.2 Possible Synthons and Interactions of LON Multi-component Systems 140
6.2.3 Co-Former Selection 140
6.2.4 Implementation and Analysis of Screening by Grinding 140
6.3 Structural Analysis of the Novel Co-Crystal and Salt Structures of LON 142

6.3.1 Structures Containing Pyridine-Related Co-Formers 142
6.3.2 Structures Containing Pyridine-Based Co-Formers 143
6.3.3 Structures Containing Pyrimidine-Based Co-Formers 150
6.3.4 Structures Containing Co-Formers with 5- and 6- Membered Rings 154
6.3.5 Structures Containing Other Co-Formers 158
6.4 Analysis of Structural Similarities in the Novel Materials 159
6.4.1 Comparisons Between ISO, NICO and BENZ 160
6.4.2 Interaction Analysis of Structures Containing NICO 161
6.4.3 Interaction Analysis of LON-2APYM and Other 2APYM-Containing Structures 162
6.4.4 Comparisons of LON-2APYD and LON-2APYM and their Interactions 164
6.4.5 Interaction Analysis of Structures Containing PIPE 164
6.4.6 Comparisons of LON Structures Displaying Carboxylic Acid···Pyridine Motifs 165
6.4.7 Analysis of Structures Displaying Tetrameric Motifs 167
6.4.8 Analysis of Structures Displaying Ladder Motifs 167
6.5 Hydrogen bonding 168
6.5.1 Hydrogen Bonds to Aromatic Nitrogen Atoms 168
6.5.2 Analysis of the Salts and Short Hydrogen Bonds 170
6.5.3 Overall Analysis of the Interactions of LON 171
6.6 Variations in the Conformation of LON 172
6.7 pK_a and Proton Transfer: Salt and Co-Crystal Formation 174
6.8 Thermal Analysis 174
6.8.1 Behaviour of the LON Solvate Structures 176
6.8.2 Behaviour of the LON Hydrate Structures 177
6.8.3 Behaviour of LON-4,4BIPY 177
6.9 Stability 177
6.9.1 Dynamic Vapour Sorption 177
6.9.2 Slurry 178
6.9.3 Accelerated Storage 179
6.10 Analysis of the Solution Properties 179

6.10.1 Solubility 179
6.10.2 Dissolution Rate 180
6.11 Conclusions 182
Chapter 7: Conclusions and Further Work 185
7.1 Conclusions 185
7.1.1 The Novel Co-Crystals of PROPY 185
7.1.2 The Novel Multi-component Systems of LON 187
7.1.3 Addressing the Research Aims 188
7.2 Further Work 193
7.2.1 PROPY Co-Former Functional Groups 193
7.2.2 Extending the Quantum Crystallography Studies 194
7.2.3 Methodology 196
7.2.4 Interesting Observations of PROPY-PGL·0.5ACN 197
Chapter 8: PROPY Experimental 199
8.1 CSD Interaction Analysis 199
8.1.1 Isostar 199
8.1.2 Contact Searching 199
8.1.3 Full Interaction Mapping 199
8.1.4 QSAR Molecular Complementarity Predictions 200
8.2 Screening by Grinding 200
8.3 Single Crystal Preparation 200
8.3.1 PROPY-25DHBA 2:1 Co-Crystal Solvate 200
8.3.2 PROPY-35DHBA 1:1 Co-Crystal 200
8.3.3 PROPY-4HBA 1:1 Co-Crystal 201
8.3.4 PROPY-45DClPA 1:1 Co-Crystal 201
8.3.5 PROPY-FA 2:1 Co-Crystal 201
8.3.6 PROPY-HQ 1:2 Co-Crystal 201
8.3.7 PROPY-MPAR 1:1 Co-Crystal 201
8.3.8 PROPY-PGL 1:1 Co-Crystal Solvate 201
8.4 Powder X-ray Diffraction Studies 202

8.5 Standard Resolution Single Crystal X-ray Diffraction Studies 202
8.5.1 Data Collection and Reduction 202
8.5.2 Structure Solution and Refinement 202
8.6 Property Measurements 203
8.6.1 Differential Scanning Calorimetry 203
8.6.2 Stability Studies 203
8.6.3 Dynamic Vapour Sorption 204
8.6.4 Solubility and Dissolution Rate 204
8.6.5 High Performance Liquid Chromatography 204
8.7 High Resolution Single Crystal X-ray Diffraction Studies 205
8.7.1 Data Collection and Reduction 205
8.7.2 Aspherical Atom Model Refinement Strategy 206
8.8 Theoretical Studies 209
8.8.1 Crystal Explorer Interaction Energies 209
8.8.2 PIXEL 209
Chapter 9: LON Experimental 211
9.1 Screening by Grinding 211
9.2 Single Crystal Preparation 211
9.2.1 α-LON 211
9.2.2 LON-246TAPYM 1:1 Salt 211
9.2.3 LON-2APYD 1:1 Salt Solvates 212
9.2.4 LON-2APYM 1:2 Co-Crystal 212
9.2.5 LON-4,4BIPY 2:1 Co-Crystal 212
9.2.6 LON-4DMAP Salts 212
9.2.7 LON-BENZ 1:1 Co-Crystal 212
9.2.8 LON-HALO 1:1 Salt Trihydrate 213
9.2.9 LON-IMID Salts / Co-Crystal Salt Hybrid Material 213
9.2.10 LON-ISO 1:1 Co-Crystal 213
9.2.11 LON-MEL 1:1 Salt 213
9.2.12 LON-NICO 1:1 Co-Crystal 213

9.2.13 LON-PIPE 2:1 Salt 213
9.3 Powder X-ray Diffraction Studies 214
9.4 Standard Resolution Single Crystal X-ray Diffraction Studies 214
9.4.1 Data Collection and Reduction 214
9.4.2 Structure Solution and Refinement 214
9.5 Physicochemical Property Measurements 215
9.5.1 Differential Scanning Calorimetry 215
9.5.2 Hot Stage Microscopy 216
9.5.3 Thermogravimetric Analysis 216
9.5.4 Stability Studies 216
9.5.5 Dynamic Vapour Sorption 216
9.5.6 Dissolution Rate 217
9.5.7 Solubility 217
9.5.8 High Performance Liquid Chromatography 217
9.5.9 Mass Spectrometry 218
9.6 CSD Searches 218
9.6.1 2APYM and Carboxylic Acid Structures 218
9.6.2 Structures with 4DMAP / 2APYD and a Carboxylic Acid 219
9.6.3 Interactions of NICO 220
9.6.4 PIPE 220
Appendices 222
Appendix A PROPY 225
A.1 CSD Knowledge Based Searching 226
A.1.1 Full Interaction Mapping[250] 226
A.1.2 Specific Contact Searching 227
A.2 Co-Former Selection 228
A.3 PXRD Patterns for Screening by Grinding 230
A.3.1 Successful Combinations of PROPY and Co-Former 230
A.3.2 Promising Combinations of PROPY and Co-Former 234
A.4 QSAR Molecular Complementarity Predictions-PROPY 238

A.5 Crystal Structure Tables 243
A.6 Hydrogen Bonding Interactions 247
A.7 Hirshfeld Surface Analysis 251
A.7.1 Hirshfeld Surfaces 251
A.7.2 Fingerprint Plots 251
A.7.3 Interaction Analysis 257
A.8 Packing Coefficients 259
A.9 Thermal Analysis 260
A.9.1 PROPY-PGL·0.5ACN 260
A.9.2 PROPY-25DHBA (1,4-dioxane solvate) 262
A.10 Stability 264
A.10.1 Slurry 264
A.10.2 Accelerated Stability 265
Appendix B PROPY Charge Density Studies 267
B.1 Choice of Experimental Multipole Models 268
B.1.1 Analysis of Models 268
B.1.2 Absorption Corretions 271
B.1.3 Refinement of κ and κ' 280
B.1.4 Multipole Population Level 283
B.1.5 Charge Comparisons 286
B.1.6 Strategy for Multipole Refinement 287
B.2 Final Experimental Multipole Models 288
B.3 Topological Analysis 291
B.3.1 Labelling of PROPY Molecule 291
B.3.2 Analysis of Models 291
B.3.3 Atomic Charges 293
B.3.4 BCP Searches 300
B.3.5 RCPs and Analysis 308
B.4 Interaction Energy Analysis 313
B.4.1 Crystal Explorer Energy Analysis 313

B.4.2 Molecule and System Energies 316
B.4.3 API and Co-Former Interactions 318
B.4.4 Strong, Moderate and Weak Energies 320
B.5 Analysis of Interactions to Water 328

Appendix C LON 331

C.1 LON Polymorph Analysis 332
C.1.1 α-LON/Form I 332
C.1.2 β-LON/Form II 333
C.1.3 Form III 335
C.1.4 Reported PXRD Data 336
C.1.5 DSC data 336
C.2 LON Material 338
C.2.1 Bulk Powder Characterisation 338
C.2.2 Control of Polymorphs 338
C.3 CSD Analysis 340
C.3.1 Carboxylic Acid Interaction Preferences 340
C.3.2 Indazole Interaction Preferences 342
C.3.3 Models used for Specific Contact Searching 346
C.4 Co-Former Selection 347
C.5 PXRD Patterns for Screening by Grinding 349
C.5.1 Successful Combinations of LON and Co-Former 349
C.5.2 Promising Combinations of LON and Co-Former 357
C.6 Crystal Structure Tables 363
C.6.1 Pharmaceutically Acceptable Co-Formers 363
C.6.2 Non-Pharmaceutically Acceptable Co-Formers 369
C.7 Hydrogen Bonding Interactions 373
C.7.1 Pharmaceutically Acceptable Co-Formers 373
C.7.1 Non-Pharmaceutically Acceptable Co-Formers 379
C.8 CSD and Structural Analysis 382

C.8.1 NICO Interactions....382
C.8.2 2APYM Co-Crystals....384
C.8.3 PIPE Interactions....387
C.8.4 Carboxylate···Pyridine Interactions....388
C.9 Novel LON Structure and Interactions....389
C.9.1 Interactions of the Indazole....389
C.9.2 Interactions of the Carboxylic Acid....390
C.9.3 Torsion Angle Analysis....392
C.10 pK_a....397
C.11 Thermal Analysis....398
C.11.1 Differential Scanning Calorimetry (DSC)....398
C.11.2 Hot Stage Microscopy (HSM)....399
C.11.3 Thermogravimetric Analysis (TGA)....402
C.12 HSM Recrystallisation Material....408
C.12.1 Mass Spectrometry....408
C.12.2 SCXRD....411
C.12.3 Other Occurrences....411
C.13 Stability....414
C.13.1 Slurry....414
C.13.2 Accelerated Stability....415
C.14 Solubility....416
List of References....433

List of Figures

Figure 1.1. Common hydrogen bonded synthons frequently implemented in synthon-based co-crystal design. 10

Figure 2.1. Example DSC thermogram showing phase transition (T_{onset} ~170 °C) followed by melting of the new phase (T_{onset} ~230 °C). 29

Figure 2.2. Example TGA curve showing three regions of mass loss with minimal regions of plateau indicating poor thermal stability between these mass-loss events. 30

Figure 4.1. Schematic showing the differing donor functional groups implemented in the Isostar search. The number of structures which contain an interaction to a carbonyl is indicated below each..... 44

Figure 4.2. Fragments used for interaction searching in Mercury with decreasing environmental and chemical constraints for the carbonyl group traversing from a) to e). 45

Figure 4.3. Map showing areas of potential interactions (left) and hotspots (right) for PROPY with a selection of different probes: N–H (uncharged) blue, O–H (alcohol) magenta, water green, aromatic C–H red, methyl carbon yellow and C=O grey. Opacity indicates the propensity of interactions; the highest opacity indicates the highest density and hence frequency of interactions..... 49

Figure 4.4. Molecular structures of propyphenazone, antipyrine, edaravone and itraconazole.50

Figure 4.5. Co-former structures that indicated promise when combined with PROPY in grinding experiments. 51

Figure 4.6. Structure of co-formers which produced a liquid, paste or gel in grinding experiments for which PXRD analysis was not viable. 52

Figure 4.7. Molecular structures of co-formers which produced co-crystals with PROPY. 54

Figure 4.8. Crystal structure of PROPY-MPAR 1:1 co-crystal displaying the main hydrogen bonding chain. 55

Figure 4.9. PROPY-PGL·0.5ACN co-crystal chains forming sheets (coloured, left) which stack into layers (right) where a single coloured layer (blue / purple) represents the red-blue-green sheet on the left. 56

F**igure 4.10**. Double chain structure viewed down the chain (left) and side-on, coloured by 2:1 units (right) in the crystal structure of PROPY-HQ 1:2 co-crystal. 57

Figure 4.11. Stepped arrangement of 2:1 PROPY-FA co-crystal containing molecules related by inversion.....58

Figure 4.12. A hydrogen bonded chain in the 1:1 PROPY-45DClPA co-crystal. 58

Figure 4.13. Main interactions in the 1:1 PROPY-4HBA co-crystal showing ladder formation (top) and packing viewed down *a*-axis (below). 60

Figure 4.14. Interactions in the PROPY-35DHBA co-crystal displaying chains of 6-component motif layers (top) and interlocking of chains *via* a second hydrogen bonded dimer in stepped packing arrangement (below), showing the protons of one disorder component only. 61

Figure 4.15. Interactions in the crystal structure of PROPY-25DHBA 2:1 1,4-dioxane solvate (above) and chains of staggered 2:1 units (below). Only the major component of the disordered co-former molecule is shown for clarity and no solvent displayed. 63

Figure 4.16. Fingerprint plots of for PROPY molecule in a) parent PROPY and the eight co-crystal crystal structures b) PROPY-25DHBA (2 independent PROPY molecules; i-ii), c) PROPY-35DHBA (4 independent PROPY molecules; i-iv), d) PROPY-45DClPA, e) PROPY-4HBA, f) PROPY-FA, g) PROPY-HQ, h) PROPY-MPAR, i) PROPY-PGL·0.5ACN (2 independent PROPY molecules; i-ii). 65

Figure 4.17. DSC plots for all co-crystals and parent material measured from 25 °C to 150 °C at heating rate 10°C min^{-1}. 69

Figure 4.18. DVS plot of sorption (solid coloured markers) and desorption (hollow markers) of PROPY and co-crystal materials. 72

Figure 4.19. Dissolution profile for PROPY and co-crystals with pharmaceutically acceptable co-formers carried out over 240 min experiment time at 37 °C in pH 7.5 phosphate buffer. 73

Figure 5.1. Molecular structures of PROPY, and co-formers 4HBA, MPAR, HQ and FA. 81

Figure 5.2. Main graphical display of Crystal Explorer v17.5 with interaction energy information showing the colours associated with each interaction energy for identification of the related molecular pair. 83

Figure 5.3. Intermolecular interaction energies for PROPY-MPAR 1:1 co-crystal determined from Crystal Explorer calculations, plotted against molecule···molecule centroid distances (R). 86

Figure 5.4. Interaction energies determined from PIXEL calculations plotted against molecule···molecule centroid distances (R) for PROPY-MPAR 1:1 co-crystal. 87

Figure 5.5. Total E_{HB} for molecule-molecule interactions (comprised of individual hydrogen bond between atoms) obtained from topological analysis of the experimental multipole model for PROPY-MPAR plotted against average R_{ij} of all interactions. 89

Figure 5.6. Intermolecular interaction energies for PROPY-4HBA 1:1 co-crystal determined from Crystal Explorer calculations, plotted against molecule···molecule centroid distances (R). 91

Figure 5.7. Interaction energies determined from PIXEL calculations plotted against molecule···molecule centroid distances (R) for PROPY-4HBA 1:1 co-crystal. 92

Figure 5.8. Total E_{HB} for molecule-molecule interactions (comprised of individual hydrogen bond between atoms) obtained from topological analysis of the experimental multipole model for PROPY-4HBA plotted against average R_{ij} of all interactions. 94

Figure 5.9. Intermolecular interaction energies for PROPY-HQ 1:2 co-crystal determined from Crystal Explorer calculations, plotted against molecule···molecule centroid distances (R). 95

Figure 5.10. Interaction energies determined from PIXEL calculations plotted against molecule···molecule centroid distances (R) for PROPY-HQ 1:2 co-crystal. 96

Figure 5.11. Total E_{HB} for molecule-molecule interactions (comprised of an individual hydrogen bond between atoms) obtained from topological analysis of the experimental multipole model for PROPY-HQ plotted against average R_{ij} of all interactions. 98

Figure 5.12. Intermolecular interaction energies for PROPY-FA 1:0.5 co-crystal determined from Crystal Explorer calculations, plotted against molecule···molecule centroid distances (R). 99

Figure 5.13. Interaction energies determined from PIXEL calculations plotted against molecule···molecule centroid distances (R) for PROPY-FA 1:0.5 co-crystal. 100

Figure 5.14. Total E_{HB} for molecule-molecule interactions (comprised of individual hydrogen bond between atoms) obtained from topological analysis of the experimental multipole model for PROPY-FA plotted against average R_{ij} of all interactions. 102

Figure 5.15. Contributions of the strong, moderate and weak interactions to the Coulombic, dispersion, repulsion and total energy components of the four PROPY systems from PIXEL.....105

Figure 5.16. Contributions of the strong, moderate and weak interactions to the Coulombic, dispersion, repulsion and total energy components of the four PROPY systems from Crystal Explorer. 105

Figure 5.17. Atomic charges (blue) and $\rho(\mathbf{r})$ (red) at the RCPs for PROPY in the four systems, using Stockholder atomic partitioning for charges. 111

Figure 5.18. PROPY co-former adduct assemblies; a) PROPY-4HBA 1:1 4-component unit, b) PROPY-FA 1:0.5 3-component unit, c) PROPY-HA 1:2 hydrogen bonded network and d) PROPY-MPAR 1:1 2-component discrete unit. 113

Figure 5.19. Atomic charges (blue) and $\rho(r)$ (red) at the RCPs for the co-former molecules in the four systems, using Stockholder atomic partitioning for charges. 114

Figure 5.20. Interaction energies determined from PIXEL calculations plotted against molecule···molecule centroid distances (R) for PROPY-PGL·0.5ACN co-crystal. Note, no PGL1···PGL1 or ACN···ACN interactions occur. 122

Figure 5.21. Interaction energies determined from PIXEL calculations plotted against molecule···molecule centroid distances (R) for PROPY-25DHBA 1:2 co-crystal. ...124

Figure 5.22. Interaction energies determined from PIXEL calculations plotted against molecule···molecule centroid distances (R) for PROPY-45DClPA 1:1 co-crystal. ..126

Figure 5.23. Interaction energies determined from PIXEL calculations plotted against molecule···molecule centroid distances (R) for PROPY (Form I, *P*c). 127

Figure 5.24. Interaction energies determined from PIXEL calculations plotted against molecule···molecule centroid distances (R) for PROPY-FA 1:0.5 co-crystal PROPY (Form II, *C*c). 128

Figure 6.1. a) Structure of LON with labelling scheme employed for all structures herein, b) main interaction pattern present in α-LON and c) main interaction pattern present in β-LON. 138

Figure 6.2. Structures of co-formers which were successful in forming a new material with LON. 141

Figure 6.3. Left, primary interaction motif in 1:1 LON-BENZ co-crystal and right, zig-zag chains. 143

Figure 6.4. Tetramer arrangement of dimers in the LON-NICO 1:1 co-crystal. 144

Figure 6.5. Tetramer arrangement of LON and ISO molecules in the 1:1 co-crystal structure. 144

Figure 6.6. LON-4,4BIPY co-crystal 2:1 units arranged in a stepped, end-to-end packing configuration with offset dichloro-substituted rings. 145

Figure 6.7. Hydrogen bonding interactions in the 1:1 LON-4DMAP·$2H_2O$ salt showing chains of water running through the crystal lattice. 146

Figure 6.8. Crystal structure of 2:1 LON-4DMAP depicting (a-c) different orientations of the 4DMAP molecule, (d) the chain structure with all disordered components and orientations and (e) the molecular arrangement with a single, uniform orientation of the disordered 4DMAP molecule. A fourth arrangement of a-c is also possible with both 4DMAP molecules forming $C–H_{methyl}\cdots O_{carboxylate}$ interactions to LON. This would occur for the adjacent LON dimers in a)..... 147

Figure 6.9. Top, zig zag chain pattern (excluding solvent) present in both 1:1 LON-2APYD salt solvate structures, below left showing the ethyl acetate solvent location and below right, the voids where acetonitrile is contained..... 148

Figure 6.10. Packing of the LON-2APYD salt solvate structures with solvent molecules removed showing the space occupied by the solvent and the effect this has on the layering. Left, EtOAc solvate and right ACN solvate..... 149

Figure 6.11. 1:2 LON-2APYM co-crystal structure. Top, tetramer formation showing the co-former molecule chain and below, end-on view of the co-former chains in two orientations located in channels between the tetramers. 151

Figure 6.12. Left, ladder arrangement in 1:1 LON-246TAPYM salt and right, ladder in 1:1 LON-MEL salt. Hydrogen bonding interactions forming the ladder are shown above whilst the images below depict the packing of the ladder structure occurring in alternating

orientations in adjacent layers (LON-246TAPYM) and all co-former pairs oriented in the same direction (LON-MEL).....153

Figure 6.13. Ladder network in the crystal structure of 2:1 LON-PIPE salt with alternating orientation of central PIPE molecules giving an ABAB type packing. 'A' PIPE molecules depicted in blue, 'B' in orange. 154

Figure 6.14. Main hydrogen bonds and structural motif present in the three LON-IMID structures. Left, LON-IMID·0.5EtOAc ladders with ABAB pattern (blue 'A' and orange 'B', solvent excluded for clarity), middle, 1:1 salt with ladders of ABBA pattern (purple 'A' and yellow 'B') and right, 2:1 structure with LON dimer interactions between 2:1 units.155

Figure 6.15. Left, chains of LON-IMID occurring in the *a*-direction in LON-IMID·0.5EtOAc (solvent molecules excluded for clarity) and right, location of solvent molecules occurring in the *b*-axis.....156

Figure 6.16. Left, chain structure in the 1:1 LON-IMID salt with ABC repeating pattern and right, layering and stacking of the chains (each given a single colour) to generate the crystal lattice. 157

Figure 6.17. Chains of 2:1 units (coloured individually) in the 2:1 LON-IMID structure. IMID molecules are arranged parallel to the *c*-axis (top) and chains layer in a parallel stacking mode (bottom). 158

Figure 6.18. Main hydrogen bonding interactions present in LON-HALO·3H_2O salt forming two tetramers. One contains two LON and two water molecules, the second is a self-assembling motif of four water molecules. 159

Figure 6.19. a) Crystal structure of 2-bromobenzoic acid-2APYM 1:2 co-crystal showing the tetrameric arrangement containing a 1:1 ratio of the molecules and additional 2APYM chain. Views down (b) and along (d) the 2APYM chain in LON-2APYM and similarly for 2-bromobenzoic acid-2APYM (c and e). 163

Figure 6.20. Primary hydrogen bonding motifs in the 1:1 isonicotinamide-benzoic acid co-crystal structure.....165

Figure 6.21. Hydrogen bonding interactions in the LON-ISO co-crystal structure displaying N–H···O and C–H···O hydrogen bonds between ISO molecules giving rise to a zig-zag pattern, in addition to the expected O–$H_{carboxylic\ acid}$···$N_{pyridine}$ motif. 166

Figure 6.22. DSC curves for LON and the new co-crystals and salts (including only LON-IMID·0.5EtOAc salt solvate of the LON-IMID materials). 176

Figure 6.23. DVS sorption (filled markers) and desorption (open markers) plots for LON and new co-crystal and salt materials with pharmaceutically acceptable co-formers. 178

Figure 6.24. Dissolution rate profile for LON and the new salts and co-crystals thereof containing pharmaceutically acceptable co-formers. 240 min experiment time in 1 % Tween 80® aqueous dissolution medium. 182

Figure 9.1. Models used to search the CSD for crystal structures containing 2APYM with a carboxylic acid group (left) and general CO_2 group (right). Z indicates any atom other than hydrogen, dotted bonds represent 'any' bond type and bonds indicated by a straight line and second, parallel, dashed line are aromatic bonds. 218

Figure 9.2. Model used to search the CSD for crystal structures containing 4DMAP (top left) and 2APYD (top right) with a CO_2 group. Z indicates any atom other than hydrogen, dotted bonds represent 'any' bond type and bonds indicated by a straight line and second, parallel, dashed line are aromatic bonds. 219

Figure 9.3. Model used to search the CSD for crystal structures containing NICO. 220

Figure 9.4. Model used for PIPE representation in CSD searches. 220

List of Accompanying Materials

Electronic appendix organised by chapter includes:

- Physicochemical property raw data and analysis
- Crystallographic Information Files (.cif) for all crystal structures reported in this thesis, both the standard resolution spherical models (PROPY and LON systems) and the four multipole models of PROPY-4HBA, PROPY-FA, PROPY-HQ and PROPY-MPAR
- Search files and related documents for the CSD and similar searches undertaken
- Hirshfeld surface interaction analysis (PROPY)
- Files containing the output from the PIXEL and Crystal Explorer interaction energy data
- Experimentally determined hydrogen bond energy data
- Analysis of the PIXEL, Crystal Explorer and experimental charge density data

DECLARATION OF AUTHORSHIP

I, Lucy Kristina Mapp

declare that this thesis and the work presented in it are my own and has been generated by me as the result of my own original research.

Novel Multi-Component Systems of Propyphenazone and Lonidamine: Characterisation, Physicochemical Properties and Quantum Crystallography Studies

I confirm that:

1. This work was done wholly or mainly while in candidature for a research degree at this University;
2. Where any part of this thesis has previously been submitted for a degree or any other qualification at this University or any other institution, this has been clearly stated;
3. Where I have consulted the published work of others, this is always clearly attributed;
4. Where I have quoted from the work of others, the source is always given. With the exception of such quotations, this thesis is entirely my own work;
5. I have acknowledged all main sources of help;
6. Where the thesis is based on work done by myself jointly with others, I have made clear exactly what was done by others and what I have contributed myself;
7. Parts of this work have been published as:

    a. Design of Cocrystals for Molecules with Limited Hydrogen Bonding Functionalities: Propyphenazone as a Model System. L. K. Mapp, S. J. Coles, S. Aitipamula, *Cryst. Growth Des.*, **2017**, *17* (1), 163–174.

    b. Novel Solid Forms of Lonidamine: Crystal Structures and Physicochemical Properties. L. K. Mapp, S. J. Coles, S. Aitipamula, CrystEngComm., **2017**,***19***, 2925-2935.

Signed: .....

Date: .....

Acknowledgements

The Agency of (A*STAR) and the University of Southampton for funding this work under the ARAP scheme, allowing me to undertake this Ph.D.

A*STAR ICES (Institute of Chemical and Engineering Sciences), in particular the Crystallisation and Particle Science group, for hosting me for 13 months enabling me to complete the majority of the synthesis and physicochemical properties determination.

Bursaries and grants from Rigaku, ICDD and the CCG allowing me to attend a number of conferences and teaching schools throughout the duration of my Ph.D. These enabled me to keep up to date with current research topics, network with many academics and companies and inspire me to continue with my research.

My supervisors Prof. Simon Coles and Dr. Srinivasulu Aitipamula for enabling the collaboration and this Ph.D, and for their continued support throughout, providing guidance where needed.

Dr. Mateusz Pitak my primary mentor for charge density introducing me to the technique and helping me to understand the process and analysis.

Dr. Thomas Gelbrich for PIXEL advice and Ms. Julie Herniman for the Mass Spectrometry data.

Dr. Graham Tizzard and Dr. Peter Horton for advice on problem crystal structures as well as offering a very different perspective and outlook making me a more 'well-rounded' person.

The rest of the Coles group and NCS past and present (Lisa, Phil, Claire, Jeppe, Wim and Gopikkaa) and Sarah for the general admin, organisation and normality.

Annie Wong and Lab Officers Lim Liling and Tan Bao Ren in ICES

To my family (my sister, mum and grandparents), and friends in Southampton. Without you all, your support and individual qualities, I don't think this would have been possible.

And finally, a special mention to Andy for pretty much everything and sticking by me over the years.

Definitions and Abbreviations

25DHBA: 2,5-Dihydroxybenzoic acid

35DHBA: 3,5-Dihydroxybenzoic acid

45DClPA: 4,5-Dichlorophthalic acid

2APYD: 2-Aminopyridine

2APYM: 2-Aminopyrimidine

4HBA: 4-Hydroxybenzoic acid

4DMAP: 4-Dimethylaminopyridine

A: Acceptor

Å: Angström

ACN: Acetonitrile

AIM: Atoms in Molecules

API: Active Pharmaceutical Ingredient

BCP: Bond Critical Point

BENZ: Benzamide

BP: Bond Path

CE: Crystal Explorer

CIF: Crystallographic Information Framework

CP: Critical Point

D: Donor

DSC: Differential Scanning Calorimetry

DVS: Dynamic Vapour Sorption

e: electron

ESP: Electrostatic Potential

EtOAc: Ethyl acetate

FA: Fumaric acid

FIM: Full Interaction Mapping

GoF: Goodness of Fit

HALO: Haloperidol

HPLC: High Performance Liquid Chromatography

HQ: Hydroquinone

HSM: Hot Stage Microscopy

IAM: Independent Atom Model

IMID: Imidazole

ISO: Isonicotinamide

LON: Lonidamine

MPAR: Methylparaben

NICO: Nicotinamide

pK_a: Acid dissociation constant

PGL: Phloroglucinol

PIPE: Piperazine

PROPY: Propyphenazone

PXRD: Powder X-ray Diffraction

QSAR: Quantitative Structure Activity Relationship

RCP: Ring Critical Point

R_{ij}: Bond Path Length

SCXRD: Single Crystal X-ray Diffraction

SHADE: Simple Hydrogen Atomic Displacement Estimator

TGA: Thermogravimetric Analysis

Chapter 1: Crystal Engineering, Co-Crystals and Multi-Component Systems

This thesis focuses on co-crystals and other multi-component systems, a specific area of crystal engineering. The work encompasses the design, synthesis, characterisation and analyses of structure and intermolecular interactions of a selection of novel materials, employing a variety of techniques in the process. This chapter will firstly provide familiarisation with important crystal engineering concepts, before introducing multi-component materials. Of particular interest to this thesis are co-crystals and salt forms. The nature, design, synthesis and importance of each of these will be presented with examples from the literature highlighting some of their main benefits and applications.

1.1 Engineering the Solid State

In 1989, Desiraju defined crystal engineering as

> "The understanding of intermolecular interactions in the context of crystal packing and in the utilization of such understanding in the design of new solids with desirable physical and chemical properties."[1]

The field of crystal engineering investigates correlations between molecular structure, crystal packing and properties. In doing so it connects many, previously unrelated, areas such as synthesis, statistical analysis of structural data and *ab initio* calculations. The intention is to aid and inform future supramolecular syntheses either in predicting the outcome, or by recommending prerequisites for a specific, desired outcome. For these syntheses, unlike synthetic chemistry, there is no 'recipe book' of named reactions which will give a required outcome from a set method. To predict the product of a supramolecular synthesis it must be known how neighbouring molecules will connect and assemble; the behaviour and interactions of different functional groups or moieties must be understood and when multiple and differing options for interactions are available the preference must be known. Hence, selective, reliable and transferable non-covalent connections are required for reliable predictions.[2]

1.1.1 Non-Covalent Interactions

Non-covalent interactions aid and direct the assembly and packing of the molecules, stabilise the molecular construct, and consequently influence the material's properties. Hence, they are central to the formation of the solid state and can be exploited in the design and control of systems. Examples of these interaction types include:

1. Electrostatic interactions

Electrostatic interactions involve charge-charge interactions such as ion-ion, ion-dipole or dipole-dipole contacts. Due to the charges these tend to be the strongest of the non-covalent interactions with bond energies in the ranges 100-350 kJ mol^{-1}, 50-200 kJ mol^{-1} and 5-50 kJ mol^{-1} for each type respectively.[3]

2. Hydrogen and halogen bonds

Hydrogen bonds occur between a partially positive hydrogen atom and an electron rich species (nucleophile) such as an electronegative atom, or one with a concentration of charge. The IUPAC definition of 2011 reports hydrogen bonds as "an attractive interaction between a hydrogen atom from a molecule or a molecular fragment X–H in which X is more electronegative than H, and an atom or a group of atoms in the same or a different molecule, in which there is evidence of bond formation".[4] These are dipole-dipole attractions forming strong interactions with energies in the range 1-160 kJ mol^{-1}.[3] Similarly, halogen bonding occurs when there is "evidence of a net attractive interaction between an electrophilic region associated with a halogen atom in a molecular entity and a nucleophilic region in another, or the same, molecular entity".[5] Due to the importance of hydrogen bonding in the solid state and crystal engineering, this will be discussed in more detail in Section 1.2.

3. Van der Waals forces

Van der Waals forces are weak electrostatic attractions involving dipoles. A positive molecular dipole or atomic nucleus can attract the negatively charged electron cloud of a proximal atom causing a temporary, induced dipole. The initial dipole can be permanent, or instantaneous, occurring due to the averaged electron movement. These forces are weak, typical energies are ≤ 5 kJ mol^{-1}, and distance dependent r^{-6}. Despite individual interactions being weak, cumulatively they can become significant. These can also be termed London dispersion forces.

4. π-Interactions

π-Interactions are present in systems that contain conjugated π-systems, such as benzene rings, containing a σ-construct with partial positive charge and a partially negative π-cloud above and below the plane. Attractive interactions can occur with positive cations or partial charges (dipoles) and the electron cloud, or other π-containing systems in π-π effects through π-orbital interactions. π-π stacking of aromatic rings can occur in three main ways: offset (slipped stacked / displaced), edge-to-face, and face-to-face where exact overlap of the rings occurs. The former is the least favoured, as the overlapping clouds of π-electrons exhibit electrostatic repulsion.[6] Slipped and edge-to-face configurations allows an attractive interaction between the negative π-cloud and the positive σ-scaffold of another. These have energies in the range of 8-10 kJ mol^{-1}.

1.2 Hydrogen Bonding

Hydrogen bonds are an attractive interaction between a hydrogen bond donor (D) and a hydrogen bond acceptor (A), usually depicted as D-H···A, or X-H···Y. The acceptor must contain a sterically accessible concentration of charge, such as a lone pair of electrons, and is often relatively electronegative, although this is not required. Common acceptor atoms include O, N, and S and the donor comprises a hydrogen atom bonded to an atom sufficiently electronegative to generate a slightly polar D–H bond.

Such interactions are possible due to the unique bonding of hydrogen. It is the only element that forms covalent σ-bonds to electronegative atoms, and uses an inner shell electron (1 S) in that covalent bond.[7] The electrons of the covalent bond are preferentially located towards the donor, exposing the proton and resulting in a partial positive charge on hydrogen, opposite to the location of the covalent bond. Thus, interactions with negatively charged species are possible.

Hydrogen bonds are highly varied with a number of influencing factors. They can occur either within a molecule (intramolecular) between atoms or groups or between those of two different molecules (intermolecular). The atoms involved, neighbouring atoms, and distances between atoms all affect the type and strength of interaction seen.[8] Stronger hydrogen bonds occur when more electronegative D atoms are present as a greater positive charge on hydrogen is generated. This results in a stronger electrostatic attraction to the acceptor. Additionally, strength has been related to shorter inter-atomic distances.[9]

Typical descriptions of hydrogen bonds include D-H···A or D···A distances and D-H···A angles. Classification is associated with these two features and an interaction strength. ‘Strong’ hydrogen

bonds have interaction energies in the range 60-120 kJ mol^{-1}, D···A distances of 2.2-2.5 Å and D-H···A angles close to linear (175-180 °). Interactions with energies of 15-60 kJ mol^{-1}, distances of 2.5-3.2 Å and angles between 130-180 ° are considered 'moderate' in strength whilst those with distances up to 4 Å, angles between 90-150 ° and energies up to 15 kJ mol^{-1} are designated 'weak'. These categories provide only a guide to classifying hydrogen bonds as in reality a continuum exists and individual interactions do not necessarily fall nicely into a defined category.[10]

1.2.1 The Importance of Hydrogen Bonding

The nature of formation of hydrogen bonds gives an inherent directionality to the interaction. This can provide control to molecular assemblies in terms of molecular arrangement and 3D packing. Strong interactions are rigid and provide spatial and directional control whilst at the other end of spectrum, weak hydrogen bonds are much more flexible and offer no structural rigidity.

3D packing, molecular arrangement and interactions dictate the properties of a solid. Hence, when present, hydrogen bonding is fundamental to the solid state and provides control over a number of physicochemical properties.[11] Hydrogen bonding as a steering force is emerging as the most important strategy in crystal engineering[2] and thus the hydrogen bond is considered the most important of all intermolecular interactions.

1.2.2 Hydrogen Bonding Interaction Preferences

Hydrogen bonds all have different characteristics which are dependent on several factors. Certain interactions are preferable to others, and stronger interactions will generally take precedence over weaker ones if alternative options are available. Many studies have been undertaken to establish an understanding into different interaction preferences.

The most well-established, and cited are Etter's rules[12, 13] which describe commonly occurring patterns and behaviours of certain groups. A second set of guidelines regarding hydrogen bond strengths are offered by Hunter.[14] From these, a hierarchical list of interactions can be determined:

- 6-membered rings are the most favoured motif pattern and will form first if possible, preferentially *via* intramolecular interactions.
- The strongest donor will then form a hydrogen bond to the strongest acceptor, after intramolecular interactions have formed.[12, 15]

- Subsequent donors and acceptors will pair accordingly until all are utilised in a favourable hydrogen bond.
- All good hydrogen bond donors and acceptors will be involved in interactions if possible.

More recently, a hydrogen bond propensity tool[16] has been developed, using data for organic crystals from the Cambridge Structural Database (CSD).[17, 18] Preferential interactions between specified functional groups can be identified in this way, and the most influential interactions in a structure determined.

1.2.3 Proton Transfer in Hydrogen Bonds

Hydrogen bonds can be considered as incipient proton transfer reactions.[9] Conventional hydrogen bonding retains the D-H covalent bond, albeit with an elongated bond length due to hydrogen bond formation. A degree of partial proton transfer occurs, however full proton transfer would result in the formation of D^- and HA^+ (as an ionic bond) and a salt would result. If proton transfer is experienced, the interaction is much stronger than a conventional hydrogen bond due to the additional, charge-related, attraction between the groups.

In some instances, the proton is not clearly covalently bonded to either D or A. It lies midway between the two and the attraction to both atoms is equal. These are designated as strong, or very strong hydrogen bonds and possess unique characteristics. They can be written as either D···H···A or D-H-A.[19] The most studied example is HF_2^- in which the proton is located midway between the two fluorine atoms.[20-22]

1.3 Multi-Component Materials: Co-Crystals and Salts

Multi-component materials are comprised of two or more different entities. They can represent a wide range of systems, such as solvates, hydrates, clathrates, inclusion structures, salts, co-crystals and combinations thereof. Of these, salts and co-crystals are of particular interest in this work, and co-crystal studies will predominate.

Co-crystals can be defined as a crystalline solid containing two or more structurally different components which are solid at room temperature.[23] These are present in their neutral form,[24] have a defined stoichiometric ratio,[24, 25] and are held together by directional non-covalent, freely-reversible intermolecular interactions[26, 27] such as hydrogen bonds, π-π stacking and electrostatics. There has been much debate over the definition of 'what constitutes a co-crystal?' from an array of authors,[23-26, 28-33] however the above will be utilised in the work of this thesis.

Conversely, salts undergo proton transfer[34] between at least two of the components present, to produce an A^+B^- complex in contrast to the neutral AB co-crystal.

Both salt and co-crystal materials can form polymorphs, solvates and hydrates producing different forms of the same material. In the latter categories further components, typically liquid at room temperature, are present in the crystal lattice. A classification system was proposed by de Gelder *et al.*[35] to help differentiate a series of multi-component systems. This classification comprises three main classes (salts, co-crystals and solvates) with seven subclasses based on the residues present. This provides a feasible way to categorise materials into a single, and appropriate, group, following from the problematic previous regulatory classification[36, 37] in which there was overlap of the regulatory classes.

1.3.1 Salt or Co-Crystal?

The nature of the crystalline solid obtained is dependent primarily on the acidity and basicity of the interacting functional groups, and whether proton transfer will occur between them. The conditions used will also have some impact.

pK_a values of the groups can provide insight into the likely product and a 'rule of three'[34, 38, 39] has been postulated. The rule is based on ΔpK_a of the acid and base ($pK_{a\,(protonated\ base)} - pK_{a\,(acid)}$) and stipulates that a salt will arise if $\Delta pK_a > 3$, and a co-crystal for if $\Delta pK_a < 0$.[38, 40] The intermediate range between these values is harder to categorise and predictions are more difficult.[41-45] Materials resulting from combinations with ΔpK_a in this range can form as either a salt, co-crystal, co-crystal salt, or disordered solid form with partial proton transfer.[45-47] Multiple, different forms have also been generated, as evidenced in the study on *p*-aminosalicylic acid by Goswami *et al*.[48]

This is a complex topic, and one under much current debate and study. Studies corroborating the rule of three have been reported, such as those of Lemmerer[49] and Mohamed *et al.*[46]. Others, such as Bhogala, Basavoju and Nangia[47] extend the limit to 3.75 as they see an intermediate bond character up to this value, and Cruz-Cabeza[38] defines the region boundaries as $\Delta pK_a < -1$, $-1 < \Delta pK_a < -4$ and $\Delta pK_a > 4$. Other studies have been able to reduce the size of this intermediate range, when a specific system or compound is considered.[45]

Accurate expectations of the behaviour of the solid state are challenging. Many studies use values that are not wholly reliable, therefore it is difficult to determine a concrete rule and 'cut-off' values. It has been observed that a crystal engineering approach, based on the intermolecular interactions that an ionisable API can partake in, rather than using pK_a values, could be more appropriate.[47]

1.3.2 Advantages of Co-Crystals and Salts

Both salts and co-crystals can be beneficial, providing alternate, or additional solid forms of a compound. To form a salt an ionisable site must be present on the molecule of interest, and the choice of salt counter ion is limited to those which can undergo proton transfer. Co-crystallisation, however, does not have these restrictions as both molecules retain their neutral state. Thus, there are many more available co-formers to select from than salt counter ions.[50]

Both forms introduce an additional molecule into the crystal lattice which alters the molecular arrangement, 3D packing and interactions. Consequently, the physicochemical properties will also be altered. Such properties include solubility, stability, crystallinity, melting point, dissolution rate and particle-related properties.[51]

The ionic nature of salts makes them inherently more likely to be more soluble[52, 53] than compounds containing neutral components, and the strong, charge-assisted interactions present produce higher melting points.[54, 55] Although salts often display the highest solubilites, co-crystals can also show improvements. Up to a factor of 50 has been reported for solubility enhancement *via* co-crystallisation, whilst salts can display a more than 2000-fold increase.[53, 56] Depending on the application, a moderate solubility and dissolution are often sought. Co-crystal solubility has been shown to be directly proportional to co-former solubility[50] however no correlation was found in the work of Aakeröy *et al.*[57, 58] Links between solubility and structure have been evidenced.[59]

Whilst salts often increase the melting points of materials, co-crystals have been shown to moderate this property. Melting points can be both increased and decreased relative to the constituent materials with judicious selection of the co-former molecule. Aakeröy, Forbes and Despar[58] show a link between co-former melting point and the melting point of the resulting co-crystal which is corroborated by Stanton and Bak[60] with co-crystals of AMG517.

A further advantage of both salts and co-crystals is the potential to design and predict new forms. Using knowledge of ΔpK_a, the hierarchy of intermolecular interactions, and physicochemical properties information it is possible to design new solids with specific requirements in mind (see Section 1.3.4 for further information).

These advantages make salts and co-crystals attractive materials for a range of different applications. There are many relevant industries and fields in which these techniques display potential, including agrochemicals, explosives, and pharmaceuticals.[25, 61-65] The latter is an area which has developed vastly in recent years and of significant relevance to this thesis. The chosen

co-former or salt counter ion must be appropriate, however, depending on the required purpose and function of the new material.

1.3.3 Pharmaceutical Applications of Co-Crystals and Salts

Many current drugs in development display some unsatisfactory properties, such as solubility, stability or bioavailability; 40 % of approved for market drugs have low solubility[66] as do 80-90 % of those in the pipeline.[31, 67, 68] Up to 77 % of screening compounds in discovery are reported to have inadequate solubility for testing[53, 69] and several marketed drugs display properties such as low solubility, low permeability, rapid metabolism and elimination from the body as well as poor safety and tolerability.[70] Hence, properties improvement is of significant interest to the pharmaceutical industry.

Most drugs (over 80 %) are administered in tablet form[56] and for optimum therapeutic effect they must exhibit satisfactory dissolution and solubility in a given time. The main interests for pharmaceutical modification are hence centred around solubility, dissolution rate, bioavailability, mechanical strength, powder stability and processing within industrial manufacturing processes.[71]

The most common method for improving solubility for acidic or basic drug molecules is through salt formation.[72] Salts are well established in the industry and regulatory guidelines exist on their classification for marketing salt form products. Co-crystals, however, were previously not well classified until the recent US FDA[37, 73] and European Medicines Agency (EMA)[74] reports. These allowed pharmaceutical companies to understand the development, marketing and intellectual property stipulations and constraints.

It has been reported that co-crystal (rather than salt formation) may be the best way to produce a drug substance with appropriate properties for *in vivo* exposure.[75, 76] One advantage of co-crystals is the lack of covalent chemical modification to the compound. The drug molecule retains its chemical composition, molecular structure and hence its biological activity.[77]

Pharmaceutical co-crystals [62, 63, 78-80] contain an Active Pharmaceutical Ingredient (API) and an acceptable co-former molecule. These can be found on US FDA (Food and Drug Administration) GRAS (generally recognised as safe) database[81] or on the EAFUS (Everything Added to Food in the United States) list.[82]

The number of literature examples of co-crystals containing an API (or API-like molecule) is growing significantly.[34] Many physicochemical property improvements have been achieved, including solubility,[42, 76, 83, 84] stability,[85-87] dissolution,[60] hygroscopicity,[88] bioavailability,[84, 89] and mechanical properties.[90] Commercialisation of a drug requires adequate stability, bioavailability

(determined by dissolution and solubility) and manufacturability (including mechanical properties),[62] hence all these reports are advances towards improved medicines.

In addition to property modification and improved solid forms, both salts and co-crystals can also be utilised to expand Intellectual Property (IP) portfolios,[91] extend the life cycles of old APIs and also protect IP.[92]

1.3.4 Design and Prediction Approaches for Co-Crystals and Salts

The generation of salt forms is well established. Counter-ions with a pK_a 2 units lower or higher (for basic and acidic molecules respectively)[93, 94] than the target molecule produces good results and is used routinely. Generating co-crystals, however, is not trivial. Numerous experimental attempts, resources and extensive time periods can provide little return, as shown by Haynes *et al.*.[95] There is no guarantee that the combination of two particular functional groups or entities will always produce a pre-defined, or expected outcome. Hence, this section will focus on the generation of co-crystal forms.

The design of co-crystals is desirable to focus experimental work and reduce the scope and breadth of experimental trials. Success of co-crystal development ultimately manifests in the identification of suitable co-formers. Wood *et al.*[96] have summarised the rational design strategies from the past and highlighted future directions of this field.

Structures are directed by both geometrical and chemical components, therefore a model based solely on close packing, or interaction hierarchy are not appropriate. The conflict between these factors needs to be appreciated for conclusive predictions of the solid form. Although the field has progressed significantly, there are still some areas in which significant advances are awaited; studies on co-former identification for improving desired physicochemical properties quantitatively have been minimal. Development in this area would allow co-former selection to obtain a new material with resulting physicochemical properties within a target range.[97]

1.3.4.1 Synthon-Based Approach

A supramolecular synthon-based, approach[16-19] is a convenient and common method used to aid design. Supramolecular synthons can be defined as

> "structural units within supermolecules which can be formed and / or assembled by known or conceivable synthetic operations involving intermolecular interactions."[98]

These can be broken down into nodes (the molecules) and node connectors (the synthons).[99] Synthons must be selective, versatile and recurrent to ensure that they provide a predictable

connectivity under different conditions and are retained in the presence of other potentially disruptive interactions or groups.[2] CSD analysis can be used to identify frequently occurring, robust, interactions and motifs of heteromeric structures. Those present in single component structures are not appropriate as they do not translate into multi-component architectures.[24] Several common motifs used in co-crystal design are shown in Figure 1.1, and can be implemented in co-former selection accompanied by knowledge of the functional group(s) present in the target molecule.[100-102]

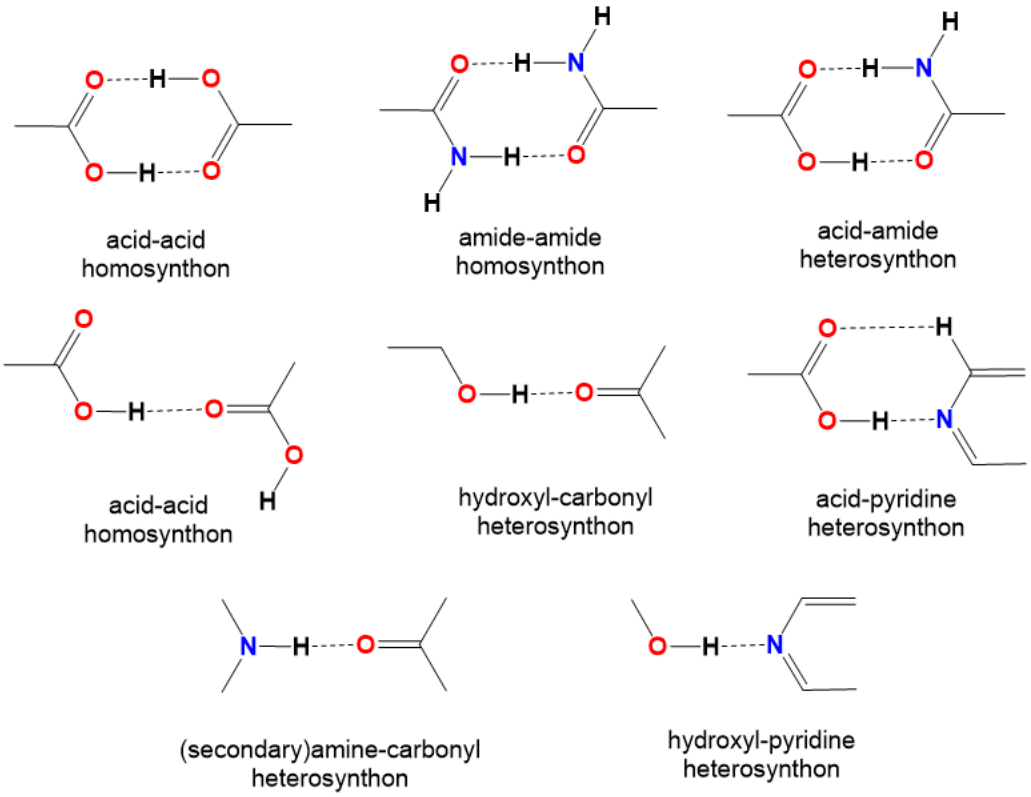

Figure 1.1. Common hydrogen bonded synthons frequently implemented in synthon-based co-crystal design.

For any design, prediction or synthetic approach, a co-crystal will only result if its formation is preferential to the isolation of the individual components. The same is also true for salt forms. Interaction preferences and the hierarchy of synthons must therefore be understood. This has been explored by various research groups, a selection of their findings highlighted below.

- $O–H_{phenol}\cdots N_{aromatic}$ and $O–H_{carboxylic\ acid}\cdots N_{aromatic}$ heterosynthons are equally competitive[101]
- However phenols dominate for basic N[103]
- $O–H_{carboxylic\ acid}\cdots N_{pyridine} > O–H_{hydroxyl}\cdots N_{pyridine}$[101]
- $O–H_{acid}\cdots N_{pyridine}$ is persistent, even with substituents on pyridine with potential for interactions[24]

- However if a cyano is present, $O–H_{hydroxyl}\cdots N_{pyridine}$ is favoured[104]
- Self association rank: amide > acid > alcoholic OH > phenolic OH.[105] Keto C=O interrupts CO_2H dimers whereas the amide equivalent are seldom interrupted.

Many molecules, particularly APIs, have structures and functionalities outside the scope of current studies and the information archived in the CSD. New and additional studies of hierarchy and competition are required to extend the data and inform about a wider variety of compounds. In response to this, Duggirala[62] proposed a scheme for the delineation of hierarchy based on CSD information and model compound experiments.

1.3.4.2 Prediction Methods

A variety of co-crystal prediction methods have emerged over recent years as an alternative, or complementary, technique to the design strategies discussed previously. One of the most prominent is that of Laszlo Fábián[25] based on molecular complementarity and implemented through a series of quantitative structure activity relationship (QSAR) based descriptors. The most discriminating factors for co-crystal formation were found to be shape and polarity related. This is now implemented in Mercury[106-108] (part of the software suite of the Cambridge Crystallographic Data Centre (CCDC)) making it widely available.

Other approaches are based on lattice energy calculations and the difference between that of the individual components and the co-crystal.[109-111] If the co-crystal is more stable (lower lattice energy, G_{cc}) than that of the sum of the pure components (G_{summ}) it will form; $-G_{cc} > -G_{sum} \rightarrow$ co-crystal.[112] The drawback of such approaches is the requirement of crystal structure predictions (CSP) which utilise significant computational resources. Additionally, energy differences are often small.[113]

One approach to overcome the necessity for CSP has been demonstrated by Abramov *et al*.[114] By treating the solid state as a supercooled liquid (which can be approximated to mixed solid phase crystals) the probability of formation can be determined from the difference in excess enthalpy (pure components and co-crystal).

Despite these promising indications of predictions, a blind test showed only 2 of 14 groups correctly predicting the experimental structure of a co-crystal.[115, 116] Hence, there is still much work needed to progress to the prediction of these structures, and known outcomes of experimental trials.

1.3.4.3 Future Directions

There are currently a wide range of approaches available, not limited to those discussed herein, to help design, inform and predict the solid state and outcomes from multi-component syntheses. Many are based on hydrogen bonding and the presence of functional groups, however pharmaceutical molecules in discovery and development are becoming ever larger, more flexible, and with fewer (accessible) functional groups.

A recent perspective article by Bučar[117] shows the field is advancing well, with property modification successes arising from changes to the crystal lattice reported. Many developments are still required and we are far from being able to successfully plan and execute the construction of any imaginable crystal lattice, if that will ever be conceivable.

The CSD is expanding considerably year on year[17] encompassing a greater breadth and depth of information as it does. With time, there is a greater likelihood that data regarding structurally similar molecules to that of interest will be available which can provide additional, directly relevant information for specific studies and help to direct syntheses.

1.3.5 Synthetic Approaches for Co-Crystals and Salts

Crystallisation is a complex event, and often produces the kinetic, rather than thermodynamic product.[118] Co-crystallisation experiments are inherently more complex than single-component systems, due to the additional component(s) involved. If favourable synthons are identified in design it is not without tribulation that these are exhibited as the appropriate experimental conditions must be identified which favour the co-crystal formation. The same is also true for salts, as the conditions must encourage proton transfer. In both instances, the co-crystal or salt must be more stable than the pure components for its formation to be favoured.

Typically, a screen is undertaken to identify systems where a change, with reference to the pure starting components, is seen. A mechanical screening approach has proved very effective[119-126] either solvent-assisted or neat (dry). The absence of solvent in dry grinding eliminates any related problems, particularly regarding solubility, however the addition of a small amount of solvent often results in greater crystallinity which is advantageous for subsequent analysis. A similar approach uses sonication in place of mechanical methods.[127]

Alternative screening methods have been reported which include thermal approaches *via* DSC,[128-130] or Hot Stage Microscopy[130-132] and various heating[89] or heating-cooling strategies,[104] allowing for a more integrated indication of promising systems. Other methods used for real-time monitoring include PXRD,[133] DSC[134] and FTIR (for solute concentration).[135]

A high-throughput approach using miscibility information indicated the most preferred combinations to guide screening[136] and theoretical approaches have also been employed such as the virtual screening of Musumeci *et al*.[137] and the use of lattice energy calculations.[112, 113]

Whilst screening, or synthesis by various methods can provide novel systems, solution methods allow full exploration of alternative phases (e.g. solvates, hydrates, polymorphs and stoichiometrically diverse combinations).[138] Solution based approaches are also advantageous for scale-up and exploring a variety of systems.[139]

Examples of solution-based approaches include droplet evaporative crystallisation,[140-142] solution mediated phase transition (slurry),[143, 144] moisture sorption,[145] vapour diffusion,[146] rapid solvent removal, supercritical antisolvent (SAS),[147] ultrasound assisted solution,[148] and the more typical evaporative techniques.[88, 138]

1.3.5.1 Factors Affecting the Synthetic Product

For solvent-based syntheses, appropriate solvent selection is crucial.[149] This can have a significant impact on the product formed with effects seen in in stoichiometry, species charges (proton location), polymorphic forms, or the inclusion or absence of solvent / water molecules within the lattice. Besides solvent choice, variables such as vessel (size, shape, material etc), crystallisation temperature including heating / cooling (and rate thereof), evaporation rate and method all impact the final product.

Stoichiometry must also be considered. 1:1 ratios are typically employed, however 1:2 and 2:1 ratios are also common. The initial input stoichiometry may not represent that in the final product, and multiple stoichiometries may arise when different conditions are used.[150 149, 151, 152] From a molecular perspective, the steric accessibility of functional groups, electronic properties, and the donor / acceptor ratio of the two components are all significant factors and control the nature of the product: single component polymorphs, co-crystals, co-crystal polymorphs and salts / other multi-component materials. With the exception of parent polymorphs these can all occur in various stoichiometries.[153]

1.4 Conclusions

An introduction to crystal engineering and multi-component systems has been presented, with salts and co-crystals highlighted as key forms for the work of this thesis. Applications, design strategies and synthetic approaches have also been discussed.

Both salts and co-crystals are advantageous new solid forms of interest to the pharmaceutical industry, and their incorporation into development programs has ensued. Salts are well-established for property modifications, particularly in pharmaceuticals, however the field of co-crystals has had a more recent expansion. Considerable research efforts are on-going and as the field develops and progresses further, more wide-ranging applications are being realised. With advancements, more diverse screening and synthetic approaches are emerging and this diversity will continue to increase with further studies.

There is a myriad of factors which can affect the final product of a salt or co-crystallisation experiment, and hence careful consideration of practices must be employed. To screen the landscape of a system, a multitude of different conditions and methods are required to explore all boundaries of a material's synthesis.

Chapter 2: Analytical Methods

Chapter 1 outlines crystal engineering and different types of solid form, the design and understanding of which is underpinned by structural chemistry. In this chapter X-ray crystallography will be introduced, along with other, complementary techniques which can provide information about the solid state. An overview of the background will be given, followed by how it can be applied and utilised in different studies. More complex studies will also be introduced and the information that they can provide analysed. Methods of analysing physicochemical properties and how these relate to the crystalline form will be discussed.

2.1 Crystallography

Crystallography is the study of molecular and crystalline structure[154] enabling the determination of relative atom location, connectivity, and molecular geometry and environment.

Crystalline materials are highly ordered and contain atoms or molecules in a regular periodic array which extends in three dimensions. The *unit cell* is a parallelepiped which represents the full symmetry of the repeat geometry of the crystal. It can be defined by three cell lengths *a*, *b* and *c* and the three angles α, β and γ. There are seven crystal systems, with differing symmetry constraints, to which the unit cell parameters must comply: triclinic, monoclinic, hexagonal, rhombohedral, orthorhombic, tetragonal, cubic. From these crystal systems there are 14 Bravais Lattices.

Diffraction is the bending of waves when a slit or obstacle of comparable size to their wavelength is encountered. The regular array of molecules in the crystal acts as such an obstacle and atoms can interact with an incoming beam resulting in diffraction which can be measured. Atomic radii are of the order ~0.3-3 Å and will therefore cause diffraction of X-rays, electrons and neutrons. These are scattered by valence shell electrons, the nucleus and surrounding electrons, and the nucleus respectively. A single atom will not give diffraction significant enough to detect, however the periodic array in the crystal magnifies the diffraction allowing it to be measured. The diffraction studies reported herein are based on X-ray diffraction, however reference neutron diffraction data is used for hydrogen atom positions for experimental charge density studies.

2.1.1 Background Theory

For diffraction from crystals to be observed, constructive interference must occur. The geometrical conditions for when this will arise (and hence diffraction is detected) were determined by the Bragg father–son partnership and led to Bragg's Law (Equation 2.1).[155]

$$2d_{hkl}sin\theta = n\lambda$$

Equation 2.1. Bragg's Law.

θ is Bragg angle, λ is the wavelength of the X-rays, d_{hkl} is the plane spacing and n is the additional path length the wave must travel. n must be a whole integer for constructive interference to occur and diffraction observed, it is generally considered as 1; Miller Indices *h*, *k*, *l* of a particular reflection can account for multiples of the wavelength.

The observed pattern is a lattice comprised from the diffracted beams observed as spots on a 2D detector. These have defined positions and intensities dependent on the crystal and form what is known as the reciprocal lattice, the geometry of it related to the crystal, or 'direct', lattice. The relationship between these is relatively simple, the reciprocal lattice comprised of reciprocal distances and perpendicular directions. The relationship between the diffraction intensities and the electron density, however, is more complex, requiring a Fourier Transformation as shown in the structure factor equation (Equation 2.2).

$$F(hkl) = \sum_{j=1}^{N} f_j \exp[2\pi i\big(hx_j + ky_j + lz\big)]$$

Equation 2.2. Structure factor equation.

The diffraction pattern is the (forward) Fourier transform of the electron density, shown in Equation 2.3. F(*hkl*) is the structure factor for reflection of indices *h, k* and *l* and comprises the amplitude and phase.

$$F(hkl) = \int_{cell} \rho(xyz) \cdot \exp\big[2\pi i\big(hx_j + ky_j + lz\big)\big]\,\mathrm{d}V$$

Equation 2.3. Structure factor equation in relation to electron density.

The reverse of the Fourier transform returns the electron density (crystal structure) from a diffraction pattern according to Equation 2.4. This is separated out to show the amplitude and phase components of the structure factors in Equation 2.5.

$$\rho(xyz) = \frac{1}{V}\sum_{h,k,l} \mathrm{F}(hkl)\ \cdot \exp[-2\pi i(hx + ky + lz)]$$

Equation 2.4. Electron density equation.

$$\rho(xyz) = \frac{1}{V}\sum_{h,k,l} |\mathrm{F}(hkl)| \cdot \exp[i\varphi(hkl)] \cdot \exp[-2\pi i(hx + ky + lz)]$$

Equation 2.5. Electron density equation split to show the amplitude and phase components of the complex number *F(hkl).*

This reverse Fourier transform corresponds to the image of electron density generating the diffraction pattern. The right-hand side of the equation can be considered as the summation of all the diffracted beams with their amplitudes and phases. The phases include the intrinsic phase, relative to the incident beam and a phase shift appropriate to each geometrical position in the image relative to the unit cell origin.[156] During the diffraction experiment, individual amplitudes are recorded as relative intensities ($I \propto |F|^2$), however the phases are lost. This is the 'phase problem' and therefore the reverse Fourier transform cannot be simply calculated from a measured diffraction pattern. To be able to reconstruct the electron density and hence solve the crystal structure from a diffraction pattern, the phase problem must be solved and this is much of the task of solving a crystal structure. To allow the reverse Fourier transform to be carried out accurate reflection amplitudes, from good quality data, are required.

2.1.2 Solving the X-ray Crystal Structure

There are three main methods for solving the phase problem in X-ray crystallography: direct methods, Patterson syntheses and charge flipping. Direct methods aims to estimate approximate phases from relationships between the structure factors. No knowledge of the crystal structure is used except for atomic nature and implications for diffraction effects. Patterson syntheses, however provides approximate positions for some of the atoms present from a Patterson map of vectors between atoms, obtained from the Patterson Function (Fourier transform of $|F_{obs}|^2$, all phases set to 0, i.e. in phase). This is most applicable when there are a few heavy atoms present among light atoms, or when there is a well-defined and rigid geometry.[156] Charge flipping, denoted as dual space iterative methods, contains algorithms which use alternating modifications in direct and reciprocal space to find a solution to the phase problem.[157]

The most commonly used approach, and that which will be discussed further, is that of direct methods. Whilst no prior information is used, there are significant restrictions on the phases arising from the properties of the electron density: it must be either positive or zero, never

negative, and concentrated in certain regions (atoms). Therefore, the waves must add up to maximise the compact regions and minimise negative ones. The most significant reflections, contributing the most to the Fourier transform are selected and phases estimated based on probable relationships. These trial phases can be entered into the forward Fourier transform equation with measured amplitudes and a set of calculated structure factors (F_{calc}) are generated. A first approximation of the phases and atomic positions are obtained. If partially correct, some resemblance of F_{obs} and F_{calc} should be seen. The accuracy can be improved by refining the atomic parameters to minimise $|F|_{calc} : |F|_{obs}$ using Fourier difference maps and the electron density equation. The new parameters can be fed back into the model and iterative cycles repeated until the refinement converges and the crystal structure is obtained. Various statistics of refinement (e.g. R, *w*R2 and residual density) can be calculated in order to inform about the model accuracy.

2.1.3 Standard Resolution Structure Analysis

The model obtained from structure solution provides a set of atomic co-ordinates which can be visualised as molecules consisting of the atoms bonded together. The interactions and bonds can be deduced from the atomic separation distances. Analysis of these spherical atoms models provides considerable structural information.

A geometric analysis provides insight into molecular bond lengths, angles and conformation arising from the relative positions of the atoms within the unit cell. Extending the structure beyond the molecule shows how the molecules pack together within the lattice and the relative positions of the functional groups. This can provide information regarding crystal form and comparisons between different forms can therefore be made.

2.1.4 Beyond Standard Resolution

The standard resolution or spherical atom model comprises atoms of a certain radius centred around the coordinates from which bonds and intermolecular interactions are inferred. It is the electrons themselves (which cause the diffraction allowing such a model to be determined) that are of particular interest with regards to the chemistry of molecules: formation of the solid state, reactivity, physicochemical properties etc. A spherical atom model gives a poor representation at electronic resolution as the electron density is distorted by bonding effects. There are a number of approaches that have emerged over the years that can be used to generate a more accurate model. These include the older approaches of Dawson,[158] Stewart[159] and Hirshfeld,[160] and some more recent developments including Jayatilaka *et al.*'s X-ray constrained wavefunction refinement approach[161] and Hirshfeld atom refinement.[162, 163] It is the multipolar model of Hansen and

Coppens[159, 164] that is the most recognised, and most commonly implemented in crystallographic approaches and programs. This approach will be used in the work of this thesis.

2.1.4.1 Hansen-Coppens Formalism

The Hansen-Coppens (HC) formalism (Equation 2.6) expands on the spherical, atom-centred functions and divides the electron density into three main parts. These relate to the spherical core density (blue), spherical valence density (green) and deformation valence density (red). The latter is distorted by chemical bonding and accounts for charge accumulation between atoms in bonds.

$$\rho_{atom}(\boldsymbol{r}) = P_{core}\rho_{core} + P_{val}\kappa^3\rho_{val}(\kappa r) + \sum_{l=0}^{l_{max}} \kappa'^3 R_l(\kappa' r) \sum_{m=0}^{l} P_{lm\pm} Y_{lm\pm}(\theta, \varphi)$$

Equation 2.6. The Hansen-Coppens Formalism for multipole model refinement, where ρ_{atom} denotes electron density, P_{core} and P_{val} denote the core and valence populations respectively, κ and κ′ are dimensionless expansion-contraction parameters, R_l are normalised Slater-type radial functions, and $Y_{lm\pm}$ the spherical harmonics each with its multipole population parameter, $P_{lm\pm}$.

As shown, many more parameters (up to 27) can be refined in this type of model, in contrast to the nine (three positional and six anisotropic displacement parameters) in a spherical atom model. Highly accurate data measured to high resolution is therefore required.

Using this alternative approach, the electron density distribution can be probed and related to the chemical nature of the molecule(s).

2.1.4.2 Properties of the Electron Density

The electron density is a scalar field across all space. Analysis of the gradient of this field allow topological analysis of the electron density distribution. From this, a number of properties can be derived, which include, but are not limited to, electron density, Laplacian of the electron density, atomic charge, bond ellipticity, bond paths, critical points and associated eigenvectors, and electrostatic potential. These are not all relevant to every study and therefore only those of interest to this thesis will be discussed.

2.1.4.2.1 Atoms and Charge

To be able to determine individual atomic properties the definition of an atom must be established and hence, atoms are enclosed within a surrounding zero-flux surface boundary.[165] This creates the perimeter of the atomic basin and entirely contains the atom. Integration of the electron density over the atomic basin can enable the determination of the atomic charge.[166]

Atomic charges depend on the partitioning method used to separate and assign the electron density to different atoms. Examples include discrete boundaries whereby electron density at a specific point is assigned to a specific atomic basin (QTAIM method) and fuzzy boundaries, in which density can be assigned to overlapping functions centred at very different locations. An alternative uses the attachment of basis functions to atomic centres. These three methods relate to Bader,[167] Stockholder (based on Hirshfeld partitioning)[168, 169] and Mulliken charges[170] respectively.

2.1.4.2.2 Critical Points

The gradient of electron density starts and ends at extrema values of the $\rho(\mathbf{r})$ which are known as critical points (CPs). These can be saddle points between electron density gradient vectors, or maxima or minima. All have a vanishing $\nabla\rho(\mathbf{r})$. They are labelled according to their rank and signature. The rank (ω) is the number of non-zero eigenvalues (and for topologically stable critical points this is always 3) whilst the signature (σ) is the algebraic sum of the signs of the eigenvalues. There are thus four different types of critical point:

- (3, -3); at this point all curvatures are negative, decreasing from the point and hence defines a local maximum. These are the core nuclei in the system.
- (3, -1); two curvatures are negative whilst one is positive - the electron density is at a maximum in a plane and perpendicular to this plane at a minimum creating a saddle point. This is known as bond critical point (BCP) and occurs between two nuclei.
- (3, +1); two curvatures are positive whilst one is negative – the electron density is at a minimum in a plane and maximum perpendicular to the plane (the opposite of a BCP). This is known as a ring critical point (RCP).
- (3, +3); all curvatures are positive hence defines a local minimum. This is known as a cage critical point (CCP).

For a bond (or interaction) to be present between two atoms, there must be a critical point. The location and analysis of this critical point can provide information about the bond. The electron density, $\rho(\mathbf{r_{CP}})$, and the Laplacian of the electron density, $\nabla^2\rho(\mathbf{r_{CP}})$, show the nature of the bond or interaction, whilst the location provides information about the atoms involved.

Covalent bonding results in an overlapping of the electron density and an accumulation of charge. The interactions are denoted open shell, or shared and $\nabla^2\rho(\mathbf{r}) < 0$. On the contrary, with no overlap of the valence shell charge concentrations (VSCCs) (no sharing of electrons) there is a depletion of charge, $\nabla^2\rho(\mathbf{r}) > 0$. These are ionic or non-covalent interactions, denoted closed shell, and the BCP is shifted towards the more electropositive atom.

2.1.4.2.3 Local Energy Density

$\rho(\mathbf{r}_{BCP})$ and $\nabla^2(\rho(\mathbf{r}_{BCP})$ values at critical points can also be used in the estimations of energy. Local kinetic energy density ($G(\mathbf{r}_{BCP})$), local potential energy density and total energy density can be calculated according to Equations 2.7 to 2.9 below of the Espinosa-Molins-Lecomte (EML) approach,[171] in conjunction with the formulae of Abramov.[172]

$$G(\boldsymbol{r}_{BCP}) = \left(\frac{3}{10}\right)(3\pi^2)^{\frac{2}{3}}\rho(\boldsymbol{r}_{BCP})^{\frac{5}{3}} + \left(\frac{1}{6}\right)\nabla^2\rho(\boldsymbol{r}_{BCP})$$

Equation 2.7. Calculation of the local kinetic energy density, where $\rho(\mathbf{r}_{BCP})$ is denoted in atomic units.

$$V(\boldsymbol{r}_{BCP}) = \left(\frac{\hbar^2}{4m}\right)\nabla^2\rho(\boldsymbol{r}_{BCP}) - 2G(\boldsymbol{r}_{BCP})$$

Equation 2.8. Calculation of the local potential energy density, where $\rho(\mathbf{r}_{BCP})$ is denoted in atomic units.

$$H(\boldsymbol{r}_{BCP}) = G(\boldsymbol{r}_{BCP}) + V(\boldsymbol{r}_{BCP})$$

Equation 2.9. Calculation of the total energy density.

Determination of these three quantities also allows the estimation of individual hydrogen bond energies, according to Equation 2.10. Conversion (from Hartrees) can be achieved through multiplication by 2625.5 $kJmol^{-1}$.

$$E_{HB} = 0.5\,(V(\boldsymbol{r}_{BCP}))$$

Equation 2.10. Calculation of the energy of the hydrogen bond (in atomic units).

Determination of these values for each interaction aids in the classification of the interaction as well as in the rationalisation of properties and the nature of the bonds.

2.1.4.2.4 High Resolution Experimental Data

Improvements in X-ray sources, detectors and cryogenic systems have made collecting diffraction data more commonplace so that standard resolution structure determination is now routine. Due to the complexity of the data collection, refinement, and interpretation, this is not the case for charge density studies. Data collection for these studies is, however, becoming more accessible than previously due to reduced time-frames and increased capability and speed of lab sources. Good quality crystals are required and data of high resolution and redundancy must be collected so that the data to parameter ratio remains above 10:1 following a full refinement. This is to avoid the correlation of individual parameters and also large uncertainties on each.[173]

High resolution data enables the deconvolution of thermal effects and nuclear positions[174] therefore it is essential to collect to at least 0.5 Å ($\sin(\theta)/\lambda$ up to at least 1.0 $Å^{-1}$). Higher resolution data provides vital information about atomic nuclear positions, as the scattering power of core electrons does not decrease rapidly with resolution, as occurs for valence electrons.[175] Low resolution reflections are equally important and provide essential information on the valence electrons. Low temperature is also required for accurate thermal displacement parameters.

2.2 Theoretical Approaches to Structural Analysis

> "With the exception of hydrogen bonding, molecular pairings responsible for the largest part of the interaction energy in a crystal show no particular atom–atom feature, no easily identifiable 'bond', not even aromatic stacks; they stick together by compatibility of minor and diffuse features in the electrostatic potential, that defy recognition and, a fortiori, classification. Only a quantitative calculation of cohesion energies can reveal true crystal structure determinants." A. Gavezzotti, 2013.[176]

Experimental charge density studies can aid in the identification and classification of hydrogen bonds. As expressed by Gavezzotti, many interactions show no particular atom···atom feature and are not easily identifiable by this method. Spackman[177] indicates that topological analyses may lack sufficient accuracy and Dunitz[178] suggests short contact analysis is too limiting. Additional, complementary methods are therefore recommended to fully understand a molecular system. Several complementary methods are available and appropriate, the two which will be used and discussed are that of Spackman,[179] implemented in Crystal Explorer,[180] and Gavezzotti,[181-184] in PIXEL.

Interaction energy can be partitioned into its constituents as indicated in Equation 2.11.

$$E_{tot} = E_{coul} + E_{pol} + E_{disp} + E_{rep}$$

Equation 2.11. Partitioning of energy in to four terms: Coulombic or electrostatic (E_{coul}), polarisation (E_{pol}), dispersion (E_{disp}), and exchange-repulsion (E_{rep}).

The coulombic (electrostatic) term is the attraction between unperturbed molecular charge densities, and can be described as shown:

$$E_{coul} = \frac{Q_1 Q_2}{4\pi\varepsilon^0 r}$$

Equation 2.12. Definition of Coulombic energy.

This (E_{coul}) is fundamentally the same for the two methods, provided they are based on the same wavefunctions.

The polarisation energy is defined differently in the two methods and polarisability is a factor for both of them. The total polarisation energy is not simply the sum of the molecule···molecule polarisation terms as it is non-additive. An increased polarisation energy denotes greater stability.

The dispersion energy is distance dependent, r^{-6}, and hence drops off considerably with distance. Outside the first co-ordination sphere it drops to zero.

(Pauli) Repulsion (not electrostatic repulsion) is short range and arises from the overlap of charge distribution and repulsion of electron spin.

The sum of these four components provides a molecule···molecule energy.[183, 184]

2.2.1 PIXEL

PIXEL uses electron densities obtained from individual molecular orbital calculations, calculated at the MP2/6-31G** level, on a grid with a standard step of 0.08 Å.[185] These are reduced to super pixels and the molecular arrangement or symmetry accounts for the duplication of the original density. In this way, the source of intermolecular potential is used as a whole rather than the atom···atom potentials of traditional approaches.[184] Molecular electron densities are therefore represented as a sum of the charged pixel volumes which can be partitioned to determine the different energy components. Intermolecular interaction energies can then be evaluated.[183]

Atomic polarisabilities and adjustable parameters are incorporated and optimised to reduce disparity between experimental sublimation energies and computational lattice energies for a representative set of crystal structures. The adjustable parameters account for short separations, damping of dispersion energies, scale factor and power law for the repulsion energy dependence.

E_{coul} is calculated as summations of the intermolecular pixel-pixel, pixel-nuclei, and nuclei-nuclei Coulombic terms.[183]

E_{disp} is based on the London formula[186] (Equation 2.13) and calculated as the sum of pixel-pixel terms with a dampening, $f(R)$, to avoid peculiarities arising from short pixel-pixel distances due to the inverse power law. The expression for E_{disp} is given in Equations 2.14 and 2.15.[185]

$$E = -\frac{3}{4}\frac{(E_{ION}\alpha^2)}{[(4\pi \in^{\circ})^2(R_{ij})^6]}$$

Equation 2.13. Dispersion energy according to the London formulation between two molecules of polarizability α and ionisation energy $E_{ION.}$ ϵ denotes electric field.

$$E_{disp,AB} = E_{ION}\left(-\frac{3}{4}\right)\sum\sum\frac{f(R)\alpha_i\alpha_j}{[(4\pi\epsilon^{\circ})^2(R_{ij})^6]}$$

Equation 2.14. PIXEL dispersion energy determined between two molecules ($E_{disp,AB}$) including the dampening factor, f(R), electric field, ϵ, and atomic polarisabilities, α.

$$E_{disp} = \frac{1}{2}\sum\sum E_{disp,AB}$$

Equation 2.15. Expression used for the PIXEL dispersion energy determination in a crystal (E_{disp}).

E_{pol} at a given pixel (i) is defined according to Equation 2.16[185] which includes a dampening (d_i) to reduced physically unrealistic contributions from high-field contributions.

$$E_{pol,i} = -1/2\ \alpha_i[\epsilon_i d_i]^2\ for\ \epsilon < \epsilon_{max}$$

Equation 2.16. Polarisation energy at a given pixel. ϵ denotes the electric field and α the polarizability.

The polarisation energy at a molecule is the sum of those at each of its electron density pixels whereas the total polarisation energy in the crystal is the sum of all A...B and B....A molecular polarisation energies.

E_{rep} is determined according to Equation 2.17 from the overlap (S_{AB}) of the electron densities of two molecules (A and B) shown in Equation 2.18.[185]

$$E_{rep,AB} = K(S_{AB})^{\gamma}$$

Equation 2.17. Calculation of E_{rep} between two molecules in the PIXEL method. K and γ are adjustable parameters, fixed at 2800 and 0.93, respectively, for Erep in kJ mol^{-1}.[185]

$$S_{AB} = \sum\sum[\rho_i(A)\ \rho_j(B)]V$$

Equation 2.18. Expression for the electron density overlap (S) of molecules A and B comprised of the electron densities in two pixels (ρ) and the pixel volume (V).

Similarly to E_{disp} calculation for the crystal, E_{rep} (Equation 2.19) is the sum of two-body interactions.

$$E_{rep} = \frac{1}{2}\sum\sum E_{rep,AB}$$

Equation 2.19. Calculation of the total repulsion energy in a crystal using the PIXEL method.

2.2.2 Crystal Explorer

A similar approach to Gavezzotti's PIXEL calculations is used by Spackman *et al.*[179] and implemented in Crystal Explorer.[180] In contrast to the breakdown of a large total energy for the interacting pair of molecules as in the PIXEL method, the total interaction energies are constructed from the individual components. Each term in the breakdown of the interaction energy has an associated scale factor (k_{coul}, k_{pol} etc,) so that Equation 2.20 is generated.

$$E_{tot} = k_{coul}E'_{coul} + k_{pol}E'_{pol} + k_{disp}E'_{disp} + k_{rep}E'_{rep}$$

Equation 2.20. Breakdown of interaction energy according to the method of Spackman *et al.*

These terms are derived as follows:[187]

E_{coul} is the classical electrostatic energy between unperturbed monomer charge distributions. These are produced from the antisymmetric combination of the monomer spin orbitals described by Su and Li.[188]

E_{pol} is estimated over the sum of nuclei with terms of the type $-(½)\alpha_{mean}|\boldsymbol{F}|^2$. The electric field, $\boldsymbol{F}$, is computed at each nucleus from the charge distribution of the other monomer and α_{mean} are isotropic atomic polarisabilities (Thakkar and Lupinetti).[189]

E_{dis} is summed over all intermolecular atom pairs and based on Grimme's D2[190] dispersion correction.

E_{rep} is also calculated between unperturbed monomer charge distributions from the antisymmetric product of the monomer spin orbitals.[188]

Calibration in this instance uses quantum mechanical results with a large set of pairwise interaction energies obtained from theory. This is in comparison to the experimental sublimation energies in PIXEL. Other comparisons of the two approaches are highlighted by Spackman *et al.*[187, 191]

2.2.3 Hirshfeld Surface Analysis

Hirshfeld surface analysis[192-196] is a tool which allows the visualisation of molecular surfaces and the size and shapes of molecules to be realised. The Hirshfeld surface defines the space occupied by a molecule in a crystal, partitioned according to a weight function (Equation 2.21) developed from that of F.L. Hirshfeld's stockholder partitioning.[174] In this the numerator is a sum over the atoms in the molecule of interest (the promolecule) and the denominator is that over the crystal (the procrystal).

$$w_A(\boldsymbol{r}) = \sum_{i \in \, molecule\ A} \rho_i^{at}(\boldsymbol{r}) \Big/ \sum_{i \in \, crystal} \rho_i^{at}(\boldsymbol{r})$$

$$= \rho_{promolecule}(\boldsymbol{r}) / \rho_{procrystal}(\boldsymbol{r})$$

Equation 2.21. Weight function used for defining a molecule in a crystal for Hirshfeld surface generation, Spackman and Jayatilaka.[196]

The Hirshfeld surface is very different from a van der Waals surface or an outer surface of the electron density, which depend only on the molecule itself. In contrast, the Hirshfeld surface is determined by both the molecule and its nearest neighbours and hence can provide information regarding intermolecular interactions.

Distances from the surface to the nearest nucleus inside or outside the surface (d_i and d_e respectively) can be mapped and when reduced to a 2D fingerprint plot[193] they can be used to analyse and compare the different interactions present. The plots are unique for a given molecule and highly sensitive to the selected molecule's immediate environment. These plots are particularly well-suited to identifying differences in structures containing the same molecule, such as polymorphs or a systematic set of structurally-related systems. The parameter d_{norm}, combines both d_i and d_e normalised by the van der Waals radii of the atoms involved in the close contact and contacts shorter than the van der Waals separation are highlighted when this property is mapped. Appendix A.7 shows example Hirshfeld surfaces and fingerprint plots.

2.3 Analysis of Intermolecular Interactions in Crystal Structures

2.3.1 Interaction Information Obtained from Experimental Studies

Values such as the electron density ($\rho(\mathbf{r}_{BCP})$) and the Laplacian of the electron density ($\nabla^2(\rho(\mathbf{r}_{BCP}))$) at a bond critical point can provide information regarding the type of bond or interaction: $\rho(\mathbf{r}_{BCP})$

values ~0.1 au are obtained for covalent bonds whereas noncovalent interactions are an order of magnitude smaller, typically around 0.01 au. A negative Laplacian indicates a concentration of charge whilst positive values show charge depletion. These are representative of shared interactions e.g. covalent bonds, and close shell interactions e.g. ionic or van der Waals type interactions including weak hydrogen bonds, respectively.

The electron density, $\rho(\mathbf{r}_{BCP})$, and the Laplacian, $\nabla^2(\rho(\mathbf{r}_{BCP})$, along with the local energy density values (Section 2.1.4.2.3), can provide further information concerning the nature of the interaction. For example, a positive Laplacian and negative total electron density ($H_{\mathbf{BCP}}$) at the BCP shows an interaction which is partly covalent in nature. Using these values, hydrogen bonds can be characterised as follows:[197]

Weak hydrogen bonds of energy $E_{HB} < 50$ kJmol^{-1} (< 12 kcal mol^{-1}) have both $\nabla^2(\rho(\mathbf{r}_{BCP})$ and $H_{BCP} > 0$. Interaction distances are typically > 1.8Å and the interactions are noncovalent.

Medium hydrogen bonds of energies $50 \leq E_{HB} \leq 100$ kJmol^{-1} (12-24 kcal mol^{-1}) have $\nabla^2(\rho(\mathbf{r}_{BCP}) > 0$ and $H_{BCP} < 0$ with typical interaction distances of 1.2-1.8 Å.

Strong hydrogen bonds, $E_{HB} > 100$ kJmol^{-1} (> 24 kcal mol^{-1}) have $\nabla^2(\rho(\mathbf{r}_{BCP})$ and $H_{BCP} < 0$ and have interaction distances of < 1.2 Å.

Very strong hydrogen bonds can give negative Laplacian values for both bonds in an interaction (e.g. both O-H bonds in an O-H···O type interaction) indicating the proton is located almost midway and shared equally between the two (oxygen) atoms.

Other terms which can be determined from $\rho(\mathbf{r}_{BCP})$ and $\nabla^2(\rho(\mathbf{r}_{BCP})$ include V_{BCP} and G_{BCP}. The ratio V_{BCP}/G_{BCP} can indicate whether an interaction is stabilised by a local concentration of charge ($V_{BCP}/G_{BCP} > 1$) in an intermediate closed-shell interaction, or whether it is electrostatic ($V_{BCP}/G_{BCP} < 1$).

2.3.2 Theoretical Approaches to Interaction Analysis

The theoretical approaches of PIXEL and Crystal Explorer produce molecular interaction energies broken down into the constituents, allowing the chemical nature of an interaction to be inferred. Coulombic and dispersive energies are perhaps the most informative, the former proving important in thermodynamic stability. Using these components, the interplay of interactions (hydrogen bonding and other interactions) in a structure can be assessed, as has been shown in several reported examples.[198, 199 200, 201] Additionally, the energies can provide information on

which molecular pair interactions are dominant in the formation of crystal structures. This has been used in CSP studies by Cruz Cabeza *et al.*[202]

2.4 Physicochemical Properties

In addition to structural analyses, physicochemical properties can be measured for materials which are crucial to understand its behaviour, and how structurally similar materials relate to one another. In many industries which have an interest in functional materials these measurements are fundamental when a new substance is produced, to assess how the substance compares to previous compounds, or to set a benchmark in a new project.

2.4.1 Thermal Properties Characterisation

The behaviour of a material over a temperature range allows its relative stability and the presence and relationships of any additional forms accessible through heat to be assessed. Both differential scanning calorimetry (DSC) and thermogravimetric analysis (TGA) have been shown to be accurate, precise and reliable analytical methods for melting point determination and quantifying solvent / water loss for pharmaceutical (and related) materials.[203] In addition, information regarding purity and polymorphism can be obtained from the same experiment.

Melting is a physical process resulting in the transition of a substance from the solid state into a liquid. The intermolecular interactions holding the molecules together in the solid state must be broken or disrupted for the phase change to occur and the sample to melt. This requires an increase in the internal energy of the system, implemented through the application of heat.

Higher melting points are associated with stronger intermolecular interactions such as strong hydrogen bonds and dipole···dipole interactions. These are often seen in polar molecules and those with hydrogen bonding functionalities.[204] Báthori *et al.*[59] showed a positive correlation of O···H interactions and inverse correlation of C···H interactions to melting point, supporting the idea that stronger hydrogen bonding interactions result in higher melting points.

Shape also plays a role in affecting the melting point of a system. Bulkier molecules pack less tightly and thus less efficiently, resulting in a lower melting point arising from the reduced cumulative strength of dispersion forces between molecules.

2.4.1.1 Differential Scanning Calorimetry

Differential scanning calorimetry (DSC) determines the heat capacity (recorded as heat flow) of a sample of known mass as it is heated or cooled. It can therefore detect transitions such as

melting, phase transitions, solid state transitions e.g. eutectic formation, glass transitions and events such as decomposition. In addition to the detection of such events, DSC can provide information regarding polymorphism, (thermal) stability, crystallinity, purity etc, and aid in the construction of phase diagrams.

Events requiring energy (endothermic) and releasing energy (exothermic) are observed as peaks and troughs originating from the base line heat flow. Depending on the instrument set-up these can be in either (but opposite) directions. An example DSC analysis is given in Figure 2.1 showing a phase transition (1, Figure 2.1) and melting point (2, Figure 2.1). The amount of energy required for melting is much greater than the phase transition, evidenced as a much larger trough than that of the phase transition.

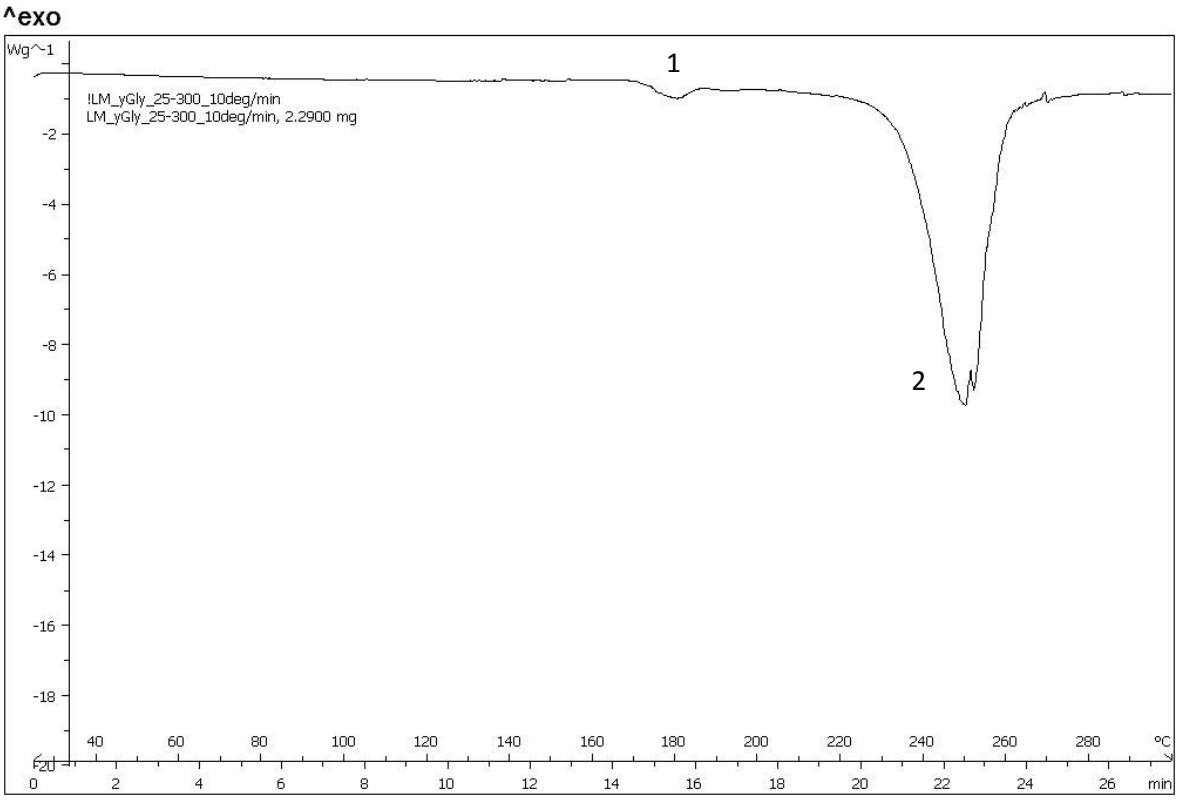

Figure 2.1. Example DSC thermogram showing phase transition (T_{onset} ~170 °C) followed by melting of the new phase (T_{onset} ~230 °C).

2.4.1.2 Thermogravimetric Analysis

Thermogravimetric analysis (TGA) indicates changes in physical and chemical properties as a function of increasing temperature at a constant heating rate. A common application is in the determination of processes which exhibit a mass loss or gain which include decomposition, evaporation, reduction, sublimation, or desorption (weight loss) and oxidation or absorption (weight gain). These events are depicted as curved sections of the trace – descending for mass

loss and an uphill gradient for an increase in mass. The gradient indicates the rate at which mass is lost / gained. Information on thermal stability can also be provided through the ranges of constant mass, i.e. plateaus in the curve. An example TGA curve is shown in Figure 2.2.

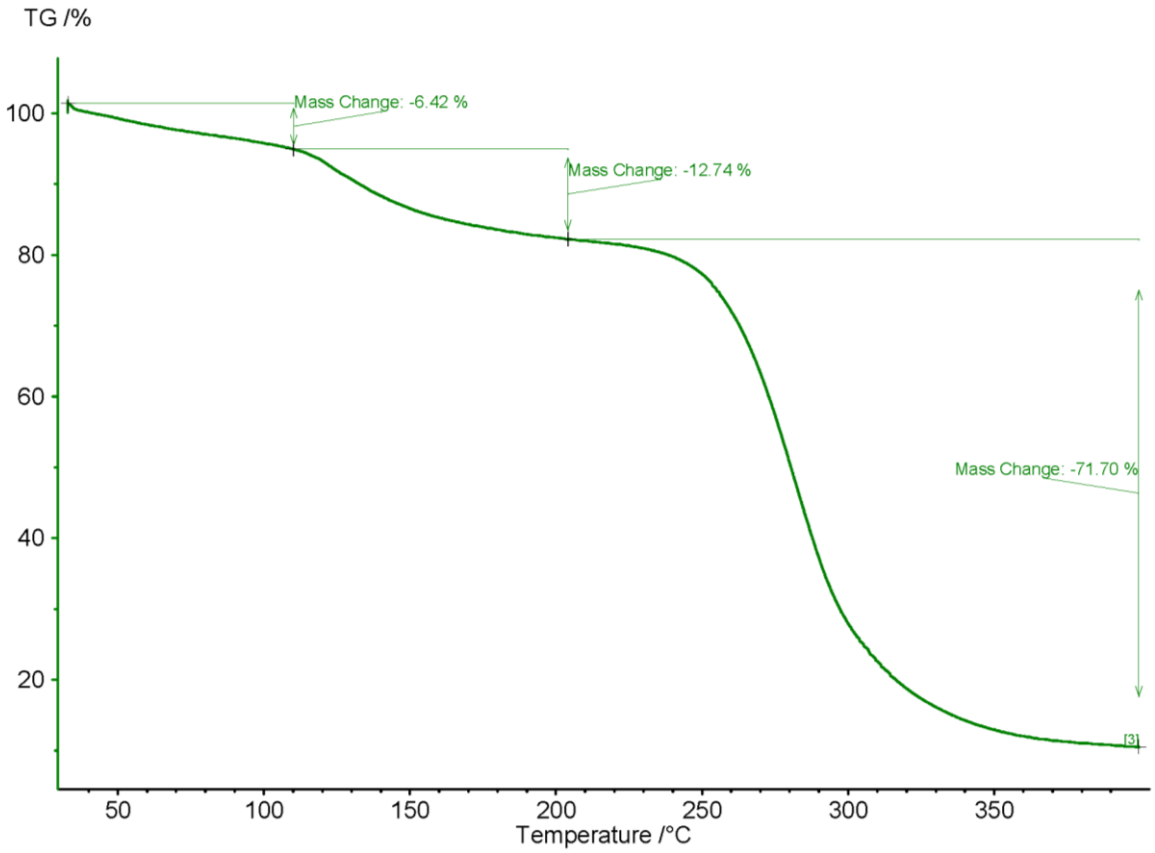

Figure 2.2. Example TGA curve showing three regions of mass loss with minimal regions of plateau indicating poor thermal stability between these mass-loss events.

In addition to the direct inferences that can be drawn from the data, TGA can also aid in determining the composition or amount of a compound in a mixture, its purity and the moisture / solvent content.[205]

2.4.2 Solution Properties

Solution-based properties provide key information regarding the release and behaviour of a molecule. This is particularly relevant to pharmaceutical applications, where understanding drug release and behaviour is paramount to ensure the correct amount of a drug is administered and to determine dose frequency. These include solubility and dissolution rate. In the context of this thesis, all solution properties are determined with respect to an aqueous environment as this is most relevant and the target environment for pharmaceutical applications.

2.4.2.1 Solubility

Solubility is a thermodynamic term, denoting the amount of solute that dissolves in a given volume of solvent, at a specific temperature and pressure.[206] This can be defined as either buffered, unbuffered or intrinsic solubility; unbuffered solubility is that of a saturated solution at the final pH of the solution, buffered (or apparent solubility) is at a given pH and measured in a pH-buffered system whilst intrinsic solubility is that of the neutral form of an ionisable compound. For a non-ionisable compound these are all concurrent as pH changes do not occur on entering solution.

Solubility is important to determine how much of a compound will be present in a resulting solution. There are two types of solubility: kinetic and thermodynamic which have different properties and provide varying information about the compound. Kinetic solubility is associated with maximum concentration in pharmaceuticals, denoting the highest concentration of the compound reached following the administration of a compound-containing product. Thermodynamic solubility is associated with equilibrium concentration, indicating the amount present over a sustained time period. This will be a trade-off between solute···solute and solute···solvent interactions to obtain a heterogeneous equilibrium. At this point, a solution is said to be saturated.[207]

Solubility of drug molecules and products is of high importance as poor solubility results in insufficient amounts for the required therapeutic effect entering the blood stream. Higher dosages are therefore required to ensure a sufficient amount is available for an adequate blood level concentration and the resultant therapeutic effect. This increases the cost of a single dose as a greater amount of drug is necessary. As discussed in Chapter 1.3.3 many drug molecules in development and approved for market display poor solubility which can lead to this problem.

2.4.2.1.1 Measuring Solubility

The type of solubility (kinetic or thermodynamic) measured is dependent on the experimental set up. Kinetic solubility is strongly time-dependent and measures the fastest precipitating species from a dissolved compound. The precipitating material is not determined and can be of any nature: neutral or charged salt, single or multi-component and range from amorphous to crystalline, including any combination thereof. Organic solution inherently favours the precipitation of metastable forms according to Ostwald's Rules.[208, 209]

Thermodynamic solubility is often deemed as the 'true' solubility of a compound. It represents the saturation solubility of a compound in equilibrium with an excess of the undissolved substance still present at the end of the test. Due to supersaturation (the solution state that

contains more material dissolved than possible under normal conditions (saturated solution)), kinetic solubility often over-predicts the thermodynamic solubility. Dissolution rate plays an important role as the crystal lattice must be disrupted and therefore amorphous or poorly crystalline materials always exhibit higher solubility than a crystalline form.[210] Determination is carried out by adding (an excess) of solid compound into a liquid and measuring the concentration, typically after 24-48 hours. To confirm equilibrium has been reached, however, the use of several time points is favoured. A rapid method, ensuring equilibrium is reached has been developed by Stuart and Box.[211]

Adequate solubility in drug compounds is considered to be greater than 100 µg mL^{-1} whilst anything less than 10 µg mL^{-1} would be poorly soluble[212] (however dose is also important in quantifying these). Poor solubility is best addressed at the discovery stage, however experimental testing is highly resource intensive. Thus, the prediction of solubility has been of high interest and many different strategies have been used to try to predict aqueous solubility.

2.4.2.1.2 Predicting and Improving Solubility

Some simple predictions of solubility have utilised melting point information as a guide,[213, 214] and it has been shown that it is possible to quantitatively relate solubility to melting point and partition coefficient.[215] Melting point, as a single predictor, however, is relatively poor, particularly for multi-component materials.[59]

A related approach to these predictions are those of Kuleshova *et al*.[112] using lattice energies to estimate solubility. Additionally, a number of computational approaches based on structure have been created[216-218] and Elder and Holm review a selection of the predictive methods, in particular *in silico* approaches.[53]

Evidencing the difficulty in predicting solubility, Llinàs *et al.* could not select a 'best' prediction method in their solubility challenge;[219] several methods performed similarly but were far from faultless. The subsequent commentary from Hewitt *et al.*[220] indicated that predictive models are only reliable within their limits; they are not applicable across all molecules. Therefore, caution should be taken when using these and it must be ensured that the model is appropriate for the molecule of interest. Predicting aqueous solubility is hence still hugely challenging.

2.4.2.2 Dissolution Rate

Dissolution rate is the speed at which a solute enters a solvent to produce a solution and dissolution profiles provide information on how a compound enters a solution over a given time. The gradient of the profile can provide information on the kinetic solubility, whilst the final

plateau denotes the maximum concentration. Such studies are important for drug compounds to model how the active drug is released from the product (e.g. tablet, or drug precursor compound). Different drug products will require different dissolution profiles depending on the nature of the treatment. A fast dissolution leads to very rapid drug release, useful for a quick-acting drug whilst other drugs require a longer activity duration and so a slower, controlled release over an extended time is required. Understanding the dissolution behaviour, and its influences, are crucial for drug products and formulations.

Dissolution involves the absorption of heat, therefore elevated temperatures increase dissolution rates due to an increased kinetic energy of the particles. This is also true for solubility. Agitation of the solution affects solvent concentration as fresh solvent will contact undissolved particles, and smaller particle sizes result in an increased rate of dissolution due to their greater surface area. Whilst also impacting solubility, these factors are more crucial in dissolution due to the kinetic nature of the measurement.

Solution-based properties in general can be influenced by a number of other influencing variables. These include the choice of solvent (polarity and viscosity (diffusion coefficient)) and sample preparation, each having a different effect on the property measurement. Experimental measurement must therefore be well-controlled to ensure equivalent conditions between all materials being tested and to ensure comparative results can be obtained. Other intrinsic factors include compound solubility (for dissolution), compound wettability, and crystallinity.

2.4.3 Stability

Any material, regardless of purpose, is likely to have a minimal required stability. A new material produced with a desirable property or activity is inadequate if it does not retain the (active) form for an appropriate time. This is applicable, but not limited to, pharmaceuticals, agrochemicals, explosives, food products etc. Different forms of the same compound often have differing stabilities and it is therefore important to test all new materials or compounds under a variety of conditions.

Over extended periods, the thermodynamic form is likely to prevail, even if it is not the first produced. This has been highly relevant in several drug molecules, most notably the case of ritonavir;[221, 222] after release on the market, crystals were observed in the capsules and effectiveness of the treatment deteriorated. The crystals turned out to be a more thermodynamically stable, but less active form of the API. Once formed, due to its stability, it was difficult to overcome and the original form could not be produced. The product had to be

withdrawn from the market and an extensive investigation carried out, with substantial associated costs.

Common stability assessments involve the use of accelerated storage and slurry conditions. Accelerated conditions comprise elevated temperature and humidity to replicate prolonged exposure at ambient conditions (and account for different temperatures and humidity across the continents) whilst slurry methods provide an indication of stability in an aqueous environment. Other techniques can also measure sample water content or moisture uptake which can be problematic for storage in more humid climates

Solid state stability has been linked to lower aqueous solubility,[53] resulting from the stronger association of molecules in the solid state. High stability is advantageous, however there is a limit. Materials with extremely high stabilities result in poor solubility which is disadvantageous.

2.4.4 pK_a

Section 1.3.1 highlights the importance of pK_a in charged and neutral species formation. To be able to use this tool, pK_a determination is required.

There are a number of methods to determine pK_a , used in some of the 'rule of three' validation studies. Examples include calculated values,[49, 223] literature reported values,[47] and experimentally determined values.[224] Consideration must be taken as pK_a values are not always straightforward to determine and those ascertained for solution species may not be applicable to hydrogen atom positions in the solid state, and hence not wholly reliable.[45, 225] Uncertainty in predictions can be greatly reduced when values are determined experimentally.[224]

2.5 Conclusions

Crystallography has been shown to be an effective method for structure determination and geometric analysis. High resolution diffraction data and enhanced modelling methods can provide information about the electron density and its distribution in the crystal structure. Topological analysis of the electron density can provide quantitative analysis for intermolecular interactions and identification of individual hydrogen bonds. Thus, interaction energies and the nature of the interactions can be determined with this data.

In addition to experimental charge density models, computational techniques can be employed providing supplementary data and complementary analyses. The combination of the data

obtained from these methods can help to understand the systems in which the interactions are occurring by probing deeper.

Physicochemical properties are also highly important when novel materials are produced, particularly multi-component systems and those of pharmaceutical interest. Determination of these properties allows full characterisation and comparison of a new material with the original components to identify the changes and modifications.

Both charge density studies and the computational approaches can probe deeper into the molecules to understand the physicochemical properties from an electronic level, each using different methods. The quantitative nature of the interaction analyses allows for comparisons to be made, and the trends observed rationalised.

Physicochemical properties are often targeted for improvement if they display as inadequate in the parent material. Quantifying these, identifying improvements and rationalising how these improvements are realised can help in future, similar studies.

Chapter 3: Aims

Chapters 1 and 2 have shown that co-crystals and salts are of importance to several fields, particularly the pharmaceutical industry, and hence are of high research interest. The ability to modify physicochemical properties is highly attractive and thus the design and synthesis of new materials is desirable. As discussed, there are several approaches for design all of which are largely dominated by the influence and presence of hydrogen bonding. This includes the salt *vs.* co-crystal determination indicating the likelihood of proton transfer, as this typically originates from hydrogen bonding preferences.

To understand the physicochemical properties and the changes which occur upon co-crystallisation it is important to understand the solid state structure. Standard resolution crystallography provides a tool for geometric analyses, however to probe these systems further, high resolution charge density studies are required. These studies enable the electron density distribution to be assessed, which differs between different co-crystals and produces the physicochemical property modifications. These changes are most easily seen in co-crystals of a single molecule or API where one component is constant in all systems. A systematic approach based on a family of related materials can show how subtleties in structure are reflected in their physicochemical properties and behaviours. Structurally related co-former molecules would allow the greatest understanding to be developed containing only small structural changes (to the co-former molecules) between the different co-crystals.

Despite the array of information that can be obtained through charge density studies, its application to multi-component systems is fairly limited with only a few reported examples.[226-233] The majority of these examples are co-crystals and include a carboxylic acid containing molecule. These include the studies of Hibbs *et al.*[228] (8-hydroxyquinoline-salicylic acid co-crystal), Wilson *et al.*[229] (isonicotinamide-oxalic acid), Gryl *et al.*[230] and Krawczuk *et al.*[231] (urea-barbituric acid and urea with rigid and flexible dicarboxylic acids respectively). The work of Guru Row *et al.*[233] is important and relevant to this thesis as they present two systems, nicotinamide-oxalic acid and nicotinamide-salicylic acid which form a salt and co-crystal respectively. This study uses experimental and theoretical approaches to identify quantitative topological features allowing salts and co-crystals to be distinguished. These include ($\rho(\mathbf{r}_{BCP})$) and $\nabla^2(\rho(\mathbf{r}_{BCP})$ to determine covalent (large $\rho(\mathbf{r}_{BCP})$ and negative $\nabla^2(\rho(\mathbf{r}_{BCP}))$ and non-covalent bonds (smaller $\rho(\mathbf{r}_{BCP})$ and positive $\nabla^2(\rho(\mathbf{r}_{BCP}))$ and features in the deformation density maps in the proton transfer region. Similar studies[229, 234, 235] have also reported these defining features. In addition to multi-component system applications, in-depth structural analyses have been undertaken on

polymorphic systems, showing their utility in subtle structural differences and relevance to understanding hydrogen bonding.[236-239] In particular, a polymorphic co-crystal system has been investigated.[230] These studies show the importance of understanding the electron density distribution to fully characterise and compare materials, and its significance for comprehensive structural studies.

The aim of the work presented in this thesis is to produce novel multi-component systems of two API molecules of interest: propyphenazone (PROPY) and lonidamine (LON). Appropriate design strategies will be employed for each, considering the molecular structure and functional groups present. Structural characterisation using X-ray crystallography and determination of physicochemical properties using a variety of methods will follow in order to fully describe each system. A systematic charge density study on structurally similar systems of the same API will allow an in-depth investigation of the electron density distribution, and intermolecular interactions present. This will involve both experimental multipole models and theoretical approaches in a quantum crystallography study from which interaction energies can be obtained. The theoretical approaches allow the energies to be deconvoluted into their component terms and investigate how the contributing terms influence the physicochemical properties. Complementary information and comparisons between the different methods will enable a deeper understanding of these systems.

The objectives of this thesis are to answer the following key research themes:

1. The application of design approaches to molecules exhibiting differing functionalities and interaction preferences to produce new multi-component systems.
2. The differences in the hydrogen bonding interactions of PROPY which contains a single, sterically hindered acceptor site, with various co-formers.
3. The differences in the hydrogen bonding and interactions of LON, a carboxylic acid containing molecule, and instances where proton transfer does / does not occur
4. The effect of different co-former molecules on the physicochemical properties of multi-component materials.
5. The effect of different co-formers on the electron density distribution and the impact this has on the physicochemical properties of structurally related co-crystals.
6. The complementarity of different techniques (experimental and theoretical), how they can be used in combination to deconvolute crystal structures in terms of the constituents and interaction energies and how this provides a better understanding of co-crystal systems.

This thesis aims to demonstrate that different co-formers affect the nature of the resulting multi-component materials. The differences, whilst observed primarily in the physicochemical properties, can be attributed to the electron density distribution. Standard resolution crystallography can be supplemented by charge density and computational studies, providing valuable information not available from other techniques. These allow the non-covalent interactions to be compared quantitatively, and linked to the physicochemical properties.

Chapter 4: Novel Co-Crystals of Propyphenazone

This chapter focuses on the design, synthesis and characterisation of co-crystals of propyphenazone. The work in this chapter has been published by Mapp, L.K.; Coles, S.J.; Aitipamula, S. in *CrystGrowthDes.,* 2017, **17,** (1), 163-174.

4.1 Propyphenazone

Propyphenazone (1,5-dimethyl-2-phenyl-4-propan-2-yl-pyrazol-3-one, PROPY) is an API with antipyretic and analgesic effects. It has been marketed as part of the combination drug Saridon,[240] used as a painkiller. The current formulation comprises propyphenazone, paracetamol and caffeine however when first marketed (Roche, 1933) it contained phenacetin and pyrithyldione in place of the now-included paracetamol. The molecular structure (Figure 4.4) contains no donor functional groups for hydrogen bonding and only a single acceptor in the form of the carbonyl, making it unsuitable for synthon-based co-former selection.

4.1.1 Polymorphs of PROPY

Three polymorphs of propyphenazone have been reported by Müller and Beer in 1982[241] with melting points of 104.3 °C, 102.5 °C and 101 °C for forms I, II and III respectively. Form II is the stable form at room temperature with I and III being metastable, and formed from the melt of Form II. Form III only occurs with the other forms rather in isolation.[242] Both metastable forms convert to Form II on storage and heating (Form I) and very quickly during handling (Form III). No further information is available on the relative stabilities and relationships of the three forms.[243] Giron-Forest *et al*.[203] also report the polymorphic behaviour, with DSC analysis showing the melting temperatures of two forms and the complex endothermic behaviours of mixtures of Forms I and II. Note in this study 'Form II' relates to crystalline modification II, which is the higher melting polymorph I. 'Form I' is the stable form and polymorph II as reported by Müller and Beer.

Form II crystallises with two morphologies (needles and plates) depending on the solvent used (polar / non-polar). The properties of the two crystal types were measured by Müller and Beer[241] and it was found that, whilst having a different morphological appearance, they had the same property values hence are not polymorphic forms. Crystal structures of Forms I (P*c*) and II (C*c*) obtained from X-ray powder diffraction data have been reported by Lemmerer *et al.*[242] Form III was only obtained as a minor component alongside the other form(s) and thus no crystal

structure has yet been produced. Although Form II affords two morphologies neither produced good quality crystals (thin, striated plates and needles) and any diffraction produced is unsuitable for structure solution. This was confirmed in this study where the crystals that formed experimentally were found to be multi-crystals comprised of stacked layers. Diffraction was not clean (multi-spots, smeared, or displaying tails on the diffraction spots) indicating the crystal was not single, even when a small fragment was tested, and also too weak for structure solution to be viable. Forms I and II are very similar in their cell parameters and in the primary intermolecular interaction (C–H···O) which occurs between the methyl substituent adjacent to the isopropyl group and the carbonyl of a second molecule. The head to tail stacking arrangement of molecules is similar in both forms however they are situated in different orientations within their respective unit cells. The difference between the forms arises from an offset (by half a unit cell) in Form II between alternate hydrogen bonded layers, leading to a *c*-centred symmetry and accordingly a larger unit cell (doubled *a*-axis length).

4.1.2 PROPY Co-Crystal and Studies on Structurally Similar APIs

Studies involving PROPY include that of the eutectic formation between paracetamol and PROPY (both present in Saridon formulations, reported by two groups, Müller and Beer[241] in 1982 and subsequently by Zalac *et al.*[243] in 1999. The latter describes the formation of a eutectic occurring in combinations containing 30-35 % paracetamol : 60-65 % propyphenazone (w/w), supported by phase diagrams determined from DSC. The eutectic temperature was determined as 56 °C, (T_m 63-65 °C). No chemical interaction between the two materials in the eutectic was indicated in FTIR spectroscopy and a decreased degree of crystallinity was observed in PXRD analysis. This conflicts with the eutectic composition of 65:35 (paracetamol:PROPY) as detailed in the earlier published report. In mixtures of such ratios, Zalac *et al*. found an excess of paracetamol in the diffraction patterns, supporting their reported eutectic composition.

Propyphenazone falls into the group of molecules with limited hydrogen bonding functionality, lacking any donor groups and containing only one acceptor atom. In addition, the presence of an isopropyl group next to the carbonyl group (Figure 4.4) creates steric hindrance restricting access of larger, or more bulky molecules and limiting the geometric possibilities of potential intermolecular interactions. One co-crystal has been reported[242, 244] containing pyrithyldione (a component of the early Saridon formulations) producing a drug-drug co-crystal. The co-crystal involves a single N–H···$O_{carbonyl}$ hydrogen bond to PROPY with additional C–H···O contacts from CH_3 and aromatic C–H groups. This indicates the potential of PROPY to form co-crystals and makes it a realistic and appropriate probe for a co-crystal study. In particular, as an example of an API with limited potential for forming intermolecular interactions.

Examples of some APIs that are similarly devoid of such donor functionalities, and for which co-crystal studies were undertaken, include griseofulvin,[245] spironolactone,[246] artemisinin[247] and iloperidone.[248] Co-former selection was primarily based on trial and error, as there is no clearly-defined methodology for such systems. Extensive co-crystal screening produced limited success; both griseofulvin and spironolactone produced one co-crystal, iloperidone formed three and artemisinin produced just two despite having some knowledge from the prediction method of Fábián[249] introduced to aid co-former choice. These predictions for artemisinin indicated 41 co-formers had potential to generate a new co-crystal, yet only two co-crystals were generated. This indicates that the molecular descriptor-based method is, as yet, perhaps not best suited to co-crystal design for such molecules (devoid of substantial hydrogen bonding functionality).

An alternative prediction method (to those aforementioned and described in Chapter 1.3.4) is to use a knowledge-based approach. A wealth of information is encompassed within the crystal structures deposited in the CSD[18] and the various software components provided by the CCDC permit its interrogation. These provide interaction and fragment searching using Isostar[250] and Conquest[106] as well as full interaction mapping and contact searching with specific interaction motifs in Mercury.[107, 108] Many of these software programs allow easy modification and variation of the environment, with the inclusion and adjustment of system and fragment constraints to best describe the chemical space of interest. Hence, it is possible to see how certain changes can affect the interaction or behaviour of a functional group. PROPY provides an appropriate case study for such an approach.

4.2 Design of Co-Crystals

4.2.1 Interaction Searching for Preferences of the Carbonyl Group

The CSD was interrogated to identify the potential interactions that could occur for PROPY and thereby aid in the selection of likely co-formers for subsequent co-crystal screening. It should be noted that a single acceptor may lack selectivity and any donor if present can, and may, interact.[2] This is, however, less applicable to PROPY due to the steric hindrance present which is expected to restrict the donor types plausible for interactions at this site. In accordance with Infantes and Motherwell,[102] and their analysis of the CSD, a carbonyl acceptor group has an average of 0.59 acceptor contacts in a crystal structure. This shows that the carbonyl, whilst being the only acceptor atom present in PROPY, does not always readily form a contact. Intermolecular contacts do not always occur as intramolecular interactions take preference over intermolecular ones.

PROPY does not possess sufficient functionality for strong intramolecular contacts therefore this should not influence predicted interactions or the synthetic outcomes.

4.2.1.1 Isostar Search for Carbonyl Interactions

Isostar[250] is a knowledge base from the CSD containing information about intermolecular interactions. These are divided according to central and contact groups of which there are over 300 and approximately 60 respectively. This analysis considers functional group interactions, rather than whole molecules, however provides a useful starting point to assess differing interactions that may occur. These interactions can also be represented in 3D to show the spatial arrangement for each structure containing the interaction in the CSD.

Donor groups of the types $–CO_2H$, O–H, $–NH_2$ and N–H (which encompass more specific functionalities such as amides, imides and ring systems) were used to search for contacts to a carbonyl group. This provides a constructive overview to determine which donors form interactions repeatedly. Compounds containing aromatic amines, aliphatic hydroxyls or carboxylic acids were found to be the most recurrent structures forming an interaction to a carbonyl group, followed by aromatic hydroxyls (Figure 4.1). This indicates these are the most likely functional groups to form an interaction with PROPY and provides a starting point for co-former selection.

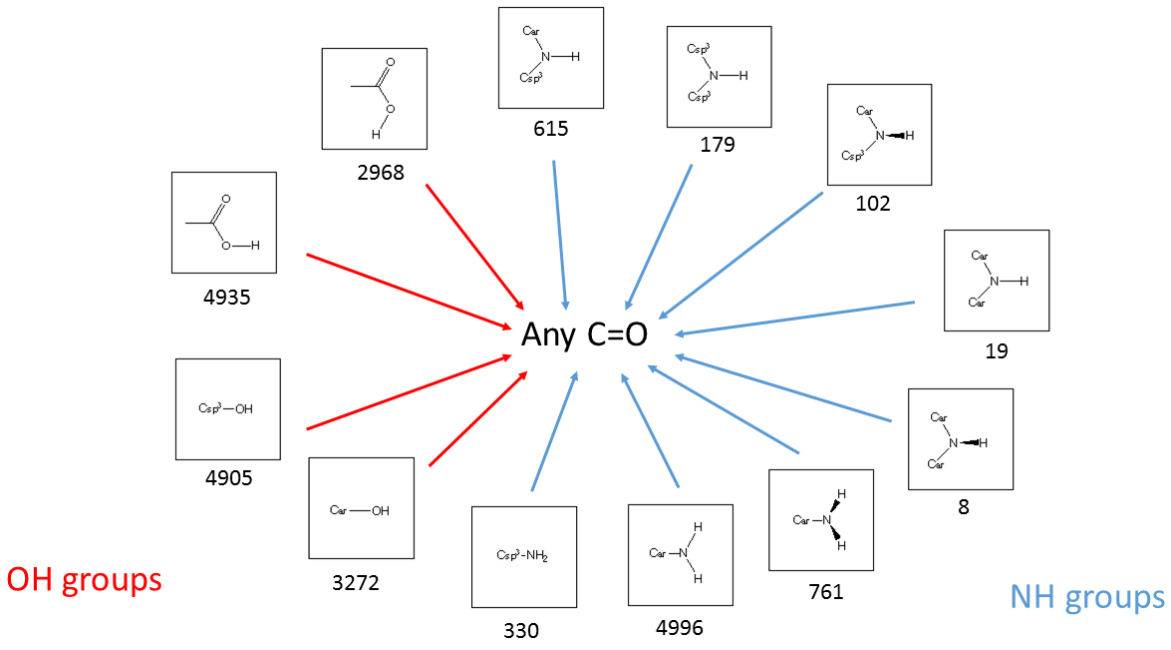

Figure 4.1. Schematic showing the differing donor functional groups implemented in the Isostar search. The number of structures which contain an interaction to a carbonyl is indicated below each.

4.2.1.2 Mercury Motif Searching for Specific Contacts

Greater flexibility and specificity in the description of the donor groups/fragments is facilitated in the searching in Mercury.[108] Very few examples of structures containing a carbonyl in a similar fragments as that in PROPY exist in the CSD. A number of models were thus employed (Figure 4.2) each with a modified carbonyl environment to be less specific to that of the carbonyl in PROPY. This was to achieve a balance of both describing the chemical environment and neighbouring atoms to reflect that of the carbonyl in PROPY, whilst also ensuring sufficient hits were returned to allow reliable conclusions to be drawn. The use of multiple models allowed a broader set of results to be generated and thus better statistics achieved; the analysis can be deemed more reliable as it is taken from a greater subset. The Supplementary File 'Specific Contact Searching' provides details of the searches carried out.

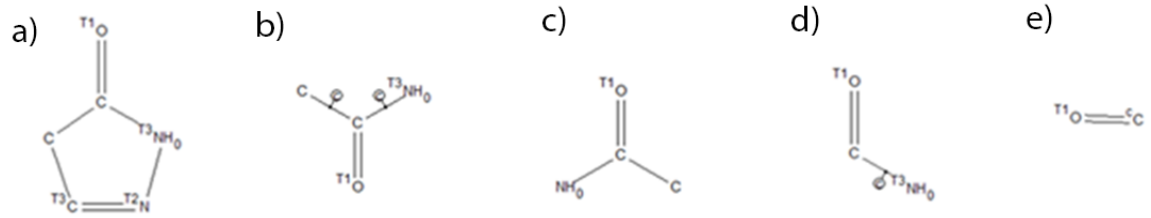

Figure 4.2. Fragments used for interaction searching in Mercury with decreasing environmental and chemical constraints for the carbonyl group traversing from a) to e).

The most representative model for the carbonyl group in PROPY is the pyrazolone ring (Figure 4.2, model a) and returned limited results with few structures to learn from. Subsequent fragments with fewer constraints returned a greater number of structures from the searches. A variety of donor groups (Table 4.1) and descriptions thereof (kept consistent for all searches) were used to provide a more detailed understanding of not only the functional groups but also their chemical environment.

Table 4.4.1. Results from interaction searching with five different carbonyl models (with reduced restraints and specificity left to right) across the top and descriptions of the 11 donor groups down the left-hand side.

	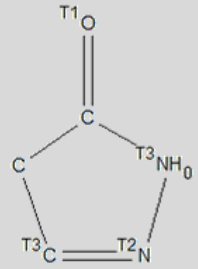		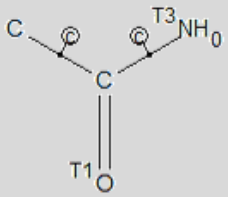		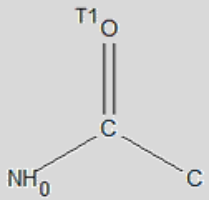		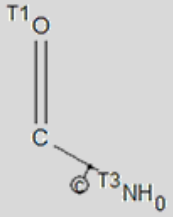		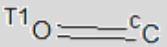	
Donor	No. structures	% Frequency	No. structures	% Frequency	No. structures	% Frequency	No. structures	% Frequency	No. structures	% Frequency
$T3NH_2$	15	45.5	529	47.3	771	49.6	1009	52.6	3302	58.6
$T3NH_1$_cyclic	14	34.1	1234	35.6	1589	37.2	2512	40.0	11708	56.1
$T3NH_1$_acyclic	18	8.5	740	28.7	1343	31.3	918	29.9	2271	31.9
$T3NH_1$	32	13.0	1967	34.2	2918	36.0	3412	38.3	14580	52.3
$T2NH_1$	0	0	0	0	1	33.3	8	16.7	20	14.7

Donor	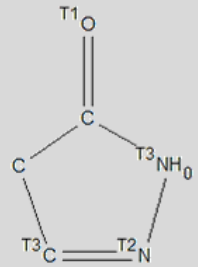		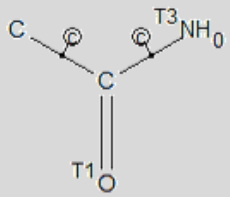		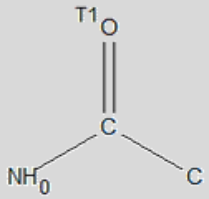		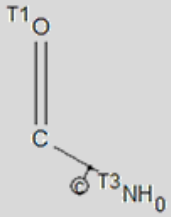		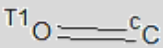	
	No. structures	% Frequency	No. structures	% Frequency	No. structures	% Frequency	No. structures	% Frequency	No. structures	% Frequency
CO_2H	1	20.0	282	29.7	389	30.9	354	30.2	1653	32.2
CO_2H_aliphatic	0	0	196	34.4	271	33.2	254	35.4	995	40.6
CO_2H_aromatic	1	50.0	68	24.3	94	28.6	77	23.8	386	30.9
OH_general	21	31.3	2571	49.4	3463	49.8	3379	48.4	14175	51.9
OH_cyclic	10	25.6	1378	51.0	1755	51.4	1782	48.4	8775	50.2
OH_acyclic	11	35.5	1227	41.6	1750	42.8	1661	39.0	5802	43.7

The most favoured donor type was found to be $–NH_2$ the however no regard to sterics is given. When considering PROPY, this may have an impact due to the isopropyl substituent in close proximity to the carbonyl. In many of the searches the statistics for $–NH_2$ groups presented as similar to hydroxyl donors. Hydroxyl groups contain less steric bulk and have a more linear arrangement hence it may be postulated that they could be favoured over a primary amine group in situations where sterics dominate. Hydroxyl groups are seen to be favoured over carboxylic acids and within these cyclic acids are preferential to acyclic. For hydroxyls, the same is seen whereby cyclic hydroxyls indicate a slight preference for interactions than their acyclic counterparts. The hydroxyl group results may contain some misrepresentation, however, as all $–CO_2H$ containing molecules will be present in the results from a general hydroxyl search. The carboxylic acid groups may not form an interaction due to the greater steric bulk of the carbonyl. Hence, O–H interaction frequencies may appear lower than they perhaps should be.

Cyclic N–H donors provide the third most favourable group (after $–NH_2$ and O–H) for forming an interaction to a carbonyl, however interactions to an acyclic N–H are less common. The least likely donor group of those tested is N–H with two bonded atoms (i.e. one double bond or delocalised aromatic system).

With reduced constraints on the model of the carbonyl fragment $–NH_2$ donors appear the most favourable and there is greater separation between the hydroxyl group results. Concurrently, carboxylic acids also become more favourable, which would indicate that less specific environments with fewer restraints favour the larger, bulkier donor groups.

4.2.1.3 Full Interaction Mapping for Preferred Location of Interactions to PROPY

The full interaction mapping (FIM) tool in Mercury[108] furthers the information obtained from Isostar, and allows molecules in their entirety to be considered. Isostar scatter plots containing interaction information and relative arrangements for each fragment of a molecule are combined into scaled density maps, with environmental effects, steric exclusion and combinative factors accounted for. This allows the generation of a map around the molecule of interest containing contoured surfaces to indicate the likelihood of an interaction at a certain point.[251] Opacity of the surfaces allows all contour surfaces to be visualised at once, the highest contour levels are depicted as the most opaque. Hotspots can also be generated showing the highest densities of interactions, and hence the preferred geometries of such groups and interactions.

FIMs was implemented to identify areas around the PROPY molecule where a donor would be most likely to be located when forming an interaction, and a number of different donor groups (types of O–H and $–NH_2$) were employed. As well as locating all potential areas for donor

molecules, hotspots indicating the most likely point surrounding the molecule for a donor were also generated. These provide an idea of how potential co-formers may arrange themselves with respect to PROPY (Figure 4.3), and give a visual indication (with respect to the PROPY structure) whether a co-crystal may be viable. These maps can be compared to the previously reported co-crystal, and also to any new structures subsequently identified. All maps, broken down by probe type can be found in Appendix A.1.1 along with alternate views of the hotspot analysis.

As might be expected, the typical hydrogen bond donor groups (alcohol O–H and N–H) favour positions around the carbonyl functionality. N–H groups are contained within a more restricted area in comparison to O–H. This supports some of the previous findings: O–H groups may be preferential in a hindered environment due to their linear geometry and smaller molecular size. Carbonyl groups are seen only around the phenyl ring where they can partake in π-π interactions. Water can act as both a donor (O–H) and acceptor (O) and therefore has a larger area in which it can locate and interact favourably. This is seen around the alkyl substituents and general framework of the molecule (Figure 4.3, green).

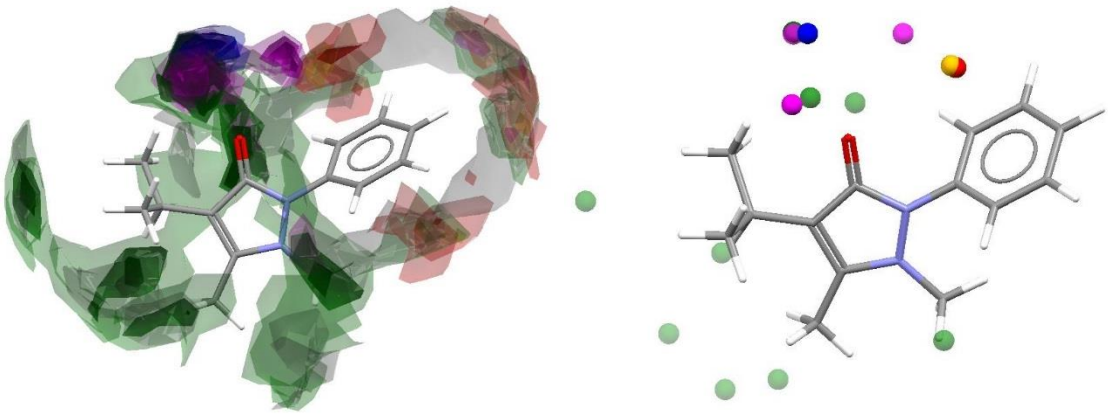

Figure 4.3. Map showing areas of potential interactions (left) and hotspots (right) for PROPY with a selection of different probes: N–H (uncharged) blue, O–H (alcohol) magenta, water green, aromatic C–H red, methyl carbon yellow and C=O grey. Opacity indicates the propensity of interactions; the highest opacity indicates the highest density and hence frequency of interactions.

4.2.2 Analysis of Structurally Related Molecules and Their Co-Crystals

PROPY shows structural similarity to two other compounds, antipyrine and edaravone, which contain the same molecular skeleton (phenylpyrazole). However, PROPY contains an adjacent isopropyl substituent at the carbonyl causing steric hindrance (Figure 4.4).

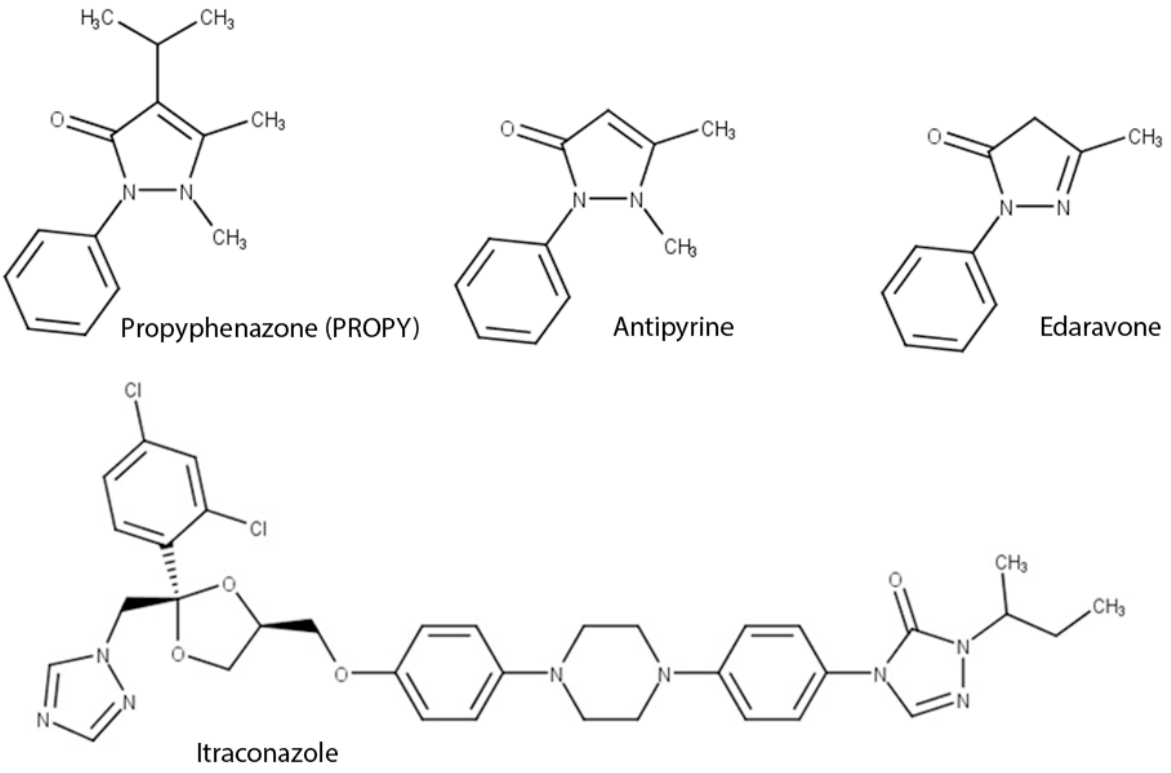

Figure 4.4. Molecular structures of propyphenazone, antipyrine, edaravone and itraconazole.

A number of multi-component systems[252-259] have been reported for antipyrine and edaravone, from which additional knowledge can be gained and used in the design and synthesis of co crystals of PROPY. An analysis of these systems indicates that most of the co-formers feature CO_2H donor groups. Structural analysis of the antipyrine co-crystals revealed that the main interactions of the carbonyl group occur predominantly from $–NH_2$ or $–CO_2H$ donor groups. This structural analysis reinforces the CSD interaction search results for PROPY and further aids in co-former selection.

Itraconazole is another similar compound to PROPY as it contains no donor groups, only acceptors (Figure 4.4, bottom). A carbonyl group in a similar environment to that of PROPY is present and experiences some steric hindrance from the adjacent 2-butyl group and phenyl ring. A number of co-crystals and two HCl salts have been synthesised.[260-263] Interestingly, all of these materials contain a dicarboxylic acid co-former, however it is the triazole ring (ar_N) with which they form an interaction, rather than the carbonyl. This indicates that hydrogen bonding to a sterically hindered carbonyl is unfavourable and if other options are available they will be preferential.

4.2.3 Co-Former Selection and Screening Approach

A variety of co-formers (Appendix A.2) containing the main functional groups identified in the CSD analyses, either in isolation or in various combinations, were selected for screening experiments. Also included were some co-formers either totally lacking in the identified functional groups, or including additional alternative ones. These acted as a control and therefore allowed investigation of the suitability of a knowledge-based prediction.

Solvent drop and neat grinding methods[122, 124, 264] were applied to the selected parent–co-former combinations and the resulting materials analysed by PXRD. The powder patterns were compared to reference data for the constituent materials to identify those which were sufficiently different and indicative of a new form. This directed subsequent experiments, focussing on promising systems only. Solution crystallisation methods were used to produce single crystals suitable for diffraction studies and crystal structure determination.

A number of combinations produced powders from grinding for which the PXRD patterns were different from those of the parent materials (Appendix A.3). These included six co-formers (given in Figure 4.7) for which single crystals were obtained (*vide infra)* and are presented with structural analyses in Section 4.3. There were also several samples which showed promise in the grinding material analysis (Appendix A.3.2) but no single crystals have yet been produced. These co-former structures for these are shown in Figure 4.5.

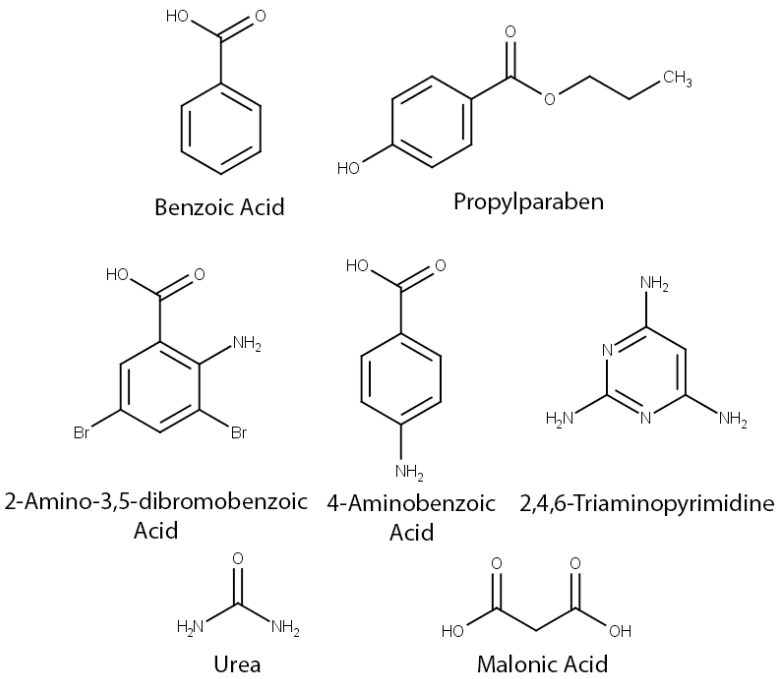

Figure 4.5. Co-former structures that indicated promise when combined with PROPY in grinding experiments.

Due to the low melting point of PROPY (~100 °C), some difficulties were encountered in screening. Several combinations resulted in a sticky paste, gel or liquid on grinding which could not be characterised by PXRD. Subsequent dry (neat) and manual grinding approaches were attempted with varying quantities of initial powders however many of these also resulted in pastes and liquids; characterisation was not viable. Figure 4.6 displays the structure of these co-formers, a number of which are similar to the co-formers in the successful co-crystals generated. For example, salicylic acid forms a co-crystal with antipyrine (PROPY equivalent lacking the isopropyl substituent), ethylparaben contains only one extra carbon in the alkyl chain relative to the successful methylparaben, and resorcinol is related to hydroquinone and phloroglucinol both of which gave new co-crystals. It is therefore a reasonable expectation that combinations may produce a new co-crystal under different, as yet untested, conditions.

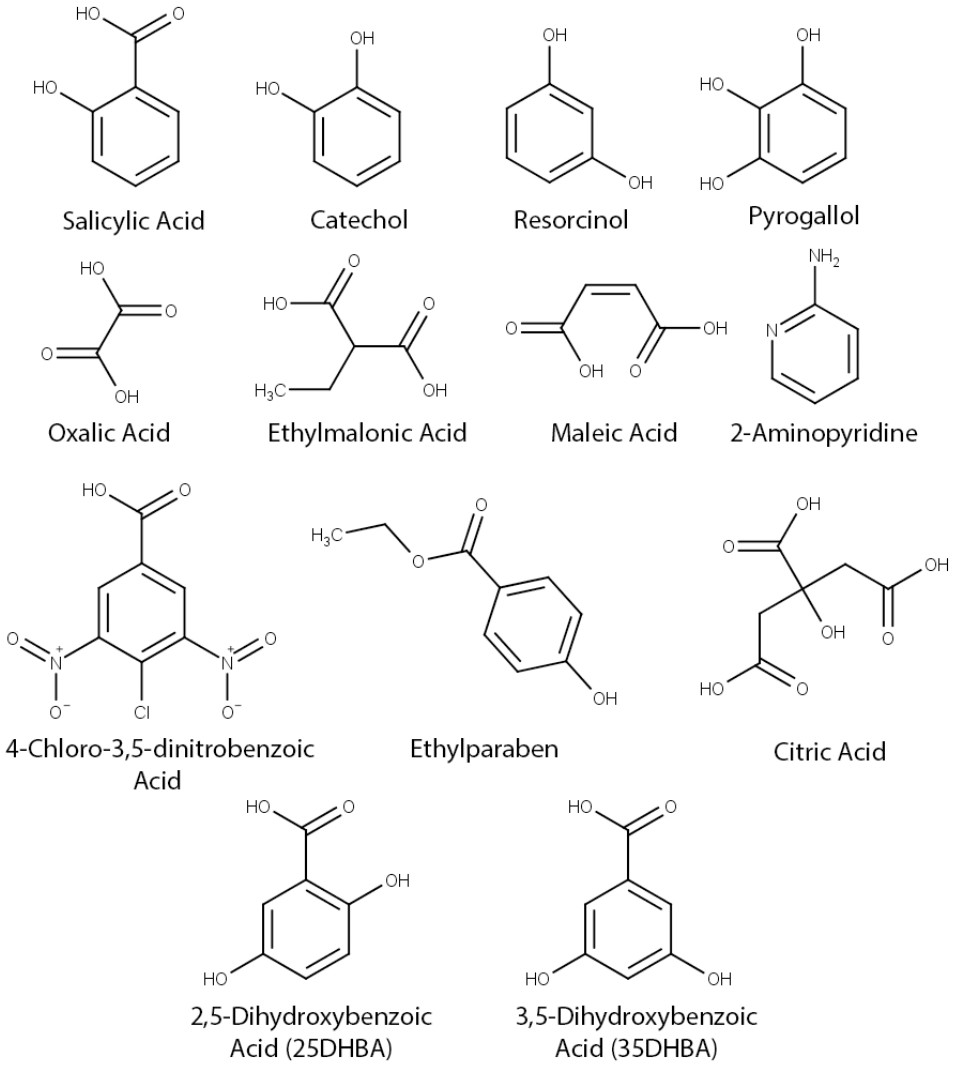

Figure 4.6. Structure of co-formers which produced a liquid, paste or gel in grinding experiments for which PXRD analysis was not viable.

Solution crystallisation experiments were attempted for some of these combinations and two co-formers, 2,5-dihydroxybenzoic acid and its 3,5-disubstituted analogue, produced single crystals suitable for characterisation and subsequent analysis.

4.2.4 Application of the Molecular Complementarity (QSAR) Prediction Method

The prediction methodology of Fábián[249] (Section 1.3.4.2) was applied to a selection of co-formers to compare to experimental findings. Mercury CSD-Materials suite[106-108] was used to generate descriptor values for the co-former molecules which were compared with the equivalent data for PROPY. Using the cut off values implemented by Fábián it could be determined whether a given pairing was likely to produce a co-crystal.

The predictions, along with experimental findings are detailed in Appendix A.4. Not all co-formers included in the predictions were tested experimentally due to restrictions such as access to, and availability of, chemicals. All the predictions can provide useful information, and be used to inform about structurally related compounds and how they may be expected to act. The eight co-formers that formed co-crystals (Figure 4.7) fall into both the pass and fail prediction lists in an almost equal distribution. Similarly, combinations from screening that indicated potential for a new form, and those which showed no changes when compared to the parent reference materials, are spread across both groups of predictions. The prediction model is hence not best suited to this class of compounds i.e. those with minimal, or no, hydrogen bonding functionalities.

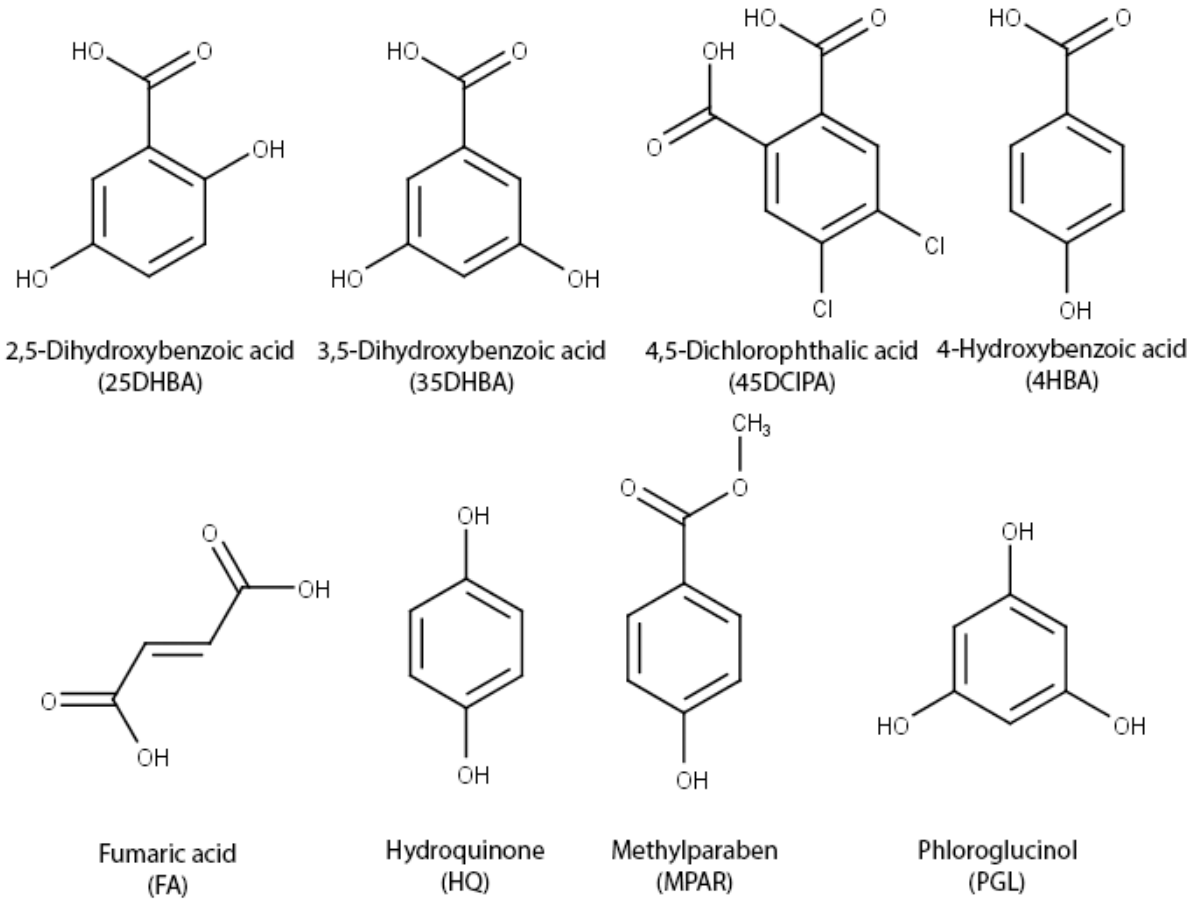

Figure 4.7. Molecular structures of co-formers which produced co-crystals with PROPY.

4.3 Structural Analysis of the Novel Co-crystals

Eight co-crystals were successfully synthesised in this study with the co-formers depicted in Figure 4.7. Combinations with 2,5-dihydroxybenzoic acid and 3,5-dihydroxybenzoic acid were not realised in initial screening by grinding due to the generation of sticky materials on every attempt. These two systems were only identified as successful through solution methods.

Two co-crystals form as solvates (those with phloroglucinol and 2,5-dihydroxybenzoic acid) and all but three co-crystal materials form in a 1:1 stoichiometric ratio. The exceptions are hydroquinone (1:2), fumaric acid (1:0.5) and 2,5-dihydroxybenzoic acid (2:1). Crystallographic information is shown in Appendix A.5 with full hydrogen bond information in Appendix A.6.

The crystal structures can be classified into three groups according to the co-former functional group(s) and the interactions exhibited:

- Co-formers containing only hydroxyl donor functionalities, forming a hydroxyl···carbonyl hydrogen bond.

- Co-formers containing only carboxylic acid donor functionalities, forming an acid···carbonyl hydrogen bond.
- Co-formers which possess both hydroxyl and carboxylic acid functional groups and form hydroxyl···carbonyl hydrogen bond.

4.3.1 Analysis of Co-Crystals Containing a Hydroxyl Functional Group

Three co-crystals were obtained with co-formers containing only O–H functional groups: hydroquinone (HQ), methylparaben (MPAR) and phloroglucinol (PGL).

4.3.1.1 PROPY-MPAR (1:1) co-crystal

The 1:1 PROPY-MPAR co-crystal crystallises in the orthorhombic space group $P2_12_12_1$ containing one of each molecule in the asymmetric unit. The assembly is based primarily on a bifurcated hydrogen bonding system, consisting of an O–H···$O_{carbonyl}$ (D···A distance 2.63 Å, D–H···A angle 174°) and a C–H···O (3.19 Å, 126°) hydrogen bond from the co-former to the PROPY carbonyl. Two further C–H···O interactions occur from a second molecule of PROPY to the carbonyl of methylparaben, generating a puckered hydrogen bonded chain (Figure 4.8). These chains occur in two orientations, each stacking into layers which run approximately along, and parallel to, the (1 0 0) plane. When viewed down the *b*-axis these can be seen as double layers propagating along the *a*-axis.

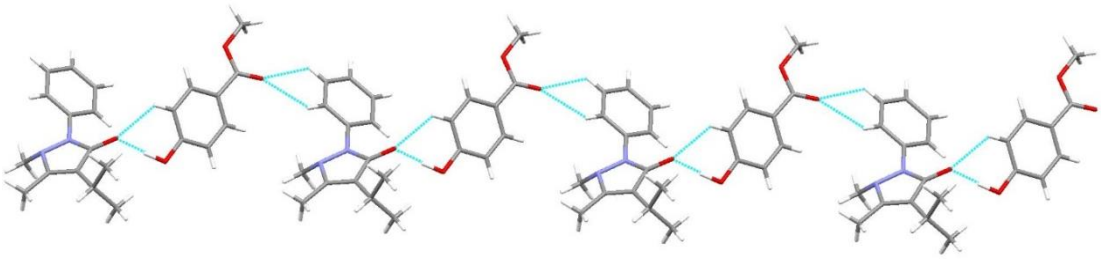

Figure 4.8. Crystal structure of PROPY-MPAR 1:1 co-crystal displaying the main hydrogen bonding chain.

4.3.1.2 PROPY-PGL acetonitrile (2:2:1) solvate

Phloroglucinol forms a co-crystal solvate (acetonitrile) with a 2:2:1 ratio (PROPY-PGL·0.5ACN) which crystallises in the monoclinic space group $P2_1/n$. The asymmetric unit contains two molecules of each of the co-former and API, along with one acetonitrile solvent molecule. The primary interaction between the co-former and PROPY is an O–H···$O_{carbonyl}$ hydrogen bonds (2.63 Å and 2.74 Å, both 169°, one hydrogen bond between each PROPY-PGL set). A bifurcated interaction to the carbonyl forms from a co-former molecule in a second set *via* a similar

O–H···$O_{carbonyl}$ hydrogen bond (2.63 Å, 168° and 2.66 Å, 176°). The two molecules of PGL are not equivalent, as one partakes in three O–H···$O_{carbonyl}$ hydrogen bonds to PROPY and the other forms one O–H···$O_{carbonyl}$ to PROPY, one O–H···$O_{hydroxyl}$ to the first PGL and an O–H···N hydrogen bond to the solvent molecule. These hydrogen bonds form a chain containing central PGL molecules, which extend into sheets *via* the bifurcated carbonyl hydrogen bonds to the second PROPY molecule. The sheets stack in layers with alternating orientations as shown in Figure 4.9.

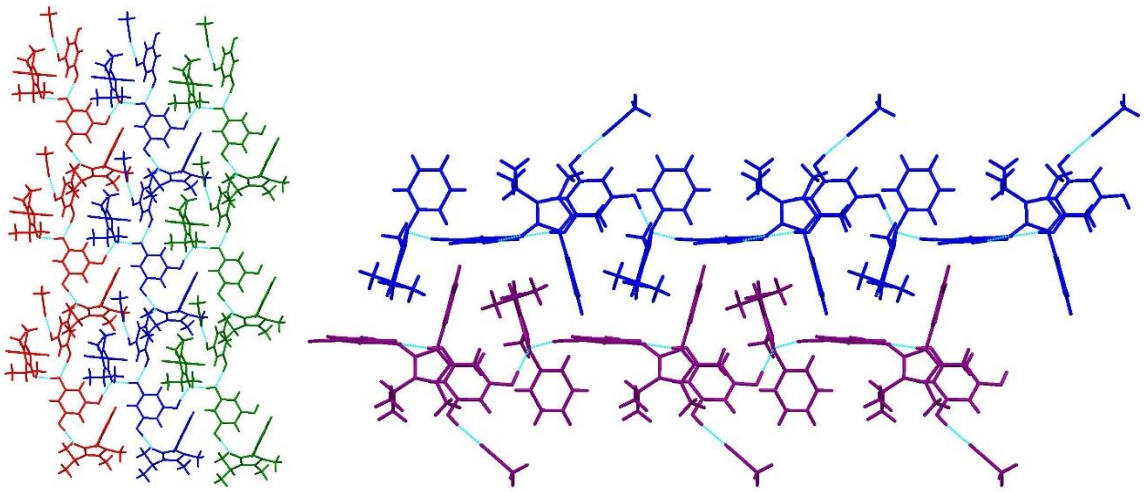

Figure 4.9. PROPY-PGL·0.5ACN co-crystal chains forming sheets (coloured, left) which stack into layers (right) where a single coloured layer (blue / purple) represents the red-blue-green sheet on the left.

4.3.1.3 PROPY-HQ (1:2) co-crystal

PROPY forms a 1:2 complex with HQ which crystallises in space group $P\bar{1}$, containing one molecule of PROPY and two of HQ in the asymmetric unit. The two HQ molecules each form a single O–H···$O_{carbonyl}$ hydrogen bond from one hydroxyl functionality to the PROPY (2.69 Å, 172° and 2.57 Å, 175°) resulting in an approximately perpendicular arrangement of the two co-former molecules. These 2:1 units extend into double layer corrugated chains *via* O–H···$O_{hydroxyl}$ hydrogen bonds between the HQ molecules (Figure 4.10). The chains propagate throughout the structure to give double layers running perpendicular to the *a*-axis.

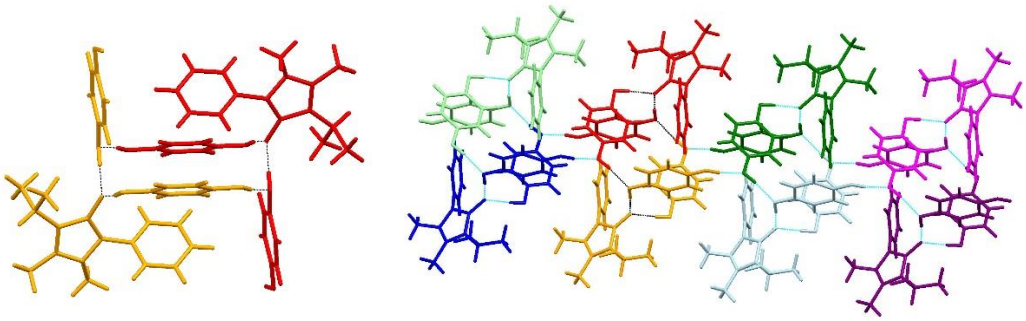

Figure 4.10. Double chain structure viewed down the chain (left) and side-on, coloured by 2:1 units (right) in the crystal structure of PROPY-HQ 1:2 co-crystal.

4.3.2 Analysis of Co-Crystals Containing a Carboxylic Acid Functional Group

Two co-crystals were obtained with co-formers containing only a carboxylic acid functional group in the molecule. These were with fumaric acid (FA) and 4,5-dichlorophthalic acid (45DClPA).

4.3.2.1 PROPY-FA (1:0.5) co-crystal

Fumaric acid forms a 1:0.5 ratio co-crystal with PROPY crystallising in the $P\bar{1}$ triclinic space group. The asymmetric unit contains one molecule of PROPY and half a molecule of FA which lies on the inversion centre. A single carboxylic acid O–H···$O_{carbonyl}$ hydrogen bond (2.57 Å, 170°) occurs between the two components, which is mirrored at the other end of the FA molecule *via* the inversion centre. These 2:1 units form a number of aromatic C–H···O contacts which result in a stepped motif in which the PROPY phenyl rings are arranged in an offset face-to-face configuration with respect to each other (Figure 4.11). These stepped chains pack into layers along the *a*-axis to give the three-dimensional crystal structure.

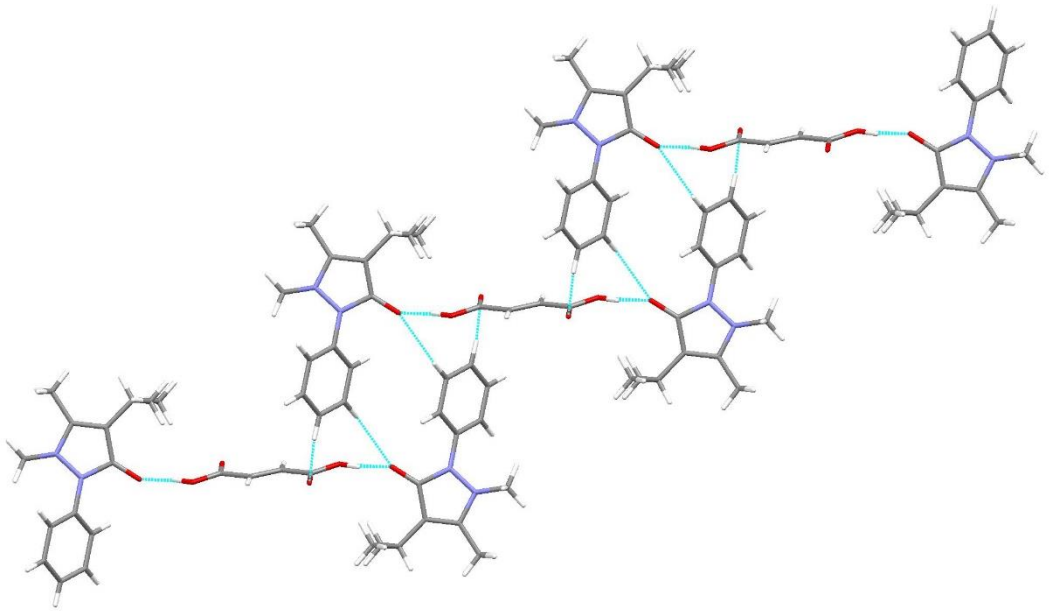

Figure 4.11. Stepped arrangement of 2:1 PROPY-FA co-crystal containing molecules related by inversion.

4.3.2.2 PROPY-45DClPA (1:1) co-crystal

A 1:1 co-crystal forms with the co-former 4,5-dichlorophthalic acid which crystallises in the orthorhombic space group *Pbca*. PROPY displays a bifurcated hydrogen bonding pattern through the carbonyl, with interactions from carboxylic acid groups of two independent co-former molecules; $O–H_{carboxylic\ acid}\cdots O_{carbonyl}$ hydrogen bonds (2.58 Å, 173° and 2.64 Å, 177°). These interactions form a chain (Figure 4.12) which are composed of double layers which stack along the *a*- and *b*-axes. An alternating motif is formed through layers related by a glide plane.

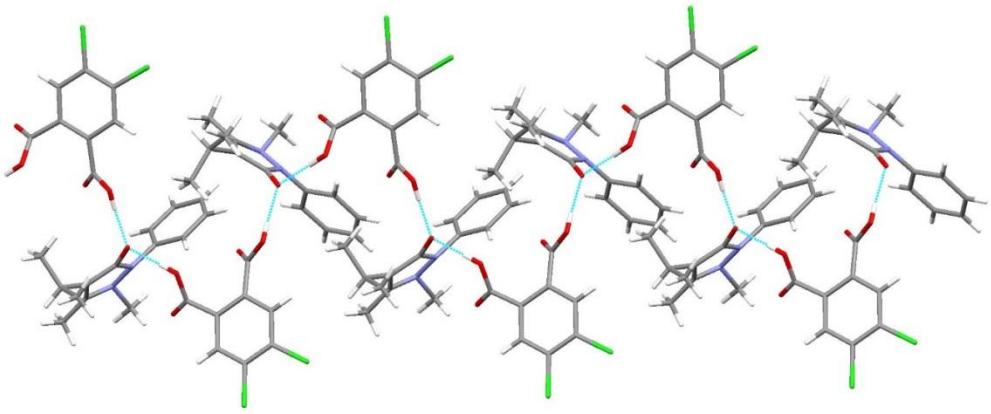

Figure 4.12. A hydrogen bonded chain in the 1:1 PROPY-45DClPA co-crystal.

4.3.3 Analysis of Co-Crystals Containing both Carboxylic Acid and Hydroxyl Functional Groups

Three co-crystals were obtained with co-formers containing both a carboxylic acid and at least one hydroxyl functional group. These were 4-hydroxybenzoic acid (4HBA), 2,5-dihydroxybenzoic acid (25DHBA) and 3,5-dihydroxybenzoic acid (35DHBA).

4.3.3.1 PROPY-4HBA (1:1) co-crystal

4-Hydroxybenzoic acid forms a 1:1 co-crystal with PROPY, crystallising in the monoclinic space group $P2_1/c$. One molecule of each component is present in the asymmetric unit and form an O–H···$O_{carbonyl}$ hydrogen bond (2.67 Å, 178°) *via* the hydroxyl functionality. Additional hydrogen bonds occur from the carboxylic acid of the co-former generating a carboxylic acid dimer with a second pair of PROPY-4HBA molecules. These 4-molecule assemblies form C–H···O interactions and stack to produce a ladder network of tapes. These consist of a central co-former dimer with peripheral PROPY molecules (Figure 4.13). The ladders have two orientations in the crystal structure, related by 45°, and pack with a square 'box' arrangement (Figure 4.13, bottom).

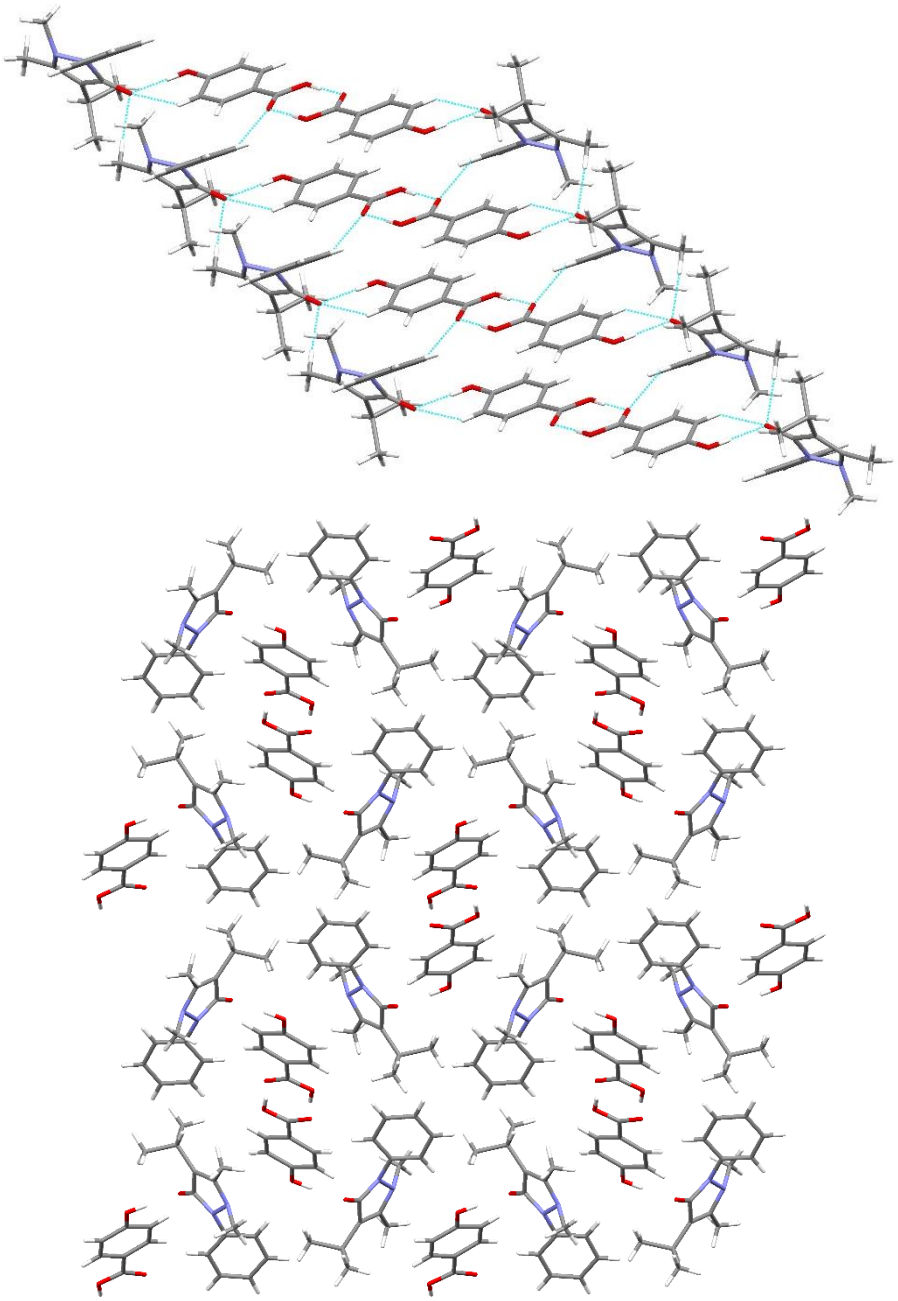

Figure 4.13. Main interactions in the 1:1 PROPY-4HBA co-crystal showing ladder formation (top) and packing viewed down *a*-axis (below).

4.3.3.2 PROPY-35DHBA (1:1) co-crystal

PROPY-35DHBA forms a 1:1 structure in the triclinic space group $P\overline{1}$ and contains four molecules of each component in the asymmetric unit. The primary interaction is an O–H···$O_{carbonyl}$ hydrogen bond occurring from a co-former hydroxyl group. This occurs twice from each molecule of 35DHBA to two independent PROPY molecules (2.63-2.74 Å, 171-177°). Co-former···co-former interactions occur to create a carboxylic acid dimer in the centre of the main structural motif (Figure 4.14, top). This dimer displays disorder of the hydrogen atom, with each hydrogen

displaying two positions and an occupancy of 0.5 at each. The remainder of the structure is free from disorder.

The aforementioned interactions form a 6-membered motif with a central co-former dimer and four surrounding PROPY molecules situated in opposite orientations on each side of the dimer (Figure 4.14, top) Two further co-formers form O–H···$O_{carbonyl}$ hydrogen bonds *via* a hydroxyl group with diagonally opposite PROPY molecules of the assembly. The 35DHBA molecules are located above and below the dimer on alternate sides. The dimer-containing chains stack in layers parallel to the co-former dimer plane, and interlock perpendicular to the plane with the additional co-former molecules. A further dimer interaction is seen between these perpendicular molecules aiding the packing of these chains and giving a stepped packing arrangement (Figure 4.14, bottom).

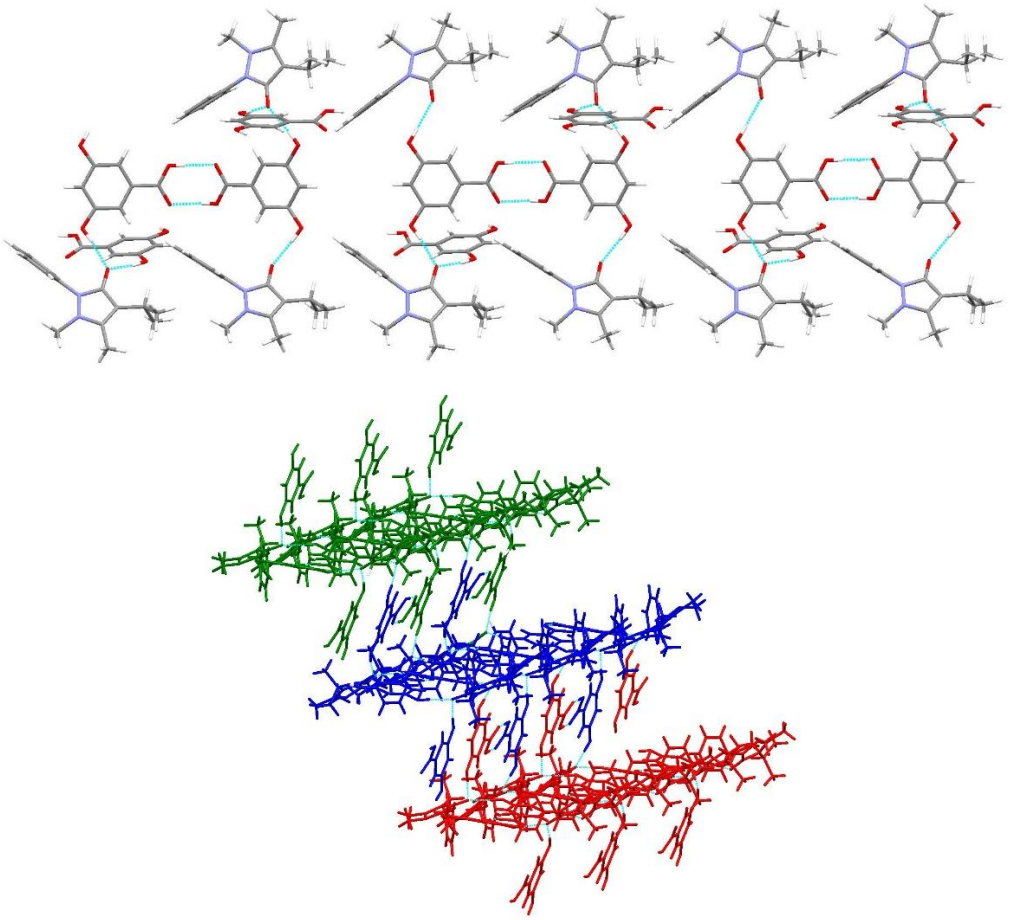

Figure 4.14. Interactions in the PROPY-35DHBA co-crystal displaying chains of 6-component motif layers (top) and interlocking of chains *via* a second hydrogen bonded dimer in stepped packing arrangement (below), showing the protons of one disorder component only.

4.3.3.3 PROPY-25DHBA (2:1) 1,4-dioxane solvate

PROPY-25DHBA forms a 2:1 ratio co-crystal solvate structure which crystallises in the monoclinic $P2_1/c$ space group. The asymmetric unit consists of one 25DHBA and two PROPY molecules (Figure 4.15). The 25DHBA is disordered over two positions, with an approximate ratio of 65:35. The solvent (1,4-dioxane) is located in voids in which it tumbles around freely. Electron density can be identified in the structure solution, visible as almost spherical areas of density generated from the tumbling hexagonal molecules. This indicates multiple positions of the solvent molecules within these voids and no suitable model for this can be employed to improve the structure or add any chemical information. By using the solvent masking routine in Olex2[265] and the SQUEEZE[266] algorithm implemented in PLATON[267, 268] it can be proposed that there is one molecule of solvent per asymmetric unit (4 per unit cell). Two void locations were found, each with 123 electrons which indicates a 2:1:1 ratio. TGA was also carried out to aid in the sample nature determination (Appendix A.9.2). This suggests a 2:1:0.5 ratio as a mass loss representative of 0.5 equivalents of 1,4-dioxane solvent is observed in the expected temperature range. This difference could be explained by a single 1,4-dioxane molecule in half of the voids, and in multiple positions within the void (free to move in the given space). Alternatively, during storage between SCXRD data collection and TGA analysis solvent loss may have occurred (the stability is known to be poor and initial breakdown likely to occur as a result of solvent loss).

The main interactions present are an $O–H_{hydroxyl}\cdots O_{carbonyl}$ (2.63 Å, 170°) and an $O–H_{carboxylic\ acid}\cdots O_{carbonyl}$ (2.55 Å, 164°) hydrogen bond from the hydroxyl and carboxylic acid respectively of a single co-former, occurring to the two independent PROPY molecules (Figure 4.15, top). $C–H\cdots O_{hydroxyl}$ contacts from the PROPY isopropyl group extend these 2:1 units into staggered chains throughout the lattice (Figure 4.15, bottom).

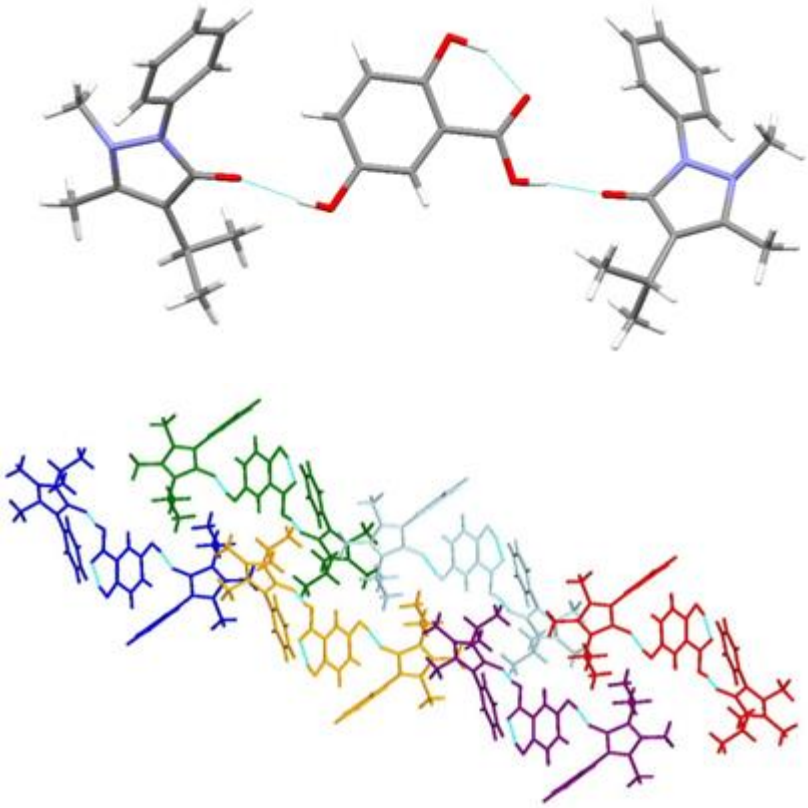

Figure 4.15. Interactions in the crystal structure of PROPY-25DHBA 2:1 1,4-dioxane solvate (above) and chains of staggered 2:1 units (below). Only the major component of the disordered co-former molecule is shown for clarity and no solvent displayed.

4.3.4 Hirshfeld Surface Analysis

Hirshfeld surfaces[192-196] can help to provide an insight into the intermolecular contacts and packing in the crystal structures. Crystal Explorer[180] was used to calculate these for PROPY and all the co-crystals, a single surface modelled for each individual component in a system as well as one encompassing the whole construct. This allows for comparisons between fingerprint plots of specific components in different systems to be made.

An example of interpreting the location of different contact types in a fingerprint plot is given in Appendix A.7.2.

Fingerprint plots of the Hirshfeld surface for the PROPY molecule in each system are shown in Figure 4.16. Where more than one discrete molecule of PROPY is present, a surface was generated for each individual entity. Hirshfeld surface images are displayed in Appendix A.7.1. There are some clear differences in the fingerprint plots of the different co-crystal systems, however they do have a number of similar features. The differences show the influence of the co-former in each system and the way they dictate the interactions occurring to PROPY.

Some similarities include a 'tail' formed from short d_e distances with relatively short d_i. This represents an O···H contact. As detailed in the crystal structure analysis, all systems display either an acid···carbonyl or, more commonly, hydroxyl···carbonyl hydrogen bond as the primary interaction between the two components. Hence, short contact distances for an $O_{inside}\cdots H_{outisde}$ contact for all co-crystals would be expected. With the exception of that for PROPY, all the fingerprint plots display the shortest contact having distance d_e ~0.6 Å and d_i ~1.0 Å and corresponding to an O···H contact.

O···H contacts originate from O-H···$O_{carbonyl}$ hydrogen bonds from either the hydroxyl (in the majority of structures), or carboxylic acid of the co-former. The relative proportion of these in the total interactions is similar in all systems at 4.3-6 % (interaction contribution data and charts are presented in Appendix A.7.3 and Supplementary File 'Hirshfeld Surfaces-Interaction Contributions Analysis'). The reciprocal H···O contacts, however, vary considerably in their contribution between systems and are dependent on the number, and relative positioning, of oxygen atoms in the co-former. Contribution values range from just 3.5 % in PROPY, to mid-range values of 7.8 % and 7.9 % (PROPY-HQ and PROPY-4HBA) and up to 13 % and 14 % in PROPY-35DHBA and PROPY-45DClPA respectively.

H···H contacts appear to dominate the interactions in all systems. This can be observed in the central region of the fingerprint plots where the paler colour indicates a higher density of interactions. These correspond to contacts between phenyl ring hydrogen atoms and those on the pyrazole ring alkyl substituents of PROPY to similar hydrogen atoms on the co-formers. The co-formers also contain aromatic rings and other alkyl groups which are also involved in H···H contacts. The H···H contribution to the total interactions varies from 73.3 % in PROPY to just 46.7 % in PROPY-45DClPA.

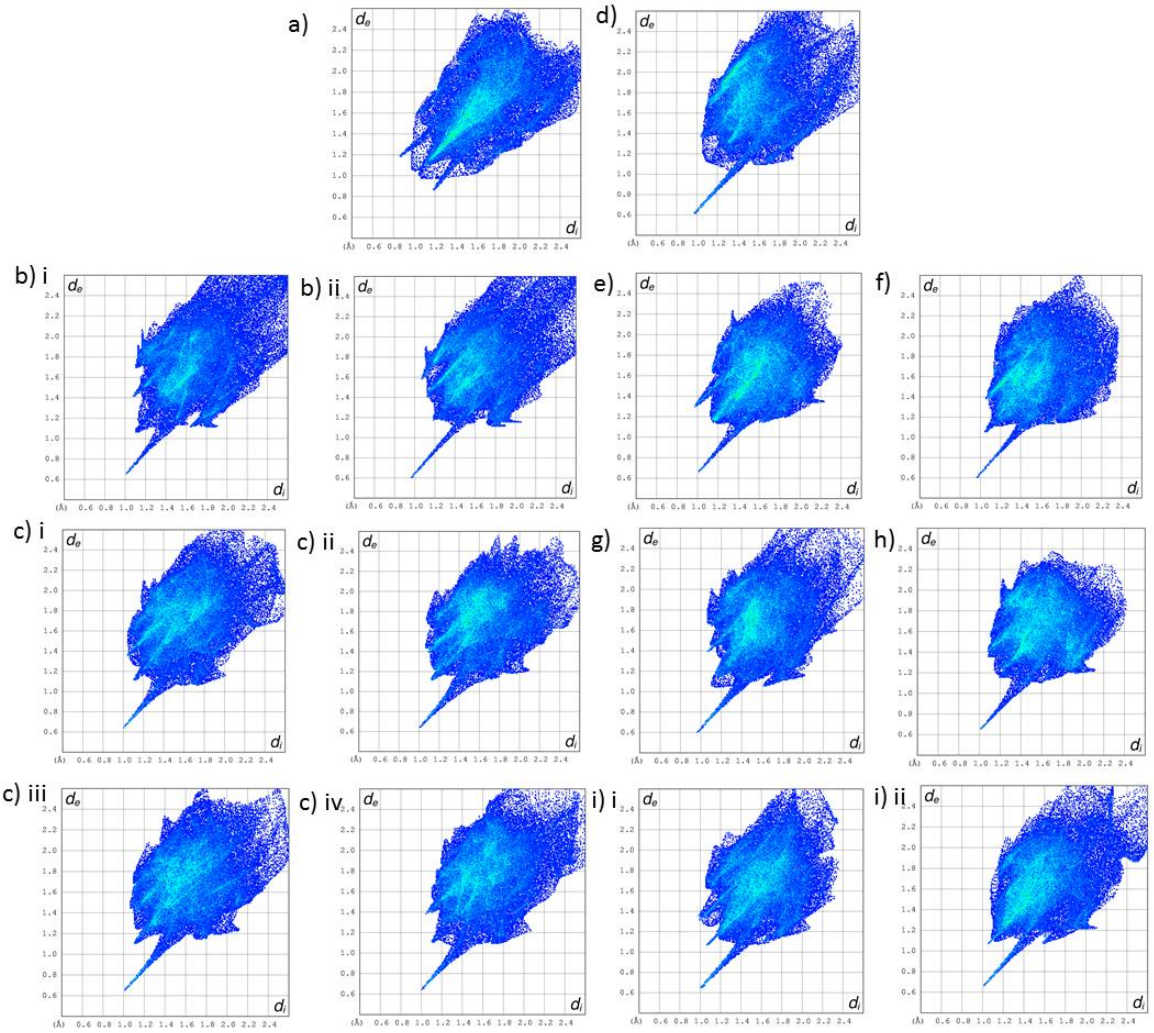

Figure 4.16. Fingerprint plots of for PROPY molecule in a) parent PROPY and the eight co-crystal crystal structures b) PROPY-25DHBA (2 independent PROPY molecules; i-ii), c) PROPY-35DHBA (4 independent PROPY molecules; i-iv), d) PROPY-45DClPA, e) PROPY-4HBA, f) PROPY-FA, g) PROPY-HQ, h) PROPY-MPAR, i) PROPY-PGL·0.5ACN (2 independent PROPY molecules; i-ii).

The 'wings' in the fingerprint plots formed from longer interaction distances represent C···H, H···C and H···H interactions and can indicate the extent of π-π stacking. The greatest contributions of H···C are seen in PROPY-35DHBA and -HQ (13.3-16.1 % and 14.8 % respectively) and are also high in PROPY-45DClPA (12 %). PROPY-FA, -PGL, -25DHBA and -MPAR all indicate a similar proportion of these interactions with values around 11 %, whilst PROPY-4HBA and PROPY have much lower contributions from such contacts (8.6 % and 6.7 % respectively). C···H contact contributions are more similar across the series occurring within the rage 7.5-10.6 % for all. PROPY-FA and PROPY-MPAR are the only two systems to have a percentage value > 10%, whilst PROPY-25DHBA and PROPY-35DHBA are the only two < 8%. Structural analyses indicate the origins of these interactions. PROPY-25DHBA, -HQ and -MPAR display edge···face π-interactions whilst

PROPY-35DHBA and -PGL display alkyl C-H···π interactions. PROPY-45DClPA has CH_3···CH_3 contacts and some offset CH_3···π interactions. PROPY-FA contains offset stacking of pyrazole rings in PROPY molecules with aromatic C–H to pyrazole ring and CH_3···$\pi_{phenyl\ ring}$ contacts between PROPY molecules.

C···C, C···N, N···C and N···O contacts are not seen in all structures and their overall contribution to the total interactions is minimal. N···N contacts are only present in PROPY-FA with a seemingly insignificant contribution of 0.2 %. 45DClPA is the only Cl-containing co-former and hence contacts to Cl are only present in this structure. Over 9.5 % of the total interactions occur to a Cl group, predominantly in the form H···Cl (9 %) with minimal C···Cl (0.3 %) contacts. The presence of additional contact types result in the reduced relative proportion of H···H contacts in this system. It is the lowest of any of the systems at just 46.7 %.

Three systems have more than one independent molecule of PROPY present in the asymmetric unit: PROPY-25DHBA (3), PROPY-35DHBA (4), and PROPY-PGL (2). All four PROPY units in PROPY-35DHBA display very similar fingerprint plots representative of their similar interactions as seen in crystal structure analysis. The two PROPY molecules in PROPY-25DHBA show differences in their interactions in crystal structure analysis – molecule 1 has the O–H···$O_{carbonyl}$ hydrogen bond occurring *via* the hydroxyl of 25DHBA, whilst that for molecule 2 occurs *via* the carboxylic acid. This is corroborated by the fingerprint plots, which have different overall shapes and the contact contributions are seen to differ in the interaction plots (Appendix A.7.3). The two PROPY molecules in PROPY-PGL display the same general fingerprint plot shape however there are differences arising from the interactions they partake in, as discussed in reference to the crystal structure.

The rank according to packing efficiency of the systems is PROPY < PROPY-45DClPA < PROPY-25HBA < PROPY-35DHBA < PROPY-PGL·0.5ACN < PROPY-HQ < PROPY-MPAR < PROPY-4HBA < PROPY-FA (Appendix A.8). Less efficient packing requires stronger interactions to mitigate it. A standard geometrical analysis (shorter hydrogen bonds / contacts are stronger) can be employed from the above fingerprint plots. The co-crystals with more efficient packing have longer contact distances (fingerprint plot apex ~1.2 Å d_i and d_e) with only a small number of shorter contacts (excluding $O_{carbonyl}$···H). The fingerprint plots with the lower apex at shorter contact distances (d_i and d_e ~1.0 Å) are those with the less efficient packing. PROPY has the least efficient packing of all systems and displays a larger number of contacts at shorter d_i···d_e distances.

A similar analysis to that described for the PROPY molecules was undertaken for the co-former molecules present in each structure. This is given in Appendix A.7.2.1.

A single surface for the entire co-crystal construct, rather than the individual components, can also be generated. Fingerprint plots determined from these surfaces are shown in Appendix A.7.2, Figure A.17. These show how the PROPY–co-former constructs as a whole interact with one another, rather than inspecting contacts of the individual molecules which are predominantly of the type PROPY···co-former. A Hirshfeld surface of the entire construct produces a very different fingerprint plot to those of the individual components. A high degree of symmetry is present as all contacts inside the surface also occur outside. These single surface fingerprint plots also show the influence of the co-former molecules in determining the structure and interactions, evident in the large variations between the different systems' plots. The crystal structure and interactions present are not underpinned by PROPY, but attributable largely to the co-former.

4.3.5 Structural Similarities and Trends in Interactions

The eight new co-crystals utilise co-formers which contain hydroxyl and / or carboxylic acid moieties. Three co-formers contain both an acid and hydroxyl group, and all demonstrate an O–H···$O_{carbonyl}$ hydrogen bond to PROPY involving the hydroxyl group. One of these, PROPY-25DHBA, also displays an O–H···$O_{carbonyl}$ hydrogen bond involving the acid. An acid···acid dimer synthon involving two co-former molecules is seen in PROPY-35DHBA and PROPY-4HBA. Both contain a co-former featuring an acid and hydroxyl functionality, and form co-crystals of a 1:1 stoichiometry.

Five of the new co-crystal structures display a bifurcated O–H···O hydrogen bonding interaction consisting of a co-former O–H or $-CO_2H$ hydrogen bond and an additional C–H contact from the co-former phenyl ring on which the O–H / $-CO_2H$ functional group is a substituent. Interestingly, the co-crystals with PGL and 45DClPA co-formers display no C-H···O contacts to the PROPY carbonyl.

The co-crystal with FA displays a single O–H···O hydrogen bond between the two components with additional C–H contacts occurring from PROPY molecules. This is the only structure which contains such an interaction pattern, with multiple API···API contacts. FA is a diacid species however the 1:0.5 ratio denotes that each acid has a carbonyl to pair with. It is the only co-former in the PROPY co-crystal series which does not contain an aromatic ring, nor does it possess additional hydrogen bonding atoms or groups besides that partaking in the main hydrogen bonding interaction. MPAR similarly does not have additional strong hydrogen bonding functionality however, unlike in PROPY-FA, weaker interactions to MPAR are possible. The formation of the 2:1 units in PROPY-FA mean no further interactions are possible except from C–H.

4.4 Thermal Analysis

All samples were analysed by differential scanning calorimetry (DSC) to ascertain their melting points and thermal behaviour. Figure 4.17 shows the DSC thermogram of the co-crystals compared to that of PROPY and Table 4.2 combines these results with the melting points of the pure co-former materials for comparison. It is shown that the co-crystals can help to improve or modify the melting point of PROPY.

Table 4.2. Tabulated melting points from DSC experiments alongside reference co-former melting points.

Sample	**Co-Crystal Melting Point T_{onset} /°C**	**Co-Former Melting Point /°C**
PROPY	102.2	-
PROPY-25DHBA	96.4	200-205
PROPY-35DHBA	136.5	236-238
PROPY-45DClPA	107.3	198-200
PROPY-4HBA	133.4	214
PROPY-FA	108.0	287
PROPY-HQ	133.9	172
PROPY-MPAR	70.2	125-128
PROPY-PGL·0.5ACN	96.5 / 109.9	219
	Recrystallisation 117.6, melt 153	

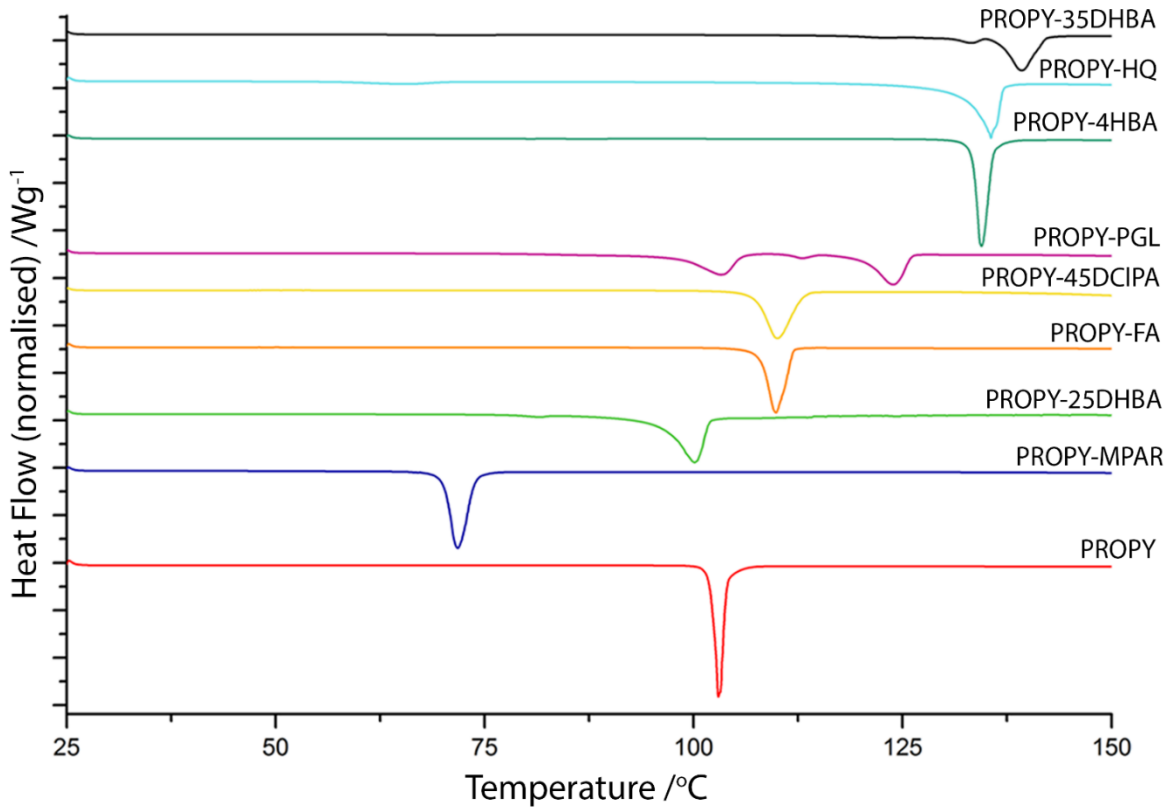

Figure 4.17. DSC plots for all co-crystals and parent material measured from 25 °C to 150 °C at heating rate 10°C min^{-1}.

The DSC thermogram of PROPY-PGL·0.5ACN indicates a number of events, which were further investigated *via* HSM (detailed in Appendix A.9.1). The behaviour can hence be ascribed from HSM to loss of acetonitrile solvent at 96 °C followed by sample melting at 110 °C. This is immediately followed by a recrystallisation event, 117 °C, which later melts at 153 °C.

The experimentally determined melting point of PROPY in this study of 102.2 °C indicates the bulk material is Form II; Form I has a slightly higher melting point reported as 104.3°C.[241]

Of the eight co-crystals, two show a lowered melting point relative to pure PROPY, three melt in a similar temperature range, with small increases seen and the remaining three melt at a higher temperature. Of the two displaying a lowered melting point one (PROPY-MPAR) contains a co-former with a relatively low melting point, the lowest of all the co-formers. Hence, it might be expected that MPAR would reduce the melting temperature (see Chapter 1.3.2). The other, PROPY-25DHBA, contains 1,4-dioxane solvent within the crystal lattice which is disordered and contained within voids. This may impact the temperature at which it melts, reducing the amount of energy required. Additionally, it has been shown that the material is unstable under a variety of conditions, (Section 4.5), which is in agreement with a lowered melting point.

Similar to PROPY-25DHBA, PROPY-PGL·0.5ACN also contains solvent within the crystal lattice, impacting the melting temperature of the material which may be lower than expected. A subsequent recrystallisation occurs after the melt which then proceeds to melt at a higer temperature. This may be a different form of PROPY-PGL with an absence of solvent as the malting point temperature does not correlate to either parent material. This material has not been characterised, however, so this cannot be confirmed at present.

Fumaric acid has a high melting point, the highest of all the co-formers, however the resulting co-crystal had a moderate melting point. PROPY-FA has a 1:0.5 ratio therefore the proportion of higher melting FA is significantly reduced and PROPY may have a greater impact on the melting temperature. Conversely, HQ has a moderate melting temperature relative to the other co-formers in the study, however its co-crystal has the second highest melting point. The stoichiometry may also influence the melting point in this system as the 1:2 ratio means twice as much HQ (higher melting point)is present than PROPY. Further discussion of the melting points are presented in Chapter 5.7.1.

4.5 Stability of Co-Crystals

The stability of the co-crystals that contain pharmaceutically acceptable co-formers (all except that containing 45DClPA) was tested under slurry and accelerated test conditions (40 °C / 75 % relative humidity), alongside pure PROPY.

4.5.1 Slurry Tests

Excess powders of the co-materials were stirred in pH 7.5 phosphate buffer solution at room temperature for 24 hours. After this time the resulting solids were filtered, air-dried and analysed by PXRD to assess stability. Solution aliquots from the filtrate were used for solubility determination (discussed later). PROPY and most of the co-crystals appear stable under these conditions with the exception of the 25DHBA and PGL systems (Appendix A.10.1). This could be due to the presence of solvent molecules in the crystal lattice of both samples, particularly PROPY-25DHBA in which the solvent is disordered and lacks strong structure retaining interactions. Analysis of the resulting solids by PXRD shows PROPY peaks indicating dissociation of the co-crystal in both cases.

4.5.2 Accelerated Storage

Storage under accelerated conditions produced similar results to the slurry conditions: dissociation of the PROPY-25DHBA co-crystal is evident from the appearance of co-former and PROPY peaks in the PXRD patterns. The PROPY-PGL·0.5ACN system, however, retains many of the original peaks and shows only a partial dissociation (Appendix A.10.2). The PROPY-PGL·0.5ACN sample is more stable under these conditions than in an aqueous slurry environment. The remaining systems all show stability.

4.5.3 Dynamic Vapour Sorption

Dynamic vapour sorption (DVS) measurements were also carried out to determine moisture uptake of the samples with an increasing relative humidity over a given time period. Figure 4.18 shows the sorption and desorption profiles for five co-crystals with pharmaceutically acceptable co-formers and the PROPY parent material. With the exception of one, PROPY-PGL, all samples display stability even at high relative humidity. The co-crystal with PGL, however, showed a significant mass change indicating water uptake and hysteresis. This structure contains small voids identified from the experimental crystal structure capable of containing a water molecule, into which absorption could occur during the test and hence explain this result. No data was obtained for PROPY-25DHBA due to the nature of the sample (degraded) at the time of equipment availability (subsequently appropriate material was available but it was not possible to collect further data). It would be predicted that this sample would indicate a significant water uptake as seen in PROPY-PGL due to the voids present in the crystal structure, and / or solvent-H_2O exchange.

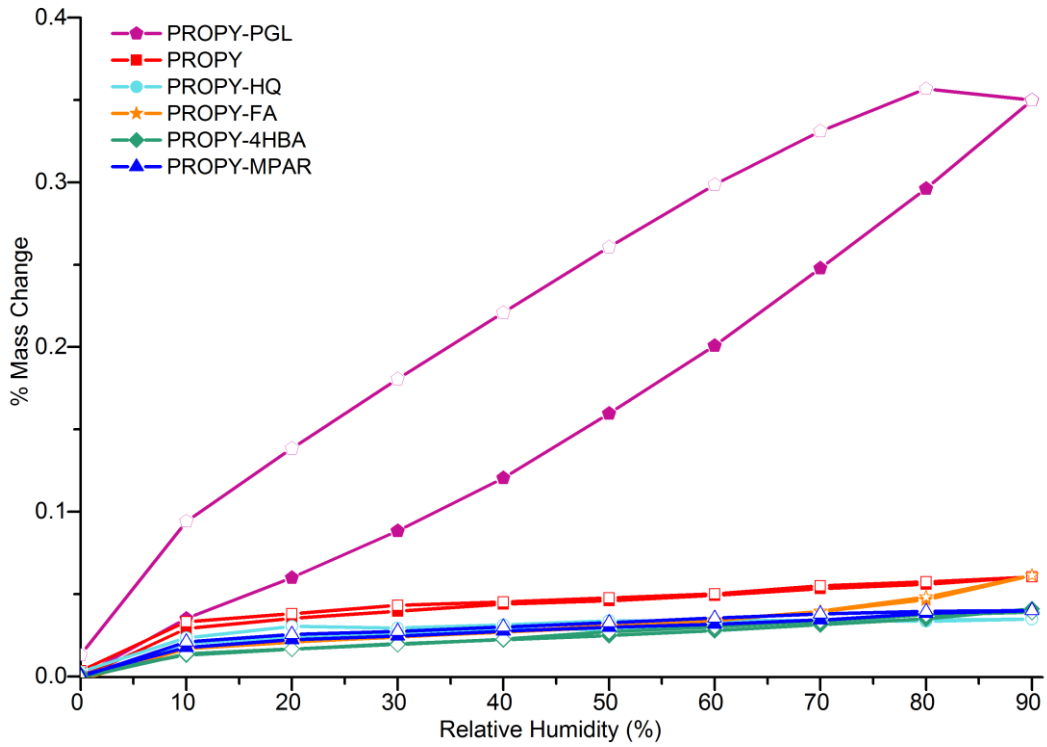

Figure 4.18. DVS plot of sorption (solid coloured markers) and desorption (hollow markers) of PROPY and co-crystal materials.

4.6 Analysis of the Solution Properties

Many drugs are delivered in a tablet form and therefore must dissolve to enter the blood stream for transport around the body. Solubility and dissolution rate are thus crucial for drug candidates as discussed in Chapter 2.4.2.

4.6.1 Dissolution Rate

An increase in the initial dissolution rate means a fast release of product from the formulation, which is advantageous for development of immediate-release drug products. Figure 4.19 displays the dissolution profiles for the co-crystals containing pharmaceutically acceptable co-formers, all of which show a significantly higher initial dissolution rate than PROPY. The dissolution rate reaches a plateau (100 % dissolution) within 60 min for most of the co-crystals, PROPY-HQ co-crystal showing the highest dissolution rate reaching the plateau within 25 min (Table 4.3). In contrast, the PROPY dissolution rate was found to be much slower, only reaching a plateau beyond the experimental time frame, after 300 min.

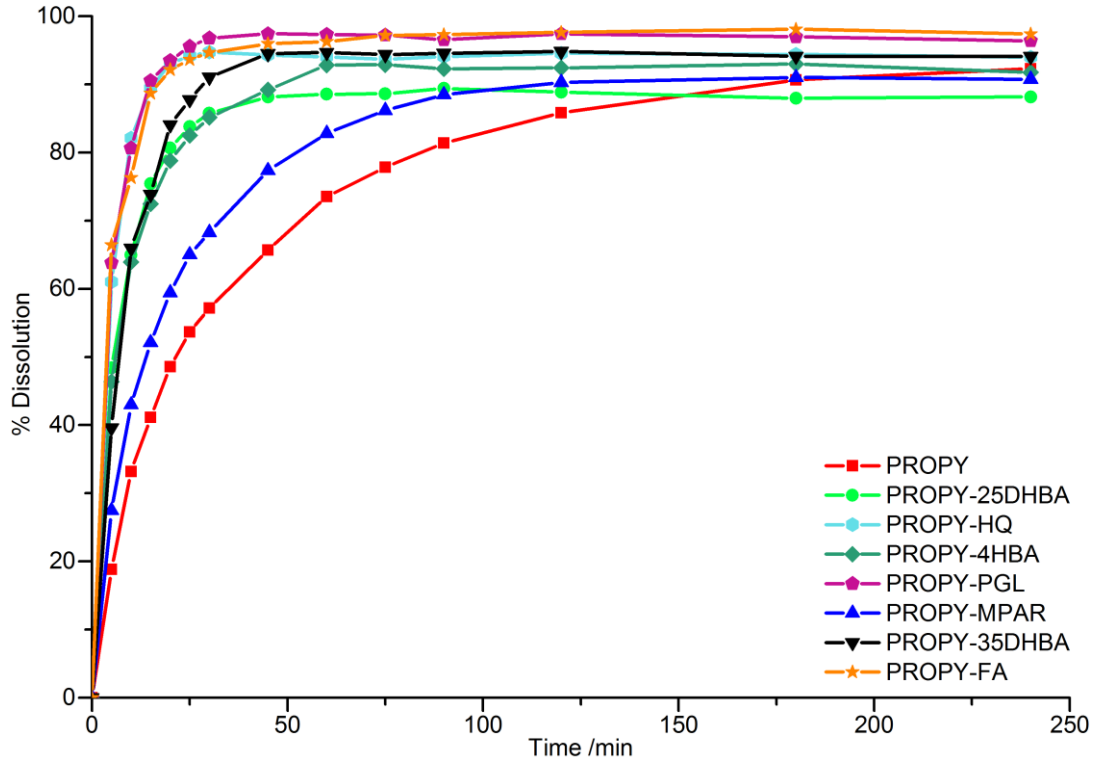

Figure 4.19. Dissolution profile for PROPY and co-crystals with pharmaceutically acceptable co-formers carried out over 240 min experiment time at 37 °C in pH 7.5 phosphate buffer.

4.6.2 Solubility

All the co-crystals were found to be stable in the slurry experiments with the exception of PROPY- 25DHBA and PROPY-PGL. For the stable co-crystals, the concentration of the aliquots taken from the slurry filtrate represents the true solubility. For the dissociable co-crystals, apparent solubility was calculated according to the literature using equation 4.1.[269, 270] Dissolution rates were taken from linear portion of the appropriate dissolution curves for the samples.

$$C_m = C_s\left(\frac{J_m}{J_s}\right)$$

Equation 4.1. Apparent solubility equation where C_m represents the apparent solubility of the unstable form, C_s represents the solubility of the thermodynamic form and J_m and J_s represent the dissolution rates of the co-crystal and thermodynamic form, respectively.

The solubility for the stable samples was determined using aliquots from the slurry filtrate, appropriately diluted and tested by HPLC. The solubility data of the co-crystals is compared with the solubility of PROPY in Table 4.3. Of the stable co-crystals, PROPY-HQ showed the highest

solubility followed by the co-crystal containing 35DHBA. The solubility of the stable co-crystals follows the trend: PROPY-HQ > PROPY-35DHBA > PROPY > PROPY-4HBA > PROPY-FA > PROPY-MPAR. The two co-crystals which dissociate under slurry conditions (with the co-formers 25DHBA and PGL) show higher (apparent) solubility than the stable co-crystals which is in accordance with many reported studies; dissociable co-crystals (which eventually produce the API or co-former) show higher apparent solubility.[31, 271]

Table 4.3. Solubility of parent API and co-crystals with pharmaceutically acceptable co-formers in pH 7.5 phosphate buffer at room temperature.

Sample	Time to reach plateau /min	Solubility /mg mL^{-1}	Ratio to API
PROPY	300	2.71	1
PROPY-4HBA	60	2.19	0.81
PROPY-MPAR	120	1.48	0.55
PROPY-FA	45	1.82	0.67
PROPY-HQ	25	3.14	1.16
PROPY-35DHBA	45	2.76	1.02
PROPY-25DHBA·X1,4-dioxane	45	5.61[a]	1.94
PROPY-PGL·0.5ACN	30	7.88[a]	3.02

[a] apparent solubility

It has been proposed that co-crystal solubility is directly proportional to the solubility of its components,[272] however factors such as API:co-former stoichiometry, solution pH, hydrogen bonding and molecular packing etc. are known to impact the solubility of co-crystals.[31] Hence, the observed solubility trends often deviate from the theoretically expected linear relationship. Of the co-formers forming the stable PROPY co-crystals, 35DHBA has the highest aqueous solubility although its co-crystal showed the second highest solubility. HQ has a lower solubility than 35DHBA, FA and 4HBA starting materials however its co-crystal exhibited the highest solubility. The reported solubility of FA, 4HBA and MPAR are higher than that of PROPY yet all the co-crystals with these co-formers presented a lower solubility than PROPY. Therefore, the observed solubility trend in PROPY co-crystals suggests that there is no clear correlation between solubility of the co-formers and the corresponding co-crystals.

This could be due to:

- Differences in hydrogen bonding – the co-crystal with HQ features two strong O–H···O hydrogen bonds involving the carbonyl of PROPY and the co-former whereas in the other co-crystals the carbonyl is involved in only one O–H···O hydrogen bond.
- Differences in PROPY-co-former stoichiometry – PROPY-HQ is a co-former rich co-crystal whereas the others contain the co-former in stoichiometrically equal or reduced amounts relative to PROPY.
- More efficient crystal packing in co-crystals than in PROPY – the calculated packing coefficients of co-crystals are higher than that of the packing coefficient of PROPY (Appendix A.8).

The dissolution rate and solubility data is perhaps not as expected with improved dissolution rates not corroborated by the solubility of the co-crystals. This could be attributed to a number of factors such as kinetics dominating the dissolution rate which are influenced largely by co-former solubility, whilst equilibrium solubility is dependent upon thermodynamics and solution equilibrium of the co-crystal, PROPY and the co-former. This will be discussed further in Chapter 5.7.4. The latter may depend upon relative ratios of the components in solution and the binding constants of complexes in solution. Other factors which may have an impact include particle size, wettability and possible tablet surface recrystallisation affecting drug release.[83, 273, 274] The solubility and dissolution experiments suggest that only one co-crystal (that with HQ) showed an increase in both solubility and dissolution rate and was stable under slurry and accelerated conditions. Other co-formers displayed the ability to modify the physicochemical properties however further investigation is required to fully understand the experimental observations.

4.7 Conclusions

Current co-crystal design strategies are not reliable for all types of compounds. In particular, compounds displaying little or no hydrogen bonding functionality (either through an absence of functional groups, steric hindrance preventing interactions or a combination of the two) pose challenges in co-former prediction and selection for the development of multi-component materials. For these types of molecules, a supramolecular synthon-based design or molecular descriptor-based predictions (primarily based on polarity and heteroatom presence) are not best-suited, or applicable. Molecules containing only hydrogen bond acceptor groups in particular present a distinct challenge.

It has been shown that a knowledge-based approach can be utilised, combining CSD statistics with other sources of knowledge, to identify the most likely interactions for a molecule and thus focus the screening to the most likely co-formers. This has been applied to the API propyphenazone to select appropriate co-formers containing different functional groups and combinations thereof, as well as no functional groups (to test predictions).

As a result, eight co-crystals have been successfully synthesised and fully characterised using a number of techniques. All of these were formed with a co-former containing either an O–H, $–CO_2H$, or both functional groups. The majority of the new materials contain a hydroxyl group confirming the findings of the initial interaction searching: O–H functionalities were found to be preferential to $–CO_2H$. This is also confirmed by the co-formers containing both functionalities as the primary interaction to PROPY is *via* the hydroxyl. Etter's rules state that carboxylic acid functional groups would preferentially form a homodimer[12] and hence direct the hydroxyl···carbonyl interaction. This dimer interaction is seen in two of the three structures.

Interaction searching also indicated that $–NH_2$ and N–H were likely functional groups to form an interaction (the latter being less favourable) however no co-crystals were obtained with co-formers containing either functional group. This may be due to steric factors as $–NH_2$ may be too bulky to access the restricted carbonyl functionality. The self-association strength of amides is greater than carboxylic acids which is in turn is greater than hydroxyls (Section 1.3.4). The prevalence of O–H and a few CO_2H interactions to carbonyl may arise from this as these co-formers are easier to break apart to form hetero-pairings than amides. Other co-crystals may be possible, but are likely to require alternative, and possibly less-routine experimental conditions beyond those attempted to fully explore the system's landscape.

The structures of the new materials can be compared to PROPY and the initial analysis carried out. Full interaction mapping (FIMs) identified areas where a particular functionality would locate to interact and also hot spots which presented the most favourable point around PROPY for that functionality. As expected the co-formers are located in these favourable areas to form their primary interaction.

Physicochemical properties such as stability, solubility and dissolution rate of those containing pharmaceutically acceptable co-formers were measured and related to the crystal structures. The stability was shown to be equivalent to parent PROPY in the majority of materials, the exceptions being the co-crystal solvates (PROPY-25DHBA$_{1,4\text{-dioxane}}$ and PROPY-PGL·0.5ACN). Initial dissolution rate was improved in all new materials and solubility increased in over half. Additionally the melting point was moderated with the different co-formers. It was observed that stoichiometry should also be considered when undertaking property modification.

To further understand some of these observations, a more in-depth structural analysis will be carried out at the electronic level on a structurally related sub-set of these materials in the following chapter. Complementary experimental and computational methods will be employed to try to rationalise some of these observations, and understand the effect differing co-formers have on the electron distribution. The information obtained can be related back to the properties discussed in this chapter to gain a deeper understanding of their nature and the structure-property relationships.

Chapter 5: Quantum Crystallography Studies of PROPY Co-Crystals

Chapter 4 describes novel co-crystal systems of the API PROPY analysed by standard resolution crystallography and with accompanying physicochemical properties measurements. To provide greater insight and to understand the differences between related systems, additional techniques have been employed and will be discussed in this chapter. These studies provide quantitative analysis of the systems at the electronic level, and hence changes in molecular charge distribution between different co-crystals can be assessed. This also permits a deeper and extended investigation of the intermolecular interactions, the associated energies and components thereof. Co-crystals are reliant on the two components being bound together in the crystal lattice and therefore an analysis of these interactions will provide insights into their physical properties.

Due to the time and resources required for experimental charge density studies, this will only be applied to a subset of the systems. The subset consists of co-crystals containing structurally related co-former molecules and allows for a systematic study to be undertaken; this develops an understanding regarding the effect of the co-former molecule on structure and properties.

5.1 Reasoning Behind Quantum Crystallography and Charge Density Studies

As highlighted in a recent communication by Dittrich,[275] topological analyses and descriptive studies of intermolecular interactions should have a clear research focus. Many studies have been criticised for being 'descriptive, but not predictive',[178] detailing in-depth topological parameters with no real focus or deeper understanding, and no resulting advancement of the technique. Reported herein are studies which aim to better understand the co-former influences on the co-crystal system and how interactions and charge distribution affect physicochemical properties. Used in this way, charge density studies can provide a tool for addressing questions regarding the foundations of crystal engineering.[275]

In a response article, Macchi[276] indicated that subtle changes observed when a molecule is embedded in a different crystal environment can provide valuable information. Such analyses and interpretation are often regarded as a discrepancy rather than interesting variations between systems, and so these investigations are rarely seen. The 'discrepancies' can represent molecular polarisability and the interplay of states generating mixed states. Specific analyses of these should be undertaken, particularly in co-crystal and similar systems.

Both experimental and theoretical approaches to charge density analysis have valid application in appropriately designed studies. Theoretical determinations can be just as accurate as experimental data,[276] however the latter is worthwhile if it can aid in answering a chemical question. Quantum crystallography "*enhancing quantum chemical calculations with experimental information"*[277] combines experimental and theoretical approaches, and properties calculated from Quantum Mechanical principles. This approach (combining and merging experimental and theoretical data sources) will be presented in this chapter to provide a range of complementary information. These complementary techniques provide a full evaluation through studying the systems at the electronic level, and offer a more holistic approach through their combination. Properties arise from electronic interactions which cannot be derived from a purely geometric analysis. Therefore, this approach and use of quantum crystallography will provide rationale and justification of the properties and structures obtained.

5.2 Selection of Co-Crystal Family

The subset of PROPY co-crystal systems chosen for experimental charge density studies comprises PROPY-4HBA (1:1), PROPY-FA (1:0.5), PROPY-HQ (1:2) and PROPY-MPAR (1:1), depicted in Figure 5.1. These are structurally similar to allow for a comparative analysis of the experimentally determined properties whilst also being diverse in their stoichiometry to assess preferences to form particular ratios. This chosen family allows for a systematic study of related systems to be undertaken.

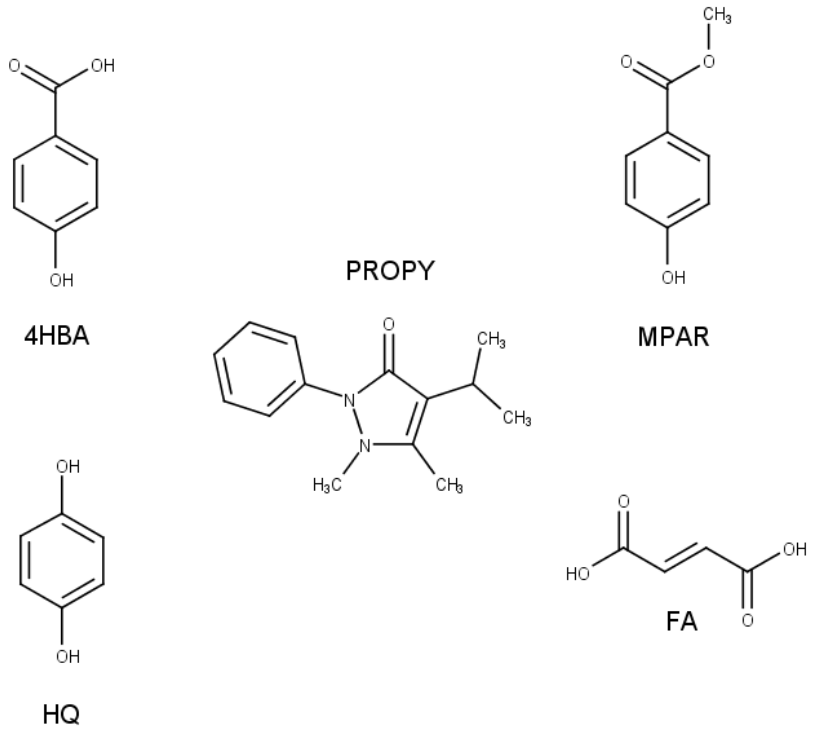

Figure 5.1. Molecular structures of PROPY, and co-formers 4HBA, MPAR, HQ and FA.

The aims of the systematic study are:

1. Structural similarities: PROPY-4HBA and PROPY-MPAR have the greatest degree of structural similarity and have been chosen to explore the effect of an additional hydrogen bonding functional group in the co-former (4HBA contains a carboxylic acid (in place of the ester) in addition to the hydroxyl group).
2. Stoichiometry: similarly to 4HBA and MPAR, HQ is also a para-substituted aromatic co-former molecule however it forms a 1:2 co-crystal with PROPY. The second hydroxyl group of HQ is less bulky (in comparison to the carboxylic acid / ester groups of 4HBA and MPAR) and so this system was chosen to identify a rationalisation for stoichiometric ratio preference based on a steric *vs.* electronic argument.
3. Primary O–H···O hydrogen bond: this is similar in all the systems and can be evaluated and compared across the series.
4. Structural diversity: PROPY-FA is structurally diverse in comparison to the other family members and is included to probe the differences between aromatic and linear co-formers as well as contrast the primary hydrogen bonding interactions: O–$H_{hydroxyl}$···O and O–$H_{carboxylic\ acid}$···O.

5.3 Methodology

Desiraju and Nangia[278] claim that a crystal structure needs to be assessed and visualised as a whole entity, rather than using localised, specific interactions. Thus, a whole system approach will be taken initially to provide a holistic view of the structure and interactions. Different computational approaches based on interaction energies provide various information which can then be used to direct the experimental data analysis.

The information obtained from the different sources will be combined for each system. Physicochemical property measurements, determined in Chapter 4, will then be considered and evaluated with consideration to the charge density distribution and information from the interaction analyses.

5.3.1 Molecular Pair Interaction Energies

The calculation of intermolecular interaction energies detailed by Spackman *et al*[187] and implemented in Crystal Explorer[180] (CE) provides an overview of molecule···molecule interactions of a system. Gaussian[279] B3LYP/6-31G(d,p) monomer wave functions for each molecule are determined within the software, from which the interaction energies are calculated[191] (Chapter 2.2.2). Each interaction energy is separated into the four constituent terms (E_{coul}, E_{pol}, E_{disp}, and E_{rep}) according to Equation 5.1. These are presented as unscaled values (E'_{coul}, E'_{pol}, E'_{disp} and E'_{rep}) however the total energy has the scaling applied. The unscaled individual contribution values allow for meaningful direct comparisons between systems whilst general trends in comparison to PIXEL values and total energies can be obtained from the scaled totals.

$$E_{tot} = k_{coul}E'_{coul} + k_{pol}E'_{pol} + k_{disp}E'_{disp} + k_{rep}E'_{rep}$$

Equation 5.1. Breakdown of interaction energy according to the method of Spackman *et al.,* each component with an associated scale factor, *k.*

With the aid of the visual display, molecular pair interaction energies can be associated with the molecules in the central graphics window (pairwise interactions occur from the central molecule to that of the colour indicated next to the interaction energy value) as indicated in Figure 5.2.

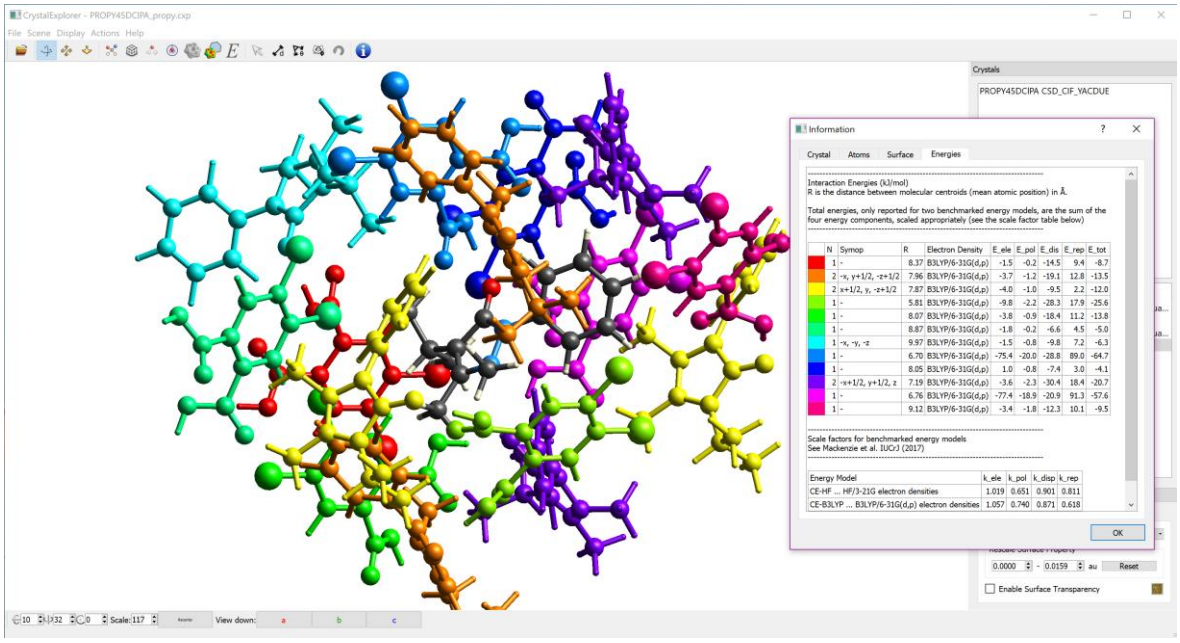

Figure 5.2. Main graphical display of Crystal Explorer v17.5 with interaction energy information showing the colours associated with each interaction energy for identification of the related molecular pair.

5.3.2 Detailed Molecular Pair Interaction Energies

Gavezzotti's PIXEL approach[181-184] (Chapter 2.2.1) is similar to that employed in Crystal Explorer, but provides further information regarding the type of interaction. The exact nature of the interactions from Crystal Explorer (e.g. API···API, API···co-former etc) can only be determined by visual inspection and correlation of the colour associated with each pairwise interaction energy to the main graphics display. PIXEL, however, separates the output by interaction type, with each calculation displaying the energies of A···A, A···B, B···A and B···B interactions (for a two component system). This provides unambiguous identification of the nature of the participants of each interaction. PIXEL interactions can be compared (*via* the molecular centroid···centroid distances) to those from Crystal Explorer and together provide a comprehensive overview of the pairwise interactions.

These computational methods offer a quantitative assessment at the molecule···molecule level and can identify the strongest, and possibly most important, interactions in a system. Both methods use different approaches for the molecular energy density calculations, however the values output are in good general agreement (see Section 5.4, Appendix B.4 and the associated Supplementary Files).

5.3.3 Experimental Charge Density

The interaction energy calculations conducted using Crystal Explorer and PIXEL provide information regarding the molecules contained within a molecular shell (of specified radius) surrounding the central molecule(s). Experimental charge density studies can investigate interactions on a more intimate level, searching for contacts between specified atoms, or within a specified distance range. The output therefore contains more contacts overall as each atom···atom, rather than molecule···molecule, pair are listed.

Each contact between individual atoms also encompasses a bond critical point (BCP) which can be identified. The properties determined (electron density, $\rho(\mathbf{r})$, and the Laplacian of the electron density, $\nabla^2\rho(\mathbf{r})$) at these points can provide further information regarding the nature of the interaction and also be used in the estimation of individual hydrogen bond energies. This technique will supplement the theoretical calculations, whilst also supporting the observations made to ensure that both methods are normalised and complementary.

Details of the experimental data, generation of the multipole model and different approaches taken for refinement are given in the experimental details (Chapter 8.7.2) and Appendix B.1, along with full details of the refinement statistics in Appendix B.2. The models were assessed using a combination of quantitative refinement statistics and visual outputs. Examples of these are shown in Appendices B.1 and B.3.

Applying Bader's AIM Theory[167] as a method of topological analysis of an experimental multipole model can generate an assortment of data including, most importantly, the location and identification of Critical Points, as well as their nature: (3,-1), (3,+1) or (3,+3). The location of a BCP (relative to the atoms) provides information concerning the two interacting atoms whilst $\rho(\mathbf{r})$ and $\nabla^2\rho(\mathbf{r})$ values provide further information regarding the bond or interaction. As described in Chapter 2.1.4.2 these indicate density accumulation or depletion and can aid in the classification of the bond. CP search data are given in Appendix B.3.4 with additional detail in the Supplementary File PROPY_XD Interaction Analysis. Individual intermolecular interaction energies between nuclei can be estimated using the Espinosa-Molins-Lecomte (EML) scheme[171] providing more specific information than that of the molecule···molecule viewpoint provided by Crystal Explorer and PIXEL.

Hydrogen bonds identified from experimental data are characterised by the presence of a BCP, within a user-specified distance. Spackman[280] has shown that, when summed, experimental energies estimated using the EML scheme of Espinosa *et al.*[171] give an underestimation in comparison to the PIXEL values. EML values depend on identifying all BCPs present between the

molecules of interest, and this is often not plausible; setting the distance too large (to include more contacts) will generate chemically unreasonable contacts which should not be analysed. An intermediate range, consistent over all searches, provides a useful overall perspective for the system, however it is unlikely that every contact present between the molecular pair is included. Some of the longer and / or weaker contacts may not be included and so the sum of all interaction energies may be below the total value of the full system taking into account all interactions, were it to be calculated. A systematic underestimate of the interaction energy occurs as a result.

5.3.4 Summary

It is hypothesised that certain intermolecular interactions (typically the strongest) have the greatest influence on structure, determining the assembly of the API–co-former adduct. Hence, these are deemed to be 'structure-directing'.

To assess each system, the interactions determined from the different methods will be correlated. Individual atom···atom interactions from experimental data can be associated with their corresponding molecule···molecule interaction from the theoretical calculations using the crystal structure and packing model. In this way, it can be determined whether it is predominantly a single interaction or several smaller contributions from different sources that are responsible for the overall energy values.

The exact values determined from the three methods are not directly comparable, particularly as those estimated from experimental charge density are highly model-dependant. They do, however, allow for relative energies to be determined and a ranking of strength and importance to be ascertained.

5.4 Overview of Co-Crystal Interactions

5.4.1 PROPY-MPAR

PROPY-MPAR is the simplest structure of the four chosen for a more detailed investigation incorporating experimental studies. The co-former molecule exhibits no additional, strong, hydrogen bonding functionality besides that partaking in the primary PROPY···co-former hydrogen bond. Hence, this system will be considered first and acts as a reference for the more complex systems.

One principal (a, Figure 5.3) and two further moderate (b, Figure 5.3) interactions are evident from the molecule···molecule energies calculated using Crystal Explorer. The principal interaction will be the most significant in determining the molecular assembly, however the two additional pairs may also play an important role. A fourth interaction (c, Figure 5.3) has an energy only slightly lower than the second 'moderate-energy' pair and may prove to be of some significance in the molecular assembly. These four interactions are seen to originate two from MPAR (a / c) and two from PROPY (b). It would be expected from the structural analysis that the strongest interaction would be that holding the two components together (PROPY···MPAR) and the strongest interaction from Crystal Explorer interaction analysis is seen to involve MPAR, showing agreement with the structural expectation.

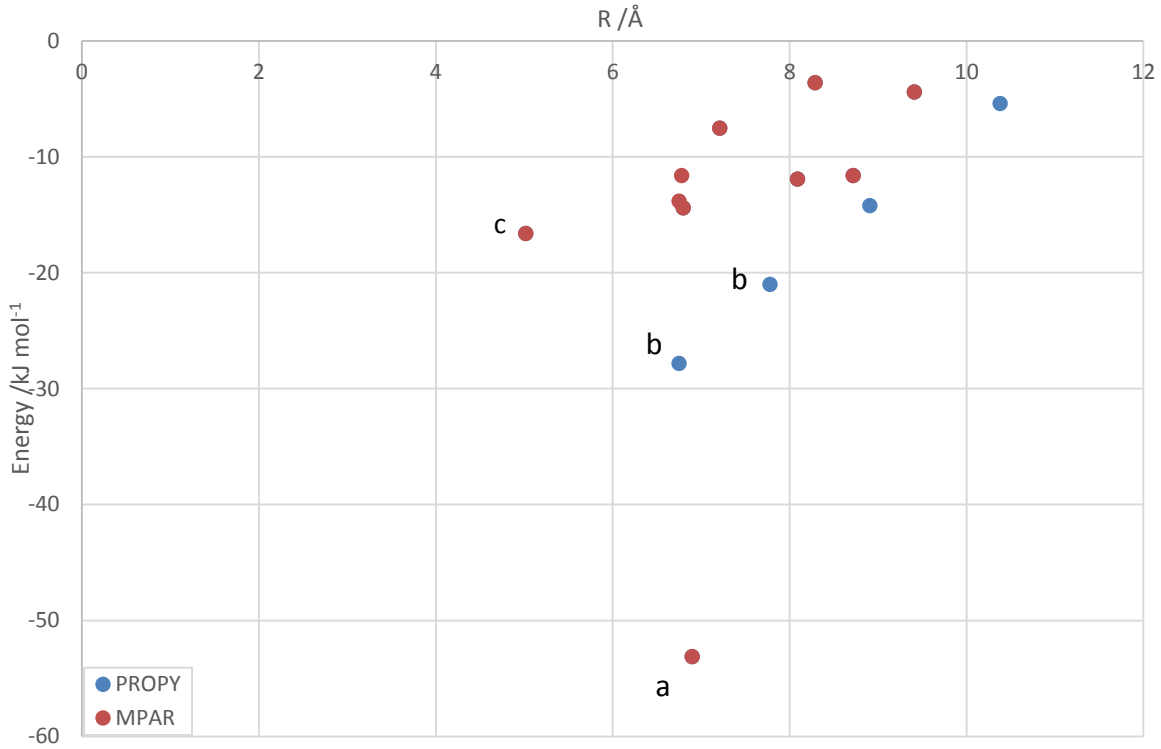

Figure 5.3. Intermolecular interaction energies for PROPY-MPAR 1:1 co-crystal determined from Crystal Explorer calculations, plotted against molecule···molecule centroid distances (R).

Figure 5.4 shows the interactions determined from PIXEL calculations which exhibit a similar distribution to that observed for the Crystal Explorer energies. The strongest interaction can be identified as that between PROPY and MPAR (a, Figure 5.4) with two PROPY···PROPY interactions as the next strongest (b and b*, Figure 5.4). The energy difference between the third and fourth strongest (b* and c) is less pronounced for PIXEL calculations than Crystal Explorer, with the data points lying just below and above -20 kJ mol^{-1}, respectively. The fourth strongest interaction (c, Figure 5.4) is identified as a PROPY···MPAR contact. Overall, these observations are in

accordance with the values and rank obtained from Crystal Explorer (strongest interaction originating from PROPY (x2) and MPAR (x2)).

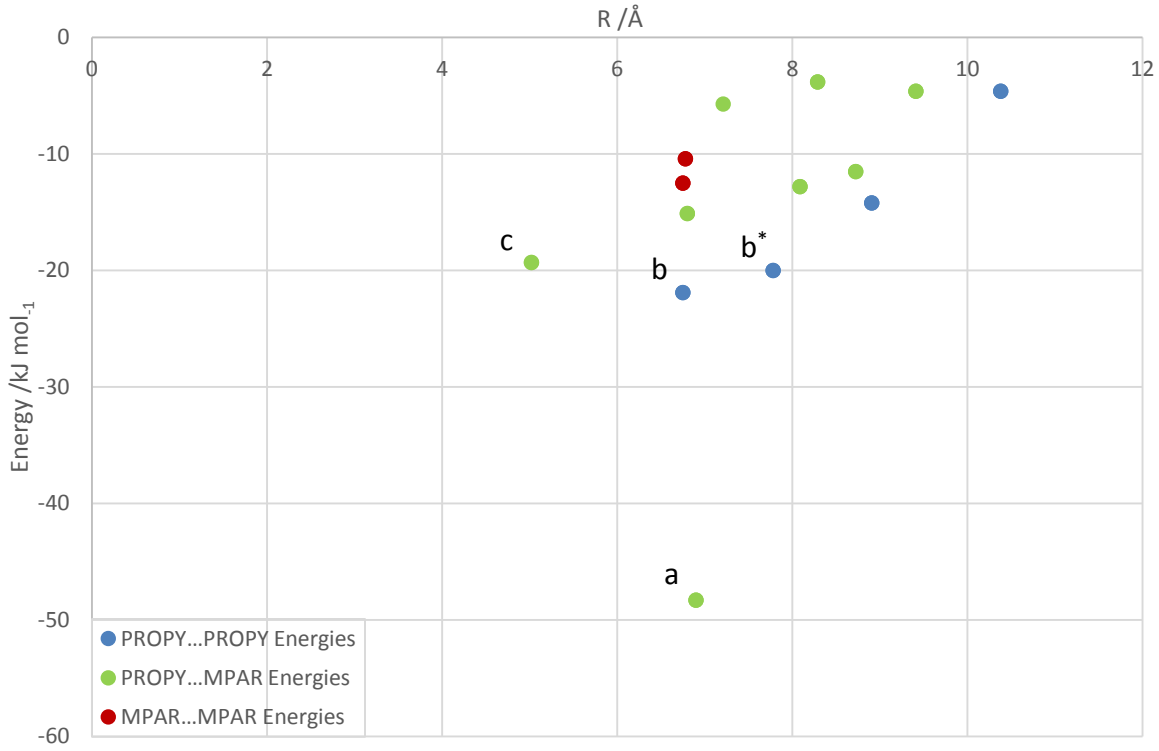

Figure 5.4. Interaction energies determined from PIXEL calculations plotted against molecule···molecule centroid distances (R) for PROPY-MPAR 1:1 co-crystal.

There is a good agreement between the two methods of energy determination, and a trend observed in which the longer molecular centroid···centroid distances have lower interaction energies. Beyond the strongest interactions discussed there are a further six with moderate energies occurring within the range -10 to -20 kJ mol^{-1} (a mix of all three molecular pair types) and four molecular pairs with energies below -10 kJ mol^{-1} (comprised predominantly of PROPY···MPAR contacts). This is true for both methods of energy determination.

The separation of the interactions according to molecule type in PIXEL permits a variety of different possible approaches for grouping and interpretation. Table 5.1 shows the grouping of the interactions according to the different constituents in the molecular pairs. Analysis of all the systems is presented in Tables 5.5 and 5.6 with full details in Appendix B.4 and Supplementary File PROPY PIXEL Calculations.

Table 5.1. Energy components for PROPY-MPAR determined from PIXEL calculations.

	Energies /kJ mol^{-1}				
	E_{coul}	E_{pol}	E_{disp}	E_{rep}	E_{tot}
PROPY···PROPY	-49.0	-19.6	-143.6	91.0	-121.4
PROPY···MPAR	-98.1	-52.0	-120.5	149.9	-121.1
MPAR···PROPY	-96.8	-50.8	-109	141.4	-115.4
MPAR···MPAR	-23.0	-10.4	-56.8	44.5	-45.8
Total	-266.9	-132.8*	-429.9	426.8	-402.8

*E_{pol} is not additive, therefore the sum of polarisation terms is not a valid indicator or value for gross comparisons.

Both combinations of PROPY and MPAR have the strongest Coulombic energy component of all the sets with the next strongest (PROPY···PROPY) having values 50 % lower. This is not reflected in the total energy however, as PROPY···PROPY pairings produce a similar total to the PROPY···MPAR and MPAR···PROPY combinations; PROPY···PROPY E_{coul} is smaller, however the dispersive forces between these pairs are greater and the repulsion significantly lower (~ 30 %) than in the API and co-former pairs. MPAR···MPAR interactions are weak and would therefore not be expected to have a great impact on the structure assembly.

The molecular pairings from the theoretical methods can be used to group the individual experimentally determined hydrogen bonds according to molecular pairs, which allow for a similar interaction analysis to be carried out. Individual hydrogen bond energies estimated from the experimental multipole model can be seen in full in the Supplementary File PIXEL_XD Interactions Analysis. The sum ($E_{HB,\,total}$) of these collective interactions for each molecular pair is plotted in Figure 5.5, against an average interaction distance ($R_{ij,\,av}$). These molecular pair energies can be deconvoluted in an alternative way to those from the theoretical calculations, allowing individual interactions which comprise the total energy to be assessed. As described in Section 5.3.3, the experimental method to determine hydrogen bonds and their energies uses a distance-based search, meaning that some interactions with longer inter-atomic distances (and likely to have weaker energies) may not be included.

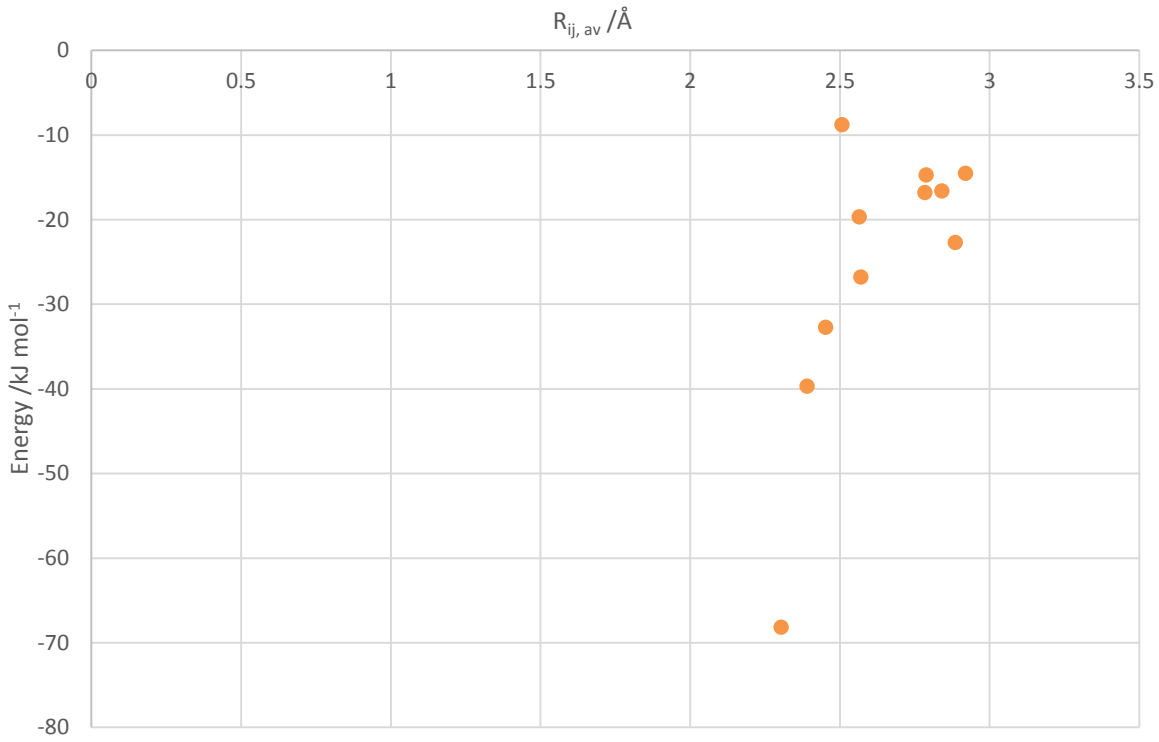

Figure 5.5. Total E_{HB} for molecule-molecule interactions (comprised of individual hydrogen bond between atoms) obtained from topological analysis of the experimental multipole model for PROPY-MPAR plotted against average R_{ij} of all interactions.

The hydrogen bond energies generated from the experimental multipole model, collated according to molecular pairings, show a similar distribution to that observed in the PIXEL and Crystal Explorer analyses (Figures 5.4 and 5.3 respectively). The distances are much shorter as atom···atom contacts, rather than longer range molecule···molecule interactions, are considered.

A single strong interaction is evident, as seen from Crystal Explorer and PIXEL, which corresponds to that between the PROPY and MPAR molecules in the asymmetric unit. This molecular pair interaction comprises one very strong hydrogen bond which dominates the molecular pair interaction and is the primary O–$H_{hydroxyl}$···$O_{carbonyl}$ hydrogen bond, as seen in the crystal structure analysis (Section 4.3.1.1). This has the greatest energy of all the experimentally determined hydrogen bonds. A further three hydrogen bonds are identified in this strong pairing, two with small hydrogen bond energies, and one with a moderate energy. These are likely to have a small contribution to the overall molecular pair interaction energy determined theoretically.

Several molecular pairs display moderate energies, similar to the theoretical calculations. On inspection of the hydrogen bonds these are seen to comprise several weaker hydrogen bonds, with energy values around 10 % that of the primary hydrogen bond. Whilst these hydrogen bonds appear strong in combination and help to maximise the energy of the adduct, they are each relatively weak individually. These interactions may impact the conformation or relative

orientation of the molecules to permit their formation but will not affect the initial adduct formation and molecular positions. Three of these next strongest pairs contain PROPY and MPAR, whilst one is a PROPY···PROPY pair.

The primary hydrogen bond has a V_{BCP}/G_{BCP} ratio of 1.056 whilst all other hydrogen bonds in this system have a ratio < 1. All but the primary hydrogen bond can be regarded as electrostatic in nature, whereas the $O–H_{hydroxyl}\cdots O_{carbonyl}$ is stabilised by a local concentration of charge in an intermediate closed-shell interaction. The R_{ij} distance of this primary hydrogen bond is 1.68 Å, the shortest of all identified hydrogen bonds, and indicates a partially covalent nature and strong interaction. All other hydrogen bonds have distances > 2.0 Å indicating a non-covalent interaction (Section 2.3.1). These observations are consistent with the energies determined across all three methods as the short, stabilised interaction has the greatest energy, whilst all others are either somewhat, or considerably, weaker especially when individual interactions are considered.

5.4.2 PROPY-4HBA

4HBA possesses a carboxylic acid group in the same position as the ester group of MPAR and forms a 1:1 co-crystal, making the two systems (PROPY-4HBA and PROPY-MPAR) directly comparable.

Two main pairwise interactions with energies greater than -50 kJ mol^{-1} (a and a^*, Figure 5.6) are observed in the Crystal Explorer interaction analysis. These occur from 4HBA and PROPY respectively. The data point for that originating from PROPY (a^*, Figure 5.6) can be ascribed to the main PROPY···4HBA interaction, as two overlapping data points are visible due a slight dissimilarity in interaction energies. This indicates an interaction from both molecules and is attributed to a PROPY···4HBA interaction. These two data points should, however, overlap exactly and appear as a single datum, as observed for PROPY-MPAR and other structures.

In addition to these two strong interactions, three interactions with an energy greater than -20 kJ mol^{-1} are observed, (b, Figure 5.6) and two further interactions occur within the range -10 to -20 kJ mol^{-1} (c and c^*, Figure 5.6). These are located at either extreme of the -10 to -20 kJ mol^{-1}, close to the range boundaries, and the lower-energy seventh interaction (c^*, PROPY) is closer to the grouping of weaker interactions than stronger ones. Of the five strong interactions (labelled a and b, Figure 5.6), two appear to originate from 4HBA whilst the others do so from PROPY.

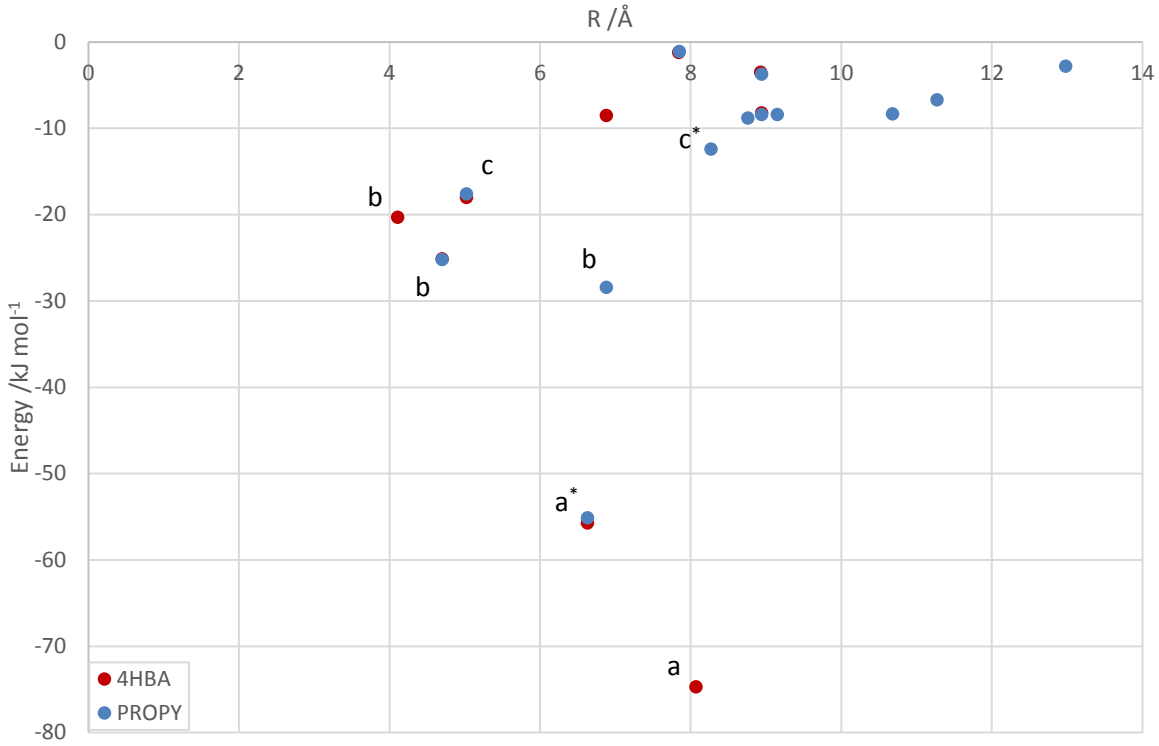

Figure 5.6. Intermolecular interaction energies for PROPY-4HBA 1:1 co-crystal determined from Crystal Explorer calculations, plotted against molecule···molecule centroid distances (R).

As seen with PROPY-MPAR, the PIXEL output scatter plot (Figure 5.7) is comparable to that from Crystal Explorer (Figure 5.6). The five largest energy interactions (labelled a and b in Figures 5.6 and 5.7) are clear and observed as one 4HBA···4HBA, one PROPY···PROPY, and three PROPY···4HBA molecular pair interactions. The strongest interaction occurs between two 4HBA molecules whilst the PROPY···4HBA adduct interaction is second strongest. The next strongest interactions (b) have energies less than 50 % that of the PROPY···4HBA interaction, and approximately 30 % that of the 4HBA···4HBA interaction.

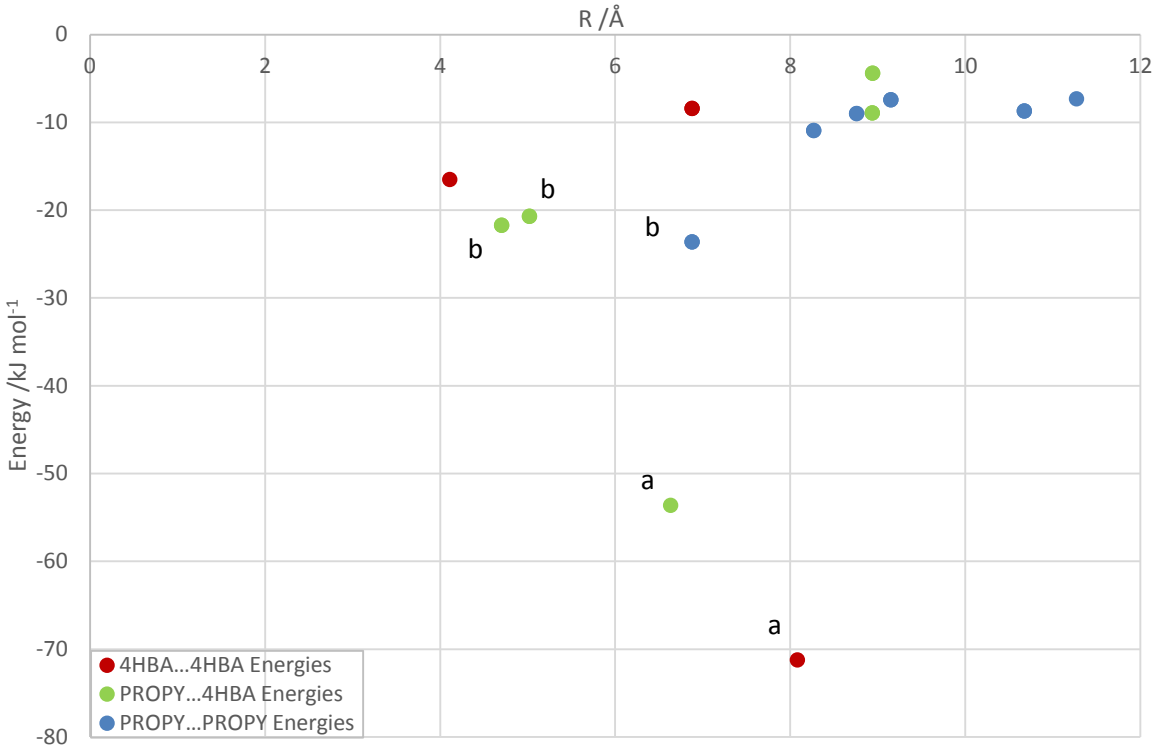

Figure 5.7. Interaction energies determined from PIXEL calculations plotted against molecule···molecule centroid distances (R) for PROPY-4HBA 1:1 co-crystal.

The total energy and its components from PIXEL calculations for the different molecular pairs are listed in Table 5.2. Unlike PROPY-MPAR, the highest Coulombic contributions are seen in the 4HBA···4HBA pairs, rather than PROPY···4HBA (even when the two PROPY···4HBA categories are combined) indicating strong interactions. The main interaction is identified from standard resolution crystallography as a carboxylic acid···carboxylic acid dimer. This is a highly favoured synthon motif comprised of strong hydrogen bonds and is the source of the large Coulombic energy observed. The total energy of both the PROPY···PROPY and 4HBA···PROPY pairs is greater than that of the 4HBA···4HBA pairs, despite the large Coulombic contribution. These co-former pairs show the lowest dispersion energy which may be a consequence of the large Coulombic energy component.

The energy of the PROPY···4HBA interaction is of a similar order to that seen in PROPY···MPAR, although appears lower in the energy rank order of the system due to the presence of the strong interactions in the co-former molecular pair. This is one difference that can be identified in response to aim number 1 (Section 5.2).

Table 5.2. Energy components for PROPY-4HBA determined from PIXEL calculations.

	Energies /kJ mol^{-1}				
	E_{coul}	E_{pol}	E_{disp}	E_{rep}	E_{tot}
PROPY···PROPY	-46.9	-23.0	-153.4	96.3	-126.5
PROPY···4HBA	-20.9	-15.4	-83.0	63.7	-55.7
4HBA···PROPY	-95.7	-50.4	-106.0	142.9	-109.3
4HBA···4HBA	-156.6	-87.5	-67.0	206.4	-104.5
Total	-320.1	-176.3*	-409.4	509.3	-320.1

*E_{pol} is not additive, therefore the sum of polarisation terms is not a valid indicator or value for gross comparisons.

The sums of the experimental hydrogen bonds for each molecular pair are presented in Figure 5.8. One very strong interaction (a, Figure 5.8) is evident and can be identified as the aforementioned strong 4HBA···4HBA molecular pair. This is comprised of two strong hydrogen bonds occurring from the acid hydroxyl to carbonyl of the second acid, and *vice versa* as expected for the dimer synthon identified in the standard resolution crystal structure. The second strongest molecular pair interaction (labelled a*, Figure 5.8) is consistent with that from PIXEL and Crystal Explorer (Figures 5.7 and 5.6 respectively) as the PROPY···4HBA adduct. This consists of one strong hydrogen bond (O–$H_{hydroxyl}$···$O_{carbonyl}$) and several other, weaker, hydrogen bonds. These have small interaction energies, approximately 12 % and 4 % of the primary hydrogen bond.

These three strong hydrogen bonds (acid dimer and PROPY···4HBA formation) all have V_{BCP}/G_{BCP} ratios greater than 1 showing a local concentration of charge, and an intermediate closed shell interaction. The value for the O–$H_{hydroxyl}$···$O_{carbonyl}$ hydrogen bond between the two main components is slightly greater than for the dimer hydrogen bonds, indicating a greater potential energy density relative to the kinetic energy density. All three hydrogen bonds have R_{ij} distances < 2 Å, those forming the acid dimer have distances of 1.60 Å, whilst the O–$H_{hydroxyl}$···$O_{carbonyl}$ distance is slightly longer, at 1.71 Å. This is marginally longer than that in PROPY-MPAR (1.68 Å) and with a smaller hydrogen bond energy (-49.6 kJ mol^{-1} compared to -53.2 kJ mol^{-1}). The presence of the strong acid···acid dimer is likely to impact this. These are further differences identified in response to aim number 1 (Section 5.2). No additional individual, strong hydrogen bonds are observed in the experimental model and full details of the experimental hydrogen bonds are given in the Supplementary File PROPY XD Interaction Analysis.

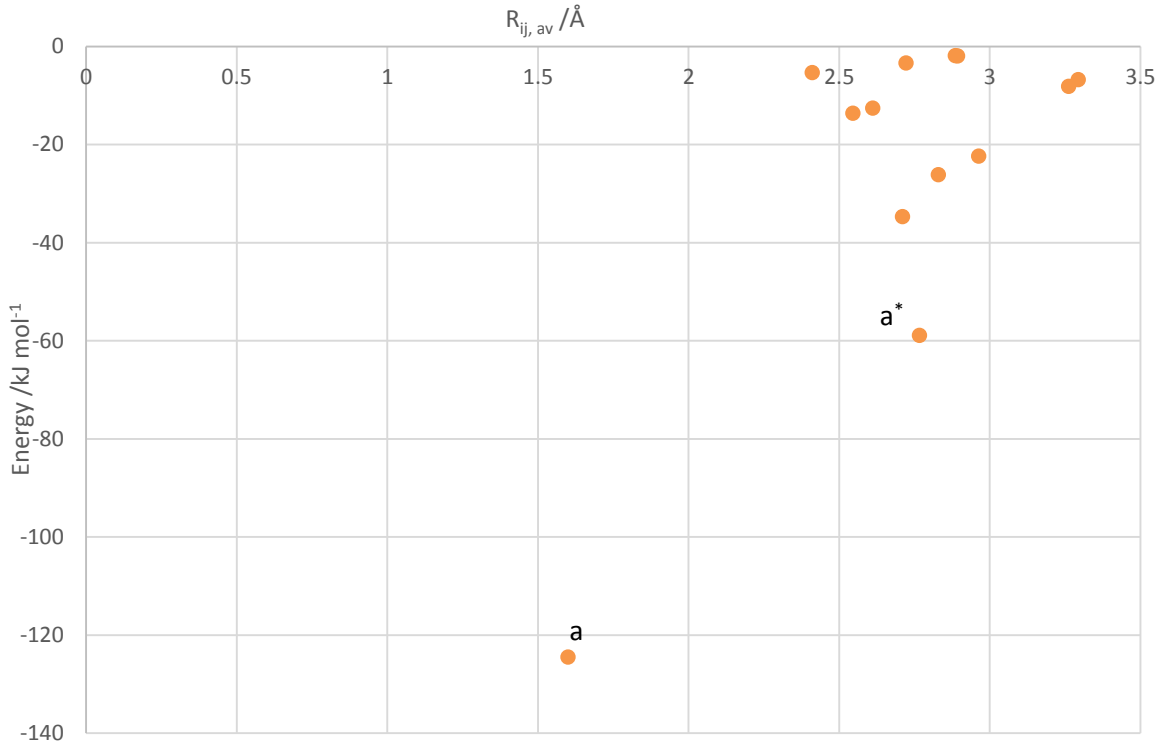

Figure 5.8. Total E_{HB} for molecule-molecule interactions (comprised of individual hydrogen bond between atoms) obtained from topological analysis of the experimental multipole model for PROPY-4HBA plotted against average R_{ij} of all interactions.

The next data points in the experimental scatter plot (Figure 5.8) are comprised of a number of weaker hydrogen bonds, with a total energy 20-25 % that of the co-former molecular pair. These occur between PROPY···PROPY (1) and PROPY···4HBA (2) and can be compared to the PIXEL energy distribution in Figure 5.7, b (PROPY···PROPY and PROPY···4HBA (2) observed between -20 and -30 kJ mol^{-1}).

The PROPY···PROPY interaction contains two hydrogen bonds with energy values approximately 15 % of the strongest hydrogen bonds (~18 % of the O–$H_{hydroxyl}$···$O_{carbonyl}$) and a further three with energies of half the strength (less than 8 % of the greatest hydrogen bond energies). The two PROPY···4HBA pairs contain a combination of hydrogen bonds, some with energies similar to the stronger components of the PROPY···PROPY pairs whilst the remainder are much weaker with energies 5 % and less of the strong hydrogen bonds. All these hydrogen bonds, and the remainder in the system can be classified as electrostatic in nature, i.e. $V_{BCP}/G_{BCP} < 1$, and R_{ij} distances > 2.2 Å.

5.4.3 PROPY-HQ

Figure 5.9 shows the Crystal Explorer energies for PROPY-HQ. In comparison to the previous two systems there is a greater number of strong or moderately strong interactions, and more molecular pair interactions overall. This is indicative of a stronger complex. The increased number

of interactions may be due partly to the 1:2 stoichiometric ratio of the system; the presence of additional HQ molecules, each containing two hydroxyl functional groups, provides additional functionality in the system through which strong intermolecular interactions can form.

The two strongest interactions involve HQ1 and HQ2 (a, Figure 5.9) with energy values in the same region as observed for PROPY···co-former pairings in the previous two systems. A clear energy gap between these and the next group of interactions (b, Figure 5.9) is evident. This second group has interactions mainly originating from HQ2 and PROPY. The weaker interactions predominantly contain HQ1 molecules with some originating from HQ2 and PROPY. The separation between the moderate and weak interactions is much less clearly defined than in the previous systems. With the exception of the strongest interaction, molecular pairs from HQ1 appear closer to the top of the scatter plot, with smaller interaction energies, than those containing HQ2.

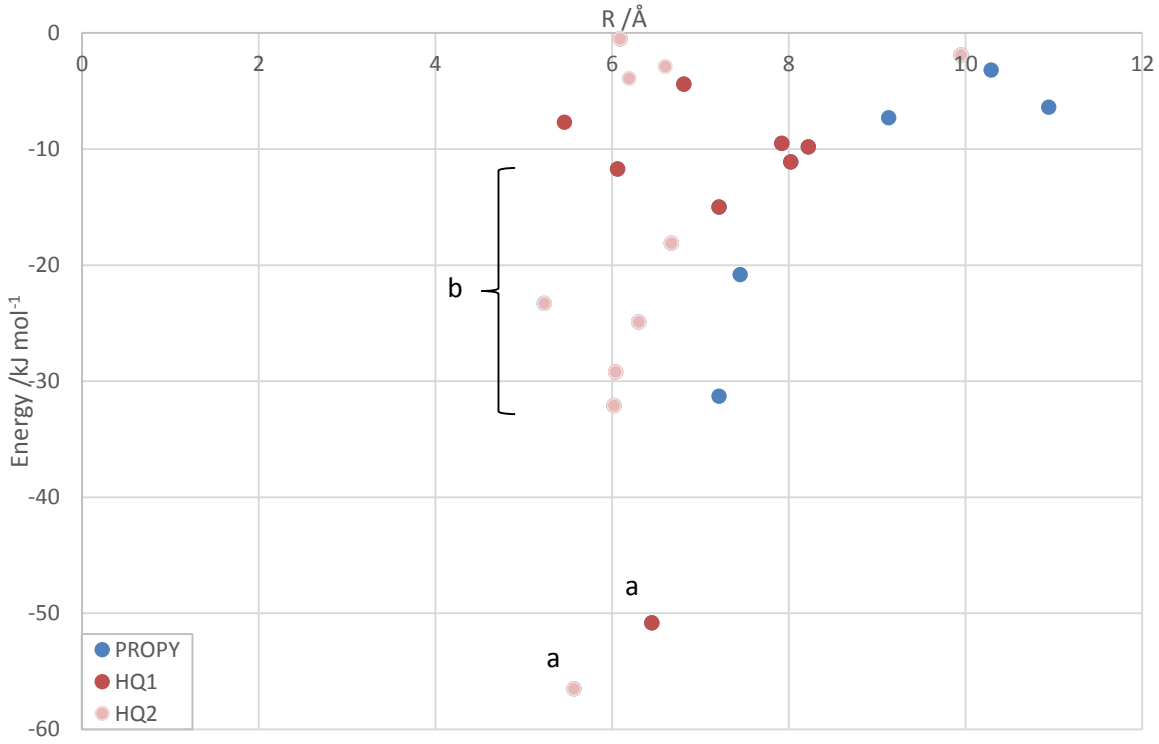

Figure 5.9. Intermolecular interaction energies for PROPY-HQ 1:2 co-crystal determined from Crystal Explorer calculations, plotted against molecule···molecule centroid distances (R).

The PIXEL energies display a similar array to Crystal Explorer, however some small differences are apparent (Figure 5.10). The two strongest interactions from Crystal Explorer (a) can be identified as PROPY···HQ1 and PROPY···HQ2, whilst the next strongest are two HQ···HQ interactions (b, Figure 5.10, displayed in purple) which occur between the two unique HQ molecules (HQ1 and HQ2).

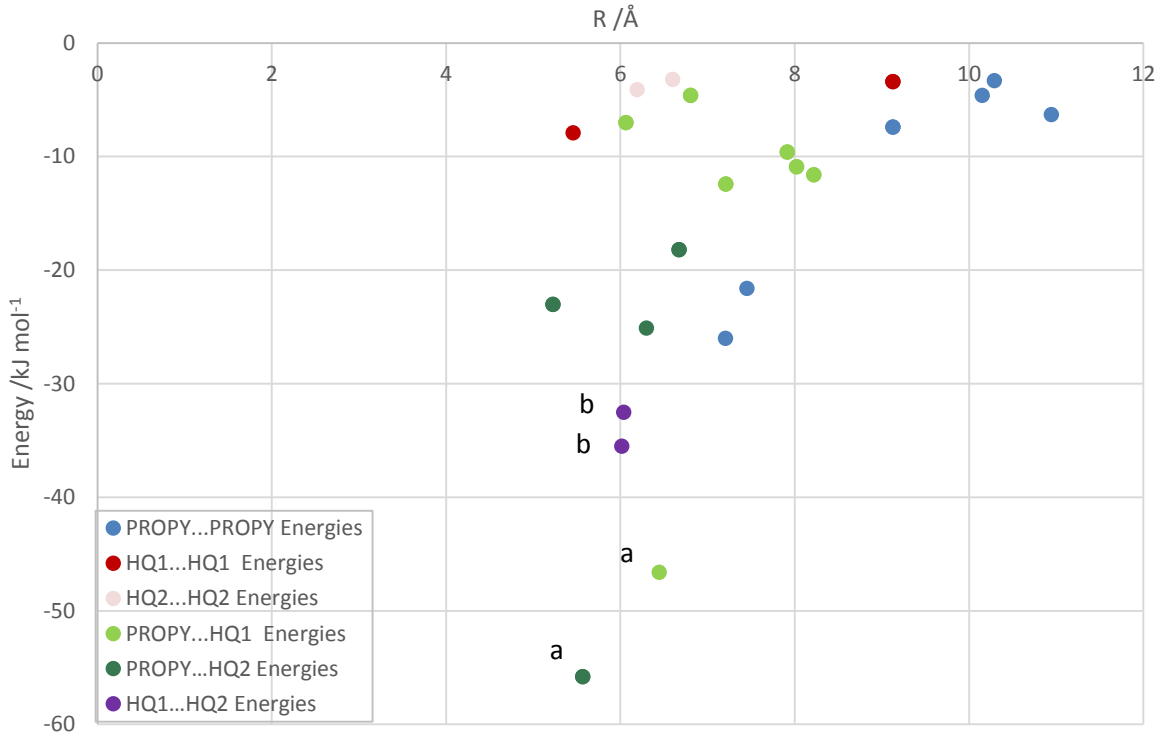

Figure 5.10. Interaction energies determined from PIXEL calculations plotted against molecule···molecule centroid distances (R) for PROPY-HQ 1:2 co-crystal.

In general, PROPY···HQ2 is stronger than the equivalent HQ1 with the majority of the latter interaction pairs located towards the top of the scatter plot. This is in accordance with the observation from the Crystal Explorer analysis that HQ1 forms interactions which are weaker than those involving HQ2. In this top region of the scatter plot there are also a number of PROPY···PROPY pairs and the homo HQ1···HQ1 and HQ2···HQ2 pairings.

Table 5.3 illustrates these observations as PROPY···HQ2 has the largest total, Coulombic and dispersion energy contributions of all the pairs. The total is more than 30 % greater than the next highest (PROPY···HQ1). PROPY···HQ1 and HQ1···HQ2 display, relatively large values for the Coulombic, and Coulombic and dispersion energy components respectively showing strong, favourable interactions. PROPY···PROPY has a similar total energy to PROPY···HQ1, however the Coulombic contribution is far greater (more than double) in the hetero PROPY···HQ1 pairing. The total energy of the HQ1···HQ2 pairs are weaker than the PROPY···PROPY and both hetero parings despite the large Coulombic energy component. Both homo HQ···HQ pairings are weak, with total energies considerably smaller than the other pairs. These appear to be dominated by dispersion contributions (HQ2···HQ2) and the dispersion and Coulombic components (HQ1···HQ1).

Table 5.3. Energy components for PROPY-HQ determined from PIXEL calculations.

	Energies /kJ mol^{-1}				
	E_{coul}	E_{pol}^{*}	E_{disp}	E_{rep}	E_{tot}
PROPY···PROPY	-65.8	-19.8	-141.0	73.0	-153.6
PROPY···HQ1	-144.3	-82.1	-176.4	244.2	-158.6
PROPY···HQ2	-204.4	-89.7	-184.0	259.0	-219.1
HQ1···HQ1	-16.4	-5.4	-30.2	22.4	-29.6
HQ2···HQ2	0.6	-1.1	-13.2	2.0	-11.7
HQ1···HQ2	-185.6	-88.3	-60.3	230.7	-103.5
Total	-575.0	-273.2*	-511.5	782.5	-580.1

$^{*}E_{pol}$ is not additive, therefore the sum of polarisation terms is not a valid indicator or value for gross comparisons.

The experimental multipole model reveals a single, very strong pairwise interaction (a, Figure 5.11) and three further pairs also with a relatively strong interaction energy (b). There is a clear energy separation between these groups, and also to the third group which comprises molecular pairs of low interaction energies. The greatest interaction energy (a, Figure 5.11) can be linked to a PROPY···HQ2 molecular pair and is dominated by a single strong O–$H_{hydroxyl}$···$O_{carbonyl}$ hydrogen bond with a high degree of local charge concentration, V_{BCP}/G_{BCP} = 1.61. The interaction distance, R_{ij} = 1.60 Å, is shorter than the equivalent primary hydrogen bond in PROPY-MPAR and PROPY-4HBA (1.68 Å and 1.71 Å respectively) and corresponds with the stronger hydrogen bond energy (aim 3, Section 5.2). Three other hydrogen bonds occur between molecules in this pair, however these are extremely weak and electrostatic in nature.

The second strongest pairing (b*, Figure 5.11) relates to PROPY-HQ1 which contains the second O–$H_{hydroxyl}$···$O_{carbonyl}$ hydrogen bond. This has a lower energy in comparison to that from HQ2 although still has V_{BCP}/G_{BCP} >1 indicating an intermediate closed-shell interaction. The R_{ij} value of 1.72 Å reflects the weaker interaction strength, and continues the correlation of R_{ij} and hydrogen bond energy seen thus far. This provides further evidence for aim 3 (Section 5.2). Several other hydrogen bonds are also present in this pairing which are electrostatic in nature, although slightly stronger (by two to five times) than those in the PROPY···HQ2 pairing.

The two other strong interactions (b) are two HQ1···HQ2 pairings, each occurring *via* an O–$H_{hydroxyl}$···$O_{hydroxyl}$ primary hydrogen bond. Both can be classified as intermediate closed-shell

interactions (V_{BCP}/G_{BCP} = 1.10 and 0.95 respectively) although that with the weaker hydrogen bond has a V_{BCP}/G_{BCP} ratio slightly less than 1. These pairings contain no other contributing hydrogen bonds discovered from the topological analysis of the experimental model. These four strongest pairings (a, b* and b, Figure 5.11) are in accordance with the PIXEL energy analysis in their composition and ranking even though the scatter plot array has a very different appearance.

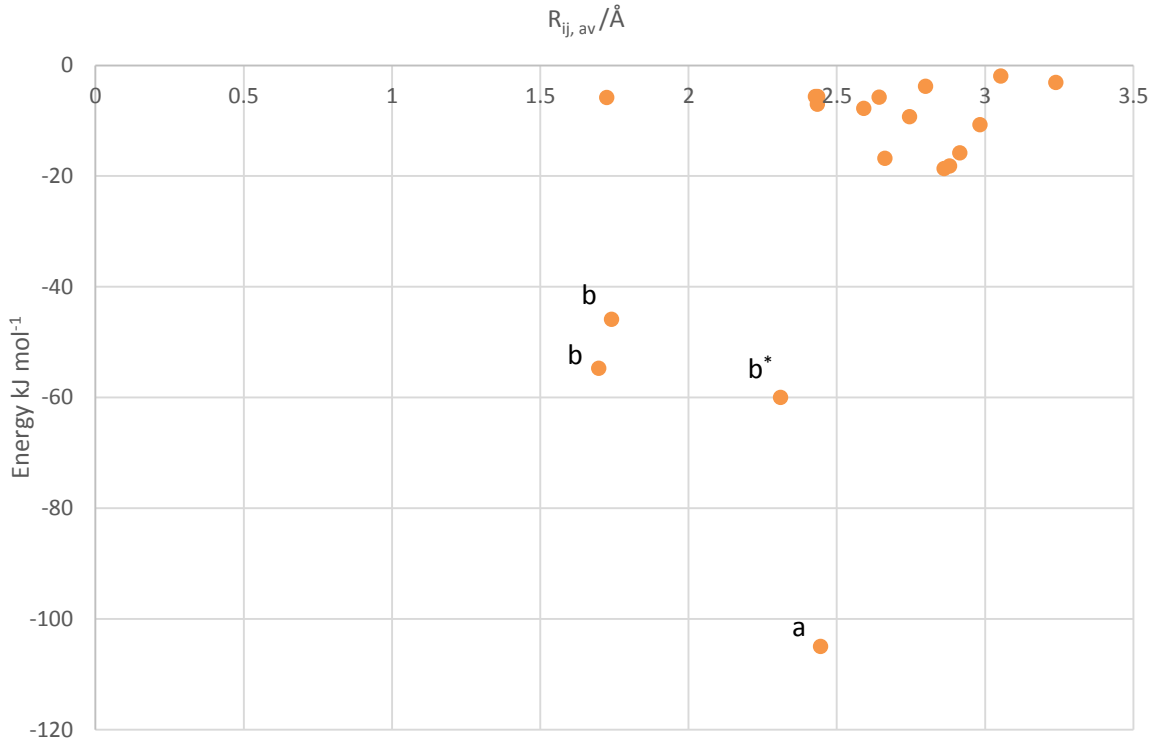

Figure 5.11. Total E_{HB} for molecule-molecule interactions (comprised of an individual hydrogen bond between atoms) obtained from topological analysis of the experimental multipole model for PROPY-HQ plotted against average R_{ij} of all interactions.

The remaining pairings (unlabelled, Figure 5.11) are quite disparate from the four strong interactions in the experimental scatter plot. This is in contrast with PIXEL and Crystal Explorer (Figures 5.10 and 5.9 respectively), in which the separation of the moderate and weak strength interactions is less defined and the two groups appear to merge into one with no clear boundary. This is likely to result from the nature of the interaction searches. The experimental values are dominated by strong hydrogen bonds, and not all weaker hydrogen bonds may be located. Hence, the molecular pairs towards the top of the plot in Figure 5.11 may not include all contacts assumed in PIXEL and Crystal Explorer analysis and the separation between the groups is greater.

5.4.4 PROPY-FA

PROPY-FA has a stoichiometry of 1:0.5 in the crystal structure. Both Crystal Explorer and PIXEL require complete molecules and therefore this system was treated as a 2:1 ratio for these

calculations, and two independent PROPY molecules are discussed (although they are in fact symmetry related).

Crystal Explorer pairwise interaction energies are shown in Figure 5.12. The two strong interactions (a, Figure 5.12) originate from FA and PROPY. There are several PROPY interactions with moderate strength interactions, whilst the majority of those from FA have lower energies and are located towards the top of the scatter plot. For similar centroid···centroid distances interactions from PROPY are stronger than those occurring from FA. This is also true for all the previous systems.

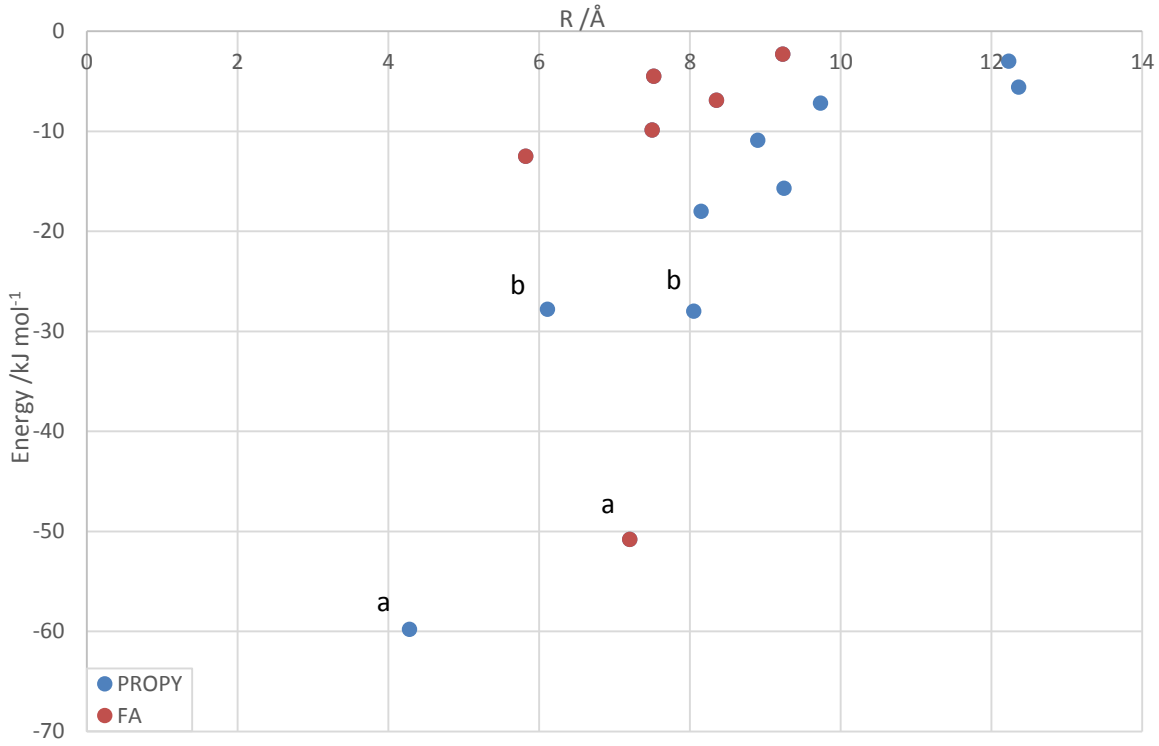

Figure 5.12. Intermolecular interaction energies for PROPY-FA 1:0.5 co-crystal determined from Crystal Explorer calculations, plotted against molecule···molecule centroid distances (R).

The PIXEL scatter plot (Figure 5.13) is similar to that obtained from Crystal Explorer. Two strong interactions (labelled a* and a) arise from PROPY1···PROPY2 and PROPY···FA pairings respectively. The latter is seen to occur with both PROPY1 and PROPY2 as the same primary hydrogen bond ($O–H_{carboxylic\ acid}\cdots O_{carbonyl}$) occurs for both symmetry related molecules. In the Crystal Explorer analysis two pairings involving PROPY, both occurring between PROPY1 and PROPY2, are seen with very similar energies but different R distances (b, Figure 5.12). PIXEL produces a greater difference in these energies (b, Figure 5.13) locating them further apart in the scatter plot. That with the longer centroid···centroid is stronger.

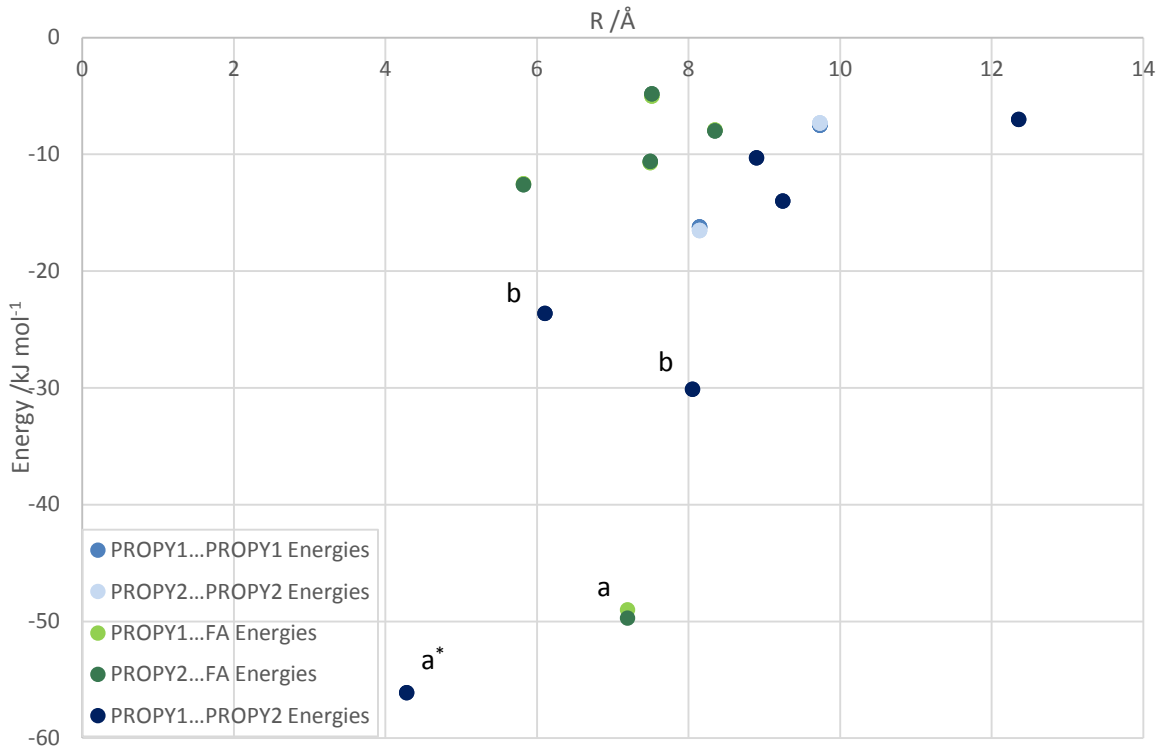

Figure 5.13. Interaction energies determined from PIXEL calculations plotted against molecule···molecule centroid distances (R) for PROPY-FA 1:0.5 co-crystal.

Unsurprisingly, PROPY1···PROPY1 and PROPY2···PROPY2 interactions are almost identical with very similar energy values presented in Table 5.4 and their data points either superimposed upon one another or located extremely close together in the scatter plot (Figure 5.13). Likewise, PROPY1···FA and PROPY2···FA pairings are also seen at the same points and have similar energy values and composition in Table 5.4.

With the exception of the strongest PROPY···PROPY and PROPY···FA interactions (a) the interactions between two PROPY molecules appear, in general, stronger than those between PROPY and FA and is evident in Figure 5.13. No FA···FA interactions are seen, as each FA is completely surrounded by PROPY due to the stoichiometric ratio.

In addition to having the strongest individual pairwise interaction, Table 5.4 shows that the sum of all PROPY1···PROPY2 pairs has the greatest total energy. These interactions also have the greatest Coulombic, dispersion and repulsion components. Both PROPY···FA sets show strong total interaction energies which are similar to that of PROPY1···PROPY2. The Coulombic components are also similar in value however the dispersive forces are significantly less. The interactions between identical PROPY molecules (e.g. PROPY1···PROPY1) are weak, as they are in neighbouring asymmetric units in the crystal structure; the closest PROPY molecules are those related by symmetry (PROPY1 and PROPY2) within the same asymmetric unit.

Table 5.4. Energy components for PROPY-FA determined from PIXEL calculations.

	Energies /kJ mol^{-1}				
	E_{coul}	E_{pol}^{*}	E_{disp}	E_{rep}	E_{tot}
PROPY1···PROPY1	-38.0	-18.8	-101.6	63.6	-38.0
PROPY2···PROPY2	-38.0	-18.4	-101.6	62.4	-38.0
PROPY1···PROPY2	-125.8	-59.8	-329.8	233.0	-125.8
PROPY1···FA	-113.9	-63.6	-105.4	161.7	-113.9
PROPY2···FA	-114.2	-63.2	-106.6	162.3	-114.2
FA···FA	-	-	-	-	-
Total	-391.9	-205.2*	-643.4	620.0	-620.5

*E_{pol} is not additive, therefore the sum of polarisation terms is not a valid indicator or value for gross comparisons.

The experimental hydrogen bond energy sums scatter plot shows one very strong interaction (a, Figure 5.14) which can be correlated to the main PROPY···FA molecular pair adduct. This is comprised of a single, strong hydrogen bond (O–$H_{carboxylic\ acid}$···$O_{carbonyl}$) with a few much weaker hydrogen bonds contributing. The strong primary hydrogen bond is the only one in the system determined with V_{BCP}/G_{BCP} >1 showing predominantly electrostatic interactions with a local concentration of charge. The R_{ij} distance is short, 0.99 Å, and the energy larger than the O–$H_{hydroxyl}$···$O_{carbonyl}$ hydrogen bonds in PROPY-MPAR, -4HBA and -HQ (the exception being a single HQ2···PROPY hydrogen bond). This provides evidence for aims 3 and 4 (Section 5.2).

This strong PROPY···FA pairwise interaction (a) is observed in the theoretical calculations however another, stronger, pair (PROPY1···PROPY2, a*) is also present. The equivalent experimental data point (a*, Figure 5.14) for this pair has the second largest energy, however it is considerably less than that of PROPY···FA (~30 %).

The theoretical calculations determine the forces present using each molecule as a whole. In contrast, experimental energies are derived from single points (BCPs) between atomic nuclei. The experimental model therefore does not account wholly for overall molecule···molecule interactions as no energy can be estimated if a BCP is not located. The experimental model appears to severely under estimate some forces present between molecules. This may be the cause for the experimental PROPY···PROPY interactions appearing weaker than PROPY···FA in

contrast to the theoretical results. Whilst summations cannot provide a true quantitative value they do however permit relative comparisons.

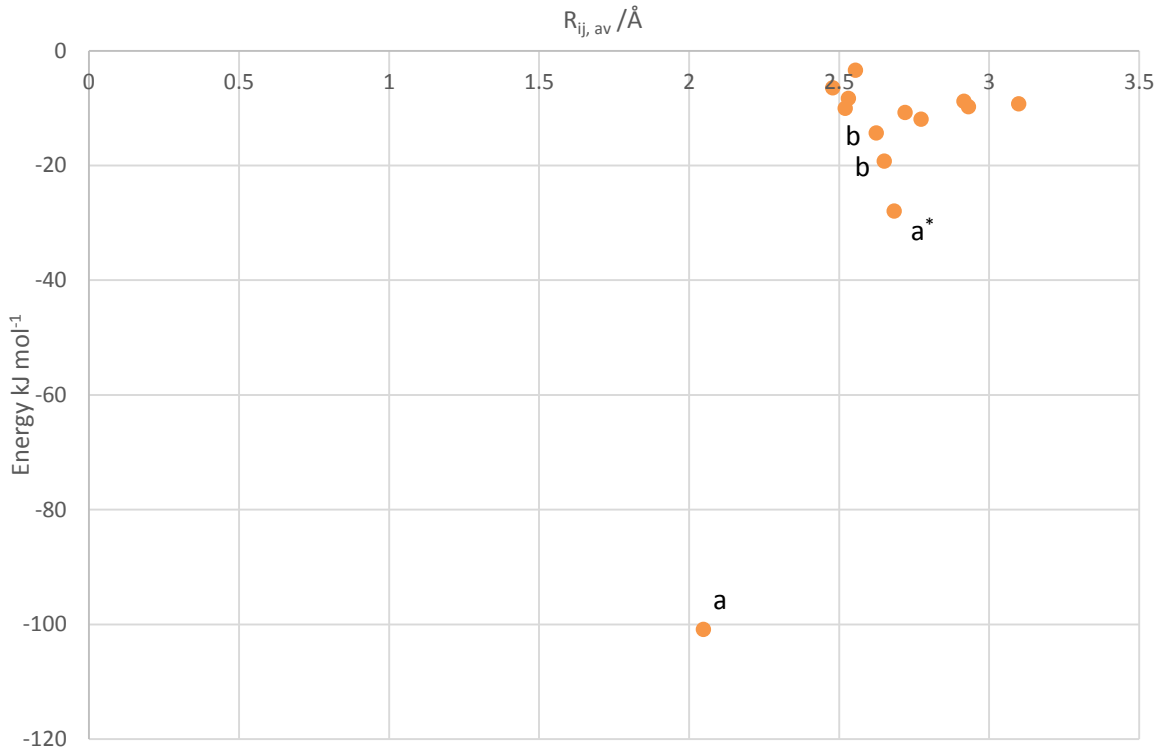

Figure 5.14. Total E_{HB} for molecule-molecule interactions (comprised of individual hydrogen bond between atoms) obtained from topological analysis of the experimental multipole model for PROPY-FA plotted against average R_{ij} of all interactions.

After PROPY···FA, the next strongest experimentally determined interaction pairs are PROPY1···PROPY 2 (as discussed), PROPY···FA and PROPY···PROPY (b, Figure 5.14). This contrasts with the rank order obtained from theoretical models which is PROPY1···PROPY2 > PROPY1···PROPY2 > PROPY1···PROPY1 and PROPY2···PROPY2. This disparity between the experimental and theoretical values and rank orders in PROPY-FA can be related to the structure. FA is the only co-former molecule which does not contain an aromatic ring and no additional hydrogen bond functionalities to form favourable hydrogen bonds besides that partaking in the primary $O–H_{carboxylic\ acid}\cdots O_{carbonyl}$ hydrogen bond. As a result, many of the forces present are less atom directed (e.g. π-stacking), and cannot be detected in this analysis leading to differences in the interactions obtained in the two approaches. This provides evidence for aim 4 (Section 5.2)

The other molecular parings contain a selection of weak hydrogen bonds, each with a hydrogen bond energy less than 5 % of the that for the primary $O–H_{carboxylic\ acid}\cdots O_{carbonyl}$ hydrogen bond. When summed, these still produce low total interaction energies.

5.5 Deconvolution of Interaction Energies

The scatter plots of PIXEL and Crystal Explorer energies exhibit three general regions: the strongest interactions (often labelled as 'a' in Section 5.4), those of moderate strength (b) and finally very weak interactions. These regions are more clearly defined in some systems than others.

5.5.1 Interaction Strengths

It is hypothesised that the strongest interactions are the most favourable in the system, and direct the structure assembly. Heterosynthons interrupt the homo API···API interactions and make the co-crystal preferential to the two individual components; the co-crystal forms rather than either component crystallising alone. These strong interactions are located towards the bottom of each scatter plot, and only a few are present in each system. When the experimental charge density is considered, each of these pairings is dominated by a single, strong hydrogen bond, and any other interactions contributing to that molecular pair are weak and comparatively non-influential. The exception to this is seen in PROPY-4HBA which contains a molecular pair with two strong hydrogen bonds forming the carboxylic acid dimer interaction. In general, these strong interactions are PROPY···co-former molecular pairs, however PROPY-4HBA and PROPY-HQ both display additional strong co-former···co-former molecular pairings in this region.

The second region contains moderate strength interactions which are comprised of several weaker hydrogen bonds, contributing to an overall interaction energy greater than any in isolation. It is conjectured that these are favourable interactions, however less influential than the main structure-directing, strong interactions. These will form if the steric-electronic balance of the API···co-former assembly allows for the appropriate orientation and positioning of molecules. They will not, however, influence or direct the main assembly. The final region contains pairwise interactions comprised of many very weak hydrogen bonds. These are weaker and / or fewer in number than the moderate strength region resulting in lower overall interaction energies. These are likely to have very little influence on structural arrangements, forming serendipitously between adjacent molecules.

5.5.1.1 Components of Theoretical Interaction Energies

Appendix B.4.4, Table B.19 summarises each system in terms of these strong, moderate and weak interactions. Each of these subgroups is divided into the separate energy components and the

contribution of each of these to the overall system is also given for both PIXEL and Crystal Explorer data. A summary across all four systems according to the energy components and the strong, moderate strength and weak interactions follows.

The Coulombic component dominates the strong interactions which is in contrast to the moderate and weak interactions which are comprised of predominantly dispersive forces. In most systems, the group of strongest interactions contains the largest proportion of the Coulombic energy of the whole system (60-70 %). PROPY-HQ is an exception, with the strongest interactions comprising only 40-45 % of the Coulombic energy. An almost equal proportion (47-48 %) is contained within the moderate strength interactions which is a far greater proportion than any of the other systems exhibit for this group type. Typically, 20-40 % of the total Coulombic energy is contained in the moderate strength interactions which is at least 20 % less than that exhibited by the strongest interactions for that system.

For the strongest interactions group dispersion energy forms a relatively small proportion of the system total. Of these, PROPY-FA displays the greatest total dispersion energy contribution (28-35 %), with the other systems containing between 9-18 % of the total in the system.

In all systems, the sum of the moderate strength interactions typically accounts for the greatest proportion of the total energy, exceeding the contribution of the strongest interactions. PROPY-HQ and PROPY-MPAR have a significantly greater percentage of the total energy contained within the moderate interactions in comparison to the strong ones. PROPY-4HBA and PROPY-FA have a more equal distribution across the two groups, with the moderate strength ones being slightly more significant. Weak interactions account for approximately 20-30 % of the total energy in most systems. The exception to this is PROPY-MPAR which contains less than 10 % of the total interaction energy within these weak molecular pairings. The Coulombic component of the weaker interactions of PROPY-MPAR is also considerably smaller than observed in the other three systems (less than 2 % of the total Coulombic energy in comparison to 13.5 % in PROPY-FA).

The total energy and contributions of each of the groups (strong, moderate strength and weak) are summarised in Figures 5.15 and 5.16 highlighting the dominance of the strong interactions in the Coulombic energy component with a relatively small dispersion energy contribution, and the large contribution of the moderate energy interactions to the dispersion energy. Variations between systems are also observed, such as in the total energy; PROPY-4HBA displays an almost equal contribution of the three groups which is similarly replicated in PROPY-FA and PROPY-HQ. In contrast, PROPY-MPAR has a very large moderate strength interaction contribution, with a reduced influence of the strong and, in particular, the weak interactions.

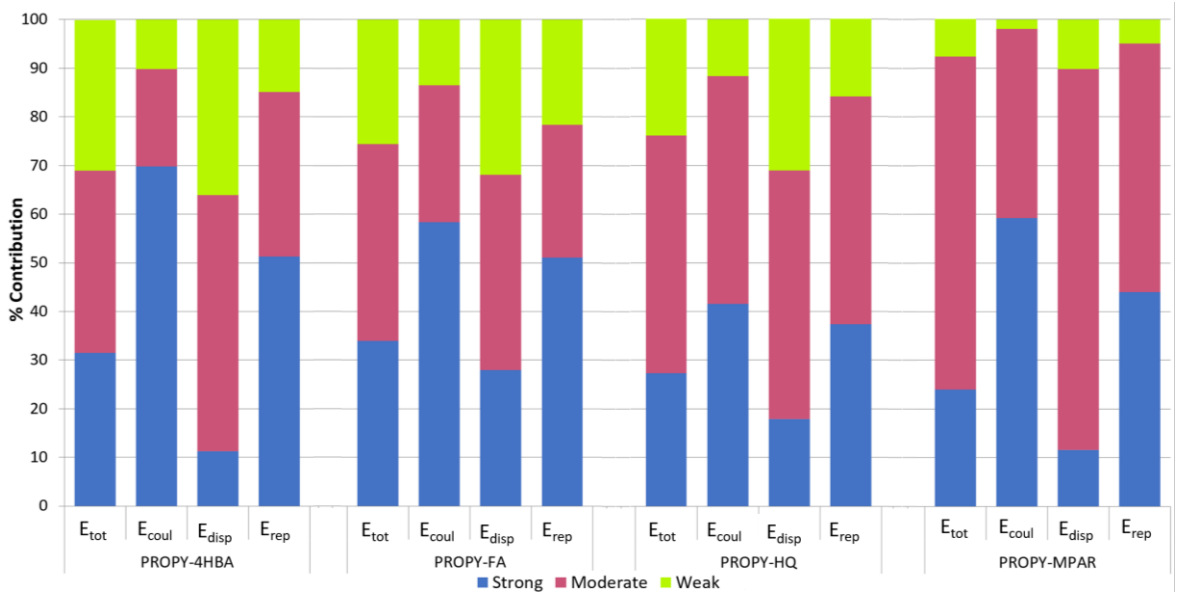

Figure 5.15. Contributions of the strong, moderate and weak interactions to the Coulombic, dispersion, repulsion and total energy components of the four PROPY systems from PIXEL.

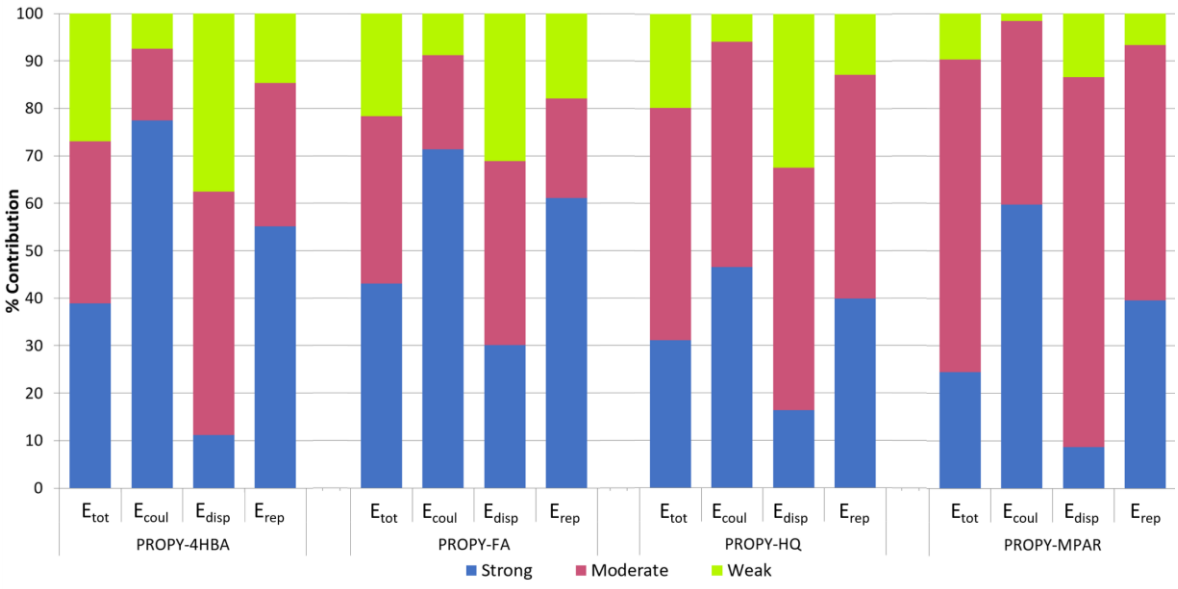

Figure 5.16. Contributions of the strong, moderate and weak interactions to the Coulombic, dispersion, repulsion and total energy components of the four PROPY systems from Crystal Explorer.

5.5.1.2 Experimental Interaction Properties

The experimental data provides additional complementary information and allows the individual O–H···O primary hydrogen bond, present in all, to be investigated. It is observed that the hydrogen bonds with the greatest energies have the shortest R_{ij} distances, and those with longer R_{ij} values are weaker. There is only one exception to this trend, the strongest $O–H_{hydroxyl}\cdots O_{carbonyl}$

hydrogen bond in PROPY-HQ has a large energy, however R_{ij} is longer than that seen in PROPY-FA (weaker hydrogen bond energy). This could, however, be interpreted that PROPY-FA is the outlier, and the trend is true for the other, structurally similar co-formers. This provides evidence for aims 3 and 4 (Section 5.2) and indicates differences between aromatic and non-aromatic systems.

A second trend is seen in the primary hydrogen bonding interactions; those with stronger hydrogen bond energies have an increased V_{BCP}/G_{BCP} ratio. This trend is seen for all with the exception of PROPY-4HBA which may be accounted for by the presence of the strongly hydrogen bonded acid dimer. The same trend is observed when all strong hydrogen bonds are considered, and the PROPY-4HBA $O–H_{hydroxyl}\cdots O_{carbonyl}$ hydrogen bond has a larger V_{BCP}/G_{BCP} ratio than expected for the interaction strength. Data available in Supplementary File XD_Interaction Analysis.

5.5.2 Contributions of the Coulombic and Dispersion Energy Components

The interaction overview (Section 5.4) compared the three techniques (Crystal Explorer, PIXEL, and energies from a topological analysis of the experimental multipole model) and showed comparative results. The methods employed in the theoretical calculations produce minor differences however the experimental models gave vastly different results in some cases. This (experimental) analysis searches for hydrogen bonds between atomic nuclei although other interactions are also likely to be present. These are more difficult to determine and analyse as they do not occur between two distinct atoms hence cannot be searched for on the electron density landscape. Hydrogen bonds manifest themselves in the Coulombic energy component of the molecular pair interactions calculated whilst others, which are harder to identify, may arise from primarily dispersive contributions.

To test this theory, some interactions which appeared significantly stronger in PIXEL and Crystal Explorer analysis in comparison to the ΣE_{HB} from the experimental model and *vice versa* were investigated. Full details of all interactions are given in Supplementary Files PROPY PIXEL calculations; PROPY Crystal Explorer Calculations; and PROPY PIXEL CE Compare.

1. The 4HBA···4HBA acid dimer appears stronger from experimental analysis, with a greater separation to the next strongest interactions (PROPY···4HBA) than the theoretical calculations. Inspection of the individual molecular pair energy identifies a large Coulombic component (-148.5 kJ mol^{-1} PIXEL; -136.8 kJ mol^{-1} CE) and a small dispersive energy (-23.1 kJ mol^{-1} PIXEL; -12.6 kJ mol-1 CE) in comparison to the PROPY···4HBA pair which has a similar dispersive component (-23 kJ mol^{-1} PIXEL; -18.3 kJ mol^{-1} CE) but a significantly smaller E_{coul} (-74.8 kJ mol^{-1} PIXEL; -66.6 kJ mol^{-1} CE). This greater Coulombic

energy is identified in the experimental analysis and the energy sum appears greater than that for PIXEL and Crystal Explorer.

2. The strongest interaction from PIXEL and Crystal Explorer for PROPY-FA is defined as a PROPY···PROPY molecular pair, followed by the PROPY···FA adduct. Experimentally, the PROPY···FA pair is observed as the strongest, and the corresponding PROPY···PROPY pair has a considerably reduced energy in comparison. PIXEL and CE show a Coulombic energy component of only -26.1 kJ mol^{-1} and -21.4 kJ mol^{-1} respectively for the PROPY···PROPY interaction and the energy is dominated by dispersive forces (-68.2 kJ mol^{-1} and -72.6 kJ mol^{-1} respectively). The PROPY···FA interaction, however, is dominated by the Coulombic energy (-88.3 / -88.2 kJ mol^{-1} PIXEL; -77.6 kJ mol^{-1} CE) with a small dispersive component (-21.6 / -22 kJ mol^{-1} PIXEL; -16.6 kJ mol^{-1} CE). Experimental energies are derived from hydrogen bonds which are principally Coulombic in nature. The differences in the constituents of the PROPY···FA and PROPY···PROPY interaction energies account for the differences in the experimental energies; the large dispersive forces in the PROPY···PROPY interaction are not considered and the experimental interaction energy appears considerably reduced.

As discussed, the strongest interactions are generally dominated by the Coulombic component, and the weakest by dispersion. However, the discrete values for dispersion energy are greatest in the moderate strength interactions.

Dispersion energy is likely to arise from the interaction of π-systems, such as the aromatic co-former and PROPY rings. The rings of PROPY are similar in all systems, and therefore it is the co-former molecule which will affect the dispersive forces more considerably. FA is structurally different to the other co-formers, lacking an aromatic ring and hence it is unsurprising that the dispersion energy in this system differs in comparison. The greatest dispersion energy is still manifested in the moderate strength interactions however, the strong interactions also have a large dispersion energy. This is significantly greater than observed in the three other systems and provides evidence for aim number 4 (Section 5.2).

FA contains a series of double bonds (carbonyl and alkene groups) in the di-acid molecule which can form π-interactions to the aromatic rings of PROPY (no FA···FA interactions occur). The $\rho(\mathbf{r})$ in these double bonds is greater than that in the co-former aromatic rings (Appendix B.3.4). Therefore, PROPY-FA would be expected to have stronger dispersive forces arising from an increased electron density.

5.5.3 Types and Contributions of the Molecular Pairs

The hypothesis that the strongest interactions dictate the molecular assembly can be explored in terms of both the additional interactions present and the types of molecules in the pairs. The strong API···co-former pair(s) will be highly favoured and direct the adduct construction. Additional molecular pairs surrounding this will either be contributory to the overall energy if they also form favourable interactions, or they may compromise the strongest interactions. This would occur if molecules are placed in unfavourable positions as a result of the primary interaction(s) formation. Weak interactions are unlikely to dictate structure, however if interactions are plausible they may impact molecular conformation or orientation. As a system strives for the most favourable energetic arrangement of molecules, the strongest interactions that are favourable and result in the largest energy will be sought primarily.

Tables 5.5 and 5.6 categorise the molecular pair energies according to the types of molecules (API or co-former), separated into constituent energy components. Crystal Explorer data (Table 5.5) shows the significant influence of the co-former molecules represented by large Coulombic energies. These are greater than the corresponding API in all systems with the exception of PROPY-MPAR. As discussed, MPAR contains no hydrogen bonding functionality beyond that involved in the API···MPAR primary interaction. The smaller co-former contribution, and lower Coulombic energy value in comparison to the other systems is expected. The rank of systems according to co-former Coulombic energy is: HQ > 4HBA > FA > MPAR, which correlates well with the number of hydrogen bonding functionalities present.

Table 5.5. Table of interaction energies for the PROPY co-crystal systems obtained from Crystal Explorer calculations, summarised into API and co-former interactions.

	API Energies /kJ mol^{-1}			Co-Former Energies /kJ mol^{-1}			Total CE energy	Total CE energy per molecule
	E_{coul}	E_{disp}	E_{rep}	E_{coul}	E_{disp}	E_{rep}	$E_{tot,\Sigma}$	
PROPY-4HBA	-127.8	-269.8	239.6	-220.8	-169.1	326.3	-476.9	-119.2
PROPY-FA	-158.9	-289.7	272.6	-177.4	-124.0	254.4	-461.9	-115.5
PROPY-HQ	-219.0	-270.3	316.3	-393.1	-288.5	588.7	-688.4	114.7
PROPY-MPAR	-132.8	-274.4	241.9	-104.0	-181.6	189.9	-433.8	-108.5

PIXEL analysis performs further separations of pairs into API···API, API···co-former and co-former···co-former interactions. As expected, API···co-former pairs form the strongest interactions, which predominantly contain the largest Coulombic and dispersive contributions. The exception is PROPY-4HBA with a large co-former···co-former Coulombic contribution (arising from the strong acid···acid dimer). PROPY-HQ also displays a large Coulombic contribution for co-former···co-former interactions arising from the $O–H_{hydroxyl}···O_{hydroxyl}$ hydrogen bonds. In both these systems the co-former···co-former dispersive component is less significant than the Coulombic energy (approximately 50 % less) showing E_{coul} to be the dominant force. These co-former interactions are highly favourable and contribute beneficially to the overall system energy. Neither PROPY-MPAR or PROPY-FA contain significant, if any (PROPY-FA), co-former···co-former interactions due to the lack of functionality beyond the primary hydrogen bond. Weak interactions form to the ester group of MPAR and constitute the small energies displayed in Table 5.6.

Table 5.6. Table of interaction energies for the PROPY co-crystal systems obtained from PIXEL calculations, summarised into API···API, API···co-former and co-former···co-former interactions.

	API···API Energies /kJ mol^{-1}			API···Co-Former Energies /kJ mol^{-1}			Co-Former···Co-Former Energies /kJ mol^{-1}			Total PIXEL energy $E_{tot,\Sigma}$	Total PIXEL energy per molecule
	E_{coul}	E_{disp}	E_{rep}	E_{coul}	E_{disp}	E_{rep}	E_{coul}	E_{disp}	E_{rep}		
PROPY-4HBA	-46.9	-153.4	96.3	-116.6	-189.0	206.6	-156.6	-67.0	206.4	-396.5	-99.1
PROPY-FA	-201.8	-533.0	359.0	-228.1	-212.0	324.0	-	-	-	-620.5	-103.4
PROPY-HQ	-65.8	-141.0	73.0	-348.7	-360.4	503.2	-201.4	-103.7	255.1	-580.1	-96.7
PROPY-MPAR	-49.0	-143.6	91.0	-194.9	-229.5	291.3	-23.0	-56.8	44.5	-402.8	-100.7

In contrast to the co-former···co-former pairs, API···API pairs are dominated by dispersive energy. PROPY-FA is the only system with a significant Coulombic component, however the dispersive energy is also large and still dominates the interactions. PROPY-4HBA, -HQ and -MPAR all have similar Coulombic, dispersive and repulsive energies between PROPY molecules. All these systems contain PROPY in a stoichiometry of 1 relative to the co-former and hence the same number of PROPY molecules are present to form interactions. PROPY-FA clearly deviates from the other three systems, arising primarily from the differences in stoichiometry. Two equivalents of PROPY results in increased PROPY···PROPY contacts.

5.6 Experimental Charge Analysis

In addition to individual hydrogen bond energies, experimental studies can also provide valuable information regarding charge and its distribution throughout molecules. Several methods are possible for the integration of the electron density and allocation of charge to atoms. Stockholder partitioning is considered the most reliable[169] and is displayed in Figures 5.17 and 5.18. Other

approaches (Mulliken[170] and Bader charges[167]) have also been applied and are included in Appendix B.3.5.

5.6.1 Analysis of the Ring Critical Points

Similar to BCPs, Ring Critical Points (RCP)s can be located at the centre of ring constructs and evaluated in a comparable way. Rings can be formed *via* covalent bonds in the molecular structure, through non-covalent inter / intra-molecular interactions, or a combination of both. PROPY contains two molecular ring fragments; a 5-membered, N-containing heterocycle and a phenyl ring. These can readily be compared across the co-crystal family series and analysis is shown in Appendix B.3.5. The most interesting property to compare across the series is $\rho(\mathbf{r}_{RCP})$ in conjunction with atomic charges. Figure 5.17 shows the Stockholder charges and $\rho(\mathbf{r}_{RCP})$ for the PROPY component of each system. Full details of atomic charges are given in Appendix B.3.3.

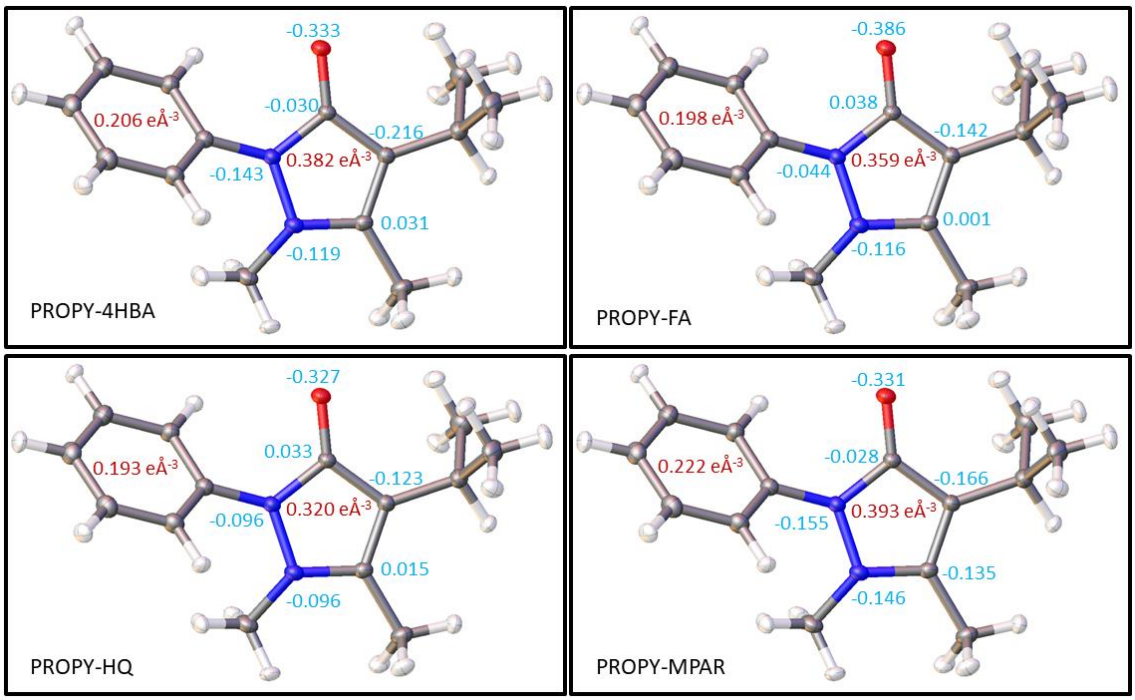

Figure 5.17. Atomic charges (blue) and $\rho(\mathbf{r})$ (red) at the RCPs for PROPY in the four systems, using Stockholder atomic partitioning for charges.

The lowest $\rho(\mathbf{r}_{RCP})$ of the 5-membered PROPY ring is seen in PROPY-HQ with a value of 0.320 eÅ^{-3}. A greater accumulation of charge is likely to result from increased hydrogen bonding. In contrast to the single strong hydrogen bond in the other systems, two hydrogen bonds form to the carbonyl and hence the density here might be expected to be larger. HQ forms two hydrogen bonds per molecule, the O–$H_{hydroxyl}$···$O_{carbonyl}$ to PROPY and an O–$H_{hydroxyl}$···$O_{hydroxyl}$ between HQ molecules. These are all classed as strong and have similar energies with one exception, the

hydrogen bond from O(31) to PROPY. This has a much larger energy determined from the experimental model and the largest $\rho(\mathbf{r}_{BCP})$ of all hydrogen bonds across the four systems. This hydrogen bond appears to act as an electron sink due to the accumulation of a greater density. The $O–H_{hydroxyl}\cdots O_{hydroxyl}$ hydrogen bonds of HQ form a linear network which extends throughout the crystal structure linking all molecules and allowing charge to be distributed evenly (Figure 5.18, b). The strong $O(31)–H_{hydroxyl}\cdots O_{carbonyl}$ forms the end of this network which terminates at PROPY, and hence charge accumulation is seen in the hydrogen bond. This manifests as a stronger hydrogen bond rather than an accumulation in any one molecule.

A ring is also generated via the dimer formation between the two 4HBA molecules in PROPY-4HBA: O(23)–C(27)–O(22)–H(22)–O(23)–C(27)–O(22)–H(22), and hence an RCP can be located. The ring, as well as the dimer hydrogen bonds, can therefore be analysed. In comparison with the covalently bonded rings of PROPY and co-formers the density accumulation here is low, however the charge contained within the atoms forming the ring is comparable to other rings.

5.6.2 PROPY···Co-Former Interactions and Assemblies

The co-former in both PROPY-4HBA and PROPY-FA forms strong hydrogen bonds at both ends of the molecule and, similarly to PROPY-HQ, the charge is distributed across the co-former and interacting molecules. PROPY-MPAR is different as no further strong hydrogen bond occurs from MPAR, besides that to the PROPY carbonyl, and discrete two component units are formed (Figure 5.18, d). There is no network of linked hydrogen bonds or other possibility for distribution of the charge beyond the two molecules and the $\rho(\mathbf{r}_{RCP})$ of the 5-membered ring in PROPY-MPAR is the highest of all the systems for that ring type (Figure 5.17). Similarly, the phenyl ring $\rho(\mathbf{r}_{RCP})$ is the largest seen across the four systems.

PROPY-4HBA displays the second highest $\rho(\mathbf{r}_{RCP})$ for both of the rings in PROPY. This might be unexpected due to the very strong carboxylic acid dimer hydrogen bonds at the opposite end of 4HBA to the PROPY interaction. This dimer interaction, however, is the reason for the greater charge accumulation in PROPY. Although charge can be redistributed across PROPY, 4HBA and into a second 4HBA molecule *via* the hydrogen bonding network (Figure 5.18, a), charge is also received from the second 4HBA molecule which is involved in an equivalent 2-component adduct. Any redistribution gain that may have been obtained is equally opposed and a net cancellation occurs. Discrete units of the PROPY-4HBA system are generated, as in PROPY-MPAR, however they are comprised of four molecules (2 PROPY···4HBA adducts connected *via* the carboxylic acid dimer) rather than two. The increased number of atoms allows for a slightly greater redistribution

of the charge and the strong acid dimer hydrogen bonds with relatively large $\rho(\mathbf{r}_{RCP})$ values indicate where some charge is relocated.

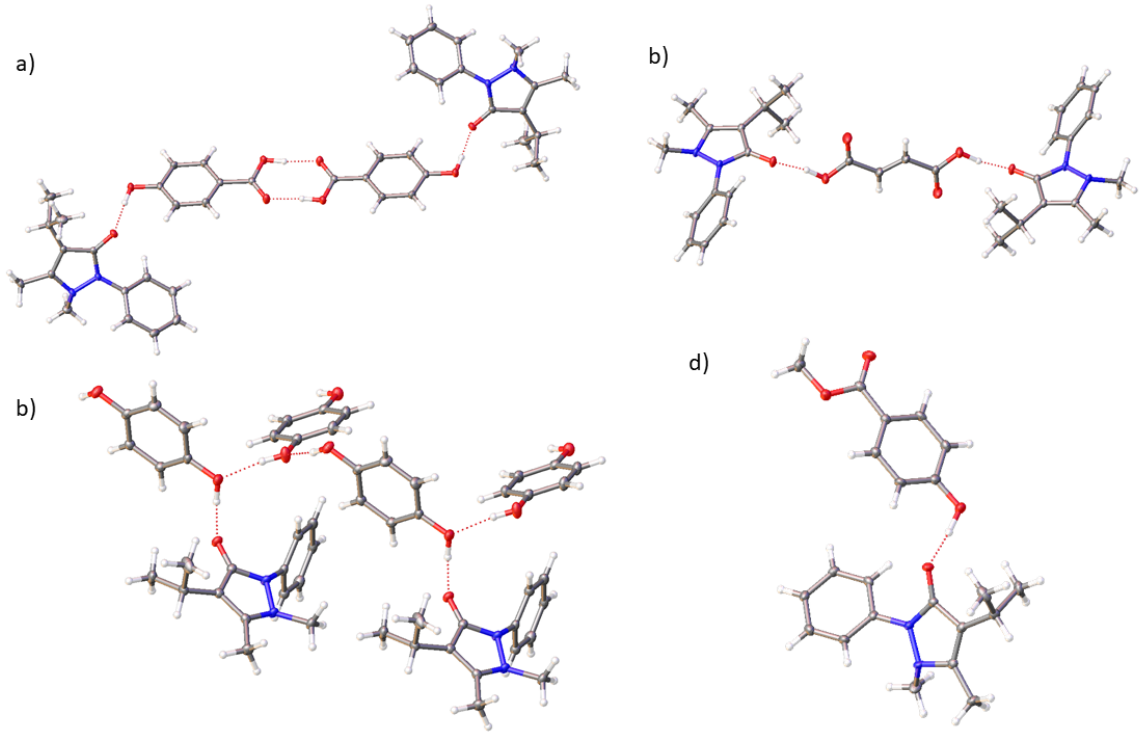

Figure 5.18. PROPY co-former adduct assemblies; a) PROPY-4HBA 1:1 4-component unit, b) PROPY-FA 1:0.5 3-component unit, c) PROPY-HA 1:2 hydrogen bonded network and d) PROPY-MPAR 1:1 2-component discrete unit.

Figure 5.19 shows the atomic charges and $\rho(\mathbf{r}_{RCP})$ for the co-former molecules. MPAR and 4HBA have identical RCP densities hence the strong acid dimer with density accumulation in PROPY-4HBA must account for the reduced accumulation of charge in PROPY.

PROPY-FA displays a moderate $\rho(\mathbf{r}_{RCP})$ for both PROPY rings despite forming discrete 2:1 ratio units with no further hydrogen bonding interaction network (Figure 5.18, b). Each FA interacts with two PROPY molecules, reducing the amount of charge available to each PROPY as the molecule is essentially halved in size. Additionally, the carboxylic acid···carbonyl hydrogen bond is strong with a high $\rho(r_{BCP})$ value, indicating where a substantial amount of charge is accumulated.

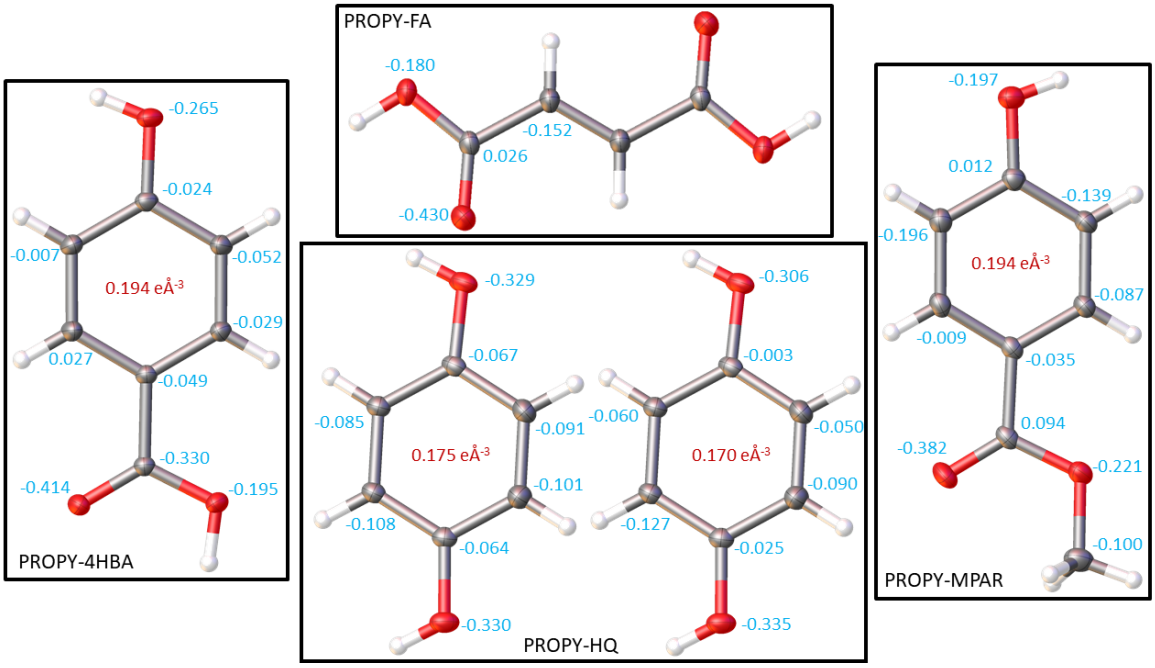

Figure 5.19. Atomic charges (blue) and ρ(r) (red) at the RCPs for the co-former molecules in the four systems, using Stockholder atomic partitioning for charges.

5.6.3 Experimental Hydrogen Bond Energies

The experimental hydrogen bond energy estimations show that O–$H_{hydroxyl}$···$O_{carbonyl}$ interactions have energies around -50 kJ mol^{-1}, whilst those from a carboxylic acid are stronger (almost -90 kJ mol^{-1} in PROPY-FA). This is due to the additional oxygen atom in the carboxylic acid providing a larger electron density initially. In comparison, the hydrogen bonds of the acid···acid dimer are seen to be of an intermediate strength. The additional electrons from the carboxylic acid present a greater density for the hydrogen bond, however density is both donated and accepted across the dimer thereby moderating the energy of each individual carboxylic acid···O hydrogen bond. The two dimer hydrogen bonds in conjunction, however, form a very strong motif.

5.7 Evaluation and Rationale of Physicochemical Properties

Assessing the intermolecular interactions present in the co-crystals provides information about the molecules in the solid state. The multiple method approach described provides extensive insight into the interplay between the different forces present in the crystalline lattice and provides a basis for relating this structural information to trends and characteristics of physicochemical properties

5.7.1 Melting Point

For a compound to melt, the network of intermolecular interactions holding the molecules together in the lattice must be broken. This allows the transition from the ordered solid state to a less ordered liquid phase to occur. The analysis discussed in this chapter provides an insight into these intermolecular interactions and the information available allows molecule···molecule interactions to be explored, broken down into energy components, as well as into individual hydrogen bonds. Appropriate analysis can provide an understanding into how the molecules are held together and hence how they break apart. A rationale behind the trend in melting points: PROPY-MPAR < PROPY-FA < PROPY-4HBA < PROPY-HQ, can be obtained.

The strongest interactions present require the most energy to break, and hence create and define the barrier to melting; a sufficiently high temperature is required to surpass the energy barrier leading to the melting point. The four systems rank PROPY-FA > PROPY-HQ > PROPY-4HBA > PROPY-MPAR according to the strong pairwise interactions (Appendix B.4.4, Table B.19). The strong interactions were seen to be dominated by a single hydrogen bond with a large hydrogen bond energy in all systems and strong co-former···co-former hydrogen bonds were also seen in PROPY-4H and PROPY-HQ. The strong hydrogen bond energy must therefore be overcome in order for the interaction to be broken.

The ranking of the individual API···co-former hydrogen bonds according to strength estimated from the experimental model is: PROPY-HQ > PROPY-FA > PROPY-4HBA > PROPY-MPAR. This is in relatively good agreement with the order of melting point however there are some anomalies to the ranking, namely PROPY-FA. PROPY-HQ contains four strong primary hydrogen bonds and PROPY-4HBA has three with both co-crystals containing strong co-former···co-former hydrogen bonds in addition to the $O–H_{hydroxyl}\cdots O_{carbonyl}$ API···co-former hydrogen bond. PROPY-FA and PROPY-MPAR have only one strong hydrogen bond each. When these numbers are considered, alongside the energies the melting point trend can be understood. Whilst PROPY-FA requires a greater energy to break the single hydrogen bond, PROPY-4HBA has three strong hydrogen bonds to break, which requires a greater energy. The theoretical analysis of PROPY-4HBA highlights that the strong interactions have a much larger Coulombic energy, which would require a larger energy to break apart.

PROPY-HQ exhibits the highest melting point and has the most interactions in total. This is in conjunction with a large Coulombic energy from the strong and moderately strong interactions. The latter is particularly important as it is significantly greater than in any of the other systems and is indicative of a stronger and therefore more stable complex which would require a larger amount of energy to break apart.

The strongest interactions produce the initial energy barrier for melting temperature, however the moderate strength interactions also play an important role. Whilst they are much weaker in energy that the strongest, they are greater in number. The individual energies and total number varies across the four systems, affecting the melting temperature. PROPY-HQ displays the highest melting point and has the strongest moderate strength interactions of all the systems. In comparison, PROPY-MPAR has the lowest energy interactions in this group and displays the lowest melting point of the series. Figures 5.15 and 5.16 show that these moderate strength interactions in PROPY-MPAR have a large contribution to the overall energy also resulting in a lower melting point.

Another aspect to consider is the composition of the energy for each system. The overall Coulombic energy per molecule can be seen to increase across the series:
PROPY-FA < PROPY-MPAR < PROPY-4HBA < PROPY-HQ which is reflected in the melting points with a positive correlation. Similarly, when dispersion energy is considered, the trend proceeds as follows: PROPY-HQ < PROPY-4HBA < PROPY-MPAR < PROPY-FA, with a negative correlation; the lowest dispersion energy is present in the system with the highest melting point. Coulombic and dispersion energy components appear to have a negative correlation with one another i.e. when Coulombic energy dominates, dispersion has little influence and *vice versa*. The exception to this trend in melting point is PROPY-FA which has a lower than expected Coulombic energy component for its melting temperature but the dispersion energy is much greater than expected.

The strongest interactions which influence melting point were seen to be dominated by the Coulombic energy term, with a much-reduced dispersion component in comparison. The co-former···co-former interactions of PROPY-4HBA and PROPY-HQ contain relatively large Coulombic energy terms which, in addition to the PROPY···co-former interactions, will contribute to the higher melting points observed. PROPY-FA however, has a dispersion energy much closer to that of the Coulombic component than observed in any other system accounting for the higher than expected melting point for the Coulombic energy component value.

Coulombic energy is influenced by atomic charges as these determine electrostatics across the molecule. Larger, more negative, charges on the PROPY carbonyl oxygen centre result in a higher melting point. PROPY-FA however, has the largest charge on oxygen for all three atomic partitioning methods used, but does not exhibit the highest melting point.

PROPY-FA is structurally different to the other three co-crystals analysed, all of which contain an aromatic ring with two para-positioned substituents (of varying type). FA contains a conjugated π-system *via* the alkene and carbonyl functionalities, however the aromaticity and degree of delocalisation of the π-electrons is far less than in aromatic rings. The trends and relationships

described above are true for systems containing aromatic co-formers, specifically those with di-substituted aromatic rings with para-substituents. Further studies would be required to confirm whether this is applicable to all aromatic co-formers, or how the relationships vary. This rule specifically accounts for the apparently anomalous PROPY-FA in the trends and properties when compared to interactions and provides evidence for aim number 4 (Section 5.2).

5.7.2 Stability

All four co-crystal materials analysed showed no indication of dissociation or breakdown in the stability tests (Chapter 4.5). Interaction analysis has shown that they all contain strong, highly favourable interactions, both at the atom···atom level *via* hydrogen bonding and at the molecular level between molecular pairs. No significant destabilising interactions have been evidenced and this therefore accounts for the good stability.

5.7.3 Dissolution

Intermolecular interaction analysis can provide insight into the assembly and some properties of the solid state. Melting involves no other factors except those concerning the molecules themselves in the lattice and therefore the interactions observed are the determining factors for this property. A similar intermolecular analysis based on strength and composition does not corroborate trends in the measured solubility and dissolution data; some of the strongest interactions are observed in PROPY-HQ yet this has a fast dissolution and high solubility, whereas those with weaker interactions, such as PROPY-MPAR, display poorer solubilities and varying dissolution rates. A comprehensive understanding is not obtained from solid state interaction analysis when other factors, beyond the molecules themselves, are involved.

Dissolution involves the breaking apart of molecular constructs *via* a disturbance to the solid state lattice cause by the solvent. A proposed mechanism is one whereby the solvent forms interactions to the solute, disrupting the intermolecular interactions of the solute. For dissolution to occur the solvent···solute interactions must be more favourable than those present in both the solvent and solute individually. Hence, the choice of solvent is paramount and different solvents will result in different rates of dissolution. Polarity is particularly important as polar molecules will dissolve better in polar solvents (due to favourable interactions) and likewise non-polar solvents will favour non-polar molecules.

To understand the dissolution behaviour of the PROPY co-crystal systems, the interactions between water (solvent used in the measured dissolution experiments) and the co-crystal components must be assessed. The crystal structures contained within the CSD can be

interrogated for the presence of water, and when present, the interactions it forms assessed. Isostar[250] compiles this information and presents the interactions of water separated into different functional groups. Hence, the propensities of interactions between water and the functional groups present in all PROPY co-crystals can be determined and are shown in Appendix B.5, Table B.22. The most favourable interaction is with a phenol O–H (present in HQ, 25DHBA, 35DHBA, 4HBA and MPAR in differing quantities) and the overall order of propensity seen as: phenol O–H > carboxylic acid > ester. All water···co-former functional group interactions are more favourable than any water···PROPY functional group interactions. It is therefore the co-former, not PROPY, which influences the dissolution and solubility of the co-crystals. This first observation explains the wide variety in dissolution rates and solubility exhibited by the different systems, despite them all containing PROPY.

The propensity of hydroxyl and carboxylic acid interactions to a carbonyl (the primary interactions in all PROPY co-crystals examined) is much lower than the equivalent interaction to a water molecule. This implies that the co-crystal would break apart and form interactions between the individual components and water, rather than stay in the co-crystal construct. This explains the dissolution behaviour for these materials, including the rate at which it proceeds.

The most favourable interaction with water occurs with phenol O–H and hence a molecule with this functionality alone would exhibit the fastest dissolution and highest solubility. Thus PROPY-HQ, containing four O–H groups (per PROPY molecule) in the 2:1 ratio co-crystal, would be expected to have a fast dissolution rate (and high solubility). This is indeed seen in the dissolution curves (Figure 4.19) where PROPY-HQ has both the fastest initial dissolution rate as well as the quickest onset of the plateau.

PGL contains three O–H groups (per PROPY) and would have the next most favourable set of interactions to water. This is confirmed as PROPY-PGL·0.5ACN has the second highest initial dissolution rate and reaches a plateau soon after PROPY-HQ.

In rank order, co-crystals of 25DHBA and 35DHBA, each containing two O–H groups and one carboxylic acid, would be expected to display the next highest dissolution, followed by 4HBA with a single O–H and a carboxylic acid. FA, with two carboxylic acid groups, would be expected to have a co-crystal dissolution rate below that of PROPY-4HBA. MPAR contains one phenol O–H group but also an ester, which forms much less favourable interactions and would likely hinder the dissolution rate despite the favourable hydroxyl interactions.

Thus, the expected dissolution rate trend would be:
PROPY-HQ > PROPY-PGL·0.5ACN > PROPY-35DHBA & PROPY-25DHBA > PROPY-4HBA > PROPY-FA > PROPY-MPAR > PROPY.

This trend almost corresponds to the experimental results, where rank orders are as follows:

Initial rate: PROPY-HQ > PROPY-PGL·0.5ACN > PROPY-35DHBA ~ PROPY-FA ~ PROPY-25DHBA > PROPY-4HBA > PROPY-MPAR > PROPY

Time to reach plateau: PROPY > PROPY-MPAR > PROPY-4HBA > PROPY-25DHBA ~ PROPY-FA ~ PROPY-35DHBA > PROPY-PGL·0.5ACN > PROPY-HQ

The only outlier evident in the experimental results from the predictions is PROPY-FA. This displays both a faster initial rate, and reduced time to reach plateau than would be expected and could result from the structure and stoichiometry. Carboxylic acid···carbonyl interactions have a lower propensity to form than the hydroxyl equivalent and hence would be easier to break on formation of a more favourable interaction (to water). A carboxylic acid···carbonyl interaction is the primary hydrogen bonding interaction in PROPY-FA whilst the remaining systems display the hydroxyl equivalent. PROPY-FA will break apart more readily resulting in the faster dissolution rate observed.

5.7.4 Solubility

Using the principles of the interaction preferences of water described above the expected order of solubility would be:

PROPY-HQ > PROPY-PGL > PROPY-35DHBA & PROPY-25DHBA > PROPY-4HBA > PROPY-FA > PROPY-MPAR > PROPY.

However, in comparison, the experimental trend is as follows:

PROPY-PGL·0.5ACN > PROPY-25DHBA > PROPY-HQ > PROPY-35DHBA > PROPY > PROPY-4HBA > PROPY-FA > PROPY-MPAR

Poorly crystalline or amorphous materials exhibit higher solubilities than the crystalline form (Chapter 2.4.2.1.1), while higher solid-state stability is linked to lower aqueous solubility (Chapter 2.4.3). PROPY-25DHBA and PROPY-PGL·0.5ACN display the highest solubilities when measured, occurring higher in the solubility trend than would be expected from the rank order of the water interaction analysis. In stability testing both demonstrate degradation with a reduced crystallinity of the final solid material. Both also contain solvent molecules which may contribute to poorer

stability. This poor stability accounts for the higher than otherwise expected solubility of these materials.

The water interaction analysis indicates that PROPY would form the least preferable interactions; all the functional groups present exhibit lower propensities than those for the functional groups of the co-formers. PROPY would be expected to have the lowest solubility, along with the slowest dissolution. This, however, is not the case and PROPY has a mid-range solubility for the series exhibiting a higher solubility than its co-crystals with 4HBA, FA and MPAR, all of which would be expected to be more soluble than the parent. Dissolution results, however, are in accordance with the expected trend. This higher than expected solubility could arise due to several reasons;

- PROPY···PROPY interactions in the solid state are weak, with no individual 'strong' hydrogen bonds present due to the lack of functional groups
- Water···PROPY interactions are seemingly less favourable than those to other functionalities, however they may be more favoured than those occurring in the solid state.
- Water···functional group interactions are favoured, yet the difference between their interactions to water, and to PROPY in the solid state, may be smaller than in the parent PROPY material
- Over time (solubility determinations are carried out over a 24 hour period) PROPY could exhibit a greater release into solution than expected due to the preference of interactions to water in comparison to those to other PROPY molecules.
- A balance between water···co-former (solution) and PROPY···co-former (solid) interactions may occur, resulting in a reduced solubility for co-crystal materials.

Either in isolation, or the interplay of these factors could result in a higher PROPY and / or lower PROPY-4HBA, -MPAR and -FA solubility than expected.

5.8 Evaluation of Additional Co-Crystal Systems

The analysis using both experimental and computational approaches of the four systems described in Sections 5.4 and 5.6 identified a number of trends and correlations in the data and in relation to the measured physicochemical properties. This analysis and evaluation appears to be particularly applicable to systems with aromatic co-formers, specifically di-substituted aromatics with a para-arrangement of substituents.

To test these theories, some of the additional PROPY co-crystal systems produced (Chapter 4) will be analysed, specifically PROPY-45DClPA, PROPY-25DHBA, and PROPY-PGL·0.5ACN, which all contain aromatic co-formers with hydroxyl and / or carboxylic acid functionalities. In contrast to the previously analysed systems, each of these co-formers has more than two ring substituents with varying arrangements and types of substituent and hence all three further systems are more complex than those previously analysed. Experimental multipole modelling would be more challenging to achieve an adequate model and only some samples are of sufficient quality for collection of satisfactory high resolution experimental data. Hence only the computational approaches will be employed for these and full details of the interaction energies are given in Appendix B.4 and Supplementary Files.

5.8.1 PROPY-PGL·0.5ACN

Of the three additional co-formers PGL displays the greatest structural resemblance to those previously analysed containing only hydroxyl functionalities on the aromatic ring. It is most similar to HQ, with an additional hydroxyl group and a resulting 2,4,6-substituent arrangement. The PROPY-PGL co-crystal contains the API and co-former in a 1:1 ratio (PROPY-HQ has a 1:2 stoichiometry) with the additional presence of solvent molecules; 0.5 equivalents of acetonitrile (ACN) solvent crystallise in the lattice adding a third component to analyse.

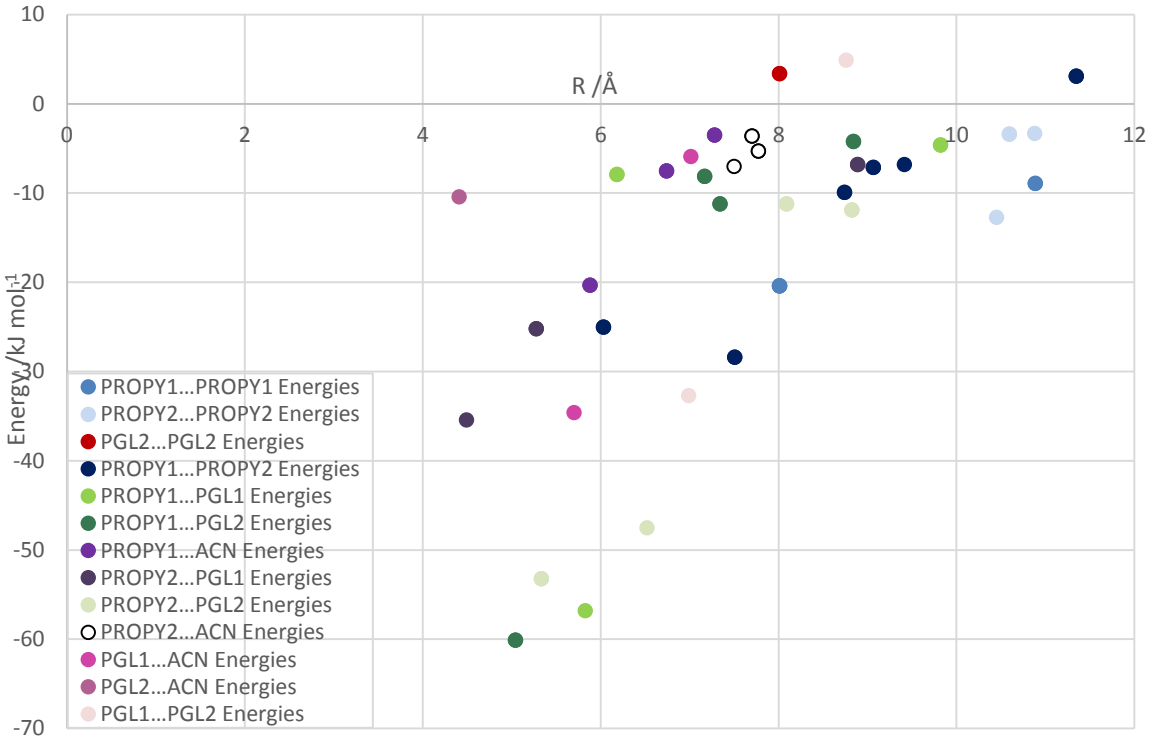

Figure 5.20. Interaction energies determined from PIXEL calculations plotted against molecule···molecule centroid distances (R) for PROPY-PGL·0.5ACN co-crystal. Note, no PGL1···PGL1 or ACN···ACN interactions occur.

The scatter plots generated from Crystal Explorer and PIXEL are shown in Appendix B.4.1 and Figure 5.20 respectively. There is good correlation between them with comparable distributions.

There are four strong interactions, all of which occur between PROPY and PGL molecules. The moderate strength interactions occur between PROPY···PGL, PGL···ACN, PGL···PGL, PROPY···PROPY and PROPY···ACN molecular pairs. These data are grouped as before into strong, moderate and weak interactions (Appendix B.4.4, Table B.20) and according to the molecules present in the pair (Appendix B.4.3 Tables B.17 and B.18).

PROPY-PGL·0.5ACN displays several events in the thermal analysis. When investigated using different techniques, these are ascribed to an initial loss of solvent observed around the solvent boiling point temperature, followed by a melt likely to be induced by the disruption to the hydrogen bond network occurring on solvent loss. A recrystallisation event follows which later melts with a continued increase in temperature. Crystal Explorer shows that ACN interactions have a significantly lower Coulombic and dispersion energy in comparison to PROPY and PGL, indicating that these are quite weak interactions. This is reinforced by the relatively easy removal of the solvent on heating. When the interactions are further broken down using PIXEL analysis PGL···ACN interactions have a greater Coulombic energy than PROPY···ACN but a smaller dispersion energy. This can be related to the type of interactions; PGL contains three hydrogen

bond donor groups which can form stronger electrostatic interactions to the solvent than PROPY, due to its lack of donor groups and minimal heteroatom presence.

The PGL···PGL interactions appear relatively weak overall, however when inspected as individual pairs there is a strong attractive pairing alongside a destabilising pairing with a positive Coulombic energy. Several of these unfavourable and destabilising interactions are present (seen with energies > 0 in Figure 5.20) which accounts for the melting upon solvent loss.

PROPY···PGL pairs have a large Coulombic energy, indicating the favourable nature of these associations, whilst PROPY···PROPY interactions have a lower Coulombic energy and are less favourable. Both sets of molecular pairs have a similar dispersion energy, likely to arise from the aromatic rings present in both molecules. The favourable nature of these pairs aids the recrystallisation and it is expected that the new material formed would maximise the favourable molecular pairings and eliminate, as far as possible, the destabilising effects present in the initial material.

5.8.2 PROPY-25DHBA

25DHBA shows some structural similarity to 4HBA, containing both a carboxylic acid and a hydroxyl group. Similarity to PGL is also apparent as both contain three functional group substituents on the main aromatic ring. Disorder is present in the 25DHBA molecule, as discussed in Chapter 4, resulting in two orientations of the co-former. The calculations discussed below were completed with a single position of 25DHBA.

The Crystal Explorer and PIXEL energy plots both display a similar scatter (Appendix B.4.1 and Figure 5.21). Some differences are seen in the moderate strength energies with the two methods producing some variations in energy values. The strongest interactions are those between PROPY and 25DHBA and contain the primary hydrogen bonds ($O–H_{hydroxyl}\cdots O_{carbonyl}$ and $O–H_{carboxylic\ acid}\cdots O_{carbonyl}$) from the para-arranged substituents. The moderate energies can be split into two sections with a clear separation evident between them. One contains two PROPY···PROPY molecular pairs and the other a range of PROPY···PROPY, PROPY···25DHBA and 25DHBA···25DHBA pairs. The grouping by interaction strength for this system has been completed with different two different separations accordingly. Tables of these values are presented in Appendix B.4.4, Tables B.20 and B.21.

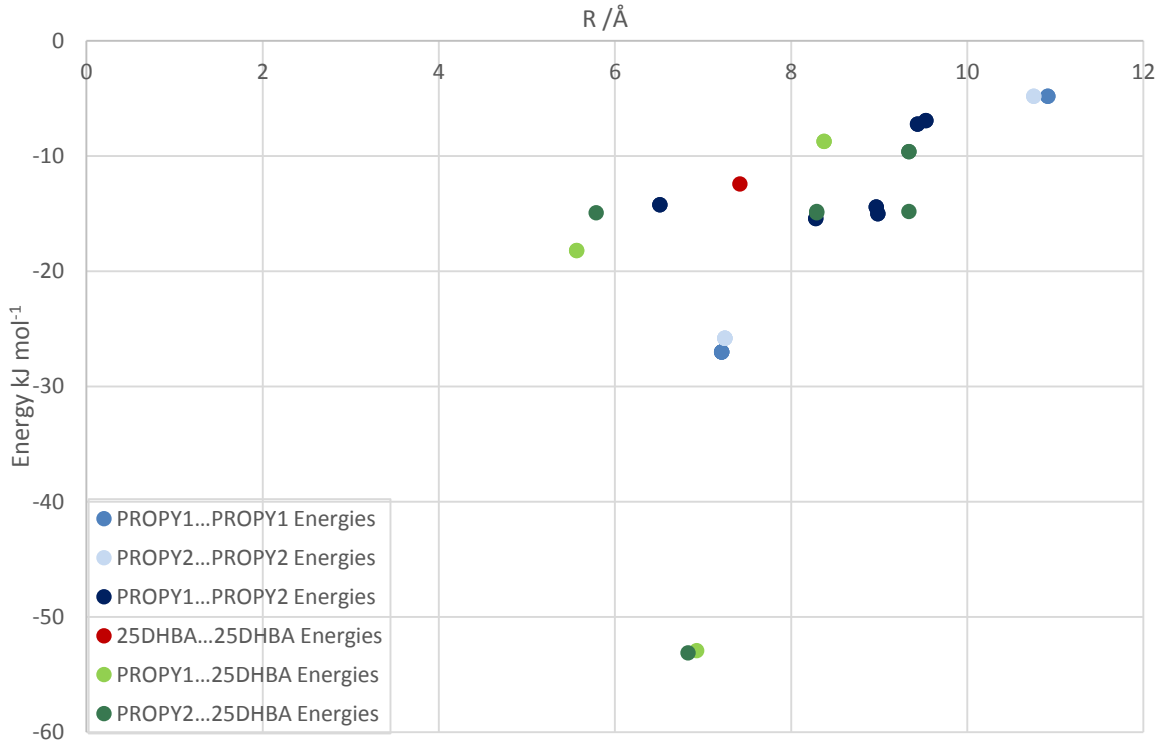

Figure 5.21. Interaction energies determined from PIXEL calculations plotted against molecule···molecule centroid distances (R) for PROPY-25DHBA 1:2 co-crystal.

Crystal Explorer indicates that PROPY forms stronger interactions than the co-former and this is corroborated by PIXEL whereby the greatest Coulombic energy is seen for PROPY···PROPY pairs. PROPY···25DHBA pairs have a smaller Coulombic and dispersion energy component in comparison, which may arise from the 2:1 ratio; there is a greater proportion of PROPY present resulting in more interactions and hence a greater overall energy. The 25DHBA···25DHBA energies are insignificant in comparison, which is again due to the ratio as each 25DHBA molecule interacts with two PROPY molecules meaning there is minimal surrounding space for the association of further 25DHBA molecules (each with its own associated two PROPY molecules).

The strong interactions have the largest Coulombic contribution, accounting for over half that in the system, with only a small dispersion component. The moderate and weak interactions can be separated in two ways: 1) using the -10 kJ mol^{-1} cut off as applied to the systems previously or 2) using the natural gap observed in the scatter plot. Using the former the moderate interactions have a significant dispersive contribution and a Coulombic energy not dissimilar from the strong interactions. The weak interactions have a small Coulombic energy with a moderate dispersion energy. For this grouping, the moderate interactions dominate this system.

Using the alternative separation both the Coulombic and dispersion energies of the moderate interactions are diminished and have almost equal values. Accordingly, the weaker interactions have an increased Coulombic and dispersion energy component, the latter significantly so. This

shows that the second area of (weaker) moderate interactions is dominated by dispersive forces with only a small Coulombic energy contribution. These energies were seen to originate from predominantly homo-pairing comprised of either PROPY or 25DHBA molecules. Both sets of pairings would partake in aromatic π-interactions rather than strong hydrogen bonds (which would contribute to the Coulombic energy) validating the dispersive energy contributions seen.

5.8.3 PROPY-45DClPA

As with FA, 45DClPA possesses only carboxylic acid functional groups with which it can form a hydrogen bond to PROPY however it does contain an aromatic ring making it comparable to the other systems in the series. 45DClPA can be considered more complex as it contains four substituents on the aromatic ring, including two chlorine atoms. No halogen atoms have been discussed previously in this work.

As with the other systems the scatter plots of the Crystal Explorer and PIXEL energies are comparable as shown in Appendix B.4.1 and Figure 5.22. There are two strong PROPY···45DClPA interactions with the highest energies and it is expected that these correspond to carboxylic acid···carbonyl hydrogen bonded pairs.

45DClPA···45DClPA pairs have favourable interactions formed *via* the carboxylic acid functionalities, however they also appear to have some unfavourable, destabilising interactions as evidenced by the data point with a positive energy. This may arise due to the molecular arrangement and positions the two electronegative chlorine atoms in close proximity.

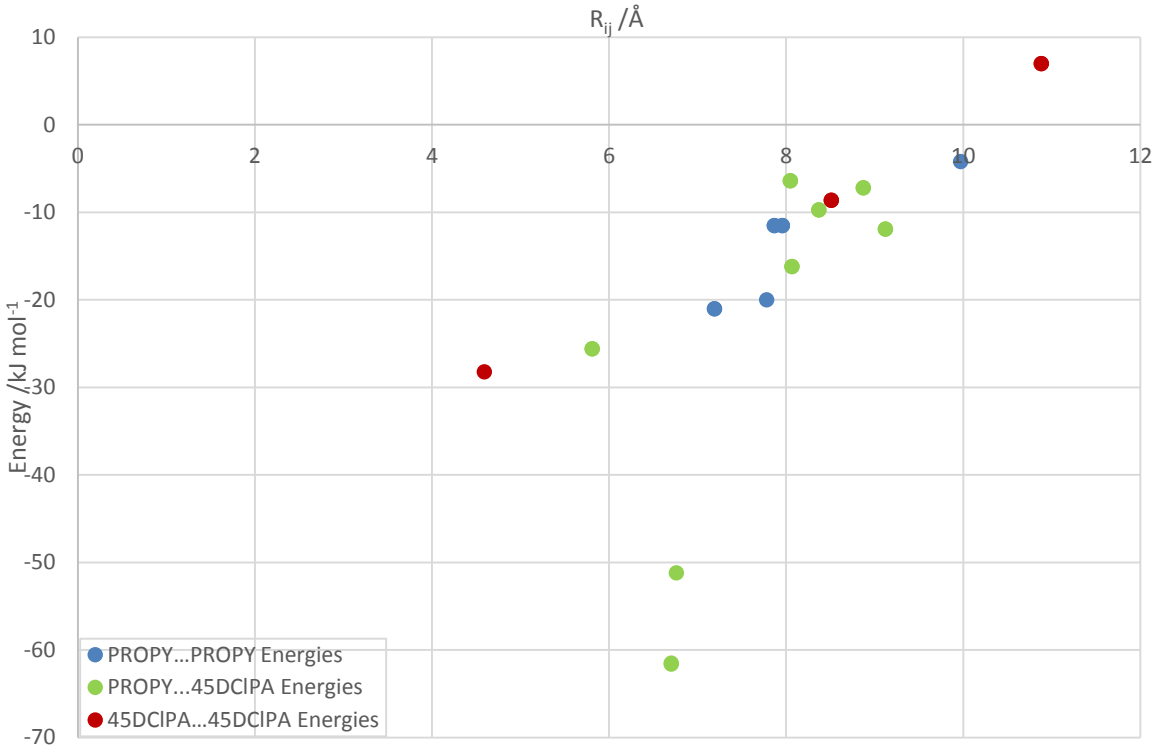

Figure 5.22. Interaction energies determined from PIXEL calculations plotted against molecule···molecule centroid distances (R) for PROPY-45DClPA 1:1 co-crystal. .

Crystal Explorer interaction analysis indicates PROPY interactions have a greater Coulombic and dispersive energy than 45DClPA interactions. Using PIXEL the large Coulombic component can be identified to originate from PROPY···45DClPA pairings. PROPY···PROPY pairs show a minimal Coulombic energy with their attractive components arising primarily from dispersive forces. A destabilising, positive Coulombic energy is observed for the total 45DClPA···45DClPA pairs (Appendix B.4.3).

5.8.4 PROPY

The same analysis was also completed on the two forms of PROPY present in the CSD. The PIXEL scatter plots produced (Figures 5.23 and 5.24) have a similar distribution of data points for both forms. Those obtained from Crystal Explorer are analogous, however a slightly greater number of interaction pairs are included (Appendix B.4.1)

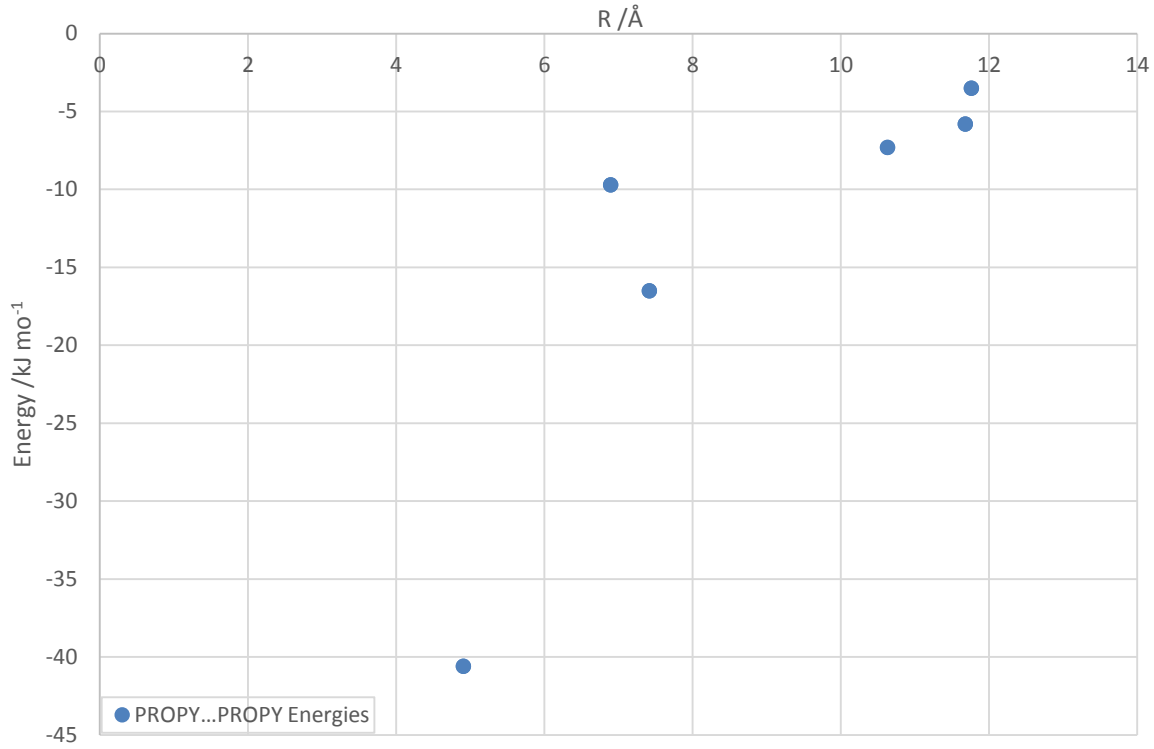

Figure 5.23. Interaction energies determined from PIXEL calculations plotted against molecule···molecule centroid distances (R) for PROPY (Form I, *P*c).

Both forms show a single, strong molecular pair interaction at the shortest molecule···molecule centroid distance. The interaction for Form I is slightly stronger than that of Form II *via* both methods. There are two moderate strength pairs and thereafter the remainder display only weak interactions. Due to the lack of functionality present in PROPY, this is expected. The energies of the systems are broken down into their component parts in Appendix B.4.2, and show that, whilst Form I appears to have the stronger interaction, the Coulombic energy of the system is greater in Form II. PIXEL exhibits a slightly greater dispersion energy in Form II than Form I, whilst Crystal Explorer indicates the opposite. The values are very similar and therefore it can be said that the dispersion is very similar in both systems.

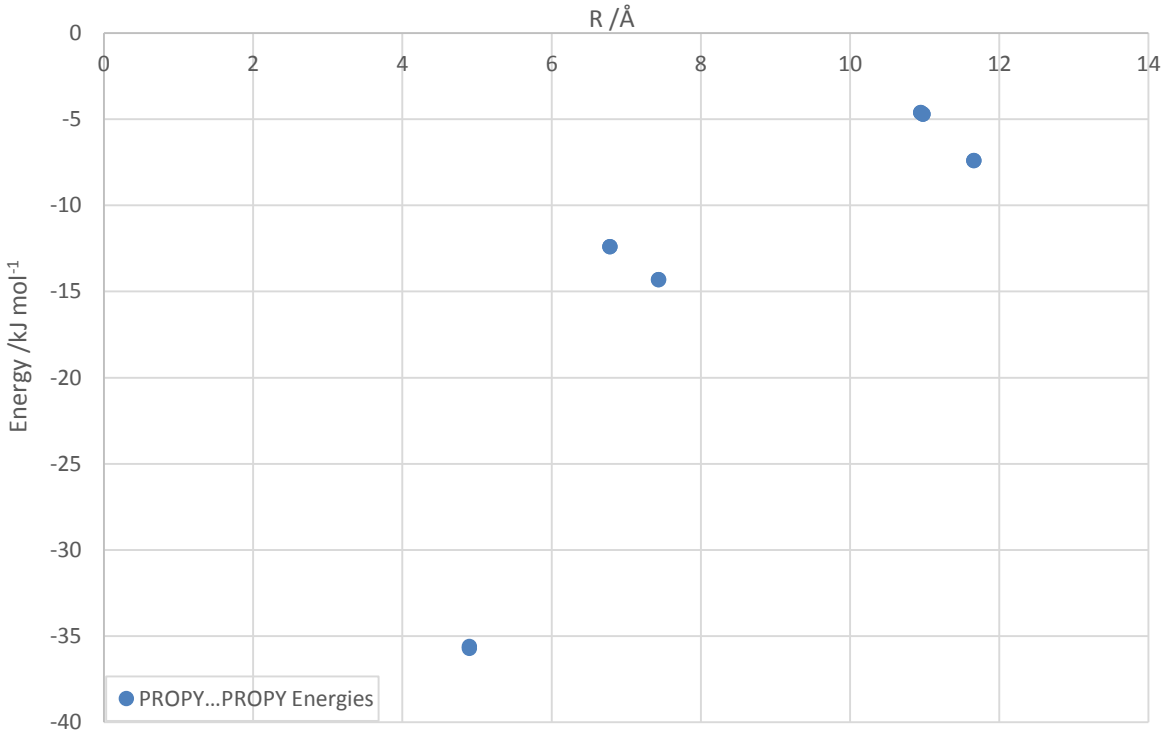

Figure 5.24. Interaction energies determined from PIXEL calculations plotted against molecule···molecule centroid distances (R) for PROPY-FA 1:0.5 co-crystal PROPY (Form II, *Cc*).

Previous studies on PROPY assert Form II as the stable form at room temperature, while Form I is metastable. The energies determined in this study and their constituent components corroborate this declaration. The overall energy is greater for Form I, which also has a greater energy for the strongest interaction, however the Coulombic energy is greater in Form II. It has been seen in melting point analyses that it is the Coulombic energy that is key to determining thermal stability.

5.9 Physicochemical Properties Analysis of All Systems

5.9.1 Melting Point

The overall melting point trend observed in Chapter 4 was:

PROPY-MPAR < PROPY-PGL·0.5ACN < PROPY < PROPY-25DHBA < PROPY-FA < PROPY-45DClPA < PROPY-4HBA < PROPY-HQ < PROPY-35DHBA.

Using the data presented in Appendix B.4 an overall analysis for the melting points based on interactions can be completed. An insight into the trend is obtained by assessing the Coulombic component of the strong and moderate interactions. Dividing the total according to the number

of molecules present, an energy per molecule can be created. (Appendix B.4.4, Table B.22) Both PROPY-25DHBA and PROPY-MPAR have low melting points and a low Coulombic energy per molecule is involved in the strong interactions. Moderate Coulombic energies are observed for the moderate strength interactions. PROPY-25DHBA has a slightly higher melting point than PROPY-MPAR, which may be due to the increased number of molecules present in the 2:1 system. More interactions are present and therefore must be broken on melting thereby requiring a higher temperature.

PROPY-PGL also has a low melting point and a moderate Coulombic energy for both the strong and moderate strength sets of interactions. In addition to the destabilising interaction seen in the scatter plots, the melting point may be reduced due to the weak ACN···ACN interactions which drive the loss of solvent and therefore system disintegration. The recrystallisation occurs beyond the boiling point of the solvent and will therefore contain no solvent molecules in the crystal lattice and PROPY···PGL interactions are likely to dominate. The strong molecular PROPY···PGL pairings in the original crystal structure were seen to be dominated by the Coulombic energy and, if similar in the new material will cause the higher melting point observed. The destabilising interactions may also be diminished from the material leading to a higher melting point.

PROPY-4HBA and PROPY-HQ both have high melting points. PROPY-4HBA has a large Coulombic energy in the strong interactions whilst PROPY-HQ has an intermediate Coulombic energy for the strong interactions. The PROPY-HQ moderate strength interactions are the strongest of all the systems and provide a greater Coulombic energy per molecule than the strongest interactions. When the strong interactions are considered in isolation the melting point would be expected to be lower than observed. It is the combination of the moderate and strong interactions in this system which give rise to the high melting point. PROPY-45DClPA contains a large Coulombic energy from the strong interactions coupled with a weaker moderate columbic energy, similar to PROPY-4HBA. The melting point, however, is lower than that of PROPY-4HBA and likely to arise from the presence of the destabilising interactions.

PROPY-FA is the final system and has an alternate structure to the other co-formers. The Coulombic energy per molecule is modest, lower than that seen for PROPY-45DClPA, however the melting point is marginally higher (PROPY-FA > PROPY-45DClPA). The Coulombic energy of the moderate interactions is also slightly greater than in PROPY-45DClPA. This Coulombic energy could be responsible, or partly so, for the higher melting point, although the nature of the co-former and the stoichiometric ratio are also likely to be factors. Perlovich[92] showed that 1:2 and 2:1 ratio co-crystal systems have a greater inclination than 1:1 systems to raise the melting temperature relative to those of the constituents.

5.9.2 Stability

Stability of all the systems, with the exception of PROPY-45DClPA (non-pharmaceutically acceptable), was tested and analysed in Chapter 4.5. Two of the materials, PROPY-PGL·0.5AGN and PROPY-25DHBA, displayed indications of dissociation during the course of these tests. Both systems have a low total energy per molecule from PIXEL values (Appendix B.4.2, Table B.16), however Crystal Explorer indicates a low value for PROPY-25DHBA but a larger energy for PROPY-PGL 0.5ACN (Appendix B.4.2, Table B.15). This is greater than those of PROPY-MPAR and PROPY-HQ and similar to that of PROPY-4HBA, all three of which are stable. Additionally, both PIXEL and Crystal Explorer show the two forms of PROPY as having the lowest energies per molecule despite exhibiting good stability.

Stability was tested in several ways:

- Slurry (for aqueous stability),
- Storage under accelerated conditions (heat and humidity influence),
- Moisture sorption in DVS (humidity influence).

All three methods involve water present in a greater quantity than ambient conditions. Poor stability is linked with higher solubility and both PROPY-25DHBA and PROPY-PGL·0.5ACN showed high solubilites enhanced by the interactions they can form with water (Section 5.7.4). These favourable interactions may provide the basis for this instability.

Both unstable systems also include solvent molecules in their crystal lattices, which can also interact favourably with water. Propensities of 42.45 % water···ether (in 1,4-dioxane, PROPY-25DHBA) and 38.49 % water···cyano (in acetonitrile, PROPY-PGL·0.5ACN) are likely to accelerate the lattice breakdown in the presence of sufficient moisture. These solvent interactions appear to have little effect on the solubility and dissolution of the materials (in large volumes of water) however they may influence the uptake of a small amount of water as experienced in DVS, accelerated stability testing and in slurry conditions when the volume of liquid is minimal.

The interaction analysis of PROPY-PGL·0.5ACN indicated both PROPY···ACN and PGL···ACN interactions, however with a significantly reduced Coulombic energy than seen for both the PROPY···PGL and PROPY···PROPY molecular pairs. These ACN interactions are likely to be weaker than water···ACN (which will occur preferentially), evidencing the poor stability results obtained. No interaction analysis involving the solvent molecules was undertaken for PROPY-25DHBA as it is located in void spaces with no clear hydrogen bonding or interactions to either co-crystal component. It is therefore free to interact with any water present and in doing so the crystal

lattice will collapse to accommodate the entry of the water molecules. The presence of the void spaces in both crystal structures may also influence water uptake and stability.

5.10 Conclusions

This chapter has shown that there are several approaches beyond the geometric and routine methods commonly employed that can be used to analyse crystal structures in more detail. At electronic resolution the charge distribution in molecules can be evaluated. When this is coupled with Quantum-based approaches intermolecular interactions can be understood at a deeper level. This aids in the rationalisation of the assembly of crystal lattices and multi-component systems and also related physicochemical properties.

The work of this thesis chapter has four primary aims which are based on:

1. Structural similarities
2. Stoichiometry
3. The primary O–H···O hydrogen bond
4. Structural diversity

5.10.1 Aim 1: Structural Similarities

This aim was addressed by using comparisons of PROPY-4HBA and PROPY-MPAR. The reduced functionality of MPAR restricts further hydrogen bonding and extension of the interaction network beyond the PROPY-MPAR $O–H_{hydroxyl}\cdots O_{carbonyl}$ primary hydrogen bond. Hence the redistribution of charge is limited and observed as an accumulation of charge in the PROPY molecule and evidenced in the $\rho(\mathbf{r})$ value at the two RCPs. Both rings show a greater electron density than that observed for the equivalent rings in PROPY-4HBA. The ring-member atomic charges of the ring components are not greatly perturbed by the additional density and only a small accumulation of charge is seen in the two PROPY ring nitrogen atoms in PROPY-MPAR. Both 4HBA and MPAR co-former molecules displayed very similar RCP properties and atomic charges showing how small structural changes of the co-formers can impact the electronic structure of PROPY (the hydrogen bond acceptor), rather than that of the co-formers themselves.

Both PROPY-MPAR and PROPY-4HBA display a strong PROPY···co-former pairwise interaction of a similar strength. This exhibits similarities to that in PROPY-HQ however differs in the structurally diverse PROPY-FA; co-former structural similarities are evidenced in the interactions.

The strongest molecular pair interaction from both PIXEL and Crystal Explorer has a slightly increased energy in PROPY-4HBA in comparison to that of PROPY-MPAR, although the experimental hydrogen bond energy is contrary; PROPY-MPAR O–$H_{hydroxyl}$···$O_{carbonyl}$ has a stronger hydrogen bond energy and can be understood when the Coulombic energy of the individual pairwise interactions from the theoretical calculations is considered.

In addition to the strong PROPY···co-former interaction both systems contain moderate strength interactions comprising PROPY···PROPY and PROPY···co-former pairs. These are of similar energies, PROPY-4HBA displaying slightly stronger interactions than those in PROPY-MPAR, and a greater separation between the moderate strength and weak interactions. The energy components of the PROPY···PROPY pairs in both systems are similar, whilst the PROPY···co-former and co-former···co-former pairs highlight the subtle differences in the structures. PROPY···4HBA pairs have a smaller Coulombic energy component than the MPAR equivalent, however the 4HBA···4HBA pairs are considerably stronger than MPAR···MPAR pairings.

The total energy of the PROPY-4HBA system is comprised in almost equal proportions of the strong, moderate and weak interactions. In contrast, PROPY-MPAR is dominated by the moderate strength interactions with a smaller contribution of the strong interactions and te weak interactions have a minimal contribution. Both the Coulombic and dispersion energy constituents display the same trend for the strong, moderate and weak interactions for the two systems; the strong interactions dominate the Coulombic energy and the moderate strength interactions do so for dispersion. Differences are seen in the relative proportions of the weak interactions, with those in PROPY-4HBA contributing more to the total than observed in PROPY-MPAR.

These comparisons and contrasting features of the two systems show the similarities of the two co-former molecules related to the *para*- substituted aromatic ring, however the difference in the functionality opposite the primary hydrogen bond is apparent.

5.10.2 Aim 2: Stoichiometry

Aim 2 (evidenced in Section 5.4.3, PROPY-HQ analysis) intended to investigate whether steric hindrances or electronic effects influence stoichiometry. Electronic factors seek to maximise the interactions and distribution of charge, which the additional hydroxyl functionality of HQ facilitates. HQ does not dimerise with itself (as with 4HBA), instead it forms strong O–H···O hydrogen bonds which stabilise the system. An increased ratio of HQ permits a greater number of interactions and larger energy of the system. This is also true for PROPY-4HBA as the additional carboxylic acid functionality has the potential to increase the number of interactions and energy of the system and therefore it was chosen for comparison.

The PROPY-HQ crystal structure demonstrates that two hydroxyl functionalities are, simultaneously, able to access and form an interaction to the PROPY carbonyl group. An additional 4HBA molecule interacting in this way would expose the carboxylic acid functional group which is known to favour acid dimer formation. In this arrangement only one further hydrogen bond would be possible as the acid···acid dimer formation would not lead to an extended hydrogen bond network. The alternative orientation of 4HBA would expose the hydroxyl group and require the carboxylic acid to form an interaction with the carbonyl. This would permit an extended hydrogen bonded network (as seen in PROPY-HQ) *via* the hydroxyl groups, however the larger carboxylic acid group may not be able to access the carbonyl due to its size. Additionally, this arrangement would force three oxygen atoms into close proximity, two of which display a lone pair of electrons. A large repulsive force would be exhibited countering the benefits of the hydrogen bond network formation from the hydroxyl groups. Hence a 1:2 ratio is not observed for PROPY-4HBA.

In contrast, PROPY-HQ can form a strong $O–H_{hydroxyl}\cdots O_{carbonyl}$ hydrogen bond whilst also extending the hydrogen bond network and distribution of charge *via* $O–H_{hydroxyl}\cdots O_{hydroxyl}$ hydrogen bonds. The presence of two hydroxyl groups interacting with the PROPY carbonyl is possible due to the small size enabling both to position in close proximity to form an interaction. This is favourable as each hydroxyl group is both donating and receiving electrons through the hydrogen bonding network so there is no charge accumulation and resultant repulsive force.

It has been shown that it is a combination of the steric and electronic effects which drives and enables the observed 1:2 ratio in PROPY-HQ.

5.10.3 Aim 3: The Primary Hydrogen Bond

The primary O–H···O hydrogen bond can be assessed using two approaches. Topological analysis of the electron density obtained from the experimental model provides information regarding the individual hydrogen bond of each system. In conjunction with the molecular pair analysis, it was seen that this interaction dominated the strongest PROPY···co-former interaction. These pairwise interactions can hence also provide information and aid in understanding the different interactions observed.

Two main primary hydrogen bond types were observed occurring from a hydroxyl or a carboxylic acid to the PROPY carbonyl. Experimental hydrogen bond estimations indicated similar energies for the hydroxyl···carbonyl hydrogen bonds in all systems (~50 kJ mol^{-1}), whilst the carboxylic acid···carbonyl (PROPY-FA) had a larger energy at almost 90 kJ mol^{-1}.

The molecular pairs investigated in the PIXEL and Crystal Explorer energy analysis indicate that the carboxylic acid···carbonyl interactions (PROPY-FA and PROPY-45DClPA) have a greater Coulombic energy than the equivalent interaction from hydroxyl-containing co-formers. The dispersion energy components are similar in both cases. This is not surprising as it is the Coulombic, not dispersion, energy which determines hydrogen bond strength.

5.10.4 Aim 4: Structural Diversity

Aim 4 is assessed using the similarities of PROPY-4HBA and PROPY-MPAR in conjunction with PROPY-HQ and contrasted with PROPY-FA. The three former systems show good correlations between their energy components, contributions and physicochemical properties forming trends, however in many cases PROPY-FA is observed as an anomaly. PROPY-FA has a large dispersion energy for the total API···API molecular pairings, much greater than seen for any other system. This indicates a difference in the co-former, which has a significant impact on the PROPY molecules. PROPY-FA is also the only system which does not contain co-former···co-former molecular pair interactions. Not only is PROPY-FA structurally different for comparisons between co-former molecules, it is also different in its primary hydrogen bonding interactions to PROPY.

These differences result in disparities in this system and show that the trends observed are true for aromatic co-former molecules specifically those with two substituents in a *para*-arrangement, however systems containing linear co-formers behave differently.

5.10.5 Physicochemical Properties

Dissolution and solubility were seen to be affected by the choice of solvent with solute···solvent interactions being the most important factor in the trends analysed and more favourable interactions between water and the co-former molecules resulting in a faster dissolution rate. Solubility was affected similarly, however equilibria conditions affect the trend somewhat. A trade-off between favourable water···co-former and PROPY···co-former interactions must occur. This reduces the solubility in some compounds, whilst water···PROPY interactions override PROPY···PROPY interactions in the parent material resulting in a higher than expected solubility.

Melting point was seen to be dominated by the Coulombic energy term, with a negative correlation to the dispersion energy component. The strong and moderate strength interactions were important in determining melting point and the energy required to break the API···co-former pairings (as well as lattice interactions between such pairs) of the system apart.

5.10.6 Additional Findings

Analysis of PROPY-25DHBA, PROPY-45DClPA and PROPY-PGL·0.5ACN using theoretical calculations has shown that with increased co-former functionality, destabilising interactions begin to emerge. This is also true when additional components are present, such as solvent in PROPY-PGL·0.5ACN. It is likely that there is a limit to the extent of co-former functionality possible, particularly for a molecule such as PROPY with minimal potential for further interactions. If the functional groups, or heteroatoms, cannot partake in favourable interactions as part of the molecular assembly, their presence is undesirable. When these begin to outweigh the strong, favourable interactions in a multi-component system, the formation is no longer advantageous and the separate components will form in preference. Initial screening included a number of co-formers with a high density of functional groups, but no co-crystals were produced corroborating this.

The study presented in this chapter is a novel approach to understanding the driving forces behind the exact interactions and important features that hold a lattice together, particularly for multi-component systems. The juxtaposition of competing favourable interactions with the 'penalties' incurred in other parts of the lattice is only understandable when traditional intermolecular interactions *vs.* molecular pairings are decomposed into their contributing components (particularly Coulombic and dispersion energies). This is a very powerful technique and provides an entirely new insight into the physiochemical properties, particularly when a systematic approach is taken.

Chapter 6: Novel Salts and Co-Crystals of Lonidamine

This chapter focuses on the design, synthesis and characterisation of co-crystals and salts of lonidamine. The work in this chapter has been published by Mapp, L.K.; Coles, S.J.; Aitipamula, S. in *CrystEngComm*, 2017, **19**, 2925 – 2935.

6.1 Lonidamine

Lonidamine (1-(2,4-dichlorobenzyl)-1H-indazole-3-carboxylic acid, LON) is a hexokinase inhibitor[281] causing inactivation of glycolysis enzymes. In this way it can help induce apoptosis as well as cause cell death through interference in angiogenesis.[282] This cell metabolism disturbance is an alternate action to other antiproliferative-antineoplastic agents which affect DNA synthesis and replication.[282] These qualities demonstrate that LON presents as a good candidate for cancer treatment for which it has been previously formulated in Italy, as doridamine.[283] Encouraging results have been reported from a number of studies utilising LON for cancer treatment either on its own[284] or as a combination treatment.[285-287] There are also uses for the drug in neurodegenerative and neuromuscular diseases, obesity and diabetes.[285, 288, 289] Thus there is reasonable evidence that this compound is of therapeutic interest. Both LON and its sodium salt exhibit very low solubility[290] creating a hindrance in drug formulation and delivery. Hence the formulation of alternate solid forms may be of interest. LON contains several functional groups including a carboxylic acid (Figure 6.1), favourable for hydrogen bonding, and a number of weaker acceptor groups. The aim of this chapter is to explore novel solid forms of LON with an objective to modify its physicochemical properties.

6.1.1 Polymorphs of LON

Three polymorphic forms of LON are known, two of which (α and β) were reported in 1993 by Benetollo *et al*.[290] More recently, a patent by Xinmin *et al*.[291] described three forms which can be identified as the two from Benetollo's work with a third, new form. Through PXRD and DSC data the work in these two papers can be correlated and α- and β- assigned to Forms I and II respectively in the patent (Appendix C.1). The third is assumed as a new γ-phase.

Benetollo *et al*. have reported the crystal structure for the β-form with an in-depth structural analysis and structure-activity relationship. They also reference the α-form and some physical properties measurements. The crystal structure for the α-form was determined during the course

of the work reported in this thesis and added to the CSD as a result. Both the polymorphs form acid···acid dimers which are connected through C–H···O interactions into 4-component motifs (Figure 6.1). In α-LON these originate from aromatic C–H groups of the fused indazole ring to the LON dimer carbonyl, whilst in β-LON they occur *via* aromatic C–H groups from the dichloro-substituted rings to the hydroxy groups in the LON dimer. In addition to the differences in the atoms partaking in the interactions, the positioning of the two LON molecules interacting with the dimer pair is also different. The orientation of the LON is flipped due to the different C–H groups involved in the interactions and as a result, the packing is also affected. Face-to-face π···π stacking of the dichloro-substituted rings is enabled in β-LON whilst stacking of the fused indazole ring and hydrogen bonded dimer interaction occurs in α-LON. The C–H···O angle is almost linear in β-LON (177.93°) indicating an almost planar arrangement, whereas in α-LON the interacting molecule is offset from the dimer plane with a C–H···O angle of 147.47°. These give rise to different $C_{aromatic}$–$O_{carbonyl}$–$O_{hydroxyl}$ (α-LON) and $C_{aromatic}$–$O_{hydroxyl}$–$O_{carbonyl}$ (β-LON) angles of 75.11° and 122.57°respectively showing how the LON molecules forming C–H···O interactions are positioned relative to the hydrogen bonded dimer.

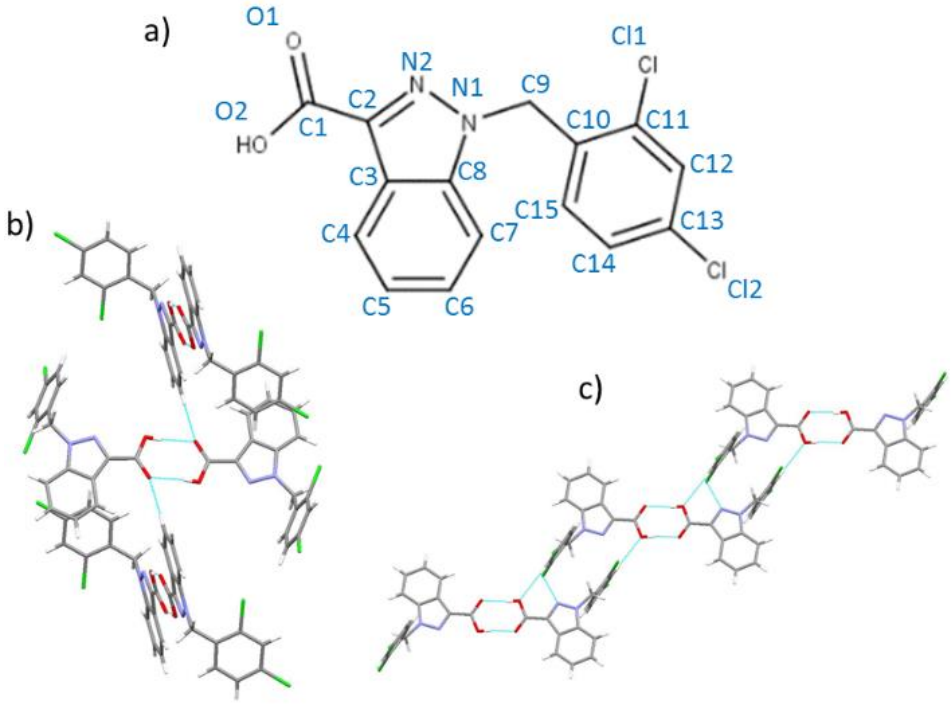

Figure 6.1. a) Structure of LON with labelling scheme employed for all structures herein, b) main interaction pattern present in α-LON and c) main interaction pattern present in β-LON.

The bulk LON material obtained and used for all experiments in this work is a mixture of both α- and β- polymorphs; β-LON is present in a greater proportion. The two polymorphs can be produced separately through careful solvent selection although formation of pure

α-form is more challenging than the β-form using solvent based crystallisation methods. Appendix C.2 provides further details on the LON material.

6.2 Design of Co-Crystals

6.2.1 Interaction Analysis to Identify the Preferred Co-Former Functional Groups

Visual inspection and structural analysis of the α- and β- polymorphs of LON indicates that the greatest potential for intermolecular interactions arises from the carboxylic acid functional group. An analysis of potential intermolecular interactions and preferred synthons was undertaken to enable the most suitable co-formers to be determined. Utilising the tools available from the CCDC, such as those implemented in Mercury[106-108] and Conquest,[106] it was found that the most preferential interactions of the carboxylic acid include those to amides, primary amines ($–NH_2$), aromatic nitrogen atoms (for example pyridines) and hydroxyls. In structures which contain these functionalities, the intermolecular interaction between the carboxylic acid and the corresponding functional group occurs at a propensity of 77.2 %, 67.2 %, 63.8 % and 35.3 % (any O–H) respectively. Hydroxyl groups can be further divided: alcoholic O–H groups are highly favoured (66 %) with general aromatic and aliphatic O–H groups displaying propensities around 50 %. The hierarchy of interactions for a carboxylic acid is therefore amides > primary amines ($–NH_2$) > aromatic nitrogen atoms > hydroxyls. Dimer interactions are also highly favoured, with 87.3 % of structures containing two carboxylic acid groups forming a dimer, and a 46.5 % frequency observed for the acid···amide equivalent. See Appendix C.3 for a detailed breakdown of this analysis.

The other main functional group present is the indazole, which, according to CSD statistics, interacts favourably with C–H groups, hydroxyls, primary amines, amides and $T3NH_1$ (nitrogen with one hydrogen atom and a total of three bonded atoms) groups. Interactions involving an indazole occur in fewer structures (smaller result sets) and with lower propensities for common hydrogen bonding functionalities. This indicates it is much weaker than the carboxylic acid in the hierarchy of interactions and synthons: a carboxylic acid group would preferentially form interactions in a molecule containing both a carboxylic acid and indazole functionality. Both may form an interaction depending on the nature and number of functionalities present with which they can interact. This is in accordance with Etter's rules of hydrogen bonding, whereby the best proton donors and acceptors, after intramolecular interactions are considered, will form interactions to one another pairing subsequently according to strength.[36]

6.2.2 Possible Synthons and Interactions of LON Multi-Component Systems

A number of examples of synthon motifs which may result from the combination of LON with some of the functional groups highlighted above are depicted in Section 1.3.4.1, Figure 1.1. The prevalence of carboxylic acid dimers,[28] acid···amide dimers,[292] and hydroxyl and carboxylic acid···pyridine interactions[101, 293] have been reported. Such literature shows that these associations are favoured over interactions to other functional groups, and are strong, robust synthons which will occur in a variety of different systems.

The aromatic N group is of particular interest especially with regards to the formation of interactions involving the carboxylic acid of LON. Carboxylic acid···N is a robust and commonly occurring synthon which has been utilised and presented in many studies including those of Zaworotko *et al.*,[293, 294] Nangia *et al.*[295, 296] and Biradha *et al.*[297] for assembly and crystal engineering strategies. As well as providing a robust supramolecular motif for engineering, carboxylic acid···pyridine interactions are also of interest with respect to the location of the hydrogen atom. A number of examples of carboxylate···pyridinium salts have been reported,[224, 298] in addition to neutral co-crystals containing the carboxylic acid···pyridine hydrogen bond.[299-301] The study of *p*-aminosalicylic acid with a selection of pyridine-containing co-formers produced 13 new materials of varying types:[223] 8 true co-crystals, 2 pure salts, 2 co-crystal salts, and 1 salt hydrate. Hence proton transfer and hydrogen atom location should be considered in any new materials synthesised.

6.2.3 Co-Former Selection

Potential co-formers for LON were selected primarily based on the findings from CSD analysis and information retrieved from literature sources regarding preferential interactions of carboxylic acid groups. A total of 87 structurally diverse compounds (see Appendix C.4) were chosen and utilised in screening by solid-state grinding (both solvent assisted and dry grinding). This diversity ensured that potential intermolecular interactions to the API were not restricted or biased towards those involving the functional groups identified, however the selection did include a large number of molecules which contained these functionalities as these were the most likely to generate a new form.

6.2.4 Implementation and Analysis of Screening by Grinding

Samples generated through grinding were analysed by PXRD and compared to reference patterns (Appendix C.5) to identify combinations which indicated a change after grinding. These directed subsequent solution crystallisation experiments to obtain suitable crystals for diffraction studies

and crystal structure determination. From these experiments, sixteen new materials were produced from twelve different co-molecules (Figure 6.2). These were a combination of salts, co-crystals and co-crystal salts with some forming as solvated and hydrated structures. Of the twelve co-formers, seven are pharmaceutically acceptable: benzamide (BENZ), haloperidol (HALO), imidazole (IMID), isonicotinamide (ISO), melamine (MEL), nicotinamide (NICO), and piperazine (PIPE). These generated nine new solid forms.

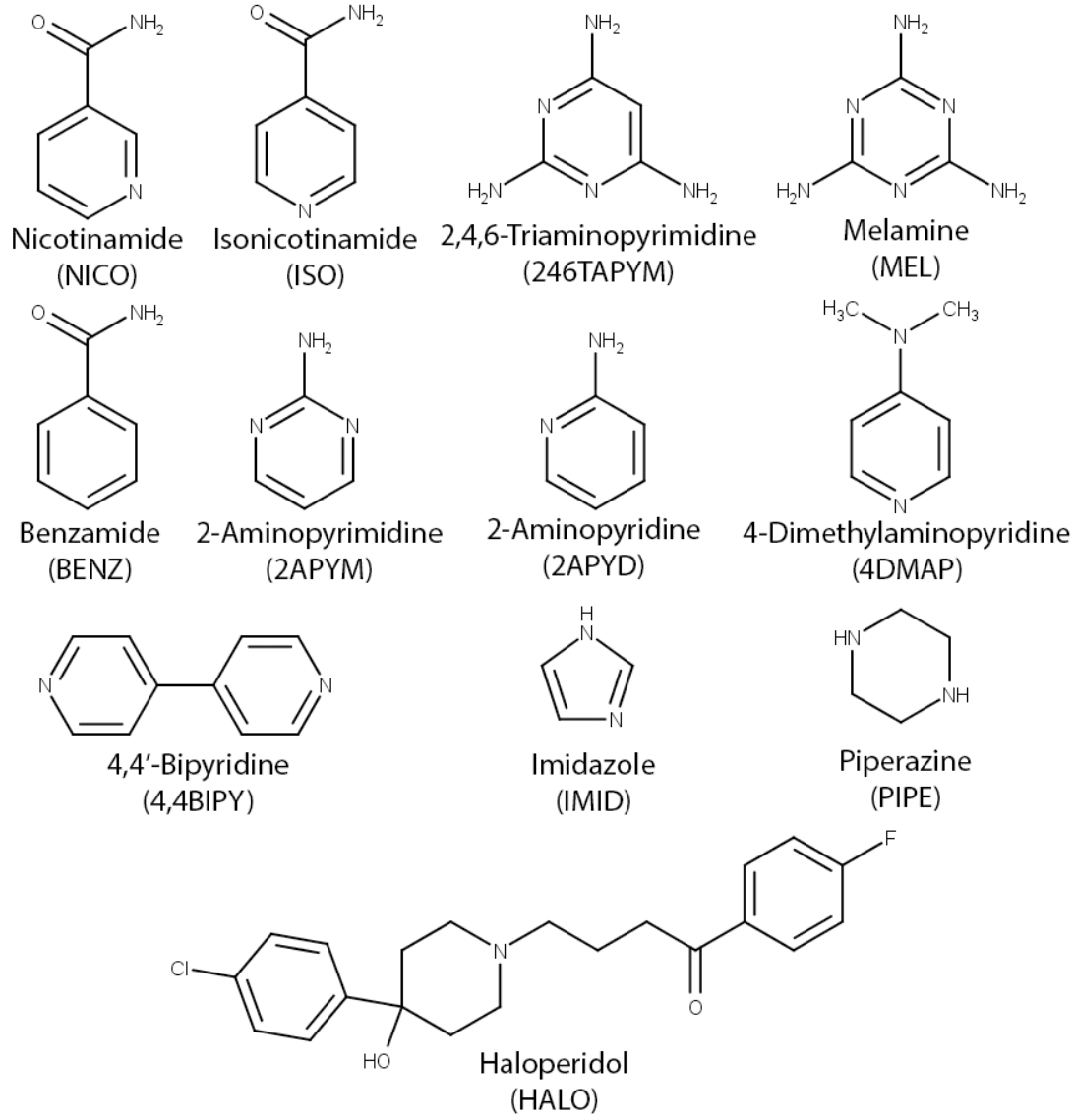

Figure 6.2. Structures of co-formers which were successful in forming a new material with LON.

In addition to the co-formers successful in producing a new form there were a number of others which, in combination with LON in grinding, were identified as promising. Details of these co-formers, along with the PXRD patterns of the material produced in grinding experiments are given in Appendix C.5.2. Despite the indication for a new form, no single crystals have yet been produced to confirm these, or identify the nature of the material.

6.3 Structural Analysis of the Novel Co-Crystal and Salt Structures of LON

Cell parameters, structural information and hydrogen bonding interactions for all sixteen materials, along with those for the α- and β- polymorphs of LON are detailed in Appendices C.6 and C.7.

The co-formers which were successful in producing a new material with LON can be grouped according to their molecular structures and functional groups present.

- Pyridine-based molecules (nicotinamide (NICO), isonicotinamide (ISO), 4,4'-bipyridine (4,4BIPY), 2-aminopyridine (2APYD), and 4-dimethylaminopyridine (4DMAP)), and the structurally similar benzamide (BENZ)
- Pyrimidine-based molecules and related 1,3,5-triazines (2-aminopyrimidine (2APYM), 2,4,6-triaminopyrimidine (246TAPYM), and melamine (MEL))
- 5- / 6- Membered rings (imidazole (IMID) and piperazine (PIPE))
- Others (haloperidol (HALO))

However, there are many cross-category correlations that can be drawn, for example 2APYD with 2APYM.

6.3.1 Structures Containing Pyridine-Related Co-Formers

6.3.1.1 LON-BENZ 1:1 co-crystal

A 1:1 ratio of LON and BENZ form a co-crystal which crystallises in the monoclinic space group $P2_1/c$. This contains a primary hydrogen bonded acid···amide dimer (O–H···O and N–H···O, D···A distances 2.55 Å and 2.88 Å, D–H···A angles 172° and 169° respectively). Additional hydrogen bonds occur from the–NH_2 in BENZ in a bifurcated pattern to a second LON molecule creating a 4-membered unit (Figure 6.3, left), similar to that seen in α-LON. This involves an N–H···$N_{indazole}$ and N–H···$O_{hydroxyl}$ hydrogen bond to the indazole and carboxylic acid groups of LON. The 4-membered units assemble into zig-zag chains and adjacent chains have a head to head arrangement (Figure 6.3, right).

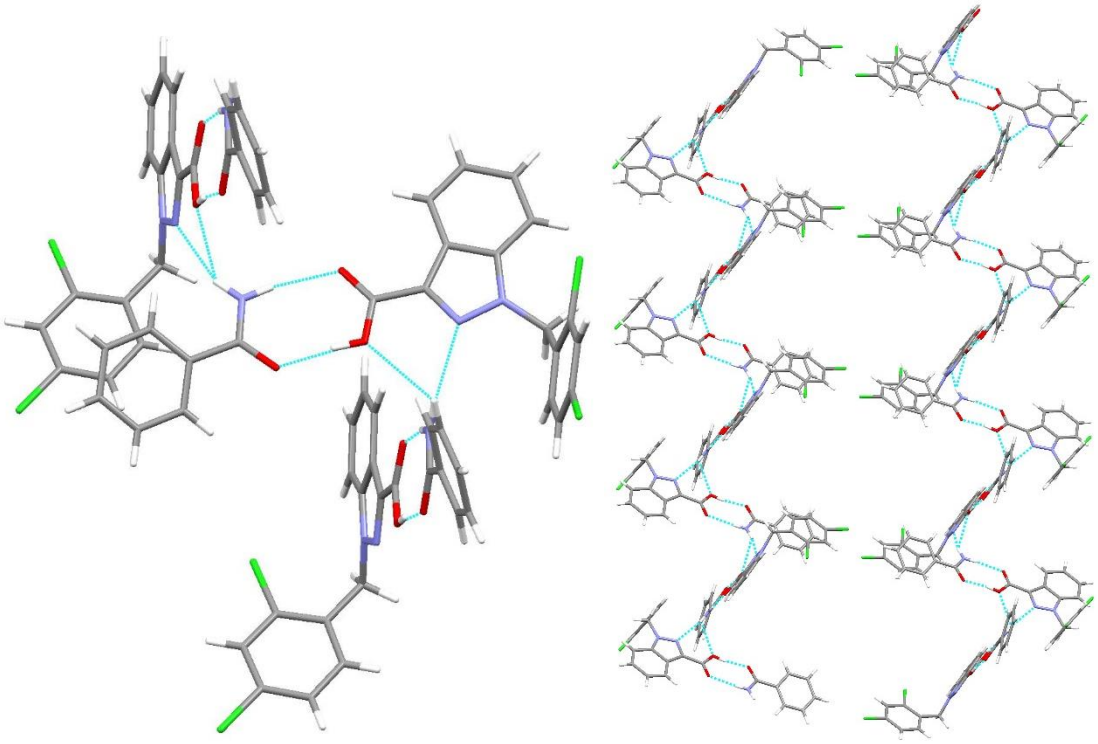

Figure 6.3. Left, primary interaction motif in 1:1 LON-BENZ co-crystal and right, zig-zag chains.

6.3.2 Structures Containing Pyridine-Based Co-Formers

6.3.2.1 LON-NICO 1:1 co-crystal

NICO forms a 1:1 co-crystal with LON, also in the monoclinic space group $P2_1/c$, and, like LON-BENZ, features an acid···amide dimer as the primary hydrogen bonding interaction. This features O–H···O and N–H···O hydrogen bonds (2.53 Å and 2.96 Å, 169° and 168° respectively). A second N–H···$O_{\text{acid carbonyl}}$ hydrogen bond (2.85 Å, 119°) forms from the NICO amide to a second dimer pair *via* the carbonyl of LON. This creates tetrameric units (Figure 6.4) which occur in two planes arranged almost perpendicularly to one another (88°). The tetramers stack into layers in these two orientations.

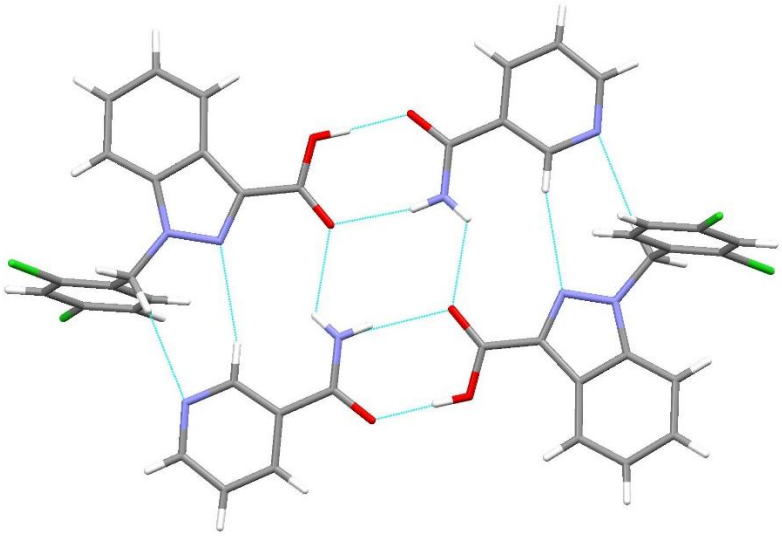

Figure 6.4. Tetramer arrangement of dimers in the LON-NICO 1:1 co-crystal.

6.3.2.2 LON-ISO 1:1 co-crystal

ISO is structurally similar to NICO and also forms a 1:1 co-crystal. This crystallises in the monoclinic space group $P2_1/n$ and also displays a tetrameric motif however this forms *via* an $O–H_{carboxylic\ acid}\cdots N_{pyridine}$ (2.64 Å, 176°) and an amide $N–H\cdots O_{carbonyl}$ (2.97 Å, 175°) hydrogen bond rather than through dimer formation (Figure 6.5). The co-former molecule is in the opposite orientation in comparison to LON-NICO (the pyridine ring rather than the amide is positioned facing the carboxylic acid) and also in contrast, the tetrameric motif is not planar; the co-former molecules sit slightly above and below the plane of the carboxylic acids with a tilted orientation. The tetramers are linked *via* $N–H_{amide}\cdots O_{carbonyl}$ hydrogen bonds and $C–H\cdots O_{carbonyl}$ interactions displaying two general orientations and stack in chains down the *b*-axis.

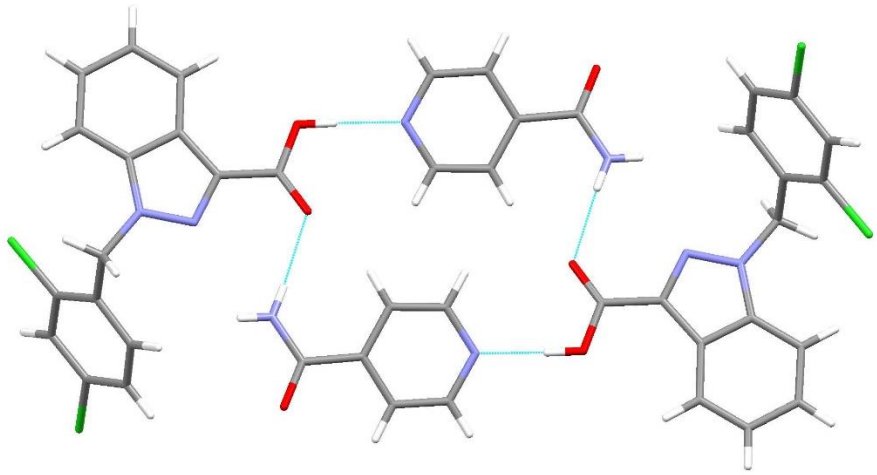

Figure 6.5. Tetramer arrangement of LON and ISO molecules in the 1:1 co-crystal structure.

6.3.2.3 LON-4,4BIPY 2:1 co-crystal

A 2:1 ratio co-crystal forms between LON and 4,4BIPY which displays discrete units of the same ratio. Two such units are present in the asymmetric unit.

The dichloro-substituted aromatic rings on all LON moieties in the crystal structure display a degree of positional disorder arising from the free rotation that is possible around the methylene linker. The disorder seen is due to an almost 180° rotation resulting in the chlorine atoms appearing in two different positions: either 2-,4- or 4-,6- relative to the methylene linker connecting the ring to the remainder of the molecule. The plane of the ring is slightly altered in some instances, arising from a slightly greater than, or less than, 180° rotation. The minor disorder component is small in each case with approximate occupancies of 7 %, 13 %, 6 % and 7 % for the four LON molecules as depicted left to right in Figure 6.6 below.

Each LON forms an $O–H_{acid}\cdots N_{pyridine}$ hydrogen bond (2.57 Å / 2.54 Å and 2.58 Å / 2.59 Å; 164° / 176 ° and 167° / 169°) to one pyridine ring of the co-former molecule (Figure 6.6). The 2:1 units pack in an end to end arrangement, offset from one another, producing stepped chains which extend into sheets through the structure.

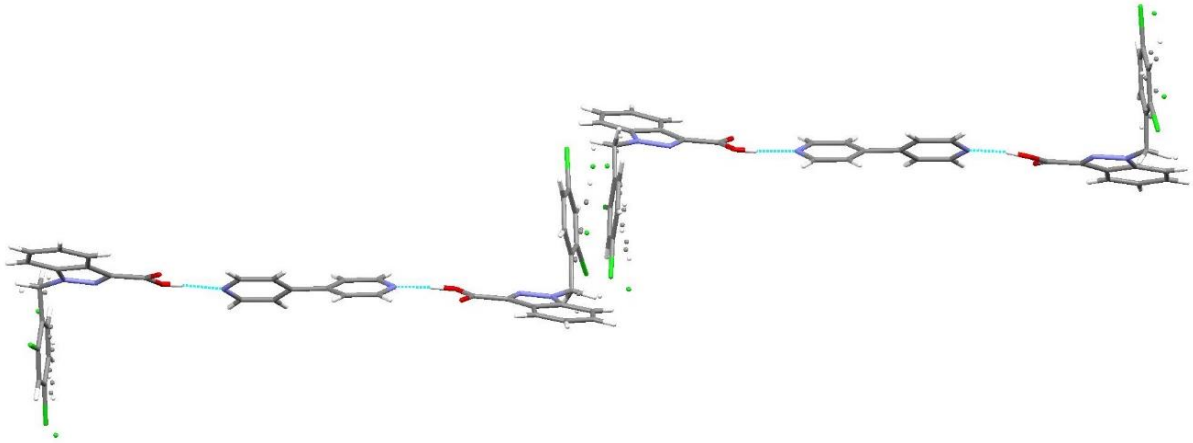

Figure 6.6. LON-4,4BIPY co-crystal 2:1 units arranged in a stepped, end-to-end packing configuration with offset dichloro-substituted rings.

6.3.2.4 LON-4DMAP

4DMAP forms two structures with LON: a 1:1 salt dihydrate and a 2:1 anhydrous salt. TGA was used to confirm the dihydrate, see Appendix C.11.3). The 1:1 dihydrate salt displays an $N^+–H\cdots O_{carboxylate}$ hydrogen bond (2.63 Å, 156°) with two additional $O–H_{water}\cdots$carboxylate hydrogen bonds (2.74 Å and 2.72 Å, 171° and 161°) from each of the two water molecules (Figure 6.7).

These water molecules occupy the site which, in the previously discussed LON-NICO and LON-BENZ crystal structures, is occupied by the co-former amide and engaged in the dimer interaction. Consequently, the 4DMAP molecule is positioned perpendicularly to the carboxylate rather than with an end-on arrangement. The LON-4DMAP pairs form chains held in place *via* the hydrogen bonds to the water molecules and two chains are connected *via* the same network of water molecules to create a layer. All LON carboxylate groups are positioned facing into the centre and directed towards the water molecules. The water molecules play an integral part in the crystal structure and packing of LON-4DMAP·2H_2O.

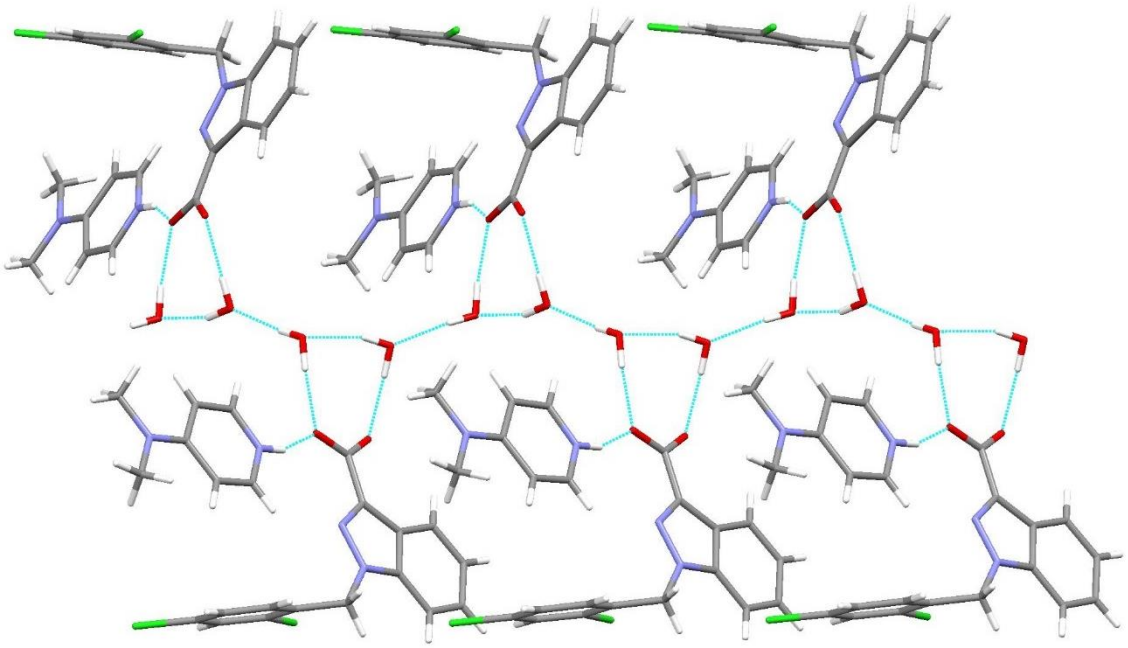

Figure 6.7. Hydrogen bonding interactions in the 1:1 LON-4DMAP·2H_2O salt showing chains of water running through the crystal lattice.

The second structure obtained from LON and 4DMAP has a 2:1 stoichiometry and can be considered as a hybrid structure or, in accordance with the categories defined by de Gelder,[35] a co-crystal salt. The co-former molecule is protonated and disordered over an inversion centre located between the acid group functionalities of the two LON molecules. Each 4DMAP location has an occupancy of 0.5 and two orientations at each site (Figure 6.8, d). The main hydrogen bond present is an O–$H_{carboxylic\ acid}$···$O_{carboxylate}$ (2.48 Å, 172°) between two molecules of LON, one protonated and one deprotonated at the acid, generating a dimer. Hydrogen bonds occur between the LON and 4DMAP *via* N^+–H···$O_{carboxylate}$ and C–H···O interactions. Units containing two LON and one full 4DMAP molecule propagate into chains in the crystal structure *via* further LON-4DMAP interactions to an adjacent LON···LON dimer. The dimers in the chains have alternating

orientations, i.e. the protonated LON molecule alternates either side of the chain of 4DMAP molecules (Figure 6.8). The chains stack to form layers.

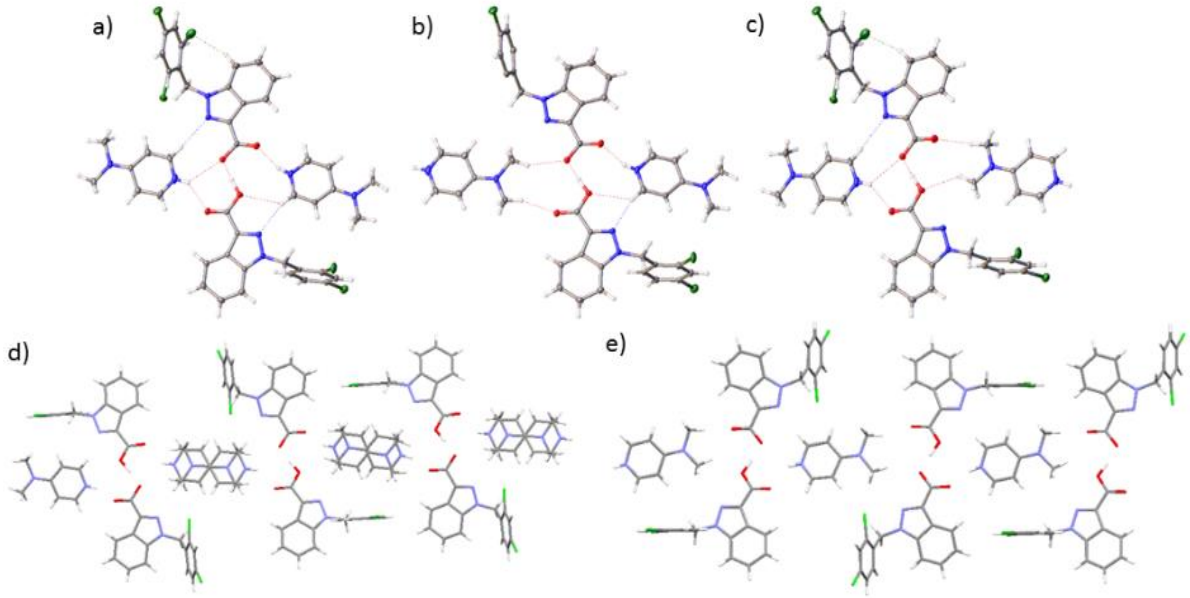

Figure 6.8. Crystal structure of 2:1 LON-4DMAP depicting (a-c) different orientations of the 4DMAP molecule, (d) the chain structure with all disordered components and orientations and (e) the molecular arrangement with a single, uniform orientation of the disordered 4DMAP molecule. A fourth arrangement of a-c is also possible with both 4DMAP molecules forming C–H_{methyl}···$O_{carboxylate}$ interactions to LON. This would occur for the adjacent LON dimers in a).

6.3.2.5 LON-2APYD 1:1 salt solvates

Two 1:1 salt solvate structures were produced with 2APYD containing ethyl acetate and acetonitrile respectively. These crystallise in monoclinic space groups: *Pc* (ethyl acetate solvate) and $P2_1/c$ (acetonitrile solvate). The ethyl acetate solvate shows a definite 1:1:1 stoichiometry with ordered solvent molecules shown in the crystal structure. This is confirmed by TGA analysis (Appendix C.11.3) and solvent loss is also seen in the DSC thermogram (Section 6.8). No discrete solvent molecules could be identified in the crystal structure of the second salt, however voids containing electron density were located. This is where the solvent molecules are located and due to the nature of the electron density, are believed to be disordered or freely mobile. The crystal was obtained from a methanol-acetonitrile solvent mix, therefore either or both solvents are plausible to be present. The electron counts obtained from the SMTBX solvent masking routine in Olex2[265] and PLATON SQUEEZE[266] indicate acetonitrile solvent was likely to be present; this was

corroborated by DSC and TGA analysis. Solvent loss was evident between 80-90 °C (boiling point of acetonitrile, 82 °C) and in TGA mass loss was observed at the same temperature equivalent to half a molecule of acetonitrile (Appendix C.11.3). Hence, this is believed to be a 1:1:0.5 acetonitrile salt solvate.

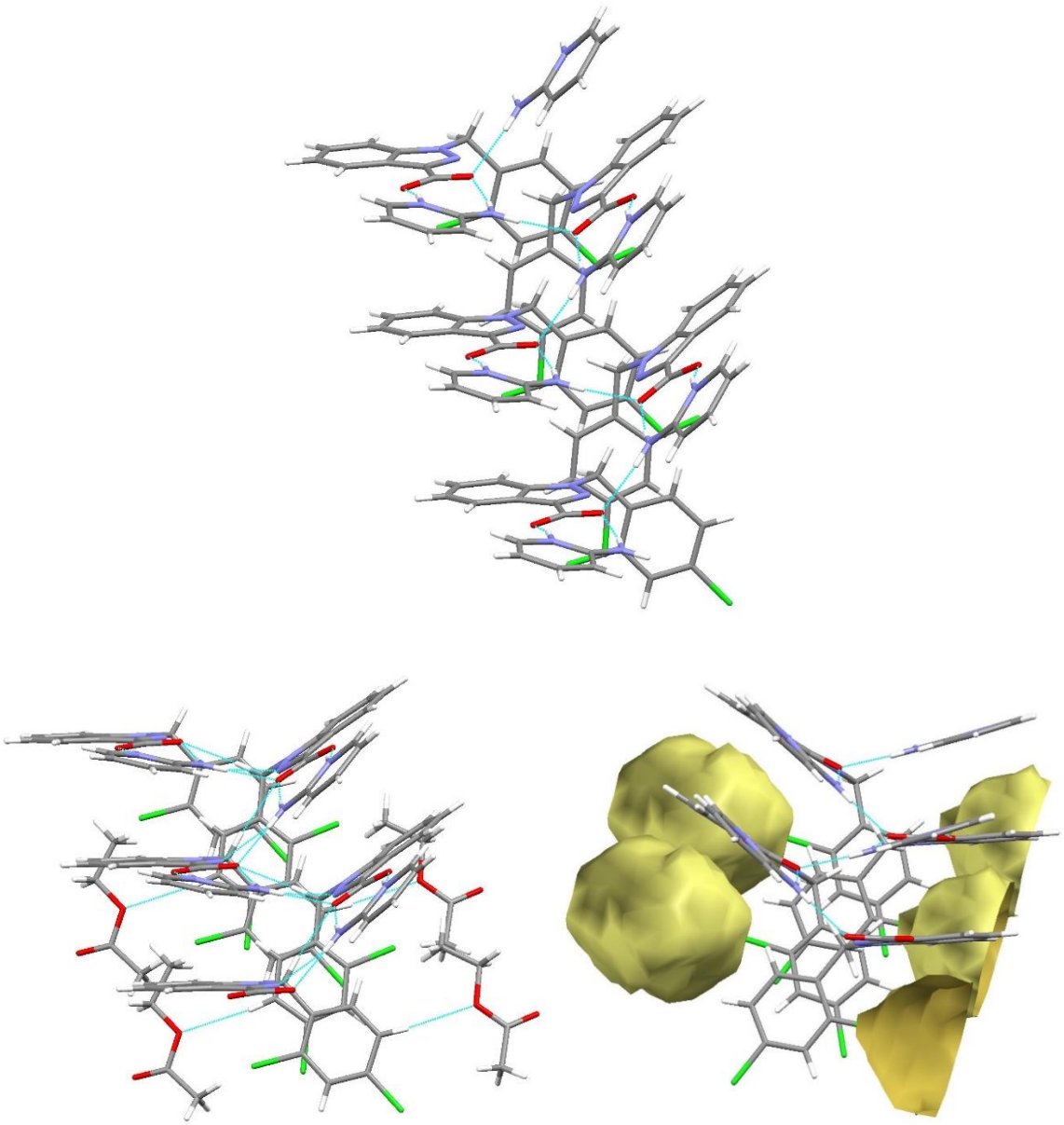

Figure 6.9. Top, zig zag chain pattern (excluding solvent) present in both 1:1 LON-2APYD salt solvate structures, below left showing the ethyl acetate solvent location and below right, the voids where acetonitrile is contained.

Both structures feature the primary hydrogen bonded interaction as a dimer between LON and 2APYD. This features N–H···$O_{carboxylate}$ and N^{+}–H···$O_{carboxylate}$ hydrogen bonds between the pyridinium nitrogen and amino group of 2APYD and the carboxylate of LON (2.78 Å and 2.67 Å, 168° and 170°, EtOAc solvate; 2.80 Å and 2.65 Å, both angles 168°, ACN solvate). The second amino hydrogen of 2APYD forms an N–H···$O_{carboxylate}$ hydrogen bond to the carboxylate of a second

LON (also partaking in a dimer interaction to its 2APYD co-former partner). This produces a zigzag chain with a bifurcated interaction to one oxygen of the LON carboxylate (Figure 6.9, top). Further interactions including amino N–H···$N_{imidazole}$ and C–H···$O_{carboxylate}$ maintain the corrugated stacking pattern.

In both structures the chains run along the *c*-axis, with solvent molecules located below the plane of the dimer interactions (Figure 6.9, bottom). The ethyl acetate solvate displays interlocking solvent molecules which occur alternately on each side of the chain according to the orientation of the LON phenyl ring. A weak C–H···O_{ester} interaction occurs between the phenyl ring and solvent ether group maintaining its fixed position. In the acetonitrile solvate, the solvent is accommodated in voids which are located in the area between the chains. There are no distinct interactions to maintain a discrete position of the solvent and no solvent was modelled in the crystal structure. Hence the solvent (ACN) is not depicted in the figures.

The chains stack into layers parallel to the *b*-axis however there are differences in the 3D packing of the two solvates. The ethyl acetate solvent molecules are larger and occupy a greater spatial volume than acetonitrile in the voids which causes separation of the stacked, repeating layers in LON-2APYD·EtOAc. A collapse of these separated layers, creating an interlocked structure of alternating orientated molecules is observed in the LON-2APYD·XACN (Figure 6.10).

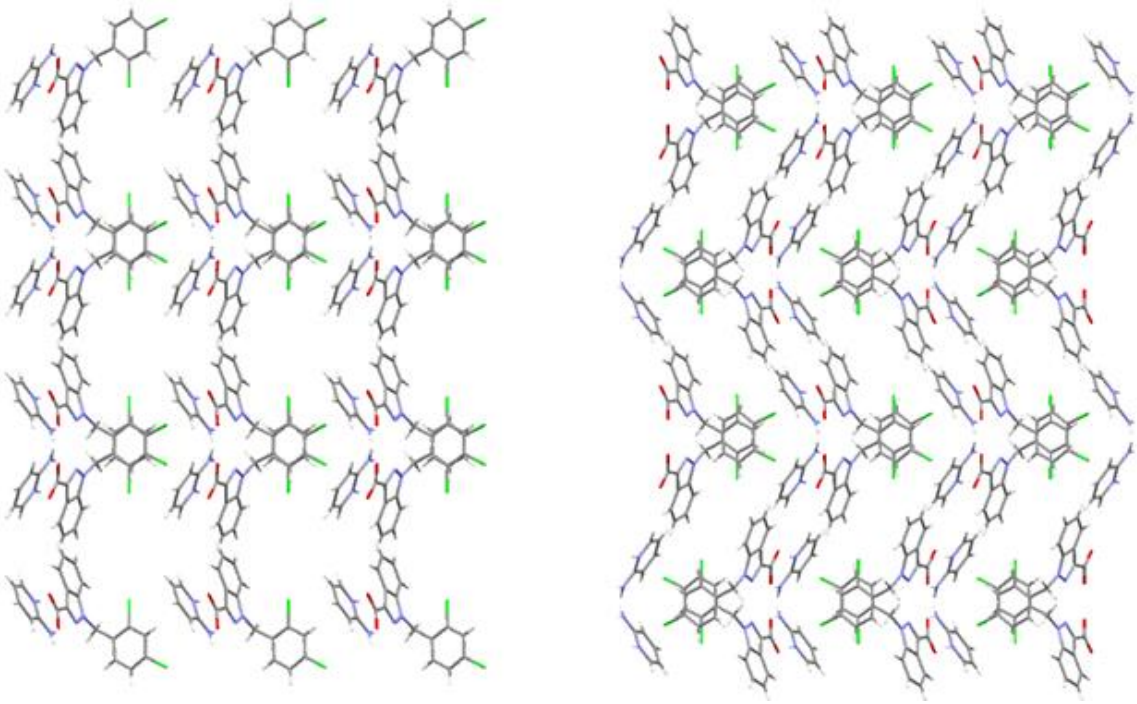

Figure 6.10. Packing of the LON-2APYD salt solvate structures with solvent molecules removed showing the space occupied by the solvent and the effect this has on the layering. Left, EtOAc solvate and right ACN solvate.

6.3.3 Structures Containing Pyrimidine-Based Co-Formers

6.3.3.1 LON-2APYM (2:1) co-crystal

LON and 2APYM form a 2:1 co-crystal containing a dimer as the primary hydrogen bonded interaction. This occurs *via* an $N–H_{amino}\cdots O_{acid\ carbonyl}$ (2.89 Å, 169°) and $O–H_{carboxylic\ acid}\cdots N_{pyrimidine}$ (2.63 Å, 169°) hydrogen bond between LON and 2APYM. Two dimers are connected *via* an $N–H_{amino}\cdots N_{indazole}$ hydrogen bond into a tetrameric unit (Figure 6.11). The tetramers have two orientations in the crystal structure and stack with a zig-zag pattern. The LON dichloro-substituted phenyl rings have an offset face···face stacking.

The second molecule of 2APYM does not partake in any interactions with LON, instead it creates a self-assembling chain containing $N–H_{amino}\cdots N_{pyrimidine}$ hydrogen bonds. The chain contains molecules of 2APYM with alternating opposite orientations. These run throughout the structure and are arranged almost perpendicularly to the tapes of tetramers (Figure 6.11, bottom).

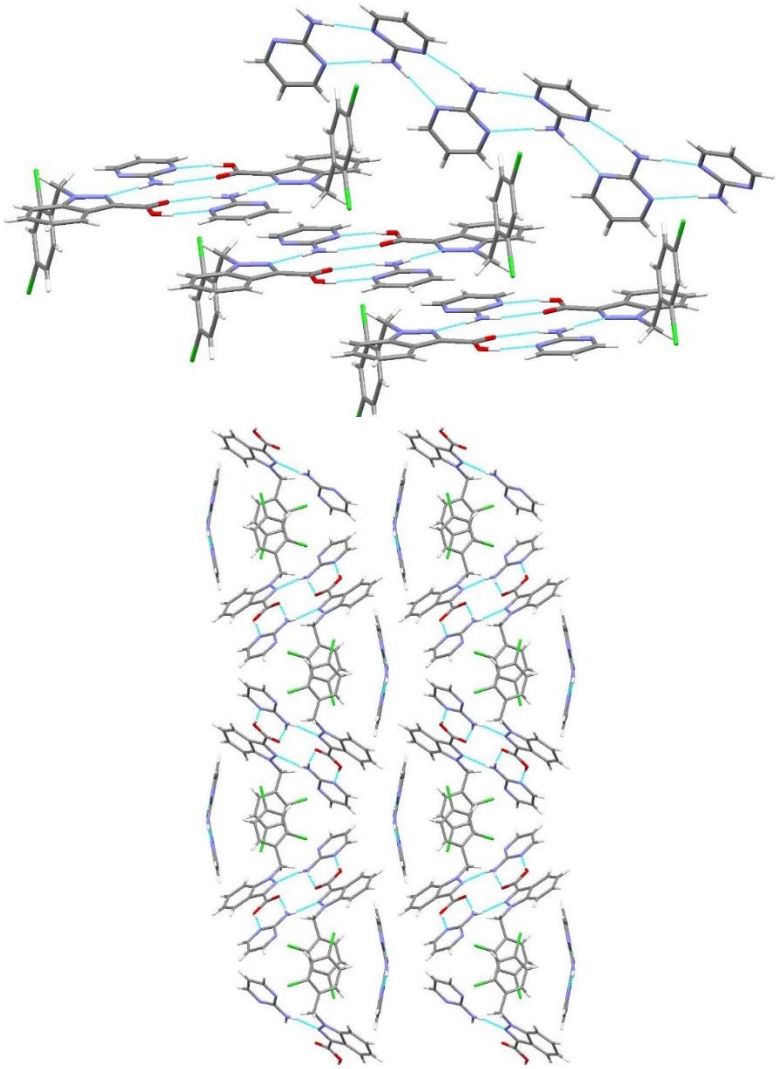

Figure 6.11. 1:2 LON-2APYM co-crystal structure. Top, tetramer formation showing the co-former molecule chain and below, end-on view of the co-former chains in two orientations located in channels between the tetramers.

6.3.3.2 LON-246TAPYM 1:1 Salt

Proton transfer occurs between LON and 246TAPYM generating a 1:1 salt. A dimer forms between the two components assembled *via* an $N–H_{amino}\cdots N_{indazole}$ hydrogen bond from the 246TAPYM amino group to LON indazole N (2.99 Å, 166°) and a bifurcated hydrogen bond arrangement to one oxygen atom of the LON carboxylate (Figure 6.12, top left). The bifurcated interaction occurs from the second amino group of 246TAPYM and the protonated pyridinium ($N–H_{amino}\cdots O^-$ 2.66 Å, 159°and $N^+–H_{pyridinium}\cdots O^-$ 2.99 Å, 136°). Each dimer pair interacts with a second dimer *via* two $N–H_{amino}\cdots O_{carboxylate}$ hydrogen bonds (2.93 Å, 166°), and a third *via* an $N–H_{amino}\cdots O_{carboxylate}$ and two

$N–H_{amino}\cdots N_{pyrimidine}$ co-former···co-former hydrogen bonds (2.99 Å, 121°). The assembly of the pairs forms a stepped ladder comprising central 246TAPYM pairs and peripheral LON molecules (Figure 6.12, bottom left)

6.3.3.3 LON-MEL 1:1 Salt

LON and MEL also form a 1:1 salt with similar hydrogen bonding interactions as displayed in the LON-246TAPYM structure. A bifurcated hydrogen bond occurs to oxygen (O1) of the LON carboxylate from MEL *via* the protonated pyrimidine N ($N^+–H_{pyridinium}\cdots O$; 2.65 Å, 157°) and adjacent amino group (N–H···O; 3.01 Å, 138°). A further hydrogen bond occurs from the same amino group to a second LON molecule *via* the second proton. This forms an $N–H_{amino}\cdots O$ hydrogen bond to O(2) of the LON carboxylate (2.99 Å, 173°), also with a weak interaction to O1. The second amino group of MEL, adjacent to the pyridinium $N^+–H$, forms an $N–H_{amino}\cdots N_{indazole}$ hydrogen bond (3.01 Å, 171°) to the LON indazole. The third MEL amino group partakes in co-former···co-former interactions forming a dimer *via* two $N–H_{amino}\cdots N_{pyrimidine}$ hydrogen bonds (2.91 Å, 175°). These interactions create a ladder network similar to that of LON-246TAPYM containing central MEL co-former pairs and peripheral LON molecules (Figure 6.12, top right). The torsion angle between the methylene linker and dichloro-substituted phenyl ring is significantly different to that in LON-246TAPYM resulting in face-to-face π···π stacking between ladders (LON-MEL) and all ladders are parallel to one another (Figure 6.12, bottom right)

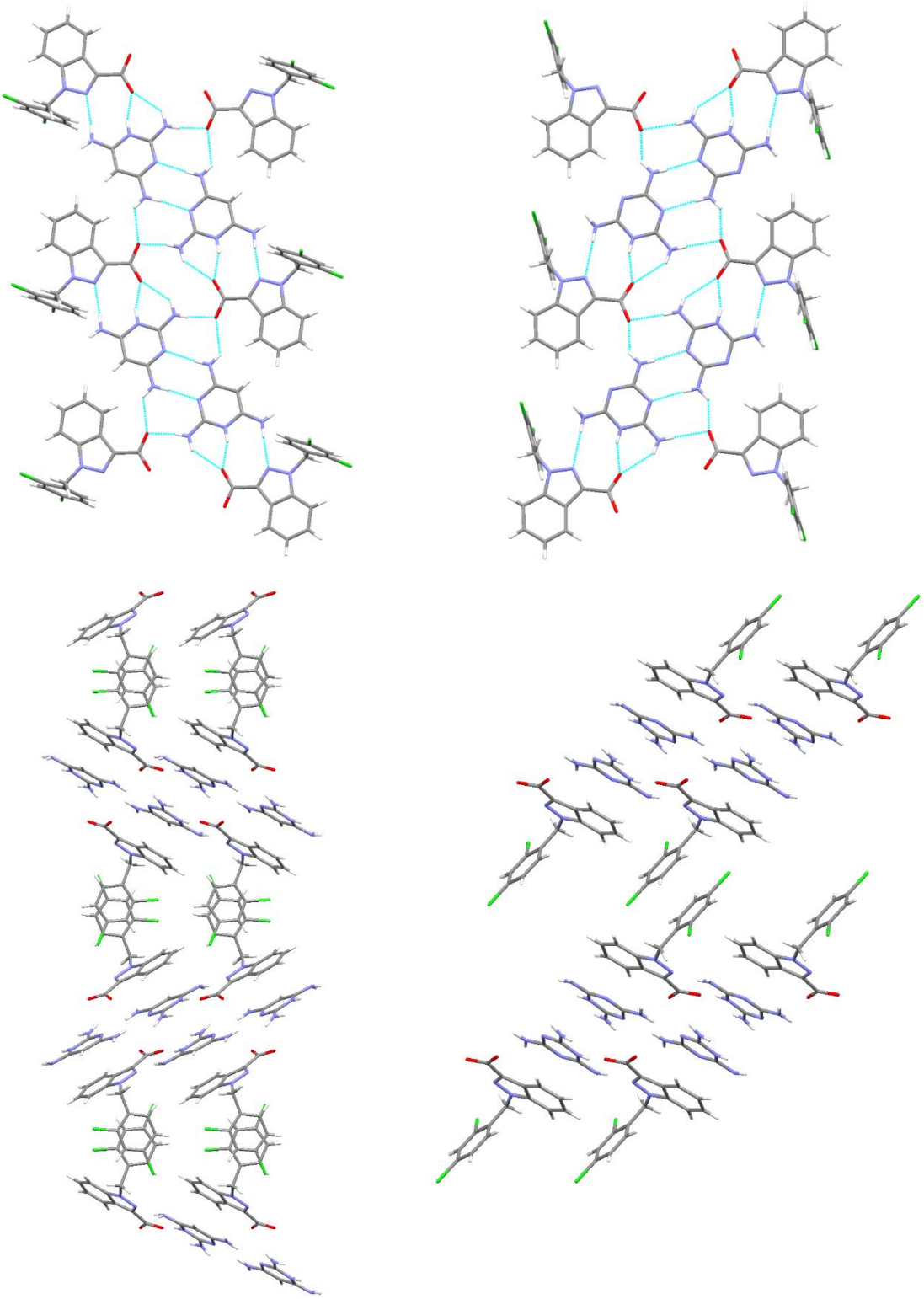

Figure 6.12. Left, ladder arrangement in 1:1 LON-246TAPYM salt and right, ladder in 1:1 LON-MEL salt. Hydrogen bonding interactions forming the ladder are shown above whilst the images below depict the packing of the ladder structure occurring in alternating orientations in adjacent layers (LON-246TAPYM) and all co-former pairs oriented in the same direction (LON-MEL).

6.3.4 Structures Containing Co-Formers with 5- and 6- Membered Rings

6.3.4.1 LON-PIPE (2:1) salt

PIPE forms a 2:1 salt with LON containing charge assisted N–H$^+$···carboxylate interactions (2.69 Å, 2.64 Å, 2.69 Å and 2.76 Å, 164°, 159°, 172° and 163°). These occur from two individual PIPE molecules to a single LON molecule and produce a ladder network, in the *a*-direction, comprised of a peripheral LON backbone and central co-former molecules. The central channel contains only a single PIPE co-former interacting with LON molecules on both sides of the ladder. This is in contrast to the co-former pairs seen in LON-MEL and LON-246TAPYM in which each co-former molecule interacts with a single LON. The PIPE molecules in the ladder occur in alternating orientations and with differing interactions giving an ABAB type layered stacking arrangement (Figure 6.13). 'A' piperazine molecules form an N–H$^+$···O$_{carboxylate}$ and a similar bifurcated interaction at either end of the piperazine molecule. The bifurcated hydrogen bond occurs to both oxygen atoms of a single carboxylate on one LON moiety. 'B' piperazine molecules also form a single N–H$^+$···O$_{carboxylate}$ interaction and a bifurcated interaction from N–H at either end of the molecule, however the latter occurs to one carboxylate oxygen and one indazole ring nitrogen.

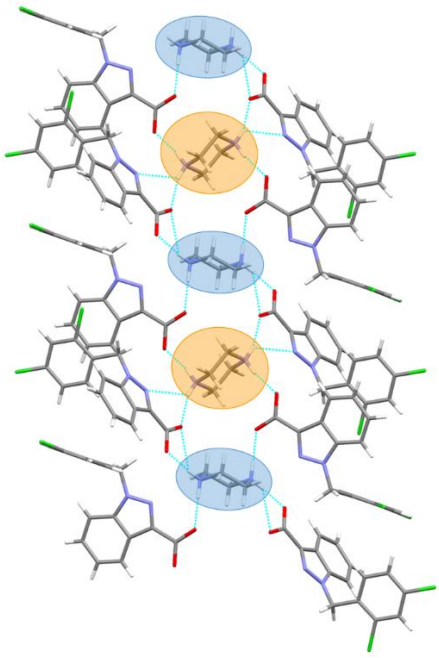

Figure 6.13. Ladder network in the crystal structure of 2:1 LON-PIPE salt with alternating orientation of central PIPE molecules giving an ABAB type packing. 'A' PIPE molecules depicted in blue, 'B' in orange.

6.3.4.2 LON-IMID

Three different structures were obtained with LON and IMID: a 1:1 salt, a 1:1:0.5 ethyl acetate salt solvate and a 2:1 co-crystal salt (hybrid structure). Figure 6.14 depicts the main structural motif of each, detailed structural discussions follow.

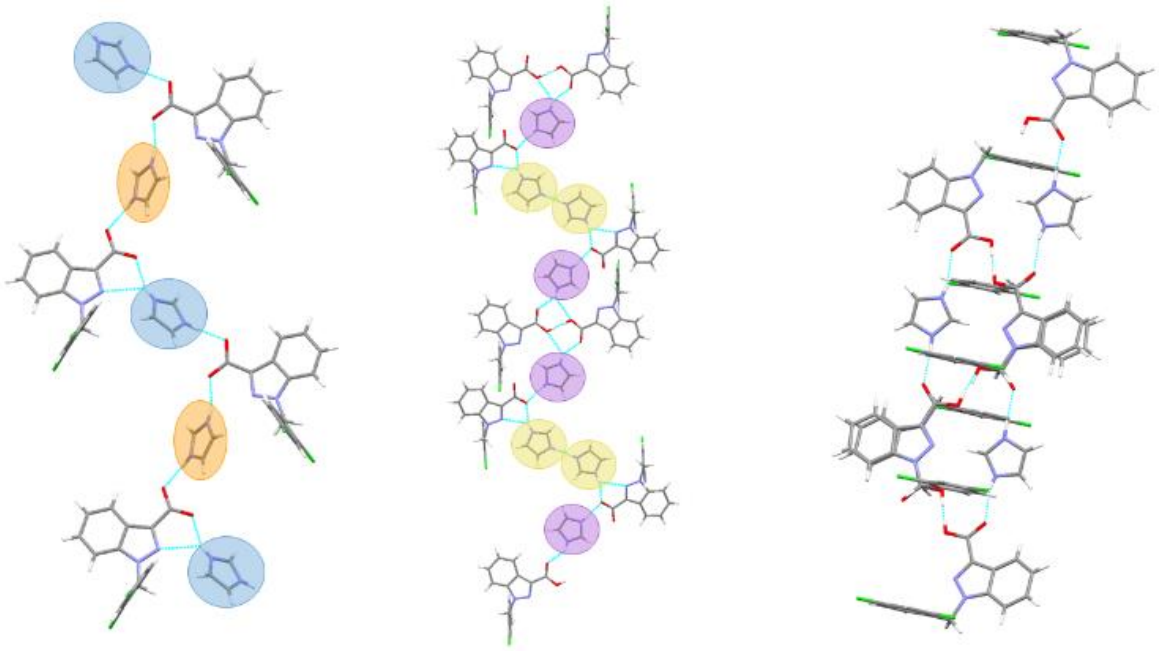

Figure 6.14. Main hydrogen bonds and structural motif present in the three LON-IMID structures. Left, LON-IMID·0.5EtOAc ladders with ABAB pattern (blue 'A' and orange 'B', solvent excluded for clarity), middle, 1:1 salt with ladders of ABBA pattern (purple 'A' and yellow 'B') and right, 2:1 structure with LON dimer interactions between 2:1 units.

The 1:1 salt solvate contains six molecules of both LON and IMID in the asymmetric unit and three EtOAc molecules. 2:1 units of LON-IMID assemble *via* two bifurcated N–H interactions. The first comprises two N–H···$O_{carboxylate}$ hydrogen bonds (e.g. 2.63 Å, 167° and 3.43 Å, 125°) whilst the second contains one N–H···$O_{carboxylate}$ and one N–H···$N_{indazole}$ hydrogen bond (2.69 Å, 153° and 3.08 Å, 125° respectively). The 2:1 units extend in zig-zag chains which contain an ABAB type pattern of IMID molecules (Figure 6.15, left) each LON contributing to two 2:1 units. All LON molecules are orientated with their dichloro-substituted phenyl rings situated above the plane of the chain however in alternating orientations complementary to the ABAB motif. The chains form parallel stacked sheets extending into layers which creates space between the dichloro-substituted phenyl rings. It is here that the solvent molecules are situated, forming a chain down the *b*-axis (Figure 6.15, right).

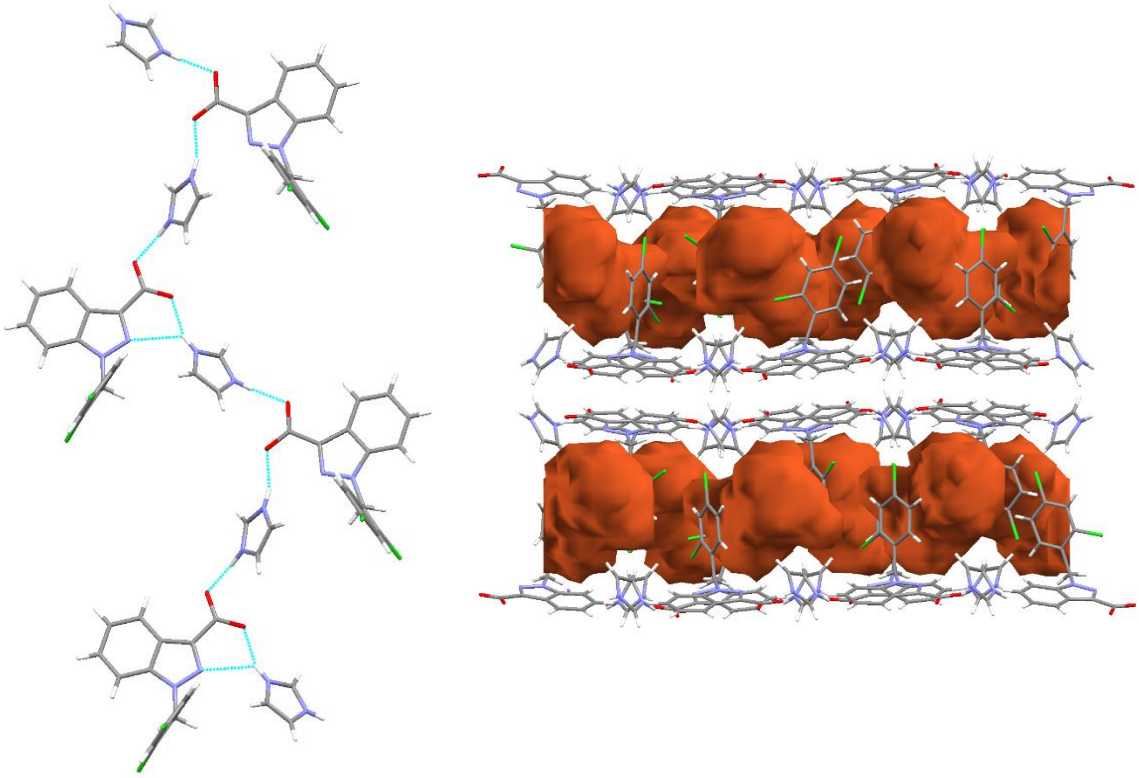

Figure 6.15. Left, chains of LON-IMID occurring in the *a*-direction in LON-IMID·0.5EtOAc (solvent molecules excluded for clarity) and right, location of solvent molecules occurring in the *b*-axis.

The 1:1 LON-IMID salt (anhydrous) contains two molecules of each component in the asymmetric unit forming two LON-IMID pairs. Complete proton transfer occurs between one pair whilst only partial transfer occurs between the second. A similar chain motif to that of the 1:1:0.5 salt solvate is formed however with an ABCABC three-layer repeat (Figure 6.16, left). The 'A' layer consists of partially protonated LON molecules which self-assemble into a dimer *via* an O–H···H–O hydrogen bond, the proton being shared between the two units. These dimers interact with a protonated IMID molecule *via* a bifurcated N–H···O hydrogen bond from IMID to both oxygen atoms of LON. The 'B' layer contains a deprotonated LON partaking in an N^+–H···O^- hydrogen bond from the 'A' IMID, and a partially protonated IMID dimer sharing a proton and formed through an N^+–H···H–N hydrogen bond. The 'C' layer contains a deprotonated LON which interacts with two independent IMID molecules. The 'B' IMID above in the chain forms an N–H···O^- hydrogen bond to LON whilst the (protonated) IMID below LON in the chain forms an N^+–H···O^- charge assisted hydrogen bond. Adjacent chains stack into layers containing face-to-face orientated LON dichloro-substituted phenyl rings (Figure 6.16, right).

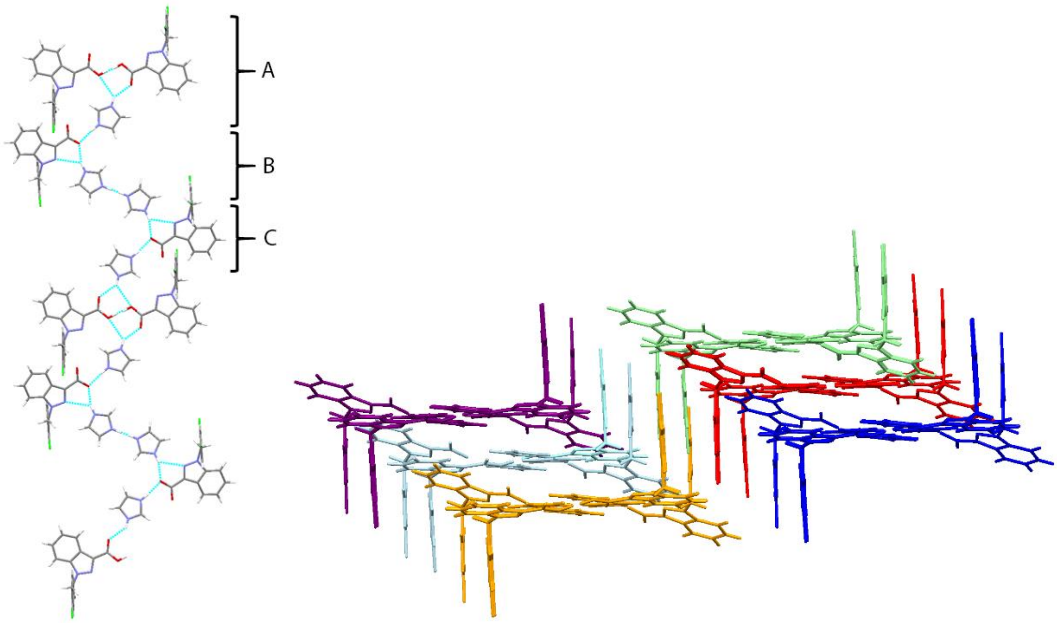

Figure 6.16. Left, chain structure in the 1:1 LON-IMID salt with ABC repeating pattern and right, layering and stacking of the chains (each given a single colour) to generate the crystal lattice.

The final IMID salt has a 2:1 ratio and contains units of the same stoichiometry held together by N–H···$O_{carbonyl}$ hydrogen bonds (2.69 Å, 159° and 2.76 Å, 169°). IMID is wholly protonated whilst both LON molecules possess a partially protonated carboxylic acid; a single proton is shared over the two carboxylic groups thus making a charge-balanced unit. The 2:1 units are connected along the crystallographic *c*-axis through LON dimer formation and an O–H···O hydrogen bond. This is similar to the 1:1 salt in which dimers form *via* the partially occupied proton in an O–H···H–O hydrogen bond. The IMID molecules of the 2:1 units lie parallel to the *c*-axis, the LON dimer interactions occurring at an angle of 68° relative to this (Figure 6.17, top). The chains stack to form parallel layers (Figure 6.17, bottom) in the *ab* plane creating the 3D lattice.

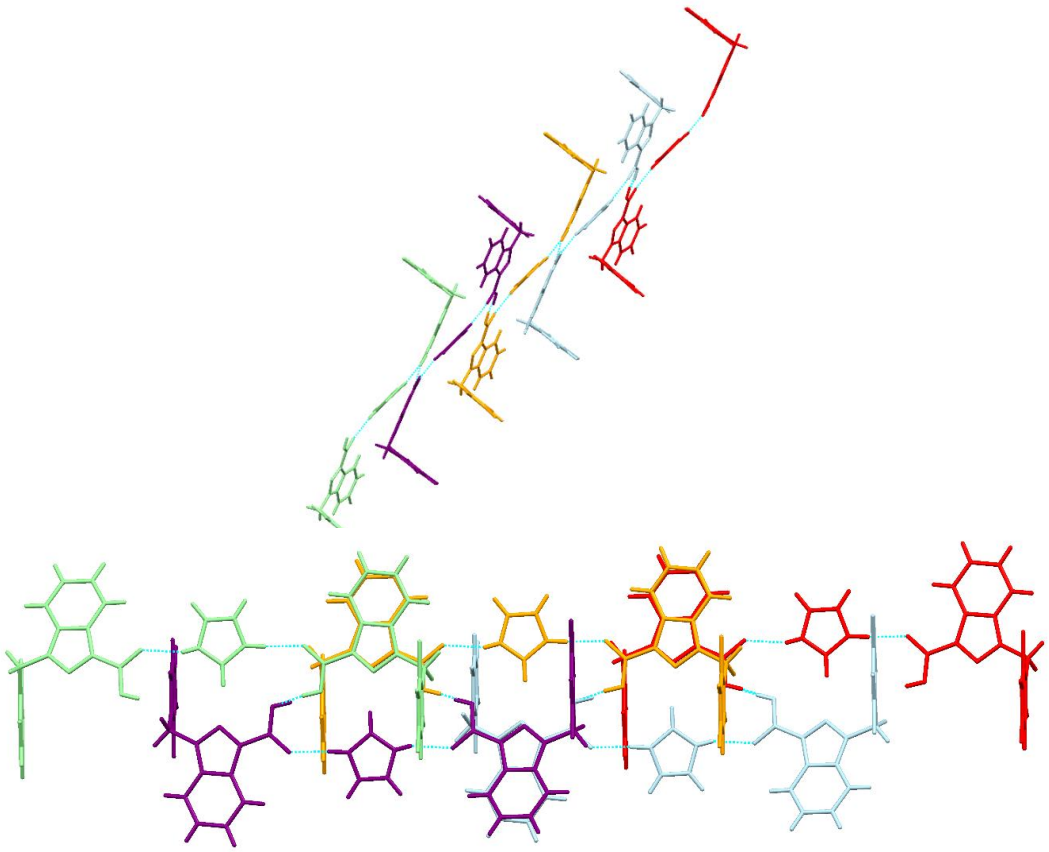

Figure 6.17. Chains of 2:1 units (coloured individually) in the 2:1 LON-IMID structure. IMID molecules are arranged parallel to the *c*-axis (top) and chains layer in a parallel stacking mode (bottom).

6.3.5 Structures Containing Other Co-Formers

6.3.5.1 LON-HALO

HALO forms a 1:1 trihydrate salt with LON crystallising in the monoclinic space group *I*2/*a*. TGA was used to confirm the trihydrate nature (Appendix C.11.3) With the exception of one, reported salts of HALO with carboxylic acids[302] all form as salt hydrates showing this structure is consistent with other observations. The three water molecules included in the lattice can each be located in a discrete position. Two of these molecules exhibit positional disorder resulting in alternative hydrogen bonds, each with approximate ratios of 60:40. The main components and their respective hydrogen bonds only are depicted in the images (Figure 6.18) for ease of the discussion and description.

LON-HALO·3H_2O contains a primary N^+–H···O^- charge assisted hydrogen bond (2.724 Å, 172°) between HALO and LON. The water molecules are central to the hydrogen bonding network and

crystal structure. An O–H···$O_{carbonyl}$ hydrogen bond occurs from one water molecule to a LON carboxylate oxygen, the same atom partaking in the primary charge assisted hydrogen bond.

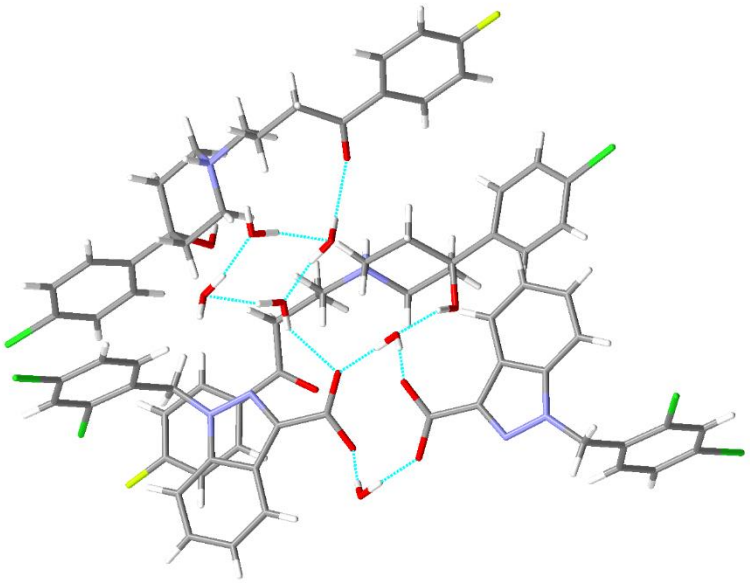

Figure 6.18. Main hydrogen bonding interactions present in LON-HALO·3H_2O salt forming two tetramers. One contains two LON and two water molecules, the second is a self-assembling motif of four water molecules.

A tetrameric supramolecular unit consisting of two LON molecules (carboxylate end) connected *via* two water molecules, forms around an inversion centre and is surrounded by two HALO molecules (Figure 6.18). The HALO molecules are situated one each above and below the plane of the tetramer. O–H···O hydrogen bonds between the water molecules extend the network and a second tetrameric motif is seen, constructed from four hydrogen bonded water molecules. The two tetramers are linked *via* an O–H_{water}···$O_{carboxylate}$ hydrogen bond and various tetramer···HALO interactions to extend the lattice. These include O–$H_{hydroxyl}$···O_{water} and O–H_{water}···$O_{carbonyl}$ hydrogen bonds.

6.4 Analysis of Structural Similarities in the Novel Materials

The new forms of LON discussed in Section 6.3 contain co-molecules which have a number of structural similarities (Figure 6.2), some of which have already been identified in the crystal structure analysis. These similarities can be investigated and, along with the crystal structure information, can help to identify correlations and illustrate comparisons between these materials.

6.4.1 Comparisons Between ISO, NICO and BENZ

ISO and NICO are very closely related in their structures, the only difference being the position of the amide substituent relative to the N in the pyridyl ring. This is located at position 3- (ISO) or 4- (NICO) relative to the amide substituent group. BENZ also has a similar structure with no ring nitrogen atom, containing just a simple phenyl ring instead.

All three co-formers produce a 1:1 co-crystal with LON therefore it might be expected that they form similar structures. Experimentally, a trend was seen in both the ease of crystal formation and crystal quality: LON-ISO > LON-NICO > LON-BENZ. The latter two formed few or only a single crystal of the new material and were thin, marked plates and needles. In comparison, LON-ISO formed large block crystals that could be produced readily.

Both LON-BENZ and LON-NICO contain an acid···amide dimer as the primary hydrogen bonding motif, however LON-ISO forms a single acid···pyridine hydrogen bond. In this arrangement, the co-former is in the opposite orientation with respect to the LON carboxylic acid as it is the pyridine ring, rather than the amide functionality, forming the interaction. The LON-ISO adduct contains a single primary hydrogen bond, however overall there are a greater number of hydrogen bonds than in LON-NICO or LON-BENZ and these contain strong donors and acceptors. A total of five 'typical' hydrogen bonds are observed in LON-ISO alongside a C–H···Cl and C–H···O contact. LON-NICO, however, forms only two N–H···O hydrogen bonds in addition to the dimer, with some weaker C–H···O contacts, and LON-BENZ displays even fewer interactions. The latter has acid···amide dimer bond lengths which are longer than in LON-NICO (see Appendix C.7.1) indicating a reduced strength.

The reduced number of hydrogen bonds in LON-NICO and LON-BENZ in comparison to LON-ISO explains the difficulty experienced in crystal formation. The slightly longer hydrogen bonding distances of LON-BENZ increases this difficulty and as a result LON-BENZ has the poorest quality crystals which are the most difficult to obtain. α-LON has a similar hydrogen bonded network to LON-BENZ and the crystals display a similar morphology. They, too, are difficult to form. This can be attributed in part to the hydrogen bonds and similar interactions present.

2-Picoline, the 2-substituted analogue of ISO and NICO was also tested in experimental screening however did not give any indications that a new material was likely. This could be attributed to the position of the N acceptor atom. The pyridine N is adjacent to the amide substituent, this proximity presenting some steric hindrance and may prevent donor atoms reaching the site to interact. This postulates that the pyridyl N, when present, may be important in hydrogen bonding and prevention of an interaction at this site results in a co-crystal being less favourable.

The positioning of the amide substituent in NICO relative to the pyridine N is overcome by the formation of a dimer between the pyridyl ring (NICO) and fused indazole ring (LON). This occurs *via* two C–H···N contacts. In this arrangement, all the hydrogen bonding functionalities can be exploited and maximal contacts formed (see Section 6.4.2). The absence of a pyridine nitrogen atom in LON-BENZ restricts the hydrogen bonding potential, however all functionalities can be involved in a hydrogen bond in a heteromeric system. The co-crystal forms but with poorer quality crystals due to the reduced number of hydrogen bonds possible (in comparison to, for example, LON-ISO).

The LON-ISO and -NICO and LON-BENZ comparison and the lack of a LON-2-picoline co-crystal supports the theory that the pyridyl nitrogen atom is key to co-crystal formation providing additional interaction functionalities. Its position, however, is important and affects the overall interaction network; sites closer to larger substituents have a greater degree of steric hindrance and restrict access for potential interacting molecules. This results in poorer quality crystals which are harder to obtain.

In contrast to 2-picoline, 2APYM does form a co-crystal with LON despite having a 2-position substituent. The 2APYM substituent (amino) is smaller and less bulky than that in 2-picoline (amide) meaning that access for hydrogen bond donors is less restricted; the pyrimidine N acceptor atoms on either side of the amino group are able to partake in hydrogen bonds with any donor functionalities present. The amino substituent of 2APYM also favours hydrogen bonding due to its position and geometry relative to the pyrimidine N atoms. Generation of a dimer interaction is possible *via* the amino N–H to an appropriate acceptor, with a reciprocal hydrogen bond forming to the pyrimidine N acceptor from a donor on the second molecule. Hence, the 2-position amino substituent is advantageous, rather than detrimental, to hydrogen bonding.

6.4.2 Interaction Analysis of Structures Containing NICO

An analysis of multi-component systems in the CSD containing NICO was conducted to investigate the interactions preferentially formed. 127 structures with ≥ 2 molecules and no metals were retrieved. Of these, eight had no co-ordinates deposited and so were not included in the subsequent analysis. The results are summarised in Appendix C.8.1 and show that amide···amide and amide···acid dimers are most favoured, as are non-dimer NICO···NICO interactions in the form of N–H···O=C hydrogen bonds. Amide···hydroxyl interactions are also preferential both from the hydroxyl to the carbonyl ($O–H_{hydroxyl}···O_{amide}$) and from the amide $–NH_2$ to the hydroxyl ($N–H_{amide}···O_{hydroxyl}$). The pyridine N acceptor most commonly forms a hydrogen bond with an O–H group (over 70 % of the structures), originating from a carboxylic acid in over 71 % of these.

Two different hydrogen bonds to the pyridine in different LON molecules are observed in four structures. These consist of either an $O–H_{acid}\cdots N$ or $O–H_{hydroxyl}\cdots N$ hydrogen bond and an $N–H_{amide}\cdots N$.

The hydrogen bonding pattern observed in the LON-NICO crystal structure (an acid···amide dimer) follows the trend seen from CSD analysis. This strong hydrogen bonded motif is supplemented by further acid···amide interactions in the tetramer formation (Figure 6.4) causing the NICO pyridine N to be poorly situated (hindered) to form a strong hydrogen bonding interaction. Two weaker C–H···N hydrogen bonds are possible from the molecular arrangement which enhance the network of interactions. This is seen in some structures retrieved from the CSD. It is postulated that the acid···pyridine hydrogen bond does not form as this would create a less favourable geometry for further hydrogen bonds to extend the network. Many structures retrieved from the CSD searches contained smaller, less bulky and often linear molecules in which molecular orientation and geometric complexity is less of an influencing factor in hydrogen bond formation.

6.4.3 Interaction Analysis of LON-2APYM and Other 2APYM-Containing Structures

The LON-2APYM co-crystal structure is of interest as Etter's hydrogen bonding rules[12] state that 2APYM will preferentially bond to a carboxylic acid rather than with itself and both N–H protons and ring nitrogen atoms will be utilised. The two protons, and likewise the ring N atoms, need not form hydrogen bonds to identical groups though. Etter establishes that $O–H_{carboxylic\ acid}\cdots N_{pyrimidine}$ is the strongest hydrogen bond and will form first. This will be followed by the association of the next best donors and acceptors[303] according to the proton donor and acceptor ranking.

Some interesting features are observed in the LON-2APYM crystal structure. Figure 6.11 illustrates a carboxylic acid···pyrimidine interaction, as expected, occurring alongside a 2APYM···2APYM association. The latter co-former···co-former interaction would not be expected with regards to Etter's rules; LON has limited functional groups besides the carboxylic acid and therefore these co-former functionalities would be the next best available hydrogen bonding donors and acceptors in the system. The 2APYM···2APYM interaction forms *via* N–H···N hydrogen bonds, utilising all amino protons and ring nitrogen atoms (as stated) in two equivalent hydrogen bonds. The tetramer which forms between two LON and two 2APYM molecules utilises only one aromatic N in hydrogen bonding in contrast to Etter's rules.

There are a number of reported co-crystals which contain 2APYM and a carboxylic acid, such as terephthalic acid,[304] *p*-phenylacetic acid,[305] 3,3,3-triphenylpropanoic acid,[306] N-methylpyrrole-2-carboxylic acid and indole-3-acetic acid,[307] and a selection of aminobenzoic, nitrobenzoic and phthalic acids.[308] Analysis of this type of reported multi-component systems as enabled *via*

interrogation of the CSD and detailed in full in Appendix C.8.2. It was found that structures with a 1:1 stoichiometry (acid-containing molecule:2APYM) are the most recurrent, many containing a di-carboxylic acid. A small proportion were seen in a 2:1 ratio and in half of these cases a degree of proton transfer was seen resulting in a co-crystal salt. Only two structures with a 1:2 ratio as observed in LON-2APYM were retrieved, both of which were neutral co-crystals. Only one, that with 2-bromobenzioc acid (CSD refcode MOZBEK),[309] contained a mono-acid and can be identified as the most closely related structure present in the CSD to LON-2APYM. This structure displays a 2APYM co-former chain connected *via* N–H···N hydrogen bonds, similar to that observed in LON-2APYM. As shown in Figure 6.19 there are slight differences in the 2APYM chains in the two co-crystal structures: when viewed down the chain the 2APYM molecules are arranged approximately parallel (177° angle) in the 2-bromobenzoic acid-2APYM structure and at an angle of around 160° for LON-2APYM (Figure 6.19, b & c). When viewed along the chain (side-on) the molecules in both chains are tilted, but in different directions: this is a sideways tilt in the 2APYM chain of 2-bromobenzoic acid-2APYM and longitudinal relative to the 2APYM molecules in LON-2APYM (Figure 6.19, d & e).

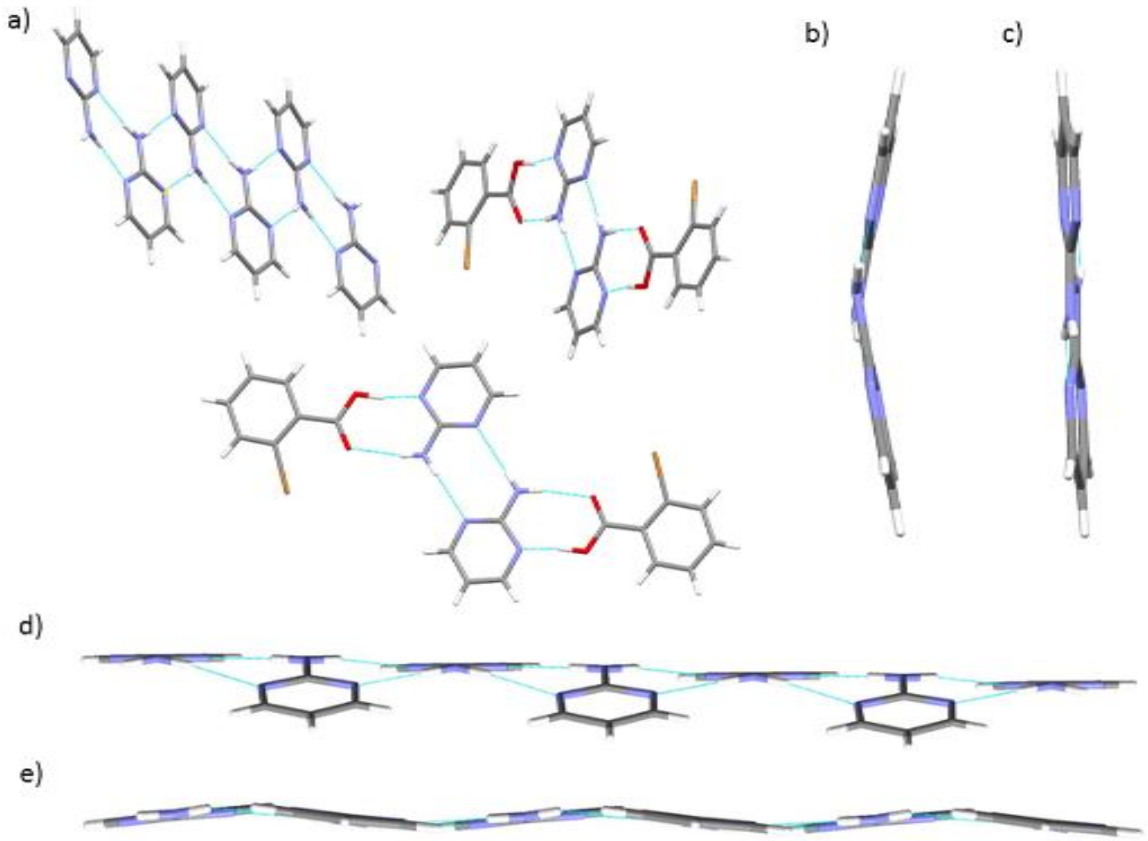

Figure 6.19. a) Crystal structure of 2-bromobenzoic acid-2APYM 1:2 co-crystal showing the tetrameric arrangement containing a 1:1 ratio of the molecules and additional 2APYM chain. Views down (b) and along (d) the 2APYM chain in LON-2APYM and similarly for 2-bromobenzoic acid-2APYM (c and e).

2-bromobenzoic acid-2APYM also forms tetrameric motifs as seen in LON-2APYM, however all available functionalities are used in hydrogen bonding. This is likely to be due to the smaller size and planar geometry of 2-bromobenzoic acid causing no steric influences. The tetramers occur in two orientations, which bisect the plane of the 2APYM chain at angles approximately 57° and 65° (Figure 6.19, a).

6.4.4 Comparisons of LON-2APYD and LON-2APYM and their Interactions

2APYD is structurally similar to 2APYM (Figure 6.2) yet behaves very differently when combined with LON. 2APYD produced two salt solvates both with a 1:1 stoichiometry whilst 2APYM formed a 1:2 neutral co-crystal. Both systems display a similar primary hydrogen bonding motif, creating a dimer between the LON carboxylic acid and pyrimidine N and adjacent amino group of the co-former. In LON-2APYM this occurs *via* $O–H_{carboxylic\ acid}\cdots N_{pyrimidine}$ and $N–H_{amino}\cdots O_{carboxylic\ acid}$ hydrogen bonds however the equivalent charge assisted $N^{+}–H_{pyridinium}\cdots O^{-}_{carboxylate}$ is seen in LON-2APYD due to the proton transfer that occurs. At the secondary level of hydrogen bonding differences are seen. The LON-2APYM neutral co-crystal forms a planar tetramer between two dimers whilst the two salts form zig zag chains with only a single N–H···O contact between (out of plane) dimers.

The pK_a of the two co-formers (Appendix C10) shows how the two different forms arise; 2APYD has a pK_a value of 6.84 whilst 2APYM pK_a is 3.62. In accordance with literature and the rules for salt formation the ΔpK_a for LON-2APYD is > 3 so salt formation would be predicted. On the contrary, 2APYM has a small difference in pK_a to LON and so no proton transfer would be expected. For more discussion of pK_a see Section 6.7.

6.4.5 Interaction Analysis of Structures Containing PIPE

PIPE can act both as a neutral and a cationic co-former to give a co-crystal or salt product with an acidic API.[56] An inspection of the CSD (Appendix C.8.3) indicated 470 compounds present that contain the piperazine ring ($C_4H_{10}N_2$) when no limitation regarding the number of hydrogen atoms bonded to N is given. Of these, 209 did not contain piperazine as an individual entity but larger molecule derivatives with additional bonds from the N atom(s). The remaining 261 can be divided into compounds with a 2+, 1+ or 0 charge according to the degree of protonation at the two N sites. 75 % (196 structures) display protonation at both N atoms, giving the 2+ piperazinium ion, 6.9 % (18 structures) had a 1+ charge with a single N protonated, and 15.7 % (41 structures) had no proton transfer leaving piperazine in its neutral form. The remaining structures contained 2 individual piperazine molecules. 4 structures (1.5 %) had one 1+ and one 2+ charged molecule, while 2 structures (0.5 %) displayed a di-protonated and a neutral molecule. These results indicate

the likelihood of proton transfer to a PIPE molecule; 84.3 % of PIPE-containing structures display a degree of proton transfer and a resulting charge. Of these charged systems, 88.7 % display di-protonation of piperazine resulting in a 2+ charge. LON-PIPE forms a salt with proton transfer to both N atoms. This is in agreement with the CSD statistics obtained and not unexpected.

6.4.6 Comparisons of LON Structures Displaying Carboxylic Acid···Pyridine Motifs

Carboxylic acid···pyridine interactions are widespread in the crystal structures of the CSD (Section 6.2.2) and are a common tool employed in crystal engineering strategies. A number of the structures for LON contain these functionalities, yet variations are seen in the hydrogen bonding interactions displayed.

The co-formers which contain a pyridine ring (single aromatic N) include: 2APYD, 4,4BIPY, 4DMAP, ISO, and NICO. Three of these (4,4BIPY, ISO and NICO) form neutral co-crystals (4,4BIPY, ISO and NICO) whilst the remaining two form salt and salt-related forms.

6.4.6.1 Co-crystal structures containing a carboxylic acid···pyridine interaction

The LON-NICO co-crystal forms an acid···amide dimer however the other two co-crystals (LON-ISO and LON-4,4BIPY) display an O–H···$N_{pyridine}$ hydrogen bond from the acid hydroxyl. Both ISO and 4,4BIPY co-formers have a *para*- arrangement of the pyridyl N and ring substituent. This geometry is likely to favour a linear arrangement of hydrogen bonds in comparison to *meta*- (NICO) or *ortho*- arranged substituents.

Aakeröy *et al*.[310] have reported the 1:1 co-crystal of ISO with benzoic acid which displays an acid···pyridine hydrogen bond and amide···amide dimer between the two ISO molecules (Figure 6.20). They also compare the interactions in a ternary co-crystal which, too, displays the acid···pyridine hydrogen bond (best acceptor and donor) alongside an acid···amide dimer (second best donor-acceptor pair). Further studies into mono- and di-carboxylic acids with ISO show that this acid···pyridine and amide···amide motif pair (Figure 6.20) is typical of the majority of these systems.[299, 311]

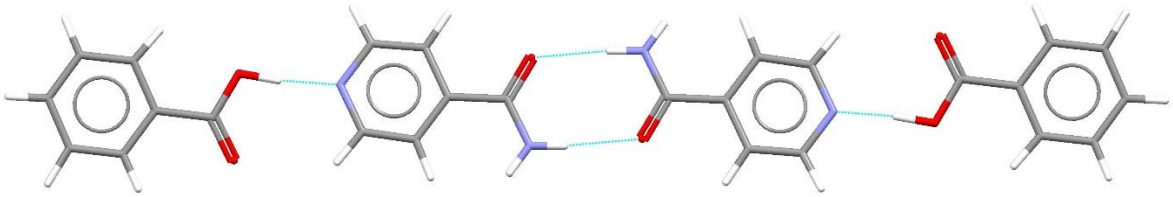

Figure 6.20. Primary hydrogen bonding motifs in the 1:1 isonicotinamide-benzoic acid co-crystal structure.

The LON-ISO co-crystal displays the acid···pyridine synthon, as expected from literature studies however the co-former···co-former hydrogen bonds deviate from those reported by Aakeröy. Instead of an amide···amide dimer formed from two N–H···O hydrogen bonds, $N–H_{amide}\cdots O_{carboxylic\ acid}$ and $C–H\cdots O_{carboxylic\ acid}$ hydrogen bonds are observed and give rise to a zig-zag, rather than linear, arrangement (Figure 6.21). This arrangement may arise due to LON, in comparison to the small, linear (ISO-like) molecules of the study. The packing and 3D geometry reflects that of the molecule.

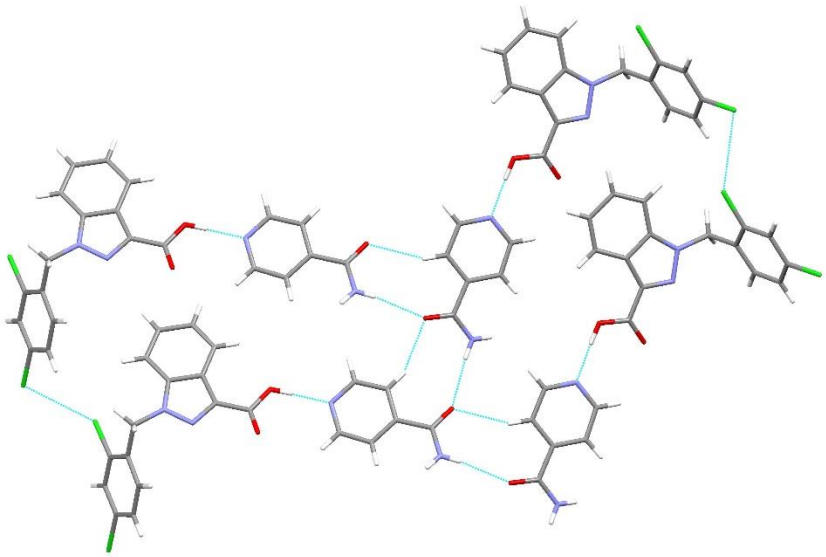

Figure 6.21. Hydrogen bonding interactions in the LON-ISO co-crystal structure displaying N–H···O and C–H···O hydrogen bonds between ISO molecules giving rise to a zig-zag pattern, in addition to the expected $O–H_{carboxylic\ acid}\cdots N_{pyridine}$ motif.

The presence of the linear $O–H_{carboxylic\ acid}\cdots N_{pyridine}$ hydrogen bond in the LON-4,4BIPY is expected due to the 4,4BIPY geometry and bi-pyridine ring system. 4,4BIPY contains no other functionalities with which it can interact with itself, other than *via* π···π stacking of the aromatic ring. Hence there are no other obvious hydrogen bonding patterns possible and the carboxylic acid groups form hydrogen bonds to either end of the 4,4BIPY molecule. Detailed interactions of the LON-NICO system are discussed in section 6.4.2.

6.4.6.2 Salt structures containing a carboxylate···pyridine interaction

2APYD and 4DMAP both form salts with LON and each produce multiple crystal structures. LON-2APYD formed two different 1:1 solvate structures, whilst 4DMAP produced two materials of differing natures: a 1:1 dihydrate salt and a 2:1 co-crystal salt in which proton transfer occurs from only one LON molecule.

A CSD search of structures containing 4DMAP and a $–CO_2$ group with filters restricting the results to contain ≥2 molecules and no metals returned 86 structures. Of these, 23 contained a 4DMAP analogue with an additional atom / group bonded to the pyridine N atom rather than the individual molecule of interest. The remaining structures (63) all contained 4DMAP in its protonated form as part of a salt or hybrid structure. Four structures contained the $–CO_2$ group as part of an ester, rather than acid and therefore did not show a carboxylic acid to pyridine proton transfer. 4DMAP was however in the protonated form resulting from an alternative proton source: two hydroxyl and two secondary amine donors. These results show the basicity of the pyridine N in 4DMAP, and the likelihood that a multi-component structure would form as a salt with either full, or at least partial, proton transfer occurring. This is in accordance with the results observed in this work.

A similar search was carried out for 2APYD. The results and analysis showed one structure did not contain an available acid ($–CO_2$ group present in an ester functionality) and only 4 out of 26 structures (15.38 %) did not exhibit proton transfer. These results indicate that 2APYD in conjunction with a carboxylic acid is likely to result in salt formation. The structures obtained herein are also in agreement with this. See Appendix C.8.4 and Supplementary File for full details.

6.4.7 Analysis of Structures Displaying Tetrameric Motifs

Both LON-NICO and LON-ISO display tetrameric motifs formed through their hydrogen bonding however they are quite different in their nature (Sections 6.3.2.1 and 6.3.2.2). A comparable tetrameric motif to that in LON-NICO is observed in the LON-2APYM 1:2 co-crystal. Hydrogen bonded dimers between 2APYM and LON ($N–H_{amine}\cdots O_{carbonyl}$ / $O–H_{carboxylic\ acid}\cdots N_{pyrimidine}$) are connected *via* a single $N–H_{amine}\cdots N_{indazole}$ hydrogen bond from the amine of 2APYM to the indazole of LON. LON-NICO contains a similar interaction from the amide of NICO to indazole ($N–H_{amide}\cdots N_{indazole}$). Both the co-crystals with NICO and 2APYM contain layers of the tetrameric motifs arranged in two orientations which lie almost perpendicular to one another.

6.4.8 Analysis of Structures Displaying Ladder Motifs

LON-246TAPYM, LON-MEL and LON-PIPE all display a ladder-type structure containing peripheral LON molecules and central salt counter ions. LON-246TAPYM and LON-MEL contain co-former···co-former interactions generating central co-former pairs with two peripheral LON molecules however in LON-PIPE, due to the PIPE 2+ charge and 2:1 stoichiometry, only a single PIPE is contained at the centre. No PIPE co-former···co-former interactions are present although each PIPE forms hydrogen bonds to two LON molecules on either side of the ladder. This is in

contrast to LON-246TAPYM and LON-MEL where the co-former forms primary hydrogen bonds to only one LON molecule.

The two 1:1 LON-IMID salt forms (EtOAc solvate and anhydrate) can be related to this set of molecules. They contain zigzag chains of LON and IMID molecules with the IMID molecules contained in the centre and LON molecules on the periphery. The unsolvated form shows similarities to the LON-PIPE structure with a single IMID molecule in the centre interacting with both LON molecules on either side. The ladders in LON-IMID·0.5EtOAc are not fully formed with gaps existing alternately on each side of the chain as a result of the three-unit repeating pattern of the co-former molecules. LON···LON interactions are also present within this ladder construct which are not seen in any of LON-MEL, LON-246TAPM or LON-PIPE.

6.5 Hydrogen bonding

Hydrogen bonds are discussed in Chapter 1.2 and show differing natures and properties according to the interaction. A number of different hydrogen bonds and bonding motifs are seen within the novel LON structure and these have differing interaction properties.

6.5.1 Hydrogen Bonds to Aromatic Nitrogen Atoms

Eight co-former molecules contain an aromatic nitrogen atom, five of which are pyridine-based (1 x N), two are pyrimidine-based (2 x N) and one contains three N atoms. 10 different crystal structures are formed from these, three of which contain neutral acid···pyridine hydrogen bonds whilst five exhibit full proton transfer and N^{+}–H···O^{-} charge assisted interactions. One structure contains a hybrid co-crystal salt material with a degree of proton transfer observed and only one structure, that of LON-NICO, does not display an acid···pyridine hydrogen bond. In this structure, the only contacts occurring to the N are from an alkyl CH_2 group and aromatic C–H. Two structures display only a single acid···N hydrogen bond between the acid and N, with D–H···A distances of 2.64 Å (LON-ISO), and 2.54-2.60 Å (LON-4,4BIPY). The remaining structures contain multiple hydrogen bonds from the acid and to the pyridine N. These show longer D–H···A distances as a result (Table 6.1).

Salt forms contain charge-assisted hydrogen bonds and hence shorter D–H···A distances may be expected however this is not seen. All the salts contain a bifurcated interaction to at least one of the carboxylate oxygen atoms, and, in the case of LON-MEL and LON-246TAPYM, to both. The

additional interactions reduce the effect of the charge in each interaction and so the degree of shortening of the bonding length is lessened.

Table 6.1. Interaction information and sample D···A distances for new materials of LON with co-formers containing an aromatic N functionality. S indicates a salt form, C a co-crystal.

Sample	S/C	Interaction	Comment	D···A /Å
LON-NICO	C	acid···amide dímer	C–H···$N_{pyridine}$ contacts only	2.531 / 2.960
		N–H···$O_{neutral}$		2.852
		C–H···N (2)		3.463; 3.445
LON-2APYM	C	acid···N/NH_2 dimer		2.889 / 2.634
LON-ISO	C	acid···pyridine		2.637
				2.971
LON-4,4BIPY	C	acid···pyridine (4)		2.565; 2.575; 2.543; 2.593
LON-2APYD·XACN	S	carboxylate···ar_N^+–H/NH_2 dimer	Bifurcated to one $O_{carboxylate}$	2.838 / 2.795
		N–H···carboxylate		2.648
LON-2APYD·EtOAc	S	$N^+_{pyridinium}$–H/NH_2···carboxylate dimer	Bifurcated to one $O_{carboxylate}$	2.856 / 2.779
		N–H···carboxylate		2.665
LON-246TAPYM	S	$N^+_{pyridinium}$–H/–NH_2···carboxylate	Bifurcated interactions	2.663 / 2.987
		N–H···O (2)		2.932 / 2.997
LON-MEL	S	$N^+_{pyridine}$H/NH_2···carboxylate	Bifurcated interactions	3.008 / 2.654
		N–H···$O_{carboxylate}$ (2)		2.789 / 2.989
LON-4DMAP·2H_2O	S	$N^+_{pyridinium}$–H···$O_{carboxylate}$	Bifurcated to second A	2.628

6.5.2 Analysis of the Salts and Short Hydrogen Bonds

Table 6.2 shows the hydrogen bonding information for the remaining salt materials which display proton transfer from the carboxylic acid. These interactions are, in general, single charge-assisted hydrogen bonds and have shorter D–H···A distances than those observed in Section 6.5.1. With the exception of 4DMAP (2:1) hybrid salt, these salts do not contain a pyridine based co-former molecule. 4DMAP is included here as the hydrogen bonding motifs in the 2:1 structure show greater similarity to IMID than the pyridine-based co-formers.

A carboxylic acid dimer is present in three structures, two of which contain a disordered proton. All display a relatively short D–H···A distance and angles close to linearity: LON-4DMAP 2:1 2.477 Å, 173° (O–H···O); LON-IMID 1:1 2.540 Å, 177° (O–H···H–O); LON-IMID 2:1 2.502 Å and 2.491 Å, 173° and 164° (O–H···H–O x2). These can be considered as short, strong hydrogen bonds (Chapter 1.2.3).

Table 6.2. Interaction information and sample D···A distances for salt materials of LON (no aromatic N) with charge-assisted hydrogen bonding.

Sample	Interaction	Comment	D···A /Å
LON-4DMAP 2:1	O–H···O dimer		2.477
LON-HALO·3H_2O	N^+–H···$O_{carboxylate}$		2.724
	O–H_{water}···$O_{carbonyl}$		2.976
	O–H_{water}···$O_{carboxylate}$ (3)		2.727 / 2.737 / 2.727
	O–H_{water}···O_{water} (2)		2.790 / 2.831
LON-IMID 1:1	O–H···H–O dimer	Disordered proton	2.540
	N–H···$O_{carboxylate}$ (2)	1 bifurcated to both O atoms	2.764 / 2.563
	N–H···$O_{neutral}$		2.673
LON-IMID 2:1	O–H···H–O dimer (2)	Disordered proton	2.502 / 2.491
	N–H···O (2)	Partial delocalised O charge	2.685 / 2.757
LON-IMID·0.5EtOAc	N–H···$O_{carboxylate}$ / N^+–H···$O_{carboxylate}$ (6)	6 independent pairings	2.633 / 2.693 2.636 / 2.708 2.657 / 2.674 2.682 / 2.688 2.653 / 2.707 2.639 / 2.718

LON-PIPE	N^+–H···$O_{carboxylate}$ (5)		2.691 / 2.688
		Bifurcated with similar interaction	3.00 / 2.754
		One bifurcated to indazole	2.644
	N^+–H···$N_{indazole}$		3.112

6.5.3 Overall Analysis of the Interactions of LON

LON contains two main functional groups which can partake in hydrogen bonding: the carboxylic acid and the indazole fused ring. Appendices C.9.1 and C.9.2 give full details of the analysis of the interactions present in all the co-crystal and salt crystal structures.

Indazole forms a hydrogen bond from a primary amine, $–NH_2$, in four structures and from an amide NH_2 ($C(=O)NH_2$) in one further structure. N–H···$N_{indazole}$ hydrogen bonds are seen in three structures from a cyclic N–H donor, one of which is a charged $–N^+H_2$ group. Four structures show an aromatic C–$H_{aromatic}$···$N_{indazole}$ interaction, which is also displayed in the β-LON polymorph, with a single structure displaying a cyclic equivalent C–H_{cyclic}···$N_{indazole}$ contact. Equivalent hydrogen bonds originating from $–CH_2$ and $–CH_3$ groups are present in two and one structure(s) respectively. There is no obvious interaction to the indazole group in three of the structures, one salt (LON-HALO), one co-crystal (LON-ISO) and the α-LON polymorph. Interactions to the indazole N are from 2 categories of functionalities: N–H containing and C–H containing. The number of structures displaying each type is approximately even, however N–H interactions are slightly more predominant. $–NH_2$ in the form of a primary amine or amide is the most favoured functional group to form a hydrogen bond to the indazole in these novel LON structures. This is followed in rank by aromatic C–H functionalities

The carboxylic acid of LON partakes in a number of different interaction types with a variety of different functionalities. Two structures feature an acid···amide dimer (LON-BENZ and LON-NICO) whilst a further two (1:1 and 2:1 LON-IMID) contain a LON dimer formed *via* a single hydrogen bond with a shared proton (O–H···H–O). LON-4DMAP 2:1 shows a similar interaction containing a single O–H···O- hydrogen bond between two LON molecules.

Seven structures (LON-2APYD (x2 solvates), -2APYM, -246TAPYM**,** -ISO, -MEL and -PIPE) display NH_2···O_{LON} interactions, originating from a neutral amino group in six, and a charged N^+H_2 group in the seventh (LON-PIPE). 14 structures contain an N**–**H···O_{LON} interaction of which six are neutral N–H hydrogen bonds displaying no proton transfer, and an aromatic (pyridyl-type) N atom is

present in eight. C–H···O_{LON} contacts are also seen in several structures and include C–H (aromatic and cyclic) and –CH_2 (alkyl and cyclic) groups.

The crystal structures obtained for the novel solid forms of LON display interactions as might be expected with regards to supramolecular synthons and known interactions. The observed intermolecular interactions are consistent with the CSD analyses and hierarchy of interactions.

The prevalence of N–H···LON interactions is slightly higher than might be expected (from Section 6.2.2). Many charge assisted hydrogen bonds are included in these structures which are favoured due to a stronger electrostatic component. The prevalence of –NH_2···O–H, –NH_2···$^-$OOC and O–H···$^-$OOC are shown by Nangia *et al*.[298] in their study of salts of benzoic acids and aminopyridines. Hence, the increased number of N–H···LON interactions is not unexpected.

6.5.3.1 Related Study

A structurally similar API, meclofenamic acid, has also been studied for multi-component systems.[56] Meclofenamic acid contains two aromatic ring systems connected *via* an N–H linker (in contrast to the methylene CH_2 in LON). Similarly to LON, a carboxylic acid substituent is present on the phenyl ring and the other has two chlorine substituents. The chlorine atoms are positioned at 2- and 6- relative to the N–H link whereas in LON they are positioned at 2- and 4- (relative to methylene). Differences between meclofenamic acid and LON are seen in the presence of the additional methyl group on the dichloro-substituted ring of meclofenamic acid (position 3) and the absence of a fused ring system and ring nitrogen atoms.

The meclofenamic acid study produced a number of co-crystals and salts and included co-formers also found to be successful for LON: 2APYD, 4,4BIPY, ISO, and PIPE. LON-4,4BIPY and LON-ISO both presented as co-crystals with LON whilst 2APYD and PIPE formed salts. This was also true for the meclofenamic acid study. 4DMAP (LON) shows similarities to the 4-aminopyridne co-former in the meclofenamic acid study and both were found to form salt hydrate materials. The inclusion of water molecules could be related to the *para*- arrangement of the ring substituents producing a linear co-former molecule. This would produce molecular packing which could permit the inclusion of the small water molecules in the lattice.

6.6 Variations in the Conformation of LON

The different interactions, motifs and packing arrangements observed in the salts and co-crystals of LON result, to some extent, from the methylene linker between the two ring systems. Some

free rotation of the carboxylic acid group also aids these variations. These areas of rotation allow for a number of conformations of LON with varying torsion angles. An analysis of the torsion angles around the methylene linker and the dihedral angle between the two ring systems has been carried out (Appendix C.9.3 Tables C.19 and C.20).

Examination of these data indicate a number of points:

- LON-4,4BIPY and LON-IMID·0.5EtOAc often occur in the same groups indicating similar conformations of LON.
- Both display a large range of torsion angles (positive and negative) showing the extent of the free-rotation possible in these structures (lack of interactions to / from the dichloro-substituted phenyl ring) and hence why disorder of the dichloro-substituted ring is evidenced in both.
- All LON-IMID structures have at least one molecule with a torsion angle in the range -148 ° < angle < -156 °.
- Very different torsion angles are observed for α- and β- LON. This would be expected as the polymorphic relationship of the two is indicative of structural differences although the primary hydrogen bonding interaction (acid···acid dimer) is present in both.
- Structurally similar co-formers ISO, NICO and BENZ all display a negative torsion angle in their co-crystal structure with LON, within the range -71 < angle < -118°. Similarly, related LON-246TAPYM and -MEL both have negative torsion angles within the range -114 < angle < -156° (although they lie close to the lower and upper limits respectively in adjacent groups).
- The three structures displaying tetrameric motifs (LON-ISO, -NICO and -2APYM) show no obvious similarities in their torsion angles or angle between planes.
- Those which display a ladder motif (LON-246TAPYM, -MEL, and -PIPE) all have a negative torsion angle. LON-246TAPYM, -114.37° whilst -MEL and -PIPE are in the range -150 < angle < -153°. Interestingly, the second torsion in LON-PIPE is almost equal but opposite to LON-246TAPYM at 114.83°.

The scatter plot (Appendix CB.9.3, Figure C.30) shows no correlation between the N1–C9–C10–C11 torsion angle and the angle between the planes. The co-former groupings also show no distinct patterns or trends (Appendix C.9.3, Figure C.31). When the formula weight (M_r) of the co-former is plotted with these there are again no clear patterns (Appendix C.8.6, Figure C.32); for each compound and related compounds the angles are spread over a relatively wide range. It can be concluded that the conformation of LON is dependent on packing, interactions and co-former position and orientation rather than the structural nature of the co-former.

6.7 pK_a and Proton Transfer: Salt and Co-Crystal Formation

The rule of three (Section 1.3.1) has been established and implemented frequently as a tool to predict co-crystal or salt formation: $\Delta pK_a < 0$ produces a neutral co-crystal whilst > 3 will generate a salt form. The intermediate range 0-3 is harder to predict.

For all the new systems formed with LON, pK_a values were predicted using the physiochemical properties calculator plugin[312] as implemented in MarvinSketch.[313] See Appendix C.10 for details on the predictions and pK_a values in Table C.21. The rule of three is applicable in more than half of the solids reported however some discrepancies are present. These are evident especially for systems with ΔpK_a values within the range 0-3. Multiple structures and / or differing degrees of protonation / deprotonation were produced experimentally for some combinations which are extremely difficult to predict and would therefore not be expected. All structures exhibiting partial proton transfer have ΔpK_a values within the range 0-3. This is the intermediate range between the prediction of a definite co-crystal and definite salt hence any hybrid structures would be expected to fall within this grouping. If the cut off values are set more leniently (e.g. the generally accepted ΔpK_a differences of greater than 2 or 3 for salt formation and less than 0 or 1 for a co-crystal assembly) all predictions for LON can be considered correct.

Many different hydrogen bonded aggregates in solution may be plausible. Nangia *et al*.[314] state that the ionic solid species is often the least soluble of these using common crystallisation solvents and the observed crystal structure is often of this nature yet may only be present in a minor proportion. This may be true for a number of the systems of LON for which salt and / or multiple forms were observed.

6.8 Thermal Analysis

The thermal behaviour of all the new materials was determined by DSC (Figure 6.22) with the exception of the LON-IMID system; only one (LON-IMID·0.5EtOAc) was tested as isolation of pure materials for the other two forms proved challenging. The melting point of the new forms are compared to that of parent LON and the co-former materials in Table C.22, Appendix C.11). The order of melting point for the pure salts is LON-MEL > LON-246TAPYM > LON-PIPE, and co-crystals LON-2APYM > LON-NICO > LON-ISO > LON-BENZ.

All results are in accordance that a lower co-former melting point (than LON) results in a lowered melting point of the material,[46,47] regardless of the nature of the material. Additionally, all pure

co-crystals (LON-NICO, LON-ISO, LON-BENZ, LON-2APYM and LON-4,4BIPY) showed a lowered melting point whilst all pure salts showed a higher melting point compared to that of LON. This can be ascribed to the presence of strong charge assisted hydrogen bonds in the salt structures.

Exceptions to this occur with the solvated and hydrated salt forms and hybrid structure: the five salt solvates / hydrates (LON-IMID·0.5EtOAc, LON-2APYD·EtOAc. LON-2APYD·ACN, LON-4DMAP·2H_2O and LON-HALO·3H_2O) displayed lowered melting points when compared to LON, which might be unexpected due to the charge assisted hydrogen bonding interactions. These lowered melting points arise from the inclusion of solvent or water molecules. Solvent loss (and water loss for hydrate forms) can cause lattice breakdown due to hydrogen bonds being broken; the network is disrupted and results in the sample melting.

The second LON-4DMAP salt (no solvent / water) has a 2:1 ratio and results in a hybrid co-crystal salt structure with proton transfer occurring from one LON only. The lack of solvent results in a higher melting point than the 1:1 dihydrate although still lower than parent LON. This can be linked to the interactions: whilst charge assisted hydrogen bonds are present, there are also hydrogen bonds which are only partially charge assisted, or in their neutral form. Additionally, disorder of the co-former is present giving rise to imperfections in the crystal lattice.

A broad endotherm following the melt was seen in a number of samples LON-HALO·3H_2O around 275 °C, LON-BENZ around 215 °C and to some extent following the melt in LON-PIPE and LON-MEL. This is most likely due to decomposition of the melt. HSM investigations of LON-HALO·3H_2O confirmed the nature of this event.

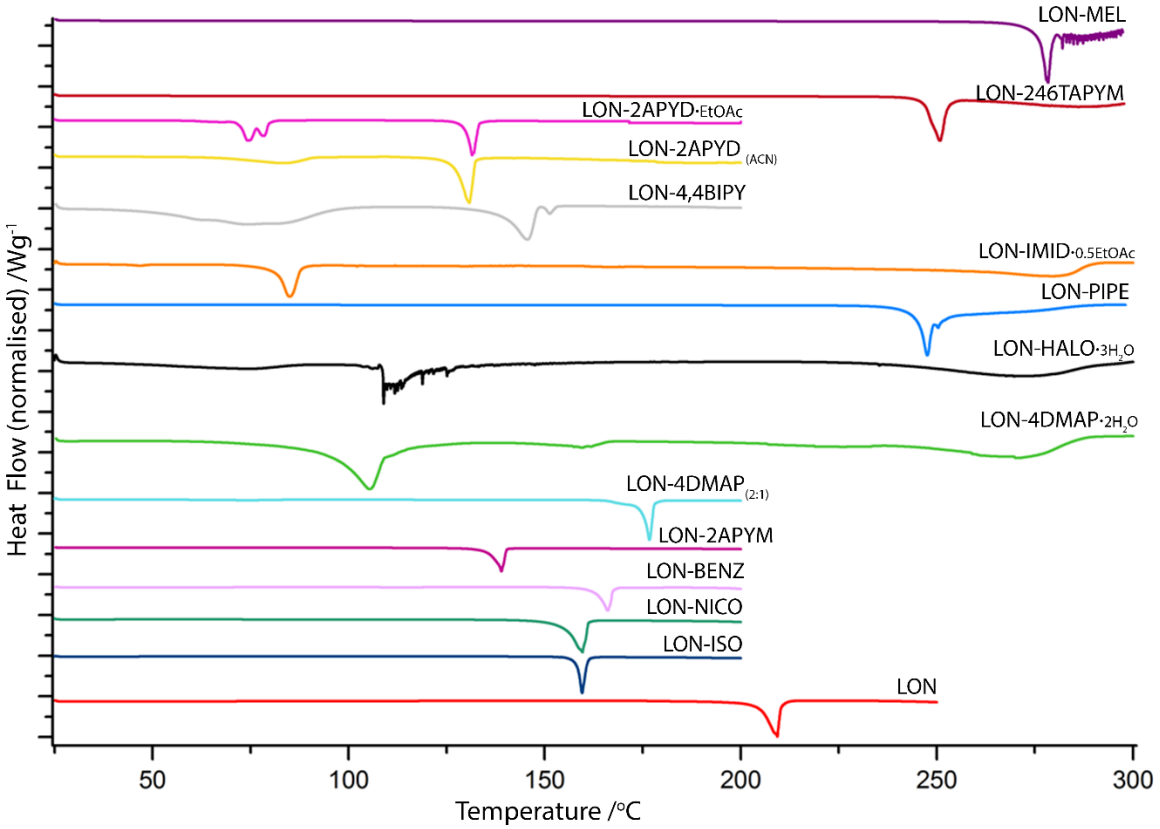

Figure 6.22. DSC curves for LON and the new co-crystals and salts (including only LON-IMID·0.5EtOAc salt solvate of the LON-IMID materials).

6.8.1 Behaviour of the LON Solvate Structures

Only two of the solvate structures displayed loss of solvent followed by a melt at a separate, higher temperature. These were the LON-2APYD salts (EtOAc and ACN). The endotherm below 100 °C in each sample corresponds to the boiling point of the respective solvent. Further confirmation of the solvent was also acquired with TGA (see Appendix C.11.3.1). The other salt solvate, LON-IMID·0.5EtOAc, displayed a low melting point with a broad endotherm at a much higher temperature. HSM and TGA (Appendix C.11.2.4 and C.11.3.4) were used to further investigate these events. Solvent loss and melting were seen to occur concomitantly, over a narrow range (81-88 °C) and the HSM investigation of LON-IMID·0.5EtOAc identified a recrystallisation event at 284 °C. This (along with some degradation) accounted for the broad endotherm observed in the DSC curve. Further analysis of the recrystallised material identified it as a possible thermal degradation product undergoing decarboxylation of some LON molecules. A poor quality single crystal X-ray diffraction data set was obtained which indicated 2 molecules of LON present in the asymmetric unit, one of which had undergone decarboxylation (see Appendix C.12). This was corroborated by mass spectrometry.

6.8.2 Behaviour of the LON Hydrate Structures

Water loss from hydrate crystals can be a complex event, dependent upon the number and location of the water molecule in the crystal lattice and the hydrogen bonds that they form with the parent molecule(s). The two hydrate structures (LON-HALO·3H2O and LON-4DMAP·2H2O) are affected by the presence of the included water molecules, in a similar way that the solvent affects LON-IMID·0.5EtOAc. HSM and TGA were conducted to provide additional data and understand the thermal behaviour (Appendices C.11.2.3 (LON-4DMAP) and C.11.3.3(LON-HALO·3H_2O). LON-HALO·3H2O shows a broad endotherm in the DSC between 60-80 °C and jagged multiple endotherms between 105-125 °C. HSM showed that water loss and melting occur simultaneously in LON-HALO·3H2O over a broad temperature range (75-125 °C) which was corroborated by TGA analysis indicating a mass loss equivalent to three molecules of water by 120°C.
LON-4DMAP·2H2O behaviour is also complex, but in a different way. The DSC indicates three main events, which, in connection with the visual HSM experiment can be interpreted as sample melting (broad endotherm 97-120 °C, DSC, HSM range 95-140 °C), a recrystallisation shortly after (onset 157 °C) and finally the recrystallisation material melting. The crystals were identified as the LON-4DMAP 2:1 form *via* SCXRD unit cell analysis and melted at the expected temperature of this material.

6.8.3 Behaviour of LON-4,4BIPY

Although neither a hydrate nor solvate, LON-4,4BIPY also showed interesting features in the DSC and was further investigated by HSM (Appendix C.11.2.1). This showed sample melting followed by recrystallisation, forming crystals of β-LON (identified *via* SCXRD unit cell analysis). These were then seen to melt at the expected temperature for pure LON.

6.9 Stability

The stability of the co-crystals and salts containing pharmaceutically acceptable co-formers was tested using a variety of different techniques and conditions.

6.9.1 Dynamic Vapour Sorption

Dynamic vapour sorption (DVS) measures water (or solvent) uptake of a powder through sample mass change, using an increasing partial pressure over a given time period. Figure 6.23 shows the sorption and desorption profiles for the new pharmaceutically acceptable materials, along with

LON. Two samples show a mass change greater than 1 % which suggests that the water uptake is beyond surface adsorption: LON-IMD·0.5EtOAc, 1.9 % and LON-HALO·3H_2O, 2.6 %. Note, both these materials are salts and contain solvent / water molecules in their crystal lattices. Further analysis of the crystal structures indicates the presence of voids (56.48 $Å^3$ LON-IMID·0.5EtOAc and 44.63 $Å^3$ LON-HALO·3H_2O), each capable of accommodating a water molecule. This explains the observed water uptake.

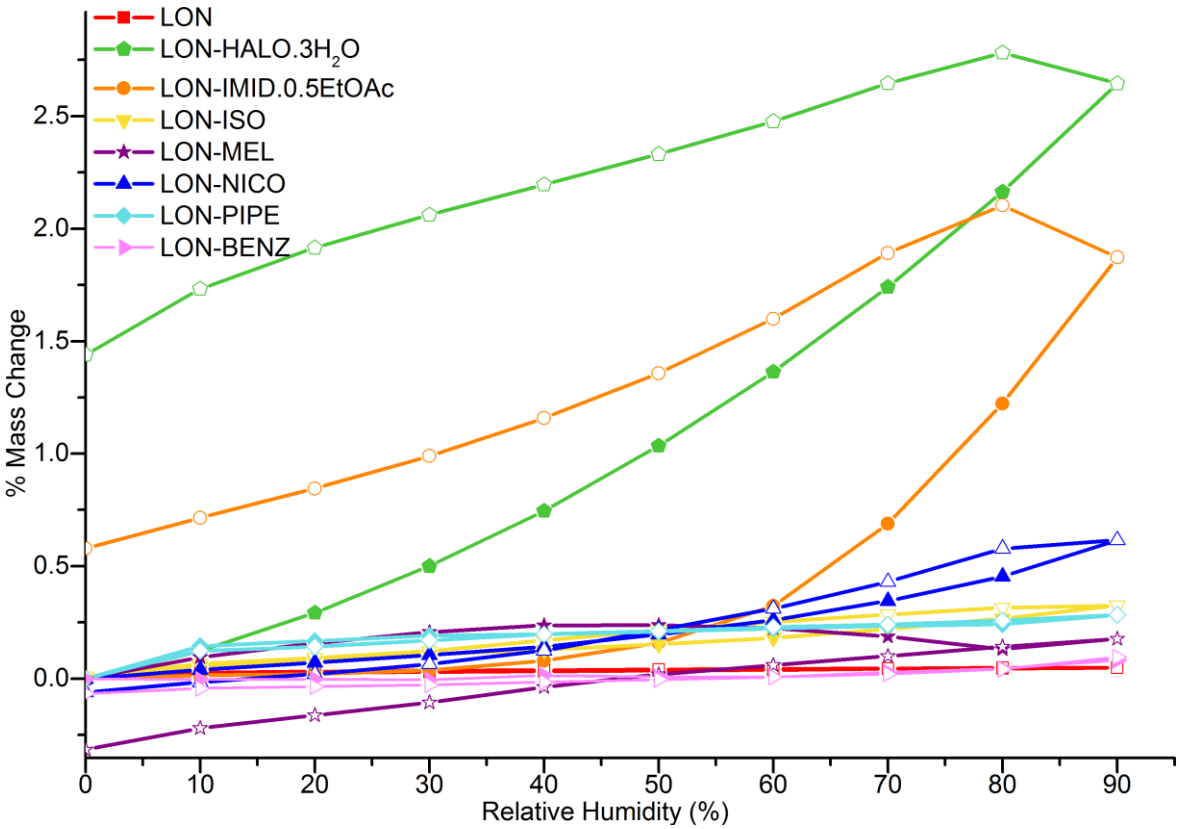

Figure 6.23. DVS sorption (filled markers) and desorption (open markers) plots for LON and new co-crystal and salt materials with pharmaceutically acceptable co-formers.

6.9.2 Slurry

Stability of the pharmaceutically acceptable solids was tested under slurry conditions: excess powders of the solids were stirred in 1 % Tween 80® aqueous media at room temperature for 24 hours. After this period the solids were filtered, dried and analysed by PXRD. Aliquots of the slurry solution were appropriately diluted and analysed for solubility estimation by high-performance liquid chromatography (HPLC).

It can be seen from the PXRD analysis (see Appendix C.13) that the LON-NICO and LON-ISO co-crystals, as well as LON-IMID·0.5EtOAc salt, demonstrated poor stability. Dissociation into component parts was apparent and evidenced by the appearance of parent LON (predominantly β-LON with a degree of both polymorphs identified in LON-NICO) and some co-former reference

peaks in the PXRD analysis. The poor stability of these co-crystals could be due to weaker hydrogen bonds compared to the charge-assisted hydrogen bonds in salts.

6.9.3 Accelerated Storage

Stability of the same materials was also tested under accelerated test conditions (40 °C / 75 % relative humidity). All samples appear stable under these conditions (Appendix C.13.2) with the exception of the IMID salt solvate. The poor stability of LON-IMID·0.5EtOAc could be attributed to the presence of solvent molecules in the crystal lattice. The EtOAc molecules are contained within void space and display no strong hydrogen bonds. Solvent removal therefore occurs readily, especially at elevated temperatures as experienced in this test. This disrupts the crystal lattice and leads to dissociation of the molecular salt into its individual components. This also helps to explain the apparent stability under these conditions of the two previously unstable (slurry conditions) LON-ISO and LON-NICO co-crystals. The water environment of the slurry test may encourage dissociation, however when less water is present (accelerated conditions) the dissociation is not observed. This may be due to the time period and with a longer testing duration, dissociation may become apparent, although DVS indicated that increased humidity results in minimal uptake in these two systems.

These stability studies suggest that the anhydrous/non-solvated salts generally showed the highest stability among the solid forms reported.

6.10 Analysis of the Solution Properties

6.10.1 Solubility

To optimise drug performance, maximum and equilibrium concentrations (kinetic and thermodynamic solubility respectively) are essential in order to understand the substances' behaviour and drug release. As shown in stability tests (Section 6.9 and Appendix C.13), the two co-crystals with ISO and NICO, and LON-IMID·0.5EtOAc salt solvate are unstable under slurry conditions. Additionally, LON-IMID·0.5EtOAc showed water uptake in DVS (Figure 6.23) and has a low melting point, reinforcing its poor stability. For these materials, apparent solubility calcuations[269, 270] were used to determine the solubility. The gradient was extracted from the linear portions of the respective dissolution curves, as demonstrated in Chapter 4.6.2. The remaining samples show good stability, remaining intact in these conditions, and hence solubility

can be determined from filtered aliquots (obtained from slurry experiments) as this will represent the true solubility of the sample.

The solubility of the new materials is compared with that of LON in Appendix C.14 and shows the highest solubility for the salt with PIPE, followed by the salts with IMID and HALO. LON-MEL is the only salt material which produced a lower solubility, and could be due to the lower aqueous solubility of the co-former (3.24 mg mL^{-1}). In general a more soluble co-former will result in a co-crystal with higher solubility and *vice versa*.[153] Sanphui's work on the NSAID meclofenamic acid[56] showed a marked increase in solubility in the salt with PIPE, the highest solubility of the new materials produced. This is also observed in this study.

Of the co-crystals, two of the three result in a lower solubility than LON, with LON-BENZ showing a slightly increased solubility. This is in accordance with the notion that salts have a greater propensity to increase the solubility of a material in comparison to co-crystals (Section 1.3.2).

The solubility can also be accounted for by the partial dissociation of the materials. In the slurry experiment, due to the extended time period, dissociation will start to occur with some conversion to parent API (evidenced in the PXRD of the resulting solid from LON-ISO and LON-NICO). This causes the lower observed solubility. LON-BENZ is stable under slurry conditions; no parent API is produced and influencing the solubility.

No comparisons and cross-correlations between solubility, melting point and energy are made as a deeper understanding of the structure and interactions is required (Chapter 5). Lower solubilities can result from a variety of factors: the relative propensities of solute-solvent interactions as well as stoichiometric ratio, supramolecular synthon formation and the drug···co-former interactions.

6.10.2 Dissolution Rate

An increase in initial dissolution rate (up to 30-45 min) is appealing and as shown in Figure 6.24 an improvement in this is seen in the salts of LON with MEL and IMID, and in and the co-crystal with BENZ. The inherent nature of salts makes them more soluble and can also raise initial dissolution rates due to more favourable interactions (charge assisted) with water or the solvent. Thus, the increase in dissolution rate for two salt materials is not unexpected.

LON-IMID·0.5EtOAc is unstable and readily dissociates, contributing to the increased dissolution rate observed. Both LON-NICO and LON-ISO showed a degree of dissociation under slurry conditions (tested over extended time period) although neither shows an increase in dissolution rate or solubility as might be expected for a dissociable co-crystal. This can be attributed to the

interactions present in the crystal structures. Both LON-NICO and LON-ISO have more hydrogen bond interactions involving LON than either of the LON polymorphs, with additional co-former···co-former hydrogen bonds also present. The increased number, as well as some shorter bonding distances, makes the hydrogen bonding network more difficult to disrupt. Hence, dissolution proceeds at a slower rate. LON-BENZ displays a similar interaction network to α- and β-LON, with fewer hydrogen bonds and slightly longer bonding interactions in the main dimer interaction in comparison to the other two co-crystals. This enables the increased dissolution rate (and solubility).

LON-PIPE displays a similar initial dissolution rate to LON, however as a salt form, and with the increased solubility observed (Appendix C.14), it might be expected that the dissolution rate would be increased too. Initial dissolution rate is dependent on kinetics but over extended time periods, such as towards the end of the dissolution experiment and in the equilibrium solubility determination, thermodynamics will have a greater influence. This is displayed in the LON-PIPE dissolution curve; towards the end of the experiment the dissolution rate for LON-PIPE is increasing at the fastest rate of all samples. The initial dissolution rate, however, is one of the slowest and less than that of LON showing there may be a kinetic barrier. This may be due to the larger relative proportion of poorly soluble LON in the 2:1 ratio, impeding the kinetics.

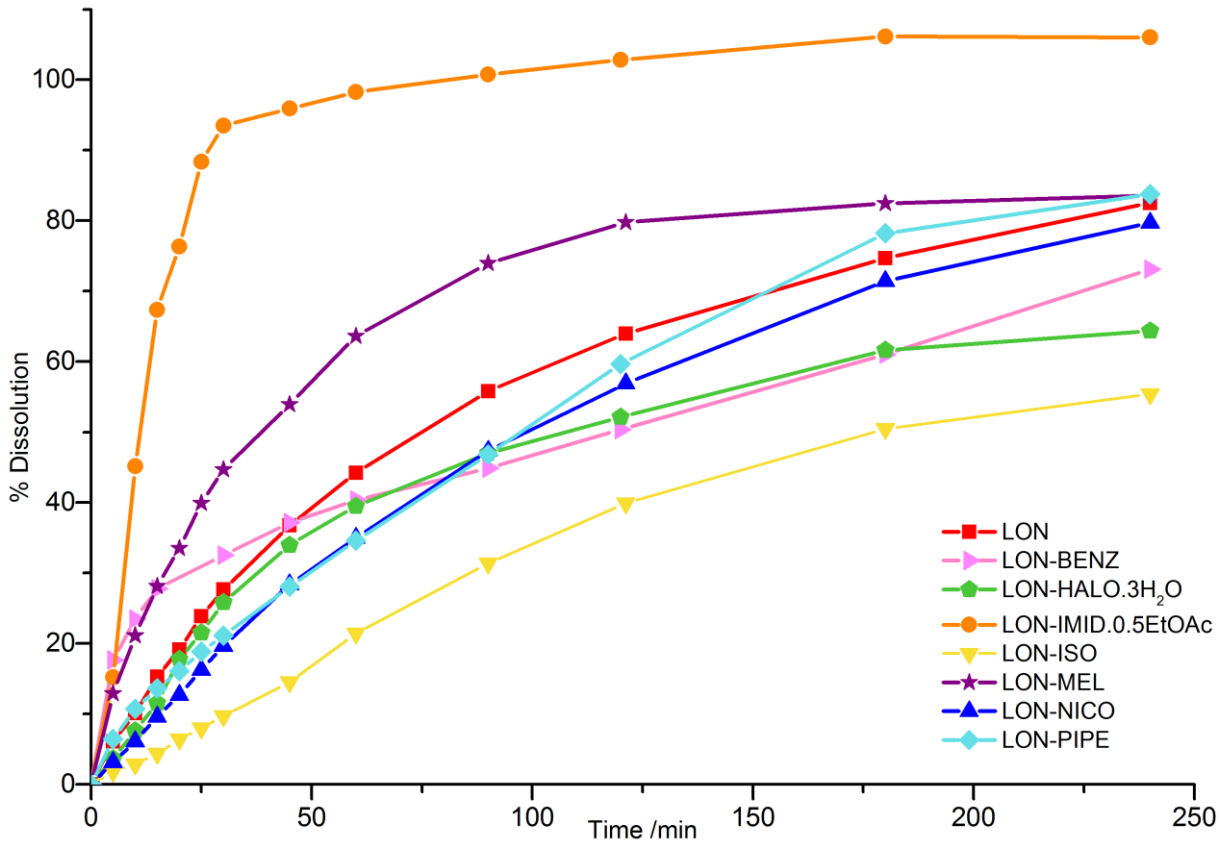

Figure 6.24. Dissolution rate profile for LON and the new salts and co-crystals thereof containing pharmaceutically acceptable co-formers. 240 min experiment time in 1 % Tween 80® aqueous dissolution medium.

6.11 Conclusions

16 new multi-component materials utilising 12 different co-former molecules have been produced with LON. As expected, the LON carboxylic acid functional group forms the primary interactions in all crystal structures, which are varied in their nature. A number of structural similarities can be seen across the set, such as the existence of tetrameric (LON-ISO, LON-NICO and LON-2APYM), ladder (LON-246TAPYM, LON-MEL and LON-PIPE) and ladder-related chain (LON-IMID) motifs. Additionally, similar interactions are seen to occur in structures containing structurally related co-formers (LON-246TAPYM, LON-2APYD and LON-2APYM).

When compared to the CSD analyses undertaken, the novel crystal structures obtained display interactions as might be expected when considering the functionalities present on LON and the co-former, the hierarchy of interactions and appropriate supramolecular synthon motifs.

Physiochemical properties were measured and it was found that the co-formers were able to modulate the properties of LON. Both increased and reduced melting points were observed across the series of compounds which can be related to the nature of the sample, co-former and

interactions present. For those materials containing pharmaceutically acceptable co-formers an equivalent or improved stability compared to LON was recognized in three of the salt materials and one co-crystal. LON-IMID·0.5EtOAc was shown to be unstable and dissociates into component materials in all conditions tested, whilst two co-crystals, LON-ISO and LON-NICO, showed a degree of dissociation under slurry conditions only.

Three new materials showed an improvement in the initial dissolution rate; LON-IMID·0.5EtOAc, LON-MEL and LON-BENZ whilst two (LON-PIPE and LON-HALO·3H_2O) were comparable to LON. Of these, LON-BENZ, LON-HALO·3H_2O, LON-IMID·0.5EtOAc, and LON-PIPE showed an improvement in solubility, the greatest being with LON-PIPE which increased the solubility by a factor of 26. LON-HALO·3H_2O demonstrated an increase in solubility of 1.5 times that of LON, with a similar initial dissolution profile, however the extended dissolution test showed a reduced release of LON and the presence of water in the trihydrate salt causes a significantly reduced melting point. LON-MEL showed the second best overall dissolution profile, after that of unstable LON-IMID·0.5EtOAc, and third best initial dissolution rate, however these results were not replicated in the solubility determination; LON-MEL demonstrated the lowest solubility of all the materials tested. This could result from the low solubility of the co-former, limiting the LON release over extended time periods.

Only LON-ISO and LON-NICO showed a reduction in both dissolution rate and solubility compared to the parent material. The ultimate goal is often to control the release of a drug therefore a reduction in the dissolution rate is ideal. By understanding these two materials it may be possible in the future to design similar such systems and control drug release if required.

LON-IMID·0.5EtOAc showed an improvement in both initial dissolution rate and solubility (over 4 times that of LON) however this was shown to be an unstable material experiencing dissociation under a number of conditions. It also displayed a low melting point. LON-BENZ also showed an increase in initial dissolution rate (up to 45 mins) as well as a slightly increased solubility (1.13 times that of LON) and an equivalent stability to LON during testing. This indicates that LON-BENZ is an ideal new form of LON, showing an improvement in several important properties.

Chapter 7: Conclusions and Further Work

7.1 Conclusions

This thesis has investigated two APIs, PROPY and LON, and novel multi-component materials of each. Two design approaches were implemented based on the different molecular structures and presence or absence of certain functional groups; a knowledge-based design for PROPY and a more typical synthon-based approach for LON. A wide-ranging set of co-formers were tested in screening with each API to explore the predictions.

Novel solids for both have been produced, eight new co-crystals formed with PROPY whilst sixteen different solids were generated with LON which comprised a mixture of co-crystals, salts and hybrid co-crystal salt materials. Structural characterisation for all the new materials produced was carried out using standard resolution X-ray crystallography to obtain crystal structures showing the geometry and molecular arrangement. Various physicochemical properties were tested: thermal behaviour, stability, solubility and dissolution. Melting point was determined for all materials whilst the tests for stability and solution properties were conducted for only those containing pharmaceutically acceptable co-molecules. The co-crystal properties were related to those of the parent materials to see the effect of the addition of the co-former. Additionally, the physicochemical properties were compared between the co-crystals of the same API to see the impact of different co-formers. Subtle differences in structurally related co-former molecules of a subset of PROPY co-crystal systems were explored in further detail using quantum crystallography studies.

7.1.1 The Novel Co-Crystals of PROPY

The sterically hindered carbonyl acceptor and overall limited hydrogen bonding functionality of PROPY meant that a supramolecular synthon based design, or one founded in hydrogen bonding, was not appropriate to identify suitable co-former molecules. Instead, a knowledge-based approach was taken collating information from a range of sources to recognise the preferred interactions of a carbonyl functional group, similar to that in PROPY. Screening and subsequent synthesis resulted in eight new co-crystals with the co-formers 25DHBA, 35DHBA, 45DClPA, 4HBA, FA, HQ, MPAR and PGL. These were primarily of 1:1 stoichiometry although several formed in alternate ratios including PROPY-25DHBA (2:1), PROPY-FA (1:0.5) and PROPY-HQ (1:2). PROPY-PGL formed as a 1:1 co-crystal although with the inclusion of acetonitrile solvent, relative ratio 0.5, to give a 1:1:0.5 system. PROPY-25DHBA also contained solvent (1,4-dioxane) in the crystal lattice,

however it was unable to be modelled successfully due to its location within voids and with no strong hydrogen bonds or interactions to maintain a fixed position.

The physicochemical properties showed that the co-formers were able to moderate the properties of parent PROPY. Melting points were generally observed to be higher than parent PROPY, although two melted at a similar temperature and one, PROPY-MPAR, had a lowered melting point. Initial dissolution rate was increased in all the new materials whilst solubility was improved in four. The stability was equivalent to that of PROPY in all but two materials (PROPY-25DHBA and PROPY-PGL·0.5ACN) when tested using three different methods and varying conditions.

7.1.1.1 Rationalisation of Structures and Properties Using Quantum Crystallography

A more in-depth analysis of the crystal structures was undertaken using a combination of experimental multipole models obtained from high resolution X-ray data and quantum-based interaction analyses. The experimental models allowed the molecular electron density distribution to be determined and a subsequent topological analysis afforded many properties. These included atomic charges, hydrogen bond locations and individual hydrogen bond energies. Theoretical calculations allowed the non-covalent interactions between molecular pairs to be investigated further and quantified in terms of the energy components of each interaction. Comparisons across a subset of co-crystals containing structurally similar co-formers were then conducted.

Structurally similar co-formers 4HBA and MPAR displayed similarities in their charge distributions and properties with correlations to HQ also observed. It was discovered that the co-former molecules have a large influence on PROPY with the structural differences of co-former molecules evidenced in the charge distribution and interactions of the PROPY molecules. The charge distribution of the system was also related to the structures formed. Those containing adducts comprised of more molecules and an extended hydrogen bonded network permit a greater redistribution of the charge. The primary hydrogen bonds were also investigated and carboxylic acids were found, in general, to form stronger interactions with a greater Coulombic energy to the PROPY carbonyl than the equivalent interaction from a hydroxyl functionality.

The molecular pair interactions were divided into strong, moderate strength and weak interaction groups for each system. The strong interactions were typically dominated by the Coulombic energy component, whilst the weaker interactions were largely dispersive in their nature. In conjunction with the experimental hydrogen bond energies this provides information regarding the nature of the interactions; strong hydrogen bonds have a large Coulombic component

stabilised by a local concentration of charge in an intermediate closed-shell interaction, whilst weaker interactions are primarily electrostatic and contain dispersive energy in the largest proportion. In most systems the moderate strength interactions had the largest contribution to the total energy.

The interaction energies from the different methods were used to compare and rationalise the measured physicochemical properties. Coulombic energy was seen to have a high correlation with melting point, and the presence of destabilising interactions justified some lower melting points. PROPY-FA was observed as an anomaly in many of the trends, linked to the very different co-former structure.

Increased co-former functionality and / or complexity of the system (e.g. additional molecules present, such as solvent) resulted in the emergence of less favourable interactions. There is likely to be a limit to the extent of co-former functionality before the co-crystal is no longer favoured over the individual components. This appears to be true for PROPY, a molecule with limited hydrogen bonding functionality itself meaning it is unable to satisfy additional or increased co-former functionality through hydrogen bond formation. This finding helps to validate some of the results from the initial screening; co-formers with a high density of functional groups were included, but none showed any indication of a new material forming when combined with PROPY.

Additional interaction analysis regarding the preference of water to form interactions with different functional helped to understand the solubility and dissolution data and the trends observed. Interactions to hydroxyl functionalities are the most favoured thus it can be understood that PROPY-HQ, containing two hydroxyl groups per HQ molecule and two HQ molecules per asymmetric unit, has the highest solubility of the stable two component materials. PROPY-MPAR which contains functional groups which form less favourable interactions has a lower solubility. The two solvate forms displayed solubilities that were higher than expected in relation to the interactions possible to water. This was due to their poor stability, which can result in an increased observed solubility.

7.1.2 The Novel Multi-Component Systems of LON

Co-crystal design with LON applied a more typical approach using supramolecular synthons and hydrogen bonding interactions. The key functionality on LON was identified as the carboxylic acid and co-former molecules likely to form a strong interaction at this site were chosen. The sixteen new materials were generated from twelve different co-former molecules and many based on the carboxylic acid···pyridine synthon or structurally-related motifs. In addition to the new

multi-component materials synthesised, crystals of α-LON were obtained and the crystal structure added to the CSD.

pK_a analysis of the new materials showed a good general agreement with the established 'rule of three' for salt and co-crystal formation. It is not possible with this simple rule to predict the occurrence of multiple forms which were seen with several of the co-molecules. These were all identified to be located within the 'difficult to predict' ΔpK_a range of 0-3 and thus in agreement with the overall rule.

A number of structural similarities were present in the co-molecules, and trends observed in the new materials. These included structural motifs such as ladders and tetramers, hydrogen bond interactions and similar relative positioning of the two components. These were compared across the series and related to the different co-formers involved, allowing the influence of the co-former to be realised. Comparisons were also made to structures in the CSD containing similar molecules to rationalise the interactions. The observed geometries and interactions present in the co-crystal and salt materials with LON were seen to be in accordance with those in the database.

Similar to the PROPY co-crystal systems, the physicochemical properties of the new materials were moderated relative to parent LON. Initial dissolution rate was seen to be increased in three of the materials, two salts and one co-crystal whilst the remaining salts and NICO co-crystal have a similar rate to that observed for LON. LON-ISO displayed a slower initial dissolution rate. The solubility was increased in the majority of the materials, only three (two co-crystals and one salt) showed a reduced solubility relative to LON. LON-IMID·0.5EtoAc did not withstand either set of conditions in stability testing whilst the NICO and ISO co-crystals showed some dissociation in the slurry conditions only. The rest of the materials displayed equal stability to parent LON.

The melting points of the new materials showed great variation due, in part, to the underlying differences between salts and co-crystals. The thermal behaviour of several systems showed interesting events, including several which underwent a recrystallisation from the melt. These included a form change (LON-4DMAP·2H_2O to LON-4DMAP 2:1), recrystallisation of parent LON (LON-4,4BIPY) and a decomposition product of LON with a single decarboxylation observed (LON, LON-IMID·0.5EtOAc and LON-4,4BIPY).

7.1.3 Addressing the Research Aims

Six key research themes were identified to be addressed in the work of this thesis:

1. The application of design approaches to molecules exhibiting differing functionalities and interaction preferences to produce new multi-component systems.

2. The differences in the hydrogen bonding interactions of PROPY which contains a single, sterically hindered acceptor site, with various co-formers.
3. The differences in the hydrogen bonding and interactions of LON, a carboxylic acid containing molecule, and instances where proton transfer does / does not occur.
4. The effect of different co-former molecules on the physicochemical properties of multi-component materials.
5. The effect of different co-formers on the electron density distribution and the impact this has on the physicochemical properties of structurally related co-crystals.
6. The complementarity of different techniques (experimental and theoretical), how they can be used in combination to deconvolute crystal structures in terms of the constituents and interaction energies and how this provides a better understanding of co-crystal systems.

These were addressed as follows:

7.1.3.1 Aim 1: Applying Appropriate Design Approaches

A different design approach for each of PROPY and LON was applied using a variety of resources particularly for the knowledge-based design of PROPY co-crystals. Both approaches resulted in appropriate co-former selection and novel materials were produced. Analysis of the CSD for the interaction preferences of a carbonyl similar to that in PROPY (Chapter 4.2.1) highlighted four functional groups (–CO_2H, –OH, –NH_2 and –N(H)–) that would be likely to form an interaction in a co-crystal system. Two of these were realised in the investigation, however no N–H···$O_{carbonyl}$ interactions were observed.

Interaction preferences of the carboxylic acid of LON from CSD structures were found to be: amides > primary amines (–NH_2) > aromatic nitrogen atoms (for example pyridines) > hydroxyls (Chapter 6.2.1). The indazole group was seen from the analysis to form less favourable interactions however when involved in an interaction C–H groups, hydroxyls, primary amines, amides and T3NH_1 groups were favoured. These preferred functionalities of the indazole group are similar in nature to those of the carboxylic acid; co-former structures containing hydroxyls, primary amines or amides (favourable interactions to both groups) would be expected to be most preferential for forming a new material.

All four of the favoured functional groups for the carboxylic acid were identified in the co-formers of the novel structures produced (Figure 6.2); amides (3 co-formers), primary amines (4 co-formers), aromatic nitrogen atoms (9 co-formers), hydroxyls (1 co-former). Aromatic nitrogen atoms appeared in a greater number of structures than expected with respect to the prevalence

of their interactions however only three of these contained the aromatic nitrogen as the sole functionality of the co-former. The other six co-formers also contained one of the favourable amide or primary amine functional groups. One structure, LON-PIPE (Chapter 6.3.4.1), formed with a co-former which contained none of these specified functionalities and instead formed interactions *via* cyclic N–H groups. Proton transfer generated an N^{+}–H group bonded to three other atoms in this structure (a T3NH group) which was seen to be a favourable group for indazole interactions.

7.1.3.2 Aim 2: PROPY Hydrogen Bonding Interactions

The novel structures of PROPY were analysed for their interactions using both a geometric-based analysis of standard resolution crystal structures (Chapter 4.3) and a more in-depth investigation combining high resolution X-ray diffraction data with theoretical approaches (Chapter 5). The co-crystal structures highlighted two main interaction types $O–H_{hydroxyl}\cdots O_{carbonyl}$ and $O–H_{carboxylic\ acid}\cdots O_{carbonyl}$; the latter observed to have stronger hydrogen bond energies determined from experimental topological analysis (Section 5.6.3 and Supplementary File XD Interactions). Whilst these interactions were stronger, the hydroxyl functionality was preferential in forming an interaction to the carbonyl in systems containing both functionalities. This is due to the strong acid dimer formation which is possible between two co-former molecules and will form first in the hierarchy of interactions. This leaves the hydroxyl to interact with the PROPY carbonyl group.

Variations within the hydroxyl···carbonyl interaction energies were observed (Section 5.6.3 and Supplementary File XD Interactions) which were linked to the extent of the hydrogen bonding network which permits the redistribution of the charge. The rank order of the energies was: PROPY-MPAR > PROPY-4HBA > PROPY-HQ (one) which form two-component, four-component and an extended hydrogen bond network respectively (Chapter 5.6.1, Figure 5.18). The second $O–H_{hydroxyl}\cdots O_{carbonyl}$ hydrogen bond in PROPY-HQ was observed as considerably stronger than the other similar interactions and also stronger than the carboxylic acid···carbonyl interactions. This hydrogen bond forms the end of the hydrogen bonded network (no further interactions from the PROPY carbonyl) and acts as an electron sink for the charge of the bonded network. This rationalises the larger than expected interaction energy.

7.1.3.3 Aim 3: LON Hydrogen Bonding Interactions

The hydrogen bonds of LON were investigated using purely a geometric analysis and hence less detail and rationalisation was possible than included for the PROPY structures. The main difference in the hydrogen bonding of the LON structures was the occurrence of proton transfer between LON and some co-former molecules, producing a salt. These contained charge-assisted

hydrogen bonds which were expected to display shorter D···A distances than neutral interactions. Most of these interactions were bifurcated, interacting with two different acceptor atoms and spreading the charge. Accordingly, a reduced shortening of each of the individual hydrogen bonds occurred and the D···A distances were not too dissimilar to their neutral counterparts. Single charge-assisted hydrogen bonds between one charged and one neutral species were observed to be shorter than the equivalent neutral interaction (e.g. N–H···carboxylate *vs.* N–H···$O_{carboxylic\ acid}$).

Water molecules were included in the structures of two materials and were central to the hydrogen bonding network (Sections 6.3.2.4 and 6.3.5). Both co-formers (HALO and 4DMAP) contain minimal hydrogen bonding functionality (Figure 6.2) and may be the reason for the inclusion of the water molecules which increase the hydrogen bonding potential of the system. Both systems are also salt forms in which the charged species form more favourable interactions to water than neutral components. This indicates why it is the salt forms only in this work which are observed as hydrate structures.

7.1.3.4 Aim 4: Effect of Co-Formers on Physicochemical Properties

Both systems, PROPY and LON, showed that the physicochemical properties of the new forms were moderated in relation to the parent API (Chapters 4.4-4.8 and 6.8-6.10) and the differences rationalised using a variety of methods of analysis. The PROPY co-crystals were subjected to a more in-depth structural analysis and this allowed the physicochemical properties to be related to the electron density distribution and molecular interactions (Chapters 5.7 and 5.9). Melting point (Chapter 5.7.1) was linked to the strength of the interactions in the system, in particular the Coulombic energy component and the strongest molecular pair interactions. These were all dominated by a single, strong, hydrogen bond which was located and investigated in the experimental interaction analysis (Chapter 5.8). Similarly, stability was linked to the interactions present (Chapter 5.7.2). Other properties (dissolution rate and solubility, Chapters 5.7.3 and 5.7.4 respectively) had additional influencing factors such as the presence of solvent. The trends observed in these properties across the series were rationalised through an additional analysis involving the interaction preferences of water (Appendix B.5).

The physicochemical properties and trends of the LON systems were explained using the standard resolution crystal structures and a more basic interaction analysis (Chapters 4.4-4.6).

7.1.3.5 Aim 5: Effect of Co-Formers on Electron Density Distribution

Experimental multipole models were generated for four PROPY systems (PROPY-4HBA, PROPY-FA, PROPY-HQ and PROPY-MPAR) which allowed the electron density distribution within the molecules to be probed (Chapter 5.6). Properties at BCPs and RCPs as well as atomic charges

showed how the different co-former molecules influenced the PROPY molecule and its charge distribution. Co-formers with additional hydrogen bonding functionalities, capable of forming additional hydrogen bonds beyond that involving the PROPY carbonyl, showed a greater ability to redistribute the charge. This was correlated with the number of molecules over which the charge could be distributed and evidenced in the electron density present at the two RCPs of PROPY (N-heterocycle and phenyl ring); a greater $\rho(\mathbf{r})$ resulting in systems with the least capacity for charge redistribution. Structurally similar co-former molecules displayed similar $\rho(\mathbf{r})$ values at the RCPs indicating that the co-formers were less perturbed by co-crystal formation than PROPY was.

7.1.3.6 Aim 6: Understanding Crystal Structures in More Detail using Complementary Techniques

PIXEL and Crystal Explorer calculations were used in combination with an experimental charge density model to determine interaction energies of the co-crystal systems (Chapter 5). Whilst the PIXEL and Crystal Explorer approaches provided detail at the molecular level the experimental model evaluated individual hydrogen bonds providing supplementary information. As a result, the crystal structure could be dissected in different ways providing a myriad of possible analyses. These included dividing the molecular pairs into the strongest, moderate strength and weakest interaction energies (Chapter 6.5.1) . These were linked to the experimentally determined hydrogen bond energies and it was found that the strongest molecular pair interactions were dominated by single, strong, hydrogen bond (Chapter 5.4 and 5.5.1). The molecular pair energies were also dissected according to the constituents involved (API or co-former and combinations thereof, Chapter 5.5.3) to investigate the differences in these pairings across the family series and the individual pairwise interactions separated into their energy components. These different insights combined to provide a wealth of detail for each co-crystal system and the measured physicochemical properties were rationalised through correlations from this work (Chapters 5.7 and 5.9). In particular, a link between melting point and the Coulombic energy contribution was determined, and it was understood that solution properties (such as dissolution rate and solubility) are influenced by not only the solid state formation of the crystal structure; solute···solvent interactions are also imperative (Chapters 5.7.1, 5.7.3 and 5.7.4).

Previously, synthons have been commonly used for the predictions of novel materials (Chapter 1.3.4) and in describing important interactions. This has been shown to be not best-suited to a range of molecules, such as those containing limited or minimal hydrogen bonding functionalities (Chapter 4.2). The combination of in-depth structural analysis, detailed interaction analysis and the complementary deconvolution of the constituent energy components shown in Chapter 5 is an entirely new way of looking at the solid state. In particular, relating the energy

components and contributions to the physicochemical properties, and doing so for multi-component systems some of which comprise three different components is novel. This new approach identifies that there are other important factors, beyond the primary hydrogen bonds and motifs, that are fundamental in controlling solid state assemblies.

7.2 Further Work

The work presented herein answers the research aims although to varying degrees. Further work focussed on those which were not fully achieved, or could be developed further, would help to develop the understanding of these systems and the application of some of the techniques and methods employed.

Two main areas for further investigation were observed: the functional groups present in the co-former molecules of the PROPY co-crystals; and increasing the quantum crystallography studies. In addition, several curiosities arose from the studies which can also be further explored.

7.2.1 PROPY Co-Former Functional Groups

The co-crystals of PROPY display predominantly O–H interactions to the PROPY carbonyl with a couple containing an interaction originating from $–CO_2H$, $–NH_2$, and N–H. Interactions were also seen to be preferential from the interaction analysis however no such interactions were identified. The generation of an N–H···O hydrogen bonded co-crystal and subsequent analysis using quantum crystallography would provide valuable interaction information and may provide insight regarding the prevalence of hydrogen bonds from hydroxyl and carboxylic acid groups shown in the eight co-crystal structures of this thesis.

The novel co-crystals provide some information regarding the primary interactions which could help to inform the appropriate selection of $–NH_2$-containing co-formers. Additional focussed screening and synthesis with specifically selected co-formers, or further trials with those showing potential from the original screening may result in a co-crystal with an N–H···O primary hydrogen bond. Only one occurrence of this interaction type, a PROPY···pyrithyldione co-crystal (Lemmerer *et al*.)[242] has been reported.

7.2.2 Extending the Quantum Crystallography Studies

7.2.2.1 PROPY

To extend the understanding of the co-former influence on PROPY and the resulting co-crystal system a systematic study, varying the electronic properties of the co-former molecule, could be instigated. This would include additional co-crystals containing hydroxyl and carboxylic acid interactions to the carbonyl as well as those containing $–NH_2$ or N–H interactions as described in Section 7.2.1. The inclusion of the latter would provide comparisons regarding the primary hydrogen bonds and supplement the hierarchy of interactions determined from CSD analysis. This could help to inform future predictions for molecules containing similar functional groups. Investigations regarding the effect of the co-former aromaticity may provide insight into the apparently anomalous PROPY-FA observations and improve the trends and relationships uncovered thus far. A selection of linear and aromatic co-formers and, if possible, a family containing a variety of stoichiometries would be most appropriate to fully understand the observations and uncover the relationships and trends for these systems.

Studies on PROPY in conjunction with the co-crystal studies would provide insight into the differences in the electron density distribution between the single and multi-component systems. Experimental studies would be challenging, due to the poor-quality crystals that PROPY forms, therefore a computational approach using a theoretical wave functions and multipole populations would be suitable. Alternatively, a combined approach could be taken using transferable multipole populations to enhance an experimental model as demonstrated by Dittrich *et al.*[315] and Coppens *et al*.[316]

7.2.2.2 LON

The PROPY study has shown how complementary techniques in quantum crystallography can provide supplementary information to a standard resolution crystal structure analysis and probe deeper into the materials, gaining an improved understanding. A similar study could be applied to LON materials using a systematic approach and family of related systems. Several structural correlations have already been evidenced and the following key areas could be investigated:

- Amide substituted pyridine ring family

  NICO and ISO are structurally very similar differing only by the amide substituent position (3- or 4-) on the pyridine ring. The 2-substituted equivalent (2-picoline) does not generate a new form and co-crystallisation attempts resulted in the individual components only. A quantitative analysis of the electron density distribution and interactions present in the

LON-ISO and LON-NICO systems could provide rationale behind the crystal quality and ease of formation observed as well as the non-existent LON-2-picoline co-crystal. A comparison of LON-BENZ to LON-ISO and -NICO may also prove insightful and indicate the role and importance (if applicable), of the pyridine nitrogen atom.

- Amide *vs.* amino pyridine ring substituent

ISO and NICO contain amide substituents on a pyridine ring, whilst 2APYD contains an amino group. 2APYM contains an amino group although situated on a pyrimidine, rather than pyridine ring as in 2APYD. Comparisons between these materials, in particular the charge distribution and interactions between the two components, would be informative.

- Tri-substituted aromatic rings

246TAPYM and MEL co-formers contain a triamino-substituted aromatic ring containing two and three ring nitrogen atoms respectively and both form a 1:1 salt with LON. These offer a suitable pair for structural similarity investigations regarding the charge distribution and interaction differences and similarities. The additional ring N atom will likely impact the overall electron density distribution which would be identified in this study.

- Salt *vs*. co-crystal

Proton transfer is seen in many of the LON systems forming salts, however the components of other systems remain in their neutral form generating a co-crystal. 2APYM and 2APYD provide an ideal pairing to investigate proton transfer as the co-former structures are almost analogous and they form a co-crystal and salt respectively. Both form a 1:1 adduct with LON *via* the primary hydrogen bonding interactions however LON-2APYM has an overall 1:2 stoichiometric ratio with additional co-former···co-former interactions present. An in-depth analysis would show the interaction differences of salts and co-crystals as well as the electron density distributions of both states (charged / uncharged) of LON and the co-molecules. Atomic charges and properties at the BCPs and RCPs could also be evaluated and compared. Molecular pair interaction analysis of other salts and co-crystals containing similar co-formers would also inform about the differing pairwise interactions in the systems as a whole. This small study could provide a great deal of information about the formation of salts and co-crystals and has the potential to improve, or alter, the current 'rule of three'[34, 38] prediction methodology.

In addition to a quantum crystallography approach, further investigations are possible with a wider experimental set. Using the materials generated herein as a basic framework, related co-former molecules could be identified and included as part of a systematic study to try to understand the rules of formation. Furthermore, the outcome (salt / co-crystal) could be predicted to see how well they adhere to the 'rule of three'. Analysis of the interactions of water were used for the PROPY systems to understand and rationalise the solution properties and trends. A similar approach could be used for LON.

These studies in isolation all provide valuable information however in combination (further experimental trials, a systematic approach, specific ΔpK_a values and probing the electron density distribution with experimental and quantum-based approaches) these offer a powerful tool to understand a number of complex behaviours and relationships.

7.2.3 Methodology

The design approaches were focussed on co-crystal formation however LON has demonstrated that salt formation is also viable and favoured with some co-molecules. A modified design process encompassing this would therefore be more appropriate for the determination of future co-former molecules, especially if there is a preference for salt / co-crystal in the resulting form. This could be achieved using CSD statistics (as before), pK_a information and the more applicable information obtained from the current study.

LON displays common functional groups and is of a similar size and flexibility to other API molecules. Therefore, the design approach could be applied to similar molecules with reasonable confidence that suitable co-formers would be identified.

The interaction analysis of PROPY systems identified that increased co-former complexity (more functional groups) resulted in the appearance of unfavourable, destabilising interactions which hinder co-crystal formation; PROPY is unable to satisfy an increased co-former functionality as it can form no further strong hydrogen bonds. Functional groups are therefore left unsatisfied and co-crystal formation is not favourable. There may be a limit to the extent of the co-former functionality that still results in co-crystals as increased functionality will favour the crystallisation of single components. This should be considered in future co-former selection and each co-former assessed for potential hydrogen bonding capacity to ensure no combinations would clearly result in unsatisfied functional groups.

7.2.4 Interesting Observations of PROPY-PGL·0.5ACN

PROPY-PGL·0.5ACN exhibited some interesting behaviour in the thermal analysis, displaying a recrystallisation from the melt. Characterisation of this new material has not yet been performed however it is postulated that the recrystallised material contains no solvent and eliminates some of the destabilising interactions observed in the original co-crystal solvate structure. Characterisation and interaction analysis using the PIXEL approach could provide confirmation of the material's nature.

Chapter 8: PROPY Experimental

PROPY was purchased from Tokyo Chemical Industry Co. Ltd, Japan, whilst all co-formers were purchased from Sigma Aldrich, Singapore and all used as received without any further purification. Analytical grade solvents were used for the crystallisation experiments and HPLC grade for all mobile phase solutions.

8.1 CSD Interaction Analysis

All CSD searches discussed in the analysis of potential PROPY carbonyl interactions were carried out using Conquest v1.18 and CSD v5.37 (+ Nov 2015 update).

8.1.1 Isostar

Interactions between differing descriptions of $–CO_2H$, O–H, $–NH_2$ and N–H groups and a carbonyl group were used in Isostar 2.2.3, 2016[250] for contact searching of generalised functional groups.

A similar approach was taken to investigate the interactions of water with the functional groups present in PROPY and the co-formers of the novel co-crystals produced. Isostar version 2.2.4, 2017 was used for this.

8.1.2 Contact Searching

Mercury[107, 108] (v3.8 build RC2) CSD-Materials Suite was used to define contacts between a selection of O–H and N–H donor groups and various models of the carbonyl group in PROPY. This returned the number of structures present in the database containing the two groups, and the percentage of times the interaction occurred to give a propensity of interaction formation. Details of the models used are given in Chapter 4.2.1.2.

8.1.3 Full Interaction Mapping

Full interaction maps (FIMs) and hotspots were generated using the CSD-Materials suite in Mercury[107, 108] to locate the most common areas for such interactions of the carbonyl in PROPY. The crystal structures deposited in the CSD for PROPY (refcodes BAQJEK and BAQJEK01) were utilised with probes of alcohol oxygen, water oxygen, uncharged N–H nitrogen and RNH_3 nitrogen.

8.1.4 QSAR Molecular Complementarity Predictions

Implemented in Mercury,[107, 108] the pre-loaded set of co-formers was utilised and supplemented with experimentally discovered results. 3D geometry optimised MOL files for were generated for these from drawn structures using the MarvinSketch software.[313] The output was inspected and analysed in spreadsheet software.

8.2 Screening by Grinding

1:1 Stoichiometric ratios of PROPY and co-former were added to a 10 mL stainless steel grinding jar with 7 mm stainless steel ball and ground for 30 min at 20 Hz using a Retsch MixerMill (models MM301 and MM200). Solvent drop grinding experiments had 1 drop of methanol added to the jars prior to grinding. PXRD was used to characterise the materials produced with reference to starting material patterns to identify whether changes were present, indicative of a new co-crystal being produced. For a number of combinations, solvent drop grinding resulted in a sticky paste or liquid which could not be characterised by PXRD. In these cases, the experiment was repeated as a dry grind, and if this still resulted in a paste then manual grinding (with much reduced time and force) was implemented. In some instances this was still unsuccessful. Observations were noted and solution trials attempted in some cases, depending on the structure of the co-former.

8.3 Single Crystal Preparation

Evaporative solution crystallisation methods were used to prepare single crystals of the new materials identified as promising from the screening by grinding, and some combinations for which the grinding material produced was unable to be characterised. These were used in single crystal X-ray diffraction experiments.

8.3.1 PROPY-25DHBA 2:1 Co-Crystal Solvate

PROPY (115.15 mg, 0.5 mmol) and 25DHBA (77.06 mg, 0.5 mmol) were dissolved in 1,4-dioxane (2 mL) at 50 °C then left at ambient conditions for evaporation of solvent to occur. After 1-2 days colourless block crystals were obtained.

8.3.2 PROPY-35DHBA 1:1 Co-Crystal

PROPY (115.15 mg, 0.5 mmol) and 35DHBA (77.06 mg, 0.5 mmol) were dissolved in 1,4-dioxane (2 mL) at 50 °C then left at ambient conditions for evaporation of solvent to occur. After 3 weeks, block crystals were formed and the same material also seen to form using ethyl acetate solvent.

8.3.3 PROPY-4HBA 1:1 Co-Crystal

PROPY (230.31 mg, 1 mmol) and 4HBA (138.12 mg, 1 mmol) were dissolved in an ethyl acetate and acetonitrile solvent mix (2 mL) at 50 °C then left at ambient conditions for evaporation of solvent to occur. After a few days thin plates / needles formed.

8.3.4 PROPY-45DClPA 1:1 Co-Crystal

PROPY (115.15 mg, 0.5 mmol) and 45DClPA (117.51 mg, 0.5 mmol) were dissolved in 1,4-dioxane (2 mL) at 50 °C then left at ambient conditions for evaporation of solvent to occur. After a week needle-like crystals formed.

8.3.5 PROPY-FA 2:1 Co-Crystal

PROPY (230.31 mg, 1 mmol) and FA (116.08 mg, 1 mmol) were dissolved in 1,4-dioxane (2 mL) at 50 °C then left at ambient conditions for evaporation of solvent to occur. After a week colourless blocks and some clusters formed. The co-crystal was also produced from ethyl acetate-acetonitrile, ethyl acetate-THF and ethyl acetate-1,4-dioxane solvent mixes.

8.3.6 PROPY-HQ 1:2 Co-Crystal

PROPY (115.15 mg, 0.5 mmol) and HQ (55.06 mg, 0.5 mmol) were dissolved in 1,4-dioxane (2 mL) at 50 °C then left at ambient conditions for evaporation of solvent to occur. After 2 weeks colourless plates formed. The co-crystal was also produced from formic acid solvent (crystals forming within a month), and the 1:2 stoichiometry was produced from both 1:1 and 1:2 stoichiometric ratios in solution crystallisation.

8.3.7 PROPY-MPAR 1:1 Co-Crystal

PROPY (230.31 mg, 1 mmol) and MPAR (152.15 mg, 1 mmol) were dissolved in an ethyl acetate-acetonitrile solvent mix (2 mL) at 50 °C then left at ambient conditions for evaporation of solvent to occur. After 2 weeks colourless plates formed.

8.3.8 PROPY-PGL 1:1 Co-Crystal Solvate

PROPY (230.31 mg, 1 mmol) and PGL (126.11 mg, 1 mmol) were dissolved in an ethyl acetate-acetonitrile solvent mix (2 mL) at 50 °C then left at ambient conditions for evaporation of solvent to occur. After a few days colourless plates formed.

8.4 Powder X-ray Diffraction Studies

For powder samples generated from grinding, stability and slurry experiments, PXRD data were collected using a Bruker D8 Advance powder X-ray diffractometer with Cu-Kα radiation (λ = 1.54060 Å), with 35 kV and 40 mA voltage and current applied. The sample was scanned from 2θ = 5 ° to 50 ° with continuous scan, and a scan rate of 5 °min-1. OriginPro 9.1 was used to plot the PXRD patterns obtained.

8.5 Standard Resolution Single Crystal X-ray Diffraction Studies

8.5.1 Data Collection and Reduction

Data for all co-crystals, except PROPY-25DBA, were collected on an Agilent Technologies Dual Source Supernova, four-circle diffractometer fitted with CCD detector and graphite monochromator using Mo-Kα radiation (λ = 0.71073 Å). CrysAlisPro[317] software was used for data collection, reduction and absorption correction using face indexing and Gaussian corrections. PROPY-25DHBA co-crystal data were collected on a Rigaku FRE+ equipped with VHF *Varimax* confocal mirrors, an AFC10 goniometer and an HG Saturn724+ detector using Mo-Kα radiation (λ = 0.71075 Å). Crystal Clear 3.1[318] software was used for data collection and CrysAlisPro[317] for data reduction and Gaussian absorption correction. All data sets were collected at 100 K and suitable crystals selected and mounted using paratone or fomblin oil on a MiTeGen Micromesh holder.

8.5.2 Structure Solution and Refinement

Structure solution for all was carried out using Direct Methods in SHELXT[319] and refined using full-matrix least squares on F^2 using SHELXL 2014[320] both implemented in the Olex2 software.[265]

Hydrogen atoms for heteroatoms (N and O) were located from the difference Fourier map and all were freely refined. The remaining protons were fixed in idealised positions with their displacement parameters riding on the values of their parent atoms. Non-hydrogen atoms were refined with anisotropic displacement parameters whilst all hydrogen atoms left as isotropic. PLATON,[267, 268] with neutron normalised hydrogen bond lengths (for O–H, N–H and C–H at 0.983 Å, 1.009 Å and 1.008 Å respectively), were used for the calculation of bond lengths and bond angles.

PROPY-25DHBA contains whole molecule disorder of 25DHBA and disordered solvent contained in voids. The solvent masking routine in Olex2[265] and PLATON SQUEEZE[266] algorithms were

implemented to determine solvent stoichiometry. PROPY-35DHBA displayed four electron density peaks in the carboxylic acid dimer indicating proton sharing. This was modelled as a 0.5 occupancy hydrogen atom on each oxygen in the dimer arrangement. All cell parameters and refinement information can be seen in Appendix A.5 along with hydrogen bonding tables (Appendix A.6).

CCDC numbers 1504450-1504457 contain the supplementary crystallographic data and can be obtained from The Cambridge Crystallographic Data Centre *via* *http://www.ccdc.cam.ac.uk/conts/retrieving.html*

8.6 Property Measurements

Synthesis of the bulk for all materials containing a pharmaceutically acceptable co-former molecule was carried out using solvent drop grinding (as per screening method with larger quantities) for PROPY-HQ and PROPY-MPAR, and using the relevant aforementioned solution techniques for the remaining samples. These bulk materials were used for all property measurements and experiments discussed below.

8.6.1 Differential Scanning Calorimetry

A TA Instruments Discovery DSC fitted with autosampler and liquid nitrogen pump cooling system was used to measure the thermal behaviour of all samples. Dried samples (free from residual solvent), of mass 2-5 mg, were placed in an aluminium pan (internal volume 20 µL) and crimp sealed with corresponding lid in a Tzero sample press. The heating range was set as 25 °C to 150 °C, with a heating rate of 10 °C min^{-1} and nitrogen gas used for purging (base purge 300 mL min^{-1}, cell flow 25 mL min^{-1}).

8.6.2 Stability Studies

Stability of PROPY and all the co-crystals except 45DCIPA (not pharmaceutically acceptable) was tested using storage under accelerated conditions (40 °C and 75 % relative humidity) for 13-15 weeks. Samples of approximately 100 mg size were stored under the test conditions and tested periodically using PXRD to identify the sample's identity.

For slurry experiments, excess co-crystal materials in pH 7.5 phosphate buffer solution were left stirring at room temperature for 24 hours before filtering and the resulting powder analysed by PXRD. Solubility of the samples was measured by taking aliquots of the filtered slurry solution and analysing by HPLC.

8.6.3 Dynamic Vapour Sorption

DVS analysis was carried out on a Surface Measurement Systems DVS Advantage machine. A preheating stage, raising the temperature to 40 °C with an isothermal hold for 5 hours, was followed by increasing the partial pressure at 0.2 % per minute from 0-90 % relative humidity and back to 0% in a similar manner *via* desorption. The system was considered to be in equilibrium if the rate change of mass was less than 0.002 % min^{-1} at one specific partial vapour pressure. The temperature was maintained at a constant 25 °C throughout the experiment. The sorption isotherms were calculated from the equilibrium mass values.

8.6.4 Solubility and Dissolution Rate

Dissolution rate was tested under sink conditions for five pharmaceutically acceptable co-crystals and PROPY using an Agilent 708-DS dissolution sampling apparatus with rotation speed of 75 rpm at 37 °C. Phosphate buffer solution (pH 7.5) was used as the dissolution medium (900 mL) with samples prepared containing 75 mg API in a 500 mg corn starch tablet, pressed for 1 minute at 2 KN using an FT-IR press. Sampling was conducted by withdrawing 2 mL of sample from the vessel and immediately replaced with fresh dissolution medium to maintain the dissolution volume. 1 mL was discarded as waste and a sample taken for analysis by HPLC after filtering through a 45 µm syringe tip filter. This was conducted at 5 minute intervals for the first 30 minutes followed by two 15 minute intervals, a 120 minute sample taken and then hourly to the end of the experiment.

Apparent solubility calculations were conducted for dissociable samples, as determined in stability tests. The apparent solubility equation was used: $C_m = C_s\left(\frac{J_m}{J_s}\right)$. C_m represents the apparent solubility of the unstable form, C_s represents the solubility of the thermodynamic form and J_m and J_s represent the dissolution rates of the co-crystal and thermodynamic form, respectively. Dissolution rates were taken from the linear portions of the appropriate dissolution curve: PROPY 0-15 mins, R^2 = 0.9595; PROPY-25DHBA 0-15 mins, R^2 = 0.8326; PROPY-PGL·0.5ACN 0-10 mins, R^2 = 0.8779.

8.6.5 High Performance Liquid Chromatography

HPLC analysis was carried out to quantitatively determine PROPY concentration by using a HP 1100 pump fitted with G1315B (Agilent Technologies) diode array detector. The LC column was an Agilent Lichrosorp-RP-18, dimensions 4.6 x 200 mm, 5 µm run at 37 °C. The mobile phase consisted of acetonitrile and water (50:50 v/v) which was filtered through a 45 µm cellulose filter

membrane under vacuum and then sonicated. The mobile phase was pumped isocratically at a flow rate of 1.5 mL min^{-1} with a 12 min run time. An injection volume of 10 µL was used and detection wavelength for all analytes was 280 nm. Retention times were: PROPY 4.29 mins, 35DHBA 0.93 mins, FA 1.05 mins, 4HBA 1.18 mins, HQ 1.73 mins and MPAR 2.32 mins. This method was created using information from the work by David *et al*.[62]

8.7 High Resolution Single Crystal X-ray Diffraction Studies

8.7.1 Data Collection and Reduction

Data was collected for all four systems on the Rigaku FRE+ diffractometer (for details see Section 8.5.1), controlled by Crystal Clear V3.1.[318] The best crystal possible was selected, and affixed to a MiTeGen MicroMesh support using two-component glue. This was allowed to cool in the cryostream air flow for 5-10 minutes before centering, to ensure no crystal contraction or movement would occur after centring.

For all systems an initial short data collection was completed using the attenuator for overload corrections. The experimental parameters were: exposure, 1 sec; redundancy, 3-4; resolution, 0.7 Å. Following this a full charge density experiment was set up, with the same crystal and in the same orientation. Experimental parameters are detailed in the Table 8.1 below.

Table 8.1. Experimental parameters for the high resolution X-ray diffraction data collections for PROPY-4HBA, PROPY-FA, PROPY-HQ and PROPY-MPAR

	PROPY-4HBA	PROPY-FA	PROPY-HQ	PROPY-MPAR
Crystal system	Monoclinic	Triclinic	Triclinic	Orthorhombic
Resolution /Å	0.41	0.41	0.41	0.41
2θ positions /°	-29 / -87	-29 / -87	-29 / -87	-29 / -87
Exposure /s	1 / 50	1 / 47	1 / 45	1 / 40
Scan width /°	0.5	0.5	0.5	0.5
Redundancy	9	10	9	20
Completeness /%	99	99	99	99
No. runs / no. frames	29 / 7051	100 / 10658	98 / 9847	27 / 5722

If time allowed, a third data collection was set up immediately after the full charge density experiment, targeting the medium resolution. This was set up with an intermediate exposure time to try to collect this region with minimal overloaded intensities (as seen in some of the high angle frames of the main experiment). Experimental set up typically collected data between 0.8-0.5 Å resolution.

Data reduction was completed using CrysalisPro software, each experiment treated separately. The long collection was treated in two parts, separated for the two 2θ positions used in the data collection, as there were some large differences in reflection intensities between the two settings. These are hence described as the low angle (θ= -29°) and high angle (θ= -87°) data.

Once each data set was processed, SORTAV[321-323] was used to combine the reflection files, merging and sorting according to the symmetry. This was completed several times using different combinations of the data to find the optimal combination. For each combination, the output statistics were inspected, and those with the highest completeness, redundancy, and lowest merging R were used for structure solution and refinement. For all cases, this consisted of the full charge density data set and the short data set with attenuation combined.

8.7.2 Aspherical Atom Model Refinement Strategy

Initially a spherical (IAM) model for the structure was generated using Olex2[265] and the process described as for the standard resolution structures (Section 8.5.2). SHELXT[319] was used for

structure solution, and SHELXL[320] for refinement, with the aim to obtain the best possible structure from the data. This model then functions as the foundation for the introduction of multipole populations, and is used as the input for the program WinXD (v2016.01).[324] The Clementi-Roeti[325] databank was used at the input stage for all systems.

8.7.2.1 Standard Refinement Method

Using WinXD, the following steps were completed for all models

- Refine scale factor
- Refine positional parameters (3) for non-hydrogen atoms against high angle data 0.0 to 0.7 Å
- Refine positional (3) and thermal parameters (6) non-hydrogen atoms against high angle data
- Refine positional parameters (3) for hydrogen atoms using low angle data (0.7 to 2.0 Å)
- Refine positional parameters (3) and one thermal parameter (isotropic) for hydrogen atoms using low angle data
- Refine all aforementioned positional and thermal parameters as appropriate for all atoms using all data
- Set hydrogen bond distances (X–H) to neutron determined values[326, 327] and ensure these are included correctly through analysis of the geometry output
- Use SHADE server 2.1 (2017)[328, 329] to estimate anisotropic displacement for hydrogen atoms and include in model
- Chemical constraints applied to equivalent atoms in a similar environment to reduce the number of parameters in the early refinements and a single κ parameter for each environment. A single κ parameter was allocated for all hydrogen atoms and fixed at the pre-determined value of 1.200. This led to 23, 19, 18, and 24 κ parameters for PROPY-4HBA, PROPY-FA, PROPY-HQ and PROPY-MPAR respectively.
- Subsequent steps introduce the multipoles sequentially: monopoles, dipoles, quadrupoles, octupoles, hexadecapoles, with κ parameters refined at all stages for non-hydrogen atoms.

  Hydrogen atoms were refined up to the quadrupole level of theory, using a single bond-directed (*z*-axis) dipole and quadrupole for each. All non-hydrogen atoms were refined to the hexadecapole level of theory. After refinement the populations and errors were scrutinised to ensure that the populations were meaningful and that refinement was sensible. As this level of theory was deemed appropriate for many non-hydrogen atoms in the systems it was applied to all to ensure consistency among atoms within and between

models. See Appendix B.1.4 for details on selection of hexadecapoles to refine and statistical meaningfulness.

- Following full multipole refinement with *κ* parameters, the chemical constraints were released to allow free refinement of all atomic environments
- Positional and thermal parameters for non-hydrogen atoms refined against the multipole model (hydrogen atoms fixed at SHADE estimated positions)
- For PROPY-FA SHADE was repeated to improve the hydrogen atom thermal displacement parameters and the resulting DMSDA (difference of mean-square displacement amplitudes) values.
- *κ* parameters fixed at their last refined values to allow for convergence of the refinement (if not obtained in previous step)

At all stages of the multipole refinement, the following checks were performed:

- ✓ DMSDA values inspected to ensure values less than 10 x 10^{-4} were obtained
- ✓ Atomic charges were sensible
- ✓ Deformation density maps were used to see the development of the multipoles, and identify any erroneous regions
- ✓ Residual density analysis to confirm density was being allocated into multipoles, and an overall reduction occurring as the refinement progressed

8.7.2.2 *κ'* refinement method

The above method was followed up to the end of the full multipole refinement with *κ* parameters. At this point, *κ'* was introduced for non-hydrogen atoms and a number of refinement cycles completed. The output was inspected for atomic charges, populations, residual electron density, and indicators of an improved model in the maps. The refinement was completed according to the steps above to allow for full model comparisons to be made.

To test the effect of *κ* and *κ'* on the model, different combinations of the *κ* parameters were refined allowing varying expansions and contractions to occur. As with *κ'*, the resulting models were compared to the initial model, and also inspected for indicators of model improvements, or deteriorations to allow a critical evaluation of which parameters to refine in the final model.

8.7.2.3 Absorption test methods

Several different absorption correction approaches were tested to account for the absence of face indexing including XABS2[330] and that implemented in SORTAV (see Appendix B.1.2 for details and example comparisons).

These were implemented during the IAM refinement, during the SORTAV process, and final refinement for SORTAV and XABS2 respectively. The XABS2[330] routine was completed in WinGX[331] using the XABS2 correction once all atoms were appropriately located, assigned and refined anisotropically in Olex2.[265] Refinement using the absorption-corrected hkl was then conducted to produce the final spherical atom model to be used as the starting model for multipole refinement. The absorption in SORTAV was combined into the SORTAV generated .hkl file and hence refinement proceeded as normal.

8.8 Theoretical Studies

8.8.1 Crystal Explorer Interaction Energies

Interaction energies for the PROPY co-crystal systems were calculated from the crystal structure (CIF file). Theoretical wavefunctions using Tonto, at the B3LYP/6-31G(d,p) level were generated, which were used to determine the energies; a molecular shell of radius 3.8 Å around one molecule was generated, all fragments completed and the energies calculated. Once complete, this was repeated in turn for the other molecule(s) present in the crystal structure, each time starting from the original CIF file.

8.8.2 PIXEL

Gavezzotti's PIXEL methodology[183, 184] was employed for all systems using the standard resolution crystal structure as the input and atomic co-ordinates. Default values were used at all stages, and Gaussian09[279] was used to generate the density files for each molecule (MP2/6-31G**).

For systems with Z > 2, a separate CIF, and calculation was conducted for each molecular pair present. For analysis, PIXEL interaction energy sums ($E_{T,\Sigma}$) were used as a final PIXEL energy is not possible for Z > 2 structures due to the number of calculations required. These sums differ slightly from the total energy of the crystal ($E_{T,Cry}$) as output by PIXEL as the polarisation energy is not pairwise additive (many-body effect). It has been shown by Gelbrich that the difference is generally small, and determined as < 2.5 % of $E_{T,\Sigma}$ for the polymorphic system investigated.[332] The PIXEL interaction energy sums will allow comparisons to be made, and relative contributions from certain groups of interactions to be assessed.

Chapter 9: LON Experimental

LON was purchased from Junda Pharmaceuticals Ltd., China whilst all co-formers were purchased from Sigma Aldrich, Singapore, except HALO, purchased from TCI Chemicals, Singapore. All were used as received without any further purification. Analytical grade solvents were used for the crystallisation experiments and HPLC grade for all mobile phase solutions.

9.1 Screening by Grinding

1:1 stoichiometric ratios of LON and co-former were added to a 10 mL stainless steel grinding jar with 7 mm stainless steel ball and ground for 30 minutes at 20 Hz using a Retsch MixerMill (models MM301 and MM200). Solvent drop grinding experiments had 2 drops of methanol added to the jars prior to grinding. PXRD was used to characterise the materials produced with reference to starting material patterns to identify whether changes were present indicative of new material being produced.

9.2 Single Crystal Preparation

Evaporative solution crystallisation methods were used to prepare single crystals of the new materials identified as promising in screening by grinding. These were used in single crystal X-ray diffraction experiments.

9.2.1 α-LON

Crystals of α-LON were obtained in a number of co-crystallisation trials in which a co-crystal was not successfully formed, predominantly using ethyl acetate as the solvent. The crystal used for structure solution was obtained from an ethyl acetate-acetonitrile solvent mix, heated to 50 °C to dissolve commercial LON and then left at ambient conditions to evaporate. Small colourless crystals formed after a week. Pure ethyl acetate also afforded such crystals.

9.2.2 LON-246TAPYM 1:1 Salt

LON (160.58 mg, 0.5 mmol) and 246TAPYM (62.54 mg, 0.5 mmol) were dissolved in DMF at 50 °C then left at ambient conditions for evaporation of solvent to occur. Within 11 days colourless block crystals in yellow solution formed of the 1:1 salt.

9.2.3 LON-2APYD 1:1 Salt Solvates

LON (160.58 mg, 0.5 mmol) and 2APYD (47.06 mg, 0.5 mmol) were dissolved in a methanol-acetonitrile solvent mix at 50 °C then left at ambient conditions for evaporation of solvent to occur. Colourless plate crystals of the 1:1 acetonitrile salt solvate formed within 3 days.

Using ethyl acetate solvent and the same procedure, clusters of colourless plates and needles of the 1:1 ethyl acetate salt solvate formed after one day.

9.2.4 LON-2APYM 1:2 Co-Crystal

LON (160.58 mg, 0.5 mmol) and 2APYM (47.55 mg, 0.5 mmol) were dissolved in ethyl acetate at 50 °C then left at ambient conditions for evaporation of solvent to occur. Within a week, colourless block crystals of the 1:2 co-crystal formed from a 1:1 ratio solution.

9.2.5 LON-4,4BIPY 2:1 Co-Crystal

LON (160.58 mg, 0.5 mmol) and 4,4BIPY (78.10 mg, 0.5 mmol) were dissolved in DMF at 50 °C then left at ambient conditions for evaporation of solvent to occur. Within 5 days clusters of colourless plate crystals formed.

9.2.6 LON-4DMAP Salts

LON (160.58 mg, 0.5 mmol) and 4DMAP were dissolved in ethyl acetate at 50 °C then left at ambient conditions for evaporation of solvent to occur. Within 5 days colourless block crystals had formed of the 1:1 dihydrate salt. Crystals of the same material were also afforded using an acetone-THF solvent mix and ethyl acetate-acetonitrile-acetone solvent combination. Using an ethyl acetate-acetonitrile solvent combination blocks of the 2:1 co-crystal salt were afforded after 2 days.

9.2.7 LON-BENZ 1:1 Co-Crystal

LON (160.58 mg, 0.5 mmol) and BENZ (60.57 mg, 0.5 mmol) were dissolved in a 50:50 solvent mix of ethyl acetate and acetonitrile at 50 °C. The solution was left at ambient conditions for evaporation of solvent to occur which resulted in small colourless plate crystals forming of the 1:1 co-crystal after 4 days.

9.2.8 LON-HALO 1:1 Salt Trihydrate

LON (160.58 mg, 0.5 mmol) and HALO (187.95 mg, 0.5 mmol) were dissolved in DMF at 50 °C then left under ambient conditions for evaporation of solvent to occur. Clusters of colourless plate crystals of the 1:1 salt formed after 6-8 weeks.

9.2.9 LON-IMID Salts / Co-Crystal Salt Hybrid Material

LON (160.58 mg, 0.5 mmol) and IMID (34.03 mg, 0.5 mmol) were dissolved in ethyl acetate at 50 °C before being left under ambient conditions for evaporation of solvent to occur. Colourless block crystals of the 1:1:0.5 salt solvate formed within one day. Crystals of the 2:1 and 1:1 salts were afforded in the same way (from a 1:1 ratio) using a methanol-acetonitrile solvent mix and were observed in the same batch (2:1 ratio material characterised first, 1:1 after some time).

9.2.10 LON-ISO 1:1 Co-Crystal

LON (160.58 mg, 0.5 mmol) and ISO (61.06 mg, 0.5 mmol) were dissolved in ethyl acetate (4 mL) at 50 °C then left at ambient conditions for evaporation of solvent to occur. After a week, large colourless block crystals of the 1:1 co-crystal formed.

9.2.11 LON-MEL 1:1 Salt

LON (160.58 mg, 0.5 mmol) and MEL (63.06 mg, 0.5 mmol) were dissolved in DMSO at 50 °C and left to evaporate at ambient conditions. Initially a gel formed however with extended time (2 weeks – 1 month) crystals of the 1:1 salt formed in the gel.

9.2.12 LON-NICO 1:1 Co-Crystal

LON (160.58 mg, 0.5 mmol) and NICO (61.06 mg, 0.5 mmol) were dissolved in an acetonitrile-ethanol solvent mix (80:20 ratio) at 50 °C then left for the solvent to evaporate under ambient conditions. Small colourless plates of the 1:1 co-crystal formed after 2 weeks.

9.2.13 LON-PIPE 2:1 Salt

LON (160.58 mg, 0.5 mmol) and PIPE (34.04 mg, 0.5 mmol) were dissolved in 50:50 methanol-acetonitrile solvent mix and left ambient conditions for evaporation of solvent to occur. Large colourless plate crystals of the 1:1 salt formed after 5 days.

9.3 Powder X-ray Diffraction Studies

For powder samples generated from grinding, stability and slurry experiments, PXRD data were collected using a Bruker D8 Advance powder X-ray diffractometer with Cu-Kα radiation (λ = 1.54060 Å), with 35 kV and 40 mA voltage and current applied. The sample was scanned from 2θ = 5 ° to 50 ° with continuous scan, and a scan rate of 5 °min-1. OriginPro 9.1 was used to plot the PXRD patterns obtained.

9.4 Standard Resolution Single Crystal X-ray Diffraction Studies

9.4.1 Data Collection and Reduction

Data for LON-NICO, LON-BENZ, LON-4,4BIPY co-crystals and LON-IMID 1:1 salt were collected on a Rigaku FRE+ equipped with VHF Varimax confocal mirrors, an AFC10 goniometer and an HG Saturn724+ detector using Mo-Kα radiation (λ = 0.71075 Å). Crystal Clear 3.1[318] software was used for data collection and CrysAlisPro[317] for data reduction and Gaussian absorption correction.

Data for the remaining samples were collected on an Agilent Technologies Dual Source Supernova, four-circle diffractometer fitted with CCD detector and graphite monochromator using Mo-Kα radiation (λ = 0.71073 Å). CrysAlisPro[317] software was used for data collection, reduction and absorption correction using face indexing and Gaussian corrections. All data was collected at 100 K and suitable crystals selected and mounted using paratone or fomblin oil on a MiTeGen Micromesh holder.

9.4.2 Structure Solution and Refinement

Structure solution for all was carried out using Direct Methods in SHELXT[319] and refined using full-matrix least squares on F^2 using SHELXL 2014[333] both implemented in the Olex2[265] software. Non-hydrogen atoms were refined with anisotropic displacement parameters. Hydrogen atoms for heteroatoms (N and O) were located from the difference Fourier map, except for one proton in the 2:1 imidazole structure which was set at standard position riding on the parent atom, and all were freely refined. The remaining protons, including those of water molecules in hydrate structures and partially occupied hydrogens in, for example 1:1 imidazole salt were fixed in idealised positions with their displacement parameters riding on the values of their parent atoms.

LON-PIPE presented as a merohedral twin (approximately 52.5 %) and LON-NICO as a pseudo-merohedral twin (approximately 3.5 %). Various restraints and constraints were used in the structures of LON-IMID·0.5EtOAc, LON-IMID 1:1 salt and LON-4,4BIPY 2:1 co-crystal structures to

give the best representation of structure. Disorder was evident in a number of structures including the dichloro-substituted rings in LON-4,4BIPY, LON-IMID·0.5EtOAc (also containing one disordered solvent molecule) and LON-4DMAP 2:1 co-crystal salt (also containing 4DMAP disordered over two positions). The 2:1 LON-IMID co-crystal salt contains disorder of one imidazole molecule and the carboxylic acid proton was observed to be shared over one IMID and one LON molecule, each with 0.5 occupancy. LON-HALO trihydrate displayed disorder of two of the water molecules. The SMTBX solvent masking routine as implemented in Olex2[330] was used for the 1:1 LON-2APYD acetonitrile solvate as the solvent was identified to be present in voids, with no apparent hydrogen bonding to maintain a fixed position of the solvent molecules. The electron count and void space volume was in line with an acetonitrile solvent molecule. PLATON,[267, 268] with neutron normalised hydrogen bond lengths (for O–H, N–H and C–H at 0.983 Å, 1.009 Å and 1.008 Å respectively), was used for the calculation of bond lengths, bond angles and torsion angles. All cell parameters and refinement information can be seen in Appendix C.5 along with hydrogen bonding tables in Appendix C.6.

CCDC (1531947-1531963) contain the crystallographic data for novel LON materials and can be obtained from The Cambridge Crystallographic Data Centre *via* *http://www.ccdc.cam.ac.uk/conts/retrieving.html.*

9.5 Physicochemical Property Measurements

Synthesis of the bulk for all materials containing a pharmaceutically acceptable co-former molecule was carried out using solvent drop grinding (as per screening method with larger quantities) for LON-NICO, LON-ISO, LON-BENZ and LON-MEL and using the relevant aforementioned solution techniques for LON-IMID, LON-HALO and LON-PIPE. These bulk materials were used for all property measurements and experiments discussed below.

9.5.1 Differential Scanning Calorimetry

A TA Instruments Discovery DSC fitted with autosampler and liquid nitrogen pump cooling system was used to measure the thermal behaviour of all samples. Dried samples (free from residual solvent), with a mass in the range 2-5 mg, were placed in an aluminium pan (internal volume 20 µL) and crimp sealed with corresponding lid in a Tzero sample press. The heating range was set as 25 °C to 150 °C, with a heating rate of 10 °C min^{-1} and nitrogen gas used for purging (base purge 300 mL min^{-1}, cell flow 25 mL min^{-1}).

9.5.2 Hot Stage Microscopy

Hot stage microscopy was used to visually observe some of the events seen through DSC analysis. This was carried out using a Leica DM2500 microscope fitted with Lumenera Infinity 1 CMOS digital microscope camera and Mettler Toledo FP82HT Hot Stage with FP90 Central Processor. Data capture was completed using Studio Capture software v3.1. Experimental parameters, such as temperature range and heating rate, were tailored to each experiment to focus on particular events but typically mimicked the DSC set up to allow comparisons to be made.

9.5.3 Thermogravimetric Analysis

Thermogravimetric analysis (TGA) was used to investigate some observations in DSC and HSM. A Netzsch TGA 209 F1 Libra was used with a ramp rate of 10 °C min^{-1} from 25-30 °C up to a maximum of 400 °C (depending on the nature of the sample and observations from DSC).

9.5.4 Stability Studies

Stability of LON and all the pharmaceutically acceptable salts and co-crystals was tested using storage under accelerated conditions (40 °C and 75 % relative humidity) for 13-15 weeks. Samples of approximately 100 mg size were stored under the test conditions and tested periodically using PXRD to identify the sample's identity.

For slurry experiments, excess co-crystal or salt materials in 1% Tween80 ® solution were left stirring at room temperature for 24 hours before filtering and the resulting powder analysed by PXRD. Solubility of the samples was measured by taking aliquots of the filtered slurry solution and analysing by HPLC.

9.5.5 Dynamic Vapour Sorption

DVS analysis was carried out on a Surface Measurement Systems DVS Advantage machine. A preheating stage, raising the temperature to 40 °C with an isothermal hold for 5 hours, was followed by increasing the partial pressure at 0.2 % per minute from 0-90 % relative humidity and back to 0 % in a similar manner *via* desorption. The system was considered to be in equilibrium if the rate change of mass was less than 0.002 % min^{-1} at one specific partial vapour pressure. The temperature was maintained at a constant 25 °C throughout the experiment. The sorption isotherms were calculated from the equilibrium mass values.

9.5.6 Dissolution Rate

Dissolution rate was tested under sink conditions for LON and the pharmaceutically acceptable co-crystals and salts using an Agilent 708-DS dissolution sampling apparatus with rotation speed of 75 rpm at 37 °C. 1% Tween 80® was used as the dissolution medium (900 mL) with samples prepared containing 25 mg API in a 250 mg corn starch tablet, pressed for 1 minute at 2 KN using an FT-IR press. Sampling was conducted by withdrawing 2 mL of sample from the vessel and immediately replaced with fresh dissolution medium to maintain the dissolution volume. 1 mL was discarded as waste and a sample taken for analysis by HPLC after filtering through a 45 µm syringe tip filter. This was conducted at 5 minute intervals for the first 30 minutes followed by two samples at 15 minute intervals, a 120 minute sample taken and then hourly to the end of the experiment.

9.5.7 Solubility

Apparent solubility of the dissociable materials, LON-ISO, LON-NICO and LON-IMID·0.5EtOAc was calculated according to the literature[269, 270] using the apparent solubility equation (Equation 9.1):

$$C_m = C_s \left(\frac{J_m}{J_s}\right)$$

Equation 9.1. Apparent Solubility Equaiton.

C_m represents the apparent solubility of the unstable form, C_s represents the solubility of the thermodynamic form, and J_m and J_s represent the dissolution rates of the co-crystal/salt and thermodynamic form, respectively. Linear portions of the dissolution curves of LON and the new materials were used to extract the dissolution rates for the required species: LON 0-30 min, R^2 = 0.9534; LON-NICO 0-30 min, R^2 = 0.9991; LON-ISO 0-30 min, R^2 = 0.9951; LON-IMID 0-30 min, R^2 = 0.9372.

9.5.8 High Performance Liquid Chromatography

HPLC analysis was carried out to quantitatively determine LON concentration by using a HP 1100 pump fitted with G1315B (Agilent Technologies) diode array detector. The LC column was an Agilent Zorbax Eclipse XDB-C18 4.6, dimensions 4.6 x 250 mm, 5 µm run at 37 °C. The mobile phase consisted of 25 mM $NaH_2PO_4.H_2O$ (pH 3) and MeOH (30 : 70 v/v) which was filtered through a 45 µm cellulose filter membrane under vacuum and then sonicated. The mobile phase was pumped isocratically at a flow rate of 1 mL min^{-1} with a 20 min run time. An injection volume of 20 µL was used and detection wavelength for all analytes was 275 nm. Retention times were: LON

11.85 min, BENZ 2.55 min, HALO 3.14 min, IMID 2.25 min and 2.55 min, ISO 2.5 min, MEL 2.3 min, 2.5 min and 3.2 min, NICO 2.5 min and PIPE 3.36 min. This method was created using information from the work by Ioele et al.[334]

9.5.9 Mass Spectrometry

High resolution mass spectra were recorded using positive ion electrospray ionisation. Samples were analysed using a MaXis (Bruker Daltonics, Bremen, Germany) mass spectrometer equipped with a Time of Flight (TOF) analyser. Samples were introduced to the mass spectrometer *via* a Dionex Ultimate 3000 autosampler and uHPLC pump. A gradient of 20 % acetonitrile (0.2 % formic acid) to 100 % acetonitrile (0.2 % formic acid) in five minutes at 0.6 mL min^{-1} was used with Acquity UPLC BEH C18 column (Waters), internal dimensions 50 mm x 2.1 mm x 1.7 µm.

9.6 CSD Searches

All CSD searches discussed in the interaction analysis of the LON co-crystals and salts were carried out using Conquest v1.19 and CSD v5.38 (+ Nov 2016 / Feb 2017 updates). Where applicable structures were visualised using Mercury 3.9. Supplementary documents also provide information on these.

9.6.1 2APYM and Carboxylic Acid Structures

CSD searches using the models shown in Figure 9.1 below were carried out to identify multi-component systems containing 2APYM and a carboxylic acid group, with any metal-containing structures filtered out. A visual inspection in Mercury was then performed to determine the stoichiometry and nature of the systems.

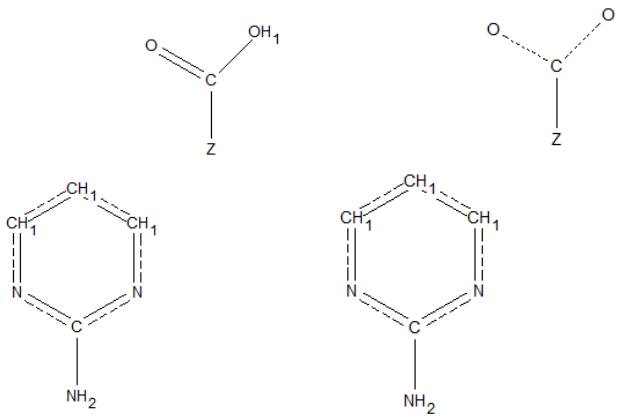

Figure 9.1. Models used to search the CSD for crystal structures containing 2APYM with a carboxylic acid group (left) and general CO_2 group (right). Z indicates any atom other

than hydrogen, dotted bonds represent 'any' bond type and bonds indicated by a straight line and second, parallel, dashed line are aromatic bonds.

9.6.2 Structures with 4DMAP / 2APYD and a Carboxylic Acid

The models shown below (Figure 9.2) was used to search the CSD for structures containing 4DMAP / 2APYD and a CO_2 group. Filters of no metals present, and the number of molecules ≥ 2, were also applied. A visual inspection was then completed on the hits returned for 4DMAP to determine whether 4DMAP was included as an independent molecule; any structures showing additional bonds from the pyridine nitrogen (excluding hydrogen) were excluded from the analysis.

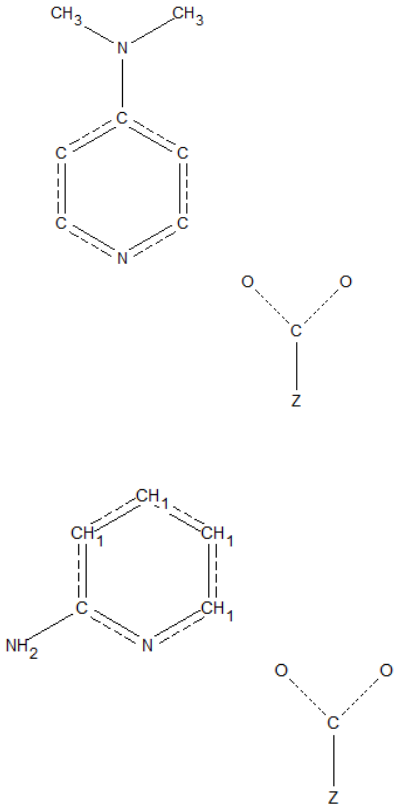

Figure 9.2. Model used to search the CSD for crystal structures containing 4DMAP (top left) and 2APYD (top right) with a CO_2 group. Z indicates any atom other than hydrogen, dotted bonds represent 'any' bond type and bonds indicated by a straight line and second, parallel, dashed line are aromatic bonds.

9.6.3 Interactions of NICO

The CSD was searched in a similar way for all structures containing NICO (model shown in figure 9.3) with ≥ 2 molecules and no metals present. The results were visually inspected using Mercury to analyse the interactions present for each of the functional groups on NICO.

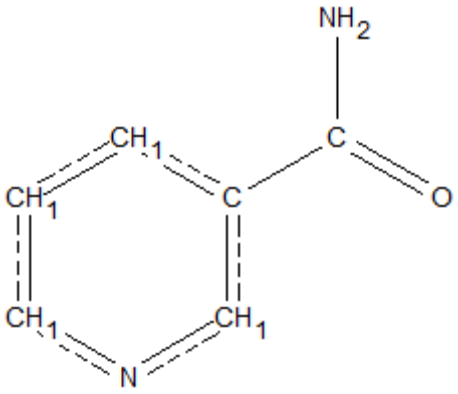

Figure 9.3. Model used to search the CSD for crystal structures containing NICO.

A search was also carried out to determine the number of structures present containing NICO and a carboxylic acid (modelled as shown previously in Figure 9.1).

9.6.4 PIPE

A search was carried out using the model of PIPE (Figure 9.4) with the restrictions of no metal present and ≥ 2 molecules. Visual inspection of the hits was carried out to sub-divide the resulting 470 structures into categories according to their degree of protonation and exclude any which did not contain PIPE and the individual molecule.

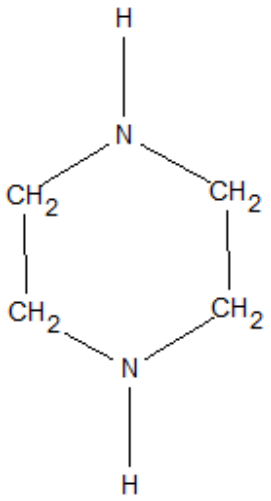

Figure 9.4. Model used for PIPE representation in CSD searches.

Appendices

The following three appendices are included, their associated electronic files detailed below

Appendix A: PROPY

Associated Files: PROPY CIFs

CSD searches and analysis:

QSAR Co-crystal prediction output (excel)

Specific Contact Searching

Interaction Contributions from Hirshfeld Surface Analysis (excel)

Appendix B: PROPY CD

Associated Files: Multipole Model CIFs – PROPY-4HBA, PROPY-FA, PROPY-HQ, PROPY-MPAR

Charge Comparisons (doc)

PIXEL calculation output (excel)

Crystal Explorer interaction energy output (excel)

PIXEL-Crystal Explorer comparisons (excel)

Strong, Moderate Weak Interaction Groupings (excel)

Topological analysis interaction energies (multipole models)

Topological analysis RCP data

Water Interaction Analysis (Isostar)

Appendix C: LON

Associated Files: LON CIFs

CSD Search Data : NICO, 2APYM, PIPE, pyridine···acid, LON interactions

Appendix A PROPY

CONTENTS

A.1 CSD Searching

A.2 Co-Former Selection

A.3 PXRD Patterns - screening by grinding

A.4 QSAR Molecular Complementarity

A.5 Crystal Structure Tables

A.6 Hydrogen Bonding Interaction Tables

A.7 Hirshfeld Surface Analysis

A.8 Packing Coefficients

A.9 Thermal Analysis

A.10 Stability

A.1 CSD Knowledge Based Searching

Related supplementary documents

- Specific Contact Searching (.doc)
- Associated search results files

A.1.1 Full Interaction Mapping

Figure A.1 shows the map for the probes used in full interaction mapping[251] separated out for clarity (combined map presented in chapter 4.2.1.3). These indicate the areas around PROPY where a particular functionality is most likely to be located and interact with PROPY, the opacity demonstrating the propensity for such an interaction.

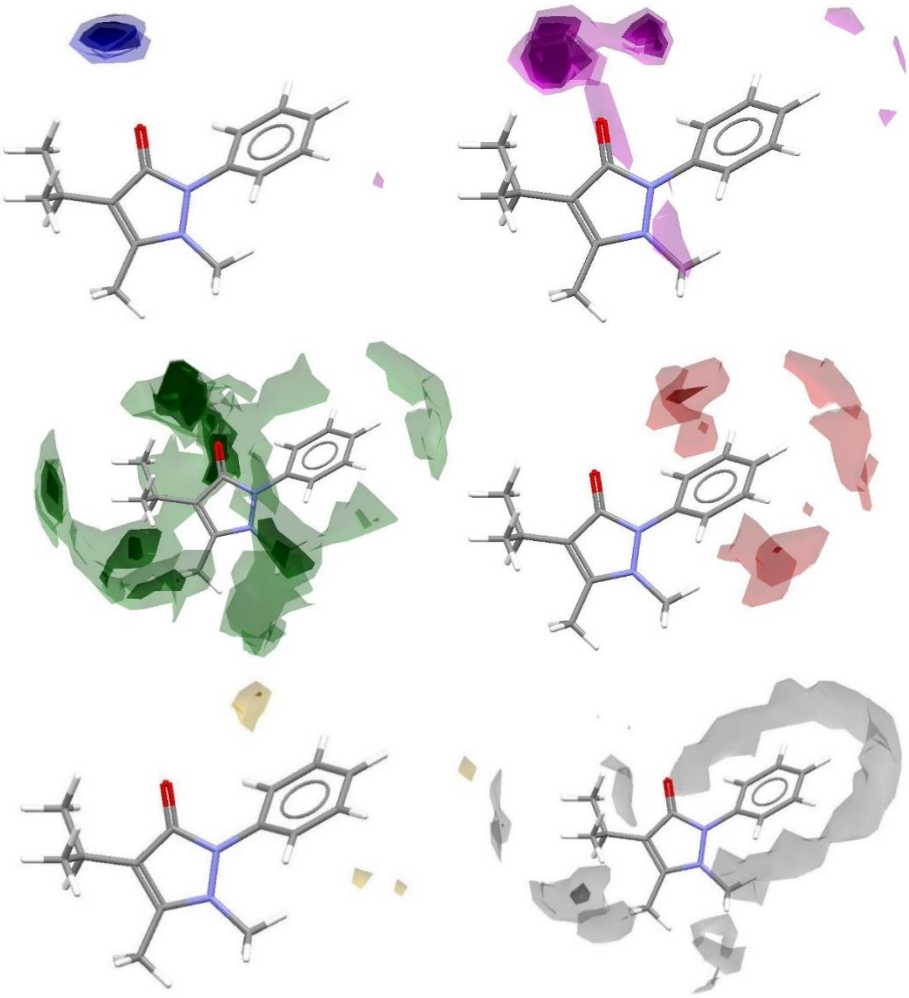

Figure A.1. Full interaction maps for PROPY with the different probes, separated by probe type to show all areas of potential interaction for a specific functional group. Top left, N–H (uncharged) blue; top right, O–H (alcohol) magenta; middle left, water green; middle right, aromatic C–H red; bottom left; methyl carbon yellow and bottom right C=O grey.

In addition, hotspots, indicating the most likely positions of functional groups can be identified. These are shown in Figure A.2 with two orientations of PROPY.

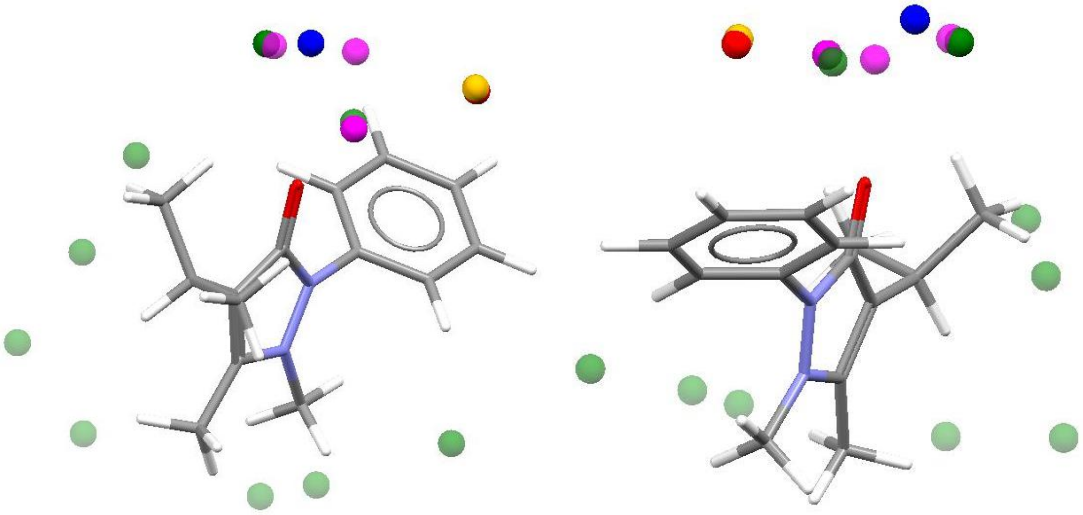

Figure A.2. Location of hotspots for the different probes from the full interaction mapping of PROPY, in two orientations. Blue, N–H (uncharged); magenta, O–H (alcohol); green, water; red, aromatic C–H; yellow methyl carbon. Note there is no hotspot for C=O (grey).

A.1.2 Specific Contact Searching

Details are given in Chapter 4 and the Supplementary Document and Files.

A.2 Co-Former Selection

A selection of co-formers were tested in initial screening experiments using solvent drop and neat grinding techniques. These are listed in Table A.1. Bold, red font indicates a new co-crystal was formed.

Table A.1. List of co-formers used in PROPY experimental work. Compounds in bold red produced a new co-crystal.

Co-Formers Tested Experimentally			
2,4,6-Triaminopyrimidine	Ascorbic acid	L-Alanine	Propionamide
~~**2,5-Dihydroxybenzoic acid (gentisic acid)**~~	Aspartame	L-Arginine	Propylparaben
2-Amino-3,5-dibromobenzoic acid	Aspirin	L-Glutamine	Pyrazinecarboxamide
2-Amino-5-bromopyrimidine	Benzamide	L-Tartaric acid	Pyridoxine
2-Aminopyridine	Benzoic Acid	L-Threonine	~~Pyrogallol~~
2-Aminopyrimidine	Caffeine	~~Maleic acid~~	~~Resorcinol~~
2-Ethoxybenzamide	Caprolactam	Malonic acid	Saccharin
2-Picolinic acid	Carbemazapine	m-Coumaric acid (trans-3-hydroxycinnamic acid)	Salbutamol
~~**3,5-Dihydroxybenzoic acid**~~	~~Citric Acid~~	Melamine	Salicylamide
3,5-Dinitrobenzoic acid	Cytosine	**Methylparaben**	Salicylhydroxamic acid
3-Aminobenzoic acid	Dacarbazine	Myo-inositol	~~salicylic acid~~
~~3-Ethynylpyridine~~	D-Methionine	Nalidixic acid	Sarcosine
~~3-Hydroxybenzoic acid~~	~~Ethylmalonic acid~~	N-cyclohexylsulfamic acid	Sebacic acid
3-Nitrobenzeneboronic acid	~~Ethylparaben~~	Nicotinamide	Suberic acid
4,5-Dichlorophthalic acid	Flufenamic acid	Nicotinic acid	Succinic acid
4-Aminobenzamide	**Fumaric acid**	Orcinol	Sulfadiazine

Co-Formers Tested Experimentally			
4-Aminobenzoic acid	Gallic acid	Orotic acid	Sulfamic acid
4-Chloro-3,5-dinitrobenzoic acid ?	(γ)-Glycine	~~Oxalic acid~~	Sulfathiazole
4-Chlorobenzeneboronic acid	~~Glutaric acid~~	Palmitic acid	Taurine
4-Hydroxybenzamide	Hippuric acid	Pamoic acid	Terephthalic acid
4-Hydroxybenzoic acid	**Hydroquinone**	Paracetamol	Theophylline
5-Aminosalicylic acid	Hydroxyurea	p-Coumaric acid (trans-4-hydroxycinnamic acid)	Thymine
5-Fluorouracil	Ibuprofen	**Phloroglucinol**	Tolfenamic acid
Acetazolamide	~~Indole-3-acetic acid~~	Phthalic acid	Uracil
Adenine	Isoniazid	Picolinamide	Urea
Adipamide	Isonicotinamide	Piperazine	Valpromide (2,2-Di-n-propylacetamide)
Adipic acid	Isonicotinic acid	Piracetam	Vanillic acid
Aminomethanesulfonic acid			

*strikethrough text indicates samples which failed in grinding, producing either a sticky paste or liquid in all experiment types (solvent drop, dry and manual grinding).

A.3 PXRD Patterns for Screening by Grinding

A.3.1 Successful Combinations of PROPY and Co-Former

Example X-ray powder patterns of the material produced from grinding are shown in Figures A.3 to A.14. The combinations of PROPY and co-former successful in producing a new co-crystal observed from grinding and suitable crystals afforded for structure solution are depicted in Figures A.3 to A.8.

A.3.1.1 PROPY-45DClPA

The PXRD pattern of the material obtained from grinding is compared to that of the parent materials (PROPY and 45DClPA) in Figure A.3. Also shown are the simulated pattern obtained from the solved crystal structure and experimental PXRD pattern of the bulk material from the solution crystallisation that afforded the crystal used in structure solution. Grinding did not result in complete conversion to a new form. Parent material peaks are still visible along with the new peaks indicating a new form is likely. The solution experiment produced complete conversion to the co-crystal; the powder pattern from the bulk experimental material is analogous to that simulated from the crystal structure.

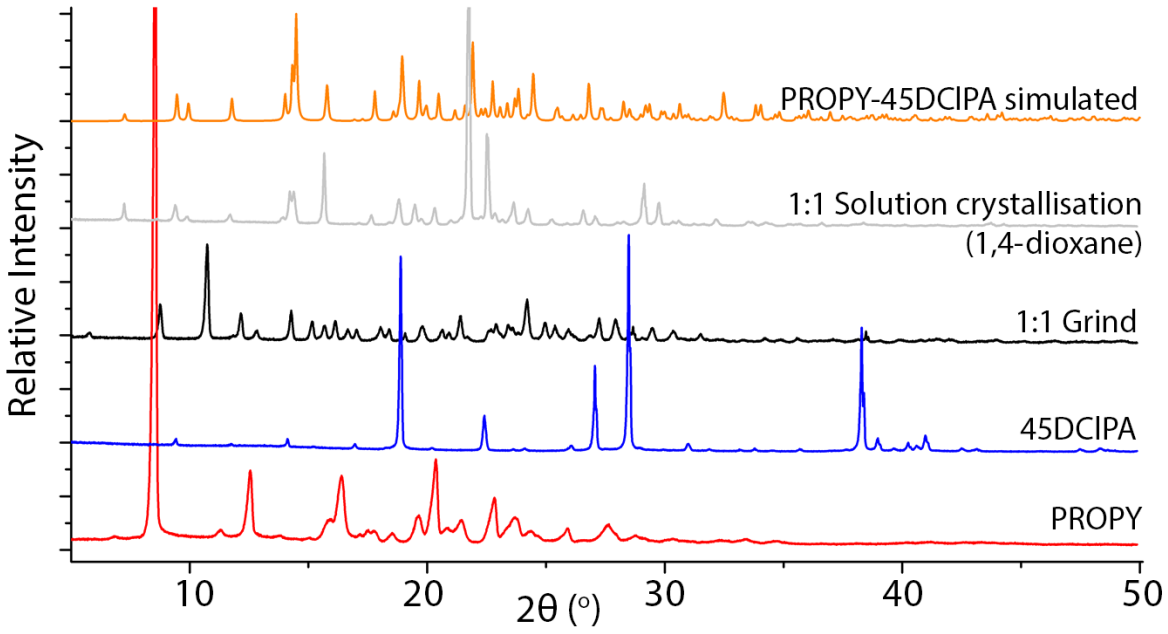

Figure A.3. PXRD pattern for 1:1 grind of PROPY with 45DClPA compared to the simulated pattern from the crystal structure obtained, and bulk material from the solution crystallisation experiment.

A.3.1.2 PROPY-4HBA

The 1:1 grinding material powder pattern and that simulated from the experimental crystal structure are depicted in Figure A.4 and show very good comparisons. Grinding afforded the co-crystal produced in solution co-crystallisation experiments, with a good conversion.

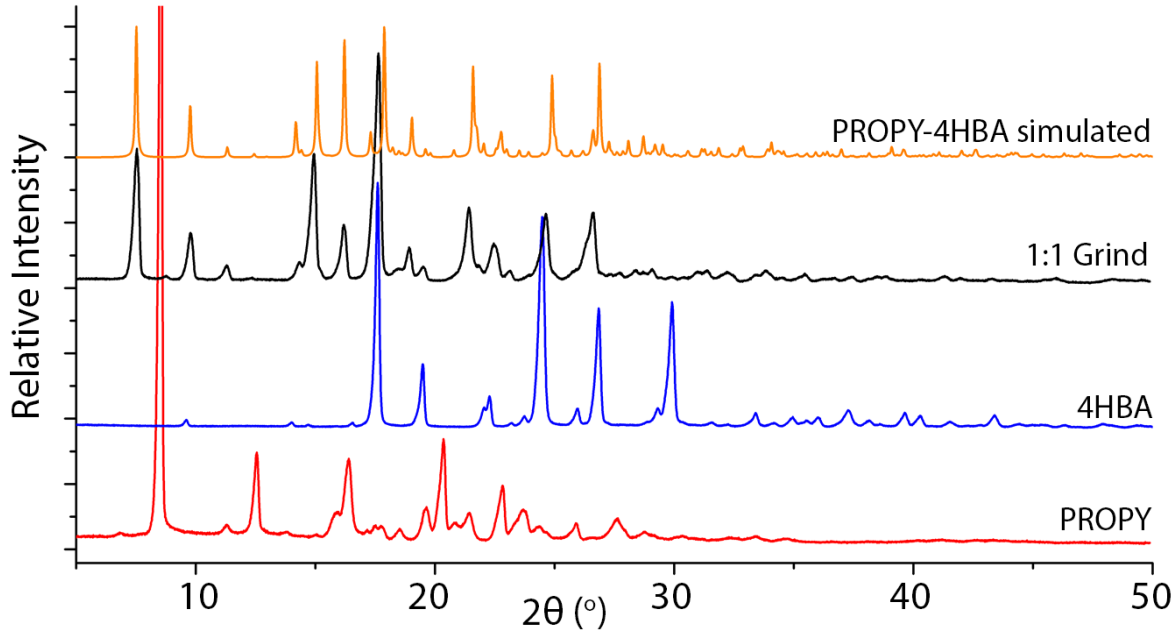

Figure A.4. PXRD pattern for 1:1 grind of PROPY with 4HBA compared to the simulated pattern from the crystal structure obtained.

A.3.1.3 PROPY-FA

Figure A.5 shows the powder pattern obtained from the 1:1 grind of PROPY and FA and that simulated from the experimetnal crytal structure. It can be seen that the 1:1 ratio produced the 2:1 experimental structure as the two patterns are comparable. Some residual FA peaks are also seen in the pattern of the grinding material as a result of the ratio and excess FA present for producing the co-crystal.

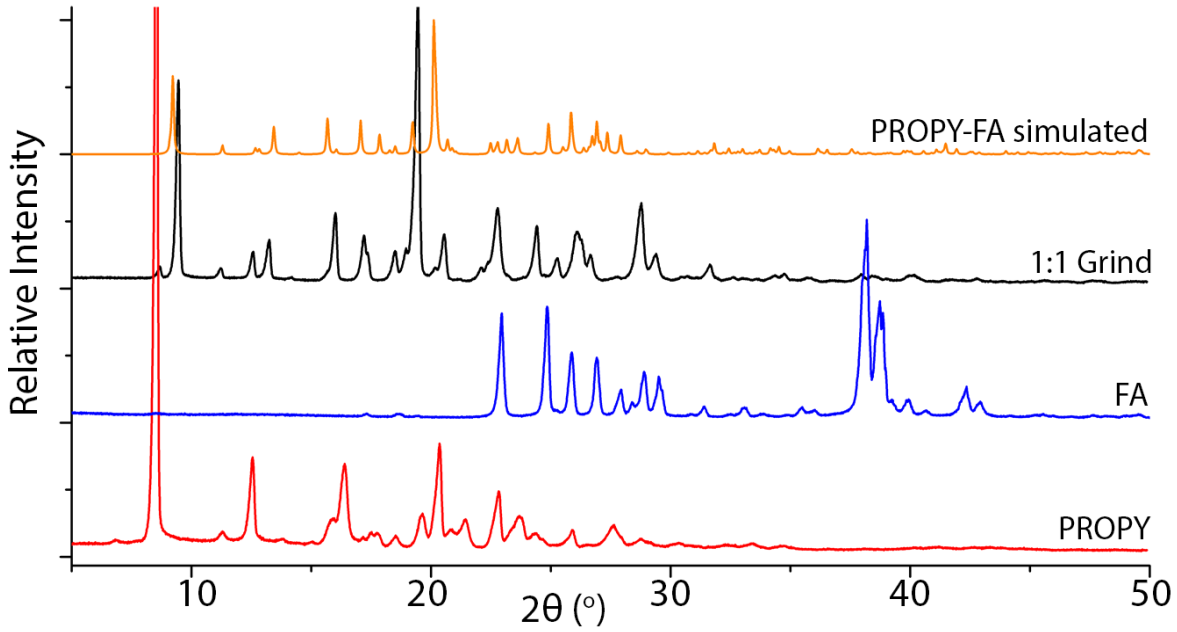

Figure A.5. PXRD pattern for 1:1 grind of PROPY with FA compared to the simulated pattern from the crystal structure obtained.

A.3.1.4 PROPY-HQ

Two grinding experiments with differing stoichiometric ratios, along with the experimentally-determined crystal structure are compared in Figure A.6. The crystal structure exhibits a 1:2 ratio, both grinding experiments producing this material however the 2:1 ratio grind gives a more complete conversion.

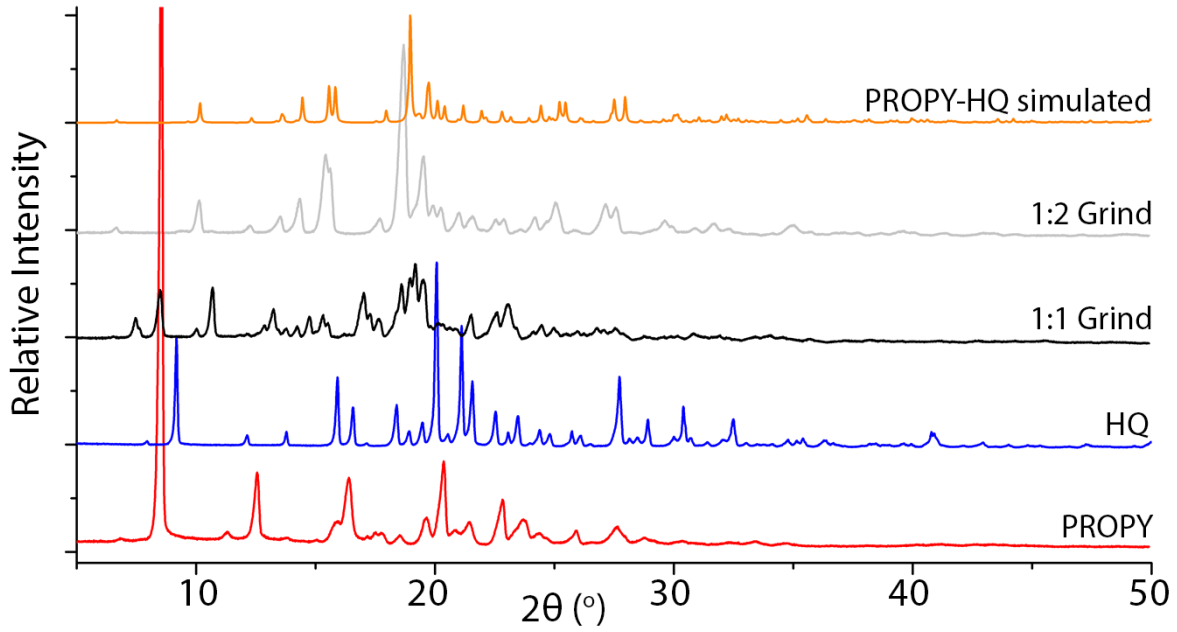

Figure A.6. PXRD pattern for 1:1 and 1:2 grinds of PROPY with HQ compared to the simulated pattern from the crystal structure (1:2) obtained.

A.3.1.5 PROPY-MPAR

The 1:1 grinding experiment and simulated pattern from the experimental crystal structure are depicted in Figure A.7. There is a good comparison between the two showing that grinding afforded the same material as the solution co-crystallisation experiments.

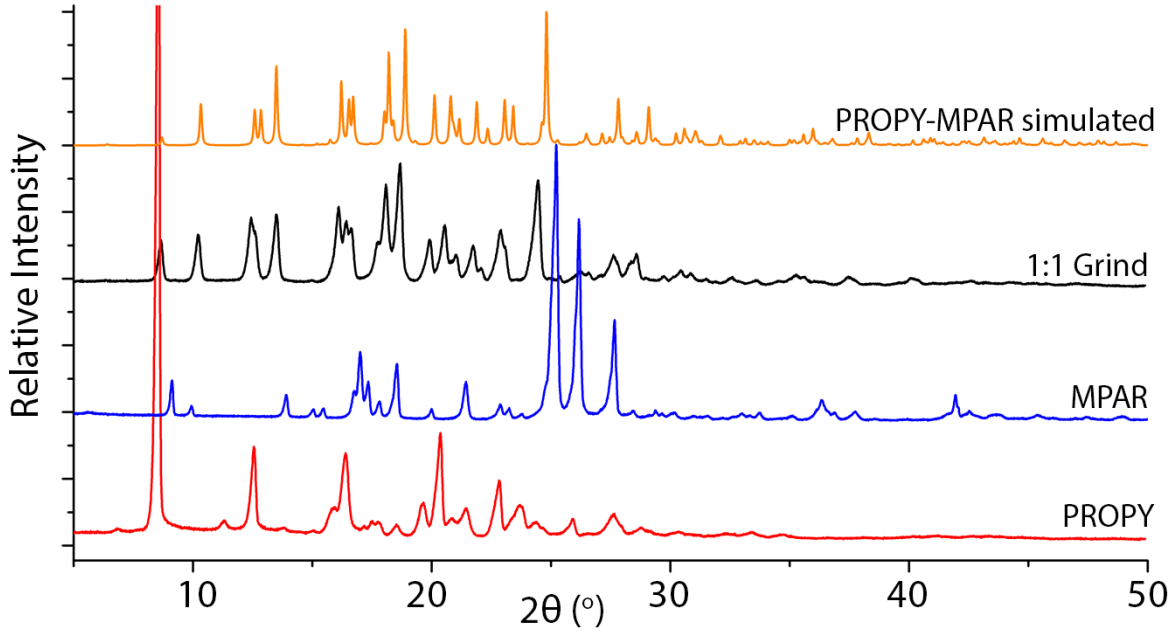

Figure A.7. PXRD pattern for 1:1 grind of PROPY with MPAR compared to the simulated pattern from the crystal structure obtained.

A.3.1.6 PROPY-PGL

Figure A.8 shows the same patterns for PROPY-PGL combinations. The crystal structure indicated an acetonitrile solvate structure however only a small amount of MeOH solvent was used in grinding. The pattern from the 1:1 grinding material shows similarities to the acetonitrile solvate crystal structure however some parent material reference peaks are also observed. This pattern indicated that a new material was likely and hence directed the subsequent solution crystallisation experiments. No MeOH solvate was observed from solution attempts, indicating that the MeOH solvent in grinding may encourage co-crystal formation with void spaces, however the solvent does not fit within these, or form favourable interactions.

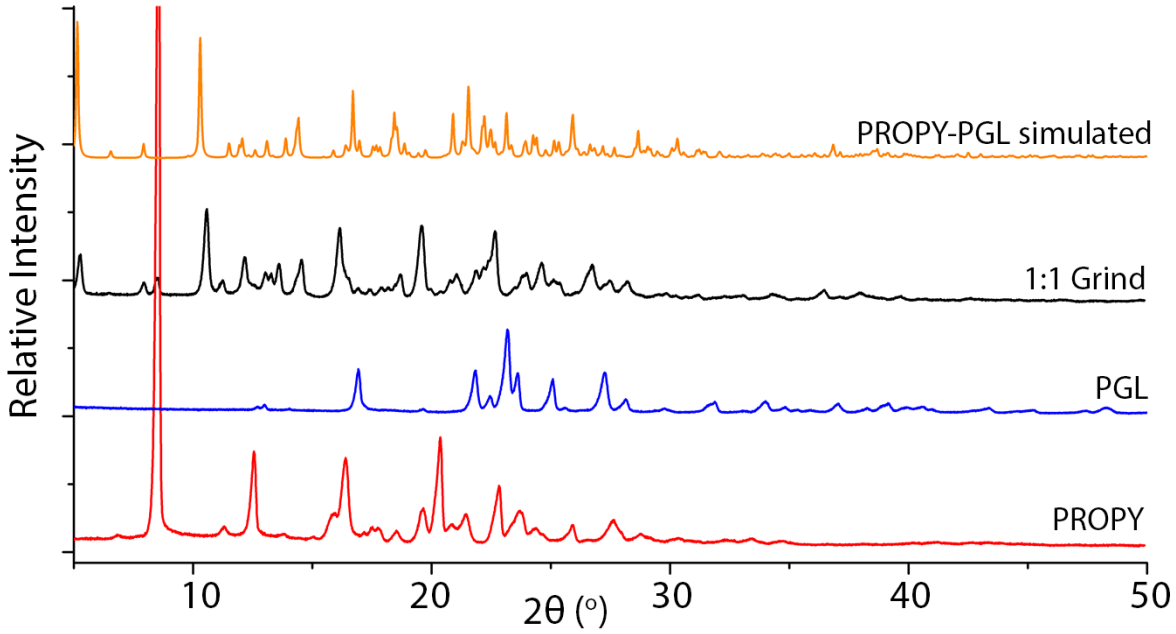

Figure A.8. PXRD pattern for 1:1 grind of PROPY with PGL compared to the simulated pattern from the crystal structure obtained.

A.3.2 Promising Combinations of PROPY and Co-Former

Figures A.9 to A.14 indicate combinations which showed promise for a new material from screening by grinding. No single crystals were produced to allow structure solution.

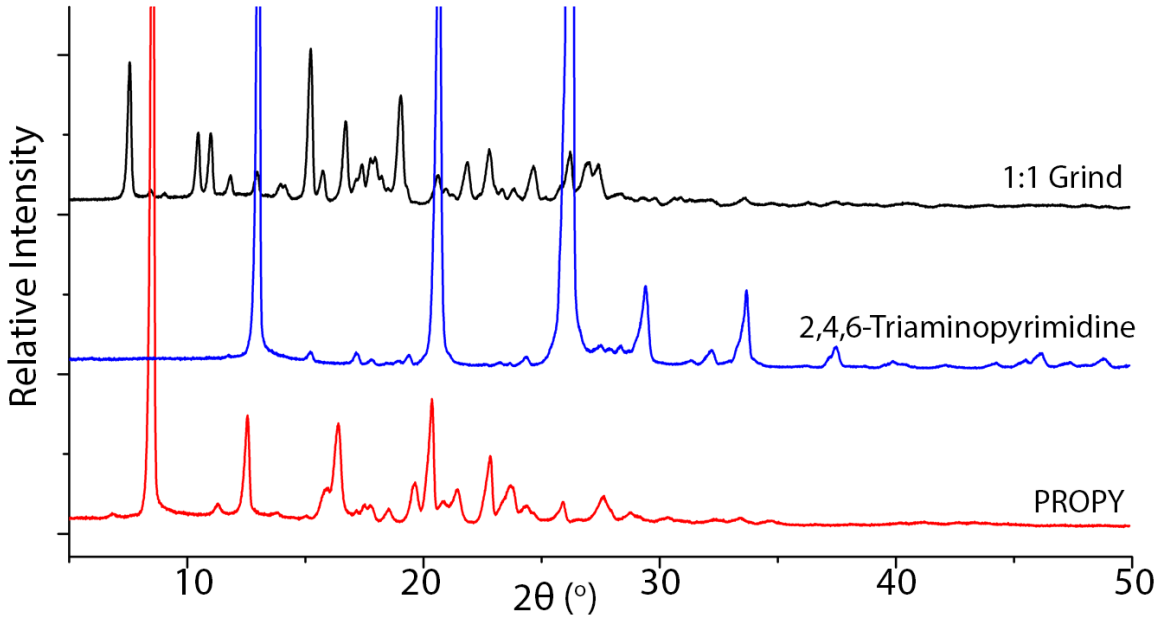

Figure A.9. PXRD pattern for 1:1 grind of PROPY with 2,4,6-triaminopyrimidine.

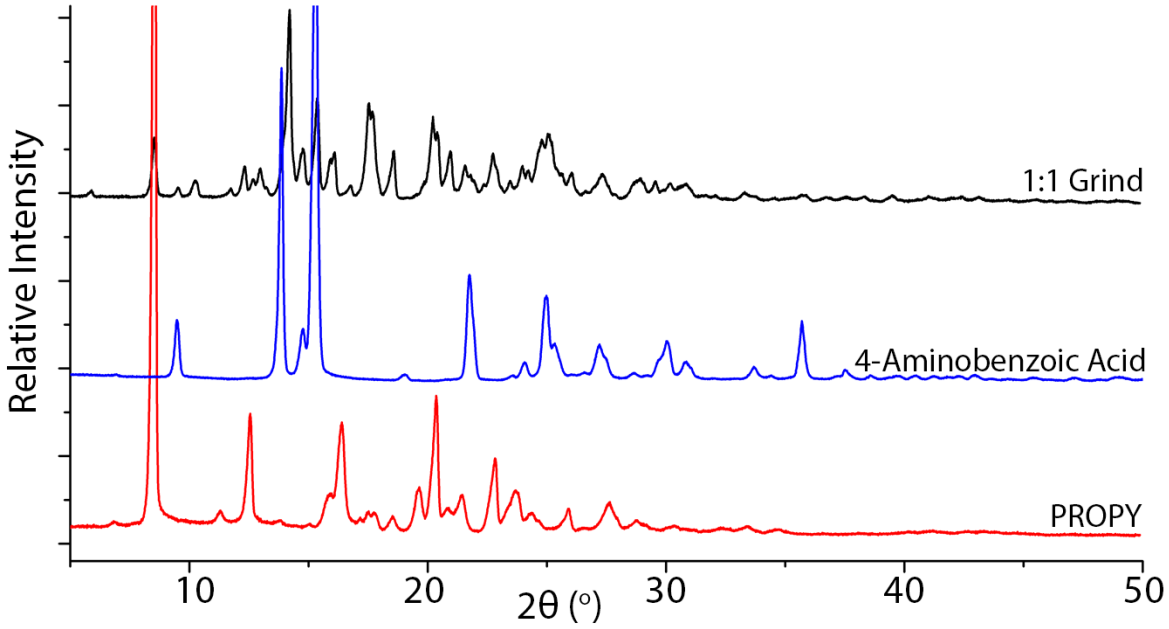

Figure A.10. PXRD pattern for 1:1 grind of PROPY with 4-aminobenzoic acid.

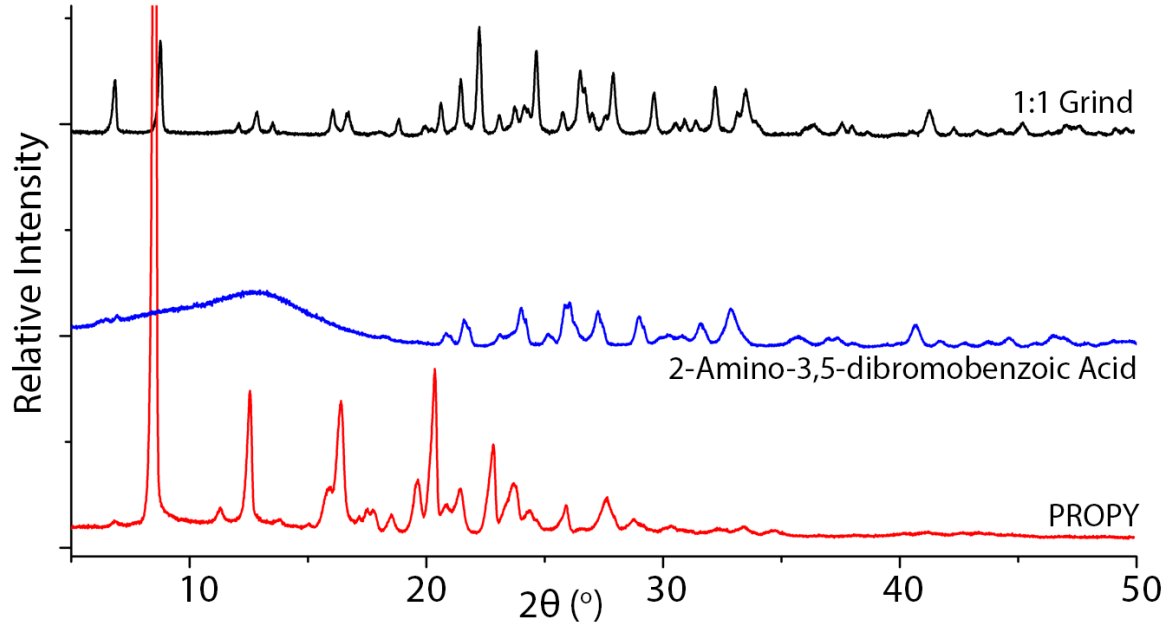

Figure A.11. PXRD pattern for 1:1 grind of PROPY with 2-amino-3,5-dibromobenzoic acid.

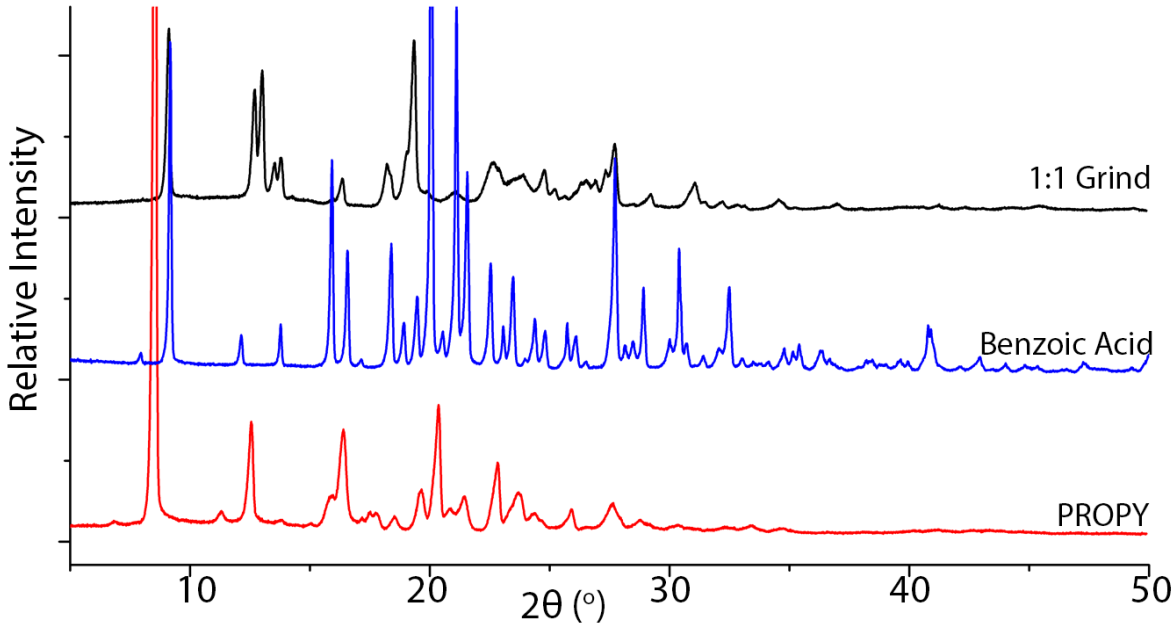

Figure A.12. PXRD pattern for 1:1 grind of PROPY with benzoic acid.

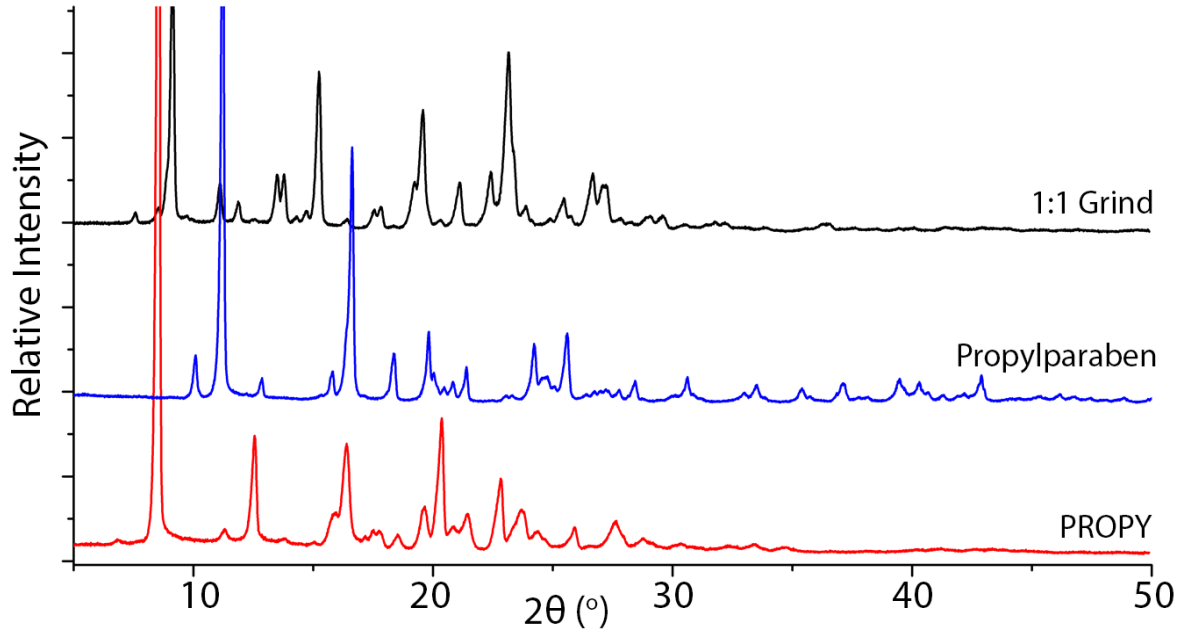

Figure A.13. PXRD pattern for 1:1 grind of PROPY with propylparaben.

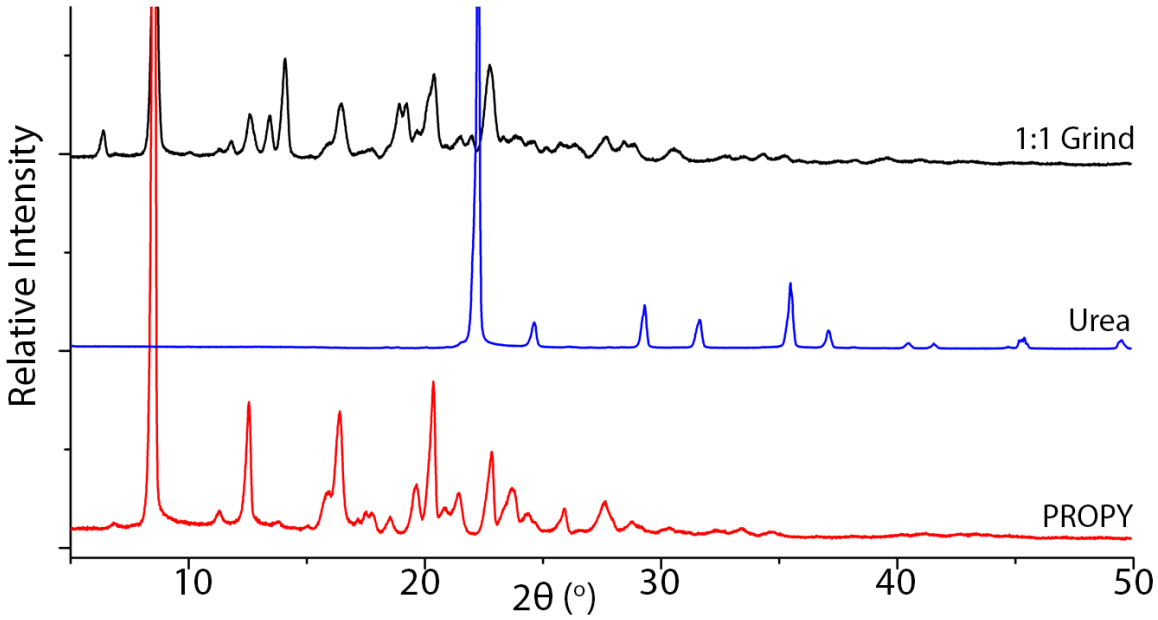

Figure A.14. PXRD pattern for 1:1 grind of PROPY with urea.

A.4 QSAR Molecular Complementarity Predictions-PROPY

Related supplementary documents

- Co-former search BAQJEK (.xls)
- QSAR co-crystal predictions search results (.xls)

Table A.2 shows the results from the QSAR molecular descriptor prediction approach applied to PROPY and a selection of co-formers. Also indicated are observations from experimental trials.

Table A.2. QSAR molecular complementarity predictions applied to PROPY and a selection of co-formers compared to experimental observations. No indication denotes the PXRD resembled either parent material or a physical mixture, possible indication denotes some changes were observed which could be indicative of a new form and blank 'experimental observation' showed no experimental trials were attempted.

Co-Former	Prediction	Experimental Observations
(-)-Camphorsulfonic acid	Yes	
(+)-Camphoric_acid	Yes	
1-Hydroxyethylidene-1,1-diphosphonic acid	No	
2-Amino-5-methylbenzoic acid	Yes	
3,5-Dihydroxybenzoic acid	Yes	Co-crystal
3-Methylpyridine	Yes	
4,5-Dichlorophthalic acid	No	Co-crystal
4-Acetamidobenzoic acid	Yes	
4-Aminobenzoic acid	Yes	Possible indication
4-Hydroxybenzoic acid	Yes	Co-crystal
Acesulfame	No	
Acetic acid	No	

Co-Former	Prediction	Experimental Observations
Acetophenone oxime	Yes	
Acetylenedicarboxylic acid	No	
Adipic acid	Yes	No indication
Alitame	Yes	
Apigenin	Yes	
Azelaic acid	Yes	
Benzoic acid	Yes	Possible indication
Biotin	Yes	
Caprolactam	No	No indication
Capsaicin	Yes	
Citric acid	No	Grinding unsuccessful
D-Alanine	No	No indication (L-)
D-Glucuronic acid	No	
D-Pantothenol	Yes	
EDTA	No	
Ethylparaben	Yes	Grinding failed
Folic acid	Yes	
Fumaric acid	No	Co-crystal
Gentisic acid (25DHBA)	Yes	Co-crystal
Glutaric acid	Yes	
Glycine	No	No indication
Glycolic acid	No	
Hesperetin	Yes	
Hippuric acid	Yes	No indication
Holic acid	Yes	

Co-Former	Prediction	Experimental Observations
Hydrocinnamic acid	Yes	
Hydroquinone	Yes	Co-crystal
Imidazole	Yes	
Isonicotinamide	Yes	No indication
Ketoglutaric acid	No	
Lactobionic acid	No	
Lactose	No	
L-Arginine	No	No indication
L-Aspartic acid	No	
L-Glutamic acid	No	
L-Glutamine	No	
L-Glutathione	Yes	
L-Lactic acid	No	
L-Leucine	Yes	
L-Mandelic acid	Yes	
L-Methionine	Yes	No indication (D-)
L-Phenylalanine	Yes	
L-Proline	Yes	
L-Serine	No	
L-Tartaric acid	No	No indication
L-Tryptophan	Yes	
L-Tyrosine	Yes	
Maleic acid	No	Grinding unsuccessful
Malic acid	No	
Malonic acid	No	Possible indication

Co-Former	Prediction	Experimental Observations
Maltitol	No	
Mannitol	No	
Methanesulfonic acid	No	
Methylparaben	Yes	Co-crystal
Monobutyrin	Yes	
N-ethylacetamide	Yes	
Nicotinamide	Yes	No indication
Oxalic acid	No	Grinding unsuccessful
Parodic acid	Yes	No indication
Phloroglucinol	No	Co-crystal
Phthalimido	No	
Pimelic acid	Yes	
Piperazine	Yes	No indication
Propylparaben	Yes	Possible indication
Pyrazine	Yes	
Riboflavin	Yes	
Saccharin	Yes	No indication
Sorbic acid	Yes	
Suberic acid	Yes	No indication
Succinic acid	No	No indication
t-Butylamine	No	
t-butylhydroxyanisole	Yes	
Theophylline	Yes	No indication
Thymidine	Yes	
Triphenylacetic acid	No	

Co-Former	Prediction	Experimental Observations
Urea	No	Possible indication
Xanthine	No	

A.5 Crystal Structure Tables

Table A.3 displays the statistics for the crystal structures of the PROPY co-crystals. All structures are published in the CSD: CCDC 1504450−1504457. CIFs are provided as supplementary electronic data to this thesis or can be obtained free of charge from www.ccdc.cam.ac.uk/data_request/cif, or by emailing data_request@ccdc.cam.ac.uk, or by contacting The Cambridge Crystallographic Data Centre, 12 Union Road, Cambridge CB2 1EZ, UK.

Table A.3. Crystal structure information for PROPY co-crystals.

	PROPY-25DHBA 2:1	**PROPY-35DHBA 1:1**	**PROPY-45DClPA 1:1**	**PROPY-4HBA 1:1**	**PROPY-FA 1:0.5**	**PROPY-HQ 1:2**	**PROPY-MPAR 1:1**	**PROPY-PGL·0.5ACN 1:1:0.5 solvate**
Chemical Formula	$2(C_{14}H_{18}N_2O)\cdot C_7H_6O_4$*	$C_{14}H_{18}N_2O\cdot C_7H_6O_4$	$C_{14}H_{18}N_2O\cdot C_8H_4Cl_2O_4$	$C_{14}H_{18}N_2O\cdot C_7H_6O_3$	$C_{14}H_{18}N_2O\cdot 0.5(C_4H_4O4)$	$C_{14}H_{18}N_2O\cdot 2(C_6H_6O_2)$	$C_{14}H_{18}N_2O\cdot C_8H_8O_3$	$2(C_{14}H_{18}N_2O)\cdot 2(C_6H_6O_3)\cdot C_2H_3N$
*M*r	614.72	384.42	465.31	368.42	288.34	450.52	382.45	753.87
Density /gcm^{-1}	1.072	1.269	1.381	1.272	1.263	1.253	11.250	1.241
Crystal size /mm	0.150 x 0.150 x 0.050	0.172 x 0.128 x 0.075	0.209 x 0.172 x 0.035	0.709 x 0.199 x 0.148	0.214 x 0.158 x 0.052	0.314 x 0.119 x 0.053	0.403 x 0.121 x 0.066	0.281 x 0.209 x 0.029
Crystal colour, morphology	Colourless, block	Colourless, block	Colourless, plate	Colourless, block	Colourless, plate	Colourless, block	Colourless, block	Colourless, plate
Crystal system	Monoclinic	Triclinic	Orthorhombic	Monoclinic	Triclinic	Triclinic	Orthorhombic	Monoclinic

	PROPY-25DHBA 2:1	**PROPY-35DHBA 1:1**	**PROPY-45DClPA 1:1**	**PROPY-4HBA 1:1**	**PROPY-FA 1:0.5**	**PROPY-HQ 1:2**	**PROPY-MPAR 1:1**	**PROPY-PGL·0.5ACN 1:1:0.5 solvate**
Space group	$P2_1/c$	$P\overline{1}$	*Pbca*	$P2_1/c$	$P\overline{1}$	$P\overline{1}$	$P2_12_12_1$	$P2_1/n$
a /Å	14.8814(3)	15.1402(4)	14.5793(7)	6.88063(17)	8.1473(3)	9.1280(3)	27.5437(10)	8.0128(2)
b /Å	18.5757(3)	16.0735(5)	12.6245(7)	15.4557(3)	9.7330(5)	9.9789(3)	10.9248(7)	14.6656(5)
c /Å	14.1318(3)	18.5380(5)	24.3122(15)	18.2615(5)	9.9869(5)	14.5941(3)	6.7514(3)	34.4109(10)
α /°	90.00	106.008(3)	90.00	90.00	85.183(4)	109.581(2)	90.00	90.00
β /°	102.9086(17)	107.361(3)	90.00	97.800(2)	76.468(4)	101.738(3)	90.00	93.607(3)
γ /°	90.00	97.595(3)	90.00	90.00	80.200(4)	98.211(3)	90.00	90.00
Cell Volume /Å^3	3807.77(12)	4024.2(2)	4474.8(4)	1924.05(8)	757.91(6)	1193.77(6)	2031.57(18)	4035.7(2)
Z	4	8	8	4	2	2	4	4
Data Collection								
Diffractometer	Rigaku FRE+	Agilent Technologies, Dual Source Supernova	Agilent Technologies, Dual Source Supernova	Agilent Technologies, Dual Source Supernova	Agilent Technologies, Dual Source Supernova	Agilent Technologies, Dual Source Supernova	Agilent Technologies, Dual Source Supernova	Agilent Technologies, Dual Source Supernova

	PROPY-25DHBA 2:1	PROPY-35DHBA 1:1	PROPY-45DClPA 1:1	PROPY-4HBA 1:1	PROPY-FA 1:0.5	PROPY-HQ 1:2	PROPY-MPAR 1:1	PROPY-PGL·0.5ACN 1:1:0.5 solvate
Temperature /K	100	100	100	100	100	100	100	100
Radiation Type	Mo K\α	Mo K\α	Mo K\α	Mo K\α	Mo K\α	Mo K\α	Mo K\α	Mo K\α
Wavelength, λ, /Å	0.71075	0.71073	0.71073	0.71073	0.71073	0.71073	0.71073	0.71073
No. measured reflections	36936	52164	49853	19926	11735	16584	14763	28247
No. unique reflections	8649	17913	5124	4388	3468	5445	4666	9225
R_{int}	0.0239	0.0379	0.0906	0.0278	0.0334	0.0345	0.0373	0.0415
Completeness /%	99.06	97.09	99.78	99.91	99.94	99.89	99.78	99.51
Refinement								
GOF, S	1.048	1.076	1.095	1.055	1.079	1.058	1.124	1.120
R_1 (I > 2σ(F))	0.0396	0.0535	0.0587	0.0373	0.0436	0.0444	0.0521	0.0555
R_1 (all data)	0.0460	0.0755	0.0872	0.0413	0.0503	0.0543	0.0557	0.0703
*w*R (I > 2σ(F))	0.1007	0.1096	0.1070	0.0933	0.1095	0.1017	0.1284	0.1216

	PROPY-25DHBA	**PROPY-35DHBA**	**PROPY-45DClPA**	**PROPY-4HBA**	**PROPY-FA**	**PROPY-HQ**	**PROPY-MPAR**	**PROPY-PGL·0.5ACN**
	2:1	**1:1**	**1:1**	**1:1**	**1:0.5**	**1:2**	**1:1**	**1:1:0.5 solvate**
*w*R	0.1048	0.1182	0.1163	0.0959	0.1135	0.1069	0.1308	0.1276
GoF	1.048	1.076	1.095	1.055	1.079	1.058	1.124	1.120

* also contains 1 molecule of disordered 1,4-dioxane solvent ($C_4H_8O_2$)

A.6 Hydrogen Bonding Interactions

Table A.4. Neutron normalised hydrogen bonding interactions present in crystal structures of the Co-crystals of PROPY. D = Donor atom, A = Acceptor atom.

Sample	D-H···A	H···A /Å	D···A /Å	D-H···A /°	Symmetry Code
PROPY-25DHBA	O(41)-H(41)···O(21)	1.59	2.5487(16)	164	
	O(43)-H(43)···O(42)	1.72	2.6173(19)	150	
	O(44)-H(44)···O(1)	1.65	2.6270(14)	169	
	C(1)-H(1B)···O(44)	2.48	3.5498(18)	168	1-*x*, 1-*y*, 1-*z*
	C(45)-H(45)···O(1)	2.40	3.176(3)	127	
PROPY-35DHBA	O(81)-H(81)···O(82)	1.69	2.6642(18)	173	-*x*, -*y*, 2-*z*
	O(83)-H(83)···O(21)	1.67	2.6466(18)	176	1-*x*, 1-*y*, 1-*z*
	O(84)-H(84)···O(1)	1.65	2.629(2)	175	-*x*, -*y*, 1-*z*
	O(91)-H(91)···O(102)	1.64	2.627(2)	179	
	O(92)-H(92)···O(101)	1.66	2.641(2)	174	
	O(93)-H(93)···O(41)	1.72	2.6994(18)	171	
	O(94)-H(94)···O(21)	1.75	2.7310(19)	177	*x*, -1+*y*, *z*
	O(101)-H(101)···O(92)	1.67	2.641(2)	170	
	O(102)-H(102)···O(91)	1.65	2.627(2)	169	
	O(103)-H(103)···O(1)	1.76	2.7410(19)	175	1-*x*, -*y*, 1-*z*
	O(104)-H(104)···O(61)	1.75	2.732(2)	176	1-*x*, 1-*y*, 1-*z*
	O(111)-H(111)···O(112)	1.67	2.6557(18)	178	1-*x*, 1-*y*, -*z*
	O(113)-H(113)···O(41)	1.66	2.635(2)	173	
	O(114)-H(114)···O(61)	1.67	2.647(2)	171	

Sample	D-H···A	H···A /Å	D···A /Å	D-H···A /°	Symmetry Code
PROPY-35DHBA	C(113)-H(11A)···O(41)	2.47	3.208(2)	124	
	C(13)-H(13)···O(83)	2.49	3.411(2)	142	
	C(14)-H(14)···O(84)	2.50	3.296(2)	130	-*x*, -*y*, 1-*z*
	C(32)-H(32)···O(103)	2.42	3.333(3)	141	*x*, 1+*y*, -1+*z*
	C(47)-H(47A)···O(102)	2.44	3.513(3)	172	2-*x*, 1-*y*, 1-*z*
	C(52)-H(52)···O(104)	2.50	3.356(2)	135	*x*, *y*, -1+*z*
	C(73)-H(73)···O(113)	2.50	3.358(2)	135	1-*x*, 1-*y*, 1-*z*
	C(83)-H(83A)···O(21)	2.35	3.128(2)	127	1-*x*, 1-*y*, 1-*z*
PROPY-45DClPA	O(22)-H(22)···O(1)	1.66	2.638(2)	177	½-*x*, -½+*y*, *z*
	O(24)-H(24)···O(1)	1.60	2.575(2)	173	
	C(8)-H(8B)···O(23)	2.43	3.288(3)	135	-½+*x*, *y*, ½-*z*
	C(14)-H(14)···O(23)	2.46	3.225(3)	126	½-*x*, ½+*y*, *z*
PROPY-4HBA	O(21)-H(21)···O(22)	1.63	2.6146(12)	175	-1-x,1-y,1-z
	O(23)-H(23)···O(1)	1.69	2.6726(12)	178	
	C(7)-H(7A)···O(1)	2.35	3.4133(14)	168	1+*x*, *y*, *z*
	C(14)-H(14)···O(22)	2.27	3.2346(15)	147	1+*x*, *y*, *z*
	C(26)-H(26)···O(1)	2.46	3.2233(14)	126	

Sample	D-H···A	H···A /Å	D···A /Å	D-H···A /°	Symmetry Code
PROPY-FA	O(21)-H(21)···O(1)	1.59	2.5673(14)	170	
	C(11)-H(11)···O(22)	2.51	3.2226(18)	122	
	C(12)-H(12)···O(22)	2.49	3.3307(18)	133	
	C(13)-H(13)···O(1)	2.46	3.4821(17)	157	
PROPY-HQ	O(21)-H(21)···O(1)	1.71	2.6865(15)	172	2-*x*, -*y*, -*z*
	O(22)-H(22)···O(31)	1.68	2.6540(17)	173	1+*x* ,*y* ,*z*
	O(31)-H(31)···O(1)	1.59	2.5671(16)	175	-1+*x*, 1+*y*, *z*
	O(32)-H(32)···O(22)	1.72	2.6961(16)	172	
	C(8)-H(8B)···O(32)	2.48	3.530(2)	164	
	C(32)-H(32A)···O(21)	2.44	3.5273(19)	179	1-*x*, 1-*y*, -*z*
PROPY-MPAR	O(21)-H(21)···O(1)	1.65	2.634(3)	174	1-*x*, -½+*y*, 3/2-*z*
	C(10)-H(10)···O(22)	2.52	3.157(4)	116	1-*x*, -½+*y*, ½-*z*
	C(11)-H(11)···O(22)	2.44	3.128(4)	120	1-*x*, -½+*y*, ½-*z*
	C(12)-H(12)···O(23)	2.50	3.359(4)	136	-½+*x*, ½-*y*, 1-*z*
	C(26)-H(26)···O(1)	2.43	3.190(4)	126	1-*x*, -½+*y*, 3/2-*z*

Sample	D-H···A	H···A /Å	D···A /Å	D-H···A /°	Symmetry Code
PROPY-PGL·0.5ACN	O(41)-H(41)···O(21)	1.65	2.6270(17)	169	
	O(42)-H(42)···O(21)	1.66	2.6350(17)	168	1+*x*, *y*, *z*
	O(43)-H(43)···O(1)	1.77	2.7390(17)	169	*x*, -1+*y*, *z*
	O(51)-H(51)···O(1)	1.69	2.6690(17)	176	
	O(52)-H(52)···O(41)	1.74	2.7173(18)	170	
	O(53)-H(53)···N(61)	1.91	2.884(3)	170	
	C(30)-H(30)···O(52)	2.36	3.435(2)	172	
	C(32)-H(32)···O(42)	2.41	3.247(2)	133	3/2-*x*, ½+*y*, ½-*z*
	C(34)-H(34)···O(52)	2.33	3.401(2)	169	-1+*x*, *y*, *z*
	C(62)-H(62A)···O(51)	2.50	3.268(3)	127	1-*x*, 2-*y*, 1-*z*
	C(62)-H(62B)···O(43)	2.40	3.312(2)	141	1-*x*, 1-*y*, 1-*z*

A.7 Hirshfeld Surface Analysis

Related supplementary documents

- Hirshfeld Surfaces - Interaction graphs
- Hirshfeld surfaces - Interaction contributions analysis

A.7.1 Hirshfeld Surfaces

Hirshfeld surfaces for the PROPY component of the eight novel co-crystals and PROPY parent material are depicted in Figure A.15. showing the areas of close contacts.

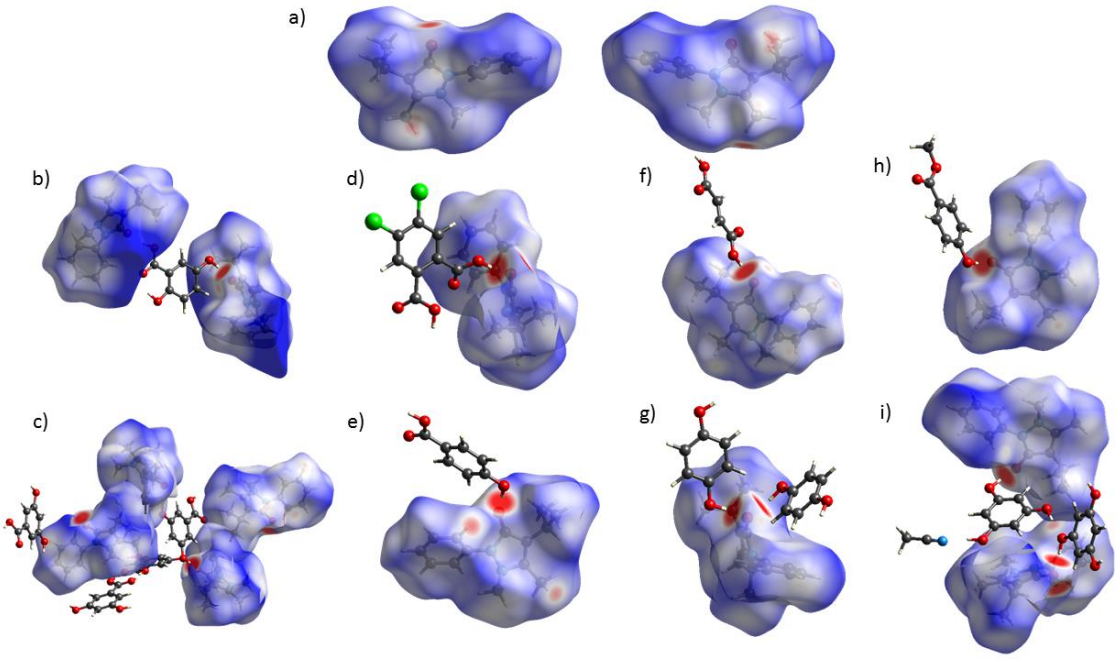

Figure A.15. Hirshfeld surface for PROPY component of all co-crystals and parent PROPY: a) PROPY (front and back), b) PROPY-25DHBA, c) PROPY-35DHBA, d) PROPY-45ClPA, e) PROPY-4HBA, f) PROPY-FA (showing all of FA molecule - 1:0.5 ratio), g) PROPY-HQ, h) PROPY-MPAR, i) PROPY-PGL·0.5ACN.

A.7.2 Fingerprint Plots

Figure A.16 shows an example fingerprint plot and the general location of the different types of contact to aid the analysis reported. The colour gradient indicates the number of contacts, from dark blue to turquoise-green as the areas of lowest to greatest density. Reciprocal contacts typically occur in symmetrically opposite locations (i.e. d_i and d_e values swapped) and homo-contacts (e.g. C···C, N···N etc.) generally occur around the centre line. H···H contacts dominate much of the fingerprint plot, in particular the central area and are not identified specifically in the example.

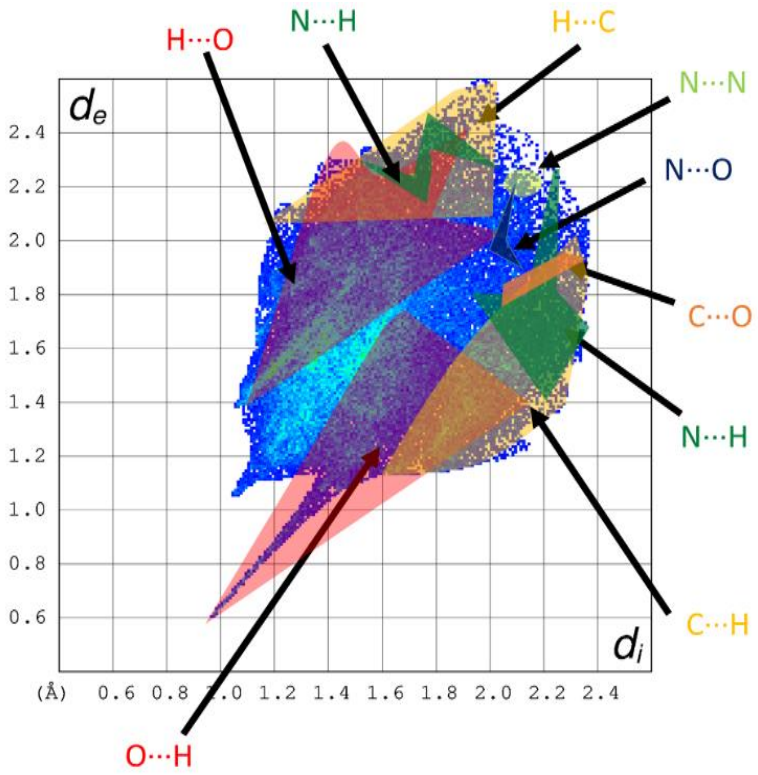

Figure A.16. Example fingerprint plot (d_i *vs.* d_e) of PROPY-FA to indicate the location of different contact types within the plot. H···H contacts cover the majority of the plot, in particular the central area and thus are not identified specifically.

Figure A.17 shows the fingerprint plots (d_i *vs.* d_e) for all eight co-crystals and parent PROPY when a single Hirshfeld surface for the entire construct is used encompassing all co-crystal components. The interactions considered are those of one set of molecules (API-co-former, or just API for the PROPY structure) with another identical set. All these plots are highly symmetrical as all contacts occurring inside the surface to outside will also occur in opposition from the reciprocal combination.

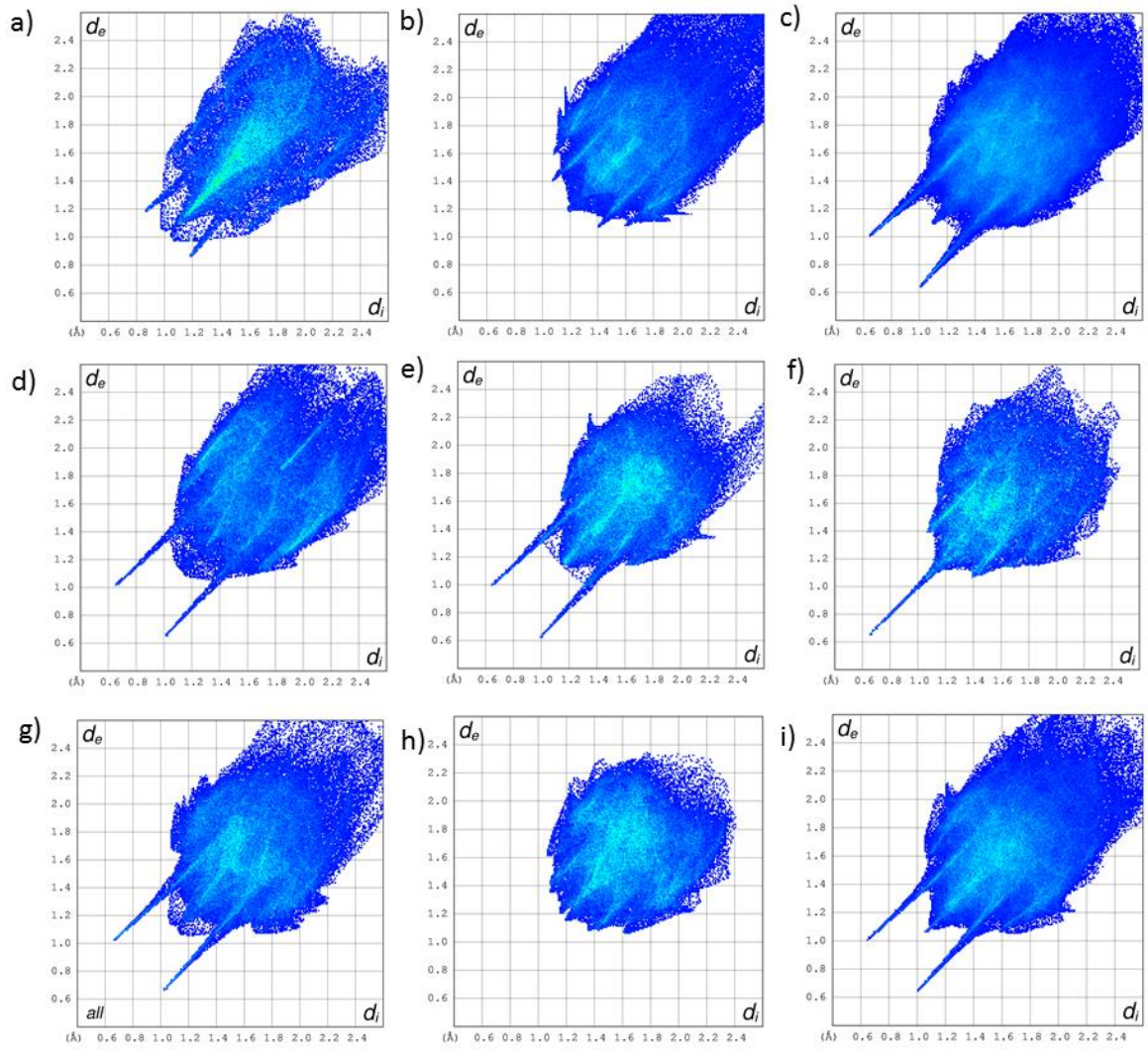

Figure A.17. Fingerprint plots (d_i *vs.* d_e) for PROPY and the eight co-crystals produced using a single Hirshfeld surface to encompass all components; a) PROPY, b) PROPY-25DHBA, c) PROPY-35DHBA, d) PROPY-45DClPA, e) PROPY-4HBA, f) PROPY-FA, g) PROPY-HQ, h) PROPY-MPAR, i) PROPY-PGL·0.5ACN.

A.7.2.1 Co-Former Plots

Similar fingerprint plots were determined for just the co-former molecules in each system, shown in Figure A.18. Few contacts to the PROPY N atoms were identified for any co-former. The greatest contributions observed were H···N in PGL (2 independent molecules), 35DHBA (2 independent molecules) and 4HBA with relative contributions to the total of 6.9, 1.5 and 1.4 % respectively. C···N contacts were also identified from 35DHBA (3 independent molecules) at 1.4 %. The other co-formers have contributions ≤ 1 % or do not exhibit that contact type.

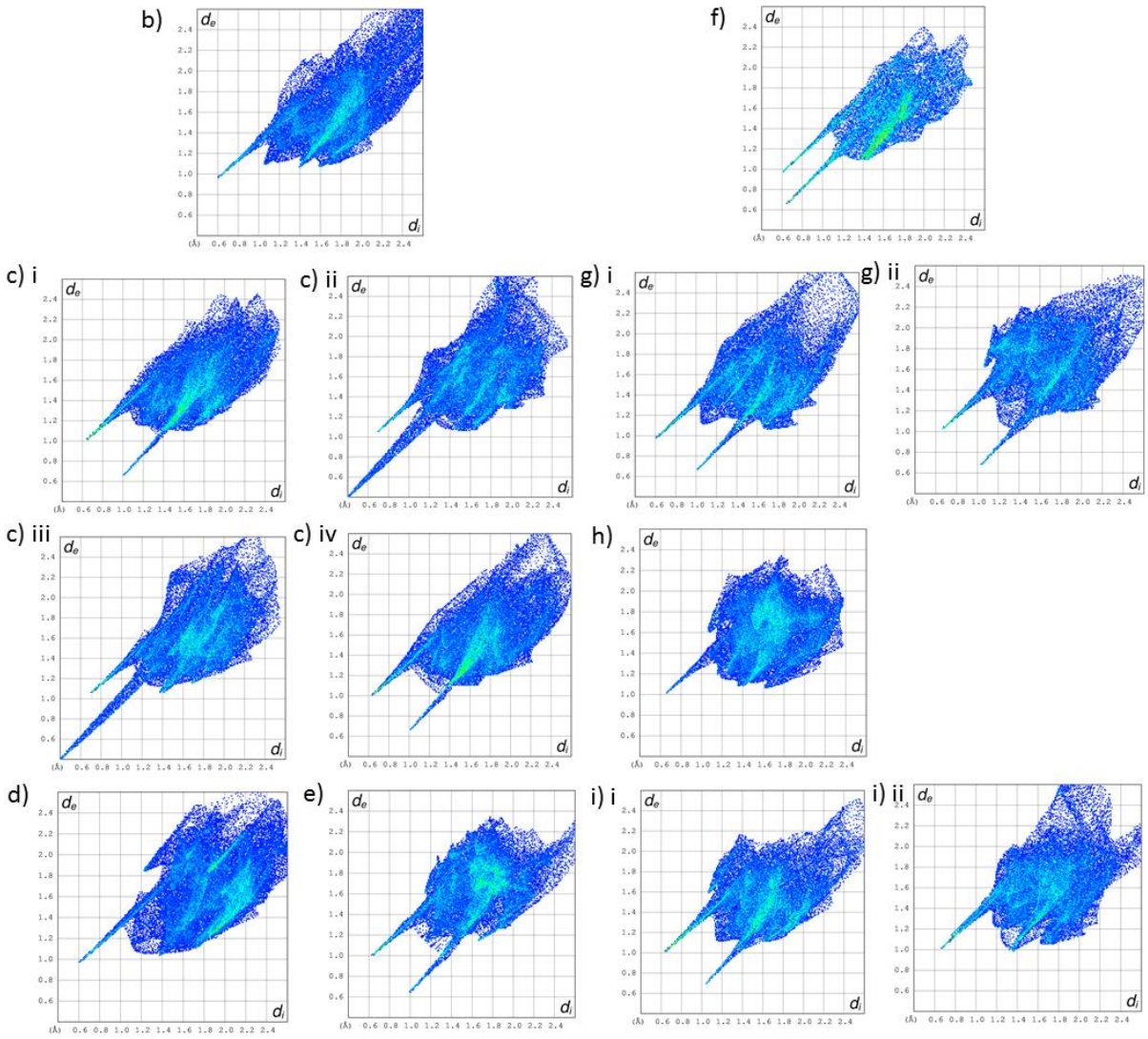

Figure A.18. Fingerprint plots (d_i *vs.* d_e) for the co-former molecules of the eight co-crystals produced. Labelling scheme retained for consistency with previous diagrams: b) PROPY-25DHBA (main component only), c) PROPY-35DHBA (4 independent 35DHBA molecules; i-iv), d) PROPY-45DClPA, e) PROPY-4HBA, f) PROPY-FA, g) PROPY-HQ (2 independent HQ molecules; i-ii), h) PROPY-MPAR, i) PROPY-PGL·0.5ACN (2 independent PGL molecules; i-ii).

25DHBA

25DHBA exhibits a tail comprised from H···O contacts with short d_i distances and marginally longer d_e. In comparison to the other co-formers many longer contacts are also present with distances up to and greater than 2.4 Å. The highest density (bright turquoise) of contacts occurs in the range 1.4···1.1 Å to 2.0···1.8 Å (d_e···d_i) consisting of mainly O···H and H···H contacts. The O···H contacts contribute almost a third (31 %) of the total contacts. This is not unsurprising due to the three co-former oxygen atoms, all of which are accessible to form intermolecular contacts.

35DHBA

Similarities between 35DHBA (ii) and (iii), and likewise (i) and (iv) can be seen. (ii) and (iii) represent the molecules which partake in the acid dimer pair and hence it would be expected that they would have similar interactions. These are dominated by the acid···acid hydrogen bonds. (i) and (iv) also form similar interactions in the crystal structure hence their fingerprint plots are also very similar. The tails correspond to O···H (lower) and H···O (upper) contacts, these regions both extending up to the top left of the plot with longer d_e than d_i distances. The two co-formers partaking in the dimer interaction display very short contact distances in some instances, arising from the proton disorder displayed over the acid···acid dimer. The main body corresponds to H···H contacts with C···H contacts located on the lower right-hand side. A small number of C···C contacts (top point) and O···O contacts (central-top) are also present.

45DClPA

The greatest proportion of contacts occurring for 45DClPA are Cl···H (23.2 %) followed by O···H and H···H (21.0 % and 17.8 % respectively). This is in contrast to the other co-formers in which H···H generally dominates followed by O···H or in some instances C···H. The contribution of H···H contacts from this co-former is less than half that observed for other structures, and the percentage of H···O contacts is also considerably less. This is due to the presence of the two chlorine atoms which partake in alternate contacts. The Cl forms contacts with four atom types, C, H, O and Cl, and these make up over a third (36.2 %) of all the contacts of 45DClPA molecules. Homoatomic Cl···Cl contacts are relatively long, with distances between 1.8-2.4 Å. These are distributed along the centre line in the fingerprint plot, towards to the top, seen in Figure A.18, d as a thin, pale turquoise line.

4HBA

The fingerprint plot for 4HBA (Figure A.18, e) is relatively symmetrical with the exception of the 'wing' protrusion formed from contacts with d_e and d_i greater than 2.0 and 2.4 Å respectively. Two tails with short d_i and d_e distances respectively are formed from O···H and H···O contacts. These can be attributed to the hydrogen bonds in the co-former acid···acid dimer and hydroxyl···carbonyl hydrogen bonds. H···H contacts account for 38.1 % of all the contacts, with 19.8 % being O···H contacts and C···H accounting for 12.3 %. In comparison to the other dihydroxybenzoic acids, 4HBA has a greater proportion of C···C and O···O contacts which are generally negligible or absent in others. This causes the proportion of other contacts to be reduced as a relative contribution to the total.

FA

FA has the greatest proportion of C···C (7.0 %) and O···H (41.6 %) of all the co-formers, and also presents one of the largest proportions of H···O (9.3 %) and H···C (5.9 %) contacts. This is due to the small size and limited number of atoms present in FA. Each has a greater contribution to the total. The fingerprint plot for FA is one of the narrowest, indicating that for a given d_i or d_e there is only a small range for the corresponding d_e or d_i. Many of the contacts have similar distances.

HQ

There are two independent molecules of HQ present both of which display similar primary hydrogen bonding interactions in the crystal structure with some differences in their other contacts. Both fingerprint plots appear relatively symmetrical however the differences in these secondary, longer and weaker contacts are seen: HQ (ii) shows the densest area of interactions (paler blue colour) further towards the top right of the plot in comparison to that observed for HQ (i), indicating longer contact distances. HQ (ii) also shows many more contacts than HQ (i) in this region which have more equal d_e and d_i values. HQ (i) has a sparser distribution of interactions in this area for long d_e and d_i values. Those present form two protrusions either side of the centre line rather than a single point or cluster as seen for HQ (ii).

Another difference is apparent in the C···H and H···C contacts. Both have similar proportions of C···H contacts (19.9 % and 19.3 %) however HQ (i) has a significantly reduced H···C contribution, (2.7 % compared to 13.1 % of (ii)). This drastic difference is compensated in the higher dominance of H···H contacts (48.5 % *vs*. 39.0 %) and O···H contacts (12.2 % *vs.* 9.8 %).

MPAR

The MPAR fingerprint plot is very compact with a small range of contact distances. The exception is the tail formed from O···H contacts. H···H contacts count for almost half of all the contacts present (49.3 %) whilst O···H and C···H contacts have an equal contribution (16.4 %). The H···C and H···O contribution are also similar (6.1 % and 7.6 % respectively). The O···H and H···O contacts are created from the three oxygen atoms of MPAR: the hydroxyl forming the primary O–H···O hydrogen bond to PROPY carbonyl, and an ester group which interacts with several different aromatic rings.

PGL

There are two independent molecules of PGL in the crystal structure each partaking in different interactions as discussed in the crystal structure analysis. The resulting fingerprint plots, whilst displaying similarities in the central area with respect to shape and contact distances, are quite

different on the periphery in their short and long contacts. PGL (i) is almost comparable to 4HBA and displays similarities to HQ and 35DHBA 4 as two tails comprised of the O···H and H···O interactions of the hydroxyl functionalities are formed at short contact distances. The interaction contributions of the two molecules are similar, the greatest difference seen in H···O contacts at 12.2 % (i) and 7.8 % (ii). PGL (ii) also displays two contact types that are not seen in (i), C···N and O···N. These occur due to the hydrogen bond formed to the acetonitrile solvent molecule.

A.7.3 Interaction Analysis

Using the fingerprint plots in Crystal Explorer, the contribution of each interaction type can be determined for a given Hirshfeld surface (here taking each molecule as an individual entity and looking at the contacts occurring to and from it within the crystal structure). The contributions for the PROPY molecule(s) in each system are shown in Figure A.19. Those with multiple independent molecules of PROPY are analysed for each PROPY individually.

H···H contacts dominate the PROPY molecules in all systems. The greatest contribution is seen for PROPY as there are few other atoms accessible to form contacts whilst the smallest percentage is seen in PROPY-45DClPA. The co-crystals have a reduced relative proportion of H···H contacts as these all have additional functional groups present which partake in stronger and alternative interactions. H···O contacts in particular, as well H···C are seen to be more dominant in the co-crystals compared to the single component PROPY.

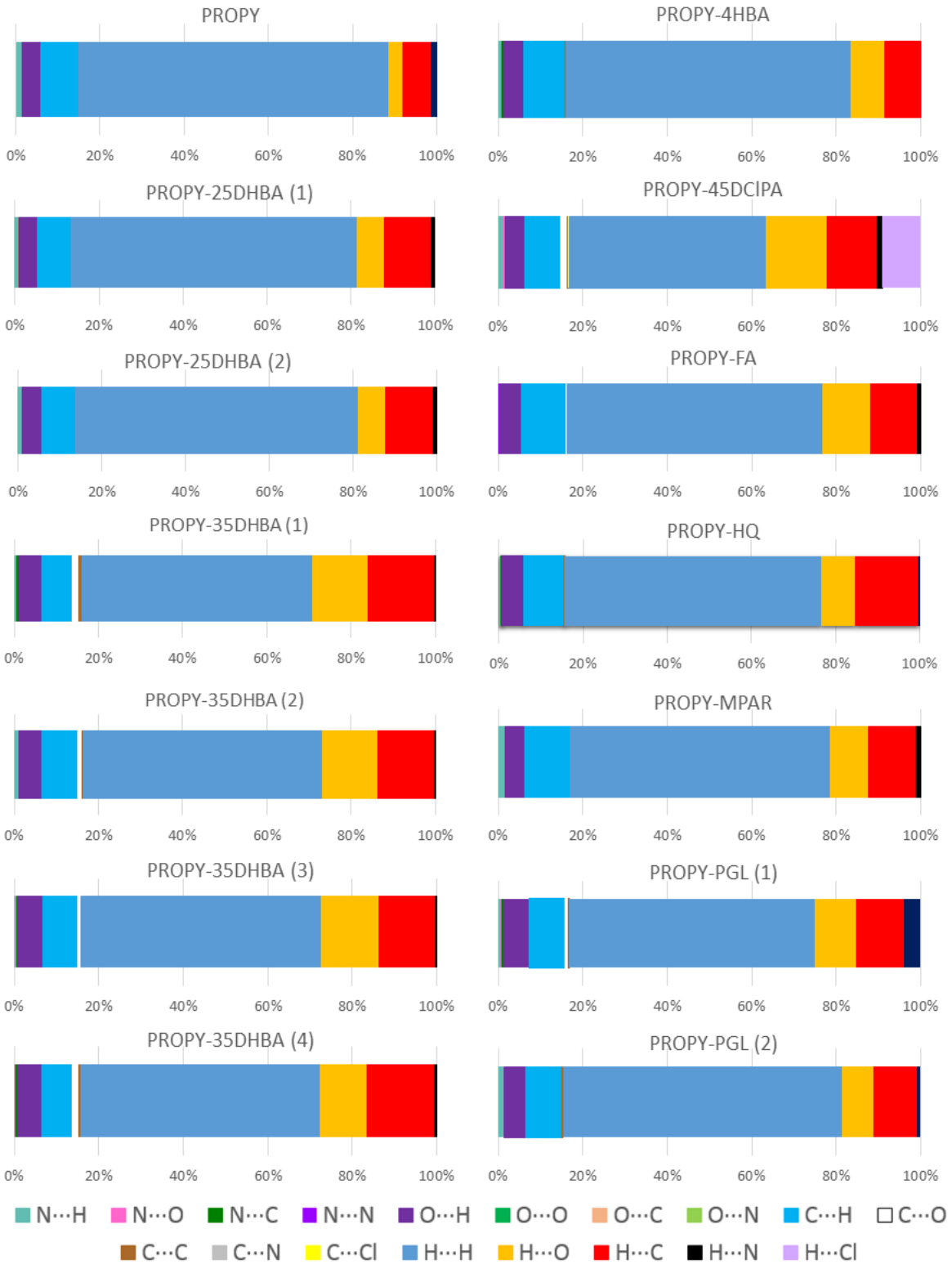

Figure A.19. Composite bars to show contribution of interaction types occurring from the PROPY molecule (inside the Hirshfeld surface, denoted first in each contact type) in each co-crystal and parent PROPY. PROPY-25DHBA, PROPY-35DHBA and PROPY-PGL·0.5ACN have multiple independent molecules of PROPY present, each has been analysed individually.

A.8 Packing Coefficients

The packing coefficients for all co-crystals and PROPY were determined to assess the efficiency at which the molecules packed together in the new forms. An increase in packing co-efficient was seen in all the new co-crystals supporting their favourable formation.

Table A.5. Unit cell and molecular volumes, Z values and packing coefficients for the eight new co-crystals and PROPY.

Sample	Z	Unit Cell Volume /Å^3	Molecular Volume[a] /Å^3	C_k[b]
PROPY Form I	2	678.7	228.24	0.6726
PROPY Form II	4	1333.9	228.24	0.6844
PROPY-25DHBA$_{(1,4\text{-dioxane})}$	5	3807.76	670.53 (excluding solvent 583.56)	0.7044 (excluding solvent 0.6130)
PROPY-35DHBA	8	4024.18	355.32	0.7064
PROPY-45DClPA	8	4474.82	393.36	0.7037
PROPY-4HBA	4	1924.05	347.3	0.7220
PROPY-FA	2	757.912	275.27	0.7264
PROPY-HQ	2	1193.76	428.4	0.7177
PROPY-MPAR	4	2031.56	364.83	0.7183
PROPY-PGL·0.5ACN	4	4035.7	718.73	0.7123

[a]Molecular volume calculated using Molinspiration Property Calculation Service (www.molinspiration.com). [b]Kitaigorodsky packing coefficient[335] calculated using the equation: $C_k = Z\, V_{mol} V_{cell}^{-1}$. V_{mol} is the molecular volume (Å^3), V_{cell} is the volume of the unit cell (Å^3), and Z is the number of molecules in the unit cell.

A.9 Thermal Analysis

A.9.1 PROPY-PGL·0.5ACN

PROPY-PGL forms an acetonitrile (ACN) solvate seen in SCXRD structure solution with a ratio of 1:1:0.5. This ratio would contain 2.72 % solvent by mass.

A.9.1.1 TGA

TGA was used to determine solvent loss and the mass loss of 2.7 % (Figure A.20) seen between 60-120 °C (boiling point of ACN: 82 °C) confirmed the expected ratio. The solvent loss appears to occur in two stages consisting of an initial, small loss of solvent up to 90 °C followed by a greater mass loss relating to a larger proportion of the solvent. The latter occurs in the temperature range seen for melting (DSC). It is therefore hypothesised that some solvent can be removed from the crystal without loss of order and crystallinity (seen in HSM, Figure A.22). As the temperature increases, the remainder of the solvent is only expelled when the crystal lattice breaks down and melting is observed releasing the solvent molecules.

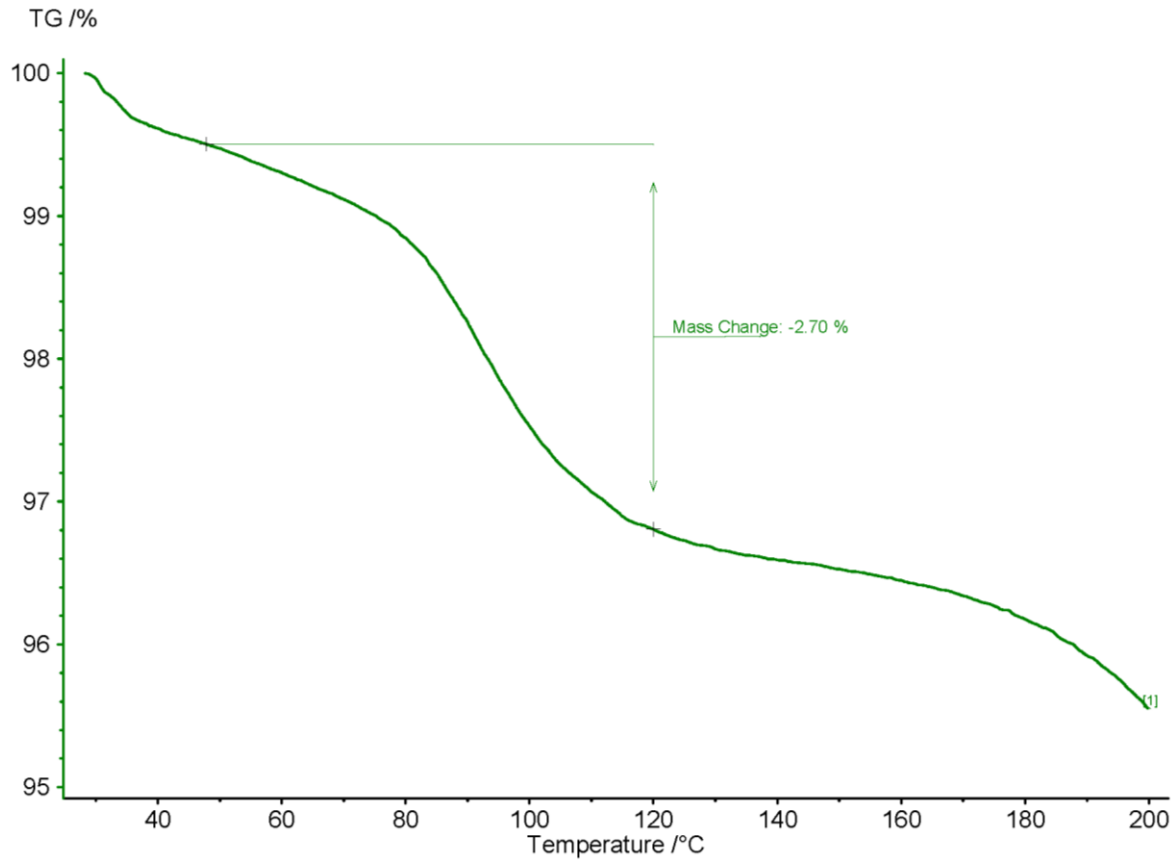

Figure A.20. TGA curve for PROPY-PGL·0.5ACN, 30-200 °C, with mass loss representing 0.5 equivalents of ACN solvent in the expected temperature range.

A.9.1.2 DSC and HSM

The DSC analysis of PROP-PGL·0.5ACN showed several events including solvent loss and sample melt (Figure A.21).

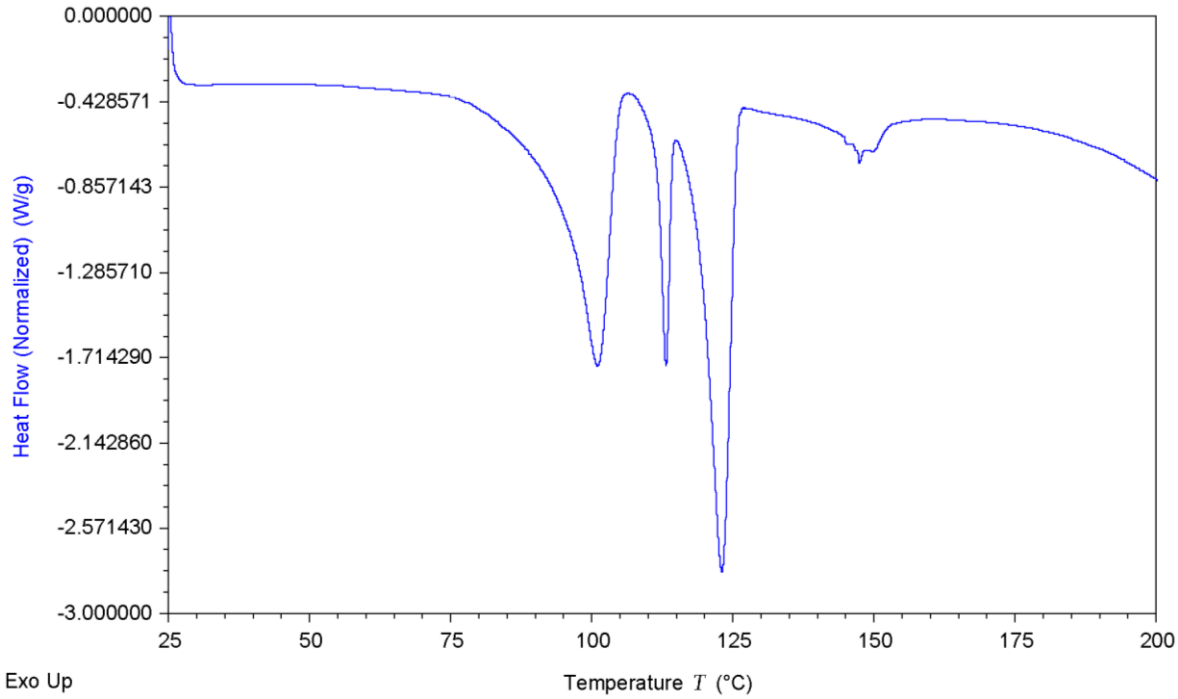

Figure A.21. DSC curve for PROPY-PGL·0.5ACN, 25-200 °C, showing solvent loss, melting with almost instantaneous recrystallisation, and melt of the new material.

To further investigate the nature of these events HSM was undertaken. This showed solvent loss, as expected, onset occurring around 90 °C followed by melting and an instantaneous recrystallisation (Figure A.22). These correspond to the events at 111 °C and 117 °C in the DSC although are seen to occur at slightly higher temperatures in HSM due to the nature of the equipment. The recrystallised material was seen to melt between 153-157 °C in HSM. These events concur with the DSC curve although at slightly lower temperatures in the quantitative DSC measurement.

It was not possible to characterise the new, recrystallised material due to the amount formed and nature of the crystals produced. It is unlikely to be either parent PROPY or PGL as they display melting points of 104 °C and 219 °C respectively. It is postulated that this could be a new anhydrous form of PROPY-PGL; TGA confirms that at this temperature all solvent is removed from the system. The additional heat, and absence of solvent, may be sufficient for an alternative form to appear which is stable as higher temperatures.

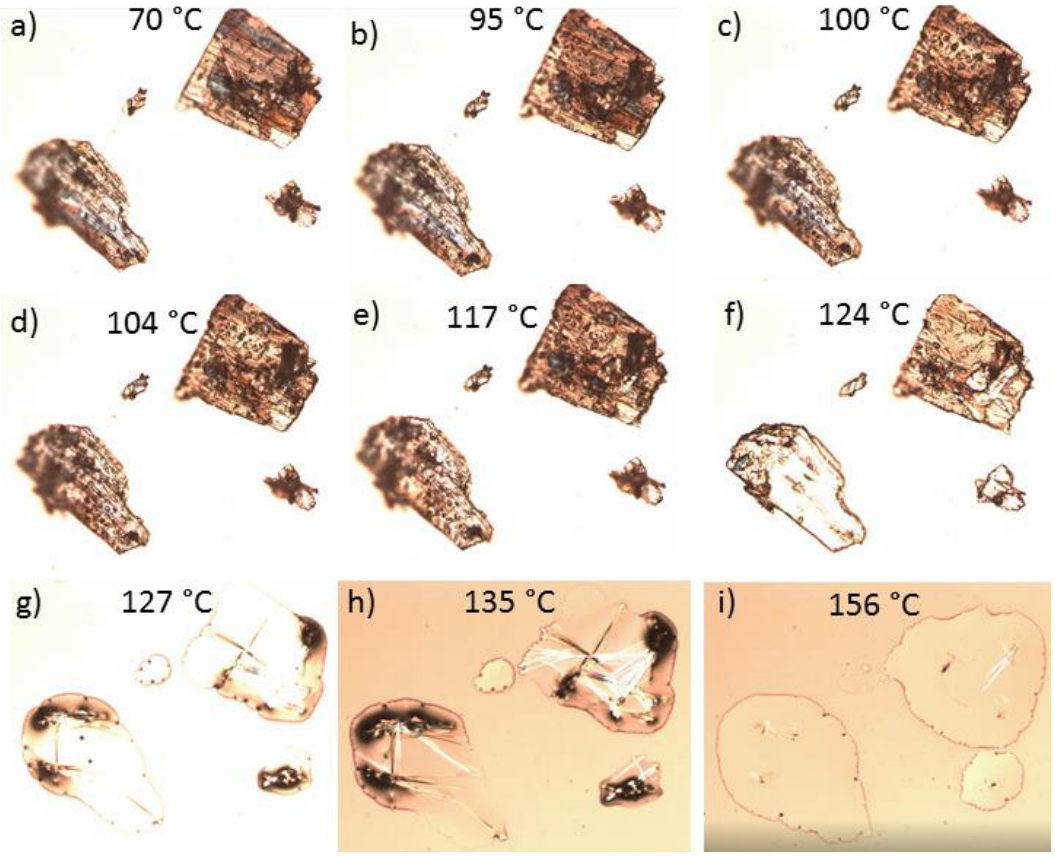

Figure A.22. Images from the PROPY-PGL·0.5ACN HSM experiment showing a) sample initially, b-e) solvent loss, f) melting onset, g) melting, h) recrystallisation from melt and i) melt of the newly recrystallised material.

A.9.2 PROPY-25DHBA (1,4-dioxane solvate)

The presence of solvent was identified in the crystal structure of the 2:1 PROPY-25DHBA co-crystal. From experimental conditions, it was identified as 1,4-dioxane and using solvent masking and SQUEEZE algorithms it was projected that there was one molecule in the asymmetric unit. This would equate to 12.54 % by mass. TGA was carried out to confirm the solvent nature and aid in the stoichiometry determination.

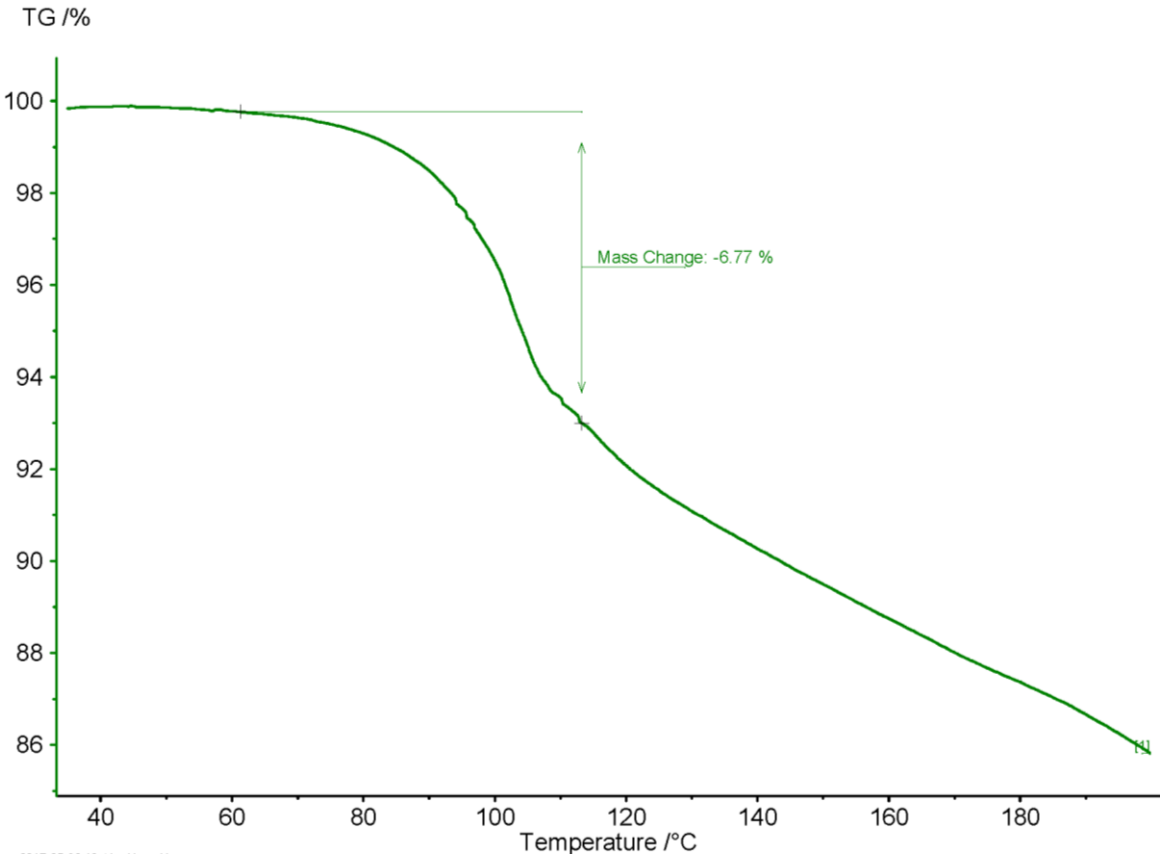

Figure A.23. TGA curve for PROPY-25DHBA, 30-200 °C, with mass loss representing 0.5 equivalents of 1,4-dioxane solvent in the appropriate temperature range.

Figure A.23 shows the TGA curve indicating a 6.77 % mass loss of in the expected temperature range for 1,4-dioxane solvent (boiling point 101 °C). This is a smaller mass loss than expected for a 2:1:1 ratio, corresponding instead to 2:1:0.5 (6.69 % solvent mass by weight). The samples were generated in advance of the TGA analysis and stored, however SCXRD data was collected when the crystals were fresh. Solvent loss during storage may have occurred (the sample is known to be unstable over extended periods of time (see A.10 for stability data) accounting for these differences. An alternative explanation is that the compound has a 0.5 stoichiometric amount of solvent present. The solvent is known to be located in voids and disordered over multiple positions. It may be possible that some voids contain solvent whilst others are empty. DVS data was not collected for this sample but it would be hypothesised that should the latter explanation be true, significant water uptake would be observed, with entry into these empty voids.

A.10 Stability

A.10.1 Slurry

When tested under slurry conditions all the samples containing pharmaceutically acceptable co-formers appeared stable with the exception of the PROPY-25DHBA and PROPY-PGL·0.5ACN co-crystals. These were seen to degrade and parent PROPY peaks apparent in the powder pattern of the resultant material (Figure A.24).

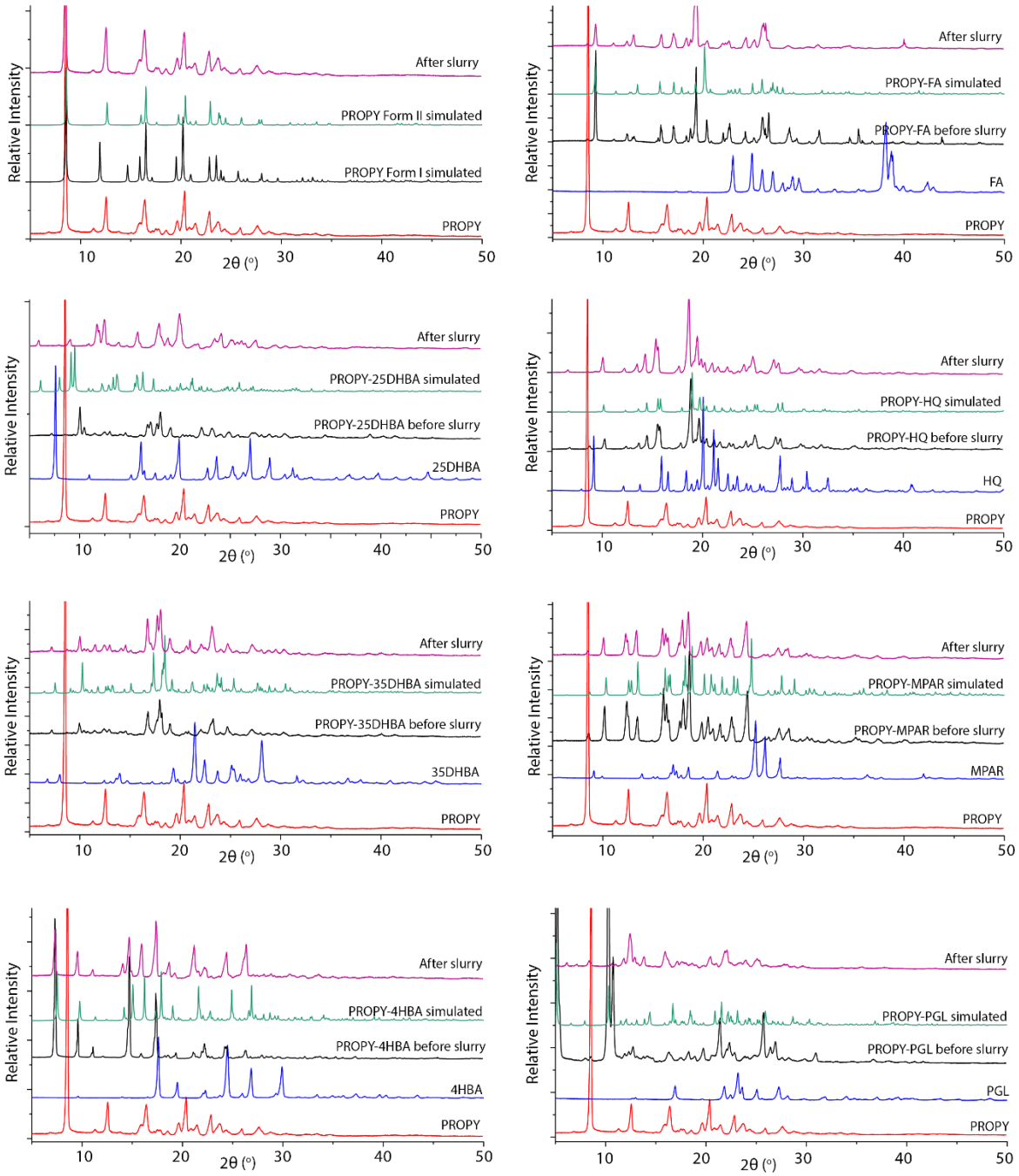

Figure A.24. Stacked PXRD patterns for co-crystals and parent material displaying data before and after 24 hour slurry experiment.

A.10.2 Accelerated Stability

As evidenced in the slurry test, Figure A.25 indicate that the all the samples are stable under accelerated conditions (13 weeks, 40 °C / 75 % relative humidity) with the exception of the PROPY-25DHBA and PROPY-PGL·0.5ACN. These showed the appearance of PROPY and co-former peaks in the sample over time indicating dissociation, either partial (PROPY-PGL·0.5ACN) or complete (PROPY-25DHBA).

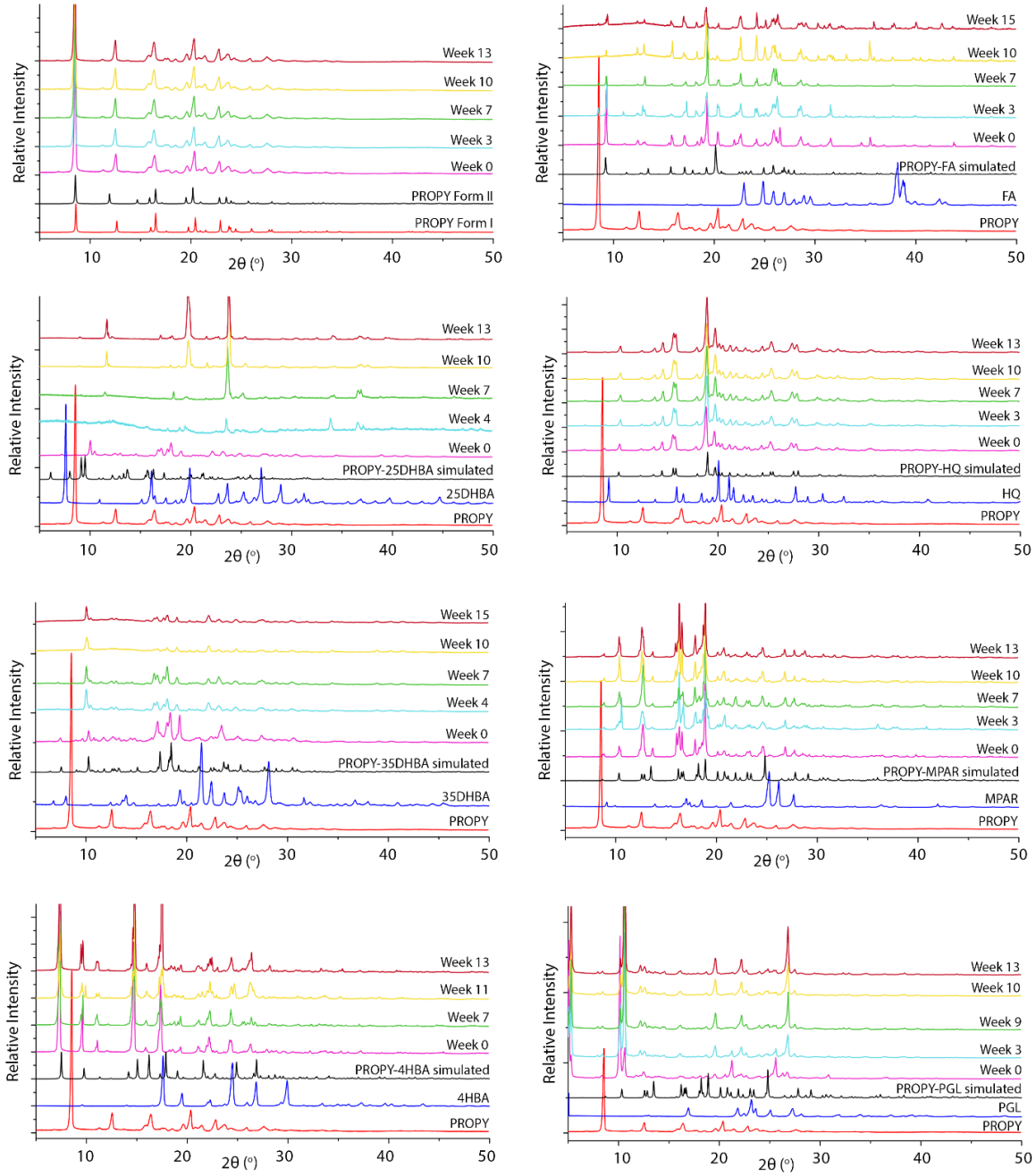

Figure A.25. Stacked PXRD patterns for 13-15 week accelerated stability testing at 75% RH, 40°C for new samples and parent materials.

Appendix B PROPY Quantum Crystallography Studies

CONTENTS

B.1 Choice of Experimental Multipole Models

B.2 Final Experimental Multipole Models

B.3 Topological Analysis

B.4 Interaction Analysis

B.5 Analysis of Interactions to Water

B.1 Choice of Experimental Multipole Models

Related supplementary documents:

- Charge Comparisons (doc)

Aspherical multipole models were produced from a routine data processing, merging and sorting approach (detailed in the Experimental, Chapter 8.7) with a typical multipolar modelling routine. Analysis of the resulting models identified a number of areas where possible improvements could be made. Several different approaches were therefore taken in data processing, manipulation and structure refinement. These included assessing the multipole populations and refining different atoms to different levels to ensure they were statistically meaningful, testing the refinement of different *κ'* parameters, and using different empirical absorption corrections. This aimed to find the most appropriate method for all the systems, producing final models in which the greatest confidence was attained.

B.1.1 Analysis of Models

The resulting models from a different refinement approaches were analysed to find the most appropriate, and representative, models of the systems. There are several methods of analysis and factors that can be considered, one of which is the residual density after a full multipole population refinement. This can be visualised and interpreted in different ways in addition to the numerical output values.

Fractal dimension distribution[336] is an iso-surface of constant value *x,* defined according to Bronstein *et al*.[337] in Equation B.1. ε is the characteristic length of a box covering the considered variation, and N (*x,ε*) is the number of boxes a desired value *x* was present in. A line-counting algorithm (described by Meindl and Henn)[336] using consecutive pairs of points in the grid file is implemented in the fractal dimension distribution plot generation.

$$d^f(\rho_0 = x) = \lim_{\varepsilon \to 0} \frac{\log N(x, \varepsilon)}{\log 1/\varepsilon}$$

Equation B.1. Fractal dimension distribution of the residual density.

These plots align all residual density distributions to the same scale to allow comparisons between models to be made. Experimental resolution, residual density flatness, minimum and maximum values of the residual density and systematic errors can all be indicated in these plots providing a valuable source to analyse models.

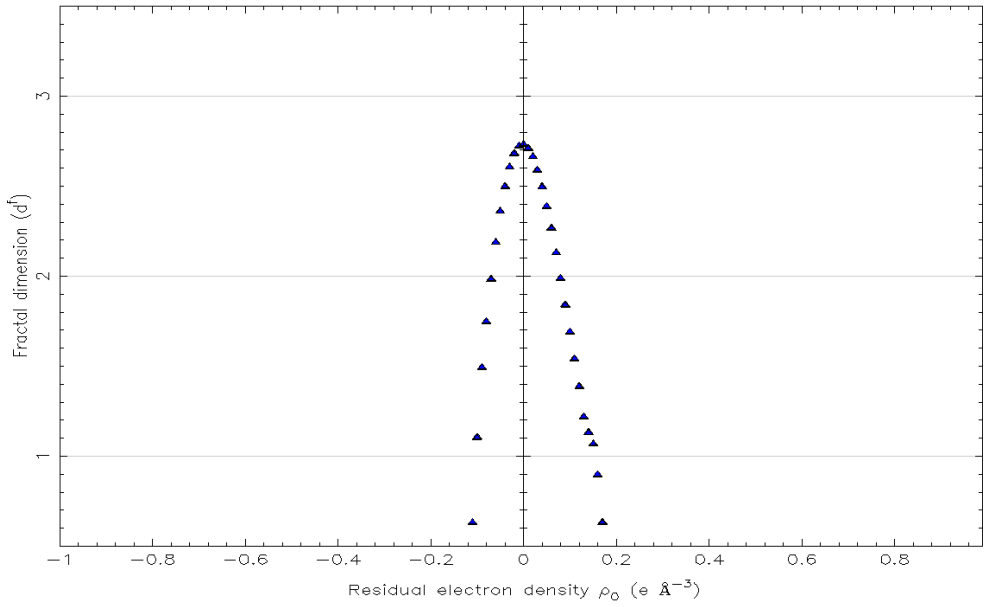

Figure B.1. Example fractal dimension distribution plot of residual density for PROPY-MPAR 1:1 co-crystal (no absorption and all non-hydrogen atoms refined to hexadecapole level).

Figure B.1 depicts the fractal dimension distribution plot for the PROPY-MPAR co-crystal with no absorption correction applied, and all non-hydrogen atoms refined to the hexadecapole level. The plot is relatively narrow indicating flatness, with low limiting values signifying small maximum and minimum residual density values. A parabolic shape with no obvious unusual features is observed (only a very slight shoulder on the lower right-hand side).

Figure B.2 shows the static deformation density map of the same system, indicating the difference between the IAM model and that in which the charge is redistributed into multipoles. The lone pair of electrons of oxygen can be easily identified, along with density deformation due to bonding and interactions. A similar map is shown in Figure B.3, depicting the Laplacian of the electron density in the same plane. This indicates charge concentration and depletion highlighting the saddle points of the covalent bonds and nuclear positions. It also depicts the charge deformation resulting from intermolecular interactions.

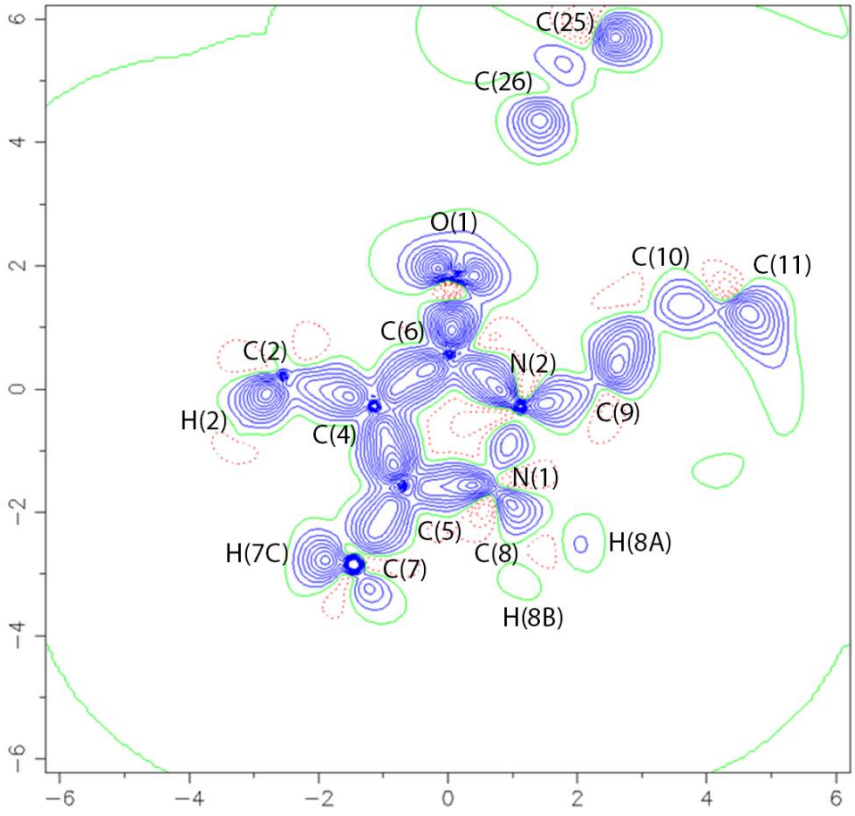

Figure B.2. Static deformation density map in the plane of the main PROPY ring for PROPY-MPAR. Contours plotted at 0.05 level.

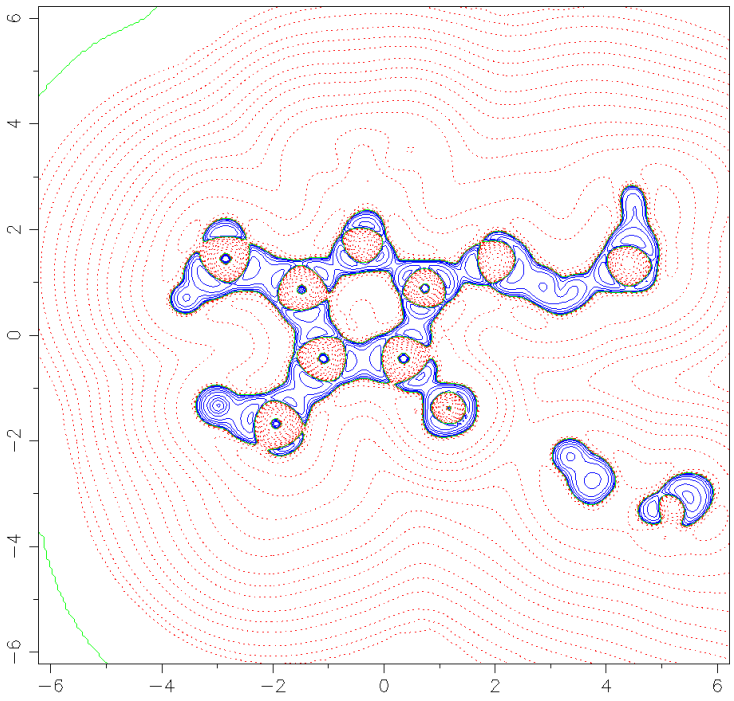

Figure B.3. Laplacian map in the plane C(6) N(2) C(5) for PROPY-MPAR. Blue contours show negative values (charge accumulation) whilst red indicate positive and charge depletion.

B.1.2 Absorption Corrections

At the time of data collection, face indexing of the crystals for which data was collected was not possible, and many of the effects seen in the initial models were thought to arise as a result of this. The main investigation was therefore into the application of post-processing empirical absorption corrections. These were implemented to try to replicate, to some extent, that which is included in a face-indexing routine.

A number of different methods for empirical absorption corrections can be applied using WinGX[331] software. These include numerical methods such as analytical[338] or Gaussian quadrature methods [339] Whilst generally agreed as the best corrections, they require full face-indexing of the crystal faces, and therefore could not be implemented for the data described herein. Semi-empirical methods rely on intensity measurements and are best applied when high redundancies are present in the data. These can be implemented in PLATON[267, 268] or SORTAV[321, 322] but were seen to have little effect (Section B.1.2.1) as a similar multiscan absorption correction[340] is applied in CrysalisPro[317] during the data processing. The final methods are refined corrections and include DIFABS,[341] XABS2[330] and SHELXA.[320] These methods calculate the absorption surface from the differences between the observed (F^2_{obs}) and calculated (F^2_{calc}) structure factors (the exact mathematical functions used to model these differences vary between the models). They rely on a refined structural model and suffer from the fact that the data are being modified to fit the model. Incorporating the parameters into a least-squares refinement can overcome this to some extent. Of the three methods, DIFABS in particular has received a lot of poor reviews with many limitations highlighted. Used within these limits it can provide a useful tool, along with the other similar methods. The methods tested for these models were XABS2 and the semi-empirical method possible through SORTAV; [321, 322] these could be easily applied to the files and data formats already available from the data processing.

B.1.2.1 SORTAV

The absorption routine available in SORTAV[321, 322] was implemented for PROPY-FA during the merging and sorting process. This system was chosen as it appeared to have the largest shoulder feature in the fractal dimension plot (Figure B.4) thought to arise from a lack of accounting correctly for the absorption effects. It was believed that this may show the greatest improvement if absorption corrections were to be beneficial. The fractal dimension distribution plots for the models generated both with and without this absorption correction are depicted in Figure B.4, and Table B.1 shows the refinement statistics. It can be seen that little difference is made to the fractal dimension plot, and the shoulder on the right-hand side persists even when this absorption correction is applied.

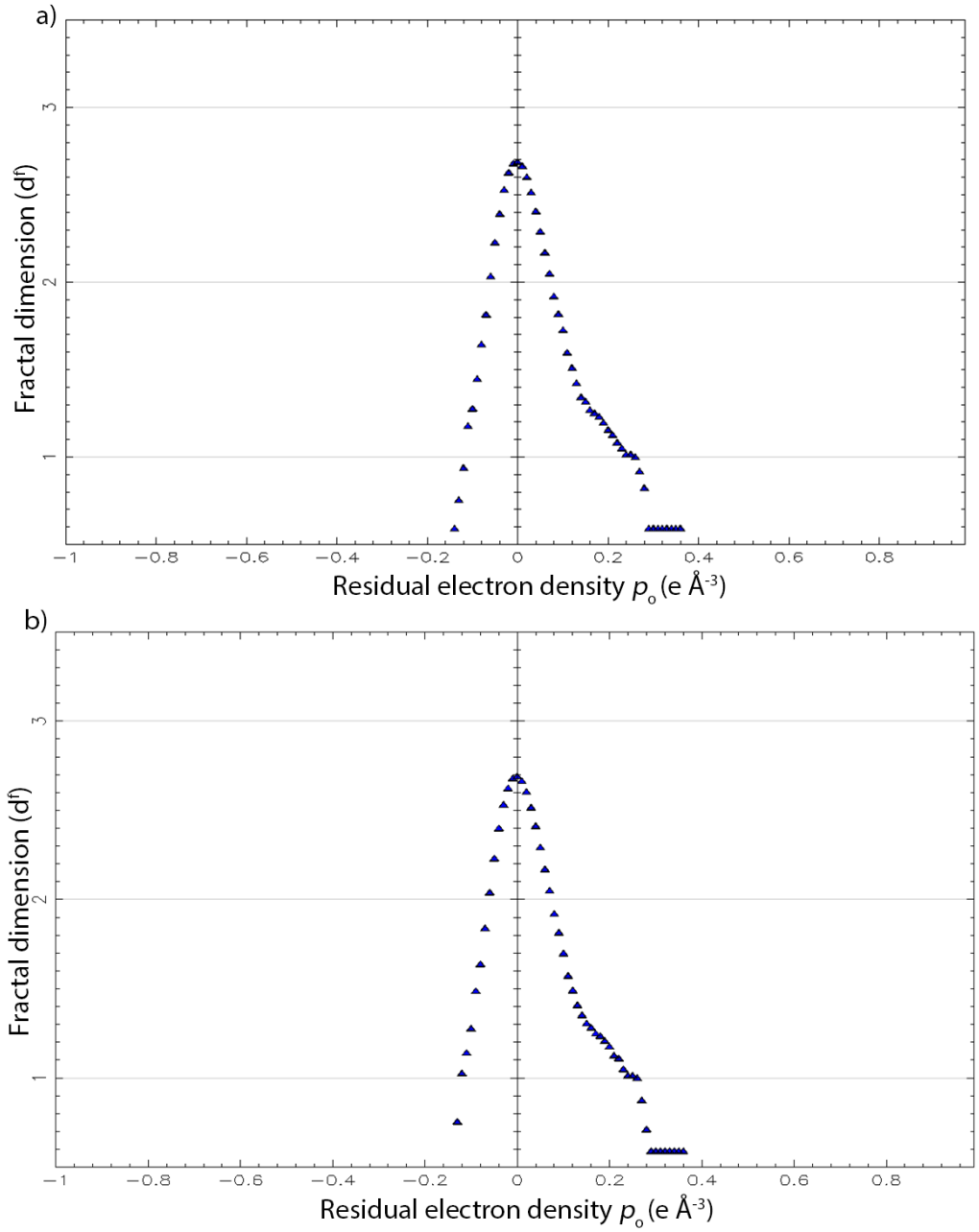

Figure B.4. Fractal dimension plots for PROPY-FA with (above, a) and without (below, b) the use of the absorption correction implemented in SORTAV.

The statistics of the refinement show a very slight improvement in the residual density and R factor after the full multipole refinement with absorption is applied although it is almost negligible. In the spherical atom model no real improvements were seen; if the applied correction were to account for absorption a marked improvement would be expected. Therefore, no further tests were carried out with this method on alternate systems as only very minimal effects on the model were observed.

Table B.1. Statistics of refinement for the two models of PROPY-FA when the absorption corrected from SORTAV was applied.

Sample	PROPY-FA	PROPY-FA (abs)
Spherical refinement		
Reflections	22567 / 22573	22567 / 22573
R_1 ($F^2 > 2\theta\{F^2\}$)	0.0365	0.0365
R_1 (all)	0.0418	0.0418
wR2 ($F^2 > 2\theta\{F^2\}$)	0.1157	0.1159
wR2 (all)	0.1200	0.1202
GOF	1.030	1.034
$\Delta\rho(\mathbf{r})$ /e Å^{-3}	-0.39 / 0.74	-0.38 / 0.74
Multipole refinement		
No. data / included in refinement	22567 / 19919	22567 / 19919
Scale	2.263602	2.26255
R{F}	0.0217	0.0216
R{F^2}	0.0275	0.0276
GoF	1.3415	1.3368
Max sin (θ/ λ) used /Å	1.22240	1.22240
Data / parameter ratio	25.7351	25.7351
Convergence	0.841400 x 10^{-11} for C(5)/Y (20 cycles)	0.688191 x 10^{-11} for N(2)/Y (15 cycles, κ fixed)
$\Delta\rho(\mathbf{r})$ /e Å^{-3}	-0.139 / 0.366 RMS = 0.028	-0.141 / 0.368 RMS = 0.027

B.1.2.2 XABS2

XABS2 was applied to all four systems. The statistics of the resulting spherical and aspherical refinements are shown in Table B.2.

Table B.2. Statistics of refinements when XABS2 is applied to the IAM model, and the multipole model resulting using this as the input model.

Sample	PROPY-4HBA	PROPY-FA	PROPY-HQ	PROPY-MPAR
Spherical refinement				
Reflections	29229	22564	35648	30871
R_1 ($F^2 > 2\theta\{F^2\}$)	0.0334	0.0333	0.0370	0.0266
R_1 (all)	0.0411	0.0387	0.0448	0.0301
wR2 ($F^2 > 2\theta\{F^2\}$)	0.1018	0.1084	0.1125	0.0694
wR2 (all)	0.1060	0. 1122	0.1127	0.0710
GOF	1.043	1.0520	1.030	1.019
$\Delta\rho(\mathbf{r})$ /e Å^{-3}	-0.41 / 0.55	-0.50 / 0.60	-0.60 / 0.61	-0.20 / 0.31
Multipole refinement				
Total data / included	29228 / 25202	22564 / 19899	35648 / 30430	30871 / 28896
Scale	1.001246	1.007510	1.003801	1.001027
R{F}	0.0229	0.0212	0.0271	0.0187
R{F^2}	0.0262	0.0275	0.0338	0.0223
GoF	1.2180	1.3101	1.4270	0.9684
Max sin (θ/ λ) used /Å	1.22089	1.22240	1.22081	1.22116
Data / parameter ratio	25.4566	25.7093	30.9248	28.0544
Convergence	0.7537 x 10^{-11} for N(2)/Z (20 cycles)	0.665965 x10^{-11} for C(11)/Y (20 cycles)	0.321040 x 10^{-11} for C(25)/Z (20 cycles)	0.6173x10^{-11} for N(2)/X (20 cycles)
$\Delta\rho(\mathbf{r})$ /e Å^{-3}	-0.287 / 0.274 RMS = 0.028	-0.183 / 0.308 RMS = 0.028	-0.414 / 0.407 RMS = 0.032	-0.127 / 0.118 RMS = 0.024

Following full refinement, a number of indicators were used to assess the quality and differences between the original multipole model and that with XABS2 applied.

1. Fractal dimension distribution plots (of residual density)

Figure B.5 shows the fractal dimension plots for the multipole models of the four systems generated from the models with and without the XABS2 absorption correction applied. PROPY-4HBA shows a narrower fractal dimension plot as a result of the absorption correction, also seen to a lesser degree in that of PORPY-MPAR. The shoulder observed in the plot of PROPY-FA is reduced slightly. No obvious differences are displayed for PROPY-HQ.

These observations, combined with the statistics of refinement in Table B.2 above show that some of the shortcomings of the models, and data, are likely to be due to absorption, as improvements are seen when some attempts at correcting for this are applied.

2. Normal Probability Distributions

Figure B.6 shows the normal probability plots for the multipole models both with and without the XABS2 absorption correction applied. Improvements are seen in the data of PROPY-MPAR however PROPY-FA and PROPY-4HBA indicate a better distribution before the correction was implemented. As observed in the fractal dimension plots, PROPY-HQ shows very little difference between the two. As determined previously, absorption may be the cause of some of the features observed in the models; the XAS2 routine appears not to be the best model for this. Some improvements, but also some worsening of models is observed across the series.

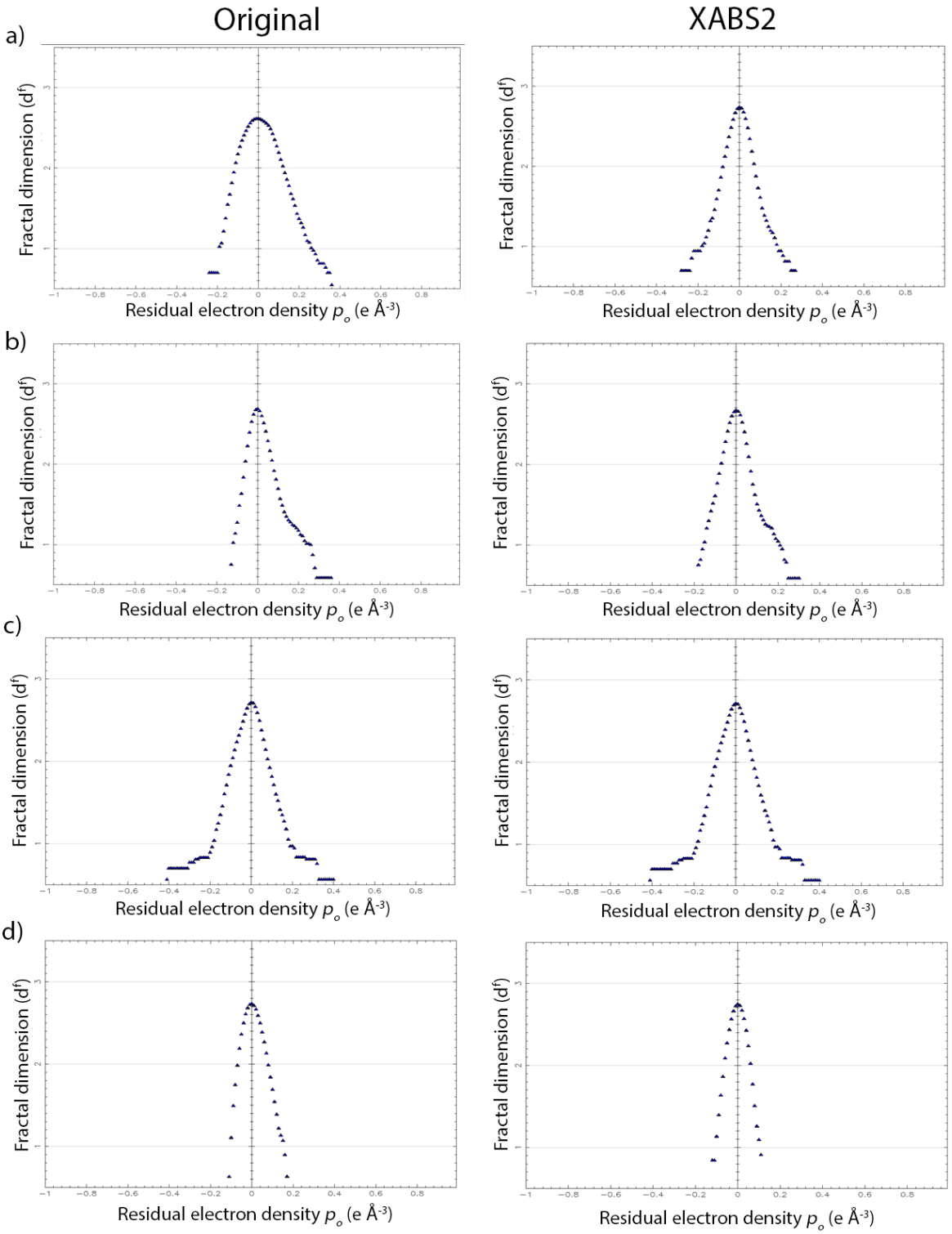

Figure B.5. Fractal dimension distribution plots for the four multipole models with and without XABS2 absorption correction applied; a) PROPY-4HBA, b) PROPY-FA, c) PROPY-HQ and d) PROPY-MPAR.

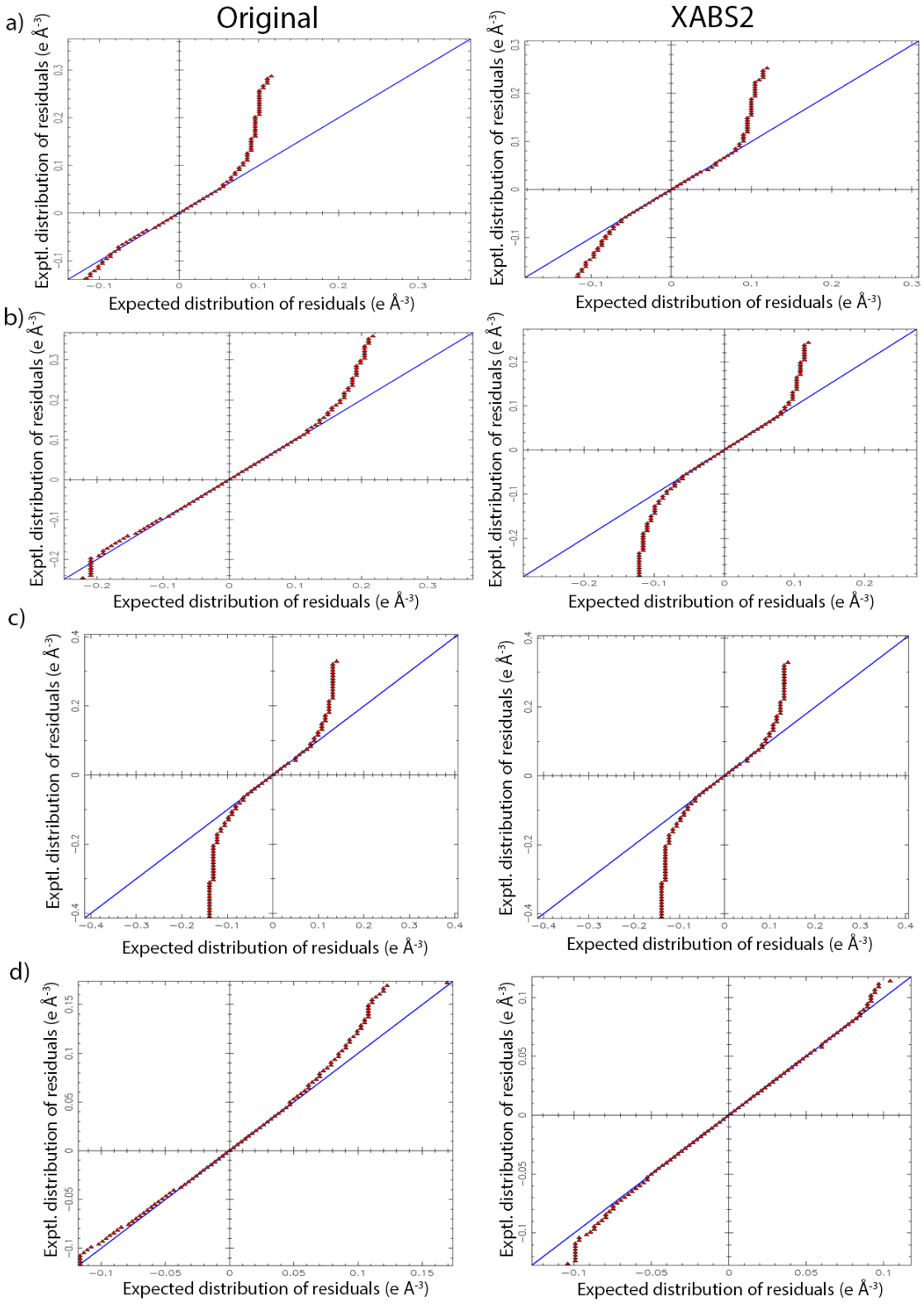

Figure B.6. Normal probability plots for the four multipole models with and without XABS2 absorption correction applied; a) PROPY-4HBA, b) PROPY-FA, c) PROPY-HQ and d) PROPY-MPAR.

3. Static Deformation Density Plots

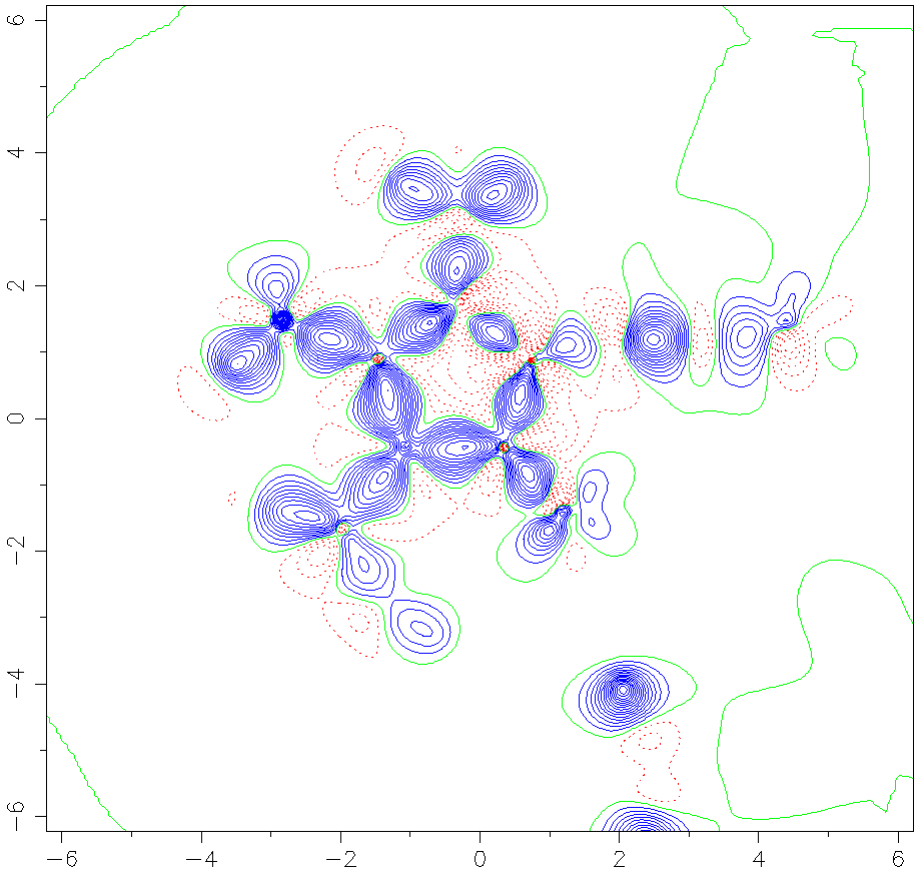

Figure B.7. Static deformation density map in the plane of the main PROPY ring (C(4) N(2) C(6)) of PROPY-HQ 1:2 co-crystal after full multipole model refinement with XABS2 empirical absorption correction applied. Contour level 0.08

Figure B.8 compares the static deformation density maps for the two versions of the multipole models, with an enlarged example map shown in Figure B.7. The models where XABS2 has been applied show some uncharacteristic atomic nuclei, with negative contours representing them. Many of the deformation contours, however, are improved with XABS2 showing more spherical and even bond contours between the nuclei.

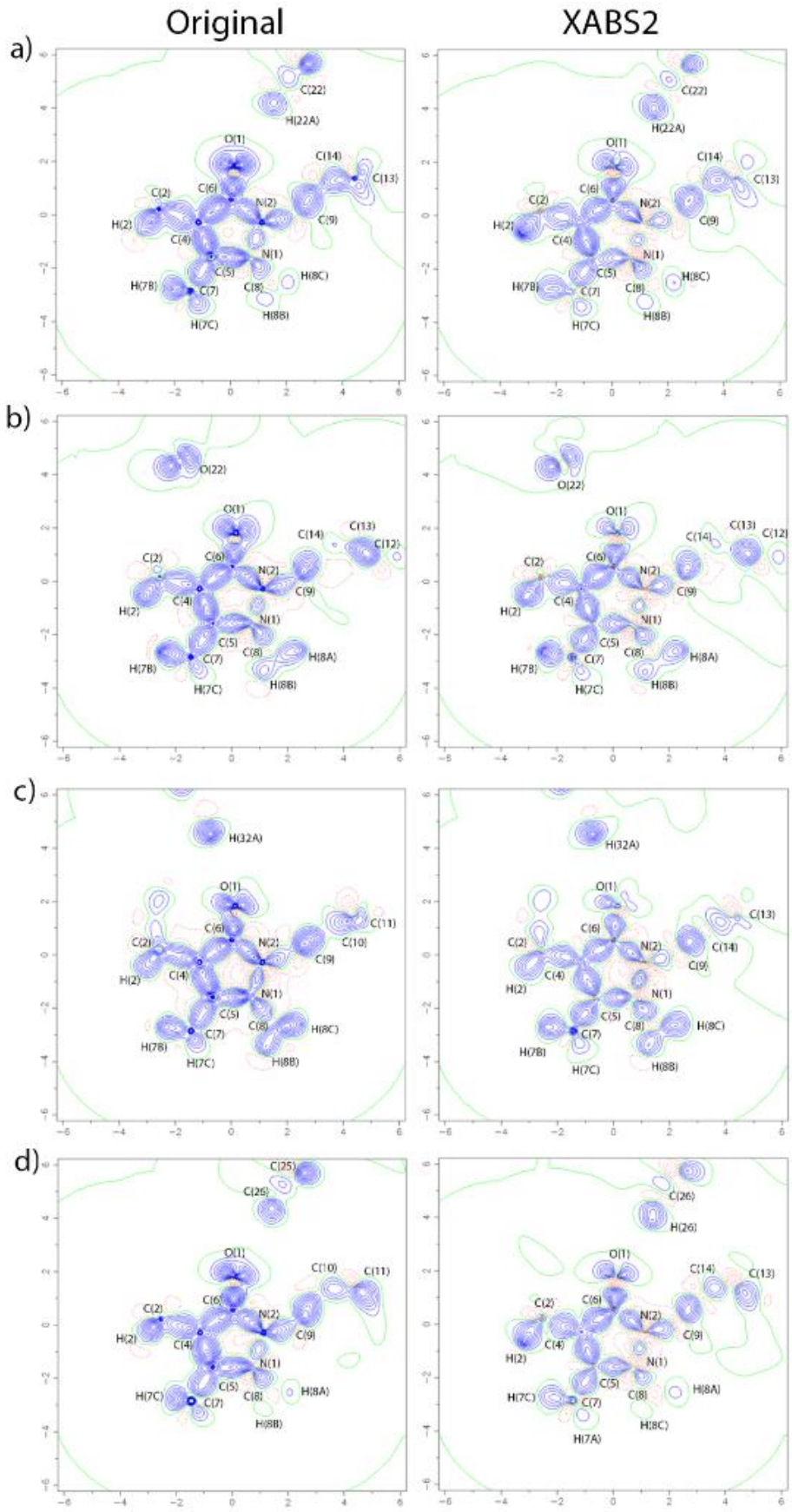

Figure B.8. Static deformation density maps for the four models with and without XABS2 applies; a) PROPY-4HBA, b) PROPY-FA, c) PROPY-HQ and d) PROPY-MPAR. XABS2 Models are all labelled according to 'standard' labels, original models have variations as described in Section B.3.1

The statistics of refinement were seen to improve with the application of XABS2. Reduced residual electron density and smoother fractal dimension plots were seen in some cases. The corresponding maps of the static deformation density display some unusual features at the atomic nuclei (seen in Figure B.7 as red atomic centres), although the contours were more rounded and typical for this property. Not all features were fully (or even partially in some instances) resolved in the fractal dimension plots. As a result, neither XABS2 nor the semi-empirical method from SORTAV were deemed appropriate for use in the final models for which subsequent topological analysis would be undertaken.

XABS2 tests show that absorption may be a likely cause of some of the residual features in the models, as some improvements were observed on application of XABS2. However, it is evident that the XABS2 routine is not the best way of treating this. While other corrections are possible many require the crystal faces to be defined and cannot be tested on these models. It is expected that improvements in all cases would be obtained should this be possible.

B.1.3 Refinement of *κ* and *κ'*

κ parameters allow for the expansion and contraction of orbitals and can be applied in different ways in multipole model refinement. Initially a single κ was refined for each atom (with the exception of hydrogen atoms, for which the value was fixed throughout), with atoms of the same type in a similar chemical environment assigned the same κ parameter. After initial refinement and the introduction of all multipoles as required, the refinement of different κ parameters was tested. Refinement statistics for the four systems with *κ'* refined are detailed in Table B.3, and Figure B.9 shows the corresponding fractal dimension distribution plots. The static deformation density maps are shown in Figure B.10.

Table B.3. Refinement parameters for the four multipole models with *κ'* refinement.

Sample	**PROPY-4HBA**	**PROPY-FA**	**PROPY-HQ**	**PROPY-MPAR**
When tested	After full model before fix kappa	After full model before fix kappa	After full model before fix kappa	After remove chem con, before xyz Uij refine
Total data / included	29829 / 25244	22567 / 19919	35655 / 30428	30926 / 28911
R{F}	0.0263	0.0218	0.0293	0.0223
$R\{F^2\}$	0.0343	0.0267	0.0389	0. 0275
GoF	1.3655	1.3581	1.5198	1.1679
Max sin (θ/ λ) used /Å	1.22089	1.22240	1.22081	1.22116
Data / parameter ratio	24.4139	24.5914	24.4205	33.7745
Convergence	0.351595 for 17/K0 (15 cycles, κ and κ' not fixed)	0.171899 x 10^2 for 3/K0 (15 cycles, κ and κ' not fixed)	0.178994 x 10^2 for C(1)/D1- (15 cycles, κ and κ' not fixed)	0.168938x 10^2 for C(22)/O0 (10 cycles, κ and κ' not fixed)
$\Delta\rho(\mathbf{r})$ /e $Å^{-3}$	-0.267 / 0.366 RMS = 0.047	-0.392 / 0.368 RMS = 0.027	-0.292 / 0.432 RMS = 0.029	-0.232 / 0.350 RMS = 0.038

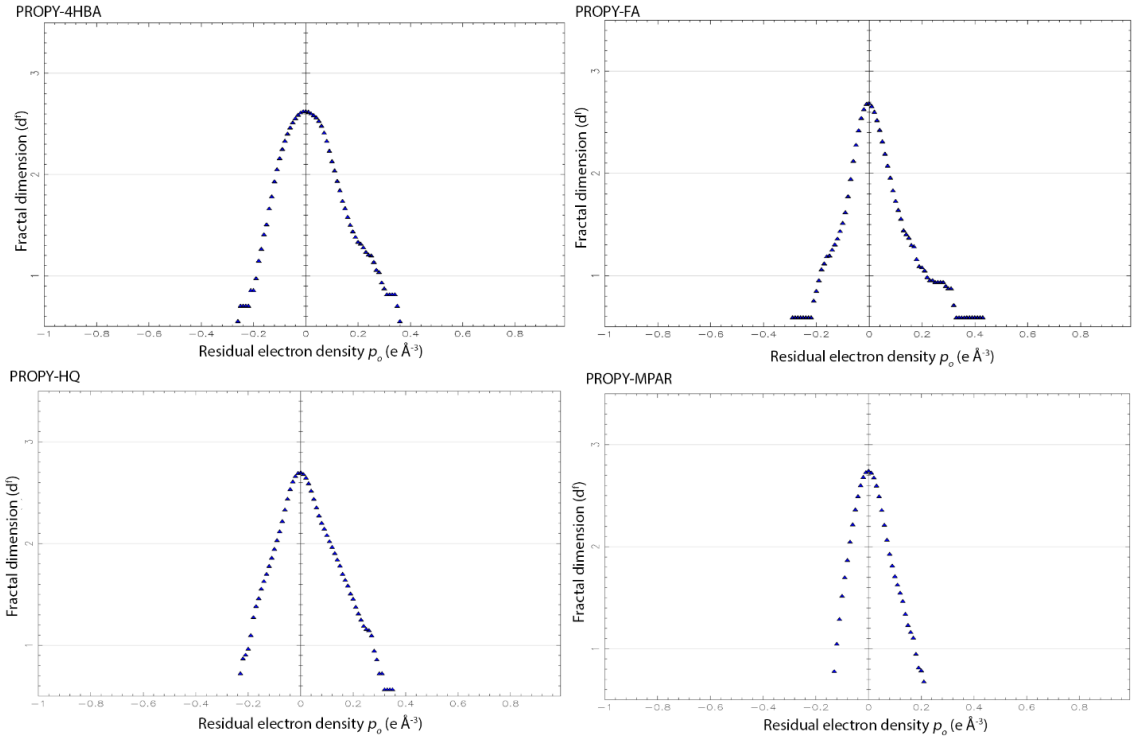

Figure B.9. Fractal dimension plots for the four PROPY systems with *κ′* refinement introduced to the aspherical model. For comparison to the original refinement (*κ* only) see Figure B.5.

The static deformation density maps in Figure B.10 show some contours which appear more rounded (see Figures B.7 and B.8 for comparisons) however the majority of the plots are deformed and display unusual, and uncharacteristic features. These features, along with the poor fractal dimension plots demonstrated above, indicate that *κ′* refinement is not advantageous for these models.

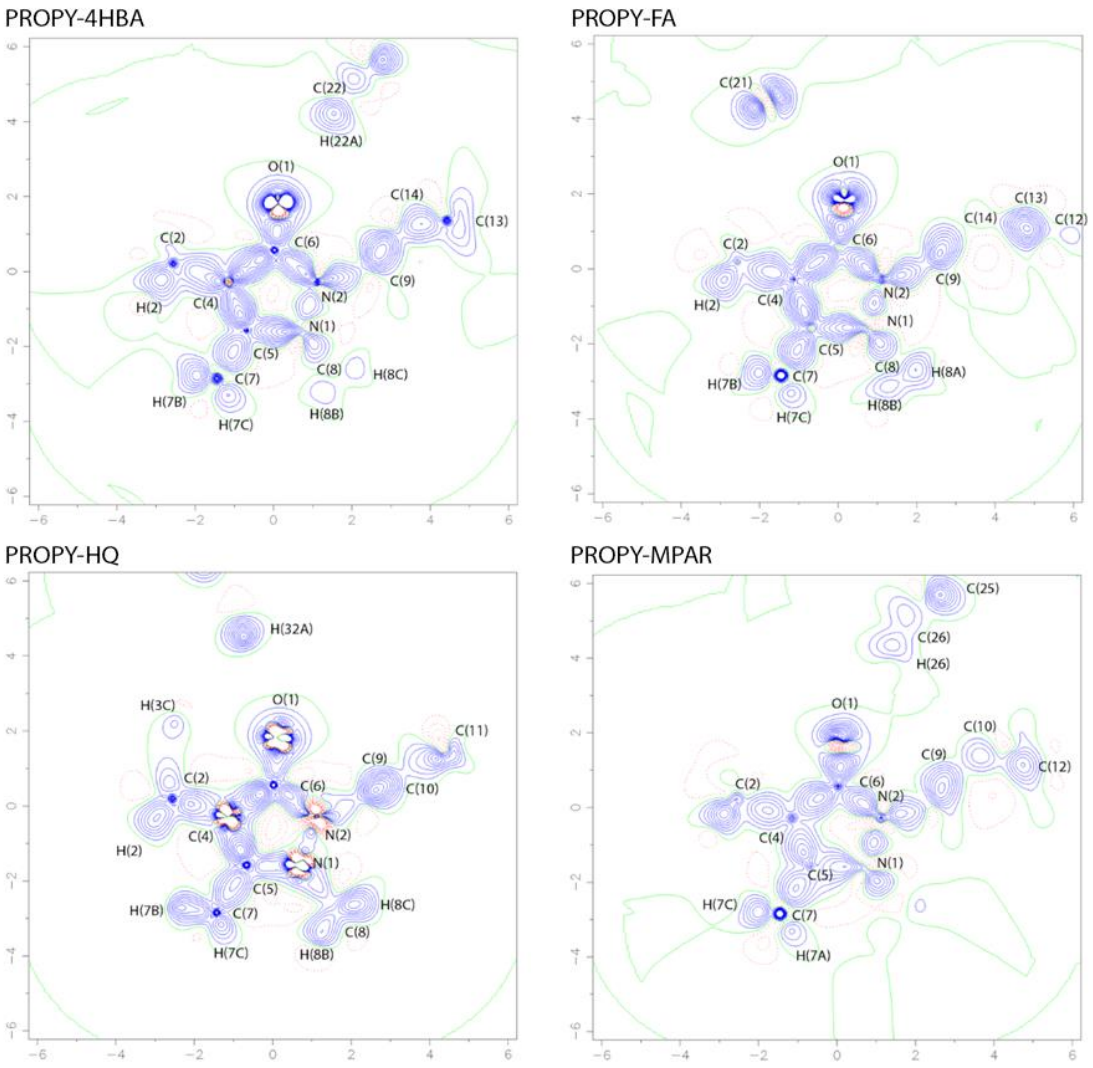

Figure B.10. Static deformation density maps for the four PROPY systems with refinement of *κ'*.

Additional, and alternative combinations of κ′ parameters were also tested to see the effect on the models. No significant improvement was achieved and in some instances the refinement deviated greatly. During refinement, warnings were given in some instances, such as Slater functions are changed more than 50% (PROPY-HQ). As a result, the final models used a single κ for all non-hydrogen atoms.

B.1.4 Multipole Population Level

The introduction of higher level multipoles increases the number of refined parameters and can reduce the data : parameter ratio. Hence, if the data are not of sufficient quality this should be approached with caution. Furthermore, the possibility of over modelling can arise.[342]

To assess the level of multipole refinement appropriate for these systems, after a full refinement (non-hydrogen atoms refined to hexadecapole level and hydrogen atoms refined with a single,

bond-directed dipole and quadrupole) the statistical meaningfulness of the populations was assessed, taking into consideration the associated error on each value. A population > 3σ was deemed meaningful. Some hexadecapole (and lower) populations were below this 3σ threshold, however many were greater (Table B.4) indicating that a hexadecapole level of refinement was appropriate.

Table B.4. Hexadecapole populations for PROPY-4HBA. Those which are statistically significant (> 3σ) are highlighted.

Atom	H40	H41+	H41-	H42+	H42-	H43+	H43-	H44+	H44-	Kappa'
O(1)	0.030(7)	0.014(7)	-0.027(7)	0.009(7)	0.011(7)	-0.013(7)	0.006(7)	0.000(7)	-0.010(7)	1.000
O(21)	0.001(8)	0.018(8)	0.012(7)	0.013(7)	-0.027(8)	0.006(7)	0.007(8)	0.029(7)	0.011(7)	1.000
O(22)	0.039(8)	-0.005(7)	0.005(7)	-0.023(7)	-0.008(7)	-0.036(7)	-0.017(7)	-0.003(7)	0.008(7)	1.000
O(23)	0.034(8)	-0.027(8)	-0.012(7)	-0.005(7)	-0.010(8)	-0.002(8)	0.035(8)	-0.003(7)	-0.020(7)	1.000
N(1)	0.020(10)	0.005(9)	0.015(9)	0.006(9)	0.041(9)	-0.007(9)	0.042(9)	0.032(8)	0.018(8)	1.000
N(2)	0.036(10)	-0.031(9)	-0.009(9)	-0.005(9)	-0.012(9)	-0.032(9)	0.044(9)	0.045(8)	-0.006(8)	1.000
C(1)	0.011(17)	0.024(15)	0.046(15)	0.000(15)	0.035(15)	-0.018(15)	0.053(16)	-0.024(16)	-0.008(15)	1.000
C(2)	0.014(16)	0.005(14)	0.017(13)	-0.002(14)	-0.004(14)	-0.017(15)	0.053(14)	0.053(15)	-0.035(14)	1.000
C(3)	-0.016(18)	-0.006(14)	-0.006(16)	-0.080(15)	0.019(15)	-0.025(15)	0.091(16)	0.027(15)	0.001(15)	1.000
C(4)	0.075(15)	-0.024(12)	0.042(14)	-0.006(14)	0.018(14)	-0.024(13)	0.049(13)	0.021(12)	-0.014(12)	1.000
C(5)	0.027(15)	0.003(12)	0.021(14)	0.011(14)	-0.001(14)	-0.008(13)	-0.039(13)	0.028(12)	0.017(12)	1.000
C(6)	0.026(14)	-0.048(12)	0.040(14)	-0.065(13)	0.016(13)	-0.016(12)	0.017(12)	-0.020(11)	0.017(11)	1.000
C(7)	-0.017(16)	-0.012(14)	0.019(13)	-0.008(13)	-0.015(13)	0.002(13)	0.071(14)	-0.016(13)	0.026(13)	1.000
C(8)	0.043(16)	-0.042(13)	-0.011(13)	-0.033(13)	-0.034(13)	0.030(13)	0.081(14)	0.022(12)	0.003(12)	1.000
C(9)	-0.018(15)	0.021(13)	-0.031(15)	-0.022(14)	-0.003(14)	-0.040(13)	-0.043(13)	0.000(12)	-0.057(11)	1.000
C(10)	-0.016(16)	0.004(13)	-0.008(15)	-0.002(14)	-0.020(14)	-0.009(13)	-0.002(14)	-0.021(13)	0.007(12)	1.000
C(11)	0.010(18)	-0.009(13)	-0.006(16)	0.021(15)	-0.006(15)	0.007(14)	-0.053(15)	-0.044(14)	0.026(14)	1.000
C(12)	0.028(18)	0.030(13)	-0.001(17)	0.003(15)	-0.013(15)	-0.004(15)	0.077(15)	0.041(15)	-0.003(15)	1.000
C(13)	-0.012(18)	-0.030(13)	0.050(16)	-0.013(15)	0.004(15)	0.025(15)	-0.013(15)	0.039(14)	-0.010(14)	1.000
C(14)	-0.011(16)	0.011(13)	-0.015(15)	0.026(14)	0.016(14)	-0.007(13)	-0.012(14)	0.010(13)	-0.040(13)	1.000
C(21)	0.049(15)	-0.012(13)	0.002(14)	0.004(13)	-0.001(14)	0.026(13)	-0.018(13)	0.014(12)	-0.006(12)	1.000
C(22)	-0.034(16)	0.015(13)	-0.011(14)	0.018(13)	-0.004(14)	-0.004(14)	0.001(14)	0.040(13)	0.013(14)	1.000
C(23)	0.056(16)	0.025(13)	-0.009(14)	-0.011(13)	-0.004(14)	0.015(14)	0.029(14)	0.008(14)	0.019(13)	1.000
C(24)	0.047(15)	0.022(13)	0.011(14)	-0.036(14)	-0.010(14)	0.019(13)	-0.033(13)	0.036(12)	-0.029(12)	1.000
C(25)	-0.010(15)	-0.019(12)	-0.003(14)	-0.010(13)	0.022(13)	0.002(13)	0.004(13)	0.040(13)	-0.002(13)	1.000
C(26)	0.016(16)	-0.016(13)	-0.034(14)	-0.006(13)	-0.014(14)	-0.009(13)	0.025(14)	-0.017(13)	-0.015(13)	1.000
C(27)	-0.009(14)	-0.044(13)	0.038(14)	-0.049(13)	-0.021(13)	0.013(12)	-0.024(12)	0.007(11)	0.007(11)	1.000

A test case, PROPY-4HBA, was used to compare the effect of refining all multipoles with only those which had significant populations. The details of the two comparative refinements are shown in Table B.5 below. The R factor is reduced with increased multipole refinement and a slightly smaller residual density observed. The data : parameter ratio is, as expected, much higher when fewer multipoles are refined and the convergence similar for both models.

Table B.5. Comparison of refinement statistics for PROPY-4HBA when all multipoles and only those statistically significant are refined.

	All multipoles refined (non-H to hexadecapole, H to single quadrupole)	**Only significant populations refined**
	κ fixed, 20 cycles	
R{F}	0.0187	0.0190
R{F^2}	0.0223	0.0231
GoF	0.9684	0.9778
Data / parameter ratio	28.054	42.000
Convergence	0.6173×10^{-11} for N(2)/X	0.5612×10^{-11} for N(2)/Z
$\Delta\rho(\mathbf{r})$ /e Å^{-3}	-0.127 / 0.118	-0.131 / 0.123

Whilst this approach, refining only statistically meaningful multiple populations, may provide more representative models with a reduced possibility of overfitting and increased data : parameter ratio, there was no pattern for the statistically meaningful octapoles and hexadecapoles across all the systems. As the primary aim of these studies was to allow for comparisons between the systems, atoms across the series were required to be modelled similarly; the hexadecapole level was deemed appropriate for all non-H atoms, accommodating those atoms with large hexadecapole populations. Using all multipoles still gave data : parameter ratios above the suggested value of 10 for all systems.

B.1.5 Charge Comparisons

See document “Charge Comparisons.doc”

Several different models were generated for each system and these were compared with theoretical data to assess their validity, in particular the atomic charges. Theoretical wave functions generated using Gaussian09 C.01 version 9.0[279, 343] provided Mulliken atomic

populations (charges) which could be compared to those determined from the various experimental models. B3LYP/6G** has been shown to be the most accurate in recent studies, whilst PIXEL energy densities are calculated using the MP2 level of theory. Both MP2 and B3LYP basis sets were therefore applied and atomic co-ordinates obtained from both spherical atom and multipolar model refinements were used. It was observed that the co-ordinates used as the input had little effect on the resulting charges; both models produced very similar charges when the same level of theory was applied. The two levels of theory produced differing populations and charges, however they were comparable to the experimental models. By comparing these different values, an assessment of the best approach to take with the experimental data could be completed, and the models to be used for topological analysis determined. Those with no absorption correction applied were seen to be the most similar to the theoretical data.

B.1.6 Strategy for Multipole Refinement

Absorption methods have their application but it was found in this instance that they were not wholly appropriate. XABS2 appeared to reduce the residual density somewhat, and smooth the fractal distribution curve, however other properties were not improved. A chemical unreasonable model resulted in some systems with positive charges on oxygen atoms. Ultimately the chemical nature of the system directed the choice of model: electronegative atoms, in particular oxygen, should have a negative charge, and any model indicating a positive oxygen is chemically inappropriate. Hexadecapoles (and lower multipoles) were refined for all non-hydrogen atoms for consistency. Whilst this may not be the most appropriate method for all models and the level of multipole refinement may be best taken on an atom by atom basis, this allows for comparisons to be made across the series. The statistics resulting from the different combinations of multipole populations did not show stark differences between them; no great improvement, or decline in model was seen, although the reduction of atoms refined to the hexadecapole level will increase the data : parameter ratio and may limit overfitting.

The overall approach taken for data processing, manipulation, and multipolar modelling was selected as providing the best overall models, whilst being consistent in the methodology across the series of structures. Using indicators described, and the statistics of the refinement, the models were critically evaluated and the best used for topological evaluation in the subsequent analysis.

B.2 Final Experimental Multipole Models

Table B.6 outlines the parameters of data collection and refinement for each of the four structures. The method used for data reduction, spherical model refinement and the following multipolar refinement is outlined in the Experimental, Section 8.7.

Table B.6. Data collection and refinement parameters for the four experimental multipole models of PROPY systems.

	PROPY-4HBA	**PROPY-FA**	**PROPY-HQ**	**PROPY-MPAR**
Chemical formula	$C_{14}H_{18}N_2O\cdot 2(C_7H_6O_3)$	$C_{14}H_{18}N_2O \cdot 0.5(C_4H_4O_4)$	$C_{14}H_{18}N_2O \cdot 2(C_6H_6O_2)$	$C_{14}H_{18}N_2O \cdot C_8H_8O_3$
M_r	368.42	288.34	450.52	382.45
Crystal system, space group	Monoclinic $P2_1/c$	Triclinic, $P\bar{1}$	Triclinic, $P\bar{1}$	Orthorhombic, $P2_12_12_1$
a/Å	6.8751(1)	8.1291(2)	9.12940(10)	6.750
b / Å	15.4396(2)	9.7073(2)	9.97660(10)	10.91420(10)
c/ Å	18.2448(2)	9.9628(2)	14.58110(10)	27.4626(2)
α / °	90.00	85.174(2)	109.5150(10)	90.00
β / °	97.781(1)	76.439(2)	101.7040(10)	90.00
γ /°	90.00	80.229(2)	98.3120(10)	90.00
Volume / $Å^3$	1918.83(4)	752.37(3)	1192.86(2)	2023.22(2)
Z	4	2	2	4
λ (Å)	0.71075	0.71075	0.71075	0.71075
Density	1.275	1.273	1.254	1.256
F (000)	784.0	308.0	480.00	816.0
Crystal morphology	Colourless block	Colourless chunk	Colourless plate	Colourless block
Crystal size	0.533 x 0.103 x 0.078	0.19 x 0.10 x 0.09	0.454 x 0.32 x 0.054	0.357 x 0.13 x 0.116

	PROPY-4HBA	PROPY-FA	PROPY-HQ	PROPY-MPAR
No. collected reflections	386876	219798	329685	325675
I/σ	16.9603	19.3673	16.4417	18.4181
R_{merge}	0.0440	0.0297	0.0386	0.0411
Completeness /%	99.90	99.40	98.00	99.93
Redundancy	12.8	9.6	9.1	10.5 (19.3)
Spherical refinement				
Total reflections/ unique	29832 / 29229	22567 / 22573	35655/35651	30931 / 30871
R_1 ($F^2 > 2\theta\{F^2\}$)	0.0383	0.0365	0.0434	0.0309
R_1 (all)	0.0460	0.0418	0.0511	0.0345
wR2 ($F^2 > 2\theta\{F^2\}$)	0.1118	0.1157	0.1246	0.0799
wR2 (all)	0.1167	0.1200	0.1306	0.0817
GoF	1.0267	1.030	1.007	1.010
$\Delta\rho(\mathbf{r})$ /e Å^{-3}	-0.34 / 0.70	-0.39 / 0.74	-0.52 / 0.73	-0.18 / 0.45
Multipole refinement				
Total data / included	29829 / 25244	22567 / 19919	35655 / 30428	30926 / 28911
Scale	1.500116	2.263602	1.214132	11.275485
R{F}	0.0273	0.0217	0.0292	0.0217
$R\{F^2\}$	0.0385	0.0275	0.0387	0.0280
GoF	1.4056	1.3415	1.5505	1.1313
Max sin (θ/λ) /Å	1.22089	1.22240	1.22081	1.22116
Data / parameter	25.4990	25.7351	25.1056	29.5613

	PROPY-4HBA	**PROPY-FA**	**PROPY-HQ**	**PROPY-MPAR**
Convergence	0.293959×10^{-4} for C(24)/U13 (20 cycles)	0.841400×10^{-11} for C(5)/Y (20 cycles)	0.262373×10^{-11} for N(1)/X (15 cycles)	0.407416×10^{-11} for C(4)/X (15 cycles)
$\Delta\rho(\mathbf{r})$ /e Å^{-3}	-0.249 / 0.368 RMS = 0.049	-0.139 / 0.366 RMS = 0.028	-0.342 / 0.497 RMS = 0.037	-0.118 / 0.174 RMS = 0.028

B.3 Topological Analysis

Topological analysis of the electron density was carried out on the final models to enable intermolecular interaction analysis. Atomic charges were determined using a variety of approaches (Mulliken populations, Stockholder moments and Bader charges) and critical point searches completed.

B.3.1 Labelling of PROPY Molecule

It was realised during analysis that the labelling of the isopropyl and ring carbon atoms of PROPY were not consistent across the systems. For ease of analysis, a conversion was applied so that atomic labels are comparable across all four models. Figure B.11 shows the original labelling scheme employed for the four models, as used in multipole model CIF files and the refinement outputs generated from WinXD.[324] PROPY-4HBA labelling has been used as the 'standard' to which all have been normalised for comparison purposes and used in tables and analysis herein.

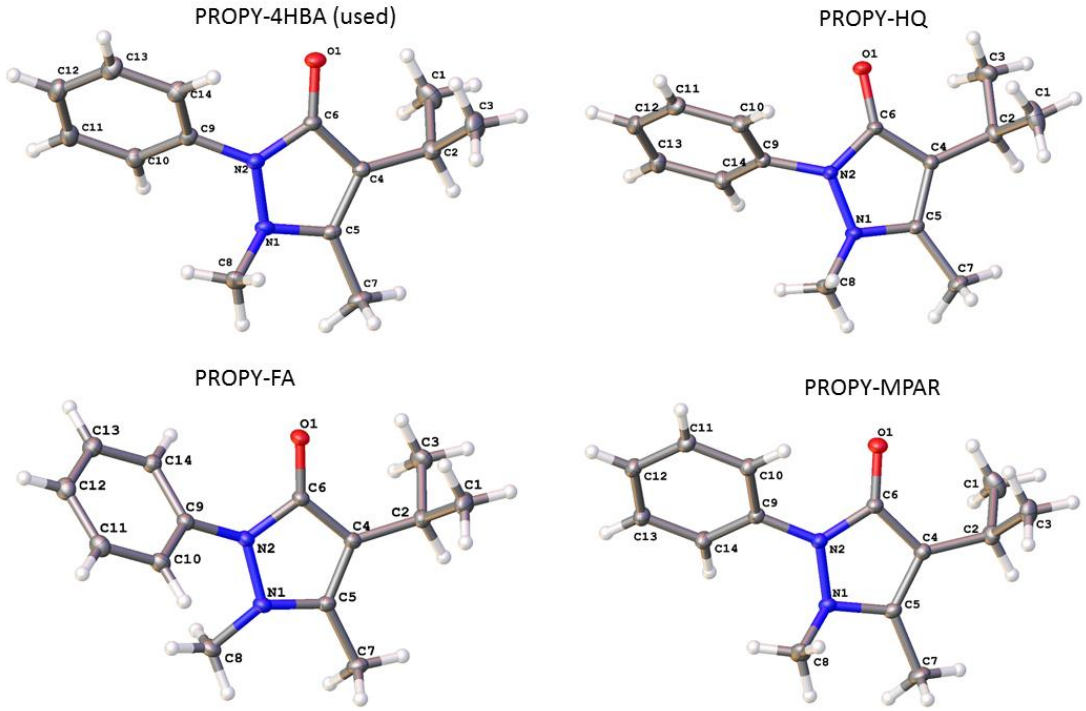

Figure B.11. Original labelling scheme of PROPY in the four structures used for multipole models.

B.3.2 Analysis of Models

Figures B.5, B.6 and B.8 show the resulting fractal dimension distribution plots, normal probability plots and static deformation density plots for the four models. There are some areas, evident in particular in the fractal dimension distribution plots, where improvements could be made. Different approaches were taken to investigate these (see Section B.1) and these models are

those best possible with the data and available approaches. It is likely that absorption has an effect on the models and has not been fully corrected for due to the absence of face-indexing. This is seen in some of the features, such as shoulders and larger widths in the fractal dimension distribution plots.

B.3.3 Atomic Charges

There are several ways to partition atomic space to determine the charge associated with each nucleus (Chapter 2.1.4.2.1). Three different partitioning schemes, Stockholder, Bader and Mulliken were applied and the associated charges determined for each of the four systems. These are given in Tables B.7 (PROPY atoms) and B.8 (co-former molecule atoms).

Table B.7. Atomic charges (Mulliken, Bader and Stockholder partitioning) for PROPY in all four systems.

PROPY charges	PROPY-4HBA			PROPY-FA			PROPY-HQ			PROPY-MPAR		
	Mulliken	Stockholder	Bader	Mulliken	Stockholder	Bader	Mulliken	Stockholder	Bader	Mulliken	Stockholder	Bader
O(1)	-0.423(16)	-0.333	-1.061	-0.523(13)	-0.386	-1.179	-0.509(17)	-0.327	-1.094	-0.389(19)	-0.331	-1.032
N(1)	-0.128(20)	-0.119	-0.752	-0.211(16)	-0.116	-0.706	-0.227(21)	-0.096	-0.687	-0.122(23)	-0.146	-0.714
N(2)	-0.201(21)	-0.143	-0.753	-0.116(17)	-0.044	-0.665	-0.242(21)	-0.096	-0.713	-0.307(24)	-0.155	-0.843
C(1)	-1.579(56)	-0.199	-1.285	-0.321(43)	-0.095	-0.253	-0.544(58)	-0.068	-0.961	-1.220(36)	-0.042	-0.505
C(2)	0.010(33)	-0.188	-0.139	0.216(28)	-0.017	0.117	0.248(34)	-0.047	-0.137	-0.064(31)	-0.040	0.090
C(3)	-1.728(51)	-0.207	-1.280	-0.319(42)	-0.023	-0.214	-0.697(60)	-0.084	-0.814	-1.103(35)	-0.051	-0.408
C(4)	-0.292(30)	-0.216	-0.243	-0.231(25)	-0.142	-0.174	-0.155(29)	-0.123	-0.127	-0.181(34)	-0.166	-0.145

PROPY charges	PROPY-4HBA			PROPY-FA			PROPY-HQ			PROPY-MPAR		
	Mulliken	Stockholder	Bader	Mulliken	Stockholder	Bader	Mulliken	Stockholder	Bader	Mulliken	Stockholder	Bader
C(5)	0.280(27)	0.031	0.393	0.058(23)	0.001	0.278	0.139(27)	0.015	0.320	-0.047(32)	-0.135	0.047
C(6)	-0.047(26)	-0.030	0.844	0.053(22)	0.038	0.959	0.004(27)	0.032	0.820	-0.025(31)	0.002	0.869
C(7)	-0.932(50)	-0.021	-0.702	-0.190(42)	-0.060	-0.271	-0.339(51)	-0.101	-0.834	-1.121(33)	-0.028	-0.326
C(8)	-1.297(49)	-0.150	-0.755	-0.372(41)	-0.155	-0.243	-0.331(48)	-0.088	-0.724	-1.195(31)	-0.046	-0.212
C(9)	-0.010(30)	-0.142	0.151	0.010(24)	-0.050	0.236	0.112(28)	0.002	0.210	0.081(31)	-0.084	0.246
C(10)	-0.520(35)	-0.158	-0.426	-0.104(30)	-0.100	-0.154	-0.166(38)	-0.078	-0.363	-0.429(33)	-0.070	-0.175
C(11)	-0.043(37)	-0.120	0.023	-0.119(31)	-0.078	-0.146	-0.072(39)	-0.063	-0.254	-0.285(36)	-0.048	-0.173
C(12)	-0.768(40)	-0.150	-0.752	-0.055(30)	-0.050	-0.139	-0.062(41)	-0.052	-0.460	-0.512(35)	-0.153	-0.108
C(13)	-0.273(38)	-0.072	-0.374	-0.022(30)	-0.029	-0.093	0.087(38)	0.017	-0.331	-0.348(34)	-0.117	0.027
C(14)	-0.355(35)	-0.117	-0.353	-0.033(28)	-0.049	-0.073	-0.122(38)	-0.018	-0.296	-0.407(32)	-0.115	-0.085
H(1A)	0.490(20)	0.105	0.409	0.086(19)	0.051	0.093	0.189(27)	0.054	0.478	0.504(19)	0.085	0.204
H(1B)	0.430(19)	0.043	0.349	0.140(20)	0.079	0.120	0.162(25)	0.066	0.343	0.425(18)	0.094	0.154

PROPY charges	PROPY-4HBA			PROPY-FA			PROPY-HQ			PROPY-MPAR		
	Mulliken	Stockholder	Bader	Mulliken	Stockholder	Bader	Mulliken	Stockholder	Bader	Mulliken	Stockholder	Bader
H(1C)	0.469(21)	0.088	0.398	0.129(19)	0.027	0.102	0.221(25)	0.070	0.397	0.464(17)	0.136	0.274
H(2)	0.369(15)	0.142	0.383	0.043(16)	0.096	0.082	0.085(21)	0.134	0.406	0.439(16)	0.147	0.146
H(3A)	0.502(20)	0.098	0.439	0.198(19)	0.052	0.136	0.228(27)	0.107	0.406	0.459(19)	0.103	0.201
H(3B)	0.504(19)	0.065	0.352	0.142(21)	0.092	0.125	0.256(26)	0.071	0.296	0.373(19)	0.080	0.097
H(3C)	0.550(20)	0.029	0.458	0.175(20)	0.094	0.167	0.286(30)	0.042	0.296	0.396(18)	0.084	0.176
H(7A)	0.351(18)	0.083	0.284	0.209(18)	0.134	0.250	0.218(26)	0.086	0.388	0.451(18)	0.124	0.193
H(7B)	0.440(18)	0.137	0.418	0.113(19)	0.119	0.159	0.104(25)	0.106	0.410	0.472(18)	0.135	0.122
H(7C)	0.341(19)	0.108	0.303	0.167(18)	0.110	0.196	0.136(24)	0.071	0.410	0.452(17)	0.111	0.162
H(8A)	0.447(19)	0.100	0.400	0.168(18)	0.061	0.219	0.214(24)	0.084	0.384	0.450(18)	0.090	0.221
H(8B)	0.449(18)	0.069	0.382	0.167(18)	0.097	0.171	0.181(23)	0.130	0.454	0.494(18)	0.134	0.224
H(8C)	0.402(18)	0.062	0.358	0.181(18)	0.099	0.222	0.267(24)	0.141	0.499	0.534(19)	0.142	0.302
H(10)	0.439(16)	0.129	0.441	0.145(16)	0.134	0.214	0.150(21)	0.098	0.355	0.389(16)	0.105	0.172

PROPY charges	PROPY-4HBA			PROPY-FA			PROPY-HQ			PROPY-MPAR		
	Mulliken	Stockholder	Bader	Mulliken	Stockholder	Bader	Mulliken	Stockholder	Bader	Mulliken	Stockholder	Bader
H(11)	0.364(17)	0.124	0.339	0.132(16)	0.121	0.165	0.083(23)	0.098	0.348	0.384(16)	0.107	0.219
H(12)	0.480(16)	0.176	0.469	0.089(18)	0.134	0.146	0.088(23)	0.123	0.380	0.419(16)	0.113	0.157
H(13)	0.399(16)	0.193	0.391	0.175(16)	0.147	0.255	0.163(22)	0.154	0.397	0.413(17)	0.137	0.162
H(14)	0.375(16)	0.179	0.425	0.145(15)	0.117	0.208	0.155(21)	0.066	0.298	0.337(16)	0.071	0.190

Note, atom re-labelling used to enable atomic comparisons between structures. Methyl hydrogen atoms may not be labelled the same, i.e. H1A/B/C may be different across the systems.

Table B.8. Atomic charges (Mulliken, Bader and Stockholder partitioning) for all co-former atoms in all four systems.

Co-former	PROPY-4HBA				PROPY-FA				PROPY-HQ				PROPY-MPAR		
	Mulliken	Stockholder	Bader		Mulliken	Stockholder	Bader		Mulliken	Stockholder	Bader		Mulliken	Stockholder	Bader
O(21)	-0.444(19)	-0.265	-1.132	**O(21)**	-0.321(16)	-0.180	-1.030	**O(21)**	-0.459(22)	-0.329	-1.124	**O(21)**	-0.583(20)	-0.197	-1.092
O(22)	-0.349(19)	-0.195	-1.091	**O(22)**	-0.465(16)	-0.430	-1.150	**O(22)**	-0.474(23)	-0.330	-1.105	**O(22)**	-0.370(20)	-0.382	-1.073
O(23)	-0.431(17)	-0.414	-1.099	**C(21)**	0.098(22)	0.026	1.183	**O(31)**	-0.415(21)	-0.306	-1.061	**O(23)**	-0.228(19)	-0.221	-1.137
C(21)	0.040(27)	-0.024	0.443	**C(22)**	-0.295(30)	-0.152	-0.283	**O(32)**	-0.446(23)	-0.335	-1.120	**C(21)**	0.292(33)	0.012	0.531
C(22)	-0.223(33)	-0.052	-0.299	**H(21)**	0.392(12)	0.176	0.700	**C(21)**	-0.039(32)	-0.067	0.294	**C(22)**	-0.553(39)	-0.139	-0.448
C(23)	-0.304(32)	-0.029	-0.300	**H(22)**	0.259(17)	0.151	0.294	**C(22)**	-0.089(39)	-0.091	-0.091	**C(23)**	-0.383(35)	-0.087	-0.350
C(24)	0.119(27)	-0.049	0.080					**C(23)**	-0.108(39)	-0.101	-0.141	**C(24)**	0.168(32)	-0.035	0.098
C(25)	-0.151(34)	0.027	-0.140					**C(24)**	-0.034(31)	-0.064	0.265	**C(25)**	-0.252(35)	-0.010	-0.192
C(26)	-0.300(33)	-0.074	-0.352					**C(25)**	-0.084(39)	-0.108	-0.105	**C(26)**	-0.634(39)	-0.196	-0.539
C(27)	0.045(26)	0.131	1.199					**C(26)**	-0.059(39)	-0.085	-0.110	**C(27)**	0.066(29)	0.094	1.159
H(21)	0.389(13)	0.169	0.693					**C(31)**	0.057(29)	-0.003	0.307	**C(28)**	-1.426(33)	-0.100	-0.781

Co-former	PROPY-4HBA			PROPY-FA			PROPY-HQ			PROPY-MPAR		
	Mulliken	Stockholder	Bader	Mulliken	Stockholder	Bader	Mulliken	Stockholder	Bader	Mulliken	Stockholder	Bader
H(22)	0.489(13)	0.327	0.756				**C(32)** -0.025(35)	-0.050	-0.053	**H(21)** 0.526(14)	0.166	0.711
H(22A)	0.403(16)	0.214	0.485				**C(33)** -0.147(36)	-0.090	-0.154	**H(22)** 0.454(16)	0.148	0.428
H(23)	0.440(16)	0.214	0.464				**C(34)** 0.040(30)	-0.025	0.329	**H(23)** 0.353(15)	0.096	0.327
H(25)	0.343(16)	0.185	0.385				**C(35)** -0.193(37)	-0.127	-0.192	**H(25)** 0.410(16)	0.136	0.370
H(26)	0.437(16)	0.234	0.455				**C(36)** -0.034(37)	-0.060	-0.067	**H(26)** 0.385(17)	0.096	0.358
							H(21) 0.309(18)	0.164	0.645	**H(28A)** 0.556(18)	0.107	0.531
							H(22) 0.291(18)	0.213	0.604	**H(28B)** 0.495(18)	0.097	0.448
							H(22A) 0.155(22)	0.096	0.160	**H(28C)** 0.540(18)	0.142	0.508
							H(23) 0.174(22)	0.145	0.212			
							H(25) 0.095(23)	0.114	0.120			
							H(26) 0.151(22)	0.158	0.200			
							H(31) 0.232(17)	0.128	0.626			

Co-former	PROPY-4HBA			PROPY-FA				PROPY-HQ			PROPY-MPAR		
	Mulliken	Stockholder	Bader	Mulliken	Stockholder	Bader		Mulliken	Stockholder	Bader	Mulliken	Stockholder	Bader
							H(32)	0.251(18)	0.205	0.604			
							H(32A)	0.137(20)	0.106	0.207			
							H(33)	0.150(21)	0.114	0.172			
							H(35)	0.136(22)	0.087	0.170			
							H(36)	0.113(22)	0.116	0.143			

B.3.4 BCP Searches

A full critical point search – (3,-1), (3,+1), (3,+3) – was carried out, with appropriate symmetry operations applied to generate equivalent molecules with which the main components interact. To ensure the correct symmetry-related molecules were generated and included in the search, the Crystal Explorer visual display was examined to identify the molecules forming the interactions. An equivalent packing structure was generated in Mercury[107] to identify the interactions and relevant symmetry operations. The number of symmetry operations that can be applied in a single search in WinXD is limited, so that several searches were required to include all necessary symmetry operations. Interactions within the atomic separation distance range 0.8-3.5 Å were detected and full output obtained for each system. When compared to the packing model generated in Mercury, any interactions which appeared likely but were not output from the original search were added into an additional, specific, search to ensure they were located, if present.

The data for the intermolecular interactions (BCPs) in each of the systems are shown in Tables B.9-B.13. All other critical point data are not applicable to the analyses carried out in this work so are omitted for clarity. For interaction analysis and energies estimated from $\rho(r_{BCP})$ and $\nabla^2\rho(\mathbf{r})$ using the EML[171] scheme see Supplementary File PROPY_XD Interactions

B.3.4.1 PROPY-4HBA

Table B.9. BCP data for PROPY-4HBA showing intermolecular interactions only.

Interaction		d_1 / Å	d_2 / Å	R_{ij} / Å	$\rho(r)$ / e Å^{-3}	$\nabla^2\rho(r)$ / e Å^{-5}	λ_1	λ_2	λ_3	ε
H(21)	O(1)	0.587	1.121	1.708	0.28	2.66	-1.80	-1.72	6.18	0.05
H(22A)	O(1)	1.065	1.472	2.536	0.05	0.85	-0.18	-0.12	1.15	0.48
H(3A)	O(21)	1.265	1.702	2.967	0.02	0.32	-0.05	-0.02	0.38	1.77
X1_H(7A)	O(1)	0.973	1.400	2.372	0.08	0.99	-0.3	-0.3	1.59	0.01
X2_H(10)	O(21)	1.230	1.652	2.882	0.04	0.49	-0.11	-0.03	0.63	2.21
X2_H(7C)	O(21)	1.163	1.546	2.709	0.04	0.50	-0.15	-0.13	0.78	0.11
X2_H(7B)	O(22)	1.251	1.554	2.805	0.03	0.52	-0.09	-0.04	0.65	1.25
X3_H(13)	O(22)	1.240	1.646	2.886	0.02	0.31	-0.09	-0.05	0.45	0.83
X3_H(22)	O(23)	0.481	1.119	1.600	0.32	3.68	-2.43	-2.39	8.49	0.02
X1_H(14)	O(23)	0.868	1.396	2.264	0.07	1.22	-0.27	-0.26	1.75	0.07
X1_O(21)	O(23)	1.634	1.634	3.268	0.03	0.48	-0.07	-0.05	0.60	0.51
H(7A)	X1_O(1)	0.973	1.399	2.372	0.08	1.00	-0.30	-0.30	1.59	0.01
H(10)	X2_O(21)	1.230	1.652	2.882	0.04	0.49	-0.11	-0.03	0.63	2.21
H(7C)	X2_O(21)	1.163	1.546	2.709	0.04	0.50	-0.15	-0.13	0.78	0.11
H(7B)	X2_O(22)	1.247	1.553	2.800	0.03	0.53	-0.09	-0.04	0.65	1.26
H(13)	X3_O(22)	1.253	1.641	2.893	0.02	0.32	-0.09	-0.05	0.45	0.68

Interaction		d_1 / Å	d_2 / Å	R_{ij} / Å	$\rho(r)$ / e Å^{-3}	$\nabla^2\rho(r)$ / e Å^{-5}	λ_1	λ_2	λ_3	ε
H(22)	X3_O(23)	0.483	1.116	1.600	0.31	3.63	-2.41	-2.37	8.41	0.02
O(21)	X1_O(23)	1.634	1.635	3.268	0.03	0.48	-0.07	-0.05	0.60	0.51
O(23)	X4_H(12)	1.466	1.062	2.527	0.05	0.78	-0.18	-0.16	1.13	0.08
H(23)	X1_N(2)	1.138	1.700	2.838	0.02	0.38	-0.09	-0.06	0.53	0.55
H(23)	X1_N(2)	1.154	1.791	2.944	0.03	0.42	-0.09	-0.03	0.54	1.85
X1_H(22A)	C(5)	1.294	1.929	3.223	0.02	0.22	-0.03	-0.01	0.27	1.20
X2_H(25)	C(5)	1.525	1.671	3.197	0.04	0.42	-0.07	-0.06	0.55	0.24
X1_H(8A)	C(12)	1.474	1.754	3.228	0.06	0.54	-0.11	-0.04	0.69	1.59
X1_H(8A)	C(13)	1.142	1.647	2.789	0.06	0.61	-0.15	-0.04	0.80	2.31
C(14)	C(22)	1.927	1.929	3.856	0.02	0.22	-0.04	-0.03	0.29	0.16
X1_H(3C)	C(22)	1.449	1.890	3.339	0.02	0.19	-0.03	-0.02	0.25	0.43
X3_C(27)	C(25)	1.639	1.655	3.294	0.04	0.42	-0.09	-0.07	0.57	0.25
H(22A)	X1_C(5)	1.294	1.929	3.223	0.02	0.22	-0.03	-0.01	0.27	1.20
H(25)	X2_C(5)	1.525	1.671	3.197	0.04	0.42	-0.07	-0.06	0.55	0.24
H(8A)	X1_C(13)	1.142	1.647	2.789	0.06	0.61	-0.15	-0.04	0.80	2.31
H(3C)	X1_C(22)	1.451	1.890	3.341	0.02	0.19	-0.03	-0.02	0.25	0.47
C(27)	X3_C(25)	1.639	1.655	3.294	0.04	0.42	-0.09	-0.07	0.57	0.25
X2_H(8C)	H(3B)	1.190	1.483	2.672	0.04	0.42	-0.10	-0.05	0.57	0.80
X2_H(26)	H(7C)	1.221	1.292	2.514	0.03	0.36	-0.07	-0.05	0.49	0.34
X2_H(3C)	H(10)	1.210	1.211	2.420	0.04	0.43	-0.14	-0.10	0.66	0.36
X2_H(3A)	H(11)	1.352	1.370	2.722	0.02	0.27	-0.06	-0.05	0.38	0.13
X4_H(2)	H(12)	1.129	1.253	2.381	0.04	0.44	-0.12	-0.10	0.66	0.17
X4_H(7B)	H(13)	1.218	1.221	2.440	0.02	0.30	-0.11	-0.07	0.48	0.60
X1_H(26)	H(22)	1.555	1.692	3.248	0.01	0.18	-0.03	-0.02	0.23	0.57
X1_H(8A)	H(22A)	1.243	1.291	2.534	0.03	0.35	-0.07	-0.06	0.48	0.12
X2_H(1A)	H(25)	1.210	1.228	2.438	0.03	0.38	-0.08	-0.07	0.53	0.24
H(8C)	X2_H(3B)	1.190	1.483	2.672	0.04	0.42	-0.10	-0.05	0.57	0.80
H(26)	X2_H(7C)	1.222	1.292	2.514	0.03	0.36	-0.07	-0.05	0.49	0.33
H(3C)	X2_H(10)	1.210	1.211	2.420	0.04	0.43	-0.14	-0.10	0.66	0.36
H(3A)	X2_H(11)	1.352	1.370	2.722	0.02	0.27	-0.06	-0.05	0.38	0.13
H(26)	X1_H(22)	1.547	1.718	3.265	0.01	0.18	-0.03	-0.02	0.22	0.46
H(1A)	X2_H(25)	1.210	1.228	2.438	0.03	0.38	-0.08	-0.07	0.53	0.24

B.3.4.2 PROPY-FA

Table B.10. BCP data for PROPY-FA showing intermolecular interactions only.

Interaction		d_1 / Å	d_2 / Å	R_{ij} / Å	$\rho(r)$ / e Å^{-3}	$\nabla^2\rho(r)$ / e Å^{-5}	λ_1	λ_2	λ_3	ε
O(21)	H(1A)	1.049	1.049	2.098	0.03	0.72	-0.11	-0.10	0.92	0.11
X2_H(8C)	O(1)	1.011	1.526	2.537	0.04	0.65	-0.16	-0.14	0.96	0.13
X2_H(13)	O(1)	0.995	1.458	2.453	0.06	0.64	-0.26	-0.25	1.15	0.05
X2_H(1C)	O(1)	1.251	1.827	3.079	0.02	0.29	-0.05	-0.02	0.37	1.44
X2_H(7A)	O(21)	1.253	1.669	2.922	0.02	0.36	-0.06	-0.03	0.45	0.89
X1_H(2)	O(21)	1.295	1.618	2.913	0.03	0.29	-0.11	-0.07	0.47	0.42
X1_H(7B)	O(21)	1.137	1.565	2.703	0.03	0.38	-0.13	-0.11	0.61	0.23
H(3C)	O(22)	1.065	1.497	2.562	0.04	0.66	-0.15	-0.15	0.96	0.03
X2_H(1B)	O(22)	1.492	1.798	3.290	0.01	0.14	-0.03	-0.03	0.20	0.21
X2_H(12)	O(22)	1.029	1.492	2.521	0.04	0.78	-0.17	-0.10	1.05	0.67
X1_H(11)	O(22)	1.037	1.457	2.494	0.06	0.95	-0.20	-0.19	1.35	0.03
H(8C)	X2_O(1)	1.011	1.526	2.537	0.04	0.65	-0.16	-0.14	0.96	0.13
H(13)	X2_O(1)	0.995	1.458	2.453	0.06	0.64	-0.26	-0.25	1.15	0.04
H(1C)	X2_O(1)	1.251	1.828	3.079	0.02	0.29	-0.05	-0.02	0.37	1.44
H(7A)	X2_O(21)	1.253	1.669	2.922	0.02	0.36	-0.06	-0.03	0.45	0.89
H(1B)	X2_O(22)	1.492	1.798	3.290	0.01	0.14	-0.03	-0.03	0.20	0.21
H(12)	X2_O(22)	1.030	1.492	2.521	0.04	0.78	-0.17	-0.10	1.05	0.64
H(2)	X1_O(21)	1.295	1.618	2.913	0.03	0.29	-0.11	-0.07	0.47	0.42
H(11)	X1_O(22)	1.037	1.457	2.494	0.06	0.95	-0.20	-0.20	1.35	0.02
X2_H(14)	C(5)	1.113	1.693	2.806	0.03	0.52	-0.07	-0.03	0.62	1.57
X2_H(3A)	C(13)	1.230	1.788	3.017	0.04	0.36	-0.08	-0.02	0.47	2.36
X2_H(3B)	C(22)	1.384	1.957	3.341	0.01	0.15	-0.03	-0.03	0.21	0.27
X1_H(3B)	C(22)	1.391	1.901	3.292	0.01	0.19	-0.03	-0.03	0.24	0.11
H(14)	X2_C(5)	1.113	1.693	2.806	0.03	0.52	-0.07	-0.03	0.62	1.57
H(7C)	X1_C(13)	1.165	1.922	3.087	0.02	0.29	-0.06	-0.02	0.37	1.73
H(3A)	X2_C(13)	1.230	1.788	3.017	0.04	0.36	-0.08	-0.02	0.47	2.36
H(3B)	X1_C(22)	1.391	1.901	3.292	0.01	0.19	-0.03	-0.03	0.24	0.11
X2_H(7A)	H(2)	1.254	1.294	2.548	0.02	0.25	-0.05	-0.03	0.33	0.42
X1_H(10)	H(3B)	1.158	1.379	2.537	0.02	0.32	-0.06	-0.02	0.39	2.80
X1_H(11)	H(3C)	1.223	1.302	2.525	0.02	0.39	-0.07	-0.05	0.51	0.41
X2_H(7B)	H(7A)	1.334	1.562	2.896	0.01	0.19	-0.04	-0.01	0.24	1.85
X2_H(1C)	H(7A)	1.249	1.457	2.705	0.03	0.41	-0.07	-0.02	0.50	2.07
X2_H(22)	H(7A)	1.074	1.089	2.163	0.03	0.50	-0.10	-0.08	0.68	0.19
X1_O(21)	H(7B)	1.137	1.137	2.274	0.03	0.38	-0.13	-0.11	0.61	0.23
X2_H(14)	H(8C)	1.114	1.261	2.375	0.04	0.38	-0.13	-0.09	0.60	0.42
X2_H(1B)	H(10)	1.205	1.579	2.784	0.03	0.48	-0.08	-0.05	0.61	0.72
X2_H(8A)	H(11)	1.166	1.313	2.479	0.03	0.51	-0.10	-0.05	0.67	0.98
X2_H(12)	H(11)	1.137	1.417	2.554	0.02	0.27	-0.08	-0.06	0.41	0.41
X1_H(8B)	H(12)	1.236	1.594	2.830	0.04	0.45	-0.09	-0.07	0.61	0.39
X2_H(14)	H(13)	1.283	1.508	2.791	0.01	0.27	-0.02	-0.01	0.31	0.82

Interaction		d_1 / Å	d_2 / Å	R_{ij} / Å	$\rho(r)$ / e Å^{-3}	$\nabla^2\rho(r)$ / e Å^{-5}	λ_1	$\lambda 2$	λ_3	ε
H(1A)	H(21)	1.049	1.498	2.547	0.03	0.72	-0.11	-0.10	0.92	0.11
O(1)	H(21)	0.493	0.493	0.985	0.43	2.52	-3.50	-3.38	9.39	0.04
X2_H(1C)	H(21)	1.489	1.744	3.233	0.01	0.12	-0.02	-0.01	0.15	0.83
H(7A)	X2_H(2)	1.254	1.313	2.567	0.02	0.24	-0.04	-0.03	0.32	0.40
H(10)	X1_H(3B)	1.158	1.379	2.537	0.02	0.32	-0.06	-0.02	0.39	2.80
H(11)	X1_H(3C)	1.223	1.303	2.525	0.02	0.39	-0.07	-0.05	0.51	0.41
H(7B)	X2_H(7A)	1.310	1.589	2.899	0.01	0.20	-0.04	-0.02	0.26	1.29
H(1C)	X2_H(7A)	1.248	1.458	2.706	0.03	0.41	-0.07	-0.02	0.50	2.05
H(22)	X2_H(7A)	1.074	1.089	2.163	0.03	0.50	-0.10	-0.08	0.68	0.19
H(14)	X2_H(8C)	1.114	1.261	2.375	0.04	0.38	-0.13	-0.09	0.60	0.42
H(1B)	X2_H(10)	1.205	1.579	2.784	0.03	0.48	-0.08	-0.05	0.61	0.72
H(8A)	X2_H(11)	1.166	1.313	2.479	0.03	0.51	-0.10	-0.05	0.67	0.98
H(12)	X2_H(11)	1.137	1.419	2.556	0.02	0.27	-0.08	-0.06	0.41	0.44
H(8B)	X1_H(12)	1.236	1.594	2.830	0.04	0.45	-0.09	-0.07	0.61	0.39
H(14)	X2_H(13)	1.277	1.524	2.801	0.01	0.27	-0.02	-0.01	0.30	1.30
H(1C)	X2_H(21)	1.489	1.745	3.233	0.01	0.12	-0.02	-0.01	0.15	0.82

Table B.11. BCP data for covalent bonds of FA in PROPY-FA showing only key bonds used in the analysis and discussion (Section 5.6.3).

Bond		d_1 / Å	d_2 / Å	R_{ij} / Å	$\rho(r)$ / e Å^{-3}	$\nabla^2\rho(r)$ / e Å^{-5}	λ_1	λ_2	λ_3	ε
O(22)	C(21)	0.479	0.479	0.958	3.10	-37.15	-28.52	-27.18	18.55	0.05
O(21)	C(21)	0.528	0.528	1.056	2.38	-26.81	-21.44	-21.06	15.69	0.02
C(21)	C(22)	0.732	0.732	1.464	1.85	-12.93	-13.46	-12.74	13.27	0.06

B.3.4.3 PROPY-HQ

Table B.12. BCP data for PROPY-HQ showing intermolecular interactions only.

Interaction		d_1 / Å	d_2 / Å	R_{ij} / Å	$\rho(r)$ / e Å^{-3}	$\nabla^2\rho(r)$ / e Å^{-5}	λ_1	λ_2	λ_3	ε
O(31)	H(1A)	1.309	1.309	2.618	0.01	0.21	-0.04	-0.03	0.27	0.22
H(3C)	O(1)	1.213	1.478	2.691	0.05	0.81	-0.13	-0.08	1.03	0.56
H(21)	O(1)	0.585	1.139	1.724	0.25	3.31	-1.64	-1.53	6.47	0.07
H(22A)	O(1)	1.069	1.483	2.552	0.05	0.80	-0.16	-0.12	1.08	0.26
H(31)	O(1)	0.534	1.066	1.600	0.48	1.78	-4.05	-3.78	9.61	0.07
H(32A)	O(1)	1.189	1.609	2.798	0.02	0.46	-0.06	-0.03	0.55	1.34
H(32A)	O(21)	0.942	1.494	2.436	0.05	0.78	-0.21	-0.2	1.19	0.06
X2_H(13)	O(21)	1.032	1.551	2.583	0.04	0.75	-0.15	-0.1	0.99	0.50
X1_H(8A)	O(21)	1.366	1.573	2.938	0.03	0.46	-0.08	-0.06	0.60	0.42
X2_H(32)	O(22)	0.596	1.145	1.741	0.24	3.72	-1.49	-1.45	6.66	0.02
X2_H(10)	O(22)	1.171	1.848	3.019	0.03	0.45	-0.1	-0.03	0.58	1.95
X2_H(7A)	O(31)	1.213	1.592	2.805	0.03	0.42	-0.09	-0.06	0.58	0.57
X2_H(2)	O(32)	1.094	1.694	2.789	0.03	0.37	-0.08	-0.04	0.49	1.17
X2_H(7B)	O(32)	1.143	1.637	2.780	0.02	0.34	-0.08	-0.07	0.49	0.06
X1_H(7C)	O(32)	1.123	1.567	2.690	0.03	0.51	-0.09	-0.08	0.69	0.15
X1_H(8B)	O(32)	0.981	1.513	2.494	0.04	0.68	-0.16	-0.15	0.99	0.11
H(13)	X2_O(21)	1.035	1.550	2.585	0.04	0.75	-0.15	-0.09	0.99	0.55
H(7C)	X2_O(22)	1.326	1.770	3.096	0.01	0.20	-0.03	-0.03	0.26	0.19
H(7A)	X2_O(31)	1.213	1.592	2.805	0.03	0.42	-0.09	-0.06	0.58	0.57
H(22)	X2_O(31)	0.585	1.112	1.698	0.29	3.30	-1.96	-1.92	7.19	0.02
H(2)	X2_O(32)	1.094	1.694	2.789	0.03	0.37	-0.08	-0.04	0.49	1.17
H(7B)	X2_O(32)	1.143	1.637	2.780	0.02	0.34	-0.08	-0.07	0.49	0.06
X2_H(1C)	C(5)	1.405	1.778	3.183	0.03	0.36	-0.06	-0.01	0.44	3.87
H(22A)	C(10)	1.087	1.704	2.791	0.04	0.58	-0.12	-0.05	0.75	1.54
X1_H(25)	C(12)	1.197	1.623	2.820	0.04	0.48	-0.12	-0.1	0.70	0.24
X1_H(26)	C(12)	1.206	1.792	2.998	0.03	0.41	-0.07	-0.02	0.51	2.70
X2_H(14)	C(21)	1.212	1.860	3.071	0.03	0.43	-0.07	-0.01	0.51	3.73
X2_H(11)	C(23)	1.280	1.872	3.152	0.02	0.31	-0.03	-0.02	0.36	0.47
X2_H(10)	C(24)	1.175	1.707	2.882	0.03	0.45	-0.10	-0.04	0.58	1.74
X2_H(3B)	C(32)	1.303	1.957	3.261	0.02	0.24	-0.03	-0.01	0.29	1.51
X2_H(12)	C(33)	1.052	1.747	2.799	0.04	0.51	-0.09	-0.04	0.63	1.53
H(25)	X1_C(12)	1.197	1.623	2.820	0.04	0.48	-0.12	-0.10	0.70	0.24
H(26)	X1_C(12)	1.206	1.792	2.998	0.03	0.41	-0.07	-0.02	0.51	2.70
H(10)	X2_C(24)	1.175	1.707	2.882	0.03	0.45	-0.10	-0.04	0.58	1.75

Interaction		d_1 / Å	d_2 / Å	R_{ij} / Å	$\rho(r)$ / e Å^{-3}	$\nabla^2\rho(r)$ / e Å^{-5}	λ_1	λ_2	λ_3	ε
H(3B)	X2_C(32)	1.303	1.957	3.261	0.02	0.24	-0.03	-0.01	0.29	1.51
X2_H(8A)	H(1B)	1.166	1.333	2.499	0.04	0.45	-0.11	-0.09	0.66	0.23
X2_H(1C)	H(1C)	1.446	1.446	2.891	0.02	0.26	-0.04	-0.02	0.31	0.98
X1_H(35)	H(3A)	1.075	1.188	2.263	0.04	0.69	-0.15	-0.08	0.92	0.87
X1_H(8A)	H(3A)	1.439	1.614	3.054	0.01	0.18	-0.02	-0.02	0.22	0.20
X2_H(1A)	H(7A)	1.162	1.290	2.452	0.03	0.42	-0.09	-0.07	0.58	0.29
X2_H(36)	H(7A)	1.325	1.361	2.686	0.02	0.30	-0.07	-0.06	0.43	0.21
X1_H(36)	H(7B)	1.080	1.526	2.606	0.02	0.43	-0.06	-0.03	0.51	0.98
X2_H(14)	H(13)	1.498	1.741	3.239	0.02	0.24	-0.04	-0.03	0.30	0.39
H(32A)	H(21)	0.942	1.487	2.429	0.05	0.78	-0.21	-0.20	1.19	0.06
C(9)	H(22A)	1.087	1.087	2.175	0.04	0.58	-0.12	-0.05	0.75	1.54
X2_H(8C)	H(25)	1.305	1.613	2.918	0.03	0.35	-0.06	-0.04	0.45	0.28
H(3C)	H(32A)	1.277	1.489	2.766	0.01	0.23	-0.02	-0.01	0.26	0.42
X2_H(1B)	H(33)	1.197	1.497	2.694	0.03	0.45	-0.10	-0.06	0.61	0.79
X2_H(35)	H(35)	1.322	1.322	2.643	0.06	0.63	-0.21	-0.13	0.97	0.64
H(8A)	X1_H(3A)	1.439	1.614	3.053	0.01	0.18	-0.02	-0.02	0.22	0.21
H(14)	X2_H(13)	1.498	1.741	3.239	0.02	0.24	-0.04	-0.03	0.30	0.39
C(14)	X2_H(13)	1.689	1.689	3.378	0.02	0.22	-0.04	-0.03	0.29	0.44
H(8A)	X2_H(1B)	1.166	1.333	2.499	0.04	0.45	-0.11	-0.09	0.66	0.23
O(31)	X2_H(22)	1.117	0.581	1.698	0.30	3.34	-2.00	-1.96	7.30	0.02
H(8C)	X2_H(25)	1.305	1.613	2.918	0.03	0.35	-0.06	-0.04	0.45	0.28
H(1B)	X2_H(33)	1.197	1.497	2.694	0.03	0.45	-0.10	-0.06	0.61	0.79
H(1A)	X2_H(7A)	1.162	1.290	2.452	0.03	0.42	-0.09	-0.07	0.58	0.29
H(36)	x2_H(7A)	1.325	1.361	2.686	0.02	0.30	-0.07	-0.06	0.43	0.21

B.3.4.4 PROPY-MPAR

Table B.13. BCP data for PROPY-MPAR showing intermolecular interactions only.

Interaction		d_1 / Å	d_2 / Å	R_{ij} / Å	$\rho(r)$ / e Å^{-3}	$\nabla^2\rho(r)$ / e Å^{-5}	λ_1	$\lambda 2$	λ_3	ε
C(10)	H(26)	1.428	1.428	2.855	0.03	0.32	-0.06	-0.03	0.41	0.86
O(1)	H(21)	1.101	0.577	1.678	0.28	3.51	-1.64	-1.58	6.72	0.04
O(1)	H(26)	1.399	0.987	2.386	0.07	1.07	-0.27	-0.19	1.53	0.44
O(21)	H(3B)	1.149	1.149	2.298	0.04	0.51	-0.11	-0.07	0.69	0.74
O(1)	X1_H(7B)	1.052	1.052	2.105	0.05	0.68	-0.16	-0.15	0.98	0.06
O(1)	X1_H(25)	1.262	1.262	2.524	0.03	0.31	-0.07	-0.03	0.41	1.64
O(21)	X3_H(2)	1.179	1.179	2.358	0.03	0.48	-0.09	-0.07	0.63	0.22
O(21)	X3_H(1B)	1.359	1.359	2.719	0.03	0.4	-0.07	-0.05	0.52	0.51
O(21)	X3_H(7C)	1.108	1.108	2.217	0.05	0.64	-0.14	-0.11	0.89	0.28
O(21)	X1_C(27)	1.660	1.810	3.469	0.03	0.36	-0.06	-0.02	0.44	1.63
O(22)	X4_C(28)	1.494	1.763	3.257	0.05	0.61	-0.12	-0.07	0.79	0.77
O(23)	X1_H(10)	1.088	1.088	2.177	0.05	0.66	-0.14	-0.12	0.92	0.20
O(23)	X4_H(12)	1.466	1.062	2.527	0.05	0.78	-0.18	-0.16	1.13	0.08
O(22)	X1_H(13)	1.037	1.037	2.074	0.07	0.99	-0.25	-0.21	1.45	0.18
O(22)	X1_H(14)	1.076	1.076	2.152	0.06	0.84	-0.19	-0.15	1.17	0.28
O(23)	X1_H(12)	-	-	-	0.03	0.32	-0.06	0.07	0.31	-
O(23)	X4_C(12)	1.464	1.925	3.389	0.06	0.79	-0.18	-0.16	1.13	0.08
H(7B)	X1_O(1)	1.053	1.477	2.530	0.05	0.68	-0.16	-0.15	0.99	0.06
H(25)	X1_O(1)	-	-	-	0.02	0.24	-0.03	0.03	0.23	-
C(27)	X1_O(21)	1.660	1.660	3.320	0.03	0.36	-0.06	-0.02	0.44	1.63
H(1B)	X3_O(21)	1.359	1.616	2.975	0.03	0.4	-0.07	-0.05	0.52	0.51
H(2)	X3_O(21)	1.179	1.592	2.771	0.03	0.48	-0.09	-0.07	0.63	0.22
H(7C)	X3_O(21)	1.110	1.534	2.643	0.05	0.64	-0.14	-0.11	0.89	0.23
H(13)	X1_O(22)	1.037	1.401	2.438	0.07	0.99	-0.25	-0.21	1.45	0.18
H(14)	X1_O(22)	1.077	1.436	2.512	0.06	0.84	-0.19	-0.15	1.18	0.28
C(28)	X4_O(22)	1.494	1.494	2.989	0.05	0.61	-0.12	-0.07	0.79	0.77
H(12)	X4_O(23)	1.065	1.464	2.529	0.06	0.79	-0.17	-0.16	1.13	0.06
H(10)	X1_O(23)	1.089	1.496	2.585	0.05	0.66	-0.14	-0.12	0.92	0.20
N(1)	X3_H(1C)	1.421	1.421	2.842	0.01	0.18	-0.02	-0.01	0.22	0.78
H(1C)	X3_N(1)	1.422	1.836	3.257	0.01	0.18	-0.02	-0.01	0.22	0.78
C(1)	X3_H(3B)	1.246	1.246	2.492	0.04	0.44	-0.09	-0.09	0.62	0.09
C(2)	X3_H(22)	1.244	1.244	2.487	0.03	0.36	-0.08	-0.07	0.51	0.23
C(3)	X3_H(1B)	1.184	1.184	2.367	0.04	0.44	-0.09	-0.09	0.62	0.09
C(4)	X3_H(3C)	1.435	1.435	2.870	0.03	0.35	-0.03	-0.01	0.39	4.38
C(5)	X1_H(26)	1.421	1.421	2.842	0.02	0.21	-0.03	-0.01	0.25	2.21
C(8)	X1_H(23)	1.331	1.331	2.661	0.02	0.22	-0.04	-0.02	0.28	1.60
C(8)	X1_H(26)	1.320	1.320	2.641	0.02	0.28	-0.05	-0.04	0.38	0.18
C(8)	X1_C(11)	1.650	1.650	3.299	0.05	0.55	-0.13	-0.07	0.76	0.75
C(9)	X4_H(12)	1.087	1.087	2.174	0.06	0.55	-0.15	-0.14	0.84	0.11
C(10)	X1_H(25)	1.306	1.306	2.611	0.02	0.25	-0.04	-0.01	0.31	1.72

Interaction		d_1 / Å	d_2 / Å	R_{ij} / Å	$\rho(r)$ / e Å^{-3}	$\nabla^2\rho(r)$ / e Å^{-5}	λ_1	λ_2	λ_3	ε
C(10)	X4_H(12)	1.618	1.087	2.705	0.06	0.55	-0.15	-0.14	0.84	0.11
C(10)	X1_H(8B)	1.163	1.163	2.326	0.05	0.55	-0.13	-0.07	0.76	0.75
C(11)	X4_H(8A)	1.398	1.398	2.797	0.02	0.20	-0.03	-0.02	0.25	0.66
C(11)	X1_H(28C)	1.158	1.158	2.315	0.03	0.38	-0.09	-0.08	0.55	0.21
C(12)	X4_H(11)	1.221	1.221	2.441	0.03	0.35	-0.05	-0.02	0.43	1.10
C(12)	X4_H(25)	1.242	1.242	2.484	0.03	0.37	-0.08	-0.06	0.50	0.32
C(21)	X1_H(3A)	1.235	1.235	2.469	0.03	0.33	-0.07	-0.06	0.45	0.14
C(21)	X1_H(28A)	1.079	1.079	2.157	0.05	0.57	-0.15	-0.08	0.79	0.90
C(22)	X3_H(2)	1.193	1.193	2.386	0.03	0.36	-0.08	-0.07	0.51	0.23
C(23)	X4_H(28B)	1.152	1.152	2.303	0.04	0.45	-0.08	-0.07	0.61	0.16
C(25)	X4_H(12)	1.223	1.223	2.447	0.03	0.37	-0.08	-0.06	0.50	0.32
C(26)	X1_H(8B)	1.301	1.301	2.601	0.02	0.28	-0.05	-0.04	0.38	0.18
C(26)	X1_H(8B)	1.301	1.301	2.601	0.02	0.28	-0.05	-0.04	0.38	0.18
C(28)	X4_H(23)	1.293	1.293	2.587	0.04	0.45	-0.08	-0.07	0.61	0.17
C(28)	X1_H(11)	1.232	1.232	2.463	0.03	0.38	-0.09	-0.08	0.55	0.21
H(3C)	X3_C(5)	1.435	1.881	3.316	0.03	0.35	-0.03	-0.01	0.39	4.39
H(8A)	X4_C(11)	1.398	2.112	3.510	0.02	0.20	-0.03	-0.02	0.25	0.69
H(11)	X4_C(12)	1.221	1.894	3.115	0.03	0.35	-0.05	-0.02	0.43	1.10
H(26)	X1_C(5)	1.421	1.954	3.375	0.02	0.21	-0.03	-0.01	0.25	2.21
H(25)	X1_C(6)	1.262	1.895	3.157	0.03	0.31	-0.07	-0.03	0.41	1.64
H(12)	X4_C(9)	1.087	2.366	3.453	0.05	0.55	-0.15	-0.14	0.84	0.11
H(3A)	X1_C(21)	1.235	2.370	3.605	0.03	0.33	-0.07	-0.06	0.45	0.14
H(28A)	X1_C(22)	1.079	1.654	2.732	0.05	0.57	-0.15	-0.08	0.79	0.90
H(7A)	X3_H(1A)	1.388	1.402	2.790	0.02	0.20	-0.04	-0.03	0.26	0.34
H(25)	X1_H(10)	1.305	1.366	2.671	0.02	0.25	-0.05	-0.02	0.31	1.92
H(23)	X1_H(8A)	1.330	1.544	2.874	0.02	0.22	-0.04	-0.02	0.28	1.60
X3_H(7A)	H(1A)	1.388	1.402	2.790	0.02	0.20	-0.04	-0.03	0.26	0.34

The location of the BCPs, along with the bond paths (showing the path the electron density takes between two atoms connecting them) for all four PROPY systems are shown in Figure 5.5.

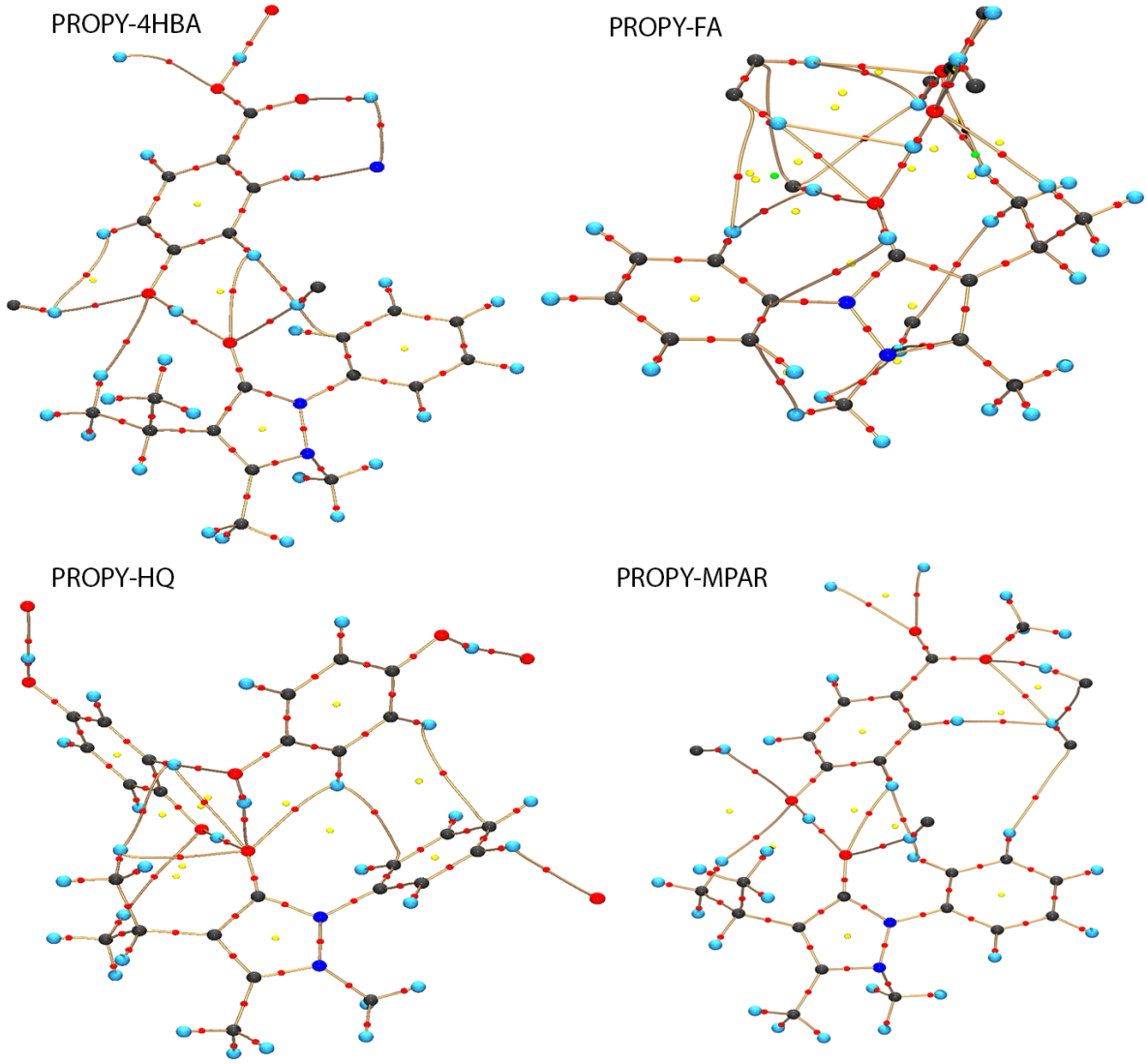

Figure B.12 Molecular graph diagrams showing atomic nuclei (coloured according to atom type), connected by bond paths (gold) with BCP (red) and RCP (yellow) displayed.

B.3.5 RCPs and Analysis

A summary of the RCPs for the main rings present in each system is presented in Table B.14, including the electron density at the RCP and sum of atomic charges around the ring. The location of the RCPs can be seen in Figure B.12.

Table B.14. Summary of RCPs for each of the four PROPY systems obtained from experimental models.

	PROPY-4HBA	PROPY-FA	PROPY-HQ	PROPY-MPAR
PROPY 5-membered ring				
$\rho(\mathbf{r})$ /e Å^{-3}	0.382	0.359	0.32	0.393
$\nabla^2\rho(\mathbf{r})$ /e Å^{-5}	7.17	7.238	8.135	7.062
Total atomic charge (Mulliken)	-0.409	-0.97	-0.99	-1.071
Total atomic charge (Stockholder)	-0.809	-0.648	-0.595	-0.96
Total atomic charge (Bader)	-1.572	-1.486	-1.481	-1.817
Total atomic charge, excluding O (Mulliken)	0.014	-0.447	-0.481	-0.682
Total atomic charge, excluding O (Stockholder)	-0.477	-0.262	-0.267	-0.629
Total atomic charge, excluding O (Bader)	-0.511	-0.307	-0.388	-0.786
PROPY phenyl ring				
$\rho(\mathbf{r})$ /e Å^{-3}	0.206	0.198	0.193	0.222
$\nabla^2\rho(\mathbf{r})$ /e Å^{-5}	3.109	3.071	3.241	2.948
Total atomic charge (Mulliken)	-1.969	-0.323	-0.223	-1.9
Total atomic charge (Stockholder)	-0.759	-0.357	-0.192	-0.588
Total atomic charge (Bader)	-1.731	-0.37	-1.494	-0.269

	PROPY-4HBA	PROPY-FA	PROPY-HQ		PROPY-MPAR
		Co-former phenyl ring			
$\rho(\mathbf{r})$ /e Å^{-3}	0.194	-	0.175	0.170	0.194
$\nabla^2\rho(\mathbf{r})$ /e Å^{-5}	2.948	-	2.894	3.115	2.972
Total atomic charge (Mulliken)	-0.819	-	-0.413	-0.302	-1.362
Total atomic charge (Stockholder)	-0.201	-	-0.515	-0.355	-0.455
Total atomic charge (Bader)	-0.568	-	0.111	0.170	-0.900
		Carboxylic acid dimer			
$\rho(\mathbf{r})$ /e Å^{-3}	0.037	-	-	-	-
$\nabla^2\rho(\mathbf{r})$ /e Å^{-5}	0.829	-	-	-	-
Total atomic charge (Mulliken)	-0.4920	-	-	-	-
Total atomic charge (Stockholder)	-0.3004	-	-	-	-
Total atomic charge (Bader)	-0.4709	-	-	-	-

Figures B.13 and B.14 depict the RCP density and atomic charges for PROPY in the four systems using the Bader and Mulliken atomic partitioning schemes respectively. Similarly, the co-formers are shown in figure B.15 and B.16.

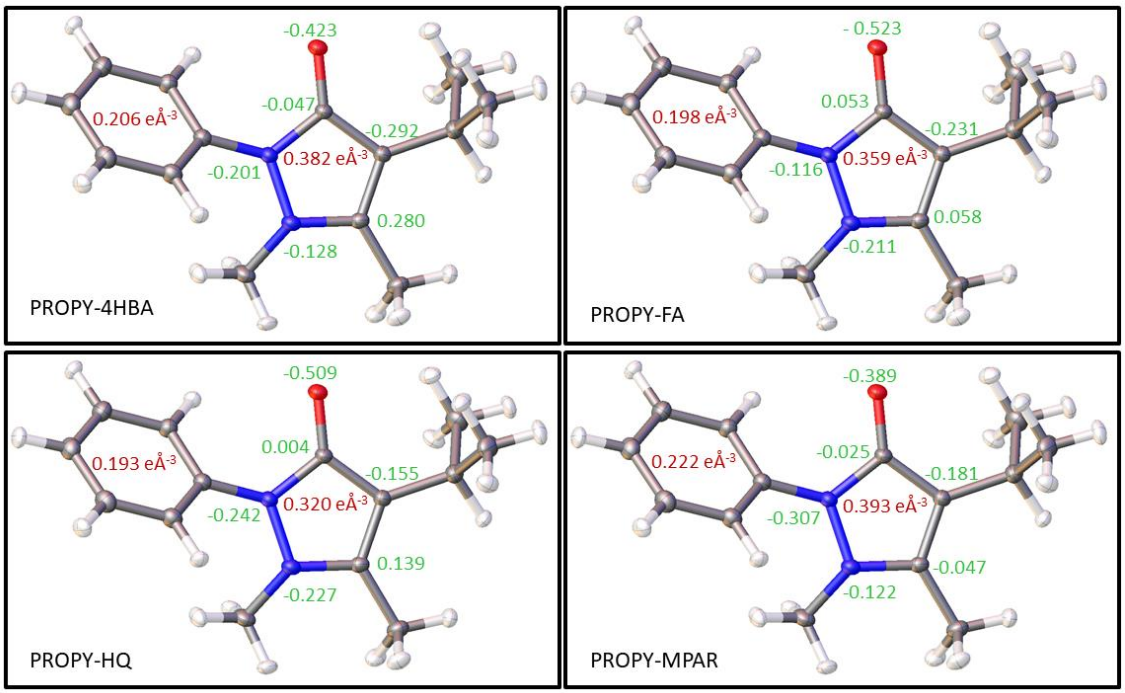

Figure B.13. Atomic charges and ρ(r) at the RCPs for PROPY in the four systems, using Mulliken atomic partitioning for charges.

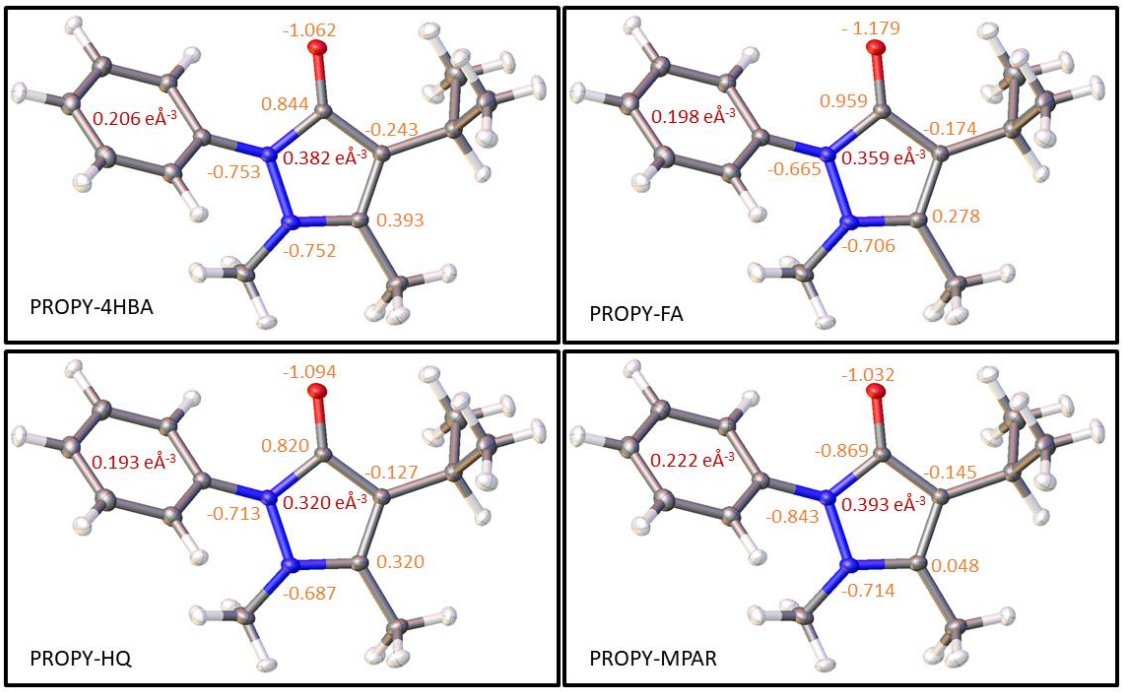

Figure B.14. Atomic charges and ρ(**r**) at the RCPs for PROPY in the four systems, using Bader atomic partitioning for charges.

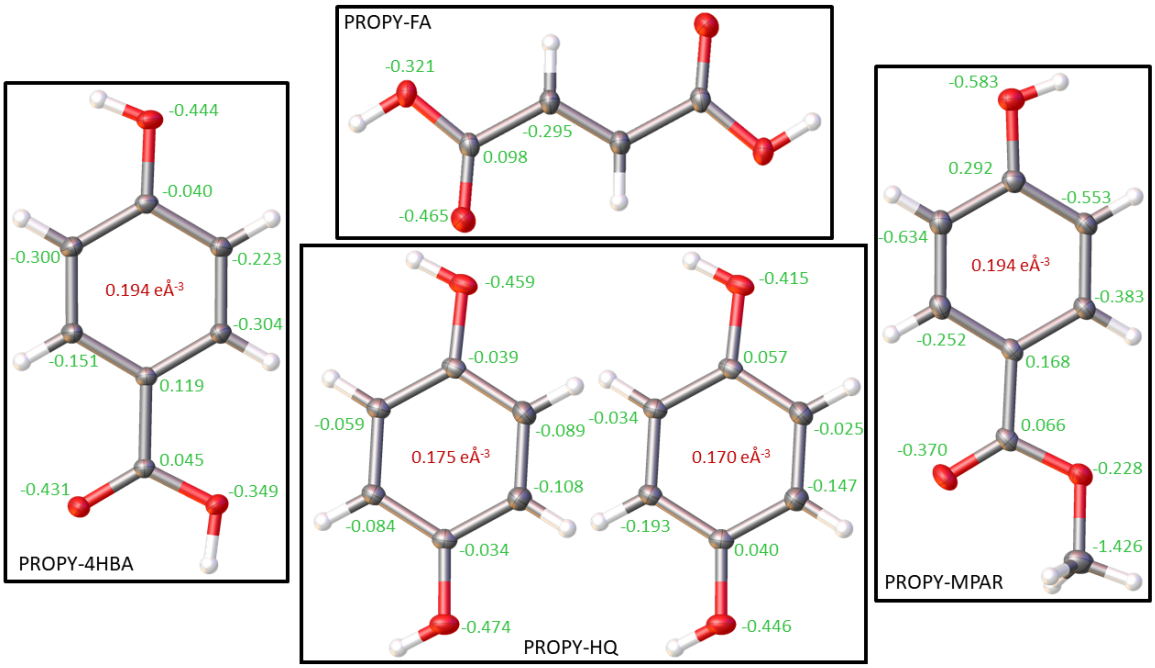

Figure B.15. Atomic charges and $\rho(\mathbf{r})$ at the RCPs for the co-former molecules in the four systems, using Mulliken atomic partitioning for charges.

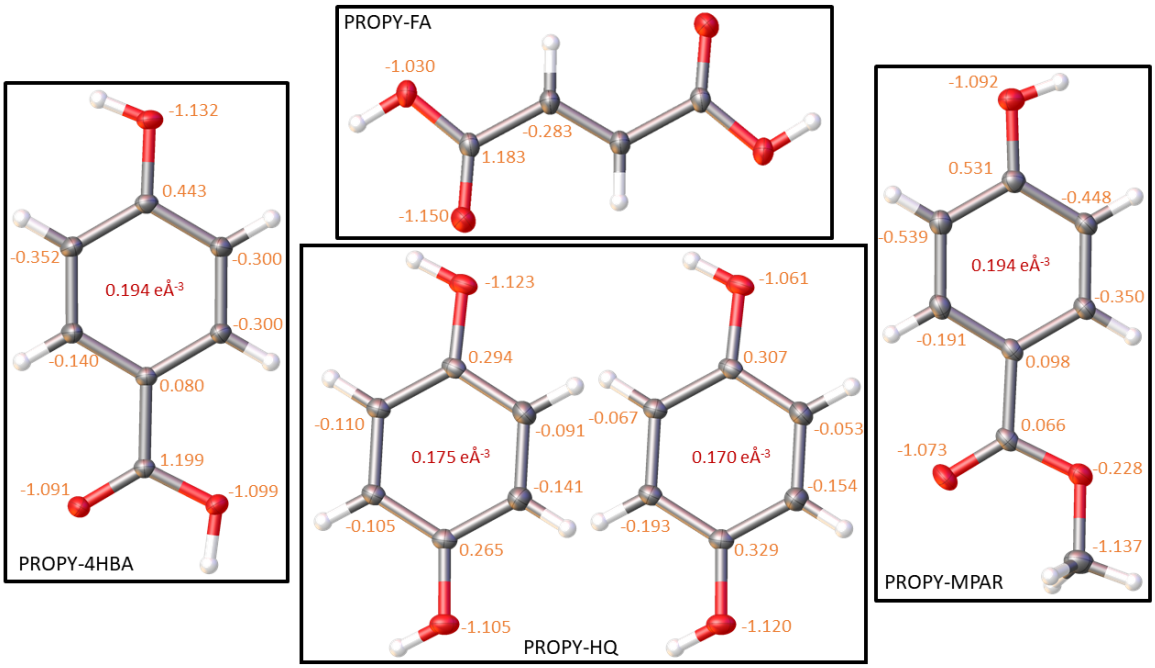

Figure B.16. Atomic charges and $\rho(\mathbf{r})$ at the RCPs for the co-former molecules in the four systems, using Bader atomic partitioning for charges

B.4 Interaction Energy Analysis

Related supplementary documents:

- PROPY_XDIinteractions Analysis
- PROPY_PIXEL Calculations
- PROPY_Crystal Explorer Calculations
- PROPY_PIXEL_CE compare
- PROPY_Interactions_strong med weak

B.4.1 Crystal Explorer Energy Analysis

The energy scatter plots generated from Crystal Explorer (CE) calculations for the additional systems (PROPY-25DHBA, PROPY-45DClPA, PROPY-PGL·0.5ACN and PROPY) are given in Figures B.17-B.21.

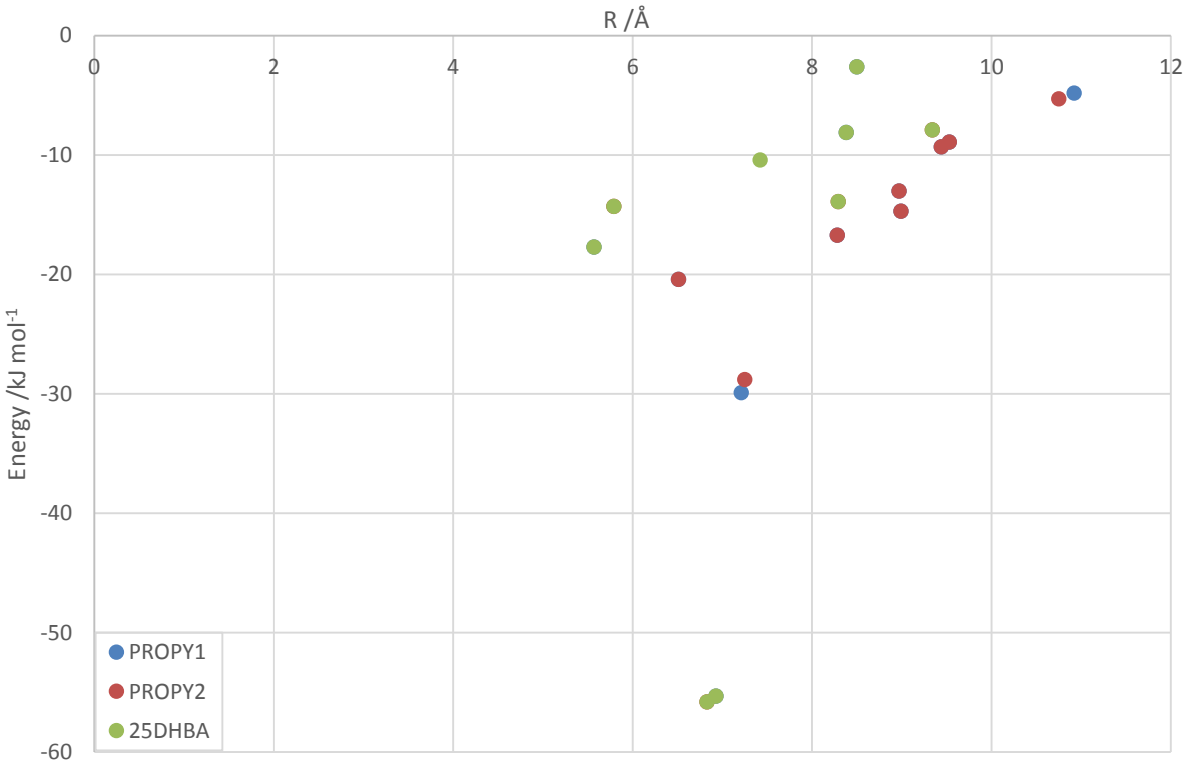

Figure B.17. Scatter plot of the energies for PROPY-25DHBA determined by Crystal Explorer plotted against R.

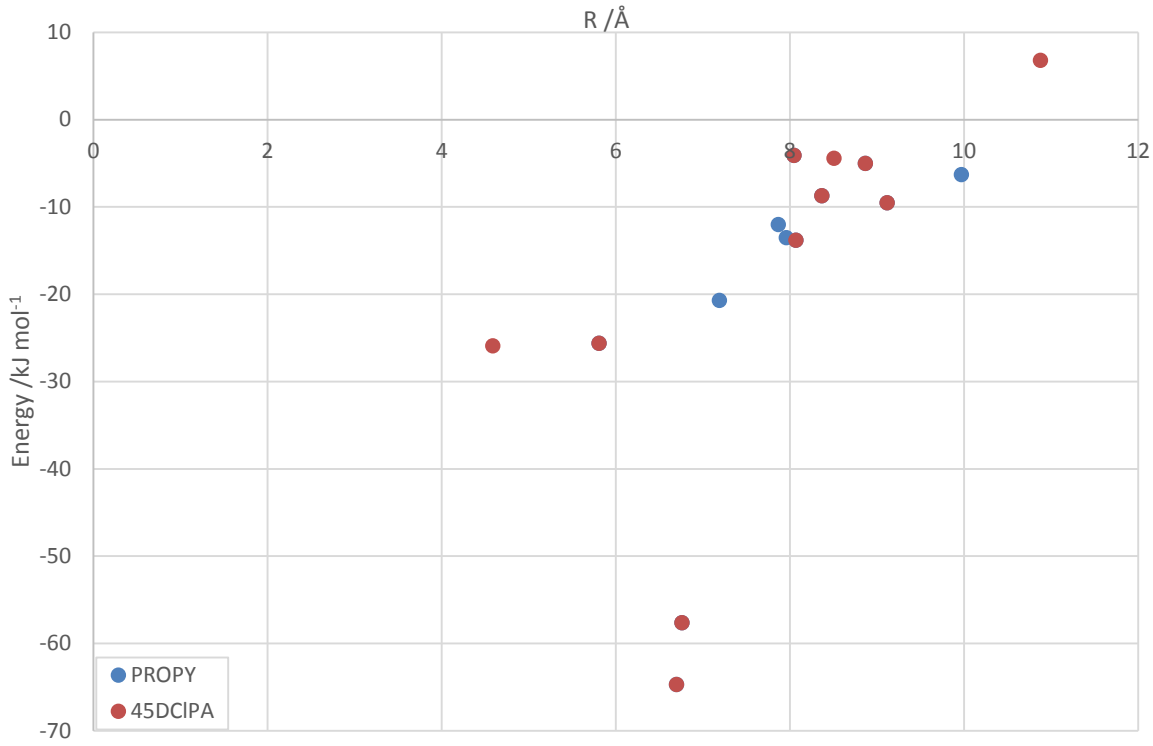

Figure B.18. Intermolecular interaction energies for PROPY-45DClPA 1:1 co-crystal obtained from Crystal Explorer calculations, plotted against R (distance between molecular centroids).

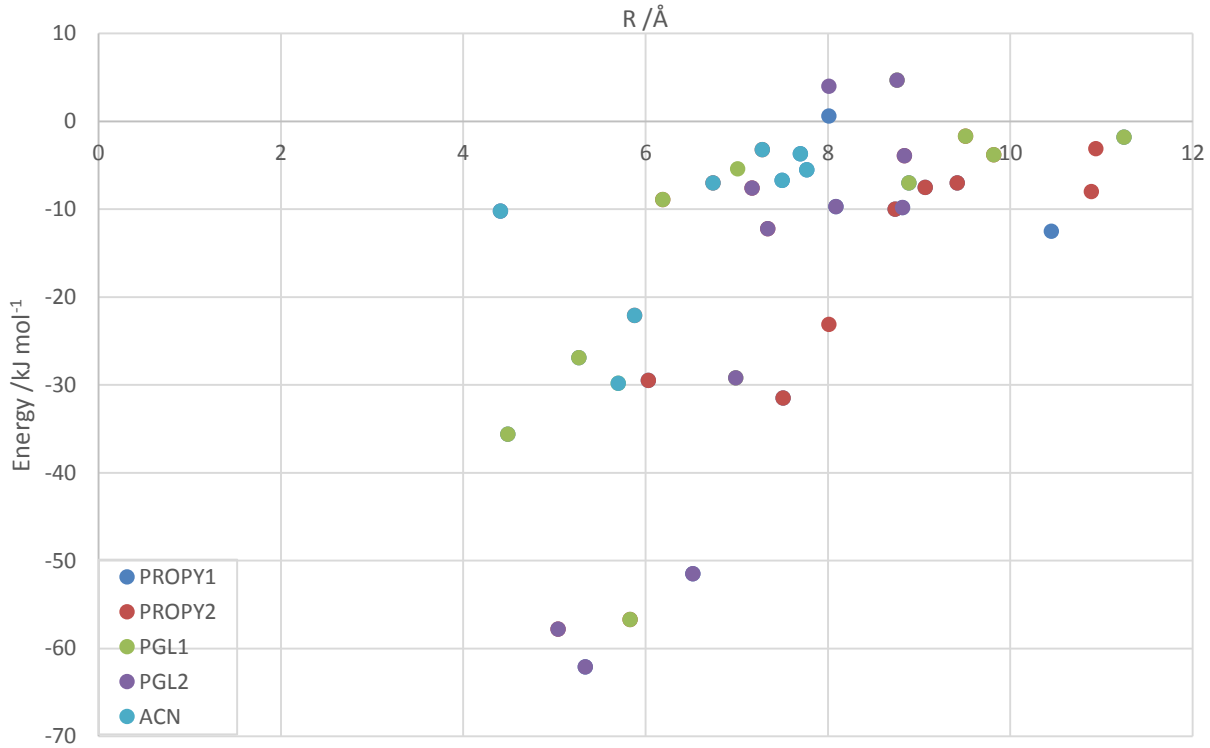

Figure B.19. Intermolecular interaction energies for PROPY-PGL·0.5ACN 1:1:0.5 co-crystal solvate obtained from Crystal Explorer calculations, plotted against R (distance between molecular centroids).

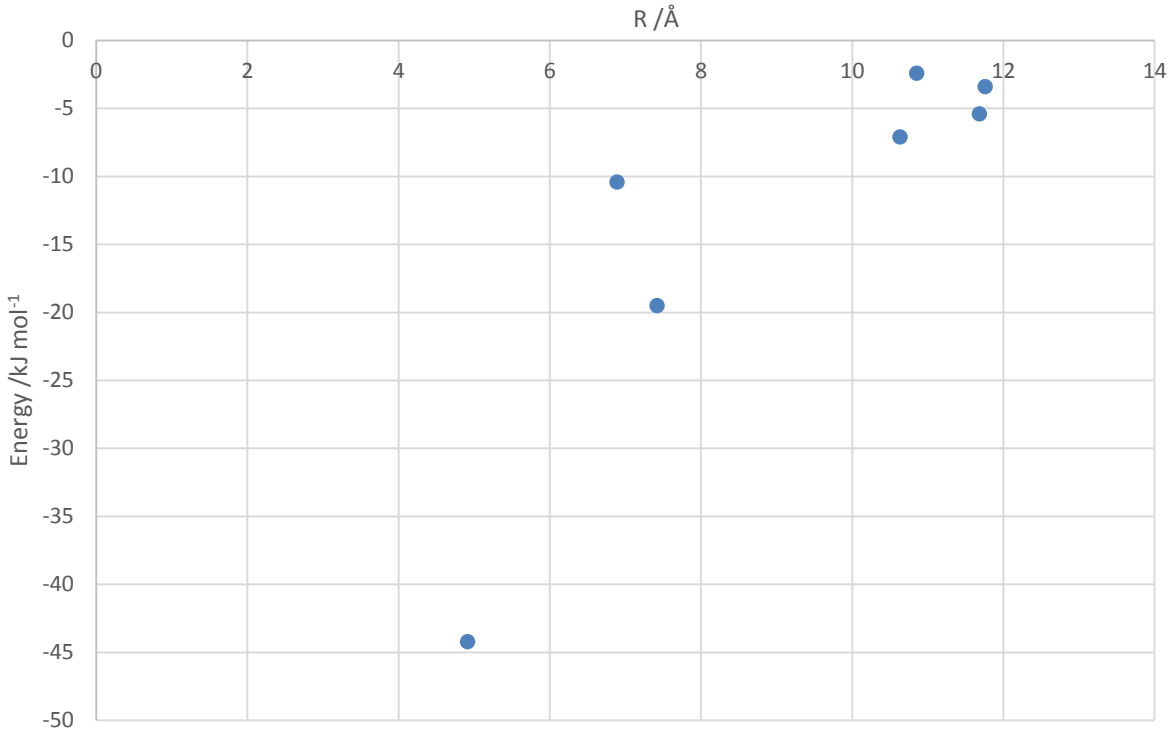

Figure B.20. Intermolecular interaction energies for PROPY Form I (*Pc*) obtained from Crystal Explorer calculations, plotted against R (distance between molecular centroids).

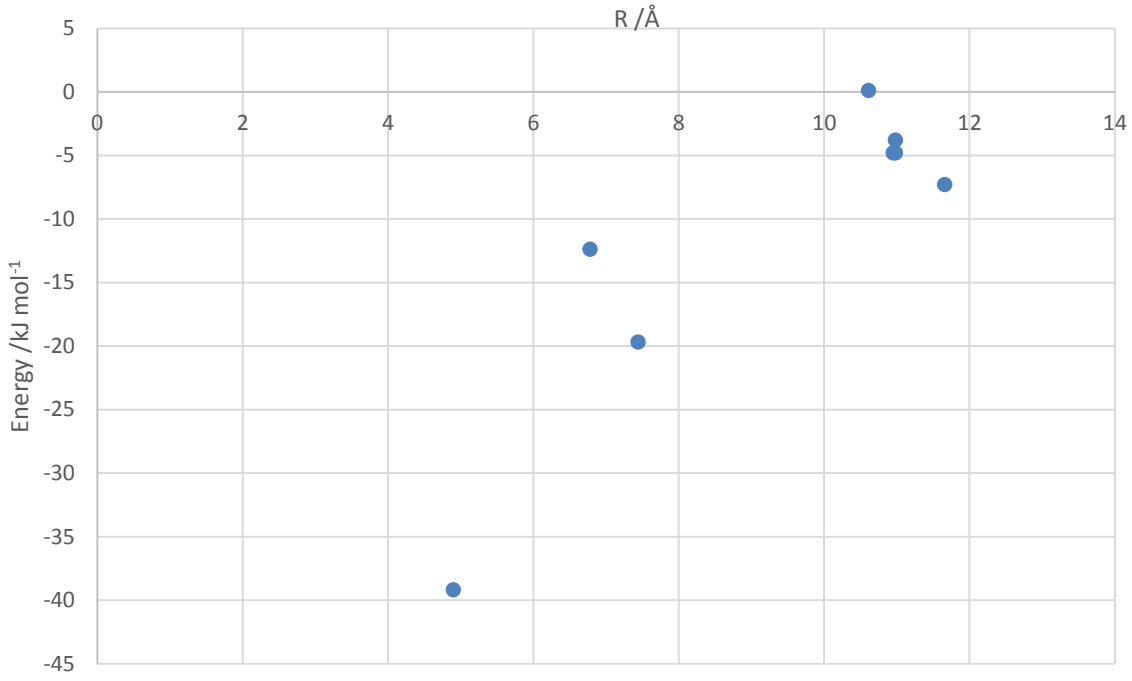

Figure B.21. Intermolecular interaction energies for PROPY Form II (*Cc*) obtained from Crystal Explorer calculations, plotted against R (distance between molecular centroids).

B.4.2 Molecule and System Energies

Energies determined by Crystal Explorer and PIXEL are given in Tables B.15 and B.16 respectively, showing the total energy and components thereof for each system. A value is also given 'per molecule' to allow comparisons between the systems as they form in a variety of stoichiometries.

Table B.15. Crystal Explorer energies for the co-crystal systems split into the four components as a total, and per molecule present.

		Crystal Explorer Energies				
		E_{coul}	E_{pol}	E_{disp}	E_{rep}	E_{tot}
PROPY I	Total	-75.8	-23.8	-232.0	186.8	-184.8
	Per molecule	-37.9	-11.9	-116.0	93.4	-92.4
PROPY II	Total	-86.0	-24.4	-225.2	237.0	-159.0
	Per molecule	-43.0	-12.2	-112.6	118.5	-79.5
PROPY-25DHBA	Total	-432.7	-130.0	-591.3	670.0	-655.1
	Per molecule	-72.1	-21.7	-98.6	111.7	-109.2
PROPY-45DClPA	Total	-361.6	-102.1	-455.8	579.7	-497.8
	Per molecule	-90.4	-25.5	-114.0	144.9	-124.5
PROPY-4HBA	Total	-348.6	-102.3	-438.9	565.9	-476.9
	Per molecule	-87.2	-25.6	-109.7	141.5	-119.2
PROPY-FA	Total	-495.2	-146.6	-703.4	799.6	-750.0
	Per molecule	-82.5	-24.4	-117.2	133.3	-125.0
PROPY-HQ	Total	-612.1	-153.6	-558.8	905.0	-688.4
	Per molecule	-102.0	-25.6	-93.1	150.8	-114.7
PROPY-MPAR	Total	-236.8	-71.8	-456.0	431.8	-433.8
	Per molecule	-59.2	-18.0	-114.0	108.0	-108.5
PROPY-PGL·0.5ACN	Total	-912.9	-269.1	-939.6	1291.1	-1184.9
	Per molecule	-91.3	-26.9	-94.0	129.1	-118.5

Table B.16. PIXEL energies for the co-crystal systems split into the four components as a total, and per molecule present.

		PIXEL Energies				
		E_{coul}	E_{pol}	E_{disp}	E_{rep}	E_{tot}
PROPY I	Total	-101.4	-46.6	-215.2	196.2	-167.0
	Per molecule	-50.7	-23.3	-107.6	98.1	-83.5
PROPY II	Total	-109.6	-56.4	-219.2	227.0	-158.2
	Per molecule	-54.8	-28.2	-109.6	113.5	-79.1
PROPY-25DHBA	Total	-236.6	-123.8	-518.7	420.2	-512.0
	Per molecule	-39.4	-20.6	-86.5	70.0	-85.3
PROPY-45DClPA	Total	-329.7	-181.9	-485.2	525.2	-471.6
	Per molecule	-82.4	-45.5	-121.3	131.3	-117.9
PROPY-4HBA	Total	-320.1	-176.3	-409.4	509.3	-396.5
	Per molecule	-80.0	-44.1	-102.4	127.3	-99.1
PROPY-FA	Total	-391.9	-205.2	-643.4	620.0	-620.5
	Per molecule	-65.3	-34.2	-107.2	103.3	-103.4
PROPY-HQ	Total	-575.0	-273.2	-511.5	782.5	-580.1
	Per molecule	-95.8	-45.5	-85.3	130.4	-96.7
PROPY-MPAR	Total	-266.9	-132.8	-429.9	426.8	-402.8
	Per molecule	-66.7	-33.2	-107.5	106.7	-100.7
PROPY-PGL·0.5ACN	Total	-963.0	-593.9	-1028.6	891.7	-932.2
	Per molecule	-96.3	-99.0	-171.4	148.6	-93.2

B.4.3 API and Co-Former Interactions

The energies determined in Crystal Explorer and PIXEL can be broken down according to molecule type. These are presented in Tables B.17 and B.18 below.

Table B.17. Table of interaction energies for all the PROPY co-crystal systems obtained from Crystal Explorer calculations, summarised into API and co-former interactions.

	API Energies /kJ mol^{-1}			Co-Former Energies /kJ mol^{-1}			Total CE energy $E_{tot,\Sigma}$
	E_{coul}	E_{disp}	E_{rep}	E_{coul}	E_{disp}	E_{rep}	
PROPY I	-75.8	-232.0	186.8				-184.8
PROPY II	-86.0	-225.2	237.0				-159.0
PROPY-25DHBA[#] (1,4-Dioxane)	-260.3	-450.3	420.3	-172.4	-141.0	249.7	-655.1
PROPY-45DClPA	-196.2	-265.0	310.4	-165.4	-190.8	269.3	-497.8
PROPY-4HBA	-127.8	-269.8	239.6	-220.8	-169.1	326.3	-476.9
PROPY-FA	-317.8	-579.4	545.2	-177.4	-124.0	254.4	-750.0
PROPY-HQ	-219.0	-270.3	316.3	-393.1	-288.5	588.7	-688.4
PROPY-MPAR	-132.8	-274.4	241.9	-104.0	-181.6	189.9	-433.8
PROPY-PGL·0.5ACN[*]	-411.3	-565.8	605.3	-428.7	-314.4	604.9	-1184.9

Calculations for PROPY-35DHBA were not completed due to the complexity of the crystal structure containing four independent molecules of each of PROPY and 35DHBA, and proton disorder present in the acid···acid dimer interaction.
[*]PROPY-PGL·0.5ACN also has the following contributions of interactions of ACN solvent: E_{coul} -72.9, E_{disp} -59.4, E_{rep} 80.9 kJ mol^{-1}.

Table B.18. shows the breakdown of the PIXEL energies according to molecular pair. Some distinct differences are evident in particular in the API···API interactions. These would be expected to be not too dissimilar across all systems, as the API is consistent; it is the co-former, and the interactions that partakes in which differs. The API will vary only slightly across the series, due to the effect of the co-former on PROPY. Some very large coulombic energies are present in the table, and these can be attributed to the number of molecules present, and the stoichiometric ratio of the co-crystal. PROPY-FA and PROPY-25DHBA both have an equivalent of 2 PROPY molecules to a single co-former, whilst PROPY-PGL has two molecules of each within the

asymmetric unit utilised in the calculations. These stoichiometries can be seen to manifest in the energy, with approximately double the expected value. Using half the values for these gives a better representation of the single API···API interactions. Likewise, the same is true for PROPY-HQ and PROPy-PGL·0.5ACN with reference to the co-formers. Both have an equivalent of 2 in comparison to the other structures. These differences in stoichiometry are normalised when the per molecule values are considered.

Table B.18. Table of interaction energies for the PIXEL calculations of PROPY co-crystal systems, summarised into API···API, API···co-former and co-former···co-former interactions.

	API···API Energies /kJ mol^{-1}			**API···Co-Former Energies /kJ mol^{-1}**			**Co-Former···Co-Former Energies /kJ mol^{-1}**			**Total PIXEL energy $E_{tot,\sum}$**
	E_{coul}	E_{disp}	E_{rep}	E_{coul}	E_{disp}	E_{rep}	E_{coul}	E_{disp}	E_{rep}	
PROPY I	-101.4	-215.2	196.2							-167.0
PROPY II	-109.6	-219.2	227.0							-158.2
PROPY-25DHBA (1,4-Dioxane)	-160.6	-378.2	237.8	-123.7	-211.8	217.2	-11.6	-15.0	5.0	-512.0
PROPY-45DClPA	-38.4	-142.9	88.0	-295.5	-279.2	402.6	4.2	-63.1	34.6	-471.6
PROPY-4HBA	-46.9	-153.4	96.3	-116.6	-189.0	206.6	-156.6	-67.0	206.4	-396.5
PROPY-FA	-201.8	-533.0	359.0	-228.1	-212.0	324.0	-	-	-	-620.5
PROPY-HQ	-65.8	-141.0	73.0	-348.7	-360.4	503.2	-201.4	-103.7	255.1	-580.1
PROPY-MPAR	-49.0	-143.6	91.0	-194.9	-229.5	291.3	-23.0	-56.8	44.5	-402.8
PROPY-PGL ·0.5ACN*	-209.8	-436.5	324.2	-547.6	-461.1	733.2	-11.2	-34.5	68.3	-932.2

Calculations for PROPY-35DHBA were not conducted due to the complexity of the crystal structure containing four independent molecules of each of PROPY and 35DHBA, and proton disorder present in the acid···acid dimer interaction.

*PROPY-PGL·0.5ACN also has the following contributions of interactions to ACN solvent: API···ACN E_{coul} -38.5, E_{disp} -63.4, E_{rep} 29.3; PGL···ACN E_{coul} -74.4, E_{disp} -47.0, E_{rep} 87.2 kJ mol^{-1}.

B.4.4 Strong, Moderate and Weak Energies

Tables B.19 and B.20 summarise the interactions in each system grouped according to the interaction strength. Each group is separated into the main energy components and the percentage that this contributes to the overall system energy is included. Differences between the two methods in the absolute values occur due to the calculated methods and included pairs (e.g. A···B and B···A or just one of these). This is also reflected in the total energy and therefore the % values are comparable. Values from a single method between systems are also comparable.

Table B.19. Interactions of the four PROPY systems for which full analyses were carried out, grouped according to interaction strength, determined from scatter plots of results.

		PIXEL		CE	
		Energy /kJ mol^{-1}	**% contribution to total**	**Energy /kJ mol^{-1}**	**% contribution to total**
PROPY-4HBA STRONG	E_{tot}	-124.80	31.48	-185.50	38.90
	E_{coul}	-223.30	69.76	-270.2	77.51
	E_{disp}	-46.10	11.26	-49.20	11.21
	E_{rep}	261.20	51.29	311.90	55.12
PROPY-4HBA MODERATE	E_{tot}	-148.50	37.45	-163.00	34.18
	E_{coul}	-64.10	20.02	-52.30	15.00
	E_{disp}	-215.50	52.64	-224.70	51.20
	E_{rep}	172.00	33.77	-171.30	30.27
PROPY-4HBA WEAK*	E_{tot}	-114.00	30.95	-128.40	26.92
	E_{coul}	-30.40	10.22	-26.10	7.49
	E_{disp}	-133.40	36.10	-165.00	37.59
	E_{rep}	66.10	14.94	82.70	14.61
PROPY-FA STRONG	E_{tot}	-210.90	33.99	-322.80	43.04
	E_{coul}	-228.70	58.36	-353.20	71.32
	E_{disp}	-180.00	27.98	-211.60	30.08
	E_{rep}	316.60	51.06	489.00	61.16

		PIXEL		CE	
		Energy /kJ mol^{-1}	% contribution to total	Energy /kJ mol^{-1}	% contribution to total
PROPY-FA MODERATE	E_{tot}	-251.00	40.45	-265.00	35.33
	E_{coul}	-110.20	28.12	-98.40	19.87
	E_{disp}	-258.00	40.10	-272.80	38.78
	E_{rep}	169.40	27.32	167.60	20.96
PROPY-FA WEAK*	E_{tot}	-158.20	25.50	-162.20	21.63
	E_{coul}	-53.00	13.52	-43.60	8.80
	E_{disp}	-205.40	31.92	-219.00	31.13
	E_{rep}	134.00	21.61	143.00	17.88
PROPY-HQ STRONG	E_{tot}	-158.20	27.27	-214.60	31.17
	E_{coul}	-238.70	41.51	-285.00	46.56
	E_{disp}	-91.60	17.91	-91.60	16.39
	E_{rep}	292.40	37.37	361.20	39.91
PROPY-HQ MODERATE	E_{tot}	-283.40	48.85	-337.30	49.00
	E_{coul}	-269.40	46.85	-291.60	47.64
	E_{disp}	-219.50	51.05	-285.70	51.13
	E_{rep}	334.90	46.73	427.50	47.24
PROPY-HQ WEAK*	E_{tot}	-142.70	24.60	-136.50	19.83
	E_{coul}	-66.70	11.60	-35.50	5.80
	E_{disp}	-166.80	32.61	-181.50	32.48
	E_{rep}	125.50	16.04	116.30	12.85

		PIXEL		CE	
		Energy /kJ mol^{-1}	% contribution to total	Energy /kJ mol^{-1}	% contribution to total
PROPY-MPAR STRONG	E_{tot}	-96.60	23.98	-106.20	24.48
	E_{coul}	-158.00	59.20	-141.60	59.80
	E_{disp}	-49.60	11.54	-39.60	8.68
	E_{rep}	187.80	44.00	170.8	39.56
PROPY-MPAR MODERATE	E_{tot}	-275.40	68.37	-285.80	65.88
	E_{coul}	-103.80	38.89	-91.40	38.60
	E_{disp}	-336.40	78.25	-355.20	77.89
	E_{rep}	217.80	51.03	232.4	53.82
PROPY-MPAR WEAK	E_{tot}	-31.70	7.87	-41.80	9.64
	E_{coul}	-5.10	1.91	-3.80	1.60
	E_{disp}	-43.9	10.21	-61.20	13.42
	E_{rep}	21.20	4.97	28.60	6.62

Some interactions are calculated differently in the different methods (e.g. both PROPY···co-former and co-former···PROPY or from just one molecule) hence there is variation in the individual values across the two methods. This is accounted for in the percentage of the totals and similar proportions of energies are seen despite these individual differences. *PROPY-4HBA, PROPY-FA and PROPY-HQ have additional weak interactions in the Crystal Explorer analysis which are not seen in PIXEL and *vice versa* for some PROPY-HQ interactions giving variation in the number of interactions and total energy. These are very weak interactions with small energy values and hence do not make a significant difference to the energies and percentages when the two methods are compared.

Table B.20. Interactions of the additional three PROPY systems for which experimental analyses were not carried out, grouped according to interaction strength, determined from scatter plots of results.

		PIXEL		CE	
		Energy /kJ mol^{-1}	**% contribution to total**	**Energy /kJ mol^{-1}**	**% contribution to total**
PROPY-25DHBA STRONG	E_{tot}	-106.00	20.70	-222.20	33.92
	E_{coul}	-174.60	53.57	-307.80	71.13
	E_{disp}	-48.90	9.06	-73.60	12.45
	E_{rep}	205.10	39.07	369.20	55.10
PROPY-25DHBA MODERATE*	E_{tot}	-331.80	64.80	-406.80	62.10
	E_{coul}	-122.00	37.43	-126.50	29.24
	E_{disp}	-401.10	74.28	-457.60	77.39
	E_{rep}	261.30	49.78	264.10	39.42
PROPY-25DHBA WEAK*	E_{tot}	-74.40	14.52	-83.70	12.78
	E_{coul}	-29.30	8.99	-25.80	5.96
	E_{disp}	-90.00	16.67	-99.30	16.79
	E_{rep}	58.50	11.14	58.30	8.70
PROPY-45DClPA STRONG	E_{tot}	-174.30	36.96	-244.60	49.14
	E_{coul}	-248.70	75.43	-305.60	84.51
	E_{disp}	-92.60	19.08	-99.40	21.81
	E_{rep}	296.40	56.44	360.60	62.20
PROPY-45DClPA MODERATE	E_{tot}	-173.80	36.85	-159.60	32.06
	E_{coul}	-60.00	18.20	-45.20	12.50
	E_{disp}	-218.80	45.09	-210.30	46.14
	E_{rep}	132.50	25.23	130.70	22.55

		PIXEL		CE	
		Energy /kJ mol^{-1}	% contribution to total	Energy /kJ mol^{-1}	% contribution to total
PROPY-45DClPA WEAK	E_{tot}	-123.80	26.25	-107.10	21.51
	E_{coul}	-21.00	6.37	-14.50	4.01
	E_{disp}	-173.80	35.82	-165.20	36.24
	E_{rep}	96.30	18.34	101.20	17.46
PROPY-PGL STRONG	E_{tot}	-330.90	35.50	-456.20	38.50
	E_{coul}	-446.00	46.31	-533.40	58.43
	E_{disp}	-183.00	17.79	-190.0	20.22
	E_{rep}	515.60	57.82	617.60	47.84
PROPY-PGL MODERATE	E_{tot}	-341.30	36.61	-455.40	38.43
	E_{coul}	-249.00	25.86	-321.00	35.16
	E_{disp}	-326.40	31.73	-387.60	41.25
	E_{rep}	355.00	39.81	458.00	35.47
PROPY-PGL WEAK	E_{tot}	-269.80	28.94	-280.10	23.64
	E_{coul}	-87.90	9.13	-64.50	7.07
	E_{disp}	-345.70	33.61	-361.00	38.42
	E_{rep}	232.10	26.03	212.50	16.46

*Medium and weak energy boundary used as -10 kJ mol^{-1}.

An alternate boundary for the separation of the moderate and weak interactions in PROPY-25DHBA was possible as a distinct energy gap is evident in the scatter plots between -26 kJ mol^{-1} and -18 kJ mol^{-1}. When this is used, the energies are as follows in Table B.21.

Table B.21. Interactions of PROPY-25DHBA when alternate boundary is used for separation of the moderate and weak interactions sectioning off the two strongest of the moderate interactions as a separate group. Strong interaction values remain as in Table B.20.

		PIXEL		CE	
		Energy /kJ mol^{-1}	**% contribution to total**	**Energy /kJ mol^{-1}**	**% contribution to total**
PROPY-25DHBA MODERATE	E_{tot}	-105.60	20.63	-117.40	17.92
	E_{coul}	-52.80	16.20	-57.00	13.17
	E_{disp}	-67.40	12.48	-77.60	13.12
	E_{rep}	33.80	6.44	43.20	6.45
PROPY-25DHBA WEAK	E_{tot}	-300.60	58.71	-315.50	48.16
	E_{coul}	-98.50	30.22	-67.90	15.69
	E_{disp}	-423.70	78.46	-440.10	74.43
	E_{rep}	286.00	54.49	257.60	38.45

In addition to the total energies for each set of interactions, a 'per molecule' value can also be determined in accordance the crystal structure (Table B.22). This allows a true comparison across the series as stoichiometric effects are negated.

Table B.22. Energies for strong and moderate interactions of all the PROPY systems determined per molecule present in the system.

		PIXEL	CE
		Energy per molecule /kJ mol^{-1}	**Energy per molecule /kJ mol^{-1}**
PROPY-25DHBA STRONG	E_{tot}	-17.67	-37.03
	E_{coul}	-29.10	-51.30
	E_{disp}	-8.15	-12.27
PROPY-25DHBA MODERATE	E_{tot}	-55.30	-67.80
	E_{coul}	-20.33	-21.08
	E_{disp}	-66.85	-76.27
PROPY-25DHBA MODERATE*	E_{tot}	-17.60	-19.57
	E_{coul}	-8.80	-9.50
	E_{disp}	-11.23	-12.93
PROPY-45DClPA STRONG	E_{tot}	-43.58	-61.15
	E_{coul}	-62.18	-76.40
	E_{disp}	-23.15	-24.85
PROPY-45DClPA MODERATE	E_{tot}	-43.45	-39.90
	E_{coul}	-15.00	-11.30
	E_{disp}	-54.70	-52.58
PROPY-4HBA STRONG	E_{tot}	-31.20	-46.38
	E_{coul}	-55.83	-67.55
	E_{disp}	-11.53	-12.30
PROPY-4HBA MODERATE	E_{tot}	-37.13	-40.75
	E_{coul}	-16.03	-13.08
	E_{disp}	-53.88	-56.18

*PROPY-25DHBA alternate grouping using separation seen in scatter plot.

		PIXEL	CE
		Energy per molecule /kJ mol^{-1}	Energy per molecule /kJ mol^{-1}
PROPY-FA STRONG	E_{tot}	-35.15	-53.80
	E_{coul}	-38.12	-58.87
	E_{disp}	-30.00	-35.27
PROPY-FA MODERATE	E_{tot}	-41.83	-44.17
	E_{coul}	-18.37	-16.40
	E_{disp}	-43.00	-45.47
PROPY-HQ STRONG	E_{tot}	-26.37	-35.77
	E_{coul}	-39.78	-47.50
	E_{disp}	-15.27	-15.27
PROPY-HQ MODERATE	E_{tot}	-47.23	-56.22
	E_{coul}	-44.90	-48.60
	E_{disp}	-36.58	-47.62
PROPY-MPAR STRONG	E_{tot}	-24.15	-26.55
	E_{coul}	-39.50	-35.40
	E_{disp}	-12.40	-9.90
PROPY-MPAR MODERATE	E_{tot}	-68.85	-71.45
	E_{coul}	-25.95	-22.85
	E_{disp}	-84.10	-88.80
PROPY-PGL STRONG	E_{tot}	-33.09	-45.62
	E_{coul}	-44.60	-53.34
	E_{disp}	-18.30	-19.00
PROPY-PGL MODERATE	E_{tot}	-34.13	-45.54
	E_{coul}	-24.90	-32.10
	E_{disp}	-32.64	-38.76

B.5 Analysis of Interactions to Water

Related supplementary documents:

- PROPY co-former to water search sol diss (.pdf) x2

Isostar[250] version 2.2.4, 2017 was used to assess the interactions between water and the functional groups present in PROPY and the co-former molecules. Propensities for each interaction were determined to assess interaction preferences calculated as the percentage of structures which contain both groups and form an interaction between them. The propensities are displayed in Table B.23 along with those determined for the main hydrogen bonds of the co-crystals ($O–H_{hydroxyl}$ or $O–H_{carboxylic\ acid}$ to carbonyl O in PROPY).

Based on this interaction analysis the expected order of dissolution / solubility is:

PROPY-HQ > PROPY-PGL > PROPY-35DHBA & PROPY-25DHBA > PROPY-4HBA > PROPY-FA > PROPY-MPAR > PROPY.

Table B.23. Propensity of interactions obtained from Isostar between water and co-former and PROPY functional groups. Ar_OH and CO_2H indicate the solid state interactions.

	Present in… (frequency)	**Interaction propensity to functional group / %**		
		Water	**Ar_OH**	**Cis CO_2H**
Water		16.18		
Phenol OH	HQ (2 x 2), 25DHBA (2), 35DHBA (2), 4HBA (1), MPAR (1)	53.00		
Carboxylic acid (cis)*	FA (2), 4HBA (1), 25DHBA (1), 35DHBA (1)	49.55		
Ester (aliphatic-aromatic)*	MPAR (1)	43.32		
Ketone (aliphatic-aromatic)	Similar to PROPY but C-C(O)-N, not C	37.74		
Pyramidal R3N	PROPY	36.92		
General alcohol OH		32.29		
Carbonyl	PROPY (1)	27.60	16.90	23.66
Any OH		24.07		
Ar_CH	25DHBA, 35DHBA, 4HBA, HQ, MPAR, PROPY	14.86		
Planar R3N		11.10		
Alkyl CH	PROPY	10.70		
Methyl	PROPY, MPAR,	6.66		
Phenyl	PROPY	4.76		

*data presented taken from named group to water interaction as no data available from water

Appendix C LON

CONTENTS

C.1 LON Polymorph Analysis

C.2 LON Material

C.3 CSD Analysis

C.4 Co-Former Selection

C.5 PXRD Patterns – screening by grinding

C.6 Crystal Structure Tables

C.7 Hydrogen Bond Interaction Tables

C.8 CSD and Structural Analysis

C.9 Novel LON Structures and Interactions

C.10 pK_a

C.11 Thermal Analysis

C.12 HSM Recrystallisation Material

C.13 Stability

C.14 Solubility

C.1 LON Polymorph Analysis

The reported work of Benetollo *et al.*[290] and the patent of Xinmin *et al.*[291] assign alternative naming schemes for the polymorphs. Analysis of the data they report in conjunction with our own findings allows these to be corroborated.

C.1.1 α-LON/Form I

Figure C.1 shows the PXRD pattern for α-LON calculated from the crystal structure and that for Form I taken from the patent shown in Figure C.2. Clear correlations can be seen between the two indicating that the labels Form I and α-LON are likely to be synonymous.

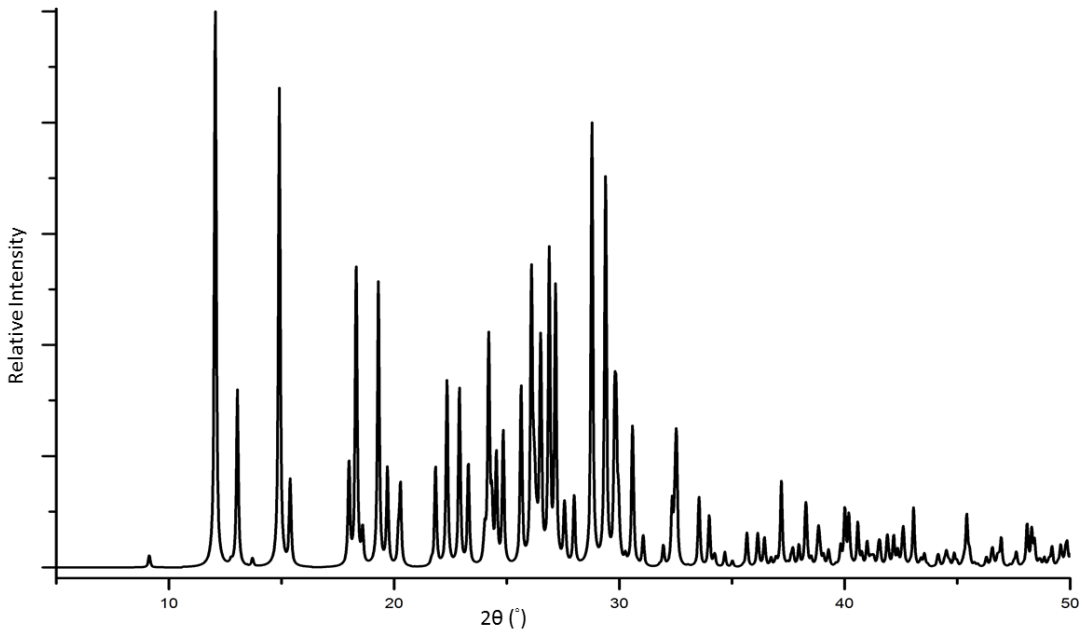

Figure C.1. PXRD pattern calculated from crystal structure data of α-LON.

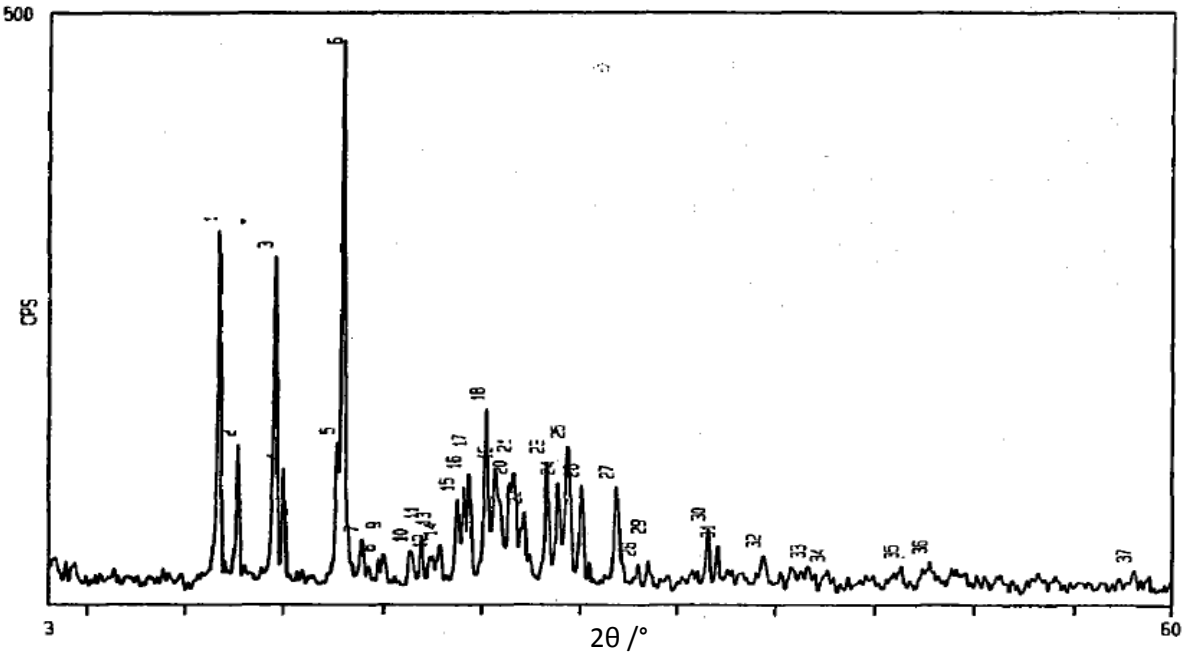

Figure C.2. Form I reported PXRD pattern taken from patent by Xinmin *et al.*[291]

C.1.2 β-LON/Form II

Figure C.3 shows the PXRD pattern for β-LON calculated from the crystal structure and shown in Figure C.4 is that for Form II taken from the patent. Reported cell parameters from the latter are: a = 7.7117 Å, b = 8.1384 Å, c = 11.987 Å, α = 106.17°, β = 93.05°, γ = 96.96°.[291] These match the experimental data (Section C.6) Clear correlations can be seen between the two patterns and also the cell parameters indicating that the labels Form II and β-LON are likely to be synonymous.

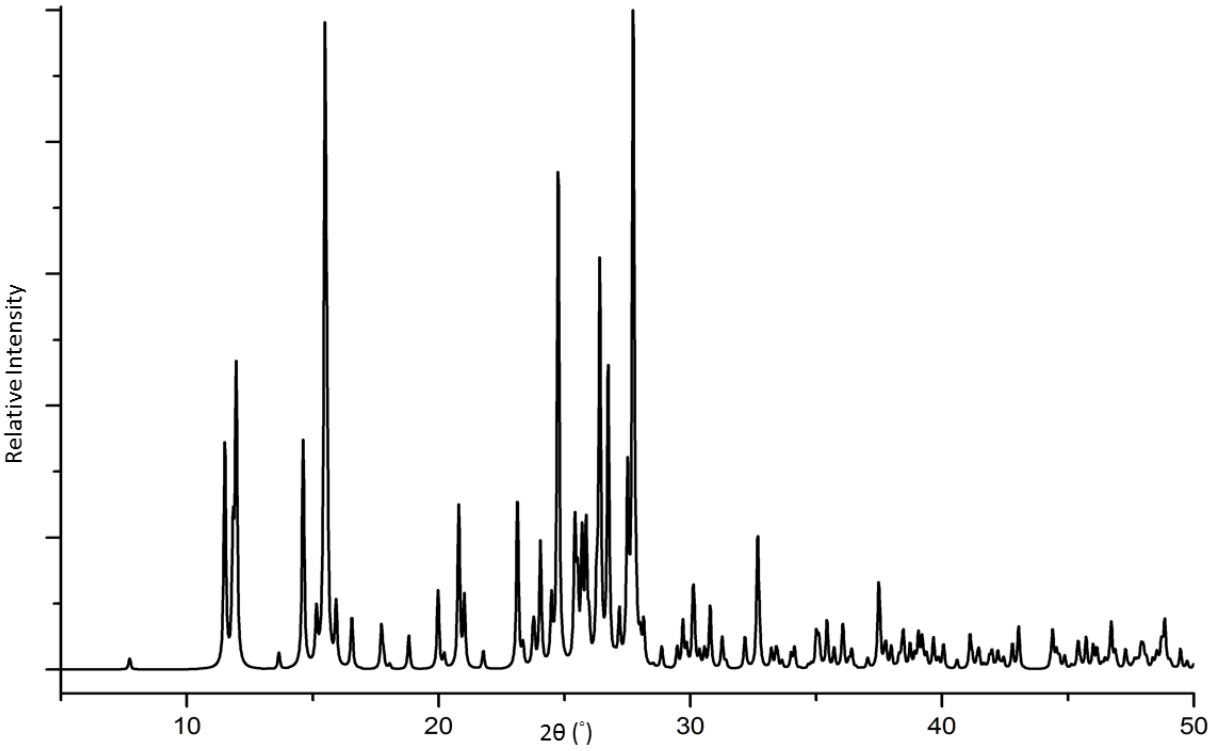

Figure C.3. PXRD pattern calculated from crystal structure of β-LON.

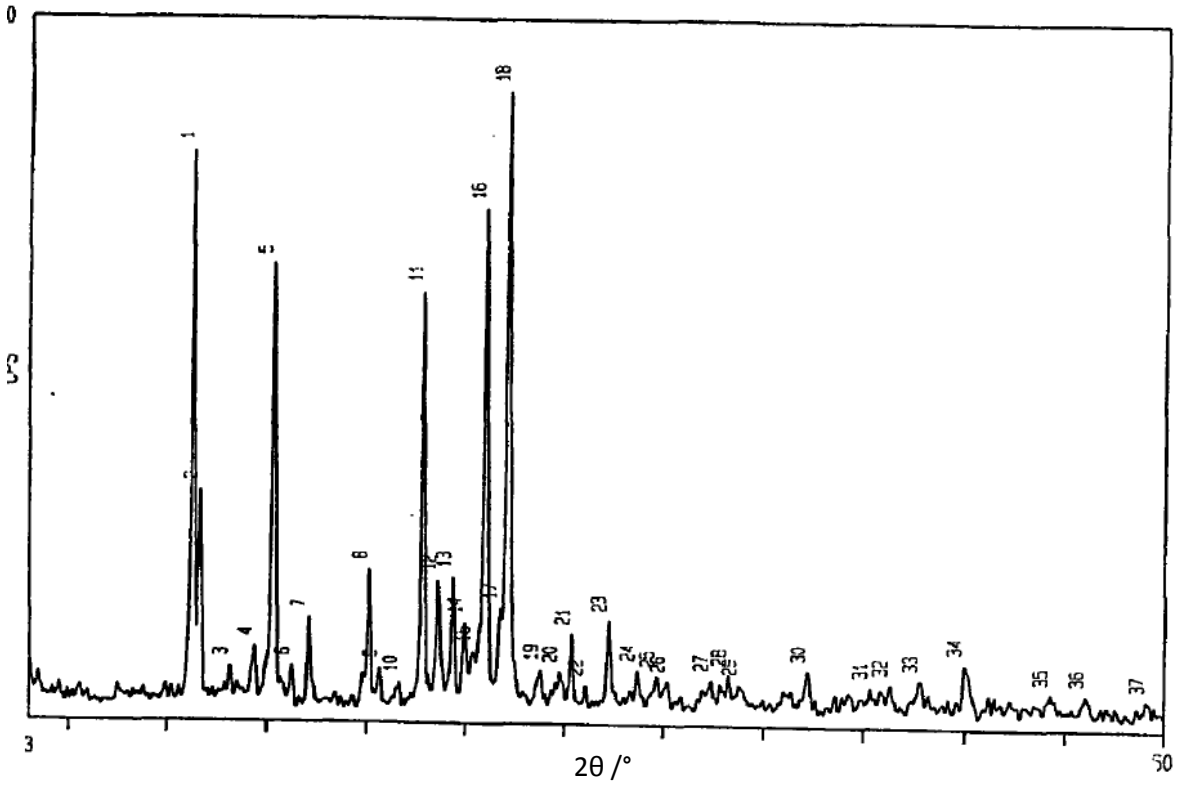

Figure C.4. Reported PXRD pattern for Form II from Xinmin *et al.*[291]

C.1.3 Form III

The PXRD pattern for Form III (Xinmin *et al.*[291]) is given in Figure C.5. Reported cell parameters are: a = 5.2879 Å, b = 8.1754 Å, c = 16.768 Å, α = 80.09°, β = 89.89°, γ = 80.65°. These are different to those experimentally determined for both α- and β-LON (section C.6). The powder pattern is also different to those generated for α- and β-LON.

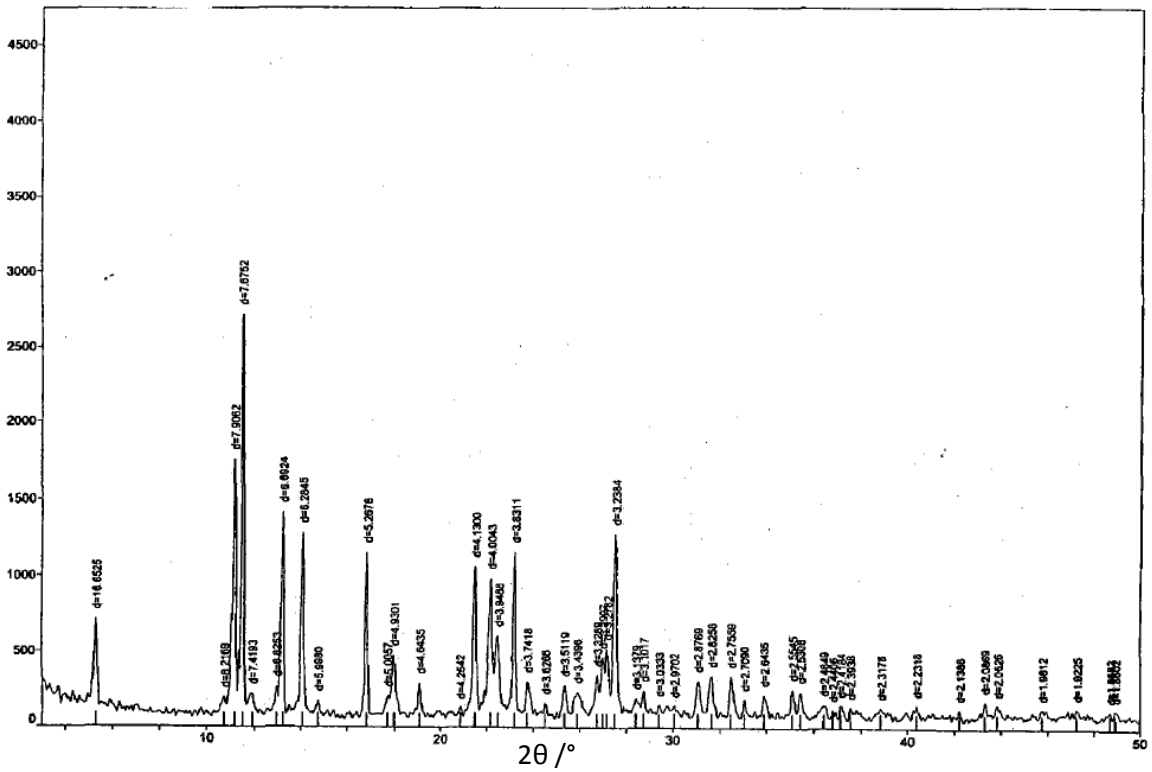

Figure C.5. Reported PXRD pattern for LON Form III from patent by Xinmin *et al*.[291]

C.1.4 Reported PXRD Data

Table C.1 collates the PXRD pattern peaks reported by Xinmin *et al*.[291] in patent CN101735151B.

Table C.1. Reported peaks from PXRD patterns for Forms I, II and III (Xinmin *et al.*[291])

FORM I		FORM II		FORM III	
2θ	**d**	**2θ**	**d**	**2θ**	**d**
11.7	7.5	11.3	7.8	5.3	16.6
12.7	6.1	11.7	7.6	11.1	7.9
14.5	5.9	15.3	5.8	11.5	7.7
15.0	5.0	20.1	4.4	13.2	6.7
17.7	4.9	22.9	3.9	14.0	6.28
17.9	3.7	26.0	3.4	16.8	5.3
24.1	3.5	27.1	3.3	21.5	4.1
25.2	3.5	32.2	2.8	22.2	4.0
25.6	3.4			22.5	3.9
26.4	3.3			23.2	3.8
27.1	3.2			27.5	3.2
28.3	3.1				
29.4	3.0				
30.0	3.0				
31.9	2.8				

C.1.5 DSC data

Xinmin *et al.*[291] report endotherms for Form I at 211.0°C and Form III and 211.3°C. Benetollo *et al*.[290] declare melting points of 211.6-212.2°C (α) and 208.5-209.5°C (β).

From all the data presented in C.1, Forms I and II from the patent can be ascribed to α- and β-LON respectively from the work of Benetollo *et al*.[290] Form III indicated in the patent is different to these two forms, and shall hence be assigned the label γ-LON.

C.2 LON Material

C.2.1 Bulk Powder Characterisation

A PXRD comparison of the calculated patterns from the experimental crystal structures of α- and β- LON and the experimental pattern from the bulk powder material used in experiments is shown in Figure C.6. This is used to determine the nature of the bulk starting material. It can be seen that the bulk sample used for all experimental work contains a mixture of the two forms however the β-form predominates; the endotherm peak in DSC experiments occurs at 209.4°C and it is this form for which some crystalline material is present and can be characterised by SCXRD. PXRD patterns indicate some peaks belonging to the α-form as well as those for the β-form, indicating a mixture of the two forms.

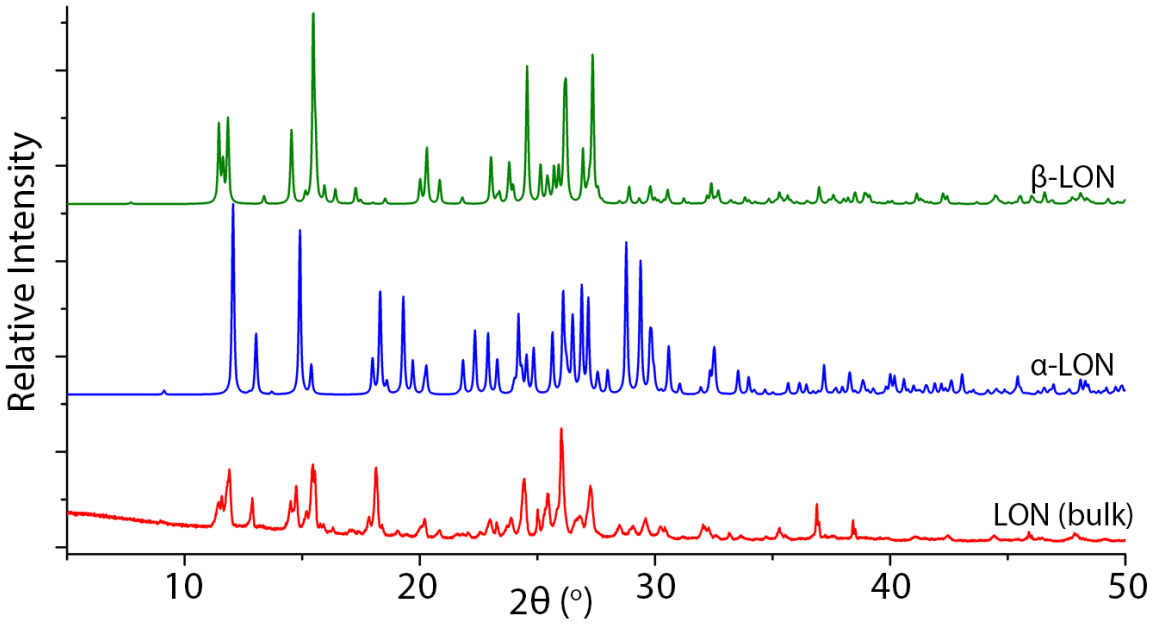

Figure C.6. PXRD comparison of bulk LON (Junda Chemicals) with the calculated patterns obtained from the crystal structures of the α- and β- polymorphs.

C.2.2 Control of Polymorphs

Rotary evaporation of solutions for fast removal of solvent was employed to investigate the effect of different solvents on polymorphic control. Fast removal of solvent reduces the thermodynamic influence and it was possible to obtain a purer sample.

Rotary evaporation of LON dissolved in ethyl acetate, ethyl acetate-H_2O and 1,4-dioxane solvents produced the α-form, whilst methanol produced the β-form (Figure C.7).

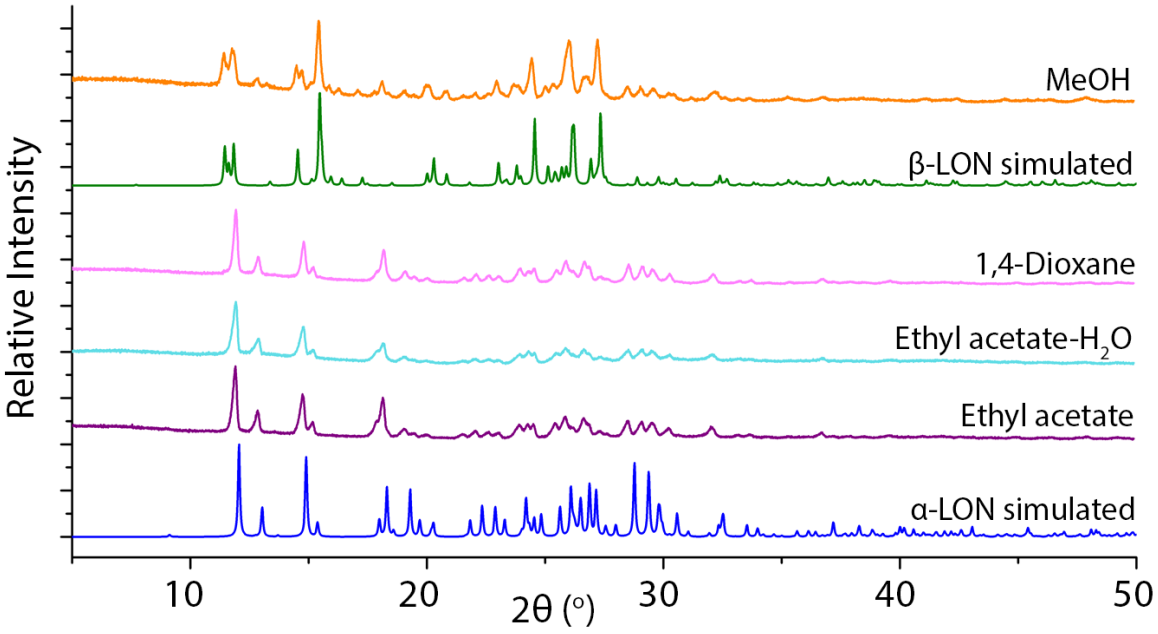

Figure C.7. PXRD comparison of solids produced from rotary evaporation of solutions of LON with various solvents and calculated patterns from the crystal structures of α- and β-LON.

Solution crystallisation experiments produced α-LON from ethyl acetate and an ethyl acetate-acetonitrile solvent mix. β-LON was obtained from MeOH, THF, DMF, DMSO, formic acid and a MeOH-acetonitrile solvent mix.

C.3 CSD Analysis

To understand the preferred interaction behaviours of LON functional groups, analysis of the CSD (v 5.3.8) was completed. A number of the different tools present in the CCDC software suite were employed. Initially Isostar,[3] v 2.2.4 was used to find the most preferential functional group pairings from pre-defined ligands and ring systems. Specific contacts were then investigated using motif searching (Mercury[4,5]) which allowed more freedom in the description of the functional groups; a wider variety of contact groups and discrimination of the precise interaction occurring (exact donor and acceptor atoms in the contact) was possible. The Conquest[6] search tool was also used to further investigate particular interactions, and different molecule fragments. Details of the models used and their labelling are given in Section C.3.3.

C.3.1 Carboxylic Acid Interaction Preferences

Tables C.2 and C.3 show the preferred interactions of a carboxylic acid group from Isostar and specific contact searching respectively.

Table C.2. Results from Isostar searches using pre-defined, general, contact groups

Uncharged carboxylic acid-CIS 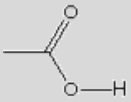	**Structures with both groups present**	**Structures with both groups and contact between**	**%**
Any polar X-H (N, O, S)	9999 (subset from 17141 structure)	2303	23.03
Alkyl CH	9999 (subset from 13315 structure)	1240	12.40
Aromatic CH	9999 (subset from 12216 structure)	1408	14.08
Any NH	7176	2100	29.26
Uncharged NH	3414	1557	45.61
Amide NH	1394	610	43.76
Uncharged C(sp^2) / C(ar)-NH2	772	531	68.78
Any OH	9999 (subset from 17141 structure)	2169	21.69
Phenol OH	1294	336	25.97
Alcohol OH	1998	1320	66.07
Water	3221	1596	49.55
Cyano	279	49	17.56
Any C=O	9999 (subset from 17141 structure)	2366	23.66
Carboxylate	2784	1494	53.66
CONH2	553	475	85.90
Aromatic or Sp2 N	4131	1871	23.03

Table C.3. Specific contact searching results showing interaction preferences.

# = number of structures % = % frequency	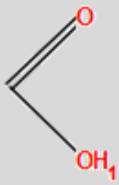			
	Carboxylic acid **OH**		Carboxylic acid **C=O**	
Contact group	#	%	#	%
OH	3764	13.3	10008	35.3
Ar_ hydroxy	227	11.5	1016	51.4
Al_hydroxy	1556	46.3	1633	48.6
Acyclic	2704	9.87	8505	31.0
Cyclic	975	23.5	1744	42.0
CO_2H	1810	6.89	7726	29.4
T3NH$_2$	521	20.7	1695	67.2
T3NH1 cyclic	409	10.1	1283	31.7
T3NH1 acyclic	222	7.25	1271	41.5
T2NH$_1$	14	51.9	8	29.6
T2N_any	3389	54.5		
CO**NH$_2$**	109	14.0	601	77.2
CONH$_2$	466	59.8		
Ar_nitrogen	2419	63.8		
Cyclic_n	601	49.8		
Acyclic_n	14	13.9		

Bold indicates the contact group used for interaction, models depicted in Section C.3.3, Figure C.8.

From these results (Tables C.2 and C.3), amide –NH_2 groups appear the most favourable to form an interaction to a carboxylic acid. This is followed by any –NH_2 group. Contact searching identifies aromatic nitrogen and T2N groups interacting with the O–H of the carboxylic acid also to be favourable. Other favourable interactions include N–H and O–H, although the latter presents the lowest apparent propensity to form. However, this low % observed in contact searching for O–H can be understood when the analyses are combined and the results from Isostar considered; phenol O–H groups have a very low tendency to form, whilst alcohol O–H groups have a much higher tendency. Hence, the O–H value from contact searching is observed as an average of these as the O–H description encompasses both and thus appears lower than may be expected. Detailed analysis indicates that cyclic hydroxyls are less likely to form an interaction than acyclic (in accordance with phenolic O–H from Isostar) and both are lower in occurrence than aliphatic and aromatic O–H (aromatic > aliphatic). –CO_2H groups appear to have a low tendency to form an interaction to the carboxylic acid group (interrogating just a single interaction). However, further investigation using Conquest indicated when two carboxylic acid

groups are present, a dimer interaction is observed in 87.3 % of structures. Similarly, the dimer interaction to an amide group is seen in 46.5 % of structures that contain both functionalities.

Further Conquest analysis of the interaction to an aromatic or sp^2 N atom identified that almost 60% of these are neutral. A large proportion also exhibit charge transfer with a protonated, positive N atom. Depending on the descriptions used, approximately 42.5 % contain a charged N atom. This is, however dependent on the charge and proton identification in the structures of the CSD. This may account for the lower than expected percentage seen in Isostar, as no information or variation on charge and protonation is possible in such searches.

C.3.2 Indazole Interaction Preferences

Tables C.4 and C.5 show the results obtained from isostar and specific contact searching respectively for the indazole group and structurally related fragments, indicating the preferred interactions. There is no directly comparable ring system to the indazole of LON implemented in Isostar. Two different systems that were the most similar in structure were analysed and results used in combination.

Table C.4. Isostar searches using first contact group (pyrazol-1-yl) most relevant to the fused indazole ring in LON.

Pyrazol-1-yl 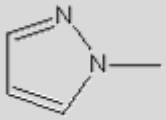	**Structures with both groups present**	**Structures with both groups and contact between them**	**%**
Any polar X-H (N, S or O)`	1137	566	49.78
Alkyl CH	2368	784	33.11
Aromatic CH	2063	845	40.96
Any NH	726	256	35.26
Uncharged NH	341	88	25.81
Amide NH	186	36	19.35
Uncharged C(sp^2) / C(ar)-NH2	52	31	59.62
Any OH	561	328	58.47
Phenol OH	90	44	48.89
Alcohol OH	122	74	60.66
Water	114	82	71.93
Cyano	177	46	25.99
Any C=O	1099	296	26.93
Carboxylate	4	1	25.00
CONH2	29	17	58.62
Aromatic or Sp2 N	2698	557	20.64

Table C.5. Isostar searches using second contact group (pyridazine) most relevant to the fused indazole ring in LON.

Pyridazine 	**Structures with both groups present**	**Structures with both groups and contact between them**	**%**
Any polar X-H (N, O, S)	178	114	64.04
Alkyl CH	367	226	61.58
Aromatic CH	472	287	60.81
Any NH	100	58	58.00
Uncharged NH	63	28	44.44
Amide NH	17	5	29.41
Any OH	96	63	65.63
Phenol OH	32	14	43.75
Alcohol OH	8	6	75.00
water	33	22	66.67
cyano	17	8	47.06
Any C=O	130	44	33.85
carboxylate	6	3	50.00
CONH2	2	2	100.00
Aromatic or Sp2 N	510	125	24.51

The specific contact searching results are shown in Table C.6 for the fused indazole ring. Analysis of the indazole group interactions was more involved than that of the carboxylic acid as fewer structures contain the exact fragment present in LON. In a similar approach to that employed in the Isostar search, a number of different fragments and functionalities were used in the searches replicating different aspects of the indazole ring and environment. The results were then combined to give an overview of the groups' behaviour.

A general trend: C–H > O–H > primary amines ($T3NH_2$) > amides > cyclic/acyclic $T3NH_1$ is observed for functionalities forming an interaction to indazole. This can be broken down into a more in-depth analysis of some of the general functional groups. C–H group analysis indicates T3C–H and aromatic C–H are the most favourable to form an interaction. A low % frequency of interactions is observed for benzene indicating that the ar_C–H interactions are more likely to occur from other ring systems, possibly containing other atom types. T4C–H is the next most likely to form an interaction followed by T3C groups. Methyl groups have a low propensity to interact, and methylene produced similar results, with low % frequencies of occurrence. For C–H groups, the overall trend can be seen as: ar_C–H / T3C–H > T4C-H >>methyl > methylene.

Table C.6. Specific contact searching.

# = number of structures % = % frequency	Pyrazoline	N-N 5 ring any	Indazole ring any	N-N=C cyclic	Ar_nitrogen
	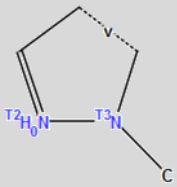	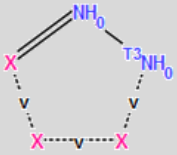	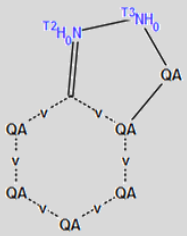	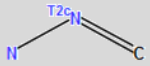	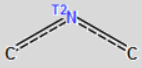

Contact group	#	%	#	%	#	%	#	%	#	%
OH	398	39	1235	28.4	7	33.3	1738	38	6276	54.8
Ar_ hydroxy	89	41.8	613	54.7	2	33.3	742	59.2	1583	52.2
Al_hydroxy	233	42.8	645	21.8	4	28.6	839	32.1	2236	45.4
Acyclic	206	42.3	458	18	4	33.3	732	28.7	3652	52.9
Cyclic	163	29.5	722	41.9	3	25	909	45.8	2072	49
CO_2H	62	40	99	16.3	0		210	26.1	2419	63.8
T3NH$_2$	178	32.3	842	28.2	2	10.5	1308	37.2	2918	49
T2NH$_1$	1	8.33	3	9.38	0		3	9.38	6	11.8
T3NH1_acyclic	102	13.1	252	9.78	1	16.7	555	17.9	2035	25.2
T3NH1_cyclic	107	19.9	347	11.6	0		1361	21.9	2117	26.8
CO**NH$_2$**	16	28.1	23	18.5	0		36	24.2	144	23
CONH$_2$	0		3	2.42	0		5	3.36	4	0.64
Methyl **CH$_3$**	167	3.99	1247	7.02	9	9.57	908	6.52	1215	5.81
Any_C-**H**	5280	86.4	24090	73	143	88.3	22343	80.8	35116	63.6
Any_**C**-H	1499	24.5	10540	32	40	24.7	9085	32.8	15810	28.6
Benzene	2	11.8	6	2.91			5	5.56	15	4.73
Methylene	2	2.82	8	2.14			8	2.84	8	1.39
Ar_C-H	2697	52.2	14705	57.3	82	53.9	14831	66.7	23921	44.4
Ar_C-H	772	14.9	5643	22	25	16.4	4952	22.3	10620	19.7
arCH1	772	14.9	5644	22	25	16.4	4953	22.3	10626	19.7
T3C	1059	17.8	7635	24.3	28	18.1	6792	26.3	11493	21.2
T3C-H	4319	72.7	16753	53.4	121	78.1	16802	65	25689	47.4
T3C-H	1061	17.9	7641	24.3	28	18.1	6797	26.3	11499	21.2
T4C	100	5.18	441	6.26	2	2.11	370	7.11	960	9.56
T4C-H	2508	44.1	13424	47	68	43	11592	51.3	16368	42.2
T4C-H	554	9.74	3835	13.4	14	8.86	2972	13.1	5239	13.5

Bold indicates the contact group used for interaction

O–H group analysis presented greater variation (than C–H) and indicated that the results are dependent on the model used. In general, –CO_2H are the least favoured O–H containing functionalities which is likely to arise due to their high propensity to form strong hydrogen bonds with other strong hydrogen bonding functionalities, as seen in the previous analyses. Ar_hydroxy functionality features as one of the most likely groups to interact across the range of models used.

Frequencies of occurrence are in the range 30-60 % which is higher than al_hydroxy groups (20-45 %). Cyclic hydroxyls appear to be slightly more favoured (25-50 %) than their acyclic counterpart (18-53 %) however the latter span the largest range showing high dependence on the model and atom environment.

C.3.3 Models used for Specific Contact Searching

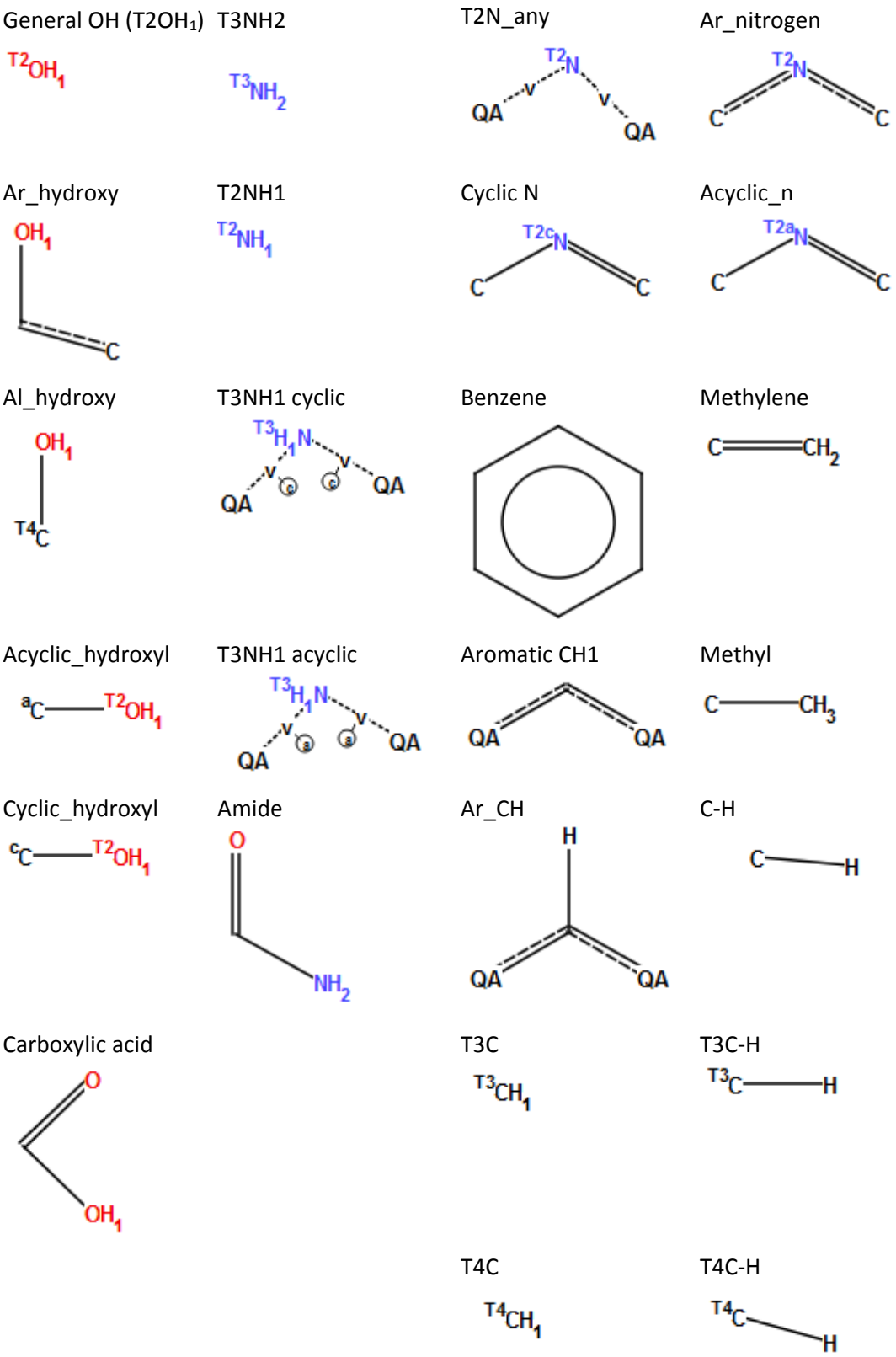

Figure C.8. Models used in specific contact searching for LON. QA denotes any atom except hydrogen, c=cyclic, a=acyclic, TX denoted of bonded atoms (eg T2 = 2 bonded atoms to atom indicated), dashed bonds indicate any bond type (not specified).

C.4 Co-Former Selection

All co-formers used in screening experiments (grinding – solvent assisted and / or neat) are listed below (Table C.7). Those on bold red font indicate a new material was formed on the combination with LON, discussed in chapter 6.3.1.

Table C.7. List of all co-formers used in experimental screening by grinding for LON. Compounds in bold red were successful in producing a new co-crystal/salt experimentally.

Co-Former		
2,2'-Di-n-propylacetamide (Valpromide)	Camphoric acid	Oxalic acid
2,4,6-Triaminopyrimidine	Caprolactam	p-Coumaric acid
2,5-Pyridinedicarboxylic acid	Catechol	Phloroglucinol
2-Amino-5-bromobenzoic acid	Chlorhexidine	Picolinamide
2-Amino-5-bromopyrimidine	Chlorpropamide	**Piperazine**
2-Aminopyridine	Cytosine	Piperine
2-Aminopyrimidine	D-Methionine	Piracetam
2-Ethoxybenzamide	Flufenamic acid	Propionamide
2-Picolinic acid	Gallic acid	Pyrazineamide
3,5-Dihydroxybenzoic acid	γ-Glycine	Pyridoxine
3-Aminobenzoic acid	**Haloperidol**	Pyrogallol
3-Ethynylpyridine	Hydroxyurea	Quinoxaline
3-Nitrobenzamide	Ibuprofen	Resorcinol
4,4'-Bipyridine	**Imidazole**	Rufinamide
4,5-Dichlorophthalic acid	Indole-3-acetic acid	Saccharin
4-Aminobenzamide	Isoniazid	Salbutamol
4-Dimethylaminopyridine	**Isonicotinamide**	Salicylamide
4-Hydroxybenzamide	Isonicotinic acid	Salicylic acid
4-Hydroxybenzoic acid	Isophthalic acid	Sarcosine

Co-Former		
5-Aminosalicylic acid	L-Alanine	Sulfamethoxypyridazine
5-Fluorouracil	L-Arginine	Sulfamic acid
Acesulfame	L-Glutamine	Taurine
Acetazolamide	L-Threonine	Terephthalic acid
Adenine	**Melamine**	Theophylline
Adipamide	Myo-inositol	Thymine
Aspartame	Nalidixic acid	Trans-3-hydroxycinnamic acid
Aspirin	**Nicotinamide**	Uracil
Benzamide	Nicotinic acid	Urea
Benzoin	Orotic acid	Vanillic acid

C.5 PXRD Patterns for Screening by Grinding

C.5.1 Successful Combinations of LON and Co-Former

Combinations of LON and co-former which were successful in producing a new material are detailed below. Indications were seen in the PXRD patterns of the powders produced from grinding. Figures C.9 to C.15 indicate those which contain pharmaceutically acceptable co-formers, whilst Figures C.16 to C.20 display successful combinations found that do not utilise a pharmaceutically acceptable co-former molecule. Crystallisation experiments afforded suitable crystals to allow the confirmation by X-ray diffraction studies and structure solution.

C.5.1.1 BENZ

The 1:1 grind of LON and BENZ afforded the 1:1 co-crystal as shown in Figure C.9. The pattern is different to the reference materials and directly comparable to that calculated from the crystal structure.

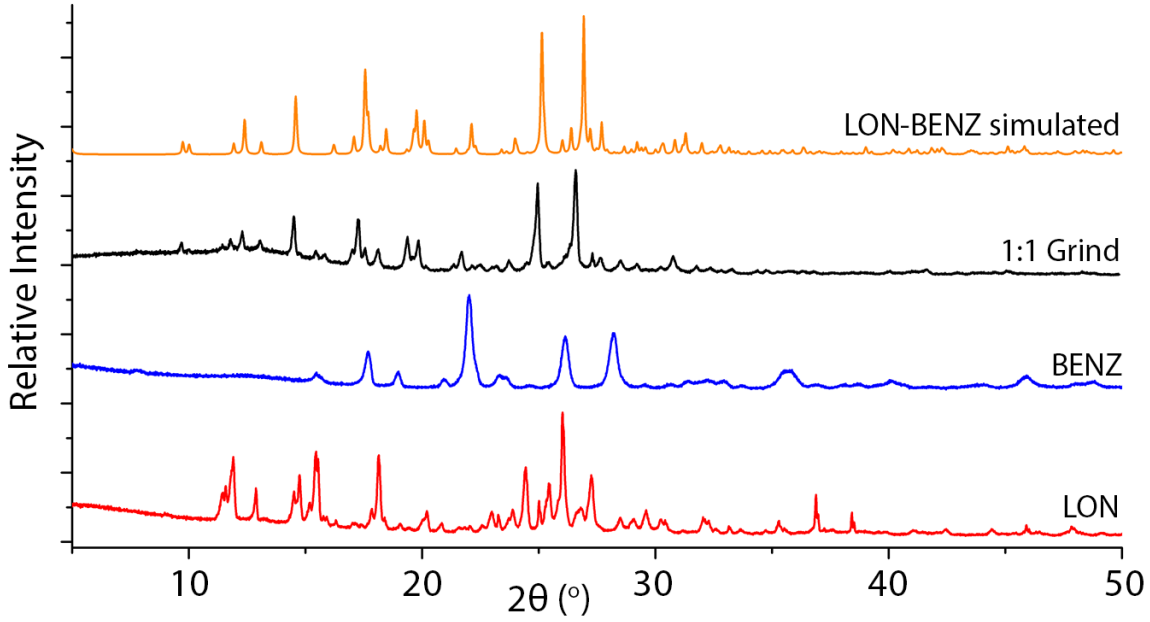

Figure C.9. PXRD for 1:1 solvent drop grind of LON with BENZ compared to the pattern calculated from the crystal structure obtained.

C.5.1.2 HALO

Figure C.10 shows the PXRD pattern of the 1:1 grinding material of LON with HALO in conjunction with that simulated from the determined crystal structure and powder generated in a solution crystallisation experiment. Grinding was not successful in producing the salt, however the resulting material was poorly crystalline and the peaks of LON and HALO similar, solution attempts were carried out. A number of these produced powders, instead of individual crystals, and PXRD analysis was performed. Solution trials were more successful than grinding at affording the new material.

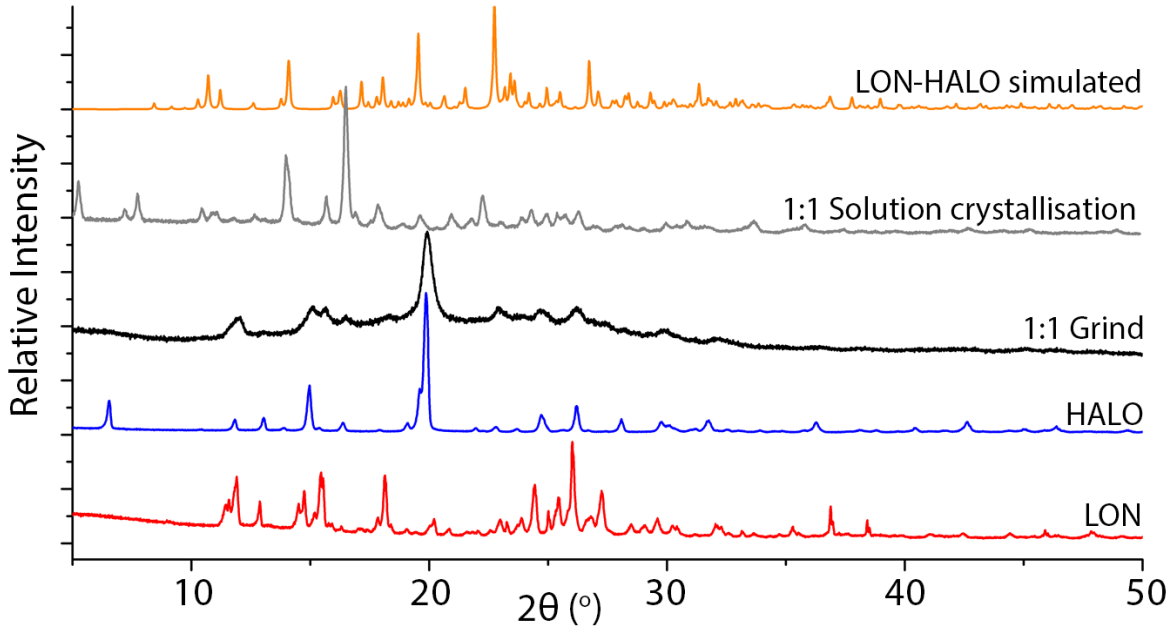

Figure C.10. PXRD for 1:1 solvent drop grind material and the powder produced from solution experiment of LON with HALO compared to the simulated pattern from the crystal structure obtained.

C.5.1.3 IMID

Similarly to HALO, the material produced from the grinding experiments with IMID was poorly crystalline. Substantial differences in the peaks, compared to the reference materials, were observed and hence solution trials were undertaken. Three different materials were obtained from these, the calculated powder pattern for each included in Figure C.11. Similarities are seen between the grinding material and 2:1 structure, however this would result in excess IMID in the grinding pattern. As with HALO, solution trials were more successful in yielding a new material for LON-IMID combinations.

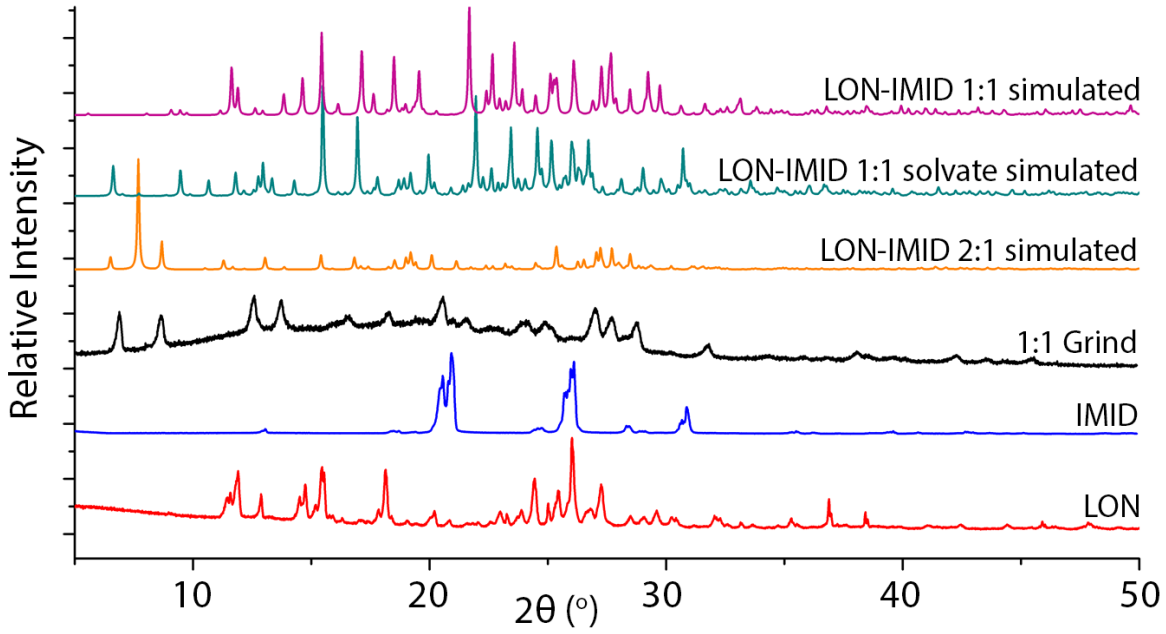

Figure C.11. PXRD for 1:1 solvent drop grind of LON with IMID compared to the simulated patterns from all three crystal structures obtained. Material was poorly crystalline but shows likeness to the 2:1 structure.

C.5.1.4 ISO

The 1:1 grind of LON and ISO produced the co-crystal as obtained from solution crystallisation attempts, the two powder patterns (calculated from the crystal structure and material from grinding) are comparable (Figure C.12).

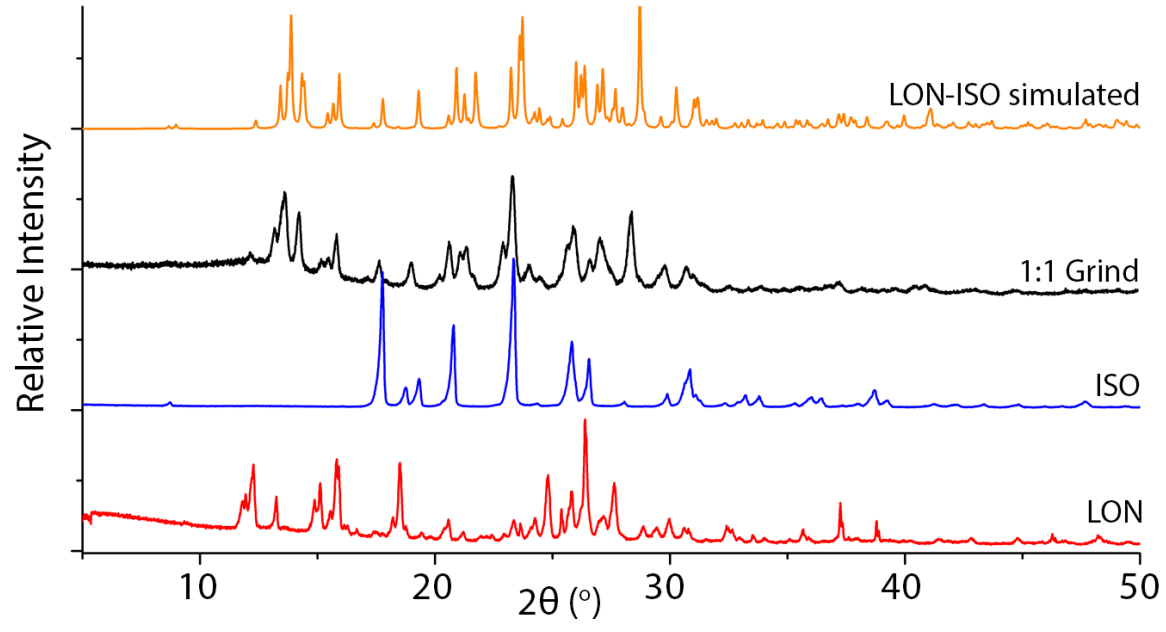

Figure C.12. PXRD pattern for 1:1 solvent drop grind of LON with ISO compared to the simulated pattern from the crystal structure obtained.

C.5.1.5 MEL

The grinding of MEL and LON resulted in the 1:1 salt being produced, identical to that obtained in solution crystallisations from which the crystal structure was obtained. The two powder patterns (simulated and 1:1 grind) in Figure C.13 are different to the reference materials, and analogous to one another.

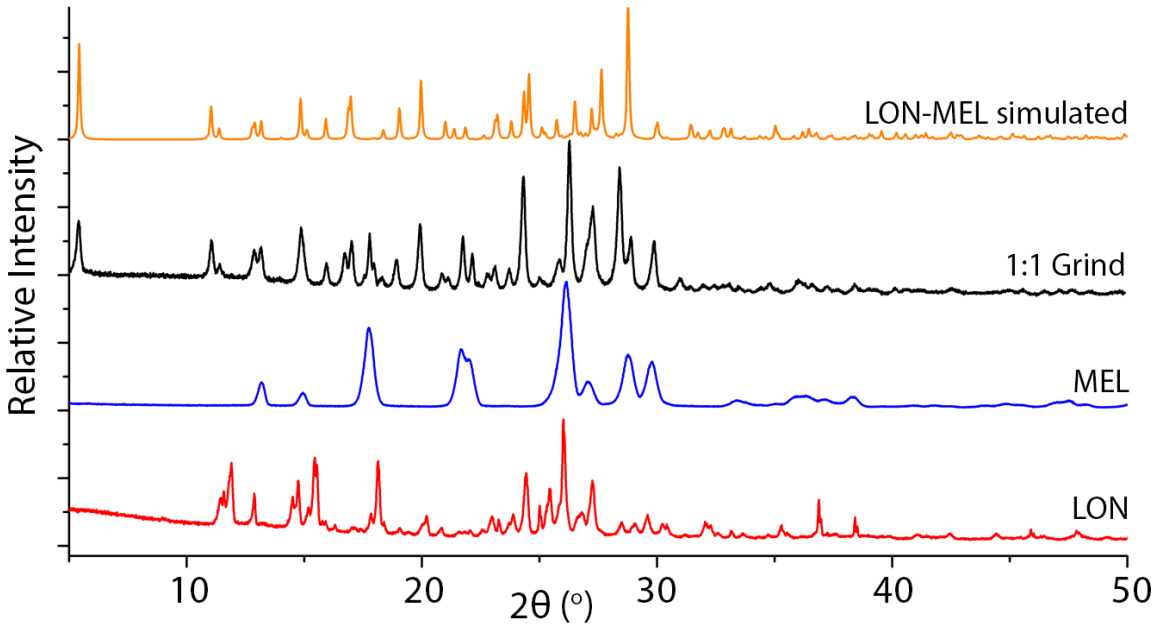

Figure C.13. PXRD for 1:1 solvent drop grind of LON with MEL compared to the simulated pattern from the crystal structure obtained.

C.5.1.6. NICO

The material produced from the 1:1 grind of LON and NICO shows clear differences to the patterns of both reference materials indicating a new form (Figure C.14). The crystallinity is fairly poor, however it can be seen that the pattern resembles that calculated from the crystal structure determined.

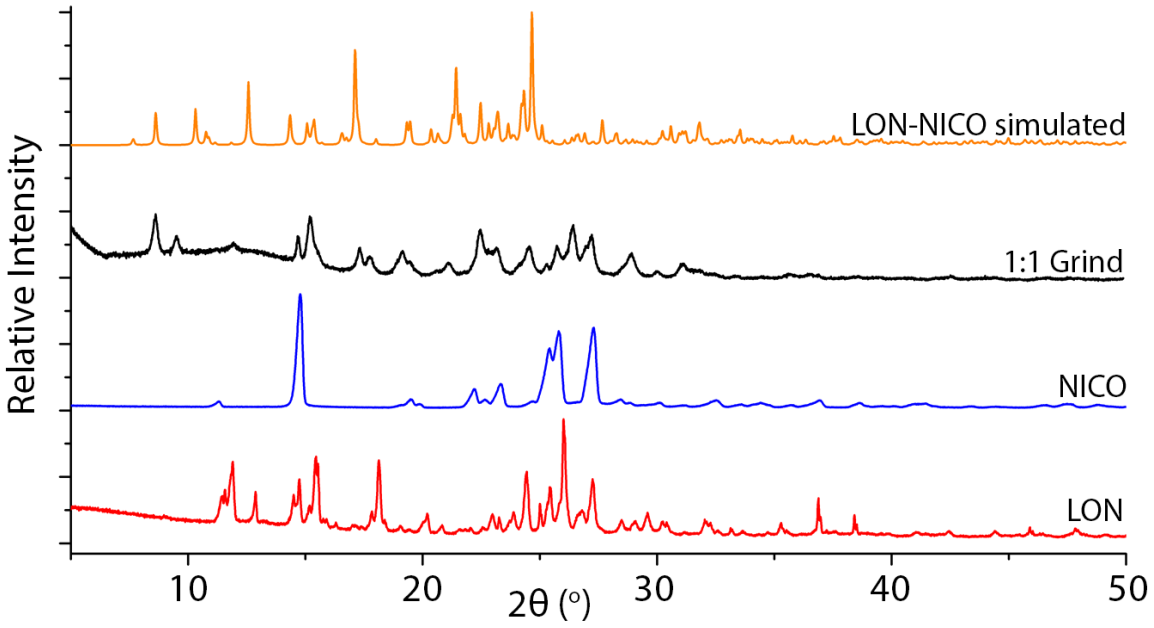

Figure C.14. PXRD for 1:1 solvent drop grind of LON with NICO compared to the simulated pattern from the crystal structure obtained.

C.5.1.7 PIPE

LON-PIPE formed a 2:1 salt, observed from crystal structure determination. The 1:1 grind material shows similarities to the powder pattern generated from this in Figure C.15 however the stoichiometry influences the pattern and excess PIPE is present for a full conversion of LON.

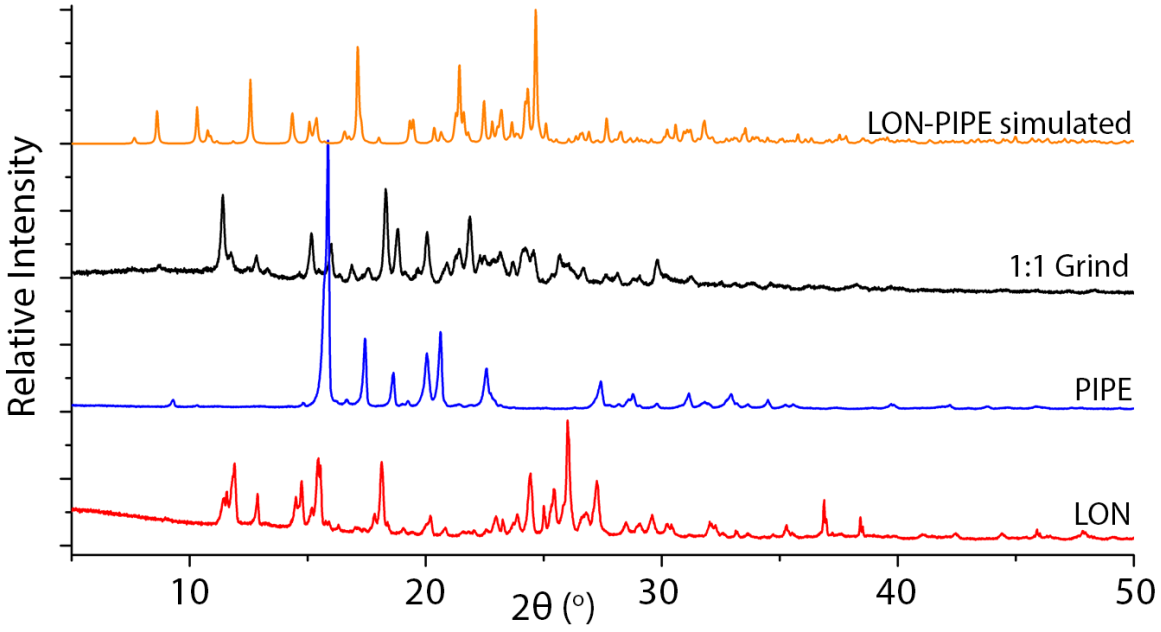

Figure C.15. PXRD for 1:1 solvent drop grind of LON with PIPE compared to the simulated pattern from the crystal structure obtained.

C.5.1.8 2APYD

The powder patterns depicted in Figure C.16 below include the 1:1 grinding material and the two crystal structures obtained from solution. These were two salt solvate forms, and hence it would be unexpected that grinding produced these as the solvents included in the crystal lattices were not present in the grinding. Some differences are seen in the 1:1 grind in comparison to the reference materials, indicating that a new form may be likely, however some parent peaks are also seen (2APYD in particular) indicating that a complete conversion to a new form did not occur.

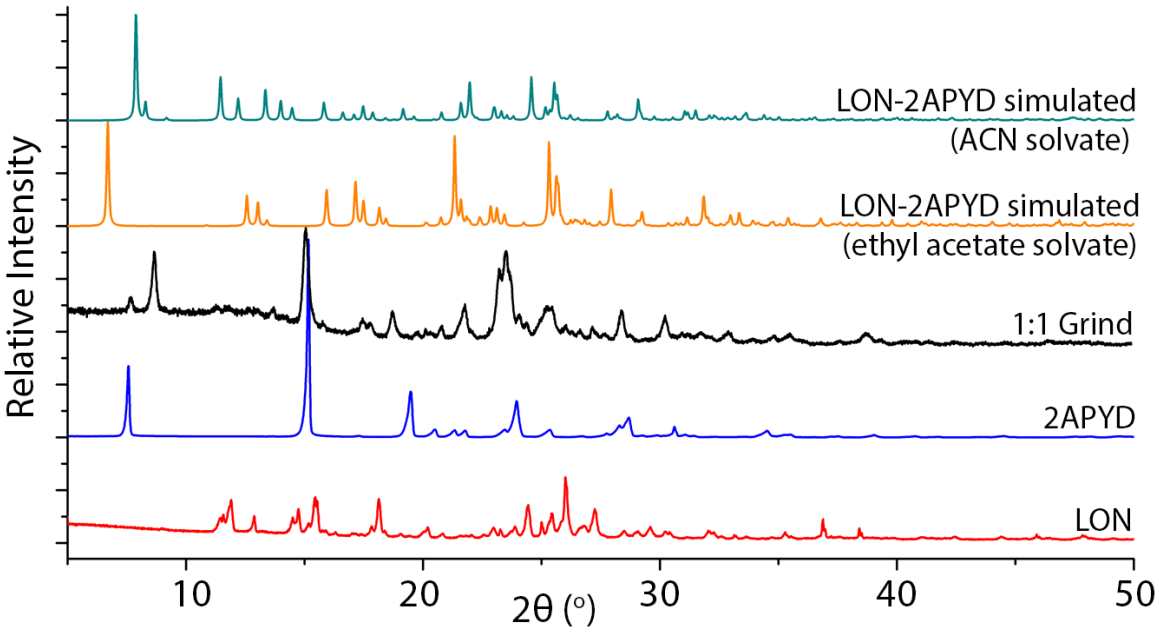

Figure C.16. PXRD for 1:1 solvent drop grind of LON with 2APYD compared to the simulated patterns from the crystal structures obtained.

C.5.1.9 2APYM

The 1:1 grind powder pattern (Figure C.17) shows clear similarities to that calculated from the crystal structure, showing that this material was likely to be formed on grinding. The crystal structure determined had a stoichiometry of 1:2 and hence residual 2APYM peaks in the pattern from grinding would be expected. Some of these are apparent however the nature of the 2APYM powder pattern leads to these not having a large influence.

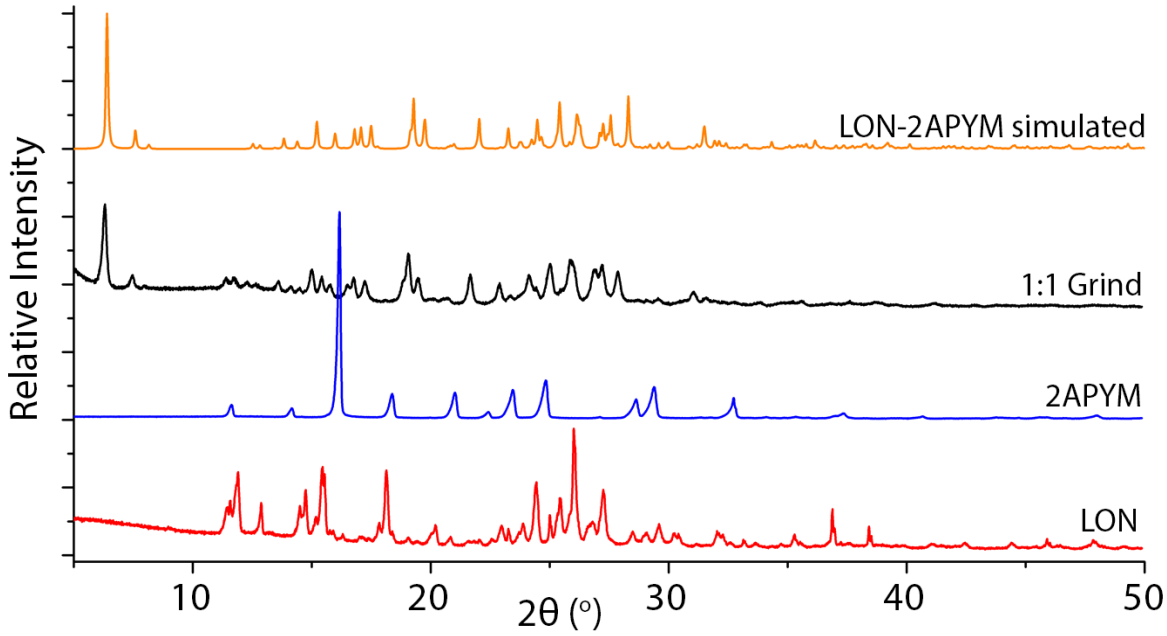

Figure C.17. PXRD for 1:1 solvent drop grind of LON with 2APYM compared to the simulated pattern from the crystal structure obtained.

C.5.1.10 246TAPYM

246TAPYM generated a 1:1 salt with LON. The material produced from grinding shows similarities in the powder pattern to that determined from the crystal structure (Figure C.18), however the crystallinity is poor and the peak heights weak relative to the background. An indication of the new form is evident, and it can be said that grinding produces this 1:1 salt.

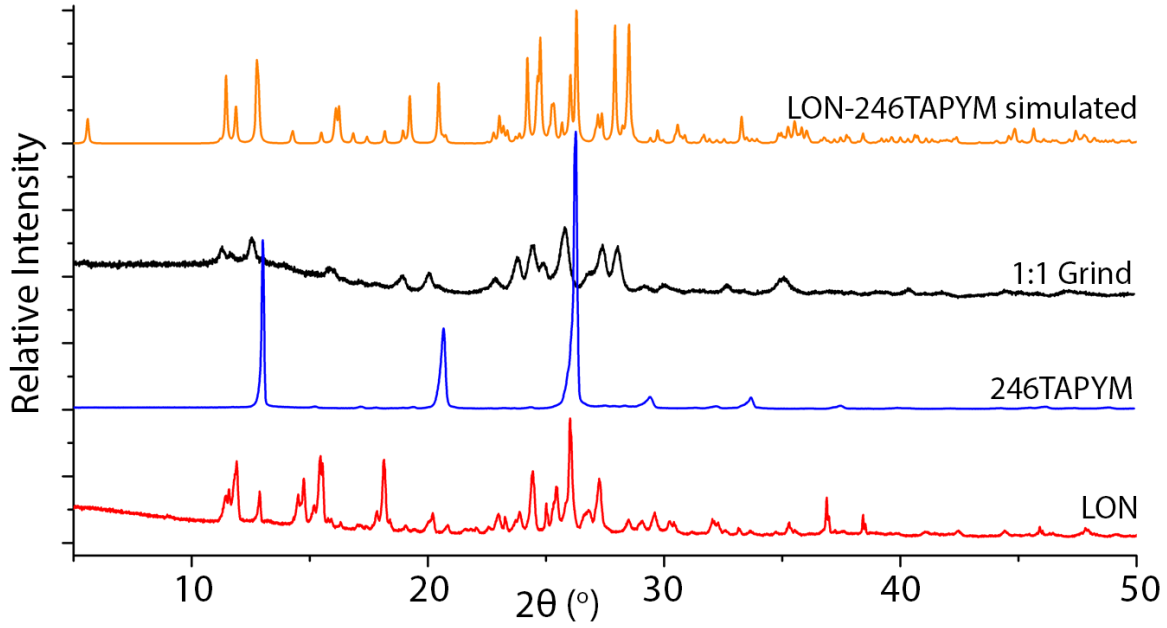

Figure C.18. PXRD for 1:1 solvent drop grind of LON with 246TAPYM compared to the simulated pattern from the crystal structure obtained.

C.5.1.11 4DMAP

Two different materials were produced from LON and 4DMAP in solution crystallisation experiments. These are both shown in Figure C.19 along with the powder pattern of the 1:1 grind. There are similarities in the pattern of the material produced in the grinding experiment to both forms, however it is most likely to be the 1:1 hydrate structure produced, to which there is a greater degree of likeness.

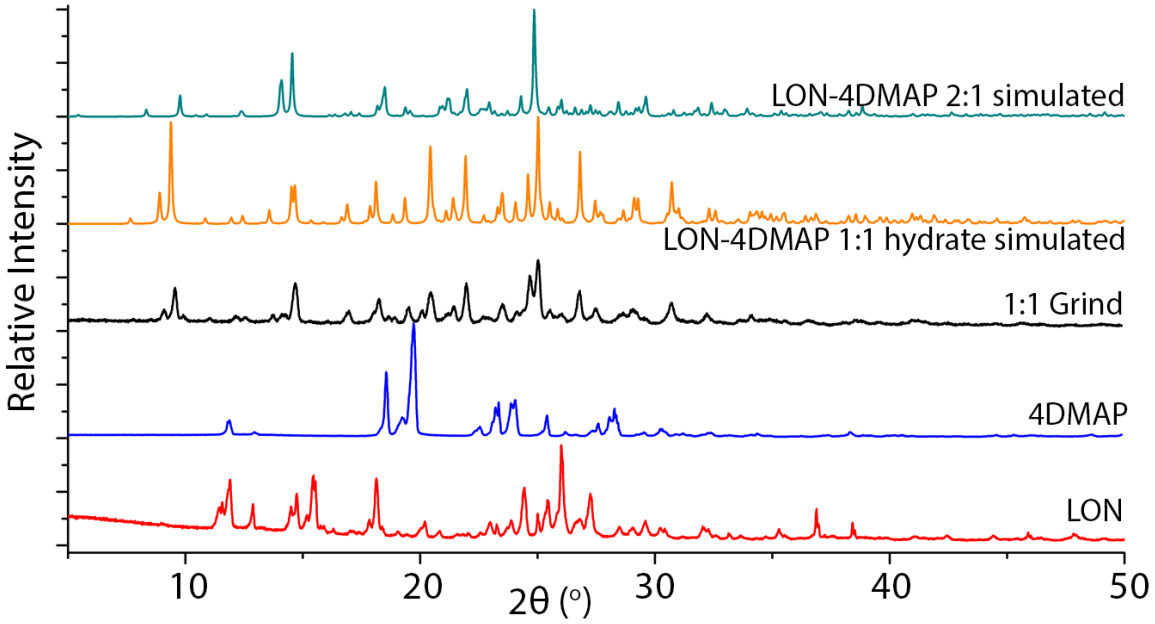

Figure C.19. PXRD for 1:1 solvent drop grind of LON with 4DMAP compared to the simulated patterns from the crystal structures obtained. It can be seen that grinding produced the 1:1 salt hydrate structure.

C.5.1.12 4,4BIPY

A 2:1 co-crystal was obtained from LON and 4,4BIPY, shown in the powder pattern in Figure C.20. The 1:1 grind material shows a close resemblance to this, indicating that this form is generated; there is residual 4,4BIPY as a result of the stoichiometry.

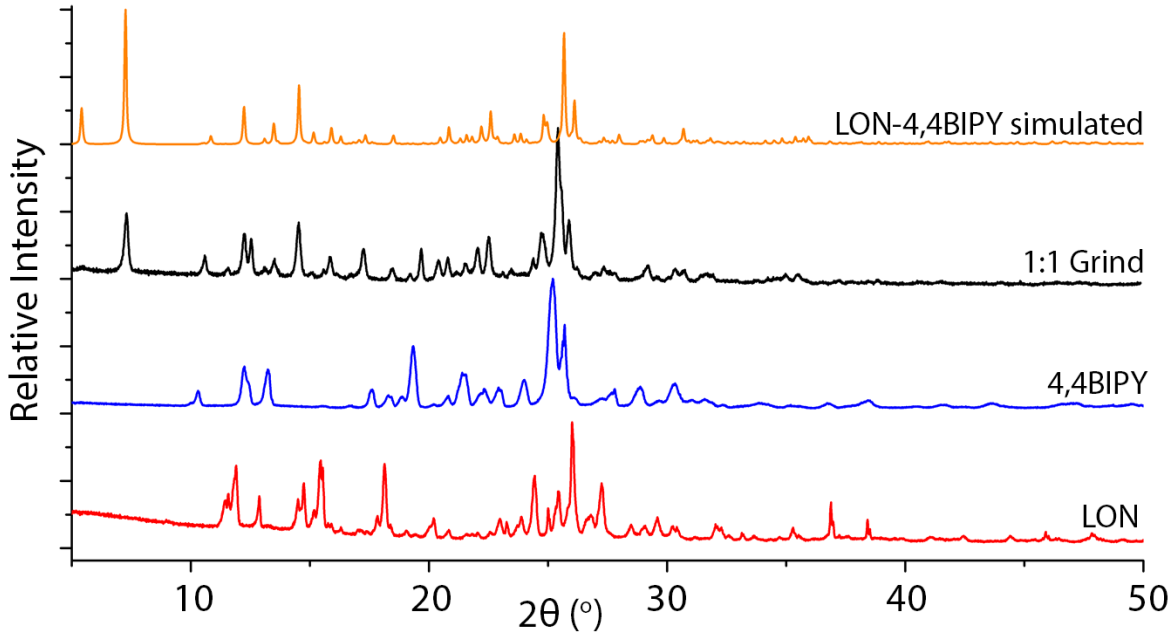

Figure C.20. PXRD for 1:1 solvent drop grind of LON with 4,4BIPY compared to the simulated pattern from the crystal structure obtained. Some peaks corresponding to 4,4'-bipyridine starting material can be seen in the powder from grinding, which is in accordance with the 2:1 stoichiometry identified from the crystal structure.

C.5.2 Promising Combinations of LON and Co-Former

Figures C.22 to C.28 show PXRD patterns of combinations of LON and co-former produced in grinding experiments which showed promise for a new material forming. No single crystals were produced to allow structure solution and confirmation of a new material. These are compared to the simulated patterns of the polymorphs of LON to indicate that the new peaks observed were not due to polymorphic conversion. Co-former structures are indicated in Figure C.21.

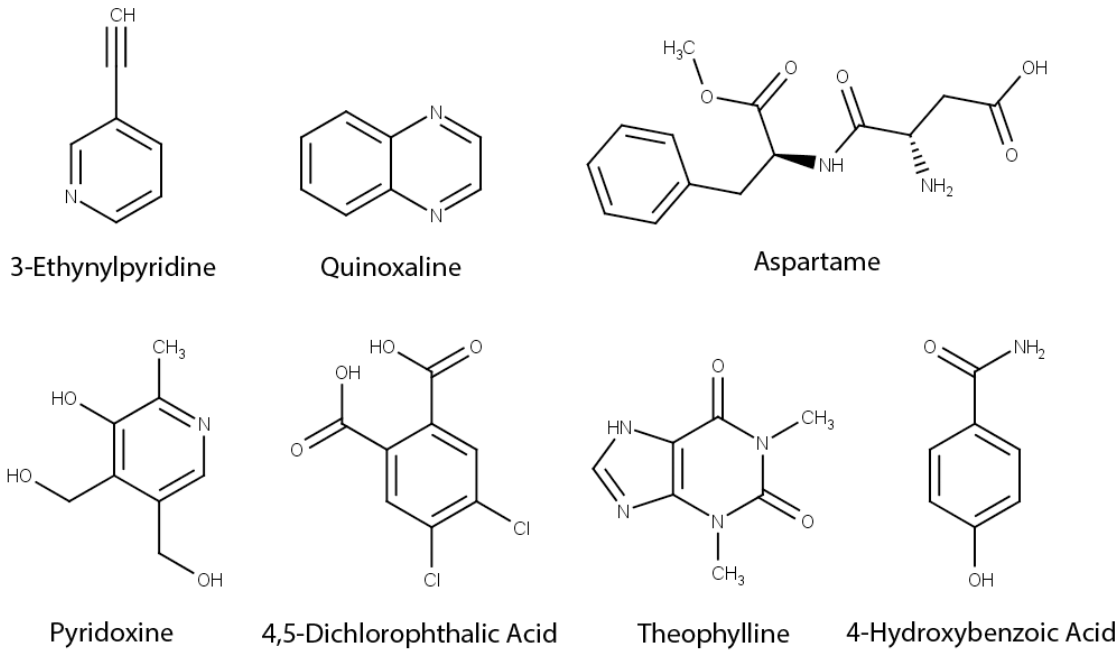

Figure C.21. Structure of co-formers which indicated potential from grinding experiments although no single crystals were produced for diffraction experiments.

C.5.2.1 3-Ethynylpyridine

The powder pattern (Figure C.22) from the material obtained when LON and 3-ethynylpyridine were combined in grinding shows a new peak at low angle not present in any of the parent reference materials. A number of other peaks also appear to be different indicating a potential new material.

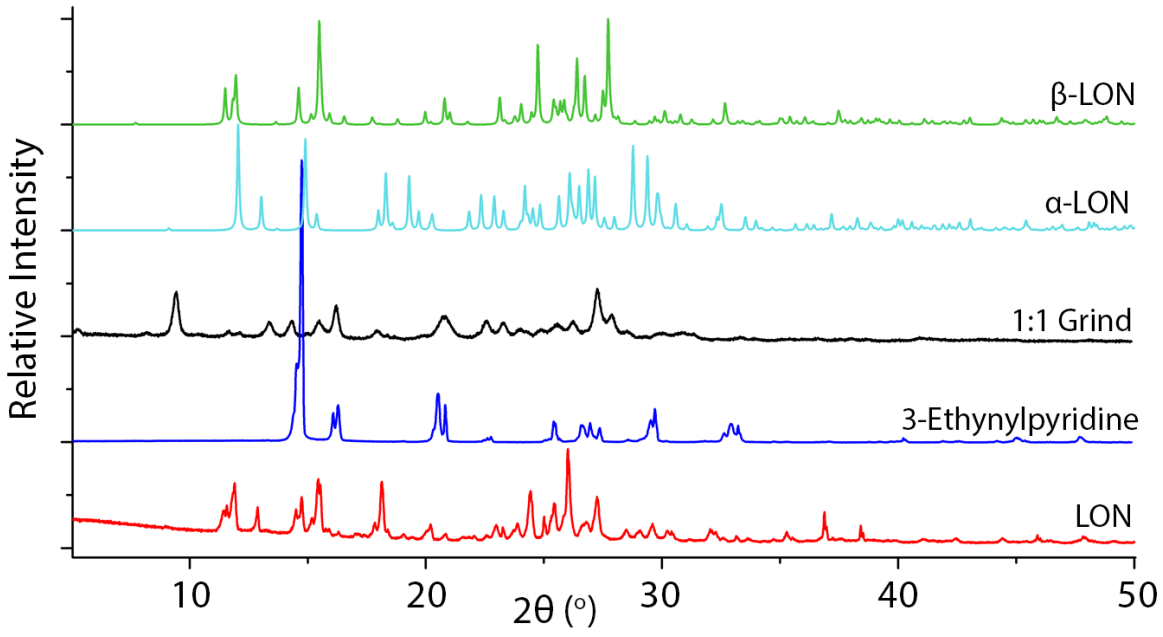

Figure C.22. PXRD for 1:1 solvent drop grind of LON with 3-ethynylpyridine.

C.5.2.2 4-Hydroxybenzamide

The 1:1 grind with LON and 4-hydroxybenzamide (Figure C.23) shows some similarities to some reference peaks, however there are many differences indicating a new form is likely.

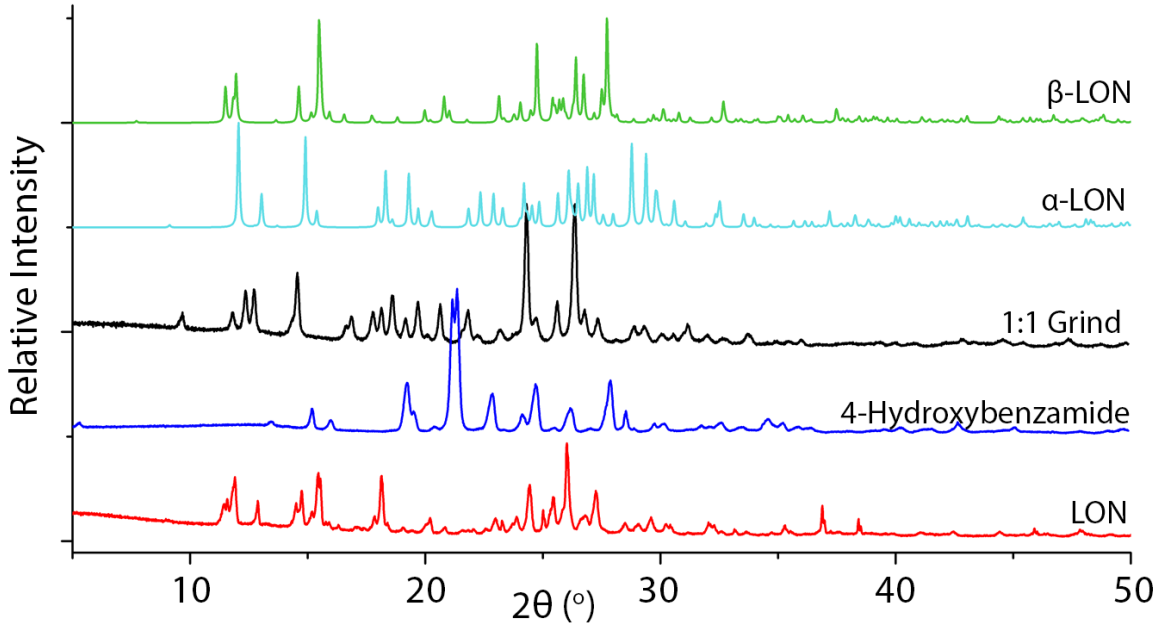

Figure C.23. PXRD for 1:1 solvent drop grind of LON with 4-hydroxybenzamide.

C.5.2.3 Aspartame

The 1:1 grind with aspartame shows new low angle peaks in the powder patterns (Figure C.24). Some aspartame peaks are also seen, indicating that either complete conversion may not have been realised, or the ratio of the new form is not 1:1 leaving residual aspartame in the grinding jar. Several solution crystallisation trials were also undertaken and are included in the figure. These, too, all indicate some residual aspartame, hence a 1:1 ratio may not be correct in this instance.

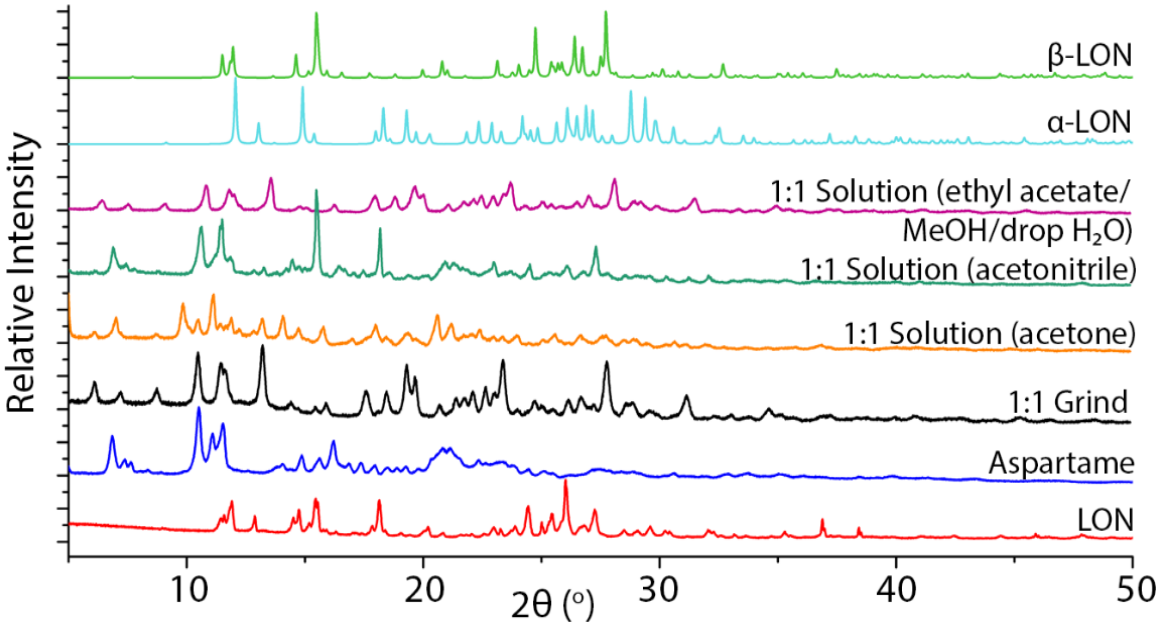

Figure C.24. PXRD for 1:1 solvent drop grind and solution attempts of LON with aspartame.

C.5.2.4 4,5-Dichlorophthalic acid

The 1:1 grinding materials obtained from the combination of LON and 4,5-dichlorophthalic acid produced a powder pattern with poor resolution and the peaks difficult to distinguish. There are, however, new low angle peaks observed (Figure C.25). Co-former reference peaks appear to be absent, indicating conversion to a different form, however there is some resemblance to LON. 4,5-dichlorophthalic acid contains two carboxylic acid groups, and therefore a 1:2 ratio may be favoured. This would account for the absence of co-former with residual LON.

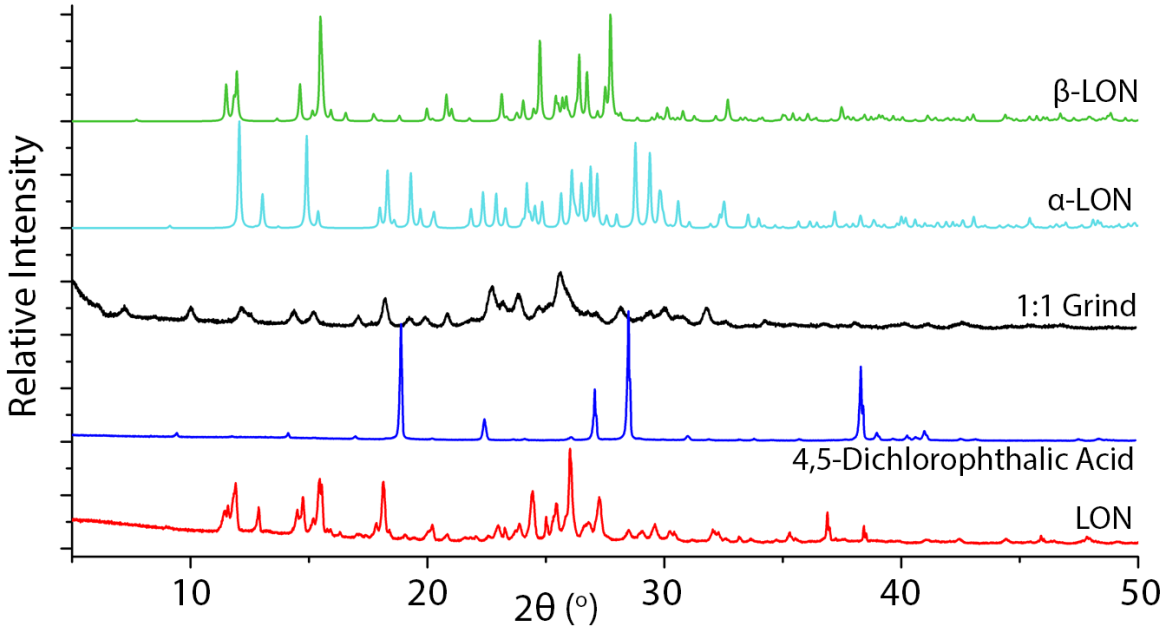

Figure C.25. PXRD for 1:1 solvent drop grind of LON with 4,5-dichlorophthalic acid.

C.5.2.5 Pyridoxine

Some clear differences are observed in the powder pattern of the 1:1 LON-pyridoxine grind in comparison to the reference patterns (Figure C.26). This indicates a new material is likely composed of these two compounds however no single crystal was obtain in solution trails to confirm this.

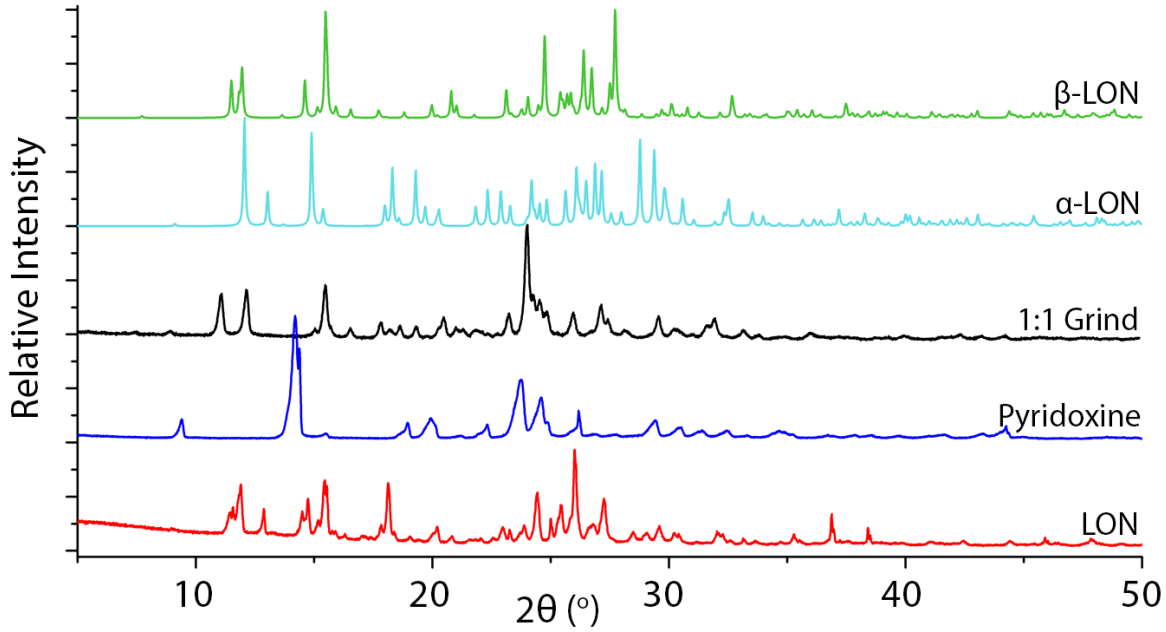

Figure C.26. PXRD for 1:1 solvent drop grind of LON with pyridoxine.

C.5.2.6 Quinoxaline

The 1:1 grind of LON with quinoxaline shows new low angle peaks in comparison to the reference materials (Figure C.27), and some differences in the peaks, although there are also similarities to the parent materials. This may be indicative of a new form which is not fully generated in the grinding or the 1:1 ratio is not the optimal stoichiometry. Further investigations would be required, and undertaken on the co-former as well to assess solvate and hydrate formation.

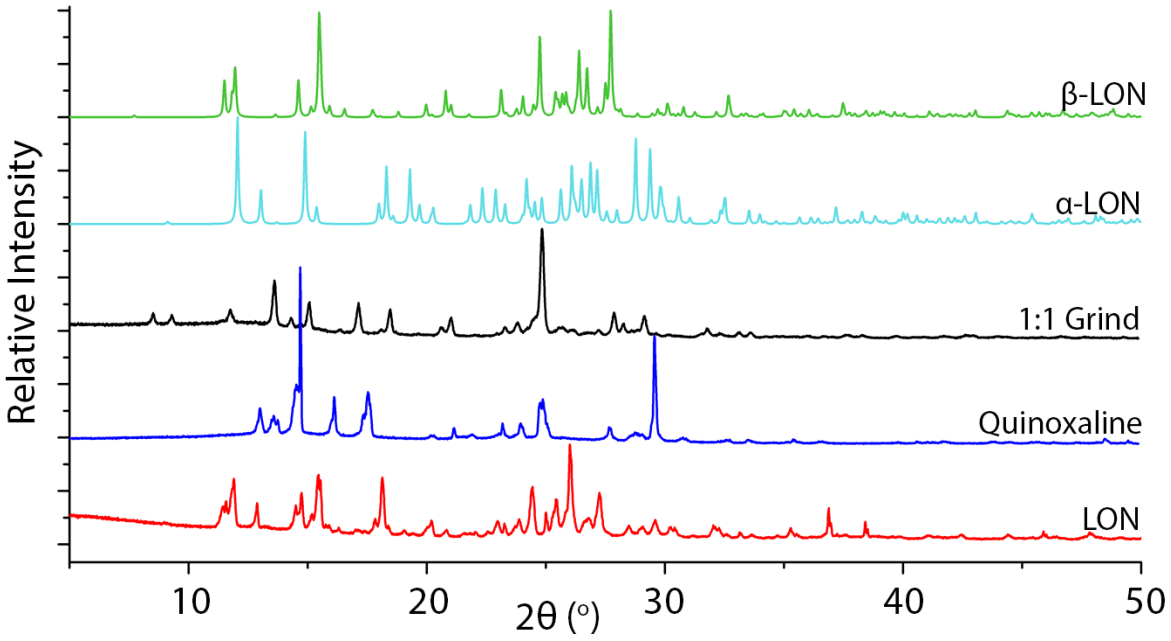

Figure C.27. PXRD for 1:1 solvent drop grind of LON with quinoxaline.

C.5.2.7 Theophylline

In addition to the grinding experiment, a number of solution crystallisation trials were also conducted for LON with theophylline. These all produced a powder solid rather than crystals suitable for structure solution. The experimental powder patterns from all of the trials show similarities (Figure C.28) and are clearly different to theophylline and the different forms of LON. This indicates that this is likely to be a new form, although single crystals were not readily produced to allow crystal structure determination to be performed.

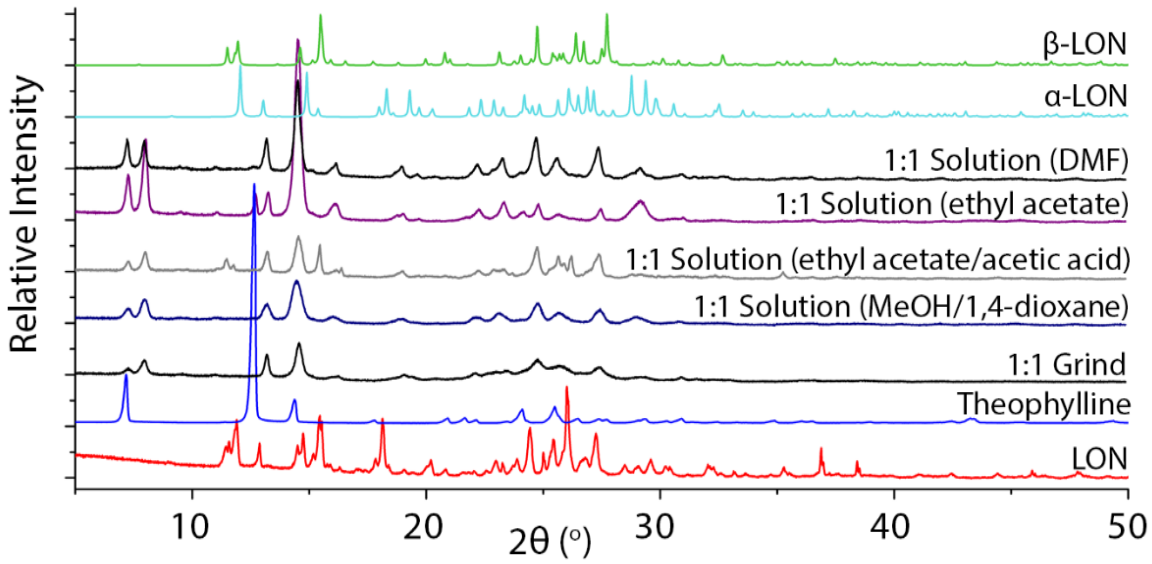

Figure C.28. PXRD for 1:1 solvent drop grind and solution attempts of LON with theophylline.

C.6 Crystal Structure Tables

Tables C.8 and C.9 display the statistics for the crystal structures of the new co-crystals, salts and hybrid materials of LON as well as for the α- and β-polymorphs. These are separated into those which contain pharmaceutically acceptable co-formers (Table C.8) and those which do not (Table C.9). All structures are published in the CSD: CCDC 1531947-1531963. CIFs are provided as supplementary electronic data to this thesis or can be obtained free of charge from www.ccdc.cam.ac.uk/data_request/cif, or by emailing data_request@ccdc.cam.ac.uk, or by contacting The Cambridge Crystallographic Data Centre, 12 Union Road, Cambridge CB2 1EZ, UK.

C.6.1 Pharmaceutically Acceptable Co-Formers

Table C.8. Crystal structure parameters for LON polymorphs and novel materials containing pharmaceutically acceptable co-formers BENZ, HALO and IMID.

	α-LON	**β-LON**	**LON-BENZ 1:1**	**LON-HALO·3H$_2$O 1:1 trihydrate**	**LON-IMID·0.5EtOAc 1:1:0.5 solvate**	**LON-IMID 2:1**	**LON-IMID 1:1**
Chemical Formula	$C_{15}H_{10}Cl_2N_2O_2$	$C_{15}H_{10}Cl_2N_2O_2$	$C_{15}H_{10}Cl_2N_2O_2 \cdot C_7H_7N_1O_1$	$C_{15}H_9Cl_2N_2O_2 \cdot C_{21}H_{24}ClFNO_2 \cdot 3(H_2O)$	$C_{15}H_9Cl_2N_2O_2 \cdot C_3H_5N_2 \cdot 0.5(C_4H_8O_2)$	$2(C_{15}H_{9.5}Cl_2N_2O_2) \cdot C_3H_5N_2$ [a]	$C_{15}H_{9.5}Cl_2N_2O_2 \cdot C_{15}H_9Cl_2N_2O_2 \cdot C_3H_5N_2 \cdot C_3H_{4.5}N_2$
Mr	321.15	321.15	442.28	751.05	433.28	710.38 [a]	778.46
Density /gcm^{-1}	1.586	1.539	1.454	1.410	1.426	1.415	1.475
Crystal size /mm	0.326 x 0.028 x 0.012	0.384 x 0.204 x 0.116	0.05 x 0.05 x 0.01	0.282 x 0.146 x 0.031	0.393 x 0.22 x 0.145	0.679 x 0.378 x 0.224	0.05 x 0.05 x 0.01
Crystal colour, morphology	Colourless, needle	Colourless, block	Colourless, plate	Colourless, plate	Colourless, block	Colourless, block	Colourless, chip

	α-LON	**β-LON**	**LON-BENZ 1:1**	**LON-HALO·3H$_2$O 1:1 trihydrate**	**LON-IMID·0.5EtOAc 1:1:0.5 solvate**	**LON-IMID 2:1**	**LON-IMID 1:1**
Crystal system	Monoclinic	Triclinic	Monoclinic	Monoclinic	Monoclinic	Triclinic	Triclinic
Space group	$P2_1/c$	$P\bar{1}$	$P2_1/c$	I_2/a	$P2_1/c$	$P\bar{1}$	$P\bar{1}$
a/Å	19.3743(10)	7.5759(3)	18.3534(8)	16.8612(5)	15.1394(5)	10.3787(7)	10.0605(5)
b/Å	4.7313(2)	8.0832(3)	10.1000(3)	10.8847(3)	29.9418(9)	11.8719(9)	11.0252(6)
c/Å	14.6770(7)	11.9077(4)	11.0376(4)	39.3807(11)	26.9456(6)	14.0409(8)	16.3298(10)
α/°	90.00	105.626(3)	90.00	90.00	90.00	105.139(6)	88.224(5)
β/°	91.886(4)	91.790(3)	99.146(4)	101.781(3)	97.628(2)	91.651(5)	76.212(5)
γ/°	90.00	98.360(3)	90.00	90.00	90.00	91.906(6)	84.969(4)
Cell volume / Å^3	1344.65(11)	692.88(5)	2020.02(13)	7075.3(3)	12106.4(6)	1667.8(2)	1752.21(17)
Z	4	2	4	8	24	2	2
Data Collection							
Diffractometer	Agilent Technologies, Dual Source Supernova	Agilent Technologies, Dual Source Supernova	Rigaku FRE+	Agilent Technologies, Dual Source Supernova	Agilent Technologies, Dual Source Supernova	Agilent Technologies, Dual Source Supernova	Rigaku FRE+
Temperature /K	100	100	100	100	100	100	100

	α-LON	β-LON	LON-BENZ 1:1	LON-HALO·3H$_2$O 1:1 trihydrate	LON-IMID·0.5EtOAc 1:1:0.5 solvate	LON-IMID 2:1	LON-IMID 1:1
Radiation Type	Mo K\α	Mo K\α	Mo K\α	Mo K\α	Mo K\α	Mo K\α	Mo K\α
Wavelength, λ, /Å	0.71073	0.71073	0.71075	0.71073	0.71073	0.71073	0.71075
No. measured reflections	9905	9562	33938	25559	86240	40327	21522
No. unique reflections	3074	3183	4631	8099	27727	12547	8029
R_{int}	0.0636	0.0208	0.0421	0.0288	0.0383	*	0.0464
Completeness /%	99.71	99.97	99.98	99.85	99.81	99.83	99.90
Refinement							
GoF, S	1.110	1.044	1.024	1.024	1.030	1.076	1.039
Final R_1 ($I > 2\sigma(I)$)	0. 0600	0.0281	0.0424	0.0478	0.0628	0.0717	0.0553
Final R_1 (all data)	0.0842	0.0306	0.0558	0.0634	0.0876	0.0830	0.0833
Final w$R\{F^2\}$ ($I > 2\sigma(I)$)	0.1318	0.0720	0.1068	0.1043	0.1575	0.2024	0.1378
Final w$R\{F^2\}$ (all data)	0.1439	0.0737	0.1143	0.1109	0.1737	0.2092	0.1521

Table C.8 continued. Crystal structure parameters for novel materials of LON containing pharmaceutically acceptable co-formers ISO, MEL, NICO and PIPE.

	LON-ISO 1:1	**LON-MEL 1:1**	**LON-NICO 1:1**	**LON-PIPE 2:1**
Chemical Formula	$C_{15}H_{10}Cl_2N_2O_2 \cdot C_6H_6N_2O_1$	$C_{15}H_9Cl_2N_2O_2 \cdot C3H_7N_6$	$C_{15}H_{10}Cl_2N_2O2 \cdot C_6H_6N_2O_1$	$2(C_{15}H_9Cl_2N_2O_2) \cdot C_4H_{12}N_2$
*M*r	443.28	447.29	443.28	728.44
Density /gcm^{-1}	1.502	1.584	1.534	1.445
Crystal size /mm	0.459 x 0.359 x 0.188	1.0 x 0.121 x 0.057	0.28 x 0.03 x 0.01	0.784 x 0.109 x 0.069
Crystal colour, morphology	Colourless, block	Colourless, needle	Colourless, plate	Colourless, block
Crystal system	Monoclinic	Triclinic	Monoclinic	Triclinic
Space group	$P2_1/n$	$P\bar{1}$	$P2_1/c$	$P\bar{1}$
a/Å	12.9910(3)	7.0752(4)	20.6918(6)	11.6186(5)
b/Å	7.6724(2)	8.1750(4)	4.61421(12)	12.3390(8)
c/Å	19.8344(5)	16.8057(10)	20.1099(5)	12.5559(7)
α/°	90.00	99.416(5)	90.00	68.926(6)
β/°	97.409(2)	100.168(5)	90.673(2)	85.447(4)
γ/°	90.00	94.778(5)	90.00	88.975(4)

	LON-ISO **1:1**	**LON-MEL** **1:1**	**LON-NICO** **1:1**	**LON-PIPE** **2:1**
Cell volume / Å^3	1960.43(9)	937.57(9)	1919.89(9)	1674.24(17)
Z	4	2	4	2
Data Collection				
Diffractometer	Agilent technologies, Dual Source Supernova	Agilent technologies, Dual Source Supernova	Rigaku FRE+	Agilent Technologies, Dual Source Supernova
Temperature /K	100	100	100	100
Radiation Type	Mo K\a	Mo K\a	Mo K\a	Mo K\a
Wavelength, λ, /Å	0.71073	0.71073	0.71075	0.71073
No. measured rflns	34896	13981	36705	36628
No. unique reflections	4486	4299	4368	13510
R_{int}	0.0456	0.0320	0.0495	*
Completeness /%	99.88	99.95	99.92	99.90
Refinement				
GoF, S	1.048	1.041	1.069	1.047
Final R_1 ($I > 2\sigma(I)$)	0.0393	0.0360	0.0532	0.0511

	LON-ISO 1:1	**LON-MEL 1:1**	**LON-NICO 1:1**	**LON-PIPE 2:1**
Final R_1 (all data)	0.0453	0.0406	0.0578	0.0622
Final w$R\{F^2\}$ ($I > 2\sigma(I)$)	0.0926	0.0892	0.1515	0.1540
Final w$R\{F^2\}$ (all data)	0.0967	0.0921	0.1569	0.1582

* Non-merohedral twin, all data are merged. [a] LON-IMID 2:1 contains voids which may contain solvent (MeOH / acetonitrile or water molecules)

C.6.2 Non-Pharmaceutically Acceptable Co-Formers

Table C.9. Crystal structure parameters for novel materials of LON containing non-pharmaceutically acceptable co-formers.

	LON-2APYD 1:1 ACN solvate	**LON-2APYD·EtOAc 1:1:1 solvate**	**LON-2AYPM 2:1**	**LON-246TAPYM 1:1**	**LON-4DMAP 2:1**	**LON-4DMAP·2H_2O 1:1 dihydrate**	**LON-4,4BIPY 2:1**
Chemical Formula	$C_{15}H_9Cl_2N_2O_2 \cdot C_5H_7N_2$	$C_{15}H_9Cl_2N_2O_2 \cdot C_5H_7N_2 \cdot C_4H_8O_2$	$C_{15}H_{10}Cl_2N_2O_2 \cdot 2(C_4H_5N_3)$	$C_{15}H_9Cl_2N_2O_2 \cdot C_4H_8N_5$	$C_{15}H_{10}Cl_2N_2O_2 \cdot C_{15}H_9Cl_2N_2O_2 \cdot C_7H_{11}N_2$	$C_{15}H_9Cl_2N_2O_2 \cdot C_7H_{11}N_2 \cdot 2(H_2O)$	$2(C_{15}H_{10}Cl_2N_2O_2) \cdot C_{10}H_8N_2$
*M*r	415.27(excluding solvent)	503.37	511.37	446.29	764.47	479.35	798.48
Density /gcm^{-1}	1.347	1.389	1.486	1.575	1.483	1.435	1.428
Crystal size /mm	0.772 x 0.092 x 0.016	1.0 x 0.156 x 0.129	0.282 x 0.147 x 0.066	0.261 x 0.201 x 0.138	0.27 x 0.089 x 0.053	0.898 x 0.122 x 0.11	0.04 x 0.03 x 0.01
Crystal colour, morphology	Colourless, plate	Colourless, block	Colourless, plate	Colourless, prism	Colourless, plate	Colourless, block	Colourless, plate
Crystal system	Monoclinic	Monoclinic	Monoclinic	Monoclinic	Triclinic	Monoclinic	Monoclinic
Space group	$P2_1/c$	Pc	$P2_1/c$	$P2_1/n$	$P\bar{1}$	$P2_1/c$	$P2_1/c$
a/Å	11.1266(5)	10.9724(3)	14.1417(6)	7.7720(12)	8.5711(2)	13.0507(6)	32.6725(11)
b/Å	22.3945(10)	13.1874(3)	21.6532(8)	31.5262(14)	12.3681(4)	9.03300(18)	26.2388(13)
c/Å	8.5821(5)	8.8415(3)	7.6525(3)	11.6214(18)	16.6270(5)	24.7738(11)	8.6827(3)
α/°	90.00	90.00	90.00	90.00	79.963(3)	90.00	90.00

	LON-2APYD 1:1 ACN solvate	**LON-2APYD·EtOAc 1:1:1 solvate**	**LON-2AYPM 2:1**	**LON-246TAPYM 1:1**	**LON-4DMAP 2:1**	**LON-4DMAP·2H$_2$O 1:1 dihydrate**	**LON-4,4BIPY 2:1**
β/°	106.718(6)	109.768(3)	102.654(4)	138.80(3)	81.329(2)	130.546(8)	93.879(3)
γ/°	90.00	90.00	90.00	90.00	84.947(3)	90.00	90.00
Cell volume / Å^3	2048.06(19)	1203.95	2286.39(16)	1875.4(8)	1712.33(9)	2219.3(2)	7426.6(5)
Z	4	2	4	4	2	4	8
Data Collection							
Diffractometer	Agilent technologies, Dual Source Supernova	Agilent technologies, Dual Source Supernova	Agilent technologies, Dual Source Supernova	Agilent technologies, Dual Source Supernova	Agilent technologies, Dual Source Supernova	Agilent technologies, Dual Source Supernova	Rigaku FRE+
Temperature /K	100	100	100	100	100	100	100
Radiation Type	Mo K\α	Mo K\α	Mo K\α	Mo K\α	Mo K\α	Mo K\α	Mo K\α
Wavelength /λ	0.71073	0.71073	0.71073	0.71073	0.71073	0.71073	0.71075
No. measured reflections	14679	9655	27846	29914	24011	19704	50025
No. unique reflections	4674	4992	5218	4304	7913	5078	17020
R_{int}	0.0330	0.0211	0.0705	0.0278	0.0363	0.0238	0.0669
Completeness /%	99.36	99.90	99.91	99.90	99.97	99.96	99.87

	LON-2APYD 1:1 ACN solvate	LON-2APYD·EtOAc 1:1:1 solvate	LON-2AYPM 2:1	LON-246TAPYM 1:1	LON-4DMAP 2:1	LON-4DMAP·2H_2O 1:1 dihydrate	LON-4,4BIPY 2:1
Refinement							
GOF, S	1.033	1.051	1.138	1.185	1.048	1.058	0.974
Final R_1 ($I > 2\sigma(I)$)	0.0499	0.0322	0.0582	0.0419	0.0466	0.0322	0.0758
Final R_1 (all data)	0.0692	0.0335	0.0815	0.0424	0.0611	0.0357	0.1561
Final w$R\{F^2\}$ ($I > 2\sigma(I)$)	0.1045	0.0820	0.1054	0.0965	0.0994	0.0822	0.1516
Final w$R\{F^2\}$ (all data)	0.1105	0.0830	0.1130	0.0967	0.1056	0.0846	0.1740

C.7 Hydrogen Bonding Interactions

The hydrogen bonding interactions for all new materials were determined using PLATON[267, 268] with neutron normalised bond lengths for X-H bonds. These are listed below in Tables C.10 and C.11 for the LON polymorphs and materials containing pharmaceutically acceptable co-formers, and those containing co-formers which are not acceptable, respectively.

C.7.1 Pharmaceutically Acceptable Co-Formers

Table C.10. Neutron normalised hydrogen bonding interactions present in LON polymorphs and novel materials containing pharmaceutically acceptable co-formers.

Sample	D–H···A	H···A /Å	D···A /Å	D–H···A /°	Symmetry code
α–LON	O(1)–H(1)···O(2)	1.67	2.648(3)	174	1–*x*, –*y*, 1–*z*
	C(5)–H(5)···O(2)	2.44	3.387(4)	146	1–*x*, ½+*y*, ½–*z*
β–LON	O(1)–H(1)···O(2)	1.64	2.6232(13)	175	2–*x*, 1–*y*, 2–*z*
	C(12)–H(12)···O(1)	2.46	3.5464(16)	178	1–*x*, 1–*y*, 1–*z*
	C(12)–H(12)···N(2)	2.56	3.1764(16)	115	1–*x*, 1–*y*, 1–*z*
LON–BENZ	O(1)–H(1)···O(21)	1.57	2.5480(17)	172	
	N(21)–H(21A)···O(2)	1.88	2.877(2)	169	
	N(21)–H(21B)···O(1)	2.51	3.113(2)	118	*x*, ½–*y*, ½+*z*
	N(21)–H(21B)···N(2)	2.19	3.107(2)	151	*x*, ½–*y*, ½+*z*
	C(6)–H(6)···O(2)	2.38	3.218(2)	133	1–*x*, ½+*y*, 3/2–*z*
	C(12)–H(12)···O(21)	2.37	3.382(2)	154	*x*, 1+*y*, *z*
	C(25)–H(25)···Cl(2)	2.70	3.728(2)	159	2–*x*, –3/2+*y*, 3/2–*z*

Sample	D–H···A	H···A /Å	D···A /Å	D–H···A /°	Symmetry code
LON–HALO·3H$_2$O	N(21)–H(21)···O(2)	1.72	2.724(2)	172	
	O(22)–H(22)···O(41)	1.78	2.727(3)	160	
	O(41)–H(41A)···O(2)	1.76	2.737(3)	175	½+*x*, 1–*y*, *z*
	O(41)–H(41B)···O(1)	1.76	2.727(3)	169	1–*x*, –½+*y*, ½–*z*
	O(42)–H(42A)···O(43)	1.91	2.831(10)	154	
	O(42)–H(42B)···O(21)	2.01	2.976(7)	166	1–*x*, –½+*y*, ½–*z*
	O(43)–H(43A)···O(42)	1.82	2.790(8)	169	3/2–*x*, 3/2–*y*, ½–*z*
	O(43)–H(43B)···O(1)	2.02	2.873(6)	143	1–*x*, –½+*y*, ½–*z*
	C(7)–H(7)···Cl(1)	2.70	3.709(2)	155	
	C(9)–H(9B)···Cl(1)	2.55	3.131(2)	113	
	C(30)–H(30A)···O(21)	2.52	3.144(2)	116	
	C(31)–H(31B)···O(1)	2.40	3.426(3)	157	1–*x*, –½+*y*, ½–*z*
LON–IMID·0.5EtOAc	N(21)_7–H(21)_7···O(2)_3	1.64	2.633(3)	167	
	N(22)_7–H(22)_7···O(1)_1	1.75	2.693(3)	153	
	N(22)_7–H(22)_7···N(2)_1	2.39	3.082(3)	125	
	N(21)_8–H(21)_8···O(1)_5	1.76	2.708(3)	155	–1+*x*, *y*, *z*
	N(21)_8–H(21)_8···N(2)_5	2.40	3.068(3)	123	–1+*x*, *y*, *z*
	N(22)_8–H(22)_8···O(2)_6	1.66	2.636(3)	162	
	N(21)_9–H(21)_9···O(2)_1	1.66	2.653(3)	166	
	N(22)_9–H(22)_9···O(1)_3	1.77	2.707(3)	153	–1+*x*, *y*, *z*
	N(22)_9–H(22)_9···N(2)_3	2.40	3.095(3)	126	–1+*x*, *y*, *z*
	N(21)_10–H(21)_10···O(2)_4	1.68	2.682(3)	171	
	N(22)_10–H(22)_10···O(1)_2	1.72	2.688(3)	159	

Sample	D–H···A	H···A /Å	D···A /Å	D–H···A /°	Symmetry code
LON–IMID·0.5EtOAc (cntd.)	N(22)_10–H(22)_10···N(2)_2	2.45	3.080(3)	120	
	N(21)_11–H(21)_11···O(1)_4	1.77	2.718(3)	155	1+*x*, *y*, *z*
	N(21)_11–H(21)_11···N(2)_4	2.38	3.055(3)	124	1+*x*, *y*, *z*
	N(22)_11–H(22)_11···O(2)_2	1.65	2.639(3)	166	
	N(21)_12–H(21)_12···O(1)_6	1.71	2.674(3)	158	
	N(21)_12–H(21)_12···N(2)_6	2.47	3.098(3)	120	
	N(22)_12–H(22)_12···O(2)_5	1.66	2.657(3)	170	
	C(6)_1–H(6)_1···O(1)_5	2.37	3.442(3)	169	*x*, ½ –*y*, –½+*z*
	C(14)_1–H(14)_1···O(31)_14	2.47	3.494(4)	157	1+*x*, ½ –*y*, –½+*z*
	C(6)_2–H(6)_2···O(1)_1	2.33	3.408(3)	174	1–*x*, 1–*y*, 1–*z*
	C(12)_2–H(12)_2···Cl(1)_4	2.69	3.597(3)	141	*x*, ½+*y*, 3/2–*z*
	C(15)_2–H(15)_2···N(2)_2	2.52	3.221(3)	121	
	C(6)_3–H(6)_3···O(1)_4	2.40	3.455(3)	165	1–*x*, 1–*y*, 1–*z*
	C(9)_4–H(9A)_4···Cl(1)_4	2.54	3.051(3)	108	
	C(15)_4–H(15)_4···N(2)_4	2.43	3.166(4)	124	
	C(9)_5–H(9B)_5···Cl(1)_5	2.53	3.069(3)	110	
	C(15)_5–H(15)_5···N(2)_5	2.50	3.223(4)	123	
	C(6)_6–H(6)_6···O(1)_3	2.32	3.392(3)	171	–1+*x*, ½–*y*, ½+*z*
	C(21)_7–H(21A)_7···O(1)_2	2.11	3.185(3)	172	
	C(21)_8–H(21A)_8···O(1)_5	2.11	3.188(3)	175	–*x*, 1–*y*, 2–*z*
	C(22)_9–H(22A)_9···O(1)_4	2.10	3.172(3)	171	
	C(22)_9–H(22A)_9···O(2)_4	2.52	3.213(3)	120	
	C(21)_10–H(21A)_10···O(1)_1	2.10	3.182(3)	176	
	C(21)_10–H(21A)···O(2)_1	2.48	3.228(3)	125	

Sample	D–H···A	H···A /Å	D···A /Å	D–H···A /°	Symmetry code
LON–IMID·0.5EtOAc (cntd.)	C(23)_10–H(23)_10···O(31A)_15	2.38	3.018(5)	116	
	C(21)_11–H(21A)_11···O(1)_3	2.11	3.190(3)	177	
	C(21)_11–H(21A)_11···O(2)_3	2.48	3.221(3)	125	
	C(21)_12–H(21A)_11···O(1)_6	2.12	3.199(3)	176	–*x*, 1–*y*, 2–*z*
LON–IMID 2:1	O(1)–H(1)···O(1)	1.52	2.502(4)	173	1–*x*, 1–*y*, 1–*z*
	O(21)–H(21)···O(21)	1.53	2.491(4)	164	1–*x*, 1–*y*, 2–*z*
	N(41)–H(41)···(O2)	1.72	2.685(5)	159	
	N(42)–H(42)···(O22)	1.76	2.757(5)	169	
	C(9)–H(9A)···Cl(1)	2.68	3.078(4)	101	
	C(29)–H(29B)···O(1)	2.47	3.391(5)	142	*x*, *y*, 1+*z*
	C(41)–H(41A)···N(21)	2.42	3.289(7)	136	1–*x*, 1–*y*, 2–*z*
LON–IMID 1:1	O(1)–H(1)···O(1)	1.56	2.540(3)	177	2–*x*, –*y*, 2–*z*
	N(41)–H(41)···O(21)	1.80	2.764(3)	160	1–*x*, 1–*y*, 1–*z*
	N(41)–H(41)···N(22)	2.46	3.119(3)	122	1–*x*, 1–*y*, 1–*z*
	N(42)–H(42)···N(42)	1.62	2.627(3)	178	1–*x*, –*y*, –*z*
	N(45)–H(45)···O(21)	1.57	2.563(17)	166	1–*x*, 1–*y*, 1–*z*
	N(46)–H(46)···O(1)	1.67	2.673(6)	170	1–*x*, 1–*y*, 1–*z*
	C(9)–H(9A)···Cl(1)	2.66	3.067(2)	101	
	C(9)–H(9A)···O(22)	2.46	3.499(3)	160	

Sample	D–H···A	H···A /Å	D···A /Å	D–H···A /°	Symmetry code
LON–IMID 1:1 (cntd.)	C(41)–H(41A)···O(22)	2.28	3.158(3)	137	*x*, *y*, –1+*z*
	C(45)–H(45A)···O(22)	2.36	2.992(7)	116	1–, 1–*y*, 1–*z*
	C(45)–H(45A)···N(2)	2.42	3.084(6)	118	1–*x*, 1–*y*, 1–*z*
	C(46)–H(46A)···O(2)	2.28	3.015(9)	124	–1+*x*, 1+*y*, –1+*z*
LON–ISO	O(2)–H(2)···N(22)	1.66	2.6366(19)	176	3/2–*x*, ½+*y*, ½–*z*
	N(21)–H(21A)···O(21)	2.30	3.241(2)	156	3/2–*x*, ½+*y*, 3/2–*z*
	N(21)–H(21B)···O(1)	1.96	2.971(2)	175	½+*x*, 3/2–*y*, ½+*z*
	C(9)–H(9A)···Cl(1)	2.66	3.1010(17)	104	
	C(9)–H(9B)···O(21)	2.22	3.287(2)	169	1–*x*, 1–*y*, 1–*z*
	C(23)–H(23)···O(1)	2.22	3.196(2)	149	½+*x*, 3/2–*y*, ½+*z*
	C(25)–H(25)···Cl(2)	2.73	3.5535(17)	132	*x*, –1+*y*, *z*
	C(26)–H(26)···O(21)	2.34	3.350(2)	155	3/2–*x*, –½+*y*, 3/2–*z*
LON–MEL	N(21)–H(21)···O(1)	1.70	2.6538(18)	157	
	N(24)–H(24A)···N(2)	2.01	3.0093(19)	171	
	N(24)–H(24B)···O(1)	2.44	3.3959(19)	157	–1+*x*, *y*, *z*
	N(25)–H(25A)···N(23)	1.91	2.9177(19)	175	2–*x*, 2–*y*, 1–*z*
	N(25)–H(25B)···O(2)	2.06	2.7888(18)	127	–1+*x*, 1+*y*, *z*
	N(26)–H(26A)···O(1)	2.18	3.0084(19)	138	
	N(26)–H(26B)···O(2)	1.99	2.9891(18)	173	3–*x*, 1–*y*, 1–*z*
	C(9)–H(9A)···Cl(1)	2.64	3.0610(16)	103	

Sample	D–H···A	H···A /Å	D···A /Å	D–H···A /°	Symmetry code
LON–NICO	O(2)–H(2)···O(21)	1.56	2.531(3)	169	
	N(21)–H(21A)···O(1)	2.23	2.852(3)	119	1–*x*, 1–*y*, 1–*z*
	N(21)–H(21B)···O(1)	1.97	2.960(4)	168	
	C(4)–H(4)···O(2)	2.48	3.000(4)	108	
	C(7)–H(7)···Cl(1)	2.67	3.679(3)	155	
	C(9)–H(9A)···Cl(1)	2.50	3.091(3)	113	
	C(9)–H(9B)···N(22)	2.43	3.463(4)	158	1–*x*, 1–*y*, 1–*z*
	C(15)–H(15)···N(22)	2.46	3.445(4)	151	1–*x*, 2–*y*, 1–*z*
	C(26)–H(26)···O(21)	2.47	3.239(4)	127	1–*x*, ½+*y*, ½–*z*
LON–PIPE	N(51)–H(51A)···O(22)	1.71	2.691(3)	164	
	N(51)–H(51B)···O(1)	1.68	2.644(3)	159	
	N(51)–H(51B)···N(2)	2.52	3.112(3)	117	
	N(61)–H(61A)···O(21)	1.69	2.688(3)	172	
	N(61)–H(61B)···O(1)	2.34	3.000(3)	122	–1+*x*, *y*, *z*
	N(61)–H(61B)···O(2)	1.77	2.754(3)	163	–1+*x*, *y*, *z*
	C(9)–H(9A)···Cl(1)	2.59	3.063(3)	106	
	C(14)–H(14)···Cl(21)	2.65	3.655(4)	154	1+*x*, *y*, *z*
	C(27)–H(27)···Cl(21)	2.65	3.665(2)	155	
	C(29)–H(29B)···Cl(21)	2.54	3.132(3)	113	
	C(52)–H(52A)···O(21)	2.32	3.360(3)	160	1–*x*, 2–*y*, 2–*z*
	C(62)–H(62B)···O(1)	2.38	3.033(3)	117	1+*x*, *y*, *z*

C.7.1 Non-Pharmaceutically Acceptable Co-Formers

Table C.11. Neutron normalised hydrogen bonding interactions present in novel materials of LON containing non-pharmaceutically acceptable co-formers. D = Donor atom, A = Acceptor atom.

Sample	D–H···A	H···A /Å	D···A /Å	D–H···A /°	Symmetry code
LON–2APYD, ACN solvate	N(21)–H(21A)···O(1)	1.84	2.838(2)	171	
	N(21)–H(21B)···O(1)	1.80	2.795(3)	168	*x*, ½–*y*, ½+*z*
	N(22)–H(22)···O(2)	1.65	2.648(2)	168	*x*, ½–*y*, ½+*z*
	C(9)–H(9A)···O(1)	2.37	3.329(3)	146	*x*, ½–*y*, ½+*z*
	C(9)–H(9A)···N(2)	2.54	3.492(3)	146	*x*, ½–*y*, ½+*z*
LON–2APYD·EtOAc	N(21)–H(21A)···O(1)	1.85	2.856(3)	177	*x*, 2–*y*, ½+*z*
	N(21)–H(21B)···O(1)	1.78	2.779(3)	168	*x*, *y*, 1+*z*
	N(22)–H(22)···O(2)	1.66	2.665(3)	170	*x*, *y*, 1+*z*
	C(9)–H(9B)···O(1)	2.49	3.451(4)	147	*x*, 2–*y*, ½+*z*
	C(23)–H(23)···Cl(2)	2.71	3.643(3)	144	–1+*x*, 2–*y*, –½+*z*
	C(25)–H(25)···O(31)	2.40	3.171(4)	127	–1+*x*, *y*, *z*
LON–2APYM	O(2)–H(2)···N(22)	1.66	2.634(3)	169	
	N(23)–H(23A)···N(2)	2.06	3.059(3)	169	1–*x*, 1–*y*, 1–*z*
	N(23)–H(23B)···O(1)	1.89	2.889(3)	169	
	N(33)–H(33A)···N(32)	1.97	2.977(3)	178	*x*, ½–*y*, ½+*z*
	N(33)–H(33B)···N(31)	2.12	3.123(3)	172	*x*, ½–*y*, –½+*z*

Sample	D–H···A	H···A /Å	D···A /Å	D–H···A /°	Symmetry code
LON–246TAPM	N(22)–H(22)···O(2)	1.69	2.663(2)	159	1+*x*, *y*, *z*
	N(23)–H(23A)··· N(21)	1.94	2.943(2)	174	1–*x*, 1–*y*, 1–*z*
	N(23)–H(23B)··· O(2)	2.35	2.997(2)	121	*x*, *y*, 1+*z*
	N(24)–H(24A)···O(1)	2.18	2.987(2)	136	1+*x*, *y*, *z*
	N(24)–H(24B)···O(2)	1.94	2.932(2)	166	–1+*x*, *y*, –1+*z*
	N(25)–H(25A)···N(2)	2.00	2.986(2)	166	1–*x*, 1–*y*, –*z*
	N(25)–H(25B)···O(2)	2.00	2.927(2)	152	1+*x*, *y*, 1+*z*
	C(9)–H(9B)···Cl(1)	2.57	3.1450(19)	112	
LON–4DMAP 2:1	O(1)–H(1)···O(21)	1.50	2.477(2)	173	
	O(1)–H(1)···O(22)	2.60	3.145(2)	115	
	N(41)–H(41)···O(22)	1.72	2.675(4)	157	
	N(41A)–H(41B)···O(2)	2.00	2.830(4)	138	2–*x*, –*y*, 2–*z*
	N(41A)–H(41B)···O(21)	2.43	3.135(4)	126	2–*x*, –*y*, 2–*z*
	C(24)–H(24)···O(22)	2.54	3.076(3)	110	
	C(30)–H(30B)···O(22)	2.44	3.459(2)	157	–1+*x*, *y*, *z*
	C(41)–(H41A)···N(2)	2.23	3.283(15)	163	
	C(41A)–H(41C)···N(22)	2.35	3.430(16)	173	2–*x*, –*y*, 2–*z*
	C(45A)–H(45A)···O(2)	2.55	3.058(17)	108	2–*x*, –*y*, 2–*z*
	C(46)–H(46A)···O(22)	2.15	3.166(11)	155	4–*x*, 1–*y*, 1–*z*
	C(46A)–H(46F)···O(2)	2.17	3.196(16)	157	
	C(47)–H(47C)···O(1)	2.34	3.145(14)	130	4–*x*, 1–*y*, 1–*z*
	C(47A)–H(47F)···O(21)	2.30	3.294(17)	152	

Sample	D–H···A	H···A /Å	D···A /Å	D–H···A /°	Symmetry code
LON–4DMAP·2H$_2$O	N(21)–H(21)···O(1)	1.67	2.6279(16)	156	
	O(21)–H(21B)···O(1)	1.76	2.7383(14)	173	
	O(21)–H(21C)···O(22)	1.76	2.7406(18)	176	½–*x*, ½+*y*, ½–*z*
	O(22)–H(22A)···O(2)	1.76	2.7210(16)	164	
	O(22)–H(22B)···O(21)	1.89	2.8102(18)	155	
	C(4)–H(4)···O(2)	2.53	3.0646(17)	109	
	C(9)–H(9A)–O(21)	2.44	3.4738(17)	160	1–*x*, 1–*y*, 1–*z*
	C(11)–H(11)···O(21)	2.41	3.3927(14)	150	1–*x*, 1–*y*, 1–*z*
LON–4,4BIPY	O(1)–H(1)···N(81)	1.61	2.565(4)	164	
	O(21)–H(21)···N(82)	1.61	2.575(4)	167	
	O(41)–H(41)···N(91)	1.56	2.543(4)	176	
	O(61)–H(61)···N(92)	1.62	2.593(4)	169	
	C(9)–H(9B)···O(1)	2.35	3.398(8)	162	*x*, ½–*y*, –½+*z*
	C(27)–H(27)···Cl(21)	2.58	3.569(4)	151	*x*, ½–*y*, ½+*z*
	C(29)–H(29B)···Cl(21)	2.62	3.076(5)	105	
	C(29)–H(29B)···O(21)	2.39	3.436(5)	163	*x*, ½–*y*, ½+*z*
	C(49)–H(49A)···Cl(41)	2.66	3.071(4)	102	
	C(49)–H(49A)···O(61)	2.34	3.405(5)	167	2–*x*, 1–*y*, –*z*
	C(69)–H(69A)···O(41)	2.43	3.475(8)	161	2–*x*, 1–*y*, –1–*z*
	C(69)–H(69A)···N(42)	2.56	3.396(8)	133	2–*x*, 1–*y*, –1–*z*
	C(91)–H(91)···O(61)	2.53	3.220(4)	121	2–*x*, 1–*y*, –1–*z*

C.8 CSD and Structural Analysis

Related supplementary documents:

- NICO CSD searches (.doc)
- NICO search interaction analysis (pdf)
- Associated NICO search files
- 2APYM and Carboxylic acid (.doc)
- Associated 2APYM search results as CIFs
- PIPE CSD Search (.doc)
- PIPE analysis (.pdf)
- Associated PIPE search file
- Carboxylate and pyridine searches (.doc)
- Associated search files
- LON Interactions Search and Analysis (.doc)
- Associated LON search files

C.8.1 NICO Interactions

Table C.12 summarises the results from the CSD search carried out for structures containing NICO with no metals and ≥ 2 molecules. More details on the search parameters are provided in the supplementary documents.

A dimer interaction pattern is seen in the majority of the structures, most commonly of the type amide···amide or acid···amide. The amide···amide dimers are predominantly homo-dimers between two NICO molecules. The occurrence of this synthon is dependent on the ratio of NICO present, and the functional groups on the other molecule(s). Fewer than 30 % of structures contain a different interaction pattern occurring from the amide group which are presented in more detail in Table C.13.

Table C.12. Summary of the CSD search results for NICO separated into the two functional groups present. Note, no co-ordinates were present for 8 structures which are not included in this analysis.

Amide interaction		**Pyridine interaction**	
Amide···acid dimer	34 (4 related C(OH)C=O)	O–$H_{(acid)}$···N	69[a] (including 1 with N–H···H–O)
Amide···amide dimer	50 (3 not nico–nico, 2 = cyclic amides)	O–$H_{(hydroxyl)}$···N	28[b]
Amide···OH dimer	3 (2 C(OH)COH; 1 $B(OH)_2$)	O–$H_{(water)}$···N	4
Individual interactions from amide[*]	32	N–$H_{(NH2)}$ ···N	11 (10 amide; 1 S–NH_2)
		N–$H_{(2ry\ amide)}$···N	3
		N–$H_{(cyclic)}$···N	2 (1 +ve)
		C–$H_{(CH2)}$···N	2 (1 cyclic)
		Ar_C–H···N	1 (2 x bifurcated)
		No contact	3

[a] 3 structures present both O-$H_{(acid)}$···N and N-H···N interactions; [b] 1 structure presents both an O-$H_{(hydroxyl)}$···N and N-H···N interaction; [*]broken down in Table C.13.

The interactions of the amide group which do not generate dimers are classified further in Table C.13. The number of structures which present an interaction are indicated, not individual interactions therefore some crystal structures may occur in several different categories, whilst others appear in only one.

Table C.13. Summary of the non-dimer interactions of the NICO amide group, separated into the two functionalities of the amide.

Amide Interactions (number of structures)			
N–H interaction		**C=O interaction**	
N–H···$OH_{(hydroxyl)}$	13	C=O···H–$N_{(amide)}$	17
N–H···$OH_{2(water)}$	2	C=O···H–$N_{(NH2–SO2)}$	2
N–H···$O_{(ether)}$	3	C=O···H–$O_{(hydroxyl)}$	9
N–H···O=$C_{(amide)}$	18	C=O···H–$O_{(water)}$	3
N–H···O=$C_{(acid)}$	5	C=O···Cl	1
N–H···O=$C_{(cyclic)}$	1		
N–H···O=$S_{(SO2)}$	4		
N–H···$N_{(ar)}$	2		

C.8.2 2APYM Co-Crystals

A CSD search was conducted using the two models shown at the top of Tables C.14 and C.15 to retrieve crystal structures which contained 2APYM and a carboxylic acid. Visual inspection in Mercury identified a number of features of each structure such as their nature (co-crystal / salt etc) and stoichiometry. The results of the analyses are presented in the tables below.

Table C.14. CSD search results for crystal structures containing 2APYM and a carboxylic acid, specified as C=O and C–OH.

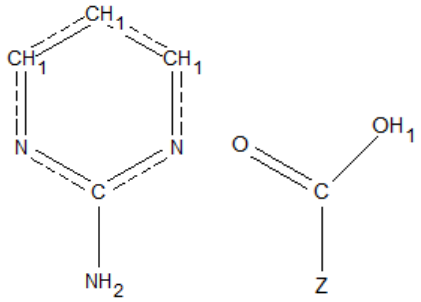

Exclude metals

	No. of structures	Repeat structures/polymorphs	Total discrete structures
1:1 co-crystal	21	2 / 2	19
1:1 dicarboxylic acid co-crystal	12	2 / 2	9
1:1 multi acid.H_2O	1		1
1:1 salt.H_2O (not CO_2H donor)	1		1
1:1 dicarboxylic acid salt co-crystal	3		3
1:1 dicarboxylic acid salt co-crystal·H_2O	1		1
1:2 co-crystal	4		4
1:2 salt co-crystal	3		3
2:1 co-crystal	1		1
2:1 dicarboxylic acid	1		1
2:1 multi acid solvate (large clathrate structure)	1		1
2:3 salt co-crystal	1		1
No co-ordinates	3		3
Containing any metal	2		2

The carboxylic acid model containing a double bond and proton specified on the hydroxyl O produced mainly co-crystals and co-crystal salt hybrid structures. These were predominantly in a 1:1 ratio although 1:2 and 2:1 structures were seen.

Table C.15. CSD search results for crystal structures containing 2APYM and a carboxylic acid, with no specificity about C-O bond types or hydrogen atom present.

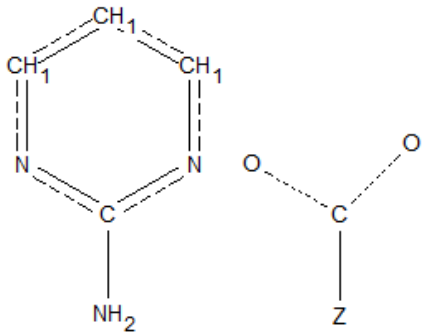

Exclude metals

	No. of structures	Repeat structures/polymorphs	Total discrete structures
1:1 co-crystal	21	2 / 2	19
1:1 dicarboxylic acid co-crystal	12	2 / 2	9
1:1 multi acid·H_2O co-crystal	1		1
1:1 salt	8		8
1:1 salt 0.5H_2O	1		1
1:1 salt·H_2O (not CO_2H donor)	1		1
1:1 dicarboxylic acid salt co-crystal	3		3
1:1 dicarboxylic acid salt co-crystal.H_2O	1		1
1:2 co-crystal	4		4
1:2 salt co-crystal	3		3
2:1 co-crystal	1		1
2:1 dicarboxylic acid	1		1
2:1 multi acid solvate (large clathrate structure)	1		1
2:3 salt co-crystal	1		1
No co-ordinates	3		3
Containing any metal	54		54

The carboxylic acid model with an unspecified bond type for C–O and no hydrogen present on the oxygen produced a further 10 structures. These were predominantly 1:1 salts. One was identified as a hemihydrate and one contained a 2APYM derivative. This was not included in the analysis. There were many more metal-containing structures filtered from this search as, without the specificity of the O proton, more charged carboxylate species were found which are more likely to co-ordinate to a metal species than when in the neutral acid form.

Only one structure contained a 2:1 ratio similar to the LON-2APYM material in this study. This was analysed in detail and comparisons made as detailed in Chapter 6.4.3.

C.8.3 PIPE Interactions

The models shown at the top of Tables C.16 were used in a CSD to find crystal structures which contained PIPE. These were visually assessed in Mercury for their degree of protonation at the N sites. Additional models were tested (detailed in the supplementary document), specifying the number of protons at each N and charges in varying combinations. These searches were not conclusive and a visual inspection of the initial hit list was deemed more thorough.

The results show that PIPE molecules contained within multi-component systems tend to undergo a degree of proton transfer. Just 15.7 % of the structures retrieved retained the neutral charge and no protonation at either nitrogen atom. Six structures contained more than one individual PIPE entity in the structure and all indicated one neutral PIPE molecule with the second either mono- or di-protonated.

Table C.16. Summary of the CSD search for PIPE; ≥ 2 molecules present, no metals.

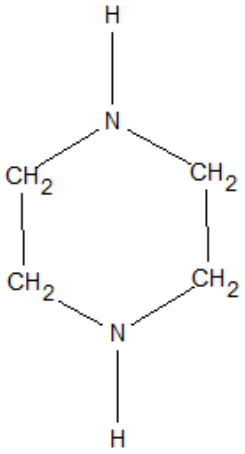

Exclude metals

Initial hits: 470	**No. of structures**
1 PIPE molecule	
NH / NH, neutral	41
N^+H_2/NH, 1+	18
N^+H_2/ N^+H_2, 2+	196
2 PIPE molecules	
N^+H_2/ N^+H_2 & NH / NH, 2+/0	2
N^+H_2/ N^+H_2 & N^+H / NH, 1+/0	4
Not pure PIPE	209

C.8.4 Carboxylate···Pyridine Interactions

See Supplementary Document

C.9 Novel LON Structure and Interactions

The crystal structures of the novel materials of LON were inspected for their interactions. These are presented below, separated into the two functional groups.

C.9.1 Interactions of the Indazole

Table C.17. Interactions of LON $N_{indazole}$ indicating the number of structures which display the interaction and details of the structures.

	No. of structures	Exclude α / β-LON	Structures
NH_2	4	4	LON-2APYD·EtOAc LON-2APYM LON-246TAPYM LON-MEL
Amide NH_2	1	1	LON-BENZ
Ar-CH	5	4	LON-NICO 2:1 LON-4DMAP LON-4DMAP·$2H_2O$ 2:1 LON-IMID (β-LON)
Cyclic NH	3	3	LON-IMID·0.5EtOAc 1:1 LON-IMID LON-PIPE (NH_2^+)
Cyclic CH	1	1	1:1 LON-IMID
CH_2	2	2	LON-2APYD$_{(ACN\ solvate)}$ LON-4,4BIPY
CH_3	1	1	2:1 LON-4DMAP
None	3	1	LON-ISO LON-HALO·$3H_2O$ (α-LON)
NH interactions	9	9	
CH interactions	9	8	

C.9.2 Interactions of the Carboxylic Acid

Table C.18. Interactions of LON carboxylic acid indicating the number of structures which display the interaction and details of the structures.

Functionality	LON CO_2H component	No of structures	Structures (no. interactions)
Ar_N	O–H	3	LON-4,4BIPY
			LON-ISO
			LON-2APYM
Ar_N^+H	O	5	LON-246TAPYM
			LON-MEL
			LON-2APYD$_{(ACN\ solvate)}$
			LON-2APYD·EtOAc
			LON-4DMAP·$2H_2O$
N^+-H	O	1	LON-HALO
	O–H	1	1:1 LON-IMID
N^+H_2	O	1	LON-PIPE (x3)
Cyclic_NH	O^-	2	LON-IMID·0.5EtOAc (multiple)
			1:1 LON-IMID (bifurcated)
	C=O	1	2:1 LON-IMID
Cyclic N^+-H	CO_2^-	1	LON-IMID·0.5EtOAc (multiple bifurcated)
NH_2	C=O	4	LON-ISO
			LON-2APYD$_{(ACN\ solvate)}$
			LON-2APYD·EtOAc
			LON-2APYM
	O	2	LON-MEL (x4)
			246TAPYM (x4)

Functionality	LON CO_2H component	No of structures	Structures (no. interactions)
CH_2	C=O	3	1:1 LON-IMID
			2:1 LON-IMID
			2:1 LON-4DMAP
	O	1	LON-PIPE
Cyclic_CH_2	O	2	LON-HALO
			LON-PIPE
Cyclic_CH	O	1	1:1 LON-IMID
	O–H	1	2:1 LON-IMID (x2)
	CO_2^-	1	LON-IMID·0.5EtOAc (multiple, bifurcated)
Ar_CH	C=O	1	LON-4,4BIPY
			LON-ISO
O-H-O / OH-H-O dimer		3	2:1 LON-4DMAP
			1:1 LON-IMID
			2:1 LON-IMID
H_2O	C=O	1	LON-4DMAP·H_2O
	O^-	2	LON-HALO (x3)
			LON-4DMAP·H_2O (x2)
Acid dimer		2	α-LON
			β-LON
Amide dimer		2	LON-BENZ
			LON-NICO

C.9.3 Torsion Angle Analysis

LON displays a variety of different conformations arising primarily from the rotation around the methylene linker connecting the dichloro-substituted and fused indazole rings. Figure C.29 shows an example of these using 6 crystal structures of novel materials containing pharmaceutically acceptable co-formers.

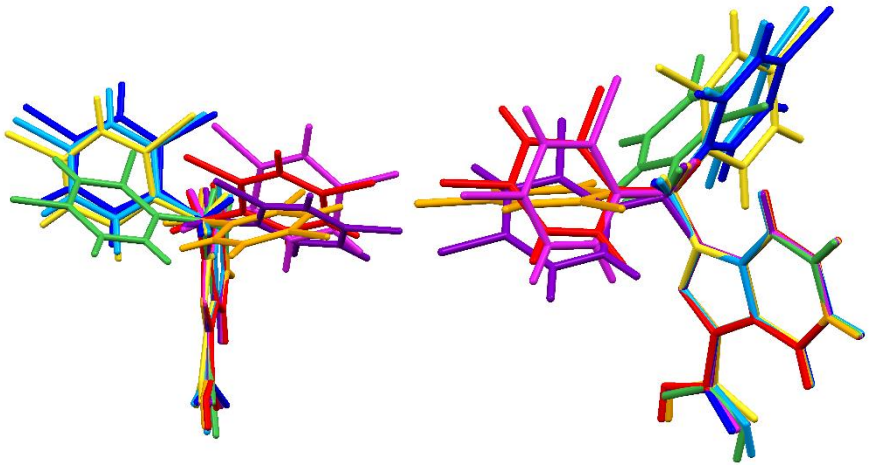

Figure C.29. Overlay of LON (2 views) for parent material and 6 co-crystals and salts containing pharmaceutically acceptable co-formers showing the variation in torsion in just 6 materials: α-LON (red), β -LON (orange), LON-ISO (green), LON-NICO (light blue), LON-HALO (royal blue), LON-IMID·EtOAc (magenta), LON-MEL (purple), LON-PIPE (yellow).

Table C.19 lists the torsion values for all the materials indicating individual angles for each independent LON molecule if more than one is present. Table C.20 groups the materials according to the angles to identify structures which show similarities. These data are also represented graphically in Figure C.30, and compared to molecular weight in Figures C.31and C.32 to allow trends based on molecular size to be identified.

Table C.19. Torsion angles around the methylene linker for each LON molecule in the previously reported and discussed co-crystal and salt crystal structures. Values in brackets denote the disordered component associated with the value for the residue immediately preceding it.

Sample	ID	Torsion angle /° (N1-C9-C10-C11)	Angle between planes /° (dichloro-substituted and fused indazole)
α-LON	1	74.11	81.75
β-LON	2	-169.05	77.70
LON-ISO	3	-90.1	66.09
LON-NICO	4	-118.80	77.96
LON-BENZ	5	-71.19	78.26
LON-2APYM	6	168.72	83.11
LON-4DMAP 2:1	7	167.52 / -76.85 (103.56)	80.33 / 72.58
LON-4DMAP·2H_2O	8	51.09	75.26
LON-MEL	9	-153.57	80.70
LON-HALO·3H_2O	10	116.33	85.70
LON-PIPE	11	-150.37 / 114.83	88.83 / 73.92
LON-IMID·0.5EtOAc	12	60.93 / 163.91 / -62.55 / -148.18 / 142.28 / -164.96	80.27 / 81.56 / 80.76 / 76.47 / 79.74 / 85.53
LON-IMID 2:1	13	-77.59 / -84.45	75.57 / 74.47
LON-IMID 1:1	14	-155.91 / -161.22	88.09 / 76.25
LON-4,4BIPY	15	60.84 (-146.78) / -154.88 (68.04) / -56.57 (139.79) / 140.08 (-64.67)	88.83 / 77.41 / 89.56 / 82.16
LON-2APYD $_{(ACN)}$	16	59.40	88.08
LON-2APYD·EtOAc	17	-62.45	85.53
LON-246TAPM	18	-114.37	86.31

Table C.20. Grouping of the LON molecules in each crystal structure according to the torsion angles and angle between planes using identification codes from Table 5.1.

Torsion angle /° (N1–C9–C10–C11)	Structures	Torsion angle /° (N1–C9–C10–C11)	Structures	Angle between planes /°	Structures
51	8	**-55 – (-65)**	12, 15, 15[a], 17	**< 70**	3
59 – 61	12, 15, 16	**-71 – (-78)**	5, 7, 13	**70 – 75**	7, 11, 13
68	15[a]	**-85**	13	**75 – 78**	2, 4, 8, 12, 13, 14, 15
74	1	**-90**	3	**78 – 80**	5, 12
114 – 116	10, 11	**-114 – (-118)**	4, 18	**80 – 82**	1, 7, 9, 12, 12, 12
140 – 142	12, 15, 15[a]	**-148 – (-156)**	9, 11, 12, 14, 15, 15[a]	**82 – 85**	6, 15
103	7[a]	**-160 – (-165)**	12, 15	**85 – 88**	10, 12, 17, 18
160 – 170	6, 7, 12	**-170**	2	**> 88**	11, 14, 15, 15, 16

[a] indicates disordered component of the structure

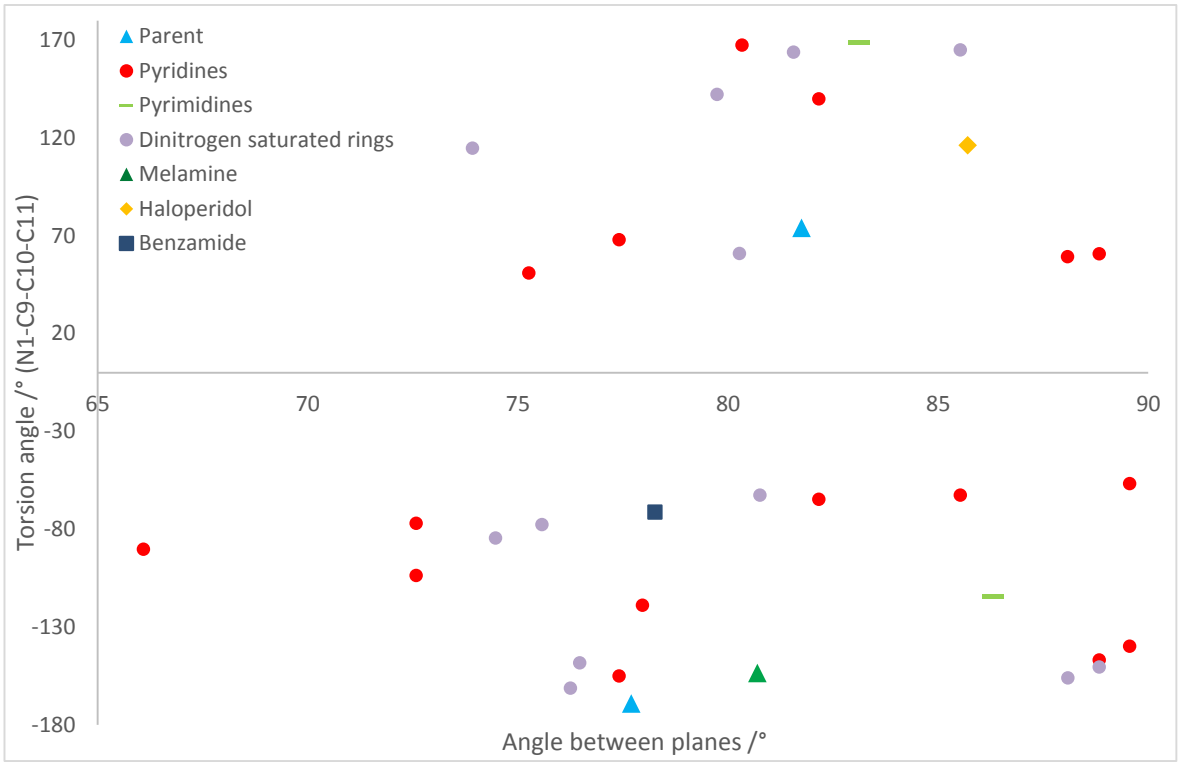

Figure C.30. Scatter plot comparing the torsion angle and angle between the planes using each independent LON molecule present in a structure; more than one data point can represent a single crystal structure.

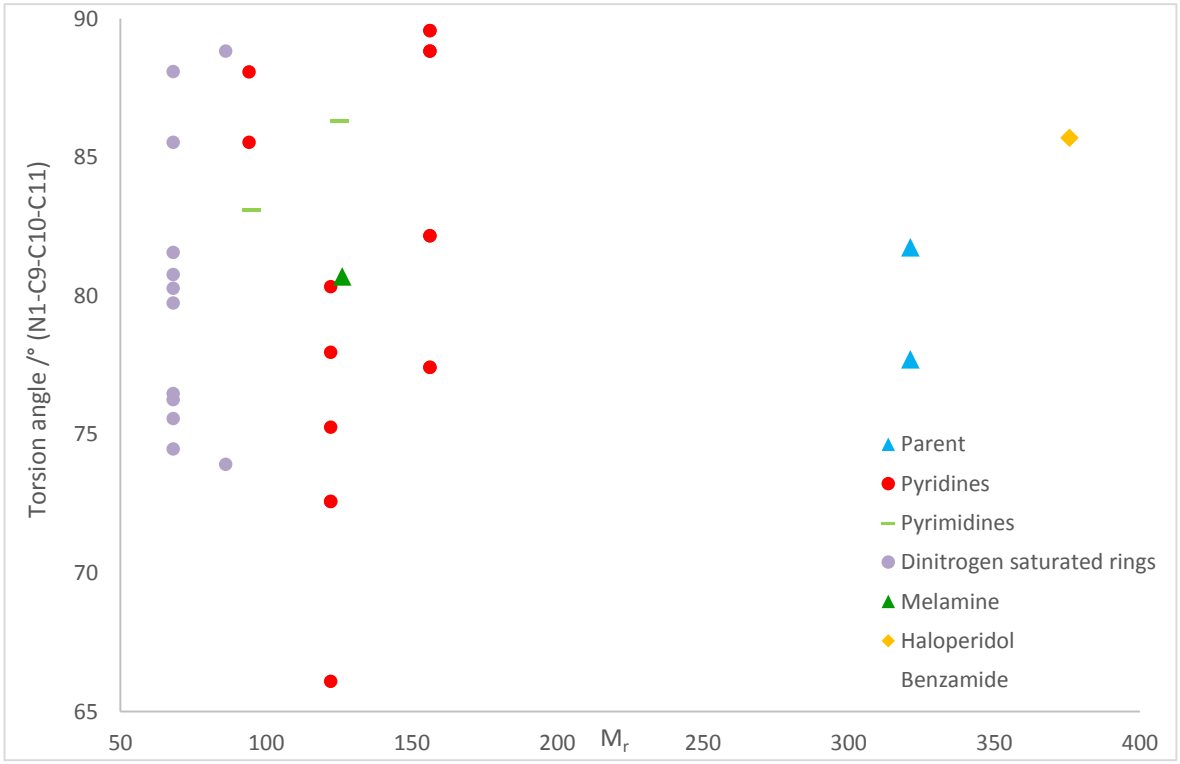

Figure C.31. Scatter plot comparing the molecular weight and torsion angle using each independent LON molecule present in a structure; more than one data point can represent a single crystal structure.

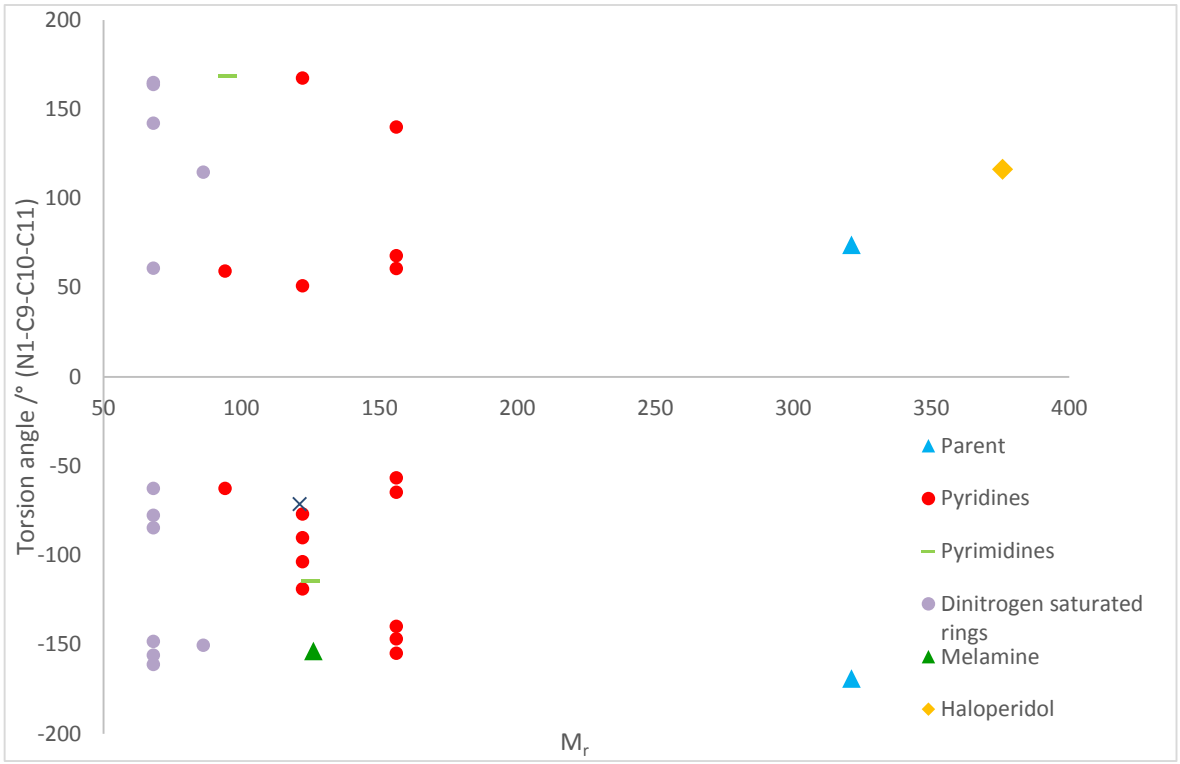

Figure C.32. Scatter plot comparing the molecular weight and angle between the planes using each independent LON molecule present in a structure; more than one data point can represent a single crystal structure.

C.10 pK_a

The pK_a values determined by the physiochemical properties calculator plugin[7] in ChemAxon's MarvinSketch[8] software for the co-former molecules are depicted in Table C.21. These are accompanied by the ΔpK_a values (pK_a (conjugate acid of base) – pK_a (carboxylic acid)) when analysed with respect to LON for prediction purposes. Two values for LON are used, one calculated using the same method as applied to the co-formers and a second taken from literature (not all values for co-formers were found in the literature therefore calculated values were used for all for consistency). The predictions based on the rule of three (> 3 = salt, 0-3 hard to predict, < 0 co-crystal) are indicated by C, co-crystal; S, salt, SC, salt-co-crystal hybrid; I, intermediate range where predictions are difficult. Experimental observations are shown alongside the predictions for comparison.

Table C.21. pK_a for all successful co-formers with ΔpK_a when analysed with respect to LON showing predicted outcome and experimental results obtained.

Co-former	pK_a (Marvinsketch predicted)	ΔpK_a (LON value 3.02[a])	Prediction	ΔpK_a (LON value 4.35[b])	Prediction	Experimental result
246TAPYM	7.28	4.26	S	2.93	M	Salt
2APYD	6.84	3.82	S	2.49	M	Salt
2APYM	3.62	0.6	M	-0.73	C	Co-Crystal
4,4BIPY	4.44[b]	1.42	M	0.09	M	Co-Crystal
4DMAP	8.78	5.76	S	4.43	S	Salt / hybrid
BENZ	-0.36	-3.38	C	-4.71	C	Co-Crystal
HALO	8.05	5.03	S	3.7	S	Salt
IMID	6.97	3.95	S	2.62	M	Salt/hybrid
ISO	3.45[b]	0.43	M	-0.9	C	Co-Crystal
MEL	8.56	5.54	S	4.21	S	Salt
NICO	3.63	0.61	M	-0.72	C	Co-Crystal
PIPE	5.18	2.16	M	0.83	M	Salt

[a] from physiochemical properties calculator plugin in MarvinSketch. [b] Reported literature value[344].

C.11 Thermal Analysis

C.11.1 Differential Scanning Calorimetry (DSC)

DSC was carried out for all samples except for the 1:1 and 2:1 salts of LON-IMID due to difficulties in isolating sufficient pure material. The melting onset taken from each DSC curve (Figure 6.22, Chapter 6.8) are reported in Table C.22 below along with reference co-former melting points.

Table C.22. Experimental melting point of LON and the new materials thereof compared with co-former reference melting points.

Sample	Melting Point (T_{onset}) /°C	Co-Former Melting Point /°C
α-LON	211.6-212.2[291]	
β-LON	208.5-209.5[291]	
$LON_{(bulk)}$	206.2	
LON-2APYD·EtOAc	129.8[a]	56-60
$LON\text{-}2APYD_{(ACN)}$	125.5[a]	56-60
LON-2APYM	137.2	123-127
LON-246TAPYM	246.7	249-251
LON-4DMAP 2:1	175.1	110-113
$LON\text{-}4DMAP{\cdot}2H_2O$	97.1[b]	110-113
LON-4,4BIPY	140.7[c]	111-114
LON-BENZ	163.3	127-130
$LON\text{-}HALO{\cdot}3H_2O$	104.7[d]	148-152
LON-IMID·0.5EtOAc	81.1[e]	88-91
LON-ISO	158.4	156
LON-MEL	276.7	345-350
LON-NICO	155.0	128-130
LON-PIPE	242.1	109-113

[a]LON-2APYD solvates show solvent loss with T_{onset} 72.1 °C (EtOAc, bp 77 °C) and 66.0 °C (CAN, bp 82 °C). The latter is a broader peak indicative of disordered solvent (contained in voids) with the peak occurring at 82 °C. [b]LON-4DMAP·2H_2O displays concomitant water loss and melting (97-120 °C), recrystallisation (T_{onset} 157.6 °C, forming 2:1 structure) and melt of the 2:1 recrystallised material at 176 °C. [c]LON-4,4BIPY displays melting at 140.7 °C preceded by solvent loss (surface solvent from crystallisation captured between the crystals) followed immediately by a recrystallisation event at 150.6 °C. This material then melts at 209 °C. [d]LON-HALO·3H_2O displays a number of events which can be described as water loss (60-80 °C), melting (105-125 °C) and decomposition 233 °C. [e]LON-IMID also displays a decomposition event from 240 °C, with the event at 81.1 °C consisting of desolvation and concomitant melting.

C.11.2 Hot Stage Microscopy (HSM)

Interesting behaviour was seen in the DSC analysis for a number of samples. In addition to the endotherm for the melt of the co-crystal/salt, additional events were evident. These were investigated using hot stage microscopy (HSM).

C.11.2.1 LON-4,4BIPY

The DSC curve of LON-4,4BIPY indicated initial surface solvent/water loss of molecules trapped in the solid crystal matrix. The sample then melted at 140.7 °C and was followed shortly after by an endotherm indicative of recrystallisation. These events were confirmed in HSM (Figure C.33) and the recrystallised material tested using SCXRD. The unit cell obtained matched that for β-LON and the new crystals were seen to melt at the expected temperature confirming this.

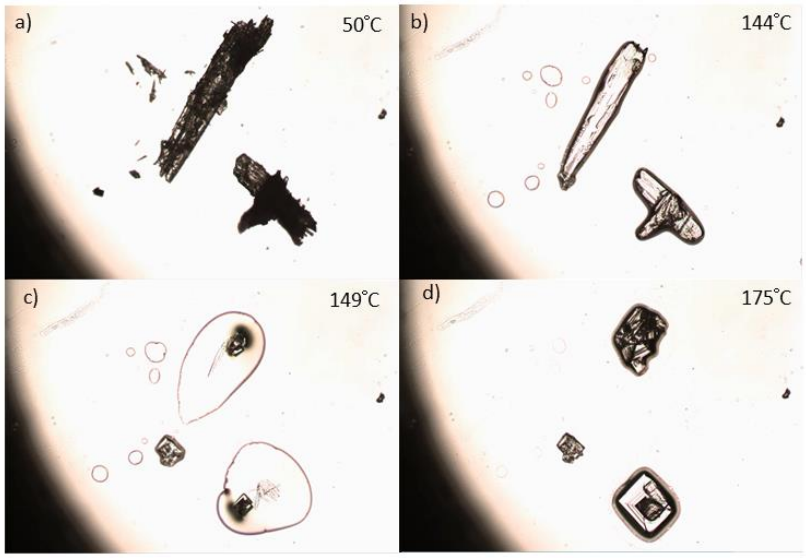

Figure C.33. Images from HSM investigation into LON-4,4BIPY salt showing a) sample initially, b) melting onset, c) recrystallisation d) resulting block crystals similar to those of β-LON (confirmed by SCXRD) which melt at 209 °C.

C.11.2.2 LON-4DMAP (1:1) salt dihydrate

LON-4DMAP·2H_2O shows a broad endotherm in the DSC at 97.1 °C followed by a second event with a smaller endotherm shortly after (157 °C). HSM investigations (Figure C.34) confirmed these as water loss concomitant with sample melting (97-120 °C) followed by a recrystallisation. SCXRD analysis of the recrystallised material confirmed it as the LON-4DMAP 2:1 salt (anhydrate) which melted as expected at 176 °C.

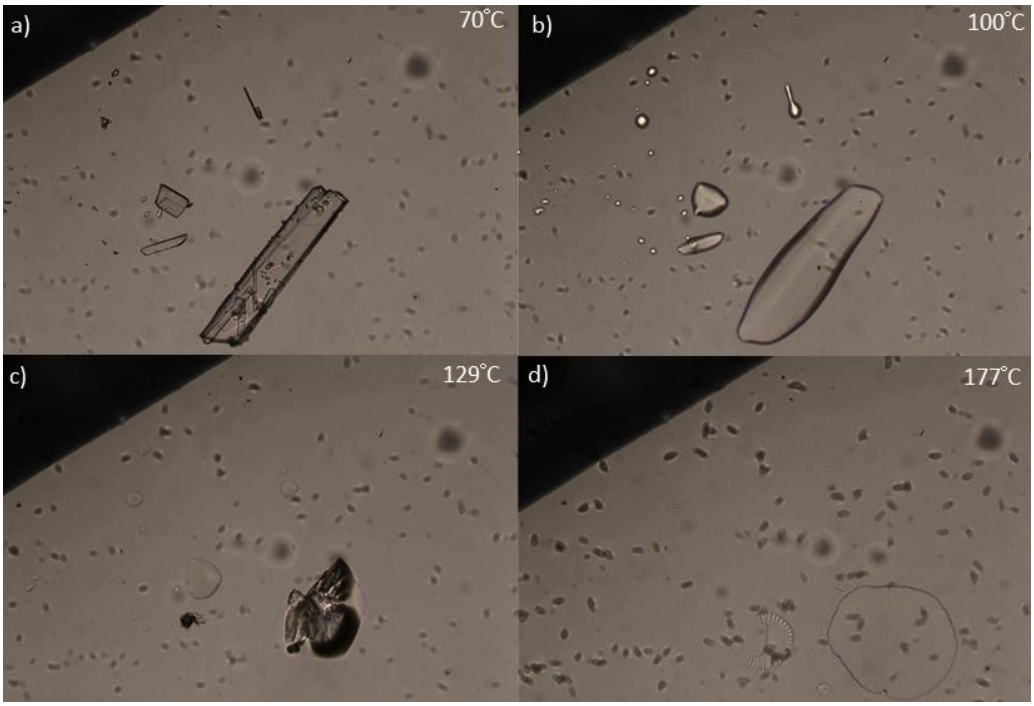

Figure C.34. Images from HSM investigation into LON-4DMAP·2H_2O salt showing a) sample initially, b) water loss and melting onset, c) recrystallisation d) recrystallisation material melting.

C.11.2.3 LON-HALO (1:1) salt trihydrate

LON-HALO·3H_2O shows a jagged endotherm (100-125 °C) in the DSC curve preceded by a small, broad endotherm (50-80 °C). These are attributed to water loss (broad endotherm) and melting due to lattice breakdown upon further water removal (100-125 °C). Water loss from hydrated crystal structures can be complex: different sites, the location within crystal and the interactions they form can all play a part. It is hypothesised that water loss is a staggered event, combined with a staged melting and produces the endotherm as observed in the DSC. The HSM investigation (Figure C.35) indicated water loss and melting occurring simultaneously over a broad temperature range, with degradation at 275 °C (also evident in the DSC).

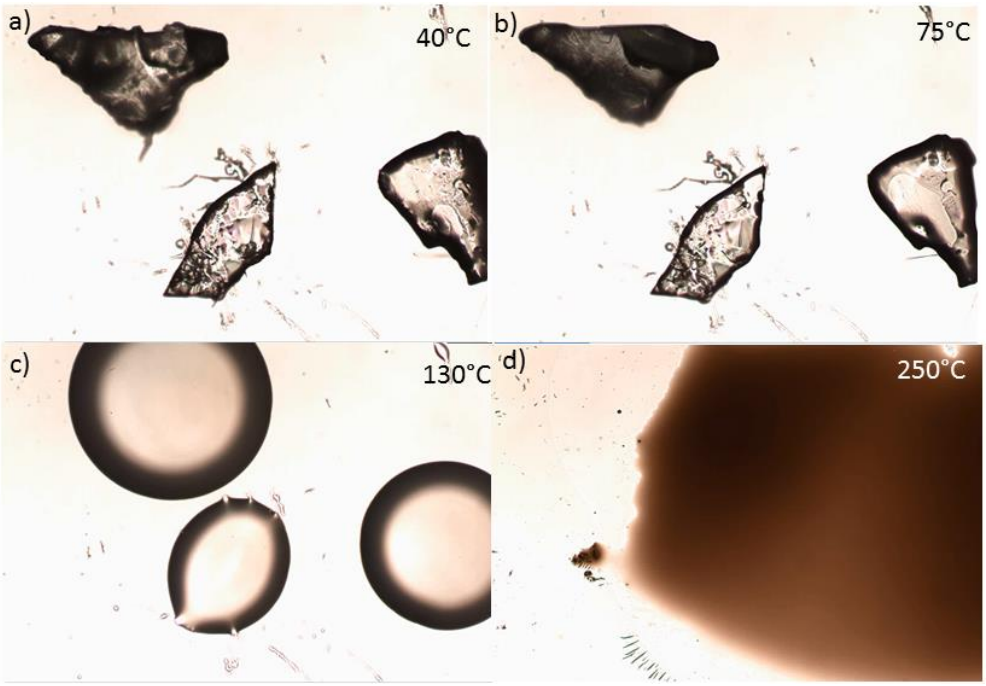

Figure C.35. Images from HSM investigation into LON-HALO·3H_2O showing a) sample initially, b) water loss onset, c) melt and d) decomposition.

C.11.2.4 LON-IMID ethyl acetate (1:1:0.5) salt solvate

LON-IMID·0.5EtOAc DSC shows an endotherm at 81 °C with a second event occurring at a much higher temperature (over 275 °C). The first event is attributed to solvent loss with concomitant melting due to lattice breakdown from the removal of solvent as evidenced in HSM (Figure C.36). The second event was observed in HSM as initial degradation of the melt (darkening of the sample, likely to be IMID degradation) followed by crystal formation at 284 °C (Figure C.36, g). See section C.12 for details regarding recrystallisation material.

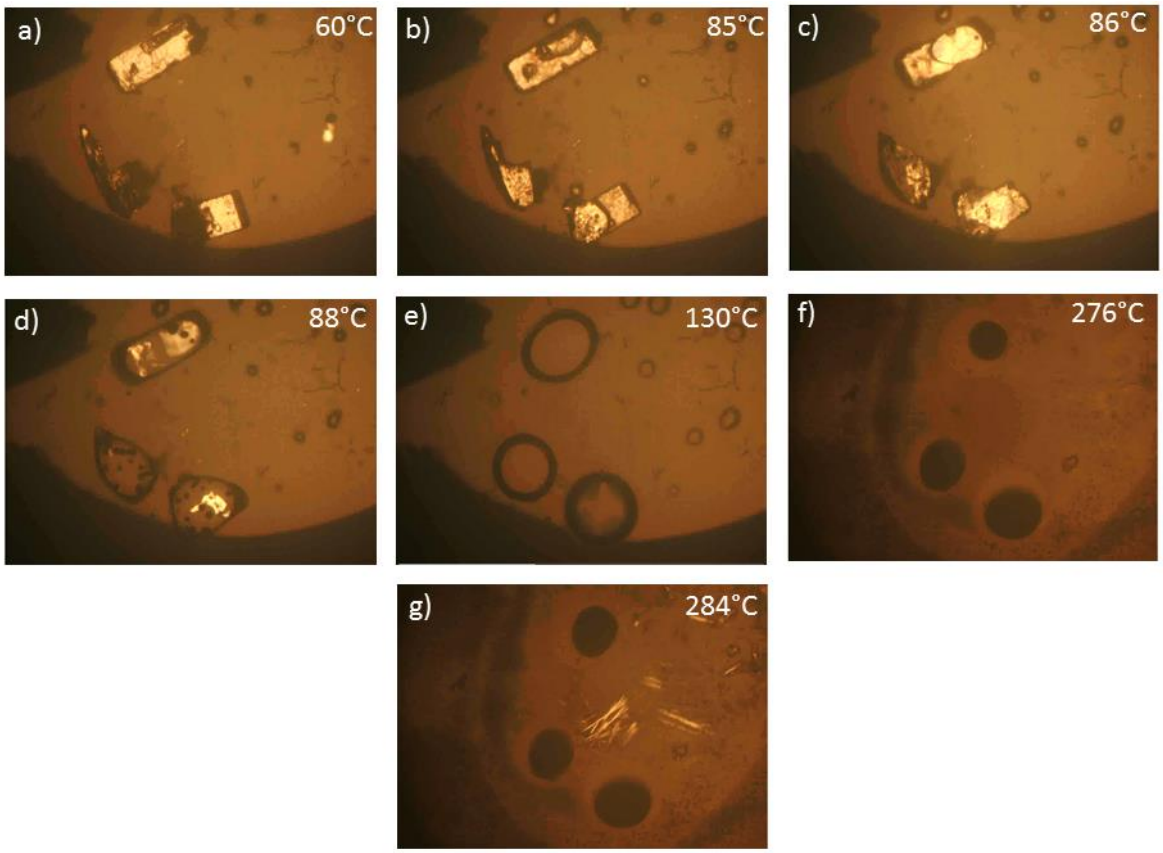

Figure C.36. Images from HSM investigation into LON-IMID.0.5EtOAc salt showing a) sample initially, b) solvent loss and melting onset, c-e) melt f) decomposition (co-former) g) recrystallisation.

C.11.3 Thermogravimetric Analysis (TGA)

TGA was used to further investigate LON-HALO·3H_2O, LON-IMID·0.5EtOAc and the two non-pharmaceutically acceptable LON-2APYD salts as all samples contained solvent / water molecules.

C.11.3.1 LON-2APYD

The TGA for the ethyl acetate salt (1:1:1 ratio) is shown Figure C.37 with solvent loss occurring in the expected temperature range for ethyl acetate (boiling point 77 °C). This % mass loss (16.75 %) is in agreement with the 1:1:1 stoichiometry determined by SCXRD. This composition would contain ethyl acetate at 17.5 % by mass. Following the loss of solvent a small gradual mass loss is seen followed by degradation (onset 250 °C) in the TGA curve.

The second salt is depicted in Figure C.38 and indicates a mass loss occurring between 70-80 °C. This corresponds to the boiling point of the assumed solvent, acetonitrile (boiling point 82 °C),

ascertained from void space analysis and electron count. The mass loss (4.06 %) corresponds with a 0.5 equivalent of acetonitrile in the crystal structure.

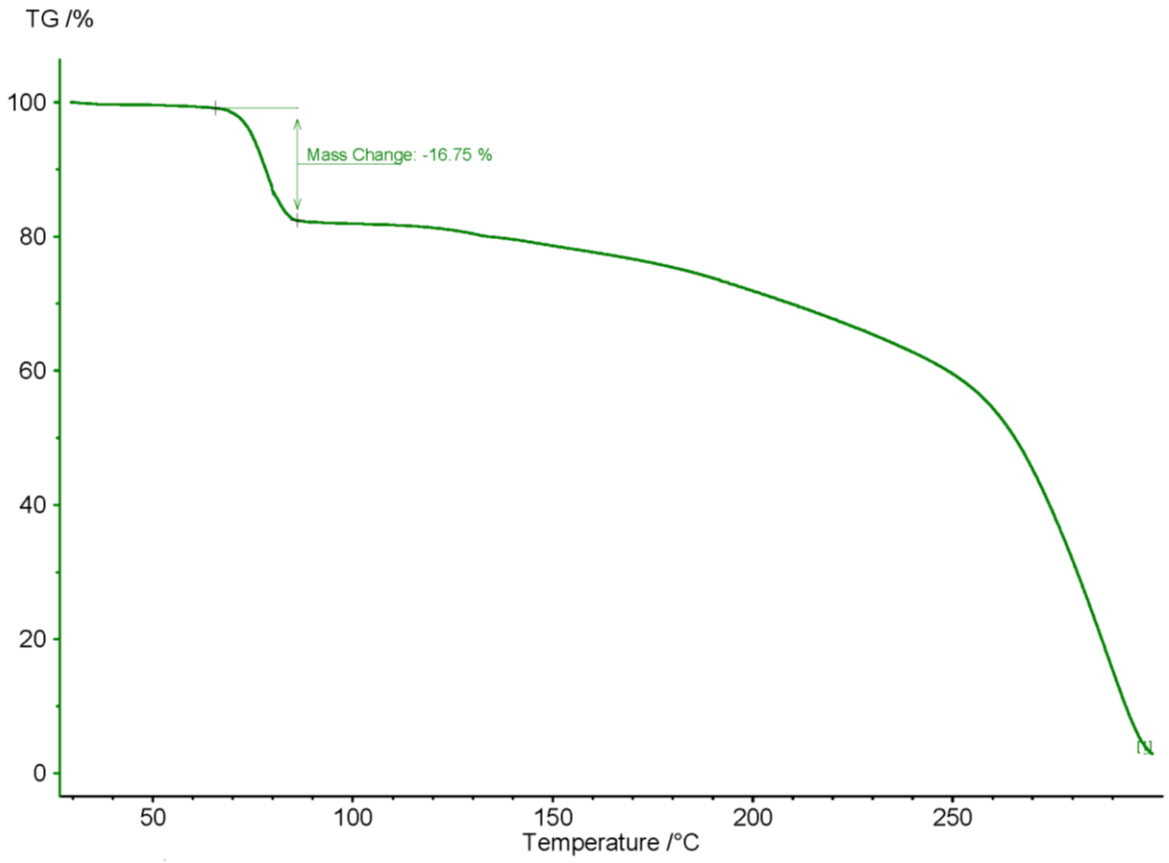

Figure C.37. TGA for LON-2APYD·EtOAc solvate 30-300 °C at 10 °C min^{-1} showing solvent loss at the expected temperature for ethyl acetate followed by sample melt and degradation from 250°C.

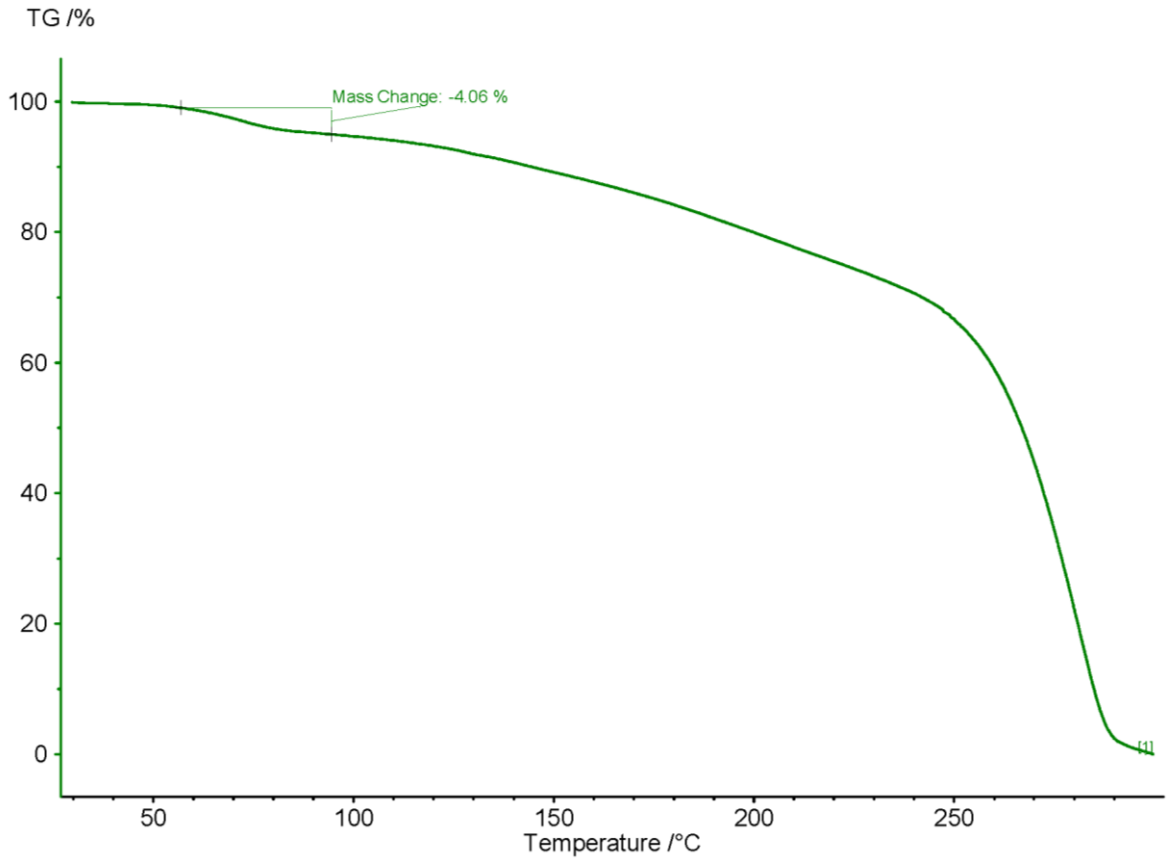

Figure C.38. TGA for LON-2APYD acetonitrile solvate 30-300 °C at 10 °Cmin^{-1} showing solvent loss at the expected temperature for acetonitrile, followed by sample melt and degradation from 250°C.

C.11.3.2 LON-4DMAP (1:1) salt dihydrate

The TGA curve for LON-DMAP·2H_2O is shown in Figure C.39 and confirms the dihydrate nature of the salt, as a mass loss representative of two water molecules occurs between 70-100 °C.

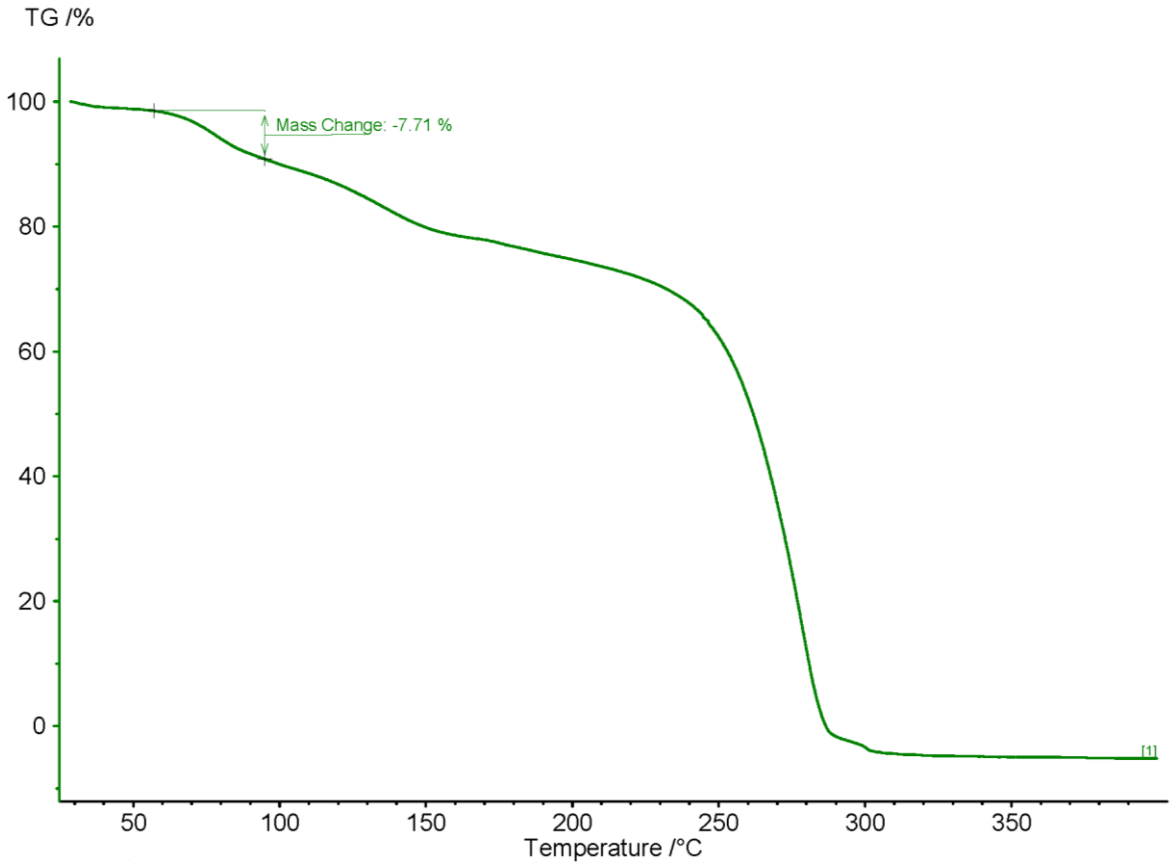

Figure C.39. TGA for LON-4DMAP·2H_2O salt 30-400 °C at 10 °C min^{-1} showing water loss (2 molecules) by 100 °C followed sample melt and degradation from 250 °C.

C.11.3.3 LON-HALO (1:1) salt trihydrate

The DSC (Figure C.40) for LON-HALO·3H_2O exhibits complex thermal behaviour. HSM provided a visual insight into this (C.11.2) TGA can provide an additional, quantitative, analysis. The TGA (Figure C.41) indicates an initial weight loss of 6.42 % up to 120 °C which corresponds to the loss of the three water molecules (7.19 % by weight of the compound) also evidenced in the HSM and DSC experiments (Figures C.35 and chapter 6.8, Figure 6.22). A further 12.74 % decrease in mass occurs between 120 °C and 250 °C followed by significant mass change which corresponds to a staggered sample degradation.

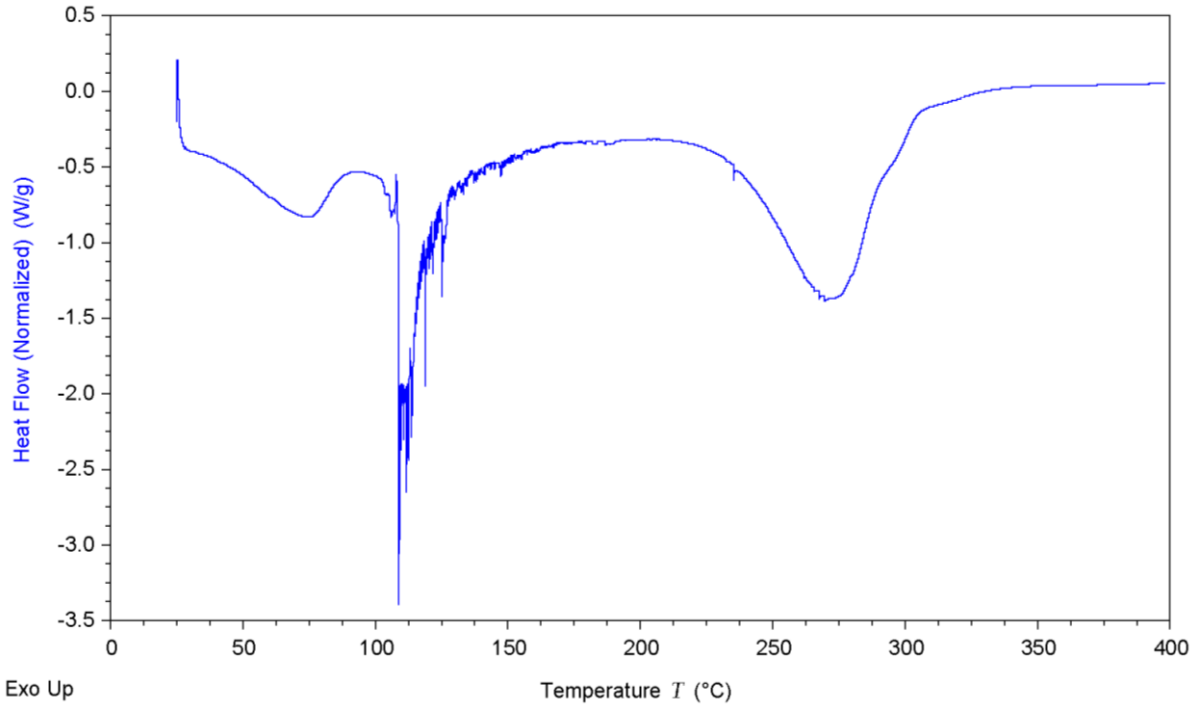

Figure C.40. DSC of LON-HALO·3H_2O salt, 25-400 °C at 10 °Cmin^{-1}. The baseline is not as expected for a usual DSC trace however this is reproducible and ascribed to the hydrate behaviour when heated (which is known to be complex and often non-conforming to standard, expected behaviours).

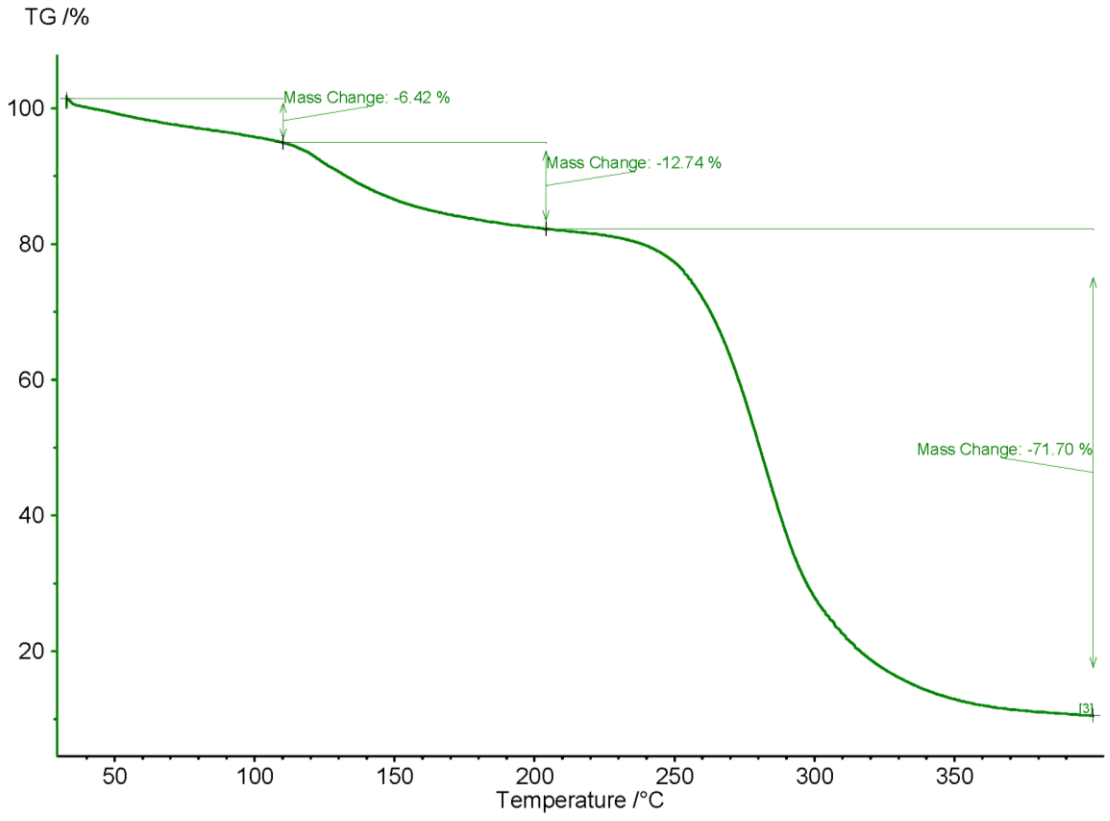

Figure C.41. TGA for LON-HALO·3H_2O 25-400°C at 10 °Cmin^{-1} showing water loss followed by sample degradation.

C.11.3.4 LON-IMID (1:1:0.5) ethyl acetate salt solvate

LON-IMID·0.5EtOAc contains 10.7 % solvent by mass. The TGA (Figure C.42) indicates an initial weight loss of 1.39 % up to 100 °C followed by a gradual and steady mass loss until 250 °C. This corresponds to some initial solvent loss (before 100 °C) which disrupts the hydrogen bonding network and causes simultaneous melting with further solvent loss. After 250 °C a significant and sharp mass change is observed which corresponds to sample degradation.

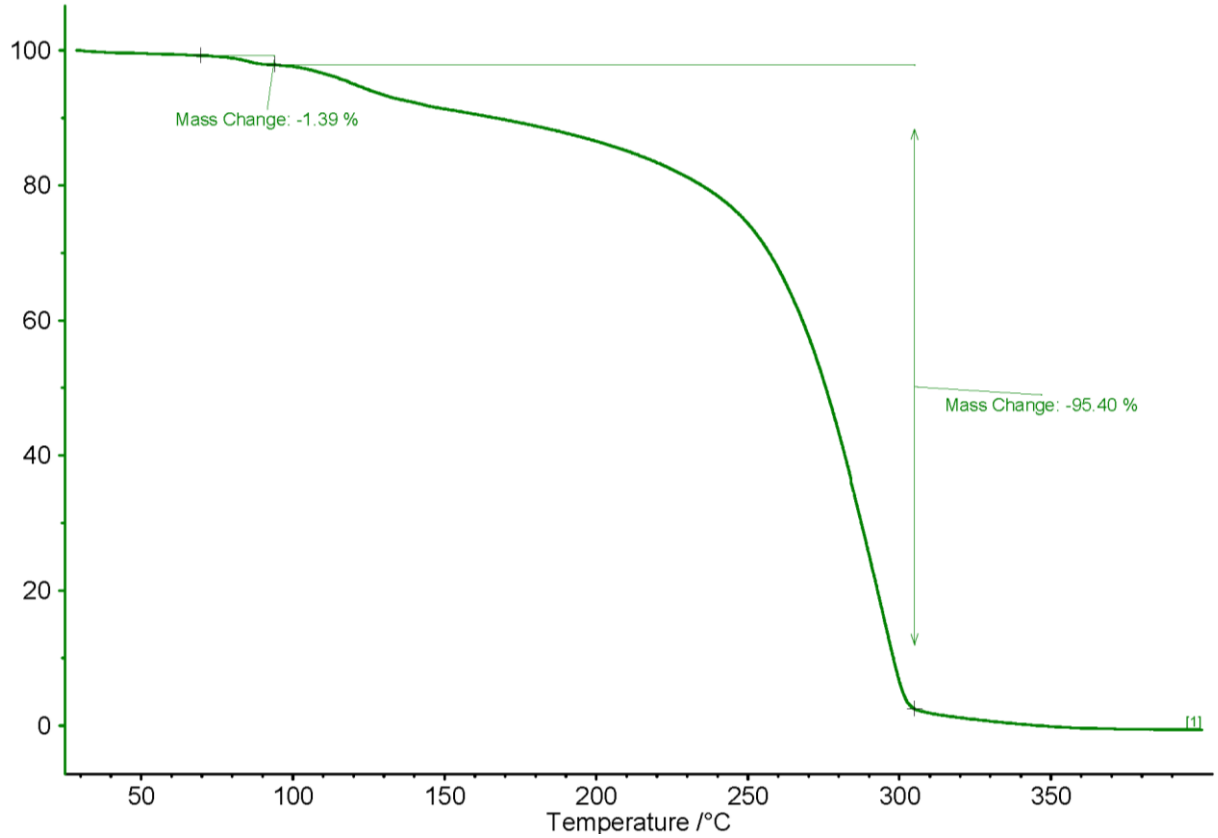

Figure C.42. TGA for LON-IMID·0.5EtOAc salt 25-400°C at 10 °Cmin^{-1} showing solvent loss occurs concomitantly with melting and sample degradation.

C.12 HSM Recrystallisation Material

To aid the identification of the recrystallisation material generated from LON-IMID·0.5EtOAc (observed in HSM experiment) a number of different techniques were applied. SCXRD data was collected on a crystal isolated from the HSM experiment however the diffraction was low resolution and weak. The data were sufficient to be able to recognise components representative of LON in the electron density, and various restraints and constraints were applied to generate a model. The structure crystallised in the tetragonal space group I $4_1/a$ with two independent molecules of LON in the asymmetric unit. The experimental electron density gave a reasonable fit to LON, with the exception of one carboxylic acid group which did not model well to the density.

C.12.1 Mass Spectrometry

To aid the modelling and structure identification, mass spectrometry was used to determine the molecular weight of the material. Positive ion electrospray ionisation (J. Herniman, University of Southampton) identified 2 peaks in the HPLC trace with retention times between 2 to 3 min (Figure C.43), indicating two different components. The area under each was analysed (Figure C.44) and showed a parent ion equating to LON in peak 1, with other fragments which can be explained using LON structure (Table C.23). Peak 2 presented fewer fragments and a parent ion equating to a decarboxylated LON molecule. This was in accordance with observations from the SCXRD data in which one molecule did not model well to the experimental electron density in the region of the carboxylic acid.

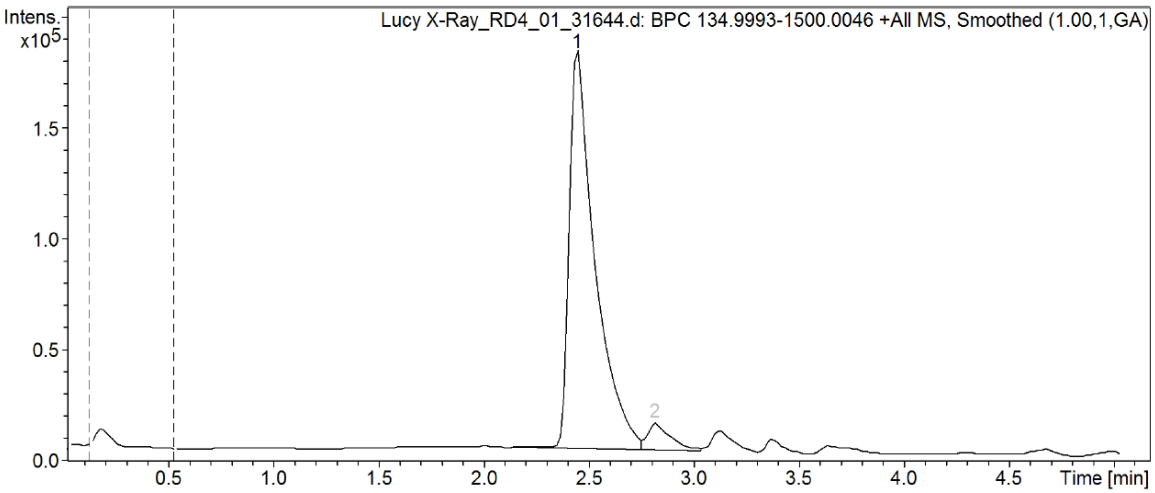

Figure C.43. HPLC trace of HSM material from mass spectrometry with two main peaks at retention times of 2.5 and 2.85 min respectively.

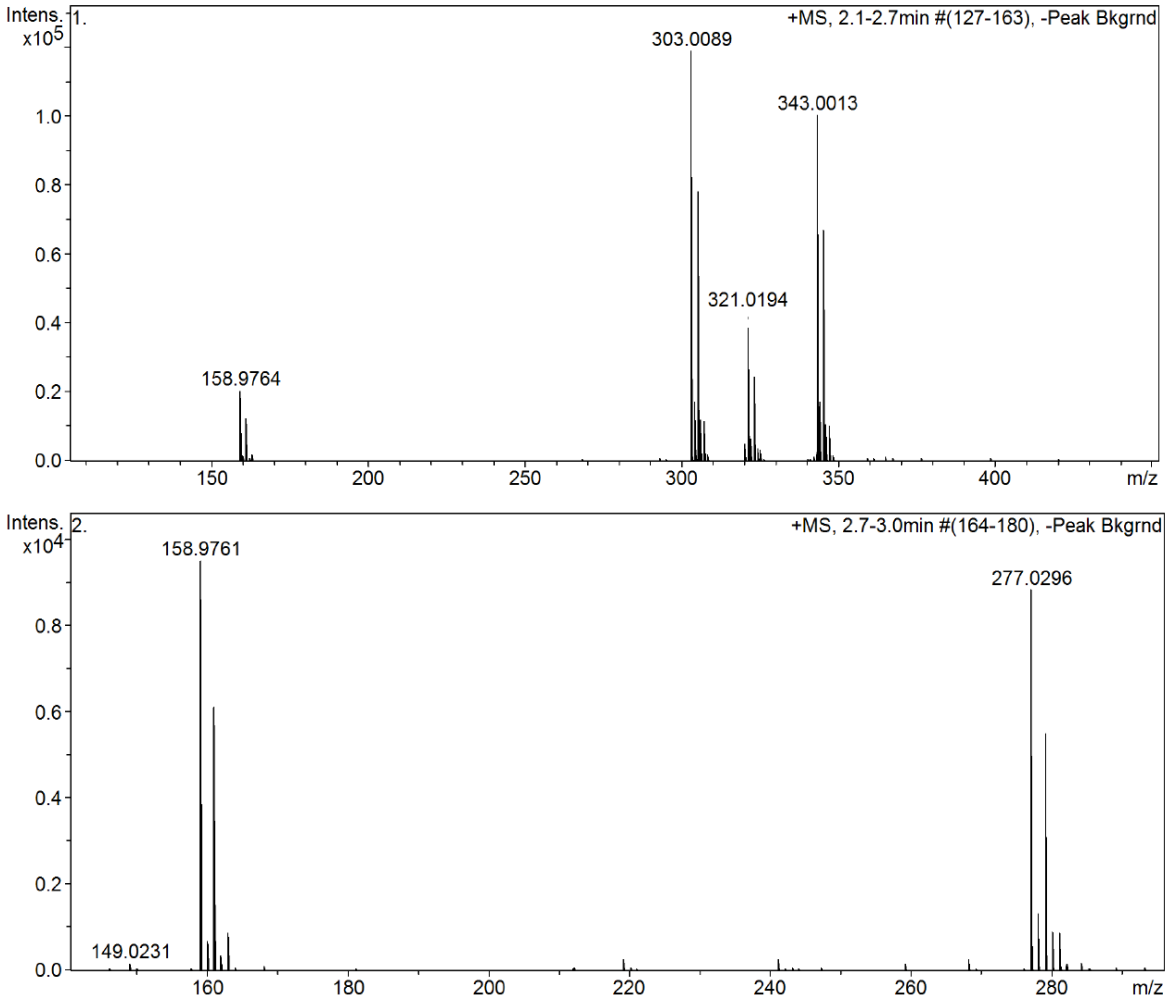

Figure C.44. Mass spectra for peak 1 (above) and peak 2 (below) obtained from analysis of the HSM recrystallisation material.

The mass spectrometry data gave confirmation to the molecular weight of the material, and the presence of two individual components. This gave confidence to the model obtained from the SCXRD (Figure C.45).

Table C.23. Fragments identified in mass spectrometry with mass, formula and associated structure.

	Mass	Formula	Fragment
Peak 1	158.9764	$C_7H_5Cl_2$	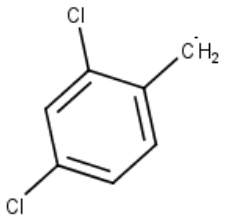

	Mass	Formula	Fragment
	303.0089	$C_{15}H_9Cl_2N_2O$	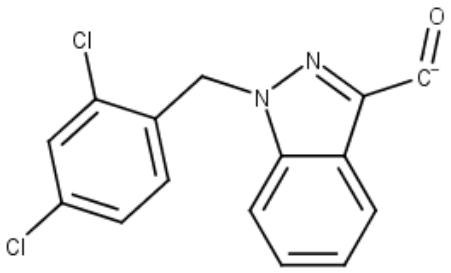
	321.0194	$C_{15}H_{11}Cl_2N_2O_2$	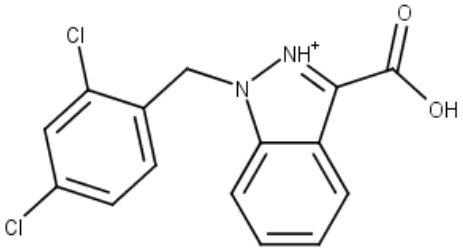
	343.0013	$C_{15}H_{10}Cl_2N_2NaO_2$	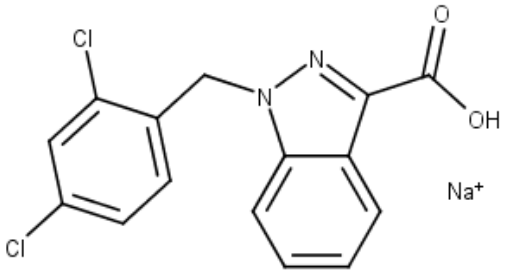
Peak 2	158.9761	$C_7H_5Cl_2$	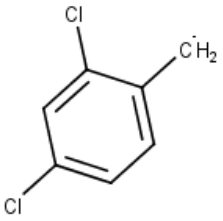
	277.0296	$C_{14}H_{11}Cl_2N_2$	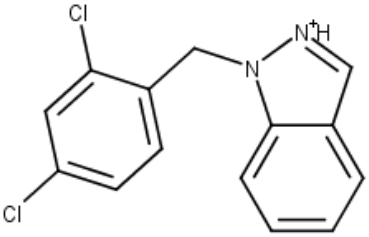

C.12.2 SCXRD

A number of crystals obtained *via* HSM were tested using SCXRD in an attempt to realise the structure of the new material. In all instances, the diffraction was weak, and of low resolution (1.6-2.0 Å) however a data set was obtained giving the tetragonal cell a = 32.700 Å, c = 11.648 Å. Structure solution and refinement in space group $I4_1/a$ produced the structure shown in Figure C.45.

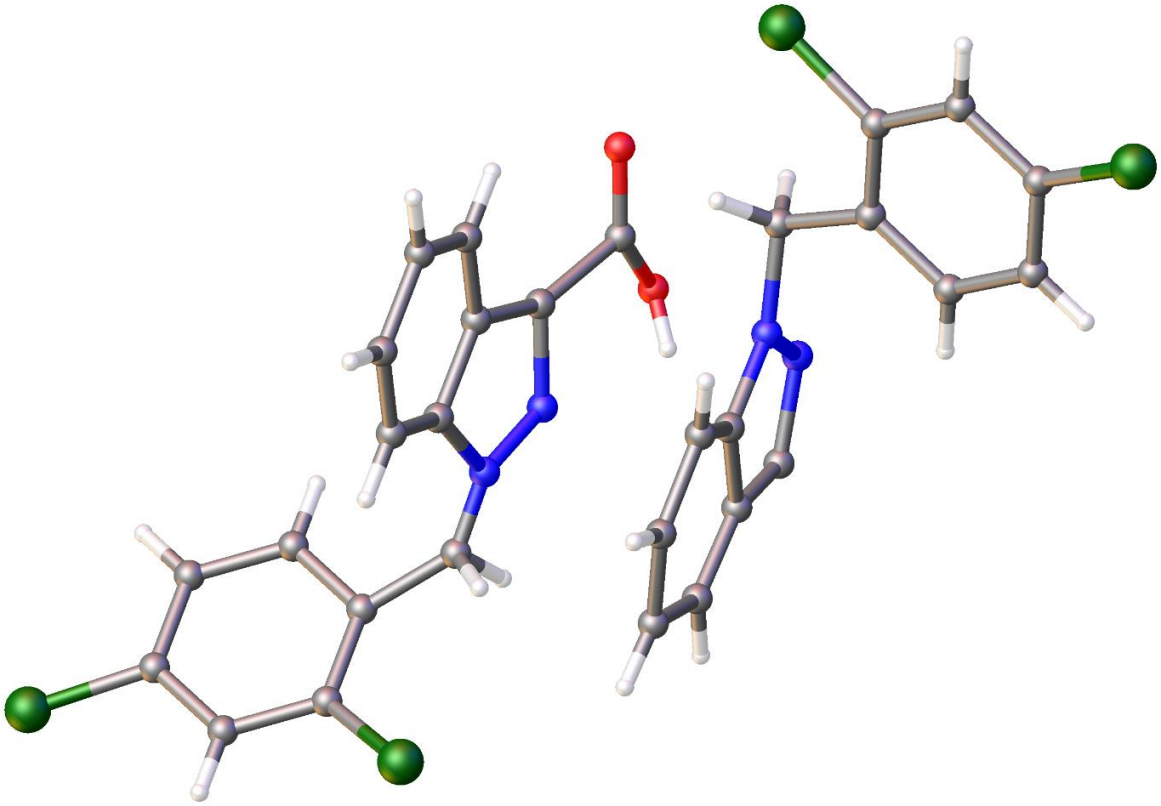

Figure C.45. Structure of material formed in the recrystallisation event seen in the HSM experiment of LON-IMID·0.5EtOAc containing two independent molecules of LON, one without the carboxylic acid group. All atoms modelled as isotropic, and viewed as a ball and stick representation for clarity.

C.12.3 Other Occurrences

Structure solution and complementary techniques identified the nature of the material formed in the HSM experiment of LON-IMID·0.5EtOAc (284 °C). This has been determined as two molecules of LON, one of which has undergone decarboxylation. As this material appears to originate from LON, the parent material was investigated up to and beyond the recrystallisation temperature range using both DSC and HSM (Figures C.46 and C.47).

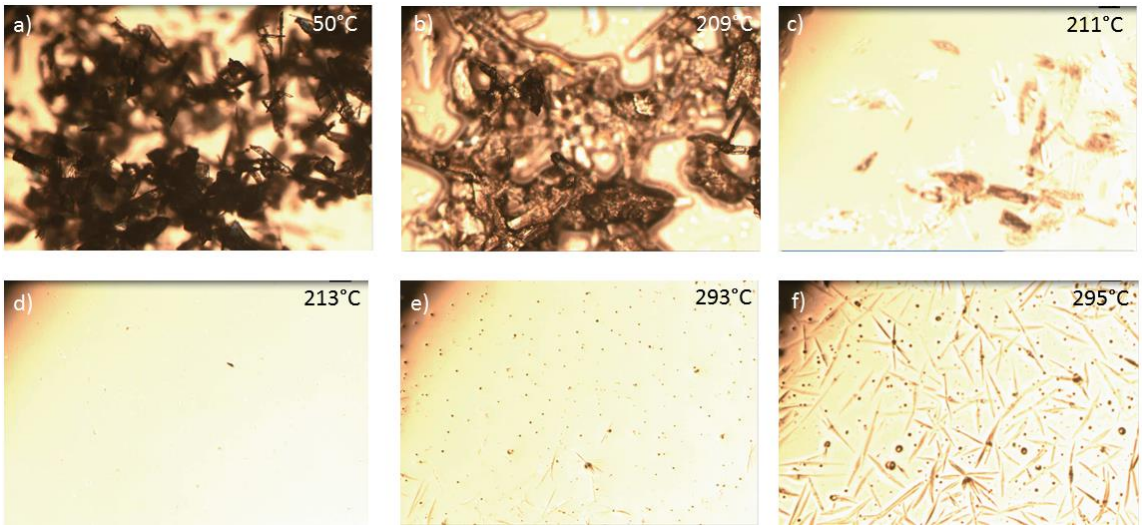

Figure C.46. Images from the HSM experiment for LON, 50-350 °C at 10 °C min^{-1} showing a) the sample initially, b) sample melt, c-d) end of melt and liquid LON, e) recrystallisation onset and f) crystals formed from the melt.

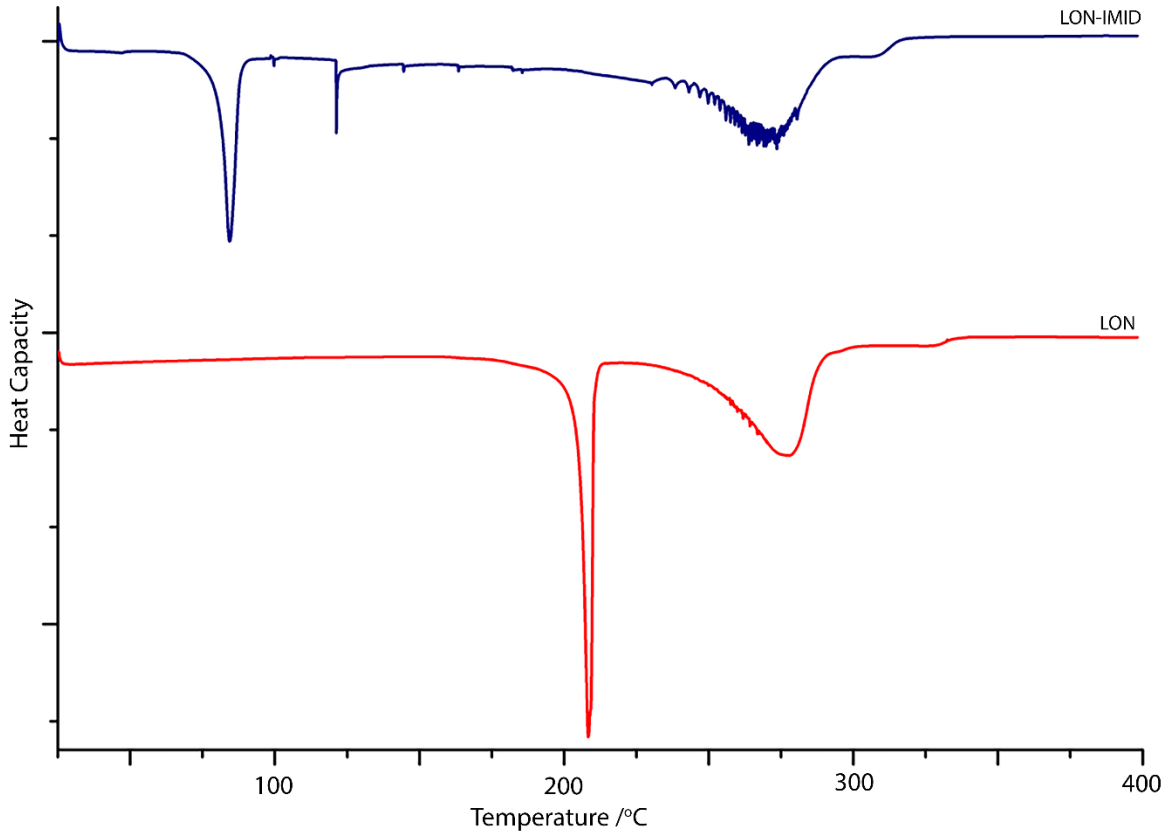

Figure C.47. DSC curves 25-400 °C for LON and LON-IMID·0.5EtOAc showing the sample melt, followed by the recrystallisation event around 280 °C.

As shown in Figure C.46 LON undergoes the same recrystallisation event as observed in the LON-IMID·0.5EtOAc sample following the initial melt. LON appears to have a slightly higher recrystallisation onset temperature in HSM than initially seen for LON-IMID·0.5EtOAc which could be due to the presence of IMID in the latter, acting as an impurity and lowering the onset temperature. The two DSC curves (Figure C.47) show a very similar endotherm corresponding to the recrystallisation event around 280 °C. This is slightly lower than observed in HSM due to the differences in heating and recording of the two techniques. On further investigation, it was also found that LON-4,4BIPY samples demonstrated the same recrystallisation event.

C.13 Stability

C.13.1 Slurry

Figure C.48 shows the PXRD patterns of the filtered materials resulting from slurry stability testing (24 hours, RT, 1 % Tween 80 ® in aqueous solution). The data indicates that LON, the co-crystal with BENZ and the salts with HALO, MEL, PIPE are stable under these conditions. The co-crystals with NICO and ISO undergo partial disociation and LON-IMID·0.5EtoAc does not withstand the conditions; a poorly crystalline material which resembles parent API results in this instance.

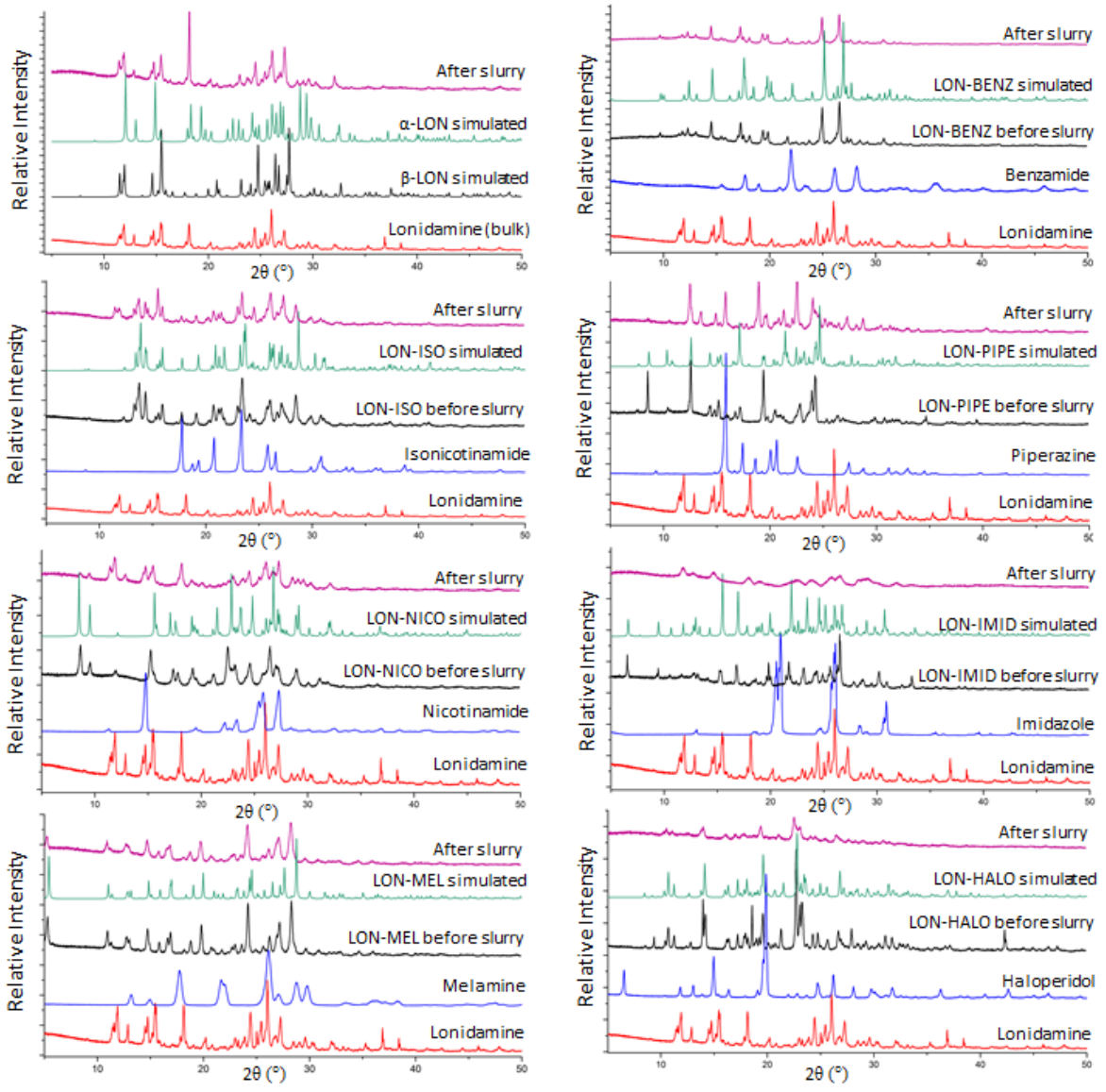

Figure C.48. Overlays of PXRD patterns resulting from slurry experiments at room temperature in 1 % Tween 80 ® aqueous solution for LON and six novel materials containing pharmaceutically acceptable co-molecules.

C.13.2 Accelerated Stability

Figure C.49 shows PXRD patterns for the LON materials containing pharmaceutically acceptable co-former molecules when tested under accelerated conditions (13 weeks, 40 °C / 75 % RH). All materials showed stability under these conditions with the exception of LON-IMID·0.5EtOAc salt solvate which showed sample degradation.

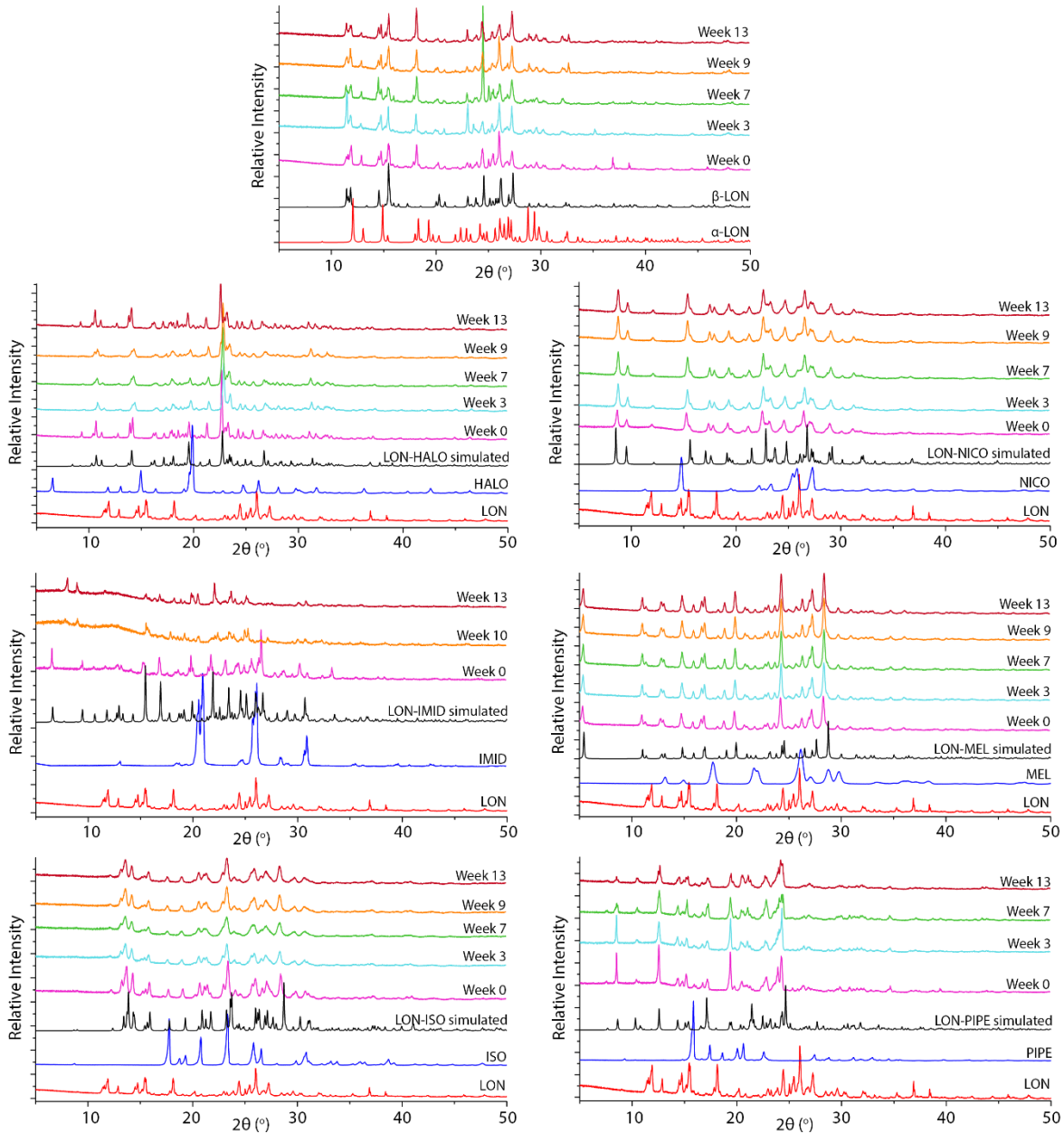

Figure C.49. Stacked PXRD patterns for storage under accelerated conditions (45 °C / 75 % RH) for LON parent material and six new materials containing pharmaceutically acceptable co-molecules.

C.14 Solubility

Solubility determination was carried out using HPLC on aliquots of the filtered slurry solution to identify the LON concentration in solution after 24h. For the samples which indicated dissociation under these conditions apparent solubility was calculated from the dissolution profiles. The solubility is presented in Table C.24 along with dissolution experiment data: % dissolution observed in 10 mins, 30 mins and the slope of the curve at the end of the experiment. This indicates the rate at which the dissolution was occurring and can provide an insight into how the dissolution may progress at further time points (i.e. reached plateau by the end of the experiment, plateau to be reached soon after the end or gradient still increasing indicating it is some time before a plateau may be reached).

Table C.24. Solubility and Dissolution data for LON and the pharmaceutically acceptable co-crystal and salt materials.

Sample	% Dissolution in 10 mins	% Dissolution in 30 mins	Gradient final 120 min	Solubility / mg mL^{-1}	Ratio to API
LON	10.4	27.7	0.156	0.115	1
LON-BENZ	22.6	32.5	0.190	0.130	1.13
LON-HALO·3H$_2$O	7.5	25.8	0.102	0.175	1.52
LON-IMID·0.5EtOAc	44.7	93.5	0.027	0.428[a]	3.73
LON-ISO	2.9	9.7	0.130	0.038[a]	0.33
LON-MEL	22.1	44.7	0.032	0.041	0.36
LON-NICO	6.5	19.7	0.192	0.078[a]	0.68
LON-PIPE	10.6	21.1	0.200	2.987	26.0

[a]Apparent solubility: $C_m = C_s\left(\frac{Jm}{J_s}\right)$

1. G. R. Desiraju, *Crystal Engineering: The Design of Organic Solids.* , Elsevier, Amsterdam, 1989.

2. C. B. Aakeröy, J. Desper, E. Elisabeth, B. A. Helfrich, B. Levin and J. F. Urbina, *Zeitschrift für Kristallographie-Crystalline Materials*, 2005, **220**, 325-332.

3. C. A. Schalley, in *Analytical Methods in Supramolecular Chemistry*, ed. C. A. Schalley, Wiley-VCH Verlag GmbH & Co. KGaA, Weinheim, Germany., 2006.

4. E. Arunan, G. R. Desiraju, R. A. Klein, J. Sadlej, S. Scheiner, I. Alkorta, D. C. Clary, R. H. Crabtree, J. J. Dannenberg, P. Hobza, H. G. Kjaergaard, A. C. Legon, B. Mennucci and D. J. Nesbitt, *Pure Appl. Chem.*, 2011, **83**, 1637-1641.

5. G. R. Desiraju, P. S. Ho, L. Kloo, A. C. Legon, R. Marquardt, P. Metrangolo, P. Politzer, G. Resnati and K. Rissanen, *Pure Appl. Chem.*, 2013, **85**, 1711-1713.

6. C. A. Hunter and J. K. M. Sanders, *J. Am. Chem. Soc.*, 1990, **112**, 5525-5534.

7. *Molecular Interactions (Noncovalent Interactions)*, http://ww2.chemistry.gatech.edu/~lw26/structure/molecular_interactions/mol_int.html#E, Accessed 17/2/2017.

8. C. Laurence and M. Berthelot, *Perspect. Drug Discovery Des.*, 2000, **18**, 39-60.

9. T. Steiner, *Angew. Chem. Int. Ed.*, 2002, **41**, 48-76.

10. G. R. Desiraju and T. Steiner, *The Weak Hydrogen Bond In Structural Chemistry and Biology*, Oxford University Press, Oxford, UK, 2001.

11. C. B. Aakeroy and K. R. Seddon, *Chem. Soc. Rev.*, 1993, **22**, 397-407.

12. M. C. Etter, *Acc. Chem. Res.*, 1990, **23**, 120-126.

13. M. C. Etter, *J. Am. Chem. Soc.*, 1982, **104**, 1095-1096.

14. C. A. Hunter, *Angew. Chem. Int. Ed.*, 2004, **43**, 5310-5324.

15. M. C. Etter, *J. Phys. Chem*, 1991, **95**, 4601-4610.

16. P. T. A. Galek, L. Fabian, W. D. S. Motherwell, F. H. Allen and N. Feeder, *Acta Crystallogr. Sect. B: Struct. Sci.*, 2007, **63**, 768-782.

17. C. R. Groom, I. J. Bruno, M. P. Lightfoot and S. C. Ward, *Acta Crystallogr. B*, 2016, **72**, 171-179.

18. F. Allen, *Acta Crystallogr. B*, 2002, **58**, 380-388.

19. J. Emsley, *Chem. Soc. Rev.*, 1980, **9**, 91-124.

20. S. J. Grabowski, *Crystals*, 2015, **6**, 3.

21. S. Humbel, *The Journal of Physical Chemistry A*, 2002, **106**, 5517-5520.

22. C. Flensburg, S. Larsen and R. F. Stewart, *J. Phys. Chem*, 1995, **99**, 10130-10141.

23. P. Vishweshwar, J. A. McMahon, J. A. Bis and M. J. Zaworotko, *J. Pharm. Sci.*, 2006, **95**, 499-516.

24. C. B. Aakeroy and D. J. Salmon, *CrystEngComm*, 2005, **7**, 439-448.

25. N. Shan and M. J. Zaworotko, *Drug Discovery Today*, 2008, **13**, 440-446.

26. N. Schultheiss and A. Newman, *Cryst. Growth Des.*, 2009, **9**, 2950-2967.

27. B. R. Bhogala and A. Nangia, *New J. Chem.*, 2008, **32**, 800-807.

28. O. Almarsson and M. J. Zaworotko, *Chem. Commun.*, 2004, 1889-1896.

29. G. P. Stahly, *Cryst. Growth Des.*, 2009, **9**, 4212-4229.

30. T. Friscic and W. Jones, *J. Pharm. Pharmacol.*, 2010, **62**, 1547-1559.

31. N. J. Babu and A. Nangia, *Cryst. Growth Des.*, 2011, **11**, 2662-2679.

32. H. G. Brittain, *Cryst. Growth Des.*, 2012, **12**, 1046-1054.

33. N. Upadhyay, T. P. Shukla, A. Mathur, Manmohana and S. K. Jha, *Int. J. Pharm. Sci. Rev. Res.*, 2011, **8**, 144-148.

34. P. H. Stahl and C. G. Wermuth, *Handbook of Pharmaceutical Salts: Properties, Selection, and Use; International Union of Pure and Applied Chemistry*, Wiley-VCH, Weinheim, NY; USA, 2002.

35. E. Grothe, H. Meekes, E. Vlieg, J. H. ter Horst and R. de Gelder, *Cryst. Growth Des.*, 2016, **16**, 3237-3243.

36. S. Aitipamula, R. Banerjee, A. K. Bansal, K. Biradha, M. L. Cheney, A. R. Choudhury, G. R. Desiraju, A. G. Dikundwar, R. Dubey, N. Duggirala, P. P. Ghogale, S. Ghosh, P. K. Goswami, N. R. Goud, R. R. K. R. Jetti, P. Karpinski, P. Kaushik, D. Kumar, V. Kumar, B. Moulton, A. Mukherjee, G. Mukherjee, A. S. Myerson, V. Puri, A. Ramanan, T. Rajamannar, C. M. Reddy, N. Rodriguez-Hornedo, R. D. Rogers, T. N. G. Row, P. Sanphui, N. Shan, G. Shete, A. Singh, C. C. Sun, J. A. Swift, R. Thaimattam, T. S. Thakur, R. Kumar Thaper, S. P. Thomas, S. Tothadi, V. R. Vangala, N. Variankaval, P. Vishweshwar, D. R. Weyna and M. J. Zaworotko, *Cryst. Growth Des.*, 2012, **12**, 2147-2152.

37. U. S. FDA, Guidance for Industry: Regulatory Classification of Pharmaceutical Co-crystals, http://www.fda.gov/downloads/Drugs/.../Guidances/UCM281764.pdf, Silver Spring, MD, 2013.

38. A. J. Cruz-Cabeza, *CrystEngComm*, 2012, **14**, 6362-6365.

39. W.-Q. T. Tong and G. Whitesell, *Pharm. Dev. Technol.*, 1998, **3**, 215-223.

40. M. Zaworotko, A. Bond, T. N. G. Row, D. E. Thurston, N. Rodriguez-Hornedo, G. Coquerel, R. Hilfiker, T. Rager, B. Jones and S. M. Reutzel-Edens, *Pharmaceutical Salts and Co-Crystals*, Royal Society of Chemistry, 2011.

41. A. Delori, P. T. A. Galek, E. Pidcock, M. Patni and W. Jones, *CrystEngComm*, 2013, **15**, 2916-2928.

42. M. L. Cheney, N. Shan, E. R. Healey, M. Hanna, L. Wojtas, M. J. Zaworotko, V. Sava, S. Song and J. R. Sanchez-Ramos, *Cryst. Growth Des.*, 2009, **10**, 394-405.

43. M. L. Cheney, D. R. Weyna, N. Shan, M. Hanna, L. Wojtas and M. J. Zaworotko, *Cryst. Growth Des.*, 2010, **10**, 4401-4413.

44. A. Delori and W. Jones, *CrystEngComm*, 2011, **13**, 6315-6318.

45. S. L. Childs, G. P. Stahly and A. Park, *Mol. Pharmaceut.*, 2007, **4**, 323-338.

46. S. Mohamed, D. A. Tocher, M. Vickers, P. G. Karamertzanis and S. L. Price, *Cryst. Growth Des.*, 2009, **9**, 2881-2889.

47. B. R. Bhogala, S. Basavoju and A. Nangia, *CrystEngComm*, 2005, **7**, 551-562.

48. P. K. Goswami, R. Thaimattam and A. Ramanan, *Cryst. Growth Des.*, 2012, **13**, 360-366.

49. A. Lemmerer, S. Govindraju, M. Johnston, X. Motloung and K. L. Savig, *CrystEngComm*, 2015.

50. D. J. Good and N. r. Rodríguez-Hornedo, *Cryst. Growth Des.*, 2009, **9**, 2252-2264.

51. S. R. Fukte, M. P. Wagh and S. Rawat, *Int J Pharm Pharm Sci*, 2014, **6**, 9-14.

52. A. P. Hill and R. J. Young, *Drug Discovery Today*, 2010, **15**, 648-655.

53. D. Elder and R. Holm, *Int. J. Pharm.*, 2013, **453**, 3-11.

54. R. Thakuria and A. Nangia, *CrystEngComm*, 2011, **13**, 1759-1764.

55. S. M. Berge, L. D. Bighley and D. C. Monkhouse, *J. Pharm. Sci.*, 1977, **66**, 1-19.

56. P. Sanphui, G. Bolla and A. Nangia, *Cryst. Growth Des.*, 2012, **12**, 2023-2036.

57. C. B. Aakeröy, S. Forbes and J. Desper, *CrystEngComm*, 2014, **16**, 5870-5877.

58. C. B. Aakeroy, S. Forbes and J. Desper, *Journal of the American Chemical Society*, 2009, **131**, 17048-17049.

59. E. Batisai, A. Ayamine, O. E. Y. Kilinkissa and N. B. Bathori, *CrystEngComm*, 2014, **16**, 9992-9998.

60. M. K. Stanton and A. Bak, *Cryst. Growth Des.*, 2008, **8**, 3856-3862.

61. A. V. Yadav, A. S. Shete, A. P. Dabke, P. V. Kulkarni and S. S. Sakhare, *Indian Journal of Pharmaceutical Sciences*, 2009, **71**, 359-370.

62. N. K. Duggirala, M. L. Perry, Ö. Almarsson and M. J. Zaworotko, *Chem. Commun.*, 2016, **52**, 640-655.

63. J. W. Steed, *Trends in pharmacological sciences*, 2013, **34**, 185-193.

64. N. Qiao, M. Li, W. Schlindwein, N. Malek, A. Davies and G. Trappitt, *International journal of pharmaceutics*, 2011, **419**, 1-11.

65. C. B. Aakeröy, T. K. Wijethunga and J. Desper, *Chemistry – A European Journal*, 2015, **21**, 11029-11037.

66. T. Takagi, C. Ramachandran, M. Bermejo, S. Yamashita, L. X. Yu and G. L. Amidon, *Mol. Pharmaceut.*, 2006, **3**, 631-643.

67. A. M. Thayer, *Chemical & Engineering News Archive*, 2010, **88**, 13-18.

68. T. Loftsson and M. E. Brewster, *J. Pharm. Pharmacol.*, 2010, **62**, 1607-1621.

69. X. Xia, E. Maliski, J. Cheetham and L. Poppe, *Pharm. Res.*, 2003, **20**, 1634-1640.

70. J. Hodgson, *Nat Biotech*, 2001, **19**, 722-726.

71. D. P. Elder, R. Holm and H. L. Diego, *International journal of pharmaceutics*, 2013, **453**, 88-100.

72. A. T. M. Serajuddin, *Adv. Drug Deliv. Rev.*, 2007, **59**, 603-616.

73. , Guidance for Industry: Regulatory Classificaiton of Pharmaceutical Co-crystals, Silver Spring, MD, 2011.

74. 2014,*Reflection Paper on the Use of Cocrystals and other Solid State Forms of*

Active Substances in Medicinal Products, European Medicines Agency.

75. L. Zhou, S. Dodd, C. Capacci-Daniel, S. Garad, R. Panicucci and V. Sethuraman, *European Journal of Pharmaceutical Sciences*, 2016, **88**, 191-201.

76. M. L. Cheney, D. R. Weyna, N. Shan, M. Hanna, L. Wojtas and M. J. Zaworotko, *J. Pharm. Sci.*, 2011, **100**, 2172-2181.

77. B. S. Sekhon, *Int Bulletin of Drug Res*, 2005, **1**, 24-39.

78. N. Blagden, S. J. Coles and D. J. Berry, *CrystEngComm*, 2014, **16**, 5753-5761.

79. A. A. Najar and Y. Azim, *Journal of the Indian Institute of Science*, 2014, **94**, 45-67.

80. G. Bolla and A. Nangia, *Chem. Commun.*, 2016, **52**, 8342-8360.

81. *Select Committee on GRAS Substances (SCOGS) Database Overview*, http://www.accessdata.fda.gov/scripts/fdcc/?set=SCOGS.

82. *Everything added to food in the United States (EUFAS) list of chemicals published by the US-FDA.*, http://www.accessdata.fda.gov/scripts/fcn/fcnnavigation.cfm?rpt=eafuslisting, Accessed 21/4/16.

83. N. Blagden, M. de Matas, P. T. Gavan and P. York, *Adv. Drug Deliv. Rev.*, 2007, **59**, 617-630.

84. T. Patole and A. Deshpande, *International Journal of Pharmaceutical Sciences and Research*, 2014, **5**, 3566.

85. Y. Gao, H. Zu and J. Zhang, *J. Pharm. Pharmacol.*, 2011, **63**, 483-490.

86. S. Aitipamula, A. B. H. Wong, P. S. Chow and R. B. H. Tan, *CrystEngComm*, 2014, **16**, 5793-5801

87. V. R. Vangala, P. S. Chow and R. B. H. Tan, *CrystEngComm*, 2011, **13**, 759-762.

88. M. Viertelhaus, R. Hilfiker, F. Blatter and M. Neuburger, *Cryst. Growth Des.*, 2009, **9**, 2220-2228.

89. D. P. McNamara, S. L. Childs, J. Giordano, A. Iarriccio, J. Cassidy, M. S. Shet, R. Mannion, E. O'Donnell and A. Park, *Pharm. Res.*, 2006, **23**, 1888-1897.

90. S. Karki, T. Friščić, L. Fábián, P. R. Laity, G. M. Day and W. Jones, *Adv. Mater.*, 2009, **21**, 3905-3909.

91. A. V. Trask, *Mol. Pharmaceut.*, 2007, **4**, 301-309.

92. G. L. Perlovich, *CrystEngComm*, 2015, **17**, 7019-7028.

93. P. Makary, *UKJ PHARMACEUTICAL & BIOSCIENCES*, 2014, **2**, 4-1.

94. S. N. Bhattachar, L. A. Deschenes and J. A. Wesley, *Drug Discovery Today*, 2006, **11**, 1012-1018.

95. H. Wahl, D. A. Haynes and T. Le Roex, *S. Afr. J. Chem.*, 2016, **69**, 35-43.

96. P. A. Wood, N. Feeder, M. Furlow, P. T. A. Galek, C. R. Groom and E. Pidcock, *CrystEngComm*, 2014, **16**, 5839-5848.

97. R. K. Gamidi and Å. C. Rasmuson, *Cryst. Growth Des.*, 2016.

98. G. R. Desiraju, *Angew. Chem., Int. Ed.*. 1995, **34**, 2311-2327.

99. C. B. Aakeröy, M. Fasulo, N. Schultheiss, J. Desper and C. Moore, *J. Am. Chem. Soc.*, 2007, **129**, 13772-13773.

100. S. G. Fleischman, S. S. Kuduva, J. A. McMahon, B. Moulton, R. D. Bailey Walsh, N. Rodríguez-Hornedo and M. J. Zaworotko, *Cryst. Growth Des.*, 2003, **3**, 909-919.

101. T. R. Shattock, K. K. Arora, P. Vishweshwar and M. J. Zaworotko, *Cryst. Growth Des.*, 2008, **8**, 4533-4545.

102. L. Infantes and W. D. S. Motherwell, *Chem. Commun.*, 2004, 1166-1167.

103. C. B. Aakeröy, K. Epa, S. Forbes, N. Schultheiss and J. Desper, *Chemistry – A European Journal*, 2013, **19**, 14998-15003.

104. J. A. Bis, P. Vishweshwar, D. Weyna and M. J. Zaworotko, *Mol. Pharmaceut.*, 2007, **4**, 401-416.

105. L. Infantes and W. D. Motherwell, *Zeitschrift für Kristallographie*, 2005, **220**, 333-339.

106. I. J. Bruno, J. C. Cole, P. R. Edgington, M. Kessler, C. F. Macrae, P. McCabe, J. Pearson and R. Taylor, *Acta Crystallogr. B*, 2002, **58**, 389-397.

107. C. F. Macrae, P. R. Edgington, P. McCabe, E. Pidcock, G. P. Shields, R. Taylor, M. Towler and J. van de Streek, *J. Appl. Crystallogr.*, 2006, **39**, 453-457.

108. C. F. Macrae, I. J. Bruno, J. A. Chisholm, P. R. Edgington, P. McCabe, E. Pidcock, L. Rodriguez-Monge, R. Taylor, J. van de Streek and P. A. Wood, *J. Appl. Crystallogr.*, 2008, **41**, 466-470.

109. N. Issa, P. G. Karamertzanis, G. W. A. Welch and S. L. Price, *Cryst. Growth Des.*, 2008, **9**, 442-453.

110. S. L. Price, *Acc. Chem. Res.*, 2008, **42**, 117-126.

111. P. G. Karamertzanis, A. V. Kazantsev, N. Issa, G. W. A. Welch, C. S. Adjiman, C. C. Pantelides and S. L. Price, *Journal of chemical theory and computation*, 2009, **5**, 1432-1448.

112. L. N. Kuleshova, D. W. M. Hofmann and R. Boese, *Chem. Phys. Lett.*, 2013, **564**, 26-32.

113. H. C. S. Chan, J. Kendrick, M. A. Neumann and F. J. J. Leusen, *CrystEngComm*, 2013, **15**, 3799-3807.

114. Y. A. Abramov, C. Loschen and A. Klamt, *J. Pharm. Sci.*, 2012, **101**, 3687-3697.

115. G. M. Day, T. G. Cooper, A. J. Cruz-Cabeza, K. E. Hejczyk, H. L. Ammon, S. X. M. Boerrigter, J. S. Tan, R. G. Della Valle, E. Venuti and J. Jose, *Acta Crystallogr. Sect. B: Struct. Sci.*, 2009, **65**, 107-125.

116. D. A. Bardwell, C. S. Adjiman, Y. A. Arnautova, E. Bartashevich, S. X. M. Boerrigter, D. E. Braun, A. J. Cruz-Cabeza, G. M. Day, R. G. Della Valle and G. R. Desiraju, *Acta Crystallogr. Sect. B: Struct. Sci.*, 2011, **67**, 535-551.

117. D.-K. Bučar, *Cryst. Growth Des.*, 2017.

118. A. Mukherjee, *Cryst. Growth Des.*, 2015, **15**, 3076-3085.

119. T. Friščić, A. V. Trask, W. Jones and W. D. S. Motherwell, *Angew. Chem. Int. Ed.*, 2006, **45**, 7546-7550.

120. S. Karki, T. Friščić, W. Jones and W. D. S. Motherwell, *Mol. Pharmaceut.*, 2007, **4**, 347-354.

121. T. Friščić and W. Jones, *Cryst. Growth Des.*, 2009, **9**, 1621-1637.

122. S. L. James, C. J. Adams, C. Bolm, D. Braga, P. Collier, T. Friscic, F. Grepioni, K. D. M. Harris, G. Hyett, W. Jones, A. Krebs, J. Mack, L. Maini, A. G. Orpen, I. P. Parkin, W. C. Shearouse, J. W. Steed and D. C. Waddell, *Chem. Soc. Rev.*, 2012, **41**, 413-447.

123. A. Delori, T. Friščić and W. Jones, *CrystEngComm*, 2012, **14**, 2350-2362.

124. A. V. Trask, W. D. S. Motherwell and W. Jones, *Chem. Commun.*, 2004, 890-891.

125. D. Braga, L. Maini and F. Grepioni, *Chem. Soc. Rev.*, 2013, **42**, 7638-7648.

126. A. V. Trask, J. van de Streek, W. D. S. Motherwell and W. Jones, *Cryst. Growth Des.*, 2005, **5**, 2233-2241.

127. D. H. Leung, S. Lohani, R. G. Ball, N. Canfield, Y. Wang, T. Rhodes and A. Bak, *Cryst. Growth Des.*, 2012, **12**, 1254-1262.

128. E. Lu, N. Rodriguez-Hornedo and R. Suryanarayanan, *CrystEngComm*, 2008, **10**, 665-668.

129. A. N. Manin, A. P. Voronin, N. G. Manin, M. V. Vener, A. V. Shishkina, A. S. Lermontov and G. L. Perlovich, *The Journal of Physical Chemistry B*, 2014, **118**, 6803-6814.

130. E. Lekšić, G. Pavlović and E. Meštrović, *Cryst. Growth Des.*, 2012, **12**, 1847-1858.

131. D. J. Berry, C. C. Seaton, W. Clegg, R. W. Harrington, S. J. Coles, P. N. Horton, M. B. Hursthouse, R. Storey, W. Jones, T. Friščić and N. Blagden, *Cryst. Growth Des.*, 2008, **8**, 1697-1712.

132. A. Lemmerer, C. Esterhuysen and J. Bernstein, *J. Pharm. Sci.*, 2010, **99**, 4054-4071.

133. I. Halasz, A. Puškarić, S. A. J. Kimber, P. J. Beldon, A. M. Belenguer, F. Adams, V. Honkimäki, R. E. Dinnebier, B. Patel and W. Jones, *Angew. Chem. Int. Ed.*, 2013, **52**, 11538-11541.

134. H.-L. Lin, G.-C. Zhang and S.-Y. Lin, *J. Therm. Anal. Calorim.*, 2014, 1-9.

135. E. Gagniere, D. Mangin, F. Puel, C. Bebon, J.-P. Klein, O. Monnier and E. Garcia, *Cryst. Growth Des.*, 2009, **9**, 3376-3383.

136. M. A. Mohammad, A. Alhalaweh and S. P. Velaga, *Int. J. Pharm.*, 2011, **407**, 63-71.

137. D. Musumeci, C. A. Hunter, R. Prohens, S. Scuderi and J. F. McCabe, *Chemical Science*, 2011, **2**, 883-890.

138. T. Leyssens, N. Tumanova, K. Robeyns, N. Candoni and S. Veesler, *CrystEngComm*, 2014, **16**, 9603-9611.

139. Z. Li, B.-S. Yang, M. Jiang, M. Eriksson, E. Spinelli, N. Yee and C. Senanayake, *Organic Process Research & Development*, 2009, **13**, 1307-1314.

140. M. Przybyłek, D. Ziółkowska, K. Mroczyńska and P. Cysewski, *European Journal of Pharmaceutical Sciences*, 2016, **85**, 132-140.

141. M. Przybyłek, P. Cysewski, M. Pawelec, D. Ziółkowska and M. Kobierski, *J. Mol. Model.*, 2015, **21**, 49.

142. P. Cysewski, M. Przybyłek, T. Miernik, M. Kobierski and D. Ziółkowska, *Struct. Chem.*, 2015, **26**, 705-712.

143. N. Takata, K. Shiraki, R. Takano, Y. Hayashi and K. Terada, *Cryst. Growth Des.*, 2008, **8**, 3032-3037.

144. G. G. Z. Zhang, R. F. Henry, T. B. Borchardt and X. Lou, *J. Pharm. Sci.*, 2007, **96**, 990-995.

145. A. Jayasankar, D. J. Good and N. Rodríguez-Hornedo, *Mol. Pharmaceut.*, 2007, **4**, 360-372.

146. G. Pinto Vitorino, N. R. Sperandeo, M. R. Caira and M. R. Mazzieri, *Cryst. Growth Des.*, 2013, **13**, 1050-1058.

147. S. Hiendrawan, B. Veriansyah, E. Widjojokusumo, S. N. Soewandhi, S. Wikarsa and R. R. Tjandrawinata, *Int J Pharm Pharm Sci*, 2016, **8**, 89-98.

148. S. Aher, R. Dhumal, K. Mahadik, A. Paradkar and P. York, *European Journal of Pharmaceutical Sciences*, 2010, **41**, 597-602.

149. T. Leyssens, G. Springuel, R. Montis, N. Candoni and S. p. Veesler, *Cryst. Growth Des.*, 2012, **12**, 1520-1530.

150. A. Jayasankar, L. S. Reddy, S. J. Bethune and N. Rodríguez-Hornedo, *Cryst. Growth Des.*, 2009, **9**, 889-897.

151. A. Alhalaweh, S. George, D. Boström and S. P. Velaga, *Cryst. Growth Des.*, 2010, **10**, 4847-4855.

152. H. Abourahma, D. D. Shah, J. Melendez, E. J. Johnson and K. T. Holman, *Cryst. Growth Des.*, 2015, **15**, 3101-3104.

153. B. Saikia, P. Bora, R. Khatioda and B. Sarma, *Cryst. Growth Des.*, 2015, **15**, 5593-5603.

154. *Online Dictionary of Crystallography*, Commission for Crystallographic Nomenclature of the International Union of Crystallography, 2012

155. W. L. Bragg, *Proceedings of the Cambridge Philosophical Society*, 1913, **17**, 43-57.

156. W. Clegg, *Crystal Structure Determination*, Oxford University Press Inc. New York, United States, 1998.

157. L. Palatinus, *Acta Crystallographica Section B: Structural Science, Crystal Engineering and Materials*, 2013, **69**, 1-16.

158. B. Dawson, *Acta Crystallographica*, 1961, **14**, 1271-1274.

159. R. F. Stewart, *Acta Crystallogr. A*, 1976, **32**, 565-574.

160. F. L. Hirshfeld, *Isr. J. Chem.*, 1977, **16**, 198-201.

161. D. Jayatilaka and B. Dittrich, *Acta Crystallogr. Sect. A: Found. Crystallogr.*, 2008, **64**, 383-393.

162. M. Woinska, D. Jayatilaka, M. A. Spackman, A. J. Edwards, P. M. Dominiak, K. Wozniak, E. Nishibori, K. Sugimoto and S. Grabowsky, *Acta Crystallogr. A*, 2014, **70**, 483-498.

163. S. C. Capelli, H.-B. Burgi, B. Dittrich, S. Grabowsky and D. Jayatilaka, *IUCrJ*, 2014, **1**, 361-379.

164. N. K. Hansen and P. Coppens, *Acta Crystallogr. A*, 1978, **A34**, 909-921.

165. R. J. Gillespie and P. L. A. Popelier, *Chemical Bonding and Molecular Geometry from Lewis to Electron Densities*, Oxford University Press, Inc., New York, USA, 2001.

166. P. Coppens, *X-Ray Charge Densities and Chemical Bonding*, Oxford University Press, New York, 1997.

167. R. F. W. Bader, *Atoms in Molecules: A Quantum Theory*, Oxford University Press, Oxford, 1990.

168. F. L. Hirshfeld, *Theoretica Chimica Acta.*, 1977, **44**, 129-138.

169. R. K. Roy, *The Journal of Physical Chemistry A*, 2003, **107**, 10428-10434.

170. R. S. Mulliken, *The Journal of Chemical Physics*, 1955, **23**, 1833-1840.

171. E. Espinosa, E. Molins and C. Lecomte, *Chem. Phys. Lett.*, 1998, **285**, 170-173.

172. Y. A. Abramov, *Acta Cryst A*, 1997, **53**, 264-272.

173. P. Macchi, *Crystallogr. Rev.*, 2013, **19**, 58-101.

174. F. Hirshfeld, *Acta Crystallogr. A*, 1976, **32**, 239-244.

175. L. Farrugia, *IUCrJ*, 2014, **1**, 265-266.

176. A. Gavezzotti, *CrystEngComm*, 2013, **15**, 4027-4035.

177. M. A. Spackman, *Cryst. Growth Des.*, 2015, **15**, 5624-5628.

178. J. D. Dunitz and A. Gavezzotti, *Angew. Chem. Int. Ed.*, 2005, **44**, 1766-1787.

179. M. J. Turner, S. P. Thomas, M. W. Shi, D. Jayatilaka and M. A. Spackman, *Chem. Commun.*, 2015, **51**, 3735-3738.

180. CrystalExplorer (Version 17.5), D. J. G. S.K. Wolff, J.J. McKinnon, M.J. Turner, D. Jayatilaka, M.A. Spackman, University of Western Australia, 2012,

181. A. Gavezzotti, *CrystEngComm*, 2003, **5**, 429-438.

182. A. Gavezzotti, *CrystEngComm*, 2003, **5**, 439-446.

183. A. Gavezzotti, *J. Phys. Chem. B*, 2002, **106**, 4145-4154.

184. A. Gavezzotti, *Zeitschrift für Kristallographie-Crystalline Materials*, 2005, **220**, 499-510.

185. A. Gavezzotti, *J. Phys. Chem. B*, 2003, **107**, 2344-2353.

186. M. Rigby, E. B. Smith, W. A. Wakeham and G. C. Maitland, *The Forces Between Molecules;*, Clarendon Press, Oxford, 1986, 34.

187. M. J. Turner, S. Grabowsky, D. Jayatilaka and M. A. Spackman, *The Journal of Physical Chemistry Letters*, 2014, **5**, 4249-4255.

188. P. Su and H. Li, *The Journal of chemical physics*, 2009, **131**, 014102.

189. A. J. Thakkar and C. Lupinetti, in *Atoms, Molecules and Clusters in Electric Fields*, ed. G. Maroulis, World Scientific, Hackensack, NJ,, 2006, pp. 505-529.

190. S. Grimme, *J. Comput. Chem.*, 2006, **27**, 1787-1799.

191. C. F. Mackenzie, P. R. Spackman, D. Jayatilaka and M. A. Spackman, *IUCrJ*, 2017, **4**.

192. J. J. McKinnon, A. S. Mitchell and M. A. Spackman, *Chemistry – A European Journal*, 1998, **4**, 2136-2141.

193. M. A. Spackman and J. J. McKinnon, *CrystEngComm*, 2002, **4**, 378-392.

194. J. J. McKinnon, M. A. Spackman and A. S. Mitchell, *Acta Crystallogr. B*, 2004, **60**, 627-668.

195. J. J. McKinnon, D. Jayatilaka and M. A. Spackman, *Chem. Commun.*, 2007, 3814-3816.

196. M. A. Spackman and D. Jayatilaka, *CrystEngComm*, 2009, **11**, 19-32.

197. I. Rozas, I. Alkorta and J. Elguero, *J. Am. Chem. Soc.*, 2000, **122**, 11154-11161.

198. F. Cozzi, S. Bacchi, G. Filippini, T. Pilati and A. Gavezzotti, *CrystEngComm*, 2009, **11**, 1122-1127.

199. S. L. Childs, P. A. Wood, N. r. Rodríguez-Hornedo, L. S. Reddy and K. I. Hardcastle, *Cryst. Growth Des.*, 2009, **9**, 1869-1888.

200. I. Mata, E. Molins, M. Amat, N. Llor and B. Checa, *Acta Crystallogr. Sect. C: Cryst. Struct. Commun.*, 2012, **68**, o114-o118.

201. K. Durka, S. Luliński, K. N. Jarzembska, J. Smętek, J. Serwatowski and K. Woźniak, *Acta Crystallographica Section B: Structural Science, Crystal Engineering and Materials*, 2014, **70**, 157-171.

202. A. J. Cruz Cabeza, G. M. Day, W. D. S. Motherwell and W. Jones, *Cryst. Growth Des.*, 2007, **7**, 100-107.

203. D. Giron-Forest, C. Goldbronn and P. Piechon, *J. Pharm. Biomed. Anal.*, 1989, **7**, 1421-1433.

204. L. Chemistry, in *Organic chemistry with emphasis on biological sciences* ed. Soderberg, Online, 2016.

205. S. Vyazovkin, in *Characterization of Materials*, ed. E. N. Kaufmann, John WIley & Sons, 2012, pp. 1-12.

206. J. Alsenz and M. Kansy, *Adv. Drug Deliv. Rev.*, 2007, **59**, 546-567.

207. P. Atkins and J. d. Paula, *Elements of Physical Chemistry*, 5th edn., Oxford University Press Inc. New York, United States, 2009.

208. R. A. Van Santen, *J. Phys. Chem*, 1984, **88**, 5768-5769.

209. W. Ostwald, *Z. Phys. Chem.*, 1879, **22**, 289.

210. C. Lipinski, in *Drug Bioavailability: Estimation of Solubility, Permeability, Absorption and Bioavailability*, ed. H. L. Han van de Waterbeemd, Per Artursson, Wiley-VCH Verlag GmbH & Co. KGaA, Weinheim, FRG, 2003, pp. 215-231.

211. M. Stuart and K. Box, *Anal. Chem.*, 2005, **77**, 983-990.

212. B. Faller and P. Ertl, *Adv. Drug Deliv. Rev.*, 2007, **59**, 533-545.

213. A. R. Katritzky, R. Jain, A. Lomaka, R. Petrukhin, U. Maran and M. Karelson, *Cryst. Growth Des.*, 2001, **1**, 261-265.

214. L. D. Hughes, D. S. Palmer, F. Nigsch and J. B. O. Mitchell, *Journal of chemical information and modeling*, 2008, **48**, 220-232.

215. S. H. Yalkowsky and S. C. Valvani, *J. Pharm. Sci.*, 1980, **69**, 912-922.

216. W. L. Jorgensen and E. M. Duffy, *Adv. Drug Deliv. Rev.*, 2002, **54**, 355-366.

217. J. S. Delaney, *Drug Discovery Today*, 2005, **10**, 289-295.

218. J. Huuskonen, *Journal of Chemical Information and Computer Sciences*, 2000, **40**, 773-777.

219. A. Llinàs, R. C. Glen and J. M. Goodman, *Journal of chemical information and modeling*, 2008, **48**, 1289-1303.

220. M. Hewitt, M. T. D. Cronin, S. J. Enoch, J. C. Madden, D. W. Roberts and J. C. Dearden, *Journal of chemical information and modeling*, 2009, **49**, 2572-2587.

221. J. Bauer, S. Spanton, R. Henry, J. Quick, W. Dziki, W. Porter and J. Morris, *Pharm. Res.*, 2001, **18**, 859-866.

222. S. R. Chemburkar, J. Bauer, K. Deming, H. Spiwek, K. Patel, J. Morris, R. Henry, S. Spanton, W. Dziki, W. Porter, J. Quick, P. Bauer, J. Donaubauer, B. A. Narayanan, M. Soldani, D. Riley and K. McFarland, *Organic Process Research & Development*, 2000, **4**, 413-417.

223. P. K. Goswami, R. Thaimattam and A. Ramanan, *Cryst. Growth Des.*, 2016, **16**, 1268-1281.

224. V. Stilinović and B. Kaitner, *Cryst. Growth Des.*, 2012, **12**, 5763-5772.

225. J. F. Remenar, S. L. Morissette, M. L. Peterson, B. Moulton, J. M. MacPhee, H. R. Guzmán and Ö. Almarsson, *J. Am. Chem. Soc.*, 2003, **125**, 8456-8457.

226. M. Gryl, S. Cenedese and K. Stadnicka, *The Journal of Physical Chemistry C*, 2015, **119**, 590-598.

227. B. L. Rodrigues, R. Tellgren and N. G. Fernandes, *Acta Crystallogr. Sect. B: Struct. Sci.*, 2001, **57**, 353-358.

228. T. H. Nguyen, P. W. Groundwater, J. A. Platts and D. E. Hibbs, *The Journal of Physical Chemistry A*, 2012, **116**, 3420-3427.

229. M. Schmidtmann, L. J. Farrugia, D. S. Middlemiss, M. J. Gutmann, G. J. McIntyre and C. C. Wilson, *J. Phys. Chem. A*, 2009, **113**, 13985-13997.

230. M. Gryl, A. Krawczuk-Pantula and K. Stadnicka, *Acta Crystallogr. B*, 2011, **67**, 144-154.

231. A. Krawczuk, M. Gryl, M. B. Pitak and K. Stadnicka, *Cryst. Growth Des.*, 2015.

232. R. Dubey, M. S. Pavan, T. N. Guru Row and G. R. Desiraju, *IUCrJ*, 2014, **1**.

233. V. R. Hathwar, R. Pal and T. N. Guru Row, *Cryst. Growth Des.*, 2010, **10**, 3306-3310.

234. P. Munshi and T. N. Guru Row, *The Journal of Physical Chemistry A*, 2005, **109**, 659-672.

235. P. Munshi and T. N. Guru Row, *CrystEngComm*, 2005, **7**, 608-611.

236. I. Sovago, M. J. Gutmann, H. M. Senn, L. H. Thomas, C. C. Wilson and L. J. Farrugia, *Acta Crystallographica Section B: Structural Science, Crystal Engineering and Materials*, 2016, **72**.

237. B. M. Craven, R. O. Fox and H. P. Weber, *Acta Crystallogr. B*, 1982, **38**, 1942-1952.

238. G. U. Kulkarni, P. Kumaradhas and C. N. R. Rao, *Chem. Mater.*, 1998, **10**, 3498-3505.

239. P. Munshi and T. N. Guru Row, *Cryst. Growth Des.*, 2006, **6**, 708-718.

240. T. A. M. Kiersch, M. R., *Curr Med Res Opin*, 2002, **18**, 18-25.

241. B. W. Müller and Y. Beer, *Acta Pharm. Technol.*, 1982, **28**, 97-102.

242. A. Lemmerer, J. Bernstein, U. J. Griesser, V. Kahlenberg, D. M. Többens, S. H. Lapidus, P. W. Stephens and C. Esterhuysen, *Chemistry – A European Journal*, 2011, **17**, 13445-13460.

243. S. Zalac, M. Z. Khan, V. Gabelica, M. Tudja, E. Mestrović and M. Romih, *Chem. Pharm. Bull*, 1999, 302-307.

244. G. Dörler, University of Innsbruck (Austria), 1982.

245. S. Aitipamula, V. R. Vangala, P. S. Chow and R. B. H. Tan, *Cryst. Growth Des.*, 2012, **12**, 5858-5863.

246. N. Takata, R. Takano, H. Uekusa, Y. Hayashi and K. Terada, *Cryst. Growth Des.*, 2010, **10**, 2116-2122.

247. S. Karki, T. Friščić, L. Fábián and W. Jones, *CrystEngComm*, 2010, **12**, 4038-4041.

248. T. Zhang, Y. Yang, H. Wang, F. Sun, X. Zhao, J. Jia, J. Liu, W. Guo, X. Cui and J. Gu, *Cryst. Growth Des.*, 2013, **13**, 5261-5266.

249. L. Fábián, *Cryst. Growth Des.*, 2009, **9**, 1436-1443.

250. I. Bruno, J. Cole, J. M. Lommerse, R. S. Rowland, R. Taylor and M. Verdonk, *J. Comput. Aided Mol. Des.*, 1997, **11**, 525-537.

251. P. A. Wood, T. S. G. Olsson, J. C. Cole, S. J. Cottrell, N. Feeder, P. T. A. Galek, C. R. Groom and E. Pidcock, *CrystEngComm*, 2013, **15**, 65-72.

252. A. Alberola, J. Rambaud and F. Sabon, *Ann. Pharm. Fr.*, 1972, **34**, 95-99.

253. S. Alberola, F. Sabon, J.Jaud and J. Galy, *Acta Cryst*, 1977, **B33**, 3337-3341.

254. N. Issa, S. A. Barnett, S. Mohamed, D. E. Braun, R. C. B. Copley, D. A. Tocher and S. L. Price, *CrystEngComm*, 2012, **14**, 2454-2464.

255. K. Lyczko, *Acta Crystallogr. Sect. Sect. E: Struct. Rep. Online*, 2013, **69**, o127-o128.

256. J. Rambaud, B. Jeanjean, B. Pauvert and S. Alberola, *Bull. Soc. Chim. Fr.*, 1986, 620-624.

257. T. P. Singh and M. Vijayan, *Acta. Cryst. Sect. B: Struct. Crystallogr. Cryst. Chem.*, 1974, **B30**, 557-562.

258. I. Tordjman, A. Durif and R. Masse, *Acta Crystallogr. Sect. C: Cryst. Struct. Commun.*, 1991, **47**, 351-353.

259. M. Veverka, T. Dubaj, J. Gallovič, E. Švajdlenka, B. Meľuchová, V. Jorík and P. Šimon, *Monatshefte für Chemie - Chemical Monthly*, 2013, **144**, 1335-1349.

260. C. A. Ober and R. B. Gupta, *AAPS PharmSciTech*, 2012, **13**, 1396-1406.

261. C. A. Ober, S. E. Montgomery and R. B. Gupta, *Powder Technol.*, 2013, **236**, 122-131.

262. A. Shevchenko, L. M. Bimbo, I. Miroshnyk, J. Haarala, K. Jelínková, K. Syrjänen, B. van Veen, J. Kiesvaara, H. A. Santos and J. Yliruusi, *Int. J. Pharm.*, 2012, **436**, 403-409.

263. A. Shevchenko, I. Miroshnyk, L.-O. Pietilä, J. Haarala, J. Salmia, K. Sinervo, S. Mirza, B. van Veen, E. Kolehmainen, Nonappa and J. Yliruusi, *Cryst. Growth Des.*, 2013, **13**, 4877-4884.

264. A. V. Trask and W. Jones, *Top. Curr. Chem.*, 2005, **254**, 41-70.

265. O. V. Dolomanov, L. J. Bourhis, R. J. Gildea, J. A. K. Howard and H. Puschmann, *J. Appl. Crystallogr.*, 2009, **42**, 339-341.

266. A. L. Spek, *Acta Crystallogr. C*, 2015, **C71**, 9-18.

267. A. L. Spek, *Acta Crystallogr. Sect. A: Found. Crystallogr.*, 1990, **46**, c34-c34.

268. PLATON, A Multipurpose Crystallographic Tool, A. L. Spek, Utrecht University, Utrecht, The Netherlands, , 1998,

269. P. Sanphui, N. R. Goud, U. B. R. Khandavilli and A. Nangia, *Cryst. Growth Des.*, 2011, **11**, 4135-4145.

270. J. H. Fagerberg, O. Tsinman, N. Sun, K. Tsinman, A. Avdeef and C. A. S. Bergström, *Mol. Pharmaceut.*, 2010, **7**, 1419-1430.

271. L. S. Reddy, S. J. Bethune, J. W. Kampf and N. r. Rodríguez-Hornedo, *Cryst. Growth Des.*, 2008, **9**, 378-385.

272. M. L. Cheney, N. Shan, E. R. Healey, M. Hanna, L. Wojtas, M. J. Zaworotko, V. Sava, S. Song and J. R. Sanchez-Ramos, *Cryst. Growth Des.*, 2010, **10**, 394-405.

273. N. Blagden, D. J. Berry, A. Parkin, H. Javed, A. Ibrahim, P. T. Gavan, L. L. De Matos and C. C. Seaton, *New J. Chem.*, 2008, **32**, 1659-1672.

274. J. Aaltonen and T. Rades, *Dissolut. Technol*, 2009, **16**, 47-54.

275. B. Dittrich, *Acta Crystallogr. B*, 2017, **73**, 325-329.

276. P. Macchi, *Acta Crystallogr. B*, 2017, **73**, 330-336.

277. S. Grabowsky, A. Genoni and H.-B. Burgi, *Chemical Science*, 2017, **8**, 4159-4176.

278. A. Nangia and G. R. Desiraju, in *Design of Organic Solids*, ed. E. Weber, Springer-Verlag, Berlin, 1998, pp. 57-95.

279. M. J. Frisch, G. W. Trucks, H. B. Schlegel, G. E. Scuseria, M. A. Robb, J. R. Cheeseman, G. Scalmani, V. Barone, B. Mennucci and G. A. Petersson, *Theor. Chem. Acc*, 2008, **120**, 215.

280. M. A. Spackman, in *Modern Charge Density Analysis*, ed. C. Gatti, Macchi, P., Springer, New York, 2012, p. 553−572.

281. L. Ravagnan, I. Marzo, P. Costantini, S. A. Susin, N. Zamzami, P. X. Petit, F. Hirsch, M. Goulbern, M.-F. Poupon and L. Miccoli, *Oncogene*, 1999, **18**, 2537-2546.

282. D. Del Bufalo, D. Trisciuoglio, M. Scarsella, G. D'Amati, A. Candiloro, A. Iervolino, C. Leonetti and G. Zupi, *Neoplasia*, 2004, **6**, 513-522.

283. *InPharma Wkly*, 1987, **583**, 19-19.

284. P. Ditonno, M. Battaglia, O. Selvaggio, L. Garofalo, V. Lorusso and F. P. Selvaggi, *Reviews in Urology*, 2005, **7**, S27-S33.

285. L. Miccoli, F. Poirson-Bichat, F. Sureau, R. B. Gonçalves, Y. Bourgeois, B. Dutrillaux, M.-F. Poupon and S. Oudard, *Journal of the National Cancer Institute*, 1998, **90**, 1400-1406.

286. L. Milane, Z. Duan and M. Amiji, *PLoS ONE*, 2011, **6**, e24075.

287. M. De Cesare, G. Pratesi, A. Giusti, D. Polizzi and F. Zunino, *British journal of cancer*, 1998, **77**, 434.

288. M. K. Brawer, *Reviews in Urology*, 2005, **7**, S21-S26.

289. S. Marrache and S. Dhar, *Proceedings of the National Academy of Sciences of the United States of America*, 2012, **109**, 16288-16293.

290. F. Benetollo, A. Pra, F. Orsini and L. Baiocchi, *Journal of Crystallographic and Spectroscopic Research*, 1993, **23**, 987-992.

291. J. Xinmin, W. Xiaoqi, G. Wu and Z. Weibin, CN 101735151 B, 2012.

292. Ö. Almarsson and M. J. Zaworotko, *Chem. Commun.*, 2004, 1889-1896.

293. D. R. Weyna, T. Shattock, P. Vishweshwar and M. J. Zaworotko, *Cryst. Growth Des.*, 2009, **9**, 1106-1123.

294. R. D. B. Walsh, M. W. Bradner, S. Fleischman, L. A. Morales, B. Moulton, N. Rodriguez-Hornedo and M. J. Zaworotko, *Chem. Commun.*, 2003, 186-187.

295. B. R. Bhogala and A. Nangia, *Cryst. Growth Des.*, 2003, **3**, 547-554.

296. B. R. Bhogala, P. Vishweshwar and A. Nangia, *Cryst. Growth Des.*, 2002, **2**, 325-328.

297. R. Santra, N. Ghosh and K. Biradha, *New J. Chem.*, 2008, **32**, 1673-1676.

298. B. Sarma, N. K. Nath, B. R. Bhogala and A. Nangia, *Cryst. Growth Des.*, 2009, **9**, 1546-1557.

299. I. D. H. Oswald, W. D. S. Motherwell and S. Parsons, *Acta Crystallogr. E*, 2004, **60**, o2380-o2383.

300. P. Vishweshwar, A. Nangia and V. M. Lynch, *Cryst. Growth Des.*, 2003, **3**, 783-790.

301. P. Vishweshwar, A. Nangia and V. M. Lynch, *The Journal of organic chemistry*, 2002, **67**, 556-565.

302. S. Aitipamula, A. B. H. Wong, P. S. Chow and R. B. H. Tan, *Cryst. Growth Des.*, 2014, **14**, 2542-2556.

303. M. C. Etter, D. A. Adsmond and D. Britton, *Acta Crystallogr. Sect. C: Cryst. Struct. Commun.*, 1990, **46**, 933-934.

304. S. Goswami, A. K. Mahapatra, K. Ghosh, G. D. Nigam, K. Chinnakali and H. K. Fun, *Acta Crystallogr. Sect. C: Cryst. Struct. Commun.*, 1999, **55**, 87-89.

305. K. Chinnakali, H. K. Fun, S. Goswami, A. K. Mahapatra and G. D. Nigam, *Acta Crystallogr. Sect. C: Cryst. Struct. Commun.*, 1999, **55**, 399-401.

306. M. F. Serafin and K. A. Wheeler, *Acta Crystallographica Section C*, 2007, **63**, o620-o621.

307. D. E. Lynch, T. Latif, G. Smith, K. A. Byriel, C. H. L. Kennard and S. Parsons, *Aust. J. Chem.*, 1998, **51**, 403-408.

308. G. Smith, J. M. Gentner, D. E. Lynch, K. A. Byriel and C. H. L. Kennard, *Aust. J. Chem.*, 1995, **48**, 1151-1166.

309. S. K. Callear, S. C. Ward, D. S. Hughes, M. B. Hursthouse and T. L. Threlfall, 2005, CCDC 1046242: Experimental Crystal Structure Determination.

310. C. B. Aakeröy, A. M. Beatty and B. A. Helfrich, *Angew. Chem. Int. Ed.*, 2001, **40**, 3240-3242.

311. C. B. Aakeröy, A. M. Beatty and B. A. Helfrich, *J. Am. Chem. Soc.*, 2002, **124**, 14425-14432.

312. J. Szegezdi and F. Csizmadia, 2007, A method for calculating the pKa values of small and large molecules, American Chemical Society Spring Meeting, March 25-29th.

313. MarvinSketch 16.4.25, ChemAxon, 2016, http://www.chemaxon.com

314. B. R. Bhogala, S. Basavoju and A. Nangia, *CrystEngComm*, 2005, **7**, 551-562.

315. B. Dittrich, C. B. Hübschle, M. Messerschmidt, R. Kalinowski, D. Girnt and P. Luger, *Acta Crystallogr. Sect. A: Found. Crystallogr.*, 2005, **61**, 314-320.

316. A. Volkov, X. Li, T. Koritsanszky and P. Coppens, *The Journal of Physical Chemistry A*, 2004, **108**, 4283-4300.

317. CrysalisPro, Agilent Technologies, Oxfordshire, 2013,

318. CrystalClear-SM Expert 3.1 b27, Rigaku, 2013,

319. G. Sheldrick, *Acta Crystallographica Section A Foundations and Advances* 2015, **71**, 3-8.

320. SHELXL Suite of Programs for Crystal Structure Analysis (Release 97-2). G. M. Sheldrick, Institüt für Anorganische Chemie der Universität, Tammanstrasse 4, D-3400 Göttingen, Germany, 1998,

321. R. H. Blessing and D. A. Langs, *J. Appl. Crystallogr.*, 1987, **20**, 427-428.

322. R. H. Blessing, *Crystallogr. Rev.*, 1987, **1**, 3-58.

323. R. H. Blessing, *J. Appl. Crystallogr.*, 1997, **30**, 421-426.

324. XD2016. A computer program for multipole refinement, topological analysis of charge densities and evaluation of intermolecular energies from experimental or theoretical structure factors, A. Volkov, P. Macchi, L. J. Farrugia, C. Gatti, P. Mallinson, T. Richter and T. Koritsanszky, 2016,

325. E. Clementi and C. Roetti, *At. Data Nucl. Data Tables*, 1974, **14**, 177-478.

326. F. H. Allen, O. Kennard, D. G. Watson, L. Brammer, A. G. Orpen and R. Taylor, *Journal of the Chemical Society, Perkin Transactions 2*, 1987, S1-S19.

327. *International Tables for X-ray Crystallography, Vol C: Mathematical, Physical and Chemical Tables*, Thrid edn., Kluwer Academic Publishers for the International Union of Crystallography, Dordrecht, The Netherlands, 2004, 801 & 808.

328. A. Madsen, *J. Appl. Crystallogr.*, 2006, **39**, 757-758.

329. *SHADE 2.1 server*, http://shade.ki.ku.dk/, 2017.

330. S. Parkin, B. Moezzi and H. Hope, *J. Appl. Crystallogr.*, 1995, **28**, 53-56.

331. L. J. Farrugia, *J. Appl. Crystallogr.*, 2012, **45**, 849-854.

332. T. Gelbrich, D. E. Braun and U. J. Griesser, *Chemistry Central Journal*, 2016, **10**, 8.

333. G. M. Sheldrick, *Acta Crystallographica Section C: Structural Chemistry*, 2015, **71**, 3-8.

334. G. Ioele, M. De Luca and G. Ragno, *Analytical Methods*, 2013, **5**, 1715.

335. A. I. Kitaigorodski, *Organic Chemical Crystallography*, Consultants Bureau, New York, 1961.

336. K. Meindl and J. Henn, *Acta Crystallogr. A*, 2008, **64**, 404-418.

337. S. Bronstein, K. A., Musiol, G. & Mühlig, H. , *Taschenbuch der Mathematik.*, Frankfurt am Main: Verlag Harry Deutsch, 1993.

338. J. t. de Meulenaer and H. Tompa, *Acta Crystallographica*, 1965, **19**, 1014-1018.

339. P. Coppens, eds. F. R. Ahmed, S. R. Hall and C. P. Hube, Copenhagen, Munksgaard, 1970, pp. 255-270.

340. R. H. Blessing, *Acta Crystallogr. Sect. A: Found. Crystallogr.*, 1995, **51**, 33-38.

341. N. Walker and D. Stuart, *Acta Crystallogr. A*, 1983, **39**, 158-166.

342. L. Krause, B. Niepotter, C. J. Schurmann, D. Stalke and R. Herbst-Irmer, *IUCrJ*, 2017, **4**.

343. Gaussian 98, M. J. Frisch, G. W. Trucks, H. B. Schlegel, G. E. Scuseria, M. A. Robb, J. R. Cheeseman, V. G. Zakrzewski, J. A. M. Jr., R. E. Stratmann, J. C. Burant, S. Dapprich, J. M. Millam, A. D. Daniels, K. N. Kudin, M. C. Strain, O. Farkas, J. Tomasi, V. Barone, M. Cossi, R. Cammi, B. Mennucci, C. Pomelli, C. Adamo, S. Clifford, J. Ochterski, G. A. Petersson, P. Y. Ayala, Q. Cui, K. Morokuma, P. Salvador, J. J. Dannenberg, D. K. Malick, A. D. Rabuck, K. Raghavachari, J. B. Foresman, J. Cioslowski, J. V. Ortiz, A. G. Baboul, B. B. Stefanov, G. Liu, A. Liashenko, P. Piskorz, I. Komaromi, R. Gomperts, R. L. Martin, D. J. Fox, T. Keith, M. A. Al-Laham, C. Y. Peng, A. Nanayakkara, M. Challacombe, P. M. W. Gill, B. Johnson, W. Chen, M. W. Wong, J. L. Andres, C. Gonzalez, M. Head-Gordon, E. S. Replogle and J. A. Pople, Gaussian Inc., Pittsburgh, PA, 1998,

344. X. Gong, S. M. Burbridge, A. C. Lewis, P. Y. D. Wong and P. Linsdell, *British Journal of Pharmacology*, 2002, **137**, 928-936.

List of References

1. G. R. Desiraju, *Crystal Engineering: The Design of Organic Solids.* , Elsevier, Amsterdam, 1989.

2. C. B. Aakeröy, J. Desper, E. Elisabeth, B. A. Helfrich, B. Levin and J. F. Urbina, *Z. Kristallogr. – Cryst. Mater.,* 2005, **220**, 325-332.

3. C. A. Schalley, *Noncovalent bonding in Supramolecular Chemistry* in *Analytical Methods in Supramolecular Chemistry*, ed. C. A. Schalley, Wiley-VCH Verlag GmbH & Co. KGaA, Weinheim, Germany., 2006.

4. E. Arunan, G. R. Desiraju, R. A. Klein, J. Sadlej, S. Scheiner, I. Alkorta, D. C. Clary, R. H. Crabtree, J. J. Dannenberg, P. Hobza, H. G. Kjaergaard, A. C. Legon, B. Mennucci and D. J. Nesbitt, *Pure Appl. Chem.*, 2011, **83**, 1637-1641.

5. G. R. Desiraju, P. S. Ho, L. Kloo, A. C. Legon, R. Marquardt, P. Metrangolo, P. Politzer, G. Resnati and K. Rissanen, *Pure Appl. Chem.*, 2013, **85**, 1711-1713.

6. C. A. Hunter and J. K. M. Sanders, *J. Am. Chem. Soc.*, 1990, **112**, 5525-5534.

7. *Molecular Interactions (Noncovalent Interactions)*, http://ww2.chemistry.gatech.edu/~lw26/structure/molecular_interactions/mol_int.html, Accessed 17/2/2017.

8. C. Laurence and M. Berthelot, *Perspect. Drug Discovery Des.*, 2000, **18**, 39-60.

9. G. R. Desiraju and T. Steiner, *The Weak Hydrogen Bond In Structural Chemistry and Biology*, Oxford University Press, Oxford, UK, 2001.

10. C. B. Aakeröy and K. R. Seddon, *Chem. Soc. Rev.*, 1993, **22**, 397-407.

11. M. C. Etter, *Acc. Chem. Res.*, 1990, **23**, 120-126.

12. M. C. Etter, *J. Am. Chem. Soc.*, 1982, **104**, 1095-1096.

13. C. A. Hunter, *Angew. Chem. Int. Ed.*, 2004, **43**, 5310-5324.

14. M. C. Etter, *J. Phys. Chem*, 1991, **95**, 4601-4610.

15. P. T. A. Galek, L. Fabian, W. D. S. Motherwell, F. H. Allen and N. Feeder, *Acta Crystallogr. Sect. B: Struct. Sci.*, 2007, **63**, 768-782.

16. C. R. Groom, I. J. Bruno, M. P. Lightfoot and S. C. Ward, *Acta Crystallogr., Sect. B: Struct. Sci.*., 2016, **72**, 171-179.

17. F. Allen, *Acta Crystallogr. Sect. B: Struct. Sci.*, 2002, **58**, 380-388.

18. T. Steiner, *Angew. Chem. Int. Ed.*, 2002, **41**, 48-76.

19. J. Emsley, *Chem. Soc. Rev.*, 1980, **9**, 91-124.

20. S. J. Grabowski, *Crystals*, 2015, **6**, 3.

21. S. Humbel, *J. Phys. Chem A*, 2002, **106**, 5517-5520.

22. C. Flensburg, S. Larsen and R. F. Stewart, *J. Phys. Chem.*, 1995, **99**, 10130-10141.

23. P. Vishweshwar, J. A. McMahon, J. A. Bis and M. J. Zaworotko, *J. Pharm. Sci.*, 2006, **95**, 499-516.

24. C. B. Aakeröy and D. J. Salmon, *CrystEngComm*, 2005, **7**, 439-448.

25. N. Shan and M. J. Zaworotko, *Drug Discovery Today*, 2008, **13**, 440-446.

26. N. Schultheiss and A. Newman, *Cryst. Growth Des.*, 2009, **9**, 2950-2967.

27. B. R. Bhogala and A. Nangia, *New J. Chem.*, 2008, **32**, 800-807.

28. O. Almarsson and M. J. Zaworotko, *Chem. Commun.*, 2004, 1889-1896.

29. G. P. Stahly, *Cryst. Growth Des.*, 2009, **9**, 4212-4229.

30. T. Friscic and W. Jones, *J. Pharm. Pharmacol.*, 2010, **62**, 1547-1559.

31. N. J. Babu and A. Nangia, *Cryst. Growth Des.*, 2011, **11**, 2662-2679.

32. H. G. Brittain, *Cryst. Growth Des.*, 2012, **12**, 1046-1054.

33. N. Upadhyay, T. P. Shukla, A. Mathur, Manmohana and S. K. Jha, *Int. J. Pharm. Sci. Rev. Res.*, 2011, **8**, 144-148.

34. P. H. Stahl and C. G. Wermuth, *Handbook of Pharmaceutical Salts: Properties, Selection, and Use; International Union of Pure and Applied Chemistry*, Wiley-VCH, Weinheim, NY; USA, 2002.

35. E. Grothe, H. Meekes, E. Vlieg, J. H. ter Horst and R. de Gelder, *Cryst. Growth Des.*, 2016, **16**, 3237-3243.

36. S. Aitipamula, R. Banerjee, A. K. Bansal, K. Biradha, M. L. Cheney, A. R. Choudhury, G. R. Desiraju, A. G. Dikundwar, R. Dubey, N. Duggirala, P. P. Ghogale, S. Ghosh, P. K. Goswami, N. R. Goud, R. R. K. R. Jetti, P. Karpinski, P. Kaushik, D. Kumar, V. Kumar, B. Moulton, A. Mukherjee, G. Mukherjee, A. S. Myerson, V. Puri, A. Ramanan, T. Rajamannar, C. M. Reddy, N. Rodriguez-Hornedo, R. D. Rogers, T. N. G. Row, P. Sanphui, N. Shan, G. Shete, A. Singh, C. C. Sun, J. A. Swift, R. Thaimattam, T. S. Thakur, R. Kumar Thaper, S. P. Thomas, S. Tothadi, V. R. Vangala, N. Variankaval, P. Vishweshwar, D. R. Weyna and M. J. Zaworotko, *Cryst. Growth Des.*, 2012, **12**, 2147-2152.

37. U.S. FDA, Guidance for Industry: Regulatory Classification of Pharmaceutical Co-crystals, http://www.fda.gov/downloads/Drugs/.../Guidances/UCM281764.pdf, Silver Spring, MD, 2013.

38. A. J. Cruz-Cabeza, *CrystEngComm*, 2012, **14**, 6362-6365.

39. M. Zaworotko, A. Bond, T. N. G. Row, D. E. Thurston, N. Rodriguez-Hornedo, G. Coquerel, R. Hilfiker, T. Rager, B. Jones and S. M. Reutzel-Edens, *Pharmaceutical Salts and Co-Crystals*, Royal Society of Chemistry, 2011.

40. A. Delori, P. T. A. Galek, E. Pidcock, M. Patni and W. Jones, *CrystEngComm*, 2013, **15**, 2916-2928.

41. M. L. Cheney, N. Shan, E. R. Healey, M. Hanna, L. Wojtas, M. J. Zaworotko, V. Sava, S. Song and J. R. Sanchez-Ramos, *Cryst. Growth Des.*, 2009, **10**, 394-405.

42. M. L. Cheney, D. R. Weyna, N. Shan, M. Hanna, L. Wojtas and M. J. Zaworotko, *Cryst. Growth Des.*, 2010, **10**, 4401-4413.

43. A. Delori and W. Jones, *CrystEngComm*, 2011, **13**, 6315-6318.

44. S. L. Childs, G. P. Stahly and A. Park, *Mol. Pharmaceut.*, 2007, **4**, 323-338.

45. S. Mohamed, D. A. Tocher, M. Vickers, P. G. Karamertzanis and S. L. Price, *Cryst. Growth Des.*, 2009, **9**, 2881-2889.

46. B. R. Bhogala, S. Basavoju and A. Nangia, *CrystEngComm*, 2005, **7**, 551-562.

47. P. K. Goswami, R. Thaimattam and A. Ramanan, *Cryst. Growth Des.*, 2012, **13**, 360-366.

48. A. Lemmerer, S. Govindraju, M. Johnston, X. Motloung and K. L. Savig, *CrystEngComm*, 2015.

49. D. J. Good and N. r. Rodríguez-Hornedo, *Cryst. Growth Des.*, 2009, **9**, 2252-2264.

50. S. R. Fukte, M. P. Wagh and S. Rawat, *Int. J. Pharm. Pharm. Sci.*, 2014, **6**, 9-14.

51. A. P. Hill and R. J. Young, *Drug Discovery Today*, 2010, **15**, 648-655.

52. D. Elder and R. Holm, *Int. J. Pharm.*, 2013, **453**, 3-11.

53. R. Thakuria and A. Nangia, *CrystEngComm*, 2011, **13**, 1759-1764.

54. S. M. Berge, L. D. Bighley and D. C. Monkhouse, *J. Pharm. Sci.*, 1977, **66**, 1-19.

55. P. Sanphui, G. Bolla and A. Nangia, *Cryst. Growth Des.*, 2012, **12**, 2023-2036.

56. C. B. Aakeröy, S. Forbes and J. Desper, *CrystEngComm*, 2014, **16**, 5870-5877.

57. C. B. Aakeröy, S. Forbes and J. Desper, *J. Am. Chem. Soc.*,, 2009, **131**, 17048-17049.

58. E. Batisai, A. Ayamine, O. E. Y. Kilinkissa and N. B. Bathori, *CrystEngComm*, 2014, **16**, 9992-9998.

59. M. K. Stanton and A. Bak, *Cryst. Growth Des.*, 2008, **8**, 3856-3862.

60. A. V. Yadav, A. S. Shete, A. P. Dabke, P. V. Kulkarni and S. S. Sakhare, *Indian J. Pharm. Sci.*, 2009, **71**, 359-370.

61. N. K. Duggirala, M. L. Perry, Ö. Almarsson and M. J. Zaworotko, *Chem. Commun.*, 2016, **52**, 640-655.

62. J. W. Steed, *Trends Pharmacol. Sci.*, 2013, **34**, 185-193.

63. N. Qiao, M. Li, W. Schlindwein, N. Malek, A. Davies and G. Trappitt, *Int. J. Pharm.,* 2011, **419**, 1-11.

64. C. B. Aakeröy, T. K. Wijethunga and J. Desper, *Chem. Eur. J.*, 2015, **21**, 11029-11037.

65. T. Takagi, C. Ramachandran, M. Bermejo, S. Yamashita, L. X. Yu and G. L. Amidon, *Mol. Pharmaceut.*, 2006, **3**, 631-643.

66. A. M. Thayer, *Chemical & Engineering News Archive*, 2010, **88**, 13-18.

67. T. Loftsson and M. E. Brewster, *J. Pharm. Pharmacol.*, 2010, **62**, 1607-1621.

68. X. Xia, E. Maliski, J. Cheetham and L. Poppe, *Pharm. Res.*, 2003, **20**, 1634-1640.

69. J. Hodgson, *Nat. Biotechnol.*, 2001, **19**, 722-726.

70. D. P. Elder, R. Holm and H. L. Diego, *Int. J. Pharm.*, 2013, **453**, 88-100.

71. A. T. M. Serajuddin, *Adv. Drug Deliv. Rev.*, 2007, **59**, 603-616.

72. FDA Guidance for Industry: Regulatory Classificaiton of Pharmaceutical Co-crystals, Silver Spring, MD, 2011.

73. European Medicines Agency, *Reflection Paper on the Use of Cocrystals and other Solid State Forms of Active Substances in Medicinal Products*, 2014.

74. L. Zhou, S. Dodd, C. Capacci-Daniel, S. Garad, R. Panicucci and V. Sethuraman, *Eur. J. Pharm. Sci.*, 2016, **88**, 191-201.

75. M. L. Cheney, D. R. Weyna, N. Shan, M. Hanna, L. Wojtas and M. J. Zaworotko, *J. Pharm. Sci.*, 2011, **100**, 2172-2181.

76. B. S. Sekhon, *Int. Bull. Drug Res.*, 2005, **1**, 24-39.

77. N. Blagden, S. J. Coles and D. J. Berry, *CrystEngComm*, 2014, **16**, 5753-5761.

78. A. A. Najar and Y. Azim, *J. Indian Inst. Sci.*, 2014, **94**, 45-67.

79. G. Bolla and A. Nangia, *Chem. Commun.*, 2016, **52**, 8342-8360.

80. *Select Committee on GRAS Substances (SCOGS) Database Overview*, http://www.accessdata.fda.gov/scripts/fdcc/?set=SCOGS.

81. *Everything added to food in the United States (EUFAS) list of chemicals published by the US-FDA.*, http://www.accessdata.fda.gov/scripts/fcn/fcnnavigation.cfm?rpt=eafuslisting, Accessed 21/4/16.

82. N. Blagden, M. de Matas, P. T. Gavan and P. York, *Adv. Drug Deliv. Rev.*, 2007, **59**, 617-630.

83. T. Patole and A. Deshpande, *Int. J. Pharm. Sci. Res.*, 2014, **5**, 3566.

84. Y. Gao, H. Zu and J. Zhang, *J. Pharm. Pharmacol.*, 2011, **63**, 483-490.

85. S. Aitipamula, A. B. H. Wong, P. S. Chow and R. B. H. Tan, *CrystEngComm*, 2014, **16**, 5793-5801

86. V. R. Vangala, P. S. Chow and R. B. H. Tan, *CrystEngComm*, 2011, **13**, 759-762.

87. M. Viertelhaus, R. Hilfiker, F. Blatter and M. Neuburger, *Cryst. Growth Des.*, 2009, **9**, 2220-2228.

88. D. P. McNamara, S. L. Childs, J. Giordano, A. Iarriccio, J. Cassidy, M. S. Shet, R. Mannion, E. O'Donnell and A. Park, *Pharm. Res.*, 2006, **23**, 1888-1897.

89. S. Karki, T. Friščić, L. Fábián, P. R. Laity, G. M. Day and W. Jones, *Adv. Mater.*, 2009, **21**, 3905-3909.

90. A. V. Trask, *Mol. Pharmaceut.*, 2007, **4**, 301-309.

91. G. L. Perlovich, *CrystEngComm*, 2015, **17**, 7019-7028.

92. P. Makary, *UK J. Pharm. Biosci*, 2014, **2**, 4-1.

93. S. N. Bhattachar, L. A. Deschenes and J. A. Wesley, *Drug Discovery Today*, 2006, **11**, 1012-1018.

94. H. Wahl, D. A. Haynes and T. Le Roex, *S. Afr. J. Chem.*, 2016, **69**, 35-43.

95. P. A. Wood, N. Feeder, M. Furlow, P. T. A. Galek, C. R. Groom and E. Pidcock, *CrystEngComm*, 2014, **16**, 5839-5848.

96. R. K. Gamidi and Å. C. Rasmuson, *Cryst. Growth Des.*, 2016.

97. G. R. Desiraju, *Angew. Chem., Int. Ed.,* 1995, **34**, 2311-2327.

98. C. B. Aakeröy, M. Fasulo, N. Schultheiss, J. Desper and C. Moore, *J. Am. Chem. Soc.*, 2007, **129**, 13772-13773.

99. S. G. Fleischman, S. S. Kuduva, J. A. McMahon, B. Moulton, R. D. Bailey Walsh, N. Rodríguez-Hornedo and M. J. Zaworotko, *Cryst. Growth Des.*, 2003, **3**, 909-919.

100. T. R. Shattock, K. K. Arora, P. Vishweshwar and M. J. Zaworotko, *Cryst. Growth Des.*, 2008, **8**, 4533-4545.

101. L. Infantes and W. D. S. Motherwell, *Chem. Commun.*, 2004, 1166-1167.

102. C. B. Aakeröy, K. Epa, S. Forbes, N. Schultheiss and J. Desper, *Chem. Eur. J.*, 2013, **19**, 14998-15003.

103. J. A. Bis, P. Vishweshwar, D. Weyna and M. J. Zaworotko, *Mol. Pharmaceut.*, 2007, **4**, 401-416.

104. L. Infantes and W. D. Motherwell, *Z. Kristallogr.*, 2005, **220**, 333-339.

105. I. J. Bruno, J. C. Cole, P. R. Edgington, M. Kessler, C. F. Macrae, P. McCabe, J. Pearson and R. Taylor, *Acta Crystallogr., Sect. B: Struct. Sci.*, 2002, **58**, 389-397.

106. C. F. Macrae, P. R. Edgington, P. McCabe, E. Pidcock, G. P. Shields, R. Taylor, M. Towler and J. van de Streek, *J. Appl. Crystallogr.*, 2006, **39**, 453-457.

107. C. F. Macrae, I. J. Bruno, J. A. Chisholm, P. R. Edgington, P. McCabe, E. Pidcock, L. Rodriguez-Monge, R. Taylor, J. van de Streek and P. A. Wood, *J. Appl. Crystallogr.*, 2008, **41**, 466-470.

108. N. Issa, P. G. Karamertzanis, G. W. A. Welch and S. L. Price, *Cryst. Growth Des.*, 2008, **9**, 442-453.

109. S. L. Price, *Acc. Chem. Res.*, 2008, **42**, 117-126.

110. P. G. Karamertzanis, A. V. Kazantsev, N. Issa, G. W. A. Welch, C. S. Adjiman, C. C. Pantelides and S. L. Price, *J. Chem. Theory Comput.*, 2009, **5**, 1432-1448.

111. L. N. Kuleshova, D. W. M. Hofmann and R. Boese, *Chem. Phys. Lett.*, 2013, **564**, 26-32.

112. H. C. S. Chan, J. Kendrick, M. A. Neumann and F. J. J. Leusen, *CrystEngComm*, 2013, **15**, 3799-3807.

113. Y. A. Abramov, C. Loschen and A. Klamt, *J. Pharm. Sci.*, 2012, **101**, 3687-3697.

114. G. M. Day, T. G. Cooper, A. J. Cruz-Cabeza, K. E. Hejczyk, H. L. Ammon, S. X. M. Boerrigter, J. S. Tan, R. G. Della Valle, E. Venuti and J. Jose, *Acta Crystallogr., Sect. B: Struct. Sci.*, 2009, **65**, 107-125.

115. D. A. Bardwell, C. S. Adjiman, Y. A. Arnautova, E. Bartashevich, S. X. M. Boerrigter, D. E. Braun, A. J. Cruz-Cabeza, G. M. Day, R. G. Della Valle and G. R. Desiraju, *Acta Crystallogr., Sect. B: Struct. Sci.*, 2011, **67**, 535-551.

116. D. K. Bučar, *Cryst. Growth Des.*, 2017.

117. A. Mukherjee, *Cryst. Growth Des.*, 2015, **15**, 3076-3085.

118. T. Friščić, A. V. Trask, W. Jones and W. D. S. Motherwell, *Angew. Chem. Int. Ed.*, 2006, **45**, 7546-7550.

119. S. Karki, T. Friščić, W. Jones and W. D. S. Motherwell, *Mol. Pharmaceut.*, 2007, **4**, 347-354.

120. T. Friščić and W. Jones, *Cryst. Growth Des.*, 2009, **9**, 1621-1637.

121. S. L. James, C. J. Adams, C. Bolm, D. Braga, P. Collier, T. Friscic, F. Grepioni, K. D. M. Harris, G. Hyett, W. Jones, A. Krebs, J. Mack, L. Maini, A. G. Orpen, I. P. Parkin, W. C. Shearouse, J. W. Steed and D. C. Waddell, *Chem. Soc. Rev.*, 2012, **41**, 413-447.

122. A. Delori, T. Friščić and W. Jones, *CrystEngComm*, 2012, **14**, 2350-2362.

123. A. V. Trask, W. D. S. Motherwell and W. Jones, *Chem. Commun.*, 2004, 890-891.

124. D. Braga, L. Maini and F. Grepioni, *Chem. Soc. Rev.*, 2013, **42**, 7638-7648.

125. A. V. Trask, J. van de Streek, W. D. S. Motherwell and W. Jones, *Cryst. Growth Des.*, 2005, **5**, 2233-2241.

126. D. H. Leung, S. Lohani, R. G. Ball, N. Canfield, Y. Wang, T. Rhodes and A. Bak, *Cryst. Growth Des.*, 2012, **12**, 1254-1262.

127. E. Lu, N. Rodriguez-Hornedo and R. Suryanarayanan, *CrystEngComm*, 2008, **10**, 665-668.

128. A. N. Manin, A. P. Voronin, N. G. Manin, M. V. Vener, A. V. Shishkina, A. S. Lermontov and G. L. Perlovich, *J. Phys. Chem. B*, 2014, **118**, 6803-6814.

129. E. Lekšić, G. Pavlović and E. Meštrović, *Cryst. Growth Des.*, 2012, **12**, 1847-1858.

130. D. J. Berry, C. C. Seaton, W. Clegg, R. W. Harrington, S. J. Coles, P. N. Horton, M. B. Hursthouse, R. Storey, W. Jones, T. Friščić and N. Blagden, *Cryst. Growth Des.*, 2008, **8**, 1697-1712.

131. A. Lemmerer, C. Esterhuysen and J. Bernstein, *J. Pharm. Sci.*, 2010, **99**, 4054-4071.

132. I. Halasz, A. Puškarić, S. A. J. Kimber, P. J. Beldon, A. M. Belenguer, F. Adams, V. Honkimäki, R. E. Dinnebier, B. Patel and W. Jones, *Angew. Chem. Int. Ed.*, 2013, **52**, 11538-11541.

133. H.-L. Lin, G.-C. Zhang and S.-Y. Lin, *J. Therm. Anal. Calorim.*, 2014, 1-9.

134. E. Gagniere, D. Mangin, F. Puel, C. Bebon, J.-P. Klein, O. Monnier and E. Garcia, *Cryst. Growth Des.*, 2009, **9**, 3376-3383.

135. M. A. Mohammad, A. Alhalaweh and S. P. Velaga, *Int. J. Pharm.*, 2011, **407**, 63-71.

136. D. Musumeci, C. A. Hunter, R. Prohens, S. Scuderi and J. F. McCabe, *Chem. Sci.*, 2011, **2**, 883-890.

137. T. Leyssens, N. Tumanova, K. Robeyns, N. Candoni and S. Veesler, *CrystEngComm*, 2014, **16**, 9603-9611.

138. Z. Li, B.-S. Yang, M. Jiang, M. Eriksson, E. Spinelli, N. Yee and C. Senanayake, *Org. Process Res. Dev.*, 2009, **13**, 1307-1314.

139. M. Przybyłek, D. Ziółkowska, K. Mroczyńska and P. Cysewski, *Eur. J. Pharm. Sci.*, 2016, **85**, 132-140.

140. M. Przybyłek, P. Cysewski, M. Pawelec, D. Ziółkowska and M. Kobierski, *J. Mol. Model.*, 2015, **21**, 49.

141. P. Cysewski, M. Przybyłek, T. Miernik, M. Kobierski and D. Ziółkowska, *Struct. Chem.*, 2015, **26**, 705-712.

142. N. Takata, K. Shiraki, R. Takano, Y. Hayashi and K. Terada, *Cryst. Growth Des.*, 2008, **8**, 3032-3037.

143. G. G. Z. Zhang, R. F. Henry, T. B. Borchardt and X. Lou, *J. Pharm. Sci.*, 2007, **96**, 990-995.

144. A. Jayasankar, D. J. Good and N. Rodríguez-Hornedo, *Mol. Pharmaceut.*, 2007, **4**, 360-372.

145. G. Pinto Vitorino, N. R. Sperandeo, M. R. Caira and M. R. Mazzieri, *Cryst. Growth Des.*, 2013, **13**, 1050-1058.

146. S. Hiendrawan, B. Veriansyah, E. Widjojokusumo, S. N. Soewandhi, S. Wikarsa and R. R. Tjandrawinata, *Int. J. Pharm. Pharm. Sci.*, 2016, **8**, 89-98.

147. S. Aher, R. Dhumal, K. Mahadik, A. Paradkar and P. York, , *Eur. J. Pharm. Sci.*, 2010, **41**, 597-602.

148. T. Leyssens, G. Springuel, R. Montis, N. Candoni and S. p. Veesler, *Cryst. Growth Des.*, 2012, **12**, 1520-1530.

149. A. Jayasankar, L. S. Reddy, S. J. Bethune and N. Rodríguez-Hornedo, *Cryst. Growth Des.*, 2009, **9**, 889-897.

150. A. Alhalaweh, S. George, D. Boström and S. P. Velaga, *Cryst. Growth Des.*, 2010, **10**, 4847-4855.

151. H. Abourahma, D. D. Shah, J. Melendez, E. J. Johnson and K. T. Holman, *Cryst. Growth Des.*, 2015, **15**, 3101-3104.

152. B. Saikia, P. Bora, R. Khatioda and B. Sarma, *Cryst. Growth Des.*, 2015, **15**, 5593-5603.

153. *Online Dictionary of Crystallography*, Commission for Crystallographic Nomenclature of the International Union of Crystallography, 2012

154. W. L. Bragg, *Proceedings of the Cambridge Philosophical Society*, 1913, **17**, 43-57.

155. W. Clegg, *Crystal Structure Determination*, Oxford University Press Inc. New York, United States, 1998.

156. L. Palatinus, *Acta Crystallogr., Sect. B: Struct. Sci., Cryst. Eng. Mater.*, 2013, **69**, 1-16.

157. B. Dawson, *Acta Crystallogr.*, 1961, **14**, 1271-1274.

158. R. F. Stewart, *Acta Crystallogr., Sect. A: Cryst. Phys., Diffr., Theor. Gen. Crystallogr.,* 1976, **32**, 565-574.

159. F. L. Hirshfeld, *Isr. J. Chem.*, 1977, **16**, 198-201.

160. D. Jayatilaka and B. Dittrich, *Acta Crystallogr., Sect. A: Found. Crystallogr.*, 2008, **64**, 383-393.

161. M. Woinska, D. Jayatilaka, M. A. Spackman, A. J. Edwards, P. M. Dominiak, K. Wozniak, E. Nishibori, K. Sugimoto and S. Grabowsky, *Acta Crystallogr., Sect. A: Found. Adv.*, 2014, **70**, 483-498.

162. S. C. Capelli, H.-B. Burgi, B. Dittrich, S. Grabowsky and D. Jayatilaka, *IUCrJ*, 2014, **1**, 361-379.

163. N. K. Hansen and P. Coppens, *Acta Crystallogr., Sect. A: Cryst. Phys., Diffr., Theor. Gen. Crystallogr.*, 1978, **A34**, 909-921.

164. R. J. Gillespie and P. L. A. Popelier, *Chemical Bonding and Molecular Geometry from Lewis to Electron Densities*, Oxford University Press, Inc., New York, USA, 2001.

165. P. Coppens, *X-Ray Charge Densities and Chemical Bonding*, Oxford University Press, New York, 1997.

166. R. F. W. Bader, *Atoms in Molecules: A Quantum Theory*, Oxford University Press, Oxford, 1990.

167. F. L. Hirshfeld, *Theor. Chim. Acta.*, 1977, **44**, 129-138.

168. R. K. Roy, *J. Phys Chem. A*, 2003, **107**, 10428-10434.

169. R. S. Mulliken, *J. Phys. Chem*, 1955, **23**, 1833-1840.

170. E. Espinosa, E. Molins and C. Lecomte, *Chem. Phys. Lett.*, 1998, **285**, 170-173.

171. Y. A. Abramov, *Acta Crystallogr., Sect. A: Found. Crystallogr.*, 1997, **53**, 264-272.

172. P. Macchi, *Crystallogr. Rev.*, 2013, **19**, 58-101.

173. F. Hirshfeld, *Acta Crystallogr., Sect. A: Cryst. Phys., Diffr., Theor. Gen. Crystallogr.*, 1976, **32**, 239-244.

174. L. Farrugia, *IUCrJ*, 2014, **1**, 265-266.

175. A. Gavezzotti, *CrystEngComm*, 2013, **15**, 4027-4035.

176. M. A. Spackman, *Cryst. Growth Des.*, 2015, **15**, 5624-5628.

177. J. D. Dunitz and A. Gavezzotti, *Angew. Chem. Int. Ed.*, 2005, **44**, 1766-1787.

178. M. J. Turner, S. P. Thomas, M. W. Shi, D. Jayatilaka and M. A. Spackman, *Chem. Commun.*, 2015, **51**, 3735-3738.

179. CrystalExplorer (Version 17.5), D. J. G. S.K. Wolff, J.J. McKinnon, M.J. Turner, D. Jayatilaka, M.A. Spackman, University of Western Australia, 2012,

180. A. Gavezzotti, *CrystEngComm*, 2003, **5**, 429-438.

181. A. Gavezzotti, *CrystEngComm*, 2003, **5**, 439-446.

182. A. Gavezzotti, *J. Phys. Chem. B*, 2002, **106**, 4145-4154.

183. A. Gavezzotti, *Z. Kristallogr.-Cyst. Mater.*, 2005, **220**, 499-510.

184. A. Gavezzotti, *J. Phys. Chem. B*, 2003, **107**, 2344-2353.

185. M. Rigby, E. B. Smith, W. A. Wakeham and G. C. Maitland, *The Forces Between Molecules;*, Clarendon Press, Oxford, 1986, 34.

186. M. J. Turner, S. Grabowsky, D. Jayatilaka and M. A. Spackman, *J. Phys. Chem. Lett.,* 2014, **5**, 4249-4255.

187. P. Su and H. Li, *J. Chem. Phys.*, 2009, **131**, 014102.

188. A. J. Thakkar and C. Lupinetti, in *Atoms, Molecules and Clusters in Electric Fields*, ed. G. Maroulis, World Scientific, Hackensack, NJ,, 2006, pp. 505-529.

189. S. Grimme, *J. Comput. Chem.*, 2006, **27**, 1787-1799.

190. C. F. Mackenzie, P. R. Spackman, D. Jayatilaka and M. A. Spackman, *IUCrJ*, 2017, **4**.

191. J. J. McKinnon, A. S. Mitchell and M. A. Spackman, *Chem. Eur. J.*, 1998, **4**, 2136-2141.

192. M. A. Spackman and J. J. McKinnon, *CrystEngComm*, 2002, **4**, 378-392.

193. J. J. McKinnon, M. A. Spackman and A. S. Mitchell, *Acta Crystallogr., Sect. B: Struct. Sci.*, 2004, **60**, 627-668.

194. J. J. McKinnon, D. Jayatilaka and M. A. Spackman, *Chem. Commun.*, 2007, 3814-3816.

195. M. A. Spackman and D. Jayatilaka, *CrystEngComm*, 2009, **11**, 19-32.

196. I. Rozas, I. Alkorta and J. Elguero, *J. Am. Chem. Soc.*, 2000, **122**, 11154-11161.

197. F. Cozzi, S. Bacchi, G. Filippini, T. Pilati and A. Gavezzotti, *CrystEngComm*, 2009, **11**, 1122-1127.

198. S. L. Childs, P. A. Wood, N. r. Rodríguez-Hornedo, L. S. Reddy and K. I. Hardcastle, *Cryst. Growth Des.*, 2009, **9**, 1869-1888.

199. I. Mata, E. Molins, M. Amat, N. Llor and B. Checa, *Acta Crystallogr., Sect. C: Cryst. Struct. Commun.*, 2012, **68**, o114-o118.

200. K. Durka, S. Luliński, K. N. Jarzembska, J. Smętek, J. Serwatowski and K. Woźniak, *Acta Crystallogr., Sect. B: Struct. Sci., Cryst. Eng. Mater.*, 2014, **70**, 157-171.

201. A. J. Cruz Cabeza, G. M. Day, W. D. S. Motherwell and W. Jones, *Cryst. Growth Des.*, 2007, **7**, 100-107.

202. D. Giron-Forest, C. Goldbronn and P. Piechon, *J. Pharm. Biomed. Anal.*, 1989, **7**, 1421-1433.

203. LibreTexts; Chemistry, 2.5 Solubility, Melting Points and Boiling Points in *Organic Chemistry with Emphasis on Biological Sciences,* ed. Soderberg, Online, 2016.

204. S. Vyazovkin, in *Characterization of Materials*, ed. E. N. Kaufmann, John WIley & Sons, 2012, pp. 1-12.

205. J. Alsenz and M. Kansy, *Adv. Drug Deliv. Rev.*, 2007, **59**, 546-567.

206. P. Atkins and J. d. Paula, *Elements of Physical Chemistry*, 5th edn., Oxford University Press Inc. New York, United States, 2009.

207. R. A. Van Santen, *J. Phys. Chem*, 1984, **88**, 5768-5769.

208. W. Ostwald, *Z. Phys. Chem.*, 1879, **22**, 289.

209. C. Lipinski, *Aqueous solubility in Discovery, Chemistry, and Assay Changes* in *Drug Bioavailability: Estimation of Solubility, Permeability, Absorption and Bioavailability*, eds. H. van de Waterbeemd, H. Lennernäs and P. Artursson, Wiley-VCH Verlag GmbH & Co. KGaA, Weinheim, FRG, 2003, pp. 215-231.

210. M. Stuart and K. Box, *Anal. Chem.*, 2005, **77**, 983-990.

211. B. Faller and P. Ertl, *Adv. Drug Deliv. Rev.*, 2007, **59**, 533-545.

212. A. R. Katritzky, R. Jain, A. Lomaka, R. Petrukhin, U. Maran and M. Karelson, *Cryst. Growth Des.*, 2001, **1**, 261-265.

213. L. D. Hughes, D. S. Palmer, F. Nigsch and J. B. O. Mitchell, *J. Chem. Inf. Model.*, 2008, **48**, 220-232.

214. S. H. Yalkowsky and S. C. Valvani, *J. Pharm. Sci.*, 1980, **69**, 912-922.

215. W. L. Jorgensen and E. M. Duffy, *Adv. Drug Deliv. Rev.*, 2002, **54**, 355-366.

216. J. S. Delaney, *Drug Discovery Today*, 2005, **10**, 289-295.

217. J. Huuskonen, *J. Chem. Inf. Comput. Sci.*, 2000, **40**, 773-777.

218. A. Llinàs, R. C. Glen and J. M. Goodman, *J. Chem. Inf. Model.*, 2008, **48**, 1289-1303.

219. M. Hewitt, M. T. D. Cronin, S. J. Enoch, J. C. Madden, D. W. Roberts and J. C. Dearden, *J. Chem. Inf. Model.*, 2009, **49**, 2572-2587.

220. J. Bauer, S. Spanton, R. Henry, J. Quick, W. Dziki, W. Porter and J. Morris, *Pharm. Res.*, 2001, **18**, 859-866.

221. S. R. Chemburkar, J. Bauer, K. Deming, H. Spiwek, K. Patel, J. Morris, R. Henry, S. Spanton, W. Dziki, W. Porter, J. Quick, P. Bauer, J. Donaubauer, B. A. Narayanan, M. Soldani, D. Riley and K. McFarland, *Org. Process Res. Dev.*, 2000, **4**, 413-417.

222. P. K. Goswami, R. Thaimattam and A. Ramanan, *Cryst. Growth Des.*, 2016, **16**, 1268-1281.

223. V. Stilinović and B. Kaitner, *Cryst. Growth Des.*, 2012, **12**, 5763-5772.

224. J. F. Remenar, S. L. Morissette, M. L. Peterson, B. Moulton, J. M. MacPhee, H. R. Guzmán and Ö. Almarsson, *J. Am. Chem. Soc.*, 2003, **125**, 8456-8457.

225. M. Gryl, S. Cenedese and K. Stadnicka, *J. Phys. Chem. C*, 2015, **119**, 590-598.

226. B. L. Rodrigues, R. Tellgren and N. G. Fernandes, *Acta Crystallogr., Sect. B: Struct. Sci.*, 2001, **57**, 353-358.

227. T. H. Nguyen, P. W. Groundwater, J. A. Platts and D. E. Hibbs, *J. Phys. Chem. A*, 2012, **116**, 3420-3427.

228. M. Schmidtmann, L. J. Farrugia, D. S. Middlemiss, M. J. Gutmann, G. J. McIntyre and C. C. Wilson, *J. Phys. Chem. A*, 2009, **113**, 13985-13997.

229. M. Gryl, A. Krawczuk-Pantula and K. Stadnicka, *Acta Crystallogr., Sect. B: Struct. Sci.*, 2011, **67**, 144-154.

230. A. Krawczuk, M. Gryl, M. B. Pitak and K. Stadnicka, *Cryst. Growth Des.*, 2015.

231. R. Dubey, M. S. Pavan, T. N. Guru Row and G. R. Desiraju, *IUCrJ*, 2014, **1**.

232. V. R. Hathwar, R. Pal and T. N. Guru Row, *Cryst. Growth Des.*, 2010, **10**, 3306-3310.

233. P. Munshi and T. N. Guru Row, *J. Phys. Chem. A*, 2005, **109**, 659-672.

234. P. Munshi and T. N. Guru Row, *CrystEngComm*, 2005, **7**, 608-611.

235. I. Sovago, M. J. Gutmann, H. M. Senn, L. H. Thomas, C. C. Wilson and L. J. Farrugia, *Acta Crystallogr., Sect. B: Struct. Sci., Cryst. Eng. Mater.*, 2016, **72**.

236. B. M. Craven, R. O. Fox and H. P. Weber, *Acta Crystallogr., Sect. B: Struct. Crystallogr. Cyst. Chem.*, 1982, **38**, 1942-1952.

237. G. U. Kulkarni, P. Kumaradhas and C. N. R. Rao, *Chem. Mater.*, 1998, **10**, 3498-3505.

238. P. Munshi and T. N. Guru Row, *Cryst. Growth Des.*, 2006, **6**, 708-718.

239. T. A. M. Kiersch, M. R., *Curr. Med. Res. Opin.*, 2002, **18**, 18-25.

240. B. W. Müller and Y. Beer, *Acta Pharm. Technol.*, 1982, **28**, 97-102.

241. A. Lemmerer, J. Bernstein, U. J. Griesser, V. Kahlenberg, D. M. Többens, S. H. Lapidus, P. W. Stephens and C. Esterhuysen, *Chem. Eur. J.*, 2011, **17**, 13445-13460.

242. S. Zalac, M. Z. Khan, V. Gabelica, M. Tudja, E. Mestrović and M. Romih, *Chem. Pharm. Bull*, 1999, 302-307.

243. G. Dörler, PhD Thesis, University of Innsbruck (Austria), 1982.

244. S. Aitipamula, V. R. Vangala, P. S. Chow and R. B. H. Tan, *Cryst. Growth Des.*, 2012, **12**, 5858-5863.

245. N. Takata, R. Takano, H. Uekusa, Y. Hayashi and K. Terada, *Cryst. Growth Des.*, 2010, **10**, 2116-2122.

246. S. Karki, T. Friščić, L. Fábián and W. Jones, *CrystEngComm*, 2010, **12**, 4038-4041.

247. T. Zhang, Y. Yang, H. Wang, F. Sun, X. Zhao, J. Jia, J. Liu, W. Guo, X. Cui and J. Gu, *Cryst. Growth Des.*, 2013, **13**, 5261-5266.

248. L. Fábián, *Cryst. Growth Des.*, 2009, **9**, 1436-1443.

249. I. Bruno, J. Cole, J. M. Lommerse, R. S. Rowland, R. Taylor and M. Verdonk, *J. Comput.-Aided Mol. Des.*, 1997, **11**, 525-537.

250. P. A. Wood, T. S. G. Olsson, J. C. Cole, S. J. Cottrell, N. Feeder, P. T. A. Galek, C. R. Groom and E. Pidcock, *CrystEngComm*, 2013, **15**, 65-72.

251. A. Alberola, J. Rambaud and F. Sabon, *Ann. Pharm. Fr.*, 1972, **34**, 95-99.

252. S. Alberola, F. Sabon, J.Jaud and J. Galy, *Acta Crystallogr.*, 1977, **B33**, 3337-3341.

253. N. Issa, S. A. Barnett, S. Mohamed, D. E. Braun, R. C. B. Copley, D. A. Tocher and S. L. Price, *CrystEngComm*, 2012, **14**, 2454-2464.

254. K. Lyczko, *Acta Crystallogr., Sect. E: Struct. Rep. Online*, 2013, **69**, o127-o128.

255. J. Rambaud, B. Jeanjean, B. Pauvert and S. Alberola, *Bull. Soc. Chim. Fr.*, 1986, 620-624.

256. T. P. Singh and M. Vijayan, *Acta. Crystallogr.,Sect. B: Struct. Crystallogr. Cryst. Chem.*, 1974, **B30**, 557-562.

257. I. Tordjman, A. Durif and R. Masse, *Acta Crystallogr., Sect. C: Cryst. Struct. Commun.*, 1991, **47**, 351-353.

258. M. Veverka, T. Dubaj, J. Gallovič, E. Švajdlenka, B. Meľuchová, V. Jorík and P. Šimon, *Monatsh. Chem.*, 2013, **144**, 1335-1349.

259. C. A. Ober and R. B. Gupta, *AAPS PharmSciTech*, 2012, **13**, 1396-1406.

260. C. A. Ober, S. E. Montgomery and R. B. Gupta, *Powder Technol.*, 2013, **236**, 122-131.

261. A. Shevchenko, L. M. Bimbo, I. Miroshnyk, J. Haarala, K. Jelínková, K. Syrjänen, B. van Veen, J. Kiesvaara, H. A. Santos and J. Yliruusi, *Int. J. Pharm.*, 2012, **436**, 403-409.

262. A. Shevchenko, I. Miroshnyk, L.-O. Pietilä, J. Haarala, J. Salmia, K. Sinervo, S. Mirza, B. van Veen, E. Kolehmainen, Nonappa and J. Yliruusi, *Cryst. Growth Des.*, 2013, **13**, 4877-4884.

263. A. V. Trask and W. Jones, *Top. Curr. Chem.*, 2005, **254**, 41-70.

264. P. Sanphui, N. R. Goud, U. B. R. Khandavilli and A. Nangia, *Cryst. Growth Des.*, 2011, **11**, 4135-4145.

265. J. H. Fagerberg, O. Tsinman, N. Sun, K. Tsinman, A. Avdeef and C. A. S. Bergström, *Mol. Pharmaceut.*, 2010, **7**, 1419-1430.

266. L. S. Reddy, S. J. Bethune, J. W. Kampf and N. r. Rodríguez-Hornedo, *Cryst. Growth Des.*, 2008, **9**, 378-385.

267. M. L. Cheney, N. Shan, E. R. Healey, M. Hanna, L. Wojtas, M. J. Zaworotko, V. Sava, S. Song and J. R. Sanchez-Ramos, *Cryst. Growth Des.*, 2010, **10**, 394-405.

268. N. Blagden, D. J. Berry, A. Parkin, H. Javed, A. Ibrahim, P. T. Gavan, L. L. De Matos and C. C. Seaton, *New J. Chem.*, 2008, **32**, 1659-1672.

269. J. Aaltonen and T. Rades, *Dissolution Technol.*, 2009, **16**, 47-54.

270. B. Dittrich, *Acta Crystallogr., Sect. B: Struct. Sci., Cyst. Eng. Mater.*, 2017, **73**, 325-329.

271. P. Macchi, *Acta Crystallogr., Sect. B: Struct. Sci., Cyst. Eng. Mater.*, 2017, **73**, 330-336.

272. S. Grabowsky, A. Genoni and H.-B. Burgi, *Chem. Sci.*, 2017, **8**, 4159-4176.

273. A. Nangia and G. R. Desiraju, *Supramolecular Synthons and Pattern Recognition* in *Design of Organic Solids*, ed. E. Weber, Springer-Verlag, Berlin, 1998, pp. 57-95.

274. M. J. Frisch, G. W. Trucks, H. B. Schlegel, G. E. Scuseria, M. A. Robb, J. R. Cheeseman, G. Scalmani, V. Barone, B. Mennucci and G. A. Petersson, *Theor. Chem. Acc*, 2008, **120**, 215.

275. M. A. Spackman, *Charge Densities and Crystal Engineering* in *Modern Charge Density Analysis*, ed. C. Gatti, Macchi, P., Springer, New York, 2012, p. 553–572.

276. L. Ravagnan, I. Marzo, P. Costantini, S. A. Susin, N. Zamzami, P. X. Petit, F. Hirsch, M. Goulbern, M.-F. Poupon and L. Miccoli, *Oncogene*, 1999, **18**, 2537-2546.

277. D. Del Bufalo, D. Trisciuoglio, M. Scarsella, G. D'Amati, A. Candiloro, A. Iervolino, C. Leonetti and G. Zupi, *Neoplasia*, 2004, **6**, 513-522.

278. Lonidamine: Angelini's anticancer agent has been approved for marketing in Italy*, Pharma Wkly*, 1987, **583**, 19.

279. P. Ditonno, M. Battaglia, O. Selvaggio, L. Garofalo, V. Lorusso and F. P. Selvaggi, *Rev. Urol.*, 2005, **7**, S27-S33.

280. L. Miccoli, F. Poirson-Bichat, F. Sureau, R. B. Gonçalves, Y. Bourgeois, B. Dutrillaux, M.-F. Poupon and S. Oudard, *J. Natl. Cancer Inst.*, 1998, **90**, 1400-1406.

281. L. Milane, Z. Duan and M. Amiji, *PLoS ONE*, 2011, **6**, e24075.

282. M. De Cesare, G. Pratesi, A. Giusti, D. Polizzi and F. Zunino, *British Journal of Cancer*, 1998, **77**, 434.

283. M. K. Brawer, *Rev. Urol.*, 2005, **7**, S21-S26.

284. S. Marrache and S. Dhar, *Proceedings of the National Academy of Sciences of the United States of America*, 2012, **109**, 16288-16293.

285. F. Benetollo, A. Pra, F. Orsini and L. Baiocchi, *J. Crystallogr. Spectrosc. Res.*, 1993, **23**, 987-992.

286. J. Xinmin, W. Xiaoqi, G. Wu and Z. Weibin*, Crystalline Form I of Lonidamine, Preparation Method Thereof and Composite Containing The Same*; CN 101735151 B, 2012.

287. Ö. Almarsson and M. J. Zaworotko, *Chem. Commun.*, 2004, 1889-1896.

288. D. R. Weyna, T. Shattock, P. Vishweshwar and M. J. Zaworotko, *Cryst. Growth Des.*, 2009, **9**, 1106-1123.

289. R. D. B. Walsh, M. W. Bradner, S. Fleischman, L. A. Morales, B. Moulton, N. Rodriguez-Hornedo and M. J. Zaworotko, *Chem. Commun.*, 2003, 186-187.

290. B. R. Bhogala and A. Nangia, *Cryst. Growth Des.*, 2003, **3**, 547-554.

291. B. R. Bhogala, P. Vishweshwar and A. Nangia, *Cryst. Growth Des.*, 2002, **2**, 325-328.

292. R. Santra, N. Ghosh and K. Biradha, *New J. Chem.*, 2008, **32**, 1673-1676.

293. B. Sarma, N. K. Nath, B. R. Bhogala and A. Nangia, *Cryst. Growth Des.*, 2009, **9**, 1546-1557.

294. I. D. H. Oswald, W. D. S. Motherwell and S. Parsons, *Acta Crystallogr., Sect. E: Struct. Rep. Online*, 2004, **60**, o2380-o2383.

295. P. Vishweshwar, A. Nangia and V. M. Lynch, *Cryst. Growth Des.*, 2003, **3**, 783-790.

296. P. Vishweshwar, A. Nangia and V. M. Lynch, *J. Org. Chem.*, 2002, **67**, 556-565.

297. S. Aitipamula, A. B. H. Wong, P. S. Chow and R. B. H. Tan, *Cryst. Growth Des.*, 2014, **14**, 2542-2556.

298. M. C. Etter, D. A. Adsmond and D. Britton, *Acta Crystallogr., Sect. C: Cryst. Struct. Commun.*, 1990, **46**, 933-934.

299. S. Goswami, A. K. Mahapatra, K. Ghosh, G. D. Nigam, K. Chinnakali and H. K. Fun, *Acta Crystallogr., Sect. C: Cryst. Struct. Commun.*, 1999, **55**, 87-89.

300. K. Chinnakali, H. K. Fun, S. Goswami, A. K. Mahapatra and G. D. Nigam, *Acta Crystallogr., Sect. C: Cryst. Struct. Commun.*, 1999, **55**, 399-401.

301. M. F. Serafin and K. A. Wheeler, *Acta Crystallogr. C: Cryst. Struct. Commun.* , 2007, **63**, o620-o621.

302. D. E. Lynch, T. Latif, G. Smith, K. A. Byriel, C. H. L. Kennard and S. Parsons, *Aust. J. Chem.*, 1998, **51**, 403-408.

303. G. Smith, J. M. Gentner, D. E. Lynch, K. A. Byriel and C. H. L. Kennard, *Aust. J. Chem.*, 1995, **48**, 1151-1166.

304. S. K. Callear, S. C. Ward, D. S. Hughes, M. B. Hursthouse and T. L. Threlfall, 2005, CCDC 1046242: Experimental Crystal Structure Determination.

305. C. B. Aakeröy, A. M. Beatty and B. A. Helfrich, *Angew. Chem. Int. Ed.*, 2001, **40**, 3240-3242.

306. C. B. Aakeröy, A. M. Beatty and B. A. Helfrich, *J. Am. Chem. Soc.*, 2002, **124**, 14425-14432.

307. J. Szegezdi and F. Csizmadia, 2007, A method for calculating the p*K*a values of small and large molecules, American Chemical Society Spring Meeting, March 25-29th.

308. MarvinSketch 16.4.25, ChemAxon, 2016, http://www.chemaxon.com.

309. B. R. Bhogala, S. Basavoju and A. Nangia, *CrystEngComm*, 2005, **7**, 551-562.

310. B. Dittrich, C. B. Hübschle, M. Messerschmidt, R. Kalinowski, D. Girnt and P. Luger, *Acta Crystallogr., Sect. A: Found. Crystallogr.*, 2005, **61**, 314-320.

311. A. Volkov, X. Li, T. Koritsanszky and P. Coppens, *J. Phys. Chem. A*, 2004, **108**, 4283-4300.

312. R. H. Blessing and D. A. Langs, *J. Appl. Crystallogr.*, 1987, **20**, 427-428.

313. R. H. Blessing, *Crystallogr. Rev.*, 1987, **1**, 3-58.

314. R. H. Blessing, *J. Appl. Crystallogr.*, 1997, **30**, 421-426.

315. XD2016. A computer program for multipole refinement, topological analysis of charge densities and evaluation of intermolecular energies from experimental or theoretical structure factors, A. Volkov, P. Macchi, L. J. Farrugia, C. Gatti, P. Mallinson, T. Richter and T. Koritsanszky, 2016,

316. E. Clementi and C. Roetti, *At. Data Nucl. Data Tables*, 1974, **14**, 177-478.

317. F. H. Allen, O. Kennard, D. G. Watson, L. Brammer, A. G. Orpen and R. Taylor, *J. Chem. Soc., Perkin Trans. 2*, 1987, S1-S19.

318. *International Tables for X-ray Crystallography, Vol C: Mathematical, Physical and Chemical Tables*, Thrid edn., Kluwer Academic Publishers for the International Union of Crystallography, Dordrecht, The Netherlands, 2004, 801 & 808.

319. A. Madsen, *J. Appl. Crystallogr.*, 2006, **39**, 757-758.

320. *SHADE 2.1 server*, http://shade.ki.ku.dk/, 2017.

321. S. Parkin, B. Moezzi and H. Hope, *J. Appl. Crystallogr.*, 1995, **28**, 53-56.

322. L. J. Farrugia, *J. Appl. Crystallogr.*, 2012, **45**, 849-854.

323. T. Gelbrich, D. E. Braun and U. J. Griesser, *Chem. Cent. J.*, 2016, **10**, 8.

324. G. Ioele, M. De Luca and G. Ragno, *Anal. Methods*, 2013, **5**, 1715.

325. A. I. Kitaigorodski, *Organic Chemical Crystallography*, Consultants Bureau, New York, 1961.

326. K. Meindl and J. Henn, *Acta Crystallogr., Sect. A: Found. Crystallogr.*, 2008, **64**, 404-418.

327. S. Bronstein, K. A., Musiol, G. & Mühlig, H. , *Taschenbuch der Mathematik.*, Frankfurt am Main: Verlag Harry Deutsch, 1993.

328. J. t. de Meulenaer and H. Tompa, *Acta Crystallogr.*, 1965, **19**, 1014-1018.

329. P. Coppens, *Crystallographic Computing*, eds. F. R. Ahmed, S. R. Hall and C. P. Hube, Copenhagen, Munksgaard, 1970, pp. 255-270.

330. A. L. Spek, *Acta Crystallogr., Sect. A: Found. Crystallogr.*, 1990, **46**, c34-c34.

331. PLATON, A Multipurpose Crystallographic Tool, A. L. Spek, Utrecht University, Utrecht, The Netherlands, , 1998,

332. R. H. Blessing, *Acta Crystallogr., Sect. A: Found. Crystallogr.*, 1995, **51**, 33-38.

333. CrysalisPro, Agilent Technologies, Oxfordshire, 2013,

334. N. Walker and D. Stuart, *Acta Crystallogr., Sect A: Found. Crystallogr.*, 1983, **39**, 158-166.

335. SHELXL Suite of Programs for Crystal Structure Analysis (Release 97-2). G. M. Sheldrick, Institüt für Anorganische Chemie der Universität, Tammanstrasse 4, D-3400 Göttingen, Germany, 1998,

336. L. Krause, B. Niepotter, C. J. Schurmann, D. Stalke and R. Herbst-Irmer, *IUCrJ*, 2017, **4**.

337. Gaussian 98, M. J. Frisch, G. W. Trucks, H. B. Schlegel, G. E. Scuseria, M. A. Robb, J. R. Cheeseman, V. G. Zakrzewski, J. A. M. Jr., R. E. Stratmann, J. C. Burant, S. Dapprich, J. M. Millam, A. D. Daniels, K. N. Kudin, M. C. Strain, O. Farkas, J. Tomasi, V. Barone, M. Cossi, R. Cammi, B. Mennucci, C. Pomelli, C. Adamo, S. Clifford, J. Ochterski, G. A. Petersson, P. Y. Ayala, Q. Cui, K. Morokuma, P. Salvador, J. J. Dannenberg, D. K. Malick, A. D. Rabuck, K. Raghavachari, J. B. Foresman, J. Cioslowski, J. V. Ortiz, A. G. Baboul, B. B. Stefanov, G. Liu, A. Liashenko, P. Piskorz, I. Komaromi, R. Gomperts, R. L. Martin, D. J. Fox, T. Keith, M. A. Al-Laham, C. Y. Peng, A. Nanayakkara, M. Challacombe, P. M. W. Gill, B. Johnson, W. Chen, M. W. Wong, J. L. Andres, C. Gonzalez, M. Head-Gordon, E. S. Replogle and J. A. Pople, Gaussian Inc., Pittsburgh, PA, 1998,

338. X. Gong, S. M. Burbridge, A. C. Lewis, P. Y. D. Wong and P. Linsdell, *Br. J. Pharmacol.*, 2002, **137**, 928-936.